surfactant science series volume **158**

Electromagnetic, Mechanical, and Transport Properties of Composite Materials

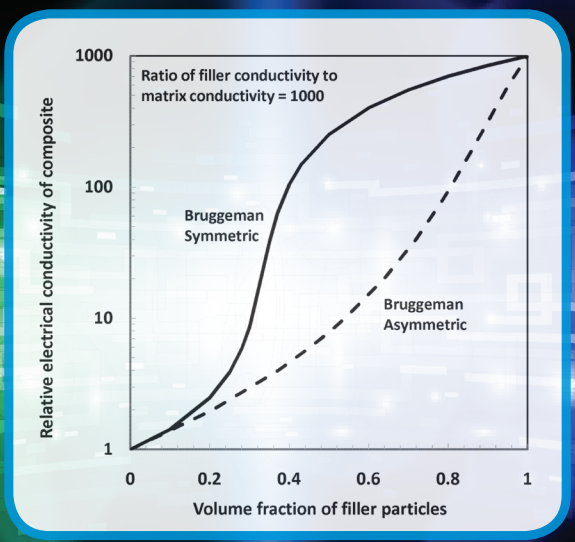

RAJINDER PAL

CRC Press
Taylor & Francis Group

Electromagnetic, Mechanical, and Transport Properties of Composite Materials

SURFACTANT SCIENCE SERIES

1. Nonionic Surfactants, *edited by Martin J. Schick* (see also Volumes 19, 23, and 60)
2. Solvent Properties of Surfactant Solutions, *edited by Kozo Shinoda* (see Volume 55)
3. Surfactant Biodegradation, *R. D. Swisher* (see Volume 18)
4. Cationic Surfactants, *edited by Eric Jungermann* (see also Volumes 34, 37, and 53)
5. Detergency: Theory and Test Methods (in three parts), *edited by W. G. Cutler and R. C. Davis* (see also Volume 20)
6. Emulsions and Emulsion Technology (in three parts), *edited by Kenneth J. Lissant*
7. Anionic Surfactants (in two parts), *edited by Warner M. Linfield* (see Volume 56)
8. Anionic Surfactants: Chemical Analysis, *edited by John Cross*
9. Stabilization of Colloidal Dispersions by Polymer Adsorption, *Tatsuo Sato and Richard Ruch*
10. Anionic Surfactants: Biochemistry, Toxicology, Dermatology, *edited by Christian Gloxhuber* (see Volume 43)
11. Anionic Surfactants: Physical Chemistry of Surfactant Action, *edited by E. H. Lucassen-Reynders*
12. Amphoteric Surfactants, *edited by B. R. Bluestein and Clifford L. Hilton* (see Volume 59)
13. Demulsification: Industrial Applications, *Kenneth J. Lissant*
14. Surfactants in Textile Processing, *Arved Datyner*
15. Electrical Phenomena at Interfaces: Fundamentals, Measurements, and Applications, *edited by Ayao Kitahara and Akira Watanabe*
16. Surfactants in Cosmetics, *edited by Martin M. Rieger* (see Volume 68)
17. Interfacial Phenomena: Equilibrium and Dynamic Effects, *Clarence A. Miller and P. Neogi*
18. Surfactant Biodegradation: Second Edition, Revised and Expanded, *R. D. Swisher*
19. Nonionic Surfactants: Chemical Analysis, *edited by John Cross*
20. Detergency: Theory and Technology, *edited by W. Gale Cutler and Erik Kissa*
21. Interfacial Phenomena in Apolar Media, *edited by Hans-Friedrich Eicke and Geoffrey D. Parfitt*
22. Surfactant Solutions: New Methods of Investigation, *edited by Raoul Zana*
23. Nonionic Surfactants: Physical Chemistry, *edited by Martin J. Schick*
24. Microemulsion Systems, *edited by Henri L. Rosano and Marc Clausse*
25. Biosurfactants and Biotechnology, *edited by Naim Kosaric, W. L. Cairns, and Neil C. C. Gray*
26. Surfactants in Emerging Technologies, *edited by Milton J. Rosen*

27. Reagents in Mineral Technology, *edited by P. Somasundaran and Brij M. Moudgil*
28. Surfactants in Chemical/Process Engineering, *edited by Darsh T. Wasan, Martin E. Ginn, and Dinesh O. Shah*
29. Thin Liquid Films, *edited by I. B. Ivanov*
30. Microemulsions and Related Systems: Formulation, Solvency, and Physical Properties, *edited by Maurice Bourrel and Robert S. Schechter*
31. Crystallization and Polymorphism of Fats and Fatty Acids, *edited by Nissim Garti and Kiyotaka Sato*
32. Interfacial Phenomena in Coal Technology, *edited by Gregory D. Botsaris and Yuli M. Glazman*
33. Surfactant-Based Separation Processes, *edited by John F. Scamehorn and Jeffrey H. Harwell*
34. Cationic Surfactants: Organic Chemistry, *edited by James M. Richmond*
35. Alkylene Oxides and Their Polymers, *F. E. Bailey, Jr., and Joseph V. Koleske*
36. Interfacial Phenomena in Petroleum Recovery, *edited by Norman R. Morrow*
37. Cationic Surfactants: Physical Chemistry, *edited by Donn N. Rubingh and Paul M. Holland*
38. Kinetics and Catalysis in Microheterogeneous Systems, *edited by M. Grätzel and K. Kalyanasundaram*
39. Interfacial Phenomena in Biological Systems, *edited by Max Bender*
40. Analysis of Surfactants, *Thomas M. Schmitt* (see Volume 96)
41. Light Scattering by Liquid Surfaces and Complementary Techniques, *edited by Dominique Langevin*
42. Polymeric Surfactants, *Irja Piirma*
43. Anionic Surfactants: Biochemistry, Toxicology, Dermatology, Second Edition, Revised and Expanded, *edited by Christian Gloxhuber and Klaus Künstler*
44. Organized Solutions: Surfactants in Science and Technology, *edited by Stig E. Friberg and Björn Lindman*
45. Defoaming: Theory and Industrial Applications, *edited by P. R. Garrett*
46. Mixed Surfactant Systems, *edited by Keizo Ogino and Masahiko Abe*
47. Coagulation and Flocculation: Theory and Applications, *edited by Bohuslav Dobiás*
48. Biosurfactants: Production Properties Applications, *edited by Naim Kosaric*
49. Wettability, *edited by John C. Berg*
50. Fluorinated Surfactants: Synthesis Properties Applications, *Erik Kissa*
51. Surface and Colloid Chemistry in Advanced Ceramics Processing, *edited by Robert J. Pugh and Lennart Bergström*
52. Technological Applications of Dispersions, *edited by Robert B. McKay*
53. Cationic Surfactants: Analytical and Biological Evaluation, *edited by John Cross and Edward J. Singer*
54. Surfactants in Agrochemicals, *Tharwat F. Tadros*
55. Solubilization in Surfactant Aggregates, *edited by Sherril D. Christian and John F. Scamehorn*
56. Anionic Surfactants: Organic Chemistry, *edited by Helmut W. Stache*
57. Foams: Theory, Measurements, and Applications, *edited by Robert K. Prud'homme and Saad A. Khan*

58. The Preparation of Dispersions in Liquids, *H. N. Stein*
59. Amphoteric Surfactants: Second Edition, *edited by Eric G. Lomax*
60. Nonionic Surfactants: Polyoxyalkylene Block Copolymers, *edited by Vaughn M. Nace*
61. Emulsions and Emulsion Stability, *edited by Johan Sjöblom*
62. Vesicles, *edited by Morton Rosoff*
63. Applied Surface Thermodynamics, *edited by A. W. Neumann and Jan K. Spelt*
64. Surfactants in Solution, *edited by Arun K. Chattopadhyay and K. L. Mittal*
65. Detergents in the Environment, *edited by Milan Johann Schwuger*
66. Industrial Applications of Microemulsions, *edited by Conxita Solans and Hironobu Kunieda*
67. Liquid Detergents, *edited by Kuo-Yann Lai*
68. Surfactants in Cosmetics: Second Edition, Revised and Expanded, *edited by Martin M. Rieger and Linda D. Rhein*
69. Enzymes in Detergency, *edited by Jan H. van Ee, Onno Misset, and Erik J. Baas*
70. Structure-Performance Relationships in Surfactants, *edited by Kunio Esumi and Minoru Ueno*
71. Powdered Detergents, *edited by Michael S. Showell*
72. Nonionic Surfactants: Organic Chemistry, *edited by Nico M. van Os*
73. Anionic Surfactants: Analytical Chemistry, Second Edition, Revised and Expanded, *edited by John Cross*
74. Novel Surfactants: Preparation, Applications, and Biodegradability, *edited by Krister Holmberg*
75. Biopolymers at Interfaces, *edited by Martin Malmsten*
76. Electrical Phenomena at Interfaces: Fundamentals, Measurements, and Applications, Second Edition, Revised and Expanded, *edited by Hiroyuki Ohshima and Kunio Furusawa*
77. Polymer-Surfactant Systems, *edited by Jan C. T. Kwak*
78. Surfaces of Nanoparticles and Porous Materials, *edited by James A. Schwarz and Cristian I. Contescu*
79. Surface Chemistry and Electrochemistry of Membranes, *edited by Torben Smith Sørensen*
80. Interfacial Phenomena in Chromatography, *edited by Emile Pefferkorn*
81. Solid–Liquid Dispersions, *Bohuslav Dobiás, Xueping Qiu, and Wolfgang von Rybinski*
82. Handbook of Detergents, editor in chief: Uri Zoller Part A: Properties, *edited by Guy Broze*
83. Modern Characterization Methods of Surfactant Systems, *edited by Bernard P. Binks*
84. Dispersions: Characterization, Testing, and Measurement, *Erik Kissa*
85. Interfacial Forces and Fields: Theory and Applications, *edited by Jyh-Ping Hsu*
86. Silicone Surfactants*, edited by Randal M. Hill*

87. Surface Characterization Methods: Principles, Techniques, and Applications, *edited by Andrew J. Milling*
88. Interfacial Dynamics, *edited by Nikola Kallay*
89. Computational Methods in Surface and Colloid Science, *edited by Malgorzata Borówko*
90. Adsorption on Silica Surfaces, *edited by Eugène Papirer*
91. Nonionic Surfactants: Alkyl Polyglucosides, *edited by Dieter Balzer and Harald Lüders*
92. Fine Particles: Synthesis, Characterization, and Mechanisms of Growth, *edited by Tadao Sugimoto*
93. Thermal Behavior of Dispersed Systems, *edited by Nissim Garti*
94. Surface Characteristics of Fibers and Textiles, *edited by Christopher M. Pastore and Paul Kiekens*
95. Liquid Interfaces in Chemical, Biological, and Pharmaceutical Applications, *edited by Alexander G. Volkov*
96. Analysis of Surfactants: Second Edition, Revised and Expanded, *Thomas M. Schmitt*
97. Fluorinated Surfactants and Repellents: Second Edition, Revised and Expanded, *Erik Kissa*
98. Detergency of Specialty Surfactants, *edited by Floyd E. Friedli*
99. Physical Chemistry of Polyelectrolytes, *edited by Tsetska Radeva*
100. Reactions and Synthesis in Surfactant Systems, *edited by John Texter*
101. Protein-Based Surfactants: Synthesis, Physicochemical Properties, and Applications, *edited by Ifendu A. Nnanna and Jiding Xia*
102. Chemical Properties of Material Surfaces, *Marek Kosmulski*
103. Oxide Surfaces, *edited by James A. Wingrave*
104. Polymers in Particulate Systems: Properties and Applications, *edited by Vincent A. Hackley, P. Somasundaran, and Jennifer A. Lewis*
105. Colloid and Surface Properties of Clays and Related Minerals, *Rossman F. Giese and Carel J. van Oss*
106. Interfacial Electrokinetics and Electrophoresis, *edited by Ángel V. Delgado*
107. Adsorption: Theory, Modeling, and Analysis, *edited by József Tóth*
108. Interfacial Applications in Environmental Engineering, *edited by Mark A. Keane*
109. Adsorption and Aggregation of Surfactants in Solution, *edited by K. L. Mittal and Dinesh O. Shah*
110. Biopolymers at Interfaces: Second Edition, Revised and Expanded, *edited by Martin Malmsten*
111. Biomolecular Films: Design, Function, and Applications, *edited by James F. Rusling*
112. Structure–Performance Relationships in Surfactants: Second Edition, Revised and Expanded, *edited by Kunio Esumi and Minoru Ueno*
113. Liquid Interfacial Systems: Oscillations and Instability, *Rudolph V. Birikh, Vladimir A. Briskman, Manuel G. Velarde, and Jean-Claude Legros*
114. Novel Surfactants: Preparation, Applications, and Biodegradability: Second Edition, Revised and Expanded, *edited by Krister Holmberg*

115. Colloidal Polymers: Synthesis and Characterization, *edited by Abdelhamid Elaissari*
116. Colloidal Biomolecules, Biomaterials, and Biomedical Applications, *edited by Abdelhamid Elaissari*
117. Gemini Surfactants: Synthesis, Interfacial and Solution-Phase Behavior, and Applications, *edited by Raoul Zana and Jiding Xia*
118. Colloidal Science of Flotation, *Anh V. Nguyen and Hans Joachim Schulze*
119. Surface and Interfacial Tension: Measurement, Theory, and Applications, *edited by Stanley Hartland*
120. Microporous Media: Synthesis, Properties, and Modeling, *Freddy Romm*
121. Handbook of Detergents, editor in chief: Uri Zoller, Part B: Environmental Impact, *edited by Uri Zoller*
122. Luminous Chemical Vapor Deposition and Interface Engineering, *Hirotsugu Yasuda*
123. Handbook of Detergents, editor in chief: Uri Zoller, Part C: Analysis, *edited by Heinrich Waldhoff and Rüdiger Spilker*
124. Mixed Surfactant Systems: Second Edition, Revised and Expanded, *edited by Masahiko Abe and John F. Scamehorn*
125. Dynamics of Surfactant Self-Assemblies: Micelles, Microemulsions, Vesicles and Lyotropic Phases, *edited by Raoul Zana*
126. Coagulation and Flocculation: Second Edition, *edited by Hansjoachim Stechemesser and Bohulav Dobiás*
127. Bicontinuous Liquid Crystals, *edited by Matthew L. Lynch and Patrick T. Spicer*
128. Handbook of Detergents, editor in chief: Uri Zoller, Part D: Formulation, *edited by Michael S. Showell*
129. Liquid Detergents: Second Edition, *edited by Kuo-Yann Lai*
130. Finely Dispersed Particles: Micro-, Nano-, and Atto-Engineering, *edited by Aleksandar M. Spasic and Jyh-Ping Hsu*
131. Colloidal Silica: Fundamentals and Applications, *edited by Horacio E. Bergna and William O. Roberts*
132. Emulsions and Emulsion Stability, Second Edition, *edited by Johan Sjöblom*
133. Micellar Catalysis, *Mohammad Niyaz Khan*
134. Molecular and Colloidal Electro-Optics, *Stoyl P. Stoylov and Maria V. Stoimenova*
135. Surfactants in Personal Care Products and Decorative Cosmetics, Third Edition, *edited by Linda D. Rhein, Mitchell Schlossman, Anthony O'Lenick, and P. Somasundaran*
136. Rheology of Particulate Dispersions and Composites, *Rajinder Pal*
137. Powders and Fibers: Interfacial Science and Applications, *edited by Michel Nardin and Eugène Papirer*
138. Wetting and Spreading Dynamics, *edited by Victor Starov, Manuel G. Velarde, and Clayton Radke*
139. Interfacial Phenomena: Equilibrium and Dynamic Effects, Second Edition, *edited by Clarence A. Miller and P. Neogi*

140. Giant Micelles: Properties and Applications, *edited by Raoul Zana and Eric W. Kaler*
141. Handbook of Detergents, editor in chief: Uri Zoller, Part E: Applications, *edited by Uri Zoller*
142. Handbook of Detergents, editor in chief: Uri Zoller, Part F: Production, *edited by Uri Zoller and co-edited by Paul Sosis*
143. Sugar-Based Surfactants: Fundamentals and Applications, *edited by Cristóbal Carnero Ruiz*
144. Microemulsions: Properties and Applications, *edited by Monzer Fanun*
145. Surface Charging and Points of Zero Charge, *Marek Kosmulski*
146. Structure and Functional Properties of Colloidal Systems, *edited by Roque Hidalgo-Álvarez*
147. Nanoscience: Colloidal and Interfacial Aspects, *edited by Victor M. Starov*
148. Interfacial Chemistry of Rocks and Soils, *Noémi M. Nagy and József Kónya*
149. Electrocatalysis: Computational, Experimental, and Industrial Aspects, *edited by Carlos Fernando Zinola*
150. Colloids in Drug Delivery, *edited by Monzer Fanun*
151. Applied Surface Thermodynamics: Second Edition, *edited by A. W. Neumann, Robert David, and Yi Y. Zuo*
152. Colloids in Biotechnology, *edited by Monzer Fanun*
153. Electrokinetic Particle Transport in Micro/Nano-fluidics: Direct Numerical Simulation Analysis, *Shizhi Qian and Ye Ai*
154. Nuclear Magnetic Resonance Studies of Interfacial Phenomena, *Vladimir M. Gun'ko and Vladimir V. Turov*
155. The Science of Defoaming: Theory, Experiment and Applications, *Peter R. Garrett*
156. Soil Colloids: Properties and Ion Binding, *Fernando V. Molina*
157. Surface Tension and Related Thermodynamic Quantities of Aqueous Electrolyte Solutions, *Norihiro Matubayasi*
158. Electromagnetic, Mechanical, and Transport Properties of Composite Materials, *Rajinder Pal*

Electromagnetic, Mechanical, and Transport Properties of Composite Materials

RAJINDER PAL
Professor of Chemical Engineering
University of Waterloo
Ontario, Canada

CRC Press
Taylor & Francis Group
Boca Raton London New York

CRC Press is an imprint of the
Taylor & Francis Group, an **informa** business

CRC Press
Taylor & Francis Group
6000 Broken Sound Parkway NW, Suite 300
Boca Raton, FL 33487-2742

Version Date: 20140624

International Standard Book Number-13: 978-1-4987-0445-8 (eBook - PDF)

To the memory of my parents,
Smt Karma-Bhari and Shri Khushal Chand

Contents

SECTION II Electromagnetic Properties of Composites: General Treatment of Electromagnetic Phenomena in Composites

SECTION III Mechanical Properties of Composites

SECTION V Transport Properties of Composites: Mass Transfer in Composites

Preface

Composite materials are blends of two or more materials of different physical properties. The individual materials are immiscible with each other and exist as distinct phases. Thus, composite materials are multiphase materials consisting of two or more phases. Different materials are mixed together with the purpose of generating superior materials having properties better than those of the individual materials. Composite materials are a rapidly growing class of materials, with applications in industries such as plastics, automotive, electronic, packaging, aircraft, space, sports, and the biomedical field.

In the design, processing, and applications of composite materials, a thorough understanding of the physical properties is required. It is important to be able to predict the variations of the electromagnetic (electrical conductivity, dielectric constant, and magnetic permeability), mechanical, thermal (thermal conductivity and coefficient of thermal expansion), and mass transport properties of composite materials with the kind, shape, and concentration of filler materials. The filler material may consist of equiaxed particles ranging anywhere from nanometers to microns in size, discontinuous short fibers or whiskers, small disk- or plate-shaped particles/flakes, or core-and-shell type of complex particles.

A number of excellent books are available on composite materials, but for the most part, they are restricted to classification, applications, and manufacturing of composite materials along with the characterization of mechanical properties. The electromagnetic, thermal, and mass transport properties of composite materials have generally received little attention as compared with the mechanical properties even though they are equally important from a practical point of view.

The study of electrical, dielectric, and magnetic properties of composite materials can reveal valuable information regarding the morphology and composition of such systems. For example, the dielectric probes could be used to probe the microstructure and to estimate the filler content of composites, especially when the dielectric constants of the individual materials are significantly different from each other. The electrical properties of composites are important in the design of plastics used in the electronics industry. Pure plastics tend to pick up electrostatic charges, especially under low-humidity conditions. When earthed, the (charged) plastics discharge and, in the process, damage electronic circuitry and equipment. To overcome the problems associated with electrostatic charge of plastics, electrically conducting filler particles (such as carbon black) are incorporated into the plastic matrix. The incorporation of electrically conducting filler particles into the plastic matrix imparts electrical conductivity to the plastic system, and as a consequence, the buildup of static charge is avoided. The magnetic properties of composite materials are of interest in many industrial applications involving electrical and electronic instruments, electrical power generators and transformers, electric motors, radio, television, telephones, computers, audio and video equipment, etc.

The thermal properties of composite materials are important in many practical applications. For example, knowledge of the coefficient of thermal expansion (CTE) of composites is required in calculating dimensional changes and buildup of internal stresses when composites are subjected to temperature changes. In designing a composite material, it is often necessary to match the CTE of different components. The other very important thermal property of composite materials is their thermal conductivity. In the electronics industry, the packaging material used to encapsulate electronic devices must have a high thermal conductivity in order to dissipate the heat generated by the device as rapidly and effectively as possible. Particulate composites consisting of polymer matrix and heat-conducting fillers are used for this purpose. Polymers filled with heat-conducting fillers provide the required thermal conductivity while maintaining the electrical insulation properties of the polymers. It has been recently discovered that the addition of a small amount of nanoparticles (such as carbon nanotubes and copper nanoparticles) can greatly improve the thermal conductivity of polymers.

The mass transport properties of composite materials are important in the design and application of composite membranes. Composite membranes are extensively used in the separation of gas mixtures. In the packaging industry, composite membranes are used as barrier films.

The aim of this book is to provide a systematic and comprehensive coverage of the electromagnetic, mechanical, thermal, and mass transport properties of composite materials. Throughout the book, the analogy between various properties is emphasized. The book draws heavily on the work of the author on physical properties of composite materials.

The first chapter of the book discusses the important applications of composite materials and the relevance of electromagnetic, mechanical, and transport properties. The book is then organized in three parts: Electromagnetic properties of composites (Sections I and II), Mechanical properties of composites (Section III), and Transport properties of composites (Sections IV and V). Section I, titled Static electromagnetic properties of composites, deals with the electromagnetic properties of composite materials subjected to time-invariant electric and magnetic fields. It consists of three chapters. Chapter 2 describes the electrical conductivity of composites, Chapter 3 the dielectric properties, and Chapter 4 describes the magnetic properties of composites. Section II, titled General treatment of electromagnetic phenomena in composites, deals with the dynamic electromagnetic properties of composite materials subjected to time-varying electric and magnetic fields. This section consists of two chapters. Chapter 5 deals with the fundamental aspects of electromagnetic phenomena. The general laws of electromagnetism (Maxwell equations) and the generalized conductivity principle are discussed. Chapter 6 describes the complex electromagnetic properties of composites. The frequency dependence of electromagnetic properties of composite materials is also discussed in details. Section III (Mechanical properties of composites) consists of seven chapters. Chapter 7 describes the mechanical properties of *dilute* particulate-filled composites. The mechanical properties of *concentrated* composites are described in Chapters 8 through 11. The influence of interfacial and interphase effects on the mechanical properties of composites is discussed in Chapter 12. The viscoelastic behavior of

composite materials is covered in Chapter 13. Section IV, titled Heat transfer in composites, consists of seven chapters. Chapters 14 and 15 cover the fundamental aspects of heat transfer. Chapters 16 and 17 describe the thermal conductivity of particulate composites. The influence of interfacial contact resistance on the thermal conductivity of composites is covered in Chapter 18. The thermal diffusivity and coefficient of thermal expansion of composites are dealt with in Chapter 19. The radiative heat transfer properties of composite materials are described in Chapter 20. Section V, titled Mass transfer in composites, consists of Chapters 21 through 24. Chapter 21 covers the fundamentals of diffusion mass transfer. The diffusion mass transfer in composite membranes is described in Chapter 22. Chapter 23 deals with the fundamentals of convective mass transfer, and Chapter 24 covers convective mass transfer in composite materials.

I hope that scientists, engineers, and students from a broad range of fields will find this book an attractive and comprehensive source of information on the subject. The book provides both an introduction to the subject for newcomers and sufficient in-depth coverage for those involved in research related to the electromagnetic, mechanical, and transport phenomena in composite materials.

Finally, I would like to thank my wife Archana and my children Anuva and Arnav for their love and constant support.

Rajinder Pal

Author

Rajinder Pal is a Professor of Chemical Engineering at the University of Waterloo, Ontario, Canada. He received the BTech degree (1981) in Chemical Engineering from the Indian Institute of Technology, Kanpur, India, and a PhD degree (1987) in Chemical Engineering from the University of Waterloo. The author of more than 120 refereed journal publications and a book in the areas of rheological, mechanical, electromagnetic, and transport properties of dispersed systems (emulsions, suspensions, foams, particulate composites, and composite membranes), Dr. Pal is a fellow of the Chemical Institute of Canada. In recognition of his distinguished contributions in chemical engineering before the age of 40, he received the Syncrude Canada Innovation Award in 1998 from the Canadian Society for Chemical Engineering. In 2001, he received the Teaching Excellence Award of the Faculty of Engineering, University of Waterloo. Dr. Pal served as Associate Editor of the *Canadian Journal of Chemical Engineering* from 1992 to 2004. He is a registered Professional Engineer in the province of Ontario, Canada.

1 Applications of Composite Materials

Composite materials are generally defined as mixtures of two or more materials of different physical properties. Different materials are mixed together with the purpose of generating superior materials having properties better than those of the individual materials. The individual materials are immiscible with each other and exist as distinct phases. Thus, composite materials are multiphase materials consisting of at least two phases (each phase being a different material). In this book, composite materials are defined as dispersed systems consisting of fine insoluble particles distributed throughout a matrix (continuous phase). The particles distributed within the matrix are collectively referred to as the particulate or dispersed phase. The particulate phase may consist of spherical particles ranging anywhere from nanometers to microns in diameter, discontinuous short fibers or whiskers, small disc- or plate-shaped particles/flakes, or core-and-shell-type spherical particles.

Three types of matrix materials are widely used in composite materials, namely, metals, ceramics, and polymers, and hence, composites are often classified as metal matrix composites (MMCs), ceramic matrix composites (CMCs), and polymer matrix composites (PMCs). Another class of composite materials is polymer/polymer blends. Physical blending of two immiscible polymer melts to generate new performance materials is of growing industrial importance [1]. A large variety of new products with desirable properties can be created by the physical blending of polymer melts without the need for synthesizing new chemical structures.

The commercial and industrial applications of composites are just too many to be discussed here in details. Several books and articles have been written describing the applications of composites in details [2–9]. Only some of the important applications of particulate-filled composites are highlighted here.

Metal matrix composites consisting of ceramic particulate filler, also called *cermets*, are widely used as a tool material for high-speed cutting of materials that are difficult to machine (for example, hardened steels) [2,3]. The ceramic material alone, although hard enough to provide the cutting surface, is extremely brittle whereas the metal alone, although tough, does not possess the requisite hardness. The combination of these two materials (ceramic and metal) in the form of a particulate composite overcomes the limitations of the individual materials. In cermets used for cutting tools, the particles of ceramic (tungsten carbide, titanium carbide, Al_2O_3, etc.) are embedded in a matrix of a ductile metal (cobalt, nickel, etc.). A large volume fraction of the dispersed particulate phase is generally used to maximize the abrasive action of the composite. Cermets are used in many other applications, such as (i) thermocouple protection tubes, (ii) mechanical seals, (iii) valve and valve seats, and (iv) turbine wheels.

Dispersion-strengthened MMCs are widely used in aircraft construction. In dispersion-strengthened MMCs, metal alloys and metals are strengthened and hardened by a uniform dispersion of very fine nanosized particles (<100 nm) of very hard and inert material such as thoria (ThO_2). The volume fraction of the dispersed phase in these dispersion-hardened metals and metal alloys is generally small (rarely exceeding 5%) [3].

Particulate-filled CMCs find applications in the manufacture of grills and flat stones for microwave heating and cooking [10]. For example, a composite material consisting of ceramic matrix and silicon carbide (SiC) whiskers is used in the form of rods (about 1 foot long and 0.5 inch wide) to form a grill for cooking in the microwave oven. The microwaves heat the ceramic composite rods preferentially over the food product, as the composite is more lossy in comparison with the food product due to the presence of SiC whiskers.

The applications of PMCs are many. The plastics industry employs a number of different types of particulate fillers to improve the mechanical properties of the plastic. In several applications, less expensive particulate fillers are added to expensive plastic materials mainly to lower the cost. Wood-derived fillers are receiving a lot of attention these days. According to some estimates, wood–plastic composites (WPCs) are the fastest growing construction materials today [11–15]. Wood filler, most often used in particulate form referred to as wood flour, has several advantages over the traditional inorganic fillers. It is derived from a renewable resource, lighter, and less expensive. Also, it is less abrasive to the processing equipment as compared with the traditional fillers. Commercially produced wood-flour filler generally consists of large-size particles (>100 μm). The weight fraction of wood in WPCs is typically 0.5, although some WPCs contain a much larger amount of wood (as high as 70 percent by weight) and others contain only little amount of wood (as low as 10 percent by weight). Both thermoset plastics and thermoplastics are used as matrix materials for WPCs although most WPCs are currently manufactured with thermoplastics such as polyethylene, polypropylene, and polyvinylchloride as the matrix.

Automobile tires are made from carbon black-reinforced rubber [16]. Nearly a quarter of the total weight of a tire is made up from carbon black. The nanosized carbon black particles (usually between 20 and 50 nm) enhance the resistance to wear and tear and increase stiffness and tensile strength of the tires. It is of interest to note that the primary nanosized particles of carbon black aggregate to form chains with various degrees of branching in the rubber matrix. It is the network of these chains of primary particles that provides the reinforcement mechanism in carbon black-reinforced rubbers.

Plastics filled with fine conductive particles, also called conductive plastics, have many practical applications [17]. Plastics are electrically insulating materials. However, the dispersion of conductive filler such as carbon black in the plastic matrix imparts conductive properties to the plastic system. The conductive carbon black particles when dispersed in a plastic matrix form a network of chainlike aggregates. Although the matrix is nonconductive, current can still flow through the network of conductive particles. Carbon-black-filled conductive plastics are used as antistatic materials in the electronic industry. Plastics, widely used as insulators, readily pick up electrostatic charges especially under low-humidity conditions. When earthed,

the plastics (carrying electrostatic charge) discharge and, in the process, damage electronic circuitry and equipment. To overcome these problems, conductive plastics are used. Conductive plastics are used in many other applications such as electromagnetic interference (EMI) shielding, heating devices, video discs, wire and cable, etc.

Polymer–clay nanocomposites are a rapidly growing class of nanoengineered materials with many applications [4,5]. They are composed of nanometer-sized clay particles dispersed uniformly in a polymeric matrix. Clays (usually aluminosilicates), in their natural form, consist of aggregates of primary plate-like particles whereas polymer–clay nanocomposites consist of an exfoliated structure; that is, the aggregates are completely separated and the individual primary particles are dispersed uniformly in the polymer matrix. The thickness of clay platelets is approximately 1 nm, and their diameter can vary anywhere from tens of nanometers to hundreds of nanometers. As the clay particles in their natural form are generally hydrophilic, they need to be treated to make them "organophilic" and compatible with hydrophobic polymers. Usually, only small quantities (less than 6% by weight) of clay are incorporated in polymer–clay nanocomposites. A small quantity of clay in exfoliated form is often enough to provide a large improvement in the mechanical and other desired properties.

Dental composites consist of a polymerizable resin matrix, usually urethane dimethacrylate (UDMA) or ethylene glycol dimethacrylate (Bis-GMA), glass particulate fillers, and a silane coupling agent [18,19]. Polymerization of the resin matrix is either light activated or chemically initiated. The silane coupling agent (usually 3-methacryloxypropyltrimethoxy silane) coats the surface of the hydrophilic filler particles, allowing them to couple with the hydrophobic resin matrix. The purpose of fillers in dental composites is to reduce shrinkage (the resin tends to shrink while it is setting) and to improve the mechanical properties (wear resistance, fracture resistance) of the material. A wide range of particle sizes is used in the manufacture of commercial dental composites [19,20]. Based on the particle size of the filler, dental composites can be classified roughly into four broad groups: (i) traditional composites with filler particle size in the micron range (>>1 μm), (ii) microfilled composites with filler particle size close to a micron (≈1 μm), (iii) nanocomposites with filler particle size in the nanometer range (<100 nm), and (iv) hybrid composites consisting of a bimodal mixture of very fine and large particles. The volume fraction of the filler in the composite is usually high, somewhere in the range of approximately 0.4 to 0.80.

The solid propellants commonly used in aerospace propulsion are particulate composites consisting of particles of solid oxidizer (usually ammonium perchlorate NH_4ClO_4) and metal fuel (usually aluminum) dispersed in a polymeric binder (usually polybutadiene). The fuel combines with oxygen provided by the oxidizer to produce gas for propulsion. The volume fraction of particles in solid propellants is typically high [21]. The composite is rubberlike material with the consistency of a rubber eraser.

Particulate-filled PMCs are widely used in the manufacture of barrier membranes for food packaging [22,23]. To ensure constant gas composition inside the package, it is important that the membrane have certain gas barrier properties. For example,

in food packaging, where long shelf life is required, it is important that oxygen and water vapor be retained inside the package to avoid ruining the organoleptic properties of the food product. The barrier properties of particulate-filled polymer composites are also being exploited in the construction and development of fuel tank and fuel line components for cars. The incorporation of filler particles in the polymer matrix inhibits the permeation of fuel solvent through the polymer.

A new class of particulate-filled polymer composite membranes is the so-called *mixed matrix membranes* composed of porous *molecular-sieve-type* inorganic fillers and polymeric matrix [24–36]. The mixed matrix membranes are very effective in the separation of gaseous mixtures. They are also used to purify a mixture of gases by removing the unwanted species from the mixture (for example, purification of natural gas by removing carbon dioxide). They offer an advantageous blend of the properties of filler particles and polymer matrix. Compared to single-phase polymeric membranes often used in gas separation, the mixed matrix membranes offer higher permeability and selectivity. The presence of shape- and size-selective pores in the molecular-sieving filler particles leads to superior separation characteristics. Examples of inorganic filler material used in mixed matrix membranes are zeolites and carbon molecular sieves. Zeolites and carbon molecular sieves have high surface area, high void volume, and uniform pore size distribution, and hence, they are the most promising candidates as inorganic fillers for mixed matrix membranes. The mixed matrix membranes are also easy to handle, process, and manufacture as compared with inorganic membranes, which are inherently brittle and fragile. Table 1.1 presents the permeability and permselectivity data for mixed membranes studied by Vu et al. [32] for the separation of CO_2/CH_4 and O_2/N_2 mixtures. The continuous phase of these filled polymer composite membranes was polyetherimide (Ultem 1000), and the filler particles were carbon molecular sieves (CMS 800-2). The addition of 35 vol.% filler to the polymer increases the permeability of CO_2 by nearly 210% and the permeability of O_2 by about 187%, as compared with the corresponding permeabilities in the pure polymer matrix. The permselectivities of CO_2 and O_2 are enhanced by nearly 38% and 9.6%, respectively, as compared with the corresponding permselectivities of the pure polymer matrix.

Particulate-filled polymer composite membranes are finding applications in polymer-electrolyte-membrane (PEM)-based fuel cells as well [37]. In the PEM fuel

TABLE 1.1
Permeability and Permselectivity Data for Mixed Membranes Studied by Vu et al. [32] for the Separation of CO_2/CH_4 and O_2/N_2 Mixtures

	Permeability (Barrer)				Permselectivity	
Mixed-Matrix Membrane	**CO_2**	**CH_4**	**O_2**	**N_2**	**CO_2/CH_4**	**O_2/N_2**
Matrix: Ultem 1000 (polyetherimide)	1.45	0.037	0.38	0.052	38.8	7.3
Filler: CMS 800-2 (carbon molecular sieves)	44	0.22	22	1.65	200	13.3
35 vol.% filler (CMS 800-2)	4.48	0.083	1.09	0.136	53.7	8

cells, the proton conductivity and mechanical strength of polymer electrolyte membrane could be improved significantly by filling the polymer matrix with inorganic particles of high proton conductivity.

Particulate-filled PMCs are widely used in the manufacture of coating materials. For example, particulate-filled polymer composite coatings of controlled thermal emissivity are applied on surfaces for the enhancement or reduction of radiative heat losses [38–46]. Particulate-filled PMCs are also used for the preparation of anticorrosive barrier coatings [47–49]. The corrosion and rust formation on iron involves the following steps:

$$\mathrm{Fe\ (s) \rightarrow Fe^{2+}\ (aq) + 2e^{-}} \tag{1.1}$$

$$\mathrm{O_2\,(g) + 2H_2O\ (l) + 4e^{-} \rightarrow 4OH^{-}\,(aq)} \tag{1.2}$$

$$\mathrm{Fe^{2+}\ (aq) + 2OH^{-}\,(aq) \rightarrow Fe(OH)_2\ (s)} \tag{1.3}$$

$$\mathrm{4Fe(OH)_2\ (s) + O_2\ (g) \rightarrow 2Fe_2O_3 \bullet H_2O\ (s) + 2H_2O\ (l)} \tag{1.4}$$

Thus, corrosion can be prevented by coating the surface of metal with a layer of particulate-filled polymer composite designed to have a very low permeability for H_2O and O_2 so as to cut off the supply of H_2O and O_2 to the metal surface.

In the electronics industry, where there is major emphasis on miniaturization and increasing power of electronic devices, particulate-filled PMCs of controlled thermal conductivity are used as conductors of heat so that the heat generated in the devices is dissipated away as quickly as possible in order to maintain the temperature of the device at the desired level [50]. Likewise, PMCs of designed electromagnetic properties (electrical conductivity, dielectric constant, magnetic permeability) find many applications in the electrical and electronic industries [51–54].

Immiscible polymer/polymer blends are also used widely in commercial and industrial applications [1]. For example, immiscible blends of polypropylene (PP) and ethylene–propylene–diene rubber (EPDM) are used in wire and cable insulation, automotive bumpers, hose, gaskets, seals, and weather stripping [55,56].

The electromagnetic, mechanical, and transport properties of particulate-filled composite materials depend on factors such as (i) the volume fraction of the dispersed phase, (ii) the geometry of the dispersed phase (shape, size, and size distribution), and (iii) the properties of the constituent phases. In order to make efficient use of composite materials in commercial and industrial applications, it is important to know the variations of the electromagnetic, mechanical, and transport properties with the kind, shape, and concentration of filler particles.

REFERENCES

1. Pal, R. 1996. Rheology of emulsions containing polymeric liquids, In: *Encyclopedia of Emulsion Technology*, ed. P. Becher, Volume 4, 93–263, New York: Marcel Dekker.
2. Berthelot, J.M. 1999. *Composite Materials*, New York: Springer.
3. Schwartz, M.M. 1992. *Composite Materials Handbook*, New York: McGraw-Hill.

4. Pinnavaia, T.J. and G.W. Beall. 2000. *Polymer–Clay Nanocomposites*, New York: John Wiley & Sons.
5. Gao, F. 2004. Clay/Polymer composites: The story. *Mater. Today* 7: 50–55.
6. Mallick, P.K. 1988. *Fiber-Reinforced Composites—Materials, Manufacturing, and Design,* New York: Marcel Dekker.
7. Hull, D. 1981. *An Introduction to Composite Materials*, Cambridge: Cambridge University Press.
8. Gay, D., S.V. Hoa and S.W. Tsai. 2003. *Composite Materials—Design and Applications,* Boca Raton: CRC Press.
9. Pal, R. 2007. *Rheology of Particulate Dispersions and Composites*, Boca Raton: CRC Press.
10. Bertram, B.D. and R.A. Gerhardt. 2010. Effects of frequency, percolation, and axisymmetric microstructure on the electrical response of hot-pressed alumina–silicon carbide whisker composites, *J. Am. Ceram. Soc.* 94: 1125–1132.
11. Dawson-Andoh, B., L.M. Matuana and J. Harrison. 2004. Mold susceptibility of rigid PVC/wood-flour composites. *J. Vinyl Addit. Tech*. 10: 179–186.
12. Clemons, C. 2002. Wood–plastic composites in the United States: The interfacing of two industries. *Forrest Prod J.* 52: 10–18.
13. Shah, B. and L.M. Matuana. 2004. Online measurement of rheological properties of PVC/wood-flour composites, *J. Vinyl Addit. Tech*. 10: 121–128.
14. Jiang, H. and D.P. Kamdem. 2004. Development of poly(vinyl chloride)/wood composites. A literature review. *J. Vinyl Addit. Tech*. 10: 59–69.
15. Pritchard, G. 2004. Two technologies merge: Wood plastic composites. *Reinf. Plast.* 48: 26–29.
16. Parkinson, D. 1951. The reinforcement of rubber by carbon black. *Brit. J. Appl. Phys.* 2: 273–280.
17. Markarian, J. 2005. Increased demands in electronics drive additive developments in conductivity. *Plast. Addit. Compound*. 7: 26–30.
18. Jones, D.W. 1998. Dental composite biomaterials. *J. Can. Dent. Assoc*. 64: 732–734.
19. Zhou, M., J.L. Drummond and L. Hanley. 2005. Barium and strontium leaching from aged glass particle/resin matrix dental composites. *Dental Mater.* 21: 145–155.
20. Li, Y., M.L. Swartz, R.W. Phillips, B.K. Moore and T.A. Roberts. 1985. Effect of filler content and size on properties of composites. *J. Dent. Res*. 64: 1396–1401.
21. Gocmez, A., C. Erisken, U. Yilmazer, F. Pekel and S. Ozkar. 1998. Mechanical and burning properties of highly loaded composite propellants. *J. Appl. Polym. Sci*. 67: 1457–1464.
22. Chen, X. and T.D. Papathanasiou. 2007. Barrier properties of flake-filled membranes: Review and numerical evaluation. *J. Plast. Film Sheet*. 23: 319–346.
23. Sapalidis, A.A., F.K. Katsaros, G.E. Romanos, N.K. Kakizis and N.K. Kanellopoulos. 2007. Preparation and characterization of novel poly-(vinyl alcohol)-Zostera flakes composites for packaging applications. *Composites B* 38: 398–404.
24. Vinh-Thang, H. and S. Kaliaguine. 2013. Predictive models for mixed-matrix membrane performance: A review. *Chem. Rev*. 113: 4980–5028.
25. Chung, T.S., L.Y. Jiang and S. Kulprathipanja. 2007. Mixed matrix membranes comprising organic polymers with dispersed inorganic fillers for gas separation. *Prog. Polym. Sci.* 32: 483–507.
26. Mahajan, R., W. J. Koros and M. Thundyil. 1999. Mixed matrix membranes: Important and challenging. *Membr. Tech*. 105: 6–8.
27. Moore, T.T., R. Mahajan, D.Q. Vu and W.J. Koros, 2004. Hybrid membrane materials comprising organic polymers with rigid dispersed phases. *AIChE J*. 50: 311–321.
28. Bouma, R.H.B., A. Checchetti, G. Chidichimo and E. Drioli. 1997. Permeation through a heterogeneous membrane: The effect of the dispersed phase. *J. Membr. Sci*. 128: 141–149.

29. Zimmerman, C.M., A. Singh and W.J. Koros. 1997. Tailoring mixed matrix composite membranes for gas separations. *J. Membr. Sci.* 137: 145–154.
30. Gonzo, E.E., M.L. Parentis and J.C. Gottifredi. 2006. Estimating models for predicting effective permeability of mixed matrix membranes. *J. Membr. Sci.* 277: 46–54.
31. Pechar, T.W., M. Tsapatsis, E. Marand and R. Davis. 2002. Preparation and characterization of a glassy fluorinated polyimide zeolite-mixed matrix membrane. *Desalination* 146: 3–9.
32. Vu, D.Q., W.J. Koros and S.J. Miller. 2003. Mixed matrix membranes using carbon molecular sieves II. Modeling permeation behavior. *J. Membr. Sci.* 211: 335–348.
33. Mahajan, R. and W.J. Koros. 2000. Factors controlling successful formation of mixed-matrix gas separation materials. *Ind. Eng. Chem. Res.* 39: 2692–2696.
34. Mahajan, R. and W.J. Koros. 2002. Mixed matrix membrane materials with glassy polymers. Part 1. *Poly. Eng. Sci.* 42: 1420–1431.
35. Mahajan, R. and W.J. Koros. 2002. Mixed matrix membrane materials with glassy polymers. Part 2. *Poly. Eng. Sci.* 42: 1432–1441.
36. Pal, R. 2008. Permeation models for mixed matrix membranes. *J. Colloid Interface Sci.* 317: 191–198.
37. Alberti, G. and M. Casciola. 2003. Composite membranes for medium-temperature PEM fuel cells. *Annu. Rev. Mater. Res.* 33: 129–154.
38. Nagar, H., R.M.A. Abdul Majeed, V.N. Bhoraskar and S.V. Bhorasker. 2008. Radiation-assisted phosphorus diffused polyimide as low thermal emissivity material. *Nucl. Instrum. Meth. B* 266: 781–785.
39. He, X., Y. Li, L. Wang, Y. Sun and S. Zhang. 2009. High emissivity coatings for high temperature application: Progress and prospect. *Thin Solid Films* 517: 5120–5129.
40. Ye, X., Y. Zhou, Y. Sun, J. Chen and Z. Wang. 2008. Structure and infrared emissivity of collagen/SiO2 composite. *Appl. Surf. Sci.* 254: 5975–5980.
41. Yu, H, G. Xu, X. Shen, X. Yan, C. Shao and C. Hu. 2009. Effects of size, shape and floatage of Cu particles on the low infrared emissivity coatings. *Prog. Org. Coat.* 66: 161–166.
42. Yu, H., G. Xu, X. Shen, X. Yan and C. Cheng. 2009. Low infrared emissivity of polyurethane/Cu composite coatings. *Appl. Surf. Sci.* 255: 6077–6081.
43. Chou, K.S. and Y.C. Lu. 2007. The application of nanosized silver colloids in far infrared low emissive coating. *Thin Solid Films* 515: 7217–7221.
44. Babrekar, H.A., N.V. Kulkarni, J.P. Jog, V. L. Mathe and S.V. Bhoraskar. 2010. Influence of filler size and morphology in controlling the thermal emissivity of aluminium/polymer composites for space applications. *Mater. Sci. Eng. B* 168: 40–44.
45. Chauhan, D.V., S.N. Misra and R.N. Shukla. 2012. Study of high emissivity coating of ceramic material for energy conservation. *Der Chemica Sinica* 3: 621–627.
46. Mauer, M., P. Kalenda, M. Honner and P. Vacikova. 2012. Composite fillers and their influence on emissivity. *J. Phys. Chem. Solids* 73: 1550–1555.
47. Yang, C., W.H. Smyrl and E.L. Cussler. 2004. Aligning flakes in barrier coating. *J. Membr. Sci*. 231: 1–12.
48. Huang, H., T. Huang, T. Yeh, C. Tsai, C. Lai, M. Tsai, J. Yeh and Y. Chou. 2011. Advanced anticorrosive materials prepared from amine-capped aniline trimer-based electroactive polyimide–clay nanocomposite materials with synergistic effects of redox catalytic capability and gas barrier properties. *Polymer* 52: 2391–2400.
49. Chang, C., T. Huang, C. Peng, T. Yeh, H. Lu, W. Hung, C. Weng, T. Yang and J. Yeh. 2012. Novel anticorrosion coatings prepared from polyaniline/graphene composites. *Carbon* 50: 5044–5051.
50. Zweben, C. 1998. Advances in composite materials for thermal management in electronic packaging. *J. Min. Met. Mater. Soc*. 50: 47–51.
51. Fiske, T.J., H. Gokturk and D.H. Kaylon. 1997. Enhancement of the relative permeability of polymeric composites with hybrid particulate fillers. *J. Appl. Polym. Sci*. 65: 1371–1377.

52. Bai, Y. 2010. The ferroelectric–ferromagnetic composite ceramics with high permittivity and high permeability in hyper-frequency. In: *Ferroelectrics*, ed. I. Coondoo, Chapter 11, New York: InTech.
53. Lei, T., Q. Xue, L. Chu, Z. Han, J. Sun, F. Xia, Z. Zhang and Q. Guo. 2013. Excellent dielectric properties of polymer composites based on core-shell structured carbon/silica nanohybrid. *Appl. Phys. Letters* 103: article 012902.
54. Dang, Z.M., Y.H. Lin and C.W. Nan. 2003. Novel ferroelectric polymer composites with high dielectric constants. *Adv. Mater*. 15: 1625–1629.
55. Khosrokhavar, R., G.R. Bakhshandeh, M.H.R. Ghoreishy and G.H. Naderi. 2009. PP/EPDM blends and their developments up to nanocomposites. *J. Reinf. Plast. Comp*. 28: 613–639.
56. Sohn, M.S., K.S. Kim, S.H. Hong and J.K. Kim. 2003. Dynamic mechanical properties of particle-reinforced EPDM composites. *J. Appl. Polym. Sci*. 87: 1595–1601.

Section I

Electromagnetic Properties of Composites

Static Electromagnetic Properties of Composites

2 Electrical Conductivity of Composites

To make efficient use of composite materials, the variations of physical properties such as electrical conductivity with the kind and concentration of filler particles should be known. For example, electrically nonconducting particles are often added to a metal matrix to enhance the mechanical properties. However, the addition of nonconducting particles can decrease the electrical conductivity of the metal by a significant amount. From a practical point of view, it is important to be able to predict this decrease in electrical conductivity with the increase in volume fraction of insulating filler. Likewise, it is important to be able to predict the increase in electrical conductivity of an insulating matrix with the increase in electrically conducting filler content; many practical applications in electronics and electrical industries require electrically conductive polymer composites (composites of nonconducting polymer matrix and electrically conducting filler particles).

2.1 BACKGROUND

The electrical conductivity (σ) of a material is a measure of its ability to conduct electrical current. The exact definition of σ comes from Ohm's law of electric conduction, given as

$$\vec{J} = \sigma \vec{E} \tag{2.1}$$

where $\vec{J}$ is current density (current per unit area, amp/m^2), $\vec{E}$ is the electric field (volts/m) in the medium, and σ is conductivity (Siemens/m). According to Ohm's law, the current density at a given location in a conductor is proportional to the electric field strength at that location and the proportionality constant is a material property called electrical conductivity.

Consider one-dimensional current conduction in a straight wire oriented in the x-direction. Let ΔV be the potential difference between the beginning and the end of a wire. The electric field, uniform and oriented along the length of the wire, is given as

$$E_x = \Delta V/L \tag{2.2}$$

where L is the length of the wire. Ohm's law in this case of one-dimensional current conduction in x-direction reduces to

$$J_x = \sigma E_x \tag{2.3}$$

or

$$\frac{I}{A} = \sigma\left(\frac{\Delta V}{L}\right) \tag{2.4}$$

where I is the current and A is the cross-sectional area of the conductor. Thus, for a given voltage gradient (ΔV/L), the current flux increases with the increase in electrical conductivity. Note that ΔV is voltage drop, that is, $V_1 - V_2$.

2.2 ELECTRICAL CONDUCTIVITY OF COMPOSITES

Over the past several decades, a number of experimental and theoretical studies have been published in the literature on the electrical properties of particulate composites [1–26]. In what follows, the key empirical and theoretical models describing the electrical conductivity of particulate composites are discussed.

2.2.1 Empirical Rules of Mixtures

According to the *Voigt* rule of mixture (ROM), the electrical conductivity of a composite material is given as

$$\sigma = \phi\sigma_d + (1 - \phi)\sigma_m \tag{2.5}$$

where σ, σ_d, and σ_m are the electrical conductivities of composite, dispersed phase and matrix, respectively, and ϕ is the volume fraction of filler particles. This formula can be derived by considering two electrical conductors, matrix and dispersed phase, in parallel with the same voltage gradients but with composite current flux proportional to the content of individual phases, that is,

$$\left(\frac{\Delta V}{L}\right) = \left(\frac{\Delta V}{L}\right)_m = \left(\frac{\Delta V}{L}\right)_d \tag{2.6}$$

$$J = (1 - \phi)J_m + \phi J_d \tag{2.7}$$

where (ΔV/L), $(\Delta V/L)_m$, and $(\Delta V/L)_d$ are the voltage gradients in composite, matrix, and dispersed phase, respectively, and J, J_m, and J_d are the current fluxes in composite, matrix, and dispersed phase, respectively. Note that the current fluxes are additive due to parallel arrangement of the matrix and dispersed phase. From Ohm's law,

$$J = \sigma\left(\frac{\Delta V}{L}\right), \quad J_m = \sigma_m\left(\frac{\Delta V}{L}\right)_m, \quad J_d = \sigma_d\left(\frac{\Delta V}{L}\right)_d \tag{2.8}$$

Upon substituting the expressions for current fluxes from Equation 2.8 into Equation 2.7 and realizing that the voltage gradients are the same, one can readily arrive at the Voigt ROM (Equation 2.5).

According to another ROM, namely the *Reuss* ROM, the electrical conductivity of a composite material is given as

$$1/\sigma = [\phi/\sigma_d] + [(1 - \phi)/\sigma_m] \tag{2.9}$$

This formula can be derived by considering two electrical conductors, matrix and dispersed phase, in series with the same current fluxes but with composite voltage gradient proportional to the content of individual phases, that is,

$$J = J_m = J_d \tag{2.10}$$

$$\left(\frac{\Delta V}{L}\right) = (1-\phi)\left(\frac{\Delta V}{L}\right)_m + \phi\left(\frac{\Delta V}{L}\right)_d \tag{2.11}$$

Note that the voltage gradients are additive due to series arrangement of the matrix and dispersed phase. From Ohm's law,

$$\left(\frac{\Delta V}{L}\right) = \frac{J}{\sigma}, \quad \left(\frac{\Delta V}{L}\right)_m = \frac{J_m}{\sigma_m}, \quad \left(\frac{\Delta V}{L}\right)_d = \frac{J_d}{\sigma_d} \tag{2.12}$$

Upon substituting the expressions for voltage gradients from Equation 2.12 into Equation 2.11 and realizing that the current fluxes are the same, one can readily arrive at the Reuss ROM (Equation 2.9).

The Voigt and Reuss ROMs are special cases of the following more general mixing rule:

$$\sigma^n = \phi\sigma_d^n + (1-\phi)\sigma_m^n \tag{2.13}$$

When n = 1, Equation 2.13 reduces to the Voigt ROM and when n = –1, the Reuss ROM is recovered. Another mixing rule that is widely recognized is the Lichtenecker logarithmic rule, given as

$$\log(\sigma) = \phi \log(\sigma_d) + (1 - \phi)\log(\sigma_m) \tag{2.14}$$

2.2.2 Theoretical Models

For an infinitely dilute composite of spherical filler particles, the exact expression for the effective electrical conductivity is given by

$$\frac{\sigma}{\sigma_m} = 1 + 3\left(\frac{\sigma_d - \sigma_m}{\sigma_d + 2\sigma_m}\right)\phi \tag{2.15}$$

where σ, σ_m, and σ_d are the electrical conductivities of composite, matrix, and filler (dispersed phase), respectively, and ϕ is the volume fraction of filler. This equation can be rewritten as

$$\sigma_r = 1 + 3\left(\frac{\lambda - 1}{\lambda + 2}\right)\phi \tag{2.16}$$

where σ_r is the relative electrical conductivity defined as σ/σ_m and λ is the electrical conductivity ratio defined as σ_d/σ_m.

For composites with electrically nonconducting filler particles and conducting matrix, $\lambda \to 0$ and Equation 2.16 reduces to

$$\sigma_r = 1 - \frac{3}{2}\phi \tag{2.17}$$

For composites with conductive filler particles and nonconductive matrix, $\lambda \to \infty$, and Equation 2.16 becomes

$$\sigma_r = 1 + 3\phi \tag{2.18}$$

Maxwell [1] developed an equation for the electrical conductivity of particulate composites using the effective medium approach. Consider a cluster of particles embedded in an infinite matrix of electrical conductivity σ_m. The cluster of particles, enclosed by a spherical region of radius R, consists of n spherical particles of radius "a" and electrical conductivity σ_d. The system is subjected to an electric potential field with a uniform potential gradient of α' at $r \to \infty$. The voltage potential distribution at $r \to \infty$ is given as $V(r, \theta) = \alpha' z$, where $z = r\cos\theta$. Assuming negligible interaction between the particles, the voltage potential at a radial distance r ($r >> R$) from the center of the spherical cluster region R is

$$V = \left(\alpha' r + n\beta\frac{1}{r^2}\right)\cos\theta \tag{2.19}$$

where the constant β is given by

$$\beta = \left(\frac{\sigma_m - \sigma_d}{\sigma_d + 2\sigma_m}\right)a^3\alpha' \tag{2.20}$$

Since $\phi = n\,(a/R)^3$, Equation 2.19 can be rewritten as

$$V = \alpha'\left[r + \phi R^3\left(\frac{\sigma_m - \sigma_d}{\sigma_d + 2\sigma_m}\right)\frac{1}{r^2}\right]\cos\theta \tag{2.21}$$

Now if the cluster of particles is treated as an "effective homogeneous medium" of radius R and electrical conductivity σ, suspended in a matrix of conductivity σ_m, the potential at any radial location r (>> R) is given as

$$V = \alpha' \left[r + R^3 \left(\frac{\sigma_m - \sigma}{\sigma + 2\sigma_m} \right) \frac{1}{r^2} \right] \cos\theta \tag{2.22}$$

Since the two expressions, Equations 2.21 and 2.22, are equivalent, it follows that

$$\left(\frac{\sigma - \sigma_m}{\sigma + 2\sigma_m} \right) = \left(\frac{\sigma_d - \sigma_m}{\sigma_d + 2\sigma_m} \right) \phi \tag{2.23}$$

This is the celebrated Maxwell equation for the electrical conductivity of particulate composites. It can be rearranged as

$$\sigma_r = \frac{\sigma}{\sigma_m} = \left[\frac{1 + 2\phi \left(\frac{\lambda - 1}{\lambda + 2} \right)}{1 - \phi \left(\frac{\lambda - 1}{\lambda + 2} \right)} \right] \tag{2.24}$$

where λ is the electrical conductivity ratio σ_d/σ_m. In the limit $\phi \to 0$, Equation 2.24 reduces to Equation 2.16.

Bruggeman [4] used a differential scheme along with the result for a dilute particulate composite, Equation 2.15, to develop the following equation for concentrated particulate composites:

$$\left(\frac{\sigma_d - \sigma}{\sigma_d - \sigma_m} \right) \left(\frac{\sigma_m}{\sigma} \right)^{\frac{1}{3}} = 1 - \phi \tag{2.25}$$

This equation is often referred to as the Bruggeman asymmetric rule. When $\lambda \to 0$, the Bruggeman equation reduces to

$$\sigma_r = \frac{\sigma}{\sigma_m} = (1 - \phi)^{3/2} \tag{2.26}$$

When $\lambda \to \infty$, the Bruggeman equation gives

$$\sigma_r = (1 - \phi)^{-3} \tag{2.27}$$

One drawback of the equations discussed thus far is that they fail to predict the correct behavior when $\phi \to \phi_m$, where ϕ_m is the maximum packing volume fraction

of particles. For random close packing of uniform spheres, ϕ_m is 0.637. When the electrical conductivity ratio is large, that is, $\lambda (= \sigma_d/\sigma_m) \to \infty$, the electrical conductivity of a composite is expected to approach infinity at $\phi \to \phi_m$.

Pal [22] recently developed new models for the electrical conductivity of particulate composites. He first generalized the exact expression for the electrical conductivity (Equation 2.15) of infinitely dilute composite of filler particles as follows:

$$\frac{\sigma}{\sigma_m} = 1 + 3\alpha\left(\frac{\sigma_d - \sigma_m}{\sigma_d + 2\sigma_m}\right)\phi \tag{2.28}$$

where α is a "correction factor" of the order of unity to account for the deviations from the assumptions made in the derivation of Equation 2.15. For example, most particulate composites of practical interest consist of nonspherical irregular-shaped fillers. Even the equiaxed particle fillers used in particulate composites are nonspherical. Furthermore, some interfacial additive is almost always present at the interface of particle–matrix.

Equation 2.28 cannot be applied at finite concentration of particles, as the interaction between the particles is not considered in its derivation. To extend the applicability of Equation 2.28 to concentrated systems, Pal [22] used a differential effective medium approach. According to the differential effective medium approach, a concentrated composite is considered to be obtained from an initial matrix phase by successively adding infinitesimally small quantities of particles to the system until the final volume fraction of filler is reached. The incremental change in electrical conductivity upon the addition of an infinitesimally small quantity of particles to the system can be determined from Equation 2.28 as

$$d\sigma = 3\alpha\sigma\left[\frac{\sigma_d - \sigma}{\sigma_d + 2\sigma}\right]d\phi \tag{2.29}$$

This equation can be rewritten as

$$\frac{1}{3\alpha}\left[\frac{1}{\sigma} + \frac{3}{\sigma_d - \sigma}\right]d\sigma = d\phi \tag{2.30}$$

Upon integration with the limit $\sigma \to \sigma_m$ at $\phi \to 0$, Equation 2.30 gives

$$\left[\frac{\sigma}{\sigma_m}\right]^{\frac{1}{3}} \left(\frac{\sigma_d - \sigma_m}{\sigma_d - \sigma}\right) = \exp(\alpha\phi) \tag{2.31}$$

or

$$\sigma_r^{1/3} \left(\frac{\lambda - 1}{\lambda - \sigma_r}\right) = \exp(\alpha\phi) \tag{2.32}$$

Equation 2.31 or 2.32, referred to as Model 1, is expected to describe the electrical conductivity of particulate composites at low to moderate values of ϕ (volume fraction of particles). This is because in the derivation of the differential equation (Equation 2.29) leading to Model 1 (Equation 2.31), it is assumed that all the volume of the existing composite, before a differential quantity of new particles are added to the existing composite, is available as free volume to the new particles. In reality, the free volume available to disperse the new particles is significantly less, due to the volume preempted by the particles already present. This means that when a differential quantity of new particles is added to the existing composite, the increase in the actual volume fraction of the dispersed phase is larger than $d\phi$. The increase in the volume fraction of the dispersed phase is $d\phi/(1 - k_o\phi)$ where k_o accounts for the "crowding effect" caused by packing difficulties of particles. k_o is equal to $1/\phi_m$, where ϕ_m is the maximum packing volume fraction of particles. Thus, Equation 2.30 should be rewritten as

$$\frac{1}{3\alpha}\left[\frac{1}{\sigma}+\frac{3}{\sigma_d-\sigma}\right]d\sigma=\frac{d\phi}{1-(\phi/\phi_m)} \tag{2.33}$$

Upon integration with the limit $\sigma \to \sigma_m$ at $\phi \to \phi_m$, Equation 2.33 gives

$$\left(\frac{\sigma}{\sigma_m}\right)^{\frac{1}{3}}\left(\frac{\sigma_d-\sigma_m}{\sigma_d-\sigma}\right)=\left(1-\frac{\phi}{\phi_m}\right)^{-\alpha\phi_m} \tag{2.34}$$

or

$$(\sigma_r)^{\frac{1}{3}}\left(\frac{\lambda-1}{\lambda-\sigma_r}\right)=\left(1-\frac{\phi}{\phi_m}\right)^{-\alpha\phi_m} \tag{2.35}$$

Equation 2.34 or 2.35, referred to as Model 2, reduces to the following expression when highly conducting particles are dispersed in a nonconducting matrix such that $\lambda \to \infty$:

$$\sigma_r=\left(1-\frac{\phi}{\phi_m}\right)^{-3\alpha\phi_m} \tag{2.36}$$

For insulating particles dispersed in a conducting matrix such that $\lambda \to 0$, Model 2 reduces to

$$\sigma_r=\left(1-\frac{\phi}{\phi_m}\right)^{\frac{3}{2}\alpha\phi_m} \tag{2.37}$$

It should be noted that the Bruggeman asymmetric equation (Equation 2.25) is a special case of Model 2 when $\alpha = 1$ and $\phi_m = 1$. Interestingly, Model 2 predicts the relative electrical conductivity of a particulate composite to be infinite when $\lambda \to \infty$ and $\phi \to \phi_m$, as expected.

Figure 2.1 shows the predictions of the relative electrical conductivity of particulate composites as a function of conductivity ratio λ using Model 2 (Equation 2.35) with $\phi_m = 0.637$ and $\alpha = 1.0$. When the electrical conductivity ratio is unity, the relative conductivity σ/σ_m of composite is unity for all values of ϕ. For $\lambda < 1.0$, σ/σ_m decreases with the increase in ϕ. For $\lambda > 1.0$, σ/σ_m increases with the increase in ϕ.

Upon comparison of experimental data with the model predictions (see Figures 2.2 through 2.4), it is found that model 1, Equation 2.31, gives good predictions of electrical conductivity of composites only at low volume fractions of the dispersed phase. This is not unexpected, as this model does not consider the crowding effect of particles. Model 2 (Equation 2.34) describes the experimental data adequately over a wide range of the volume fraction of filler ϕ.

Another useful model, presented here for the first time without proof, which considers the crowding effect of particles, is the following generalization of Equation 2.32:

$$\sigma_r^{1/3} \left(\frac{\lambda - 1}{\lambda - \sigma_r} \right) = \exp\left(\frac{\alpha\phi}{1 - \dfrac{\phi}{\phi_m}} \right) \tag{2.38}$$

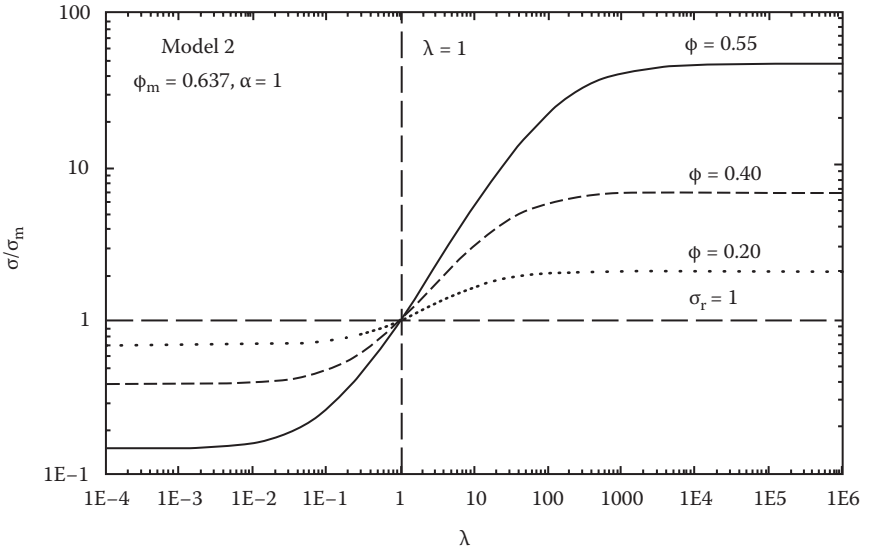

FIGURE 2.1 Effect of volume fraction of filler particles (ϕ) on the relative electrical conductivity σ/σ_m. The plots are generated from Model 2 (Equation 2.35) using $\alpha = 1$ and $\phi_m = 0.637$. (From Pal, R., *J. Composite Mater.* 41: 2499–2511, 2007.)

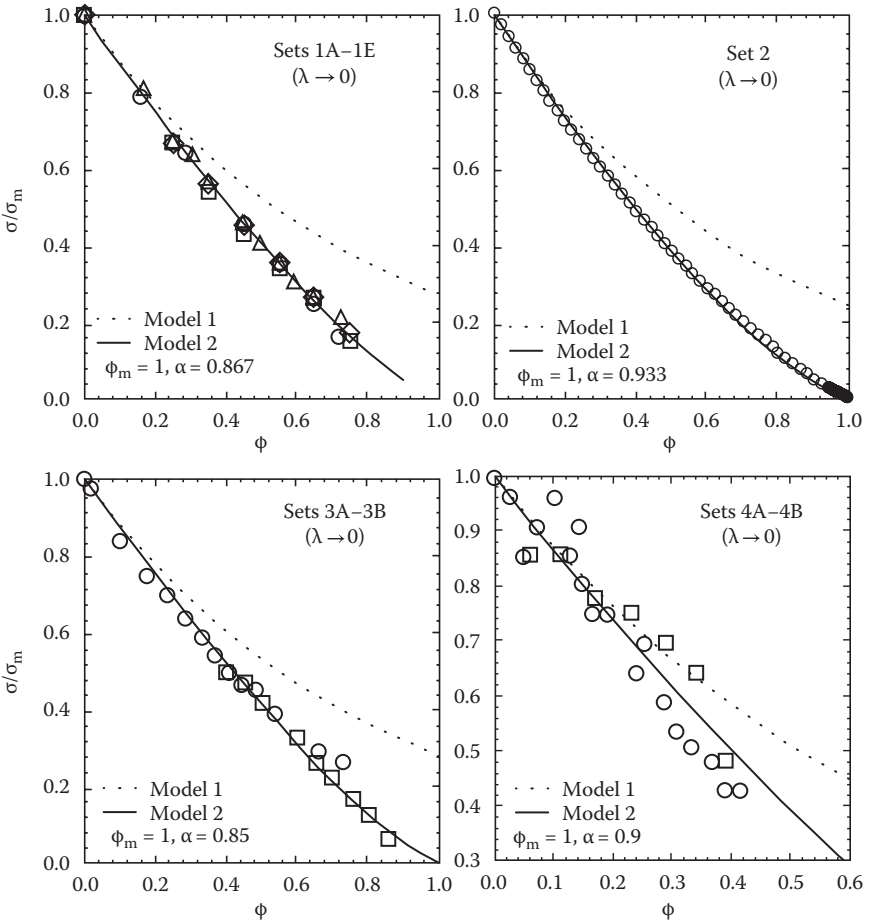

FIGURE 2.2 Comparison between experimental σ/σ_m data of particulate composites and Models 1 and 2. The values of α and ϕ_m used in the models are indicated in the figure. Note that the same value of α is used in Models 1 and 2. (From Pal, R., *J. Composite Mater.* 41: 2499–2511, 2007.)

The Lewis–Nielsen model [27–30] also considers the crowding effect of particles. Lewis and Nielsen [28–30] modified and adapted the Halpin–Tsai equation for elastic moduli of composite materials to conductivity of particulate-filled composites. The Lewis–Nielsen equation is given as

$$\sigma_r = \left[\frac{1 + A\left(\frac{\lambda - 1}{\lambda + A}\right)\phi}{1 - \phi\psi\left(\frac{\lambda - 1}{\lambda + A}\right)}\right] \tag{2.39a}$$

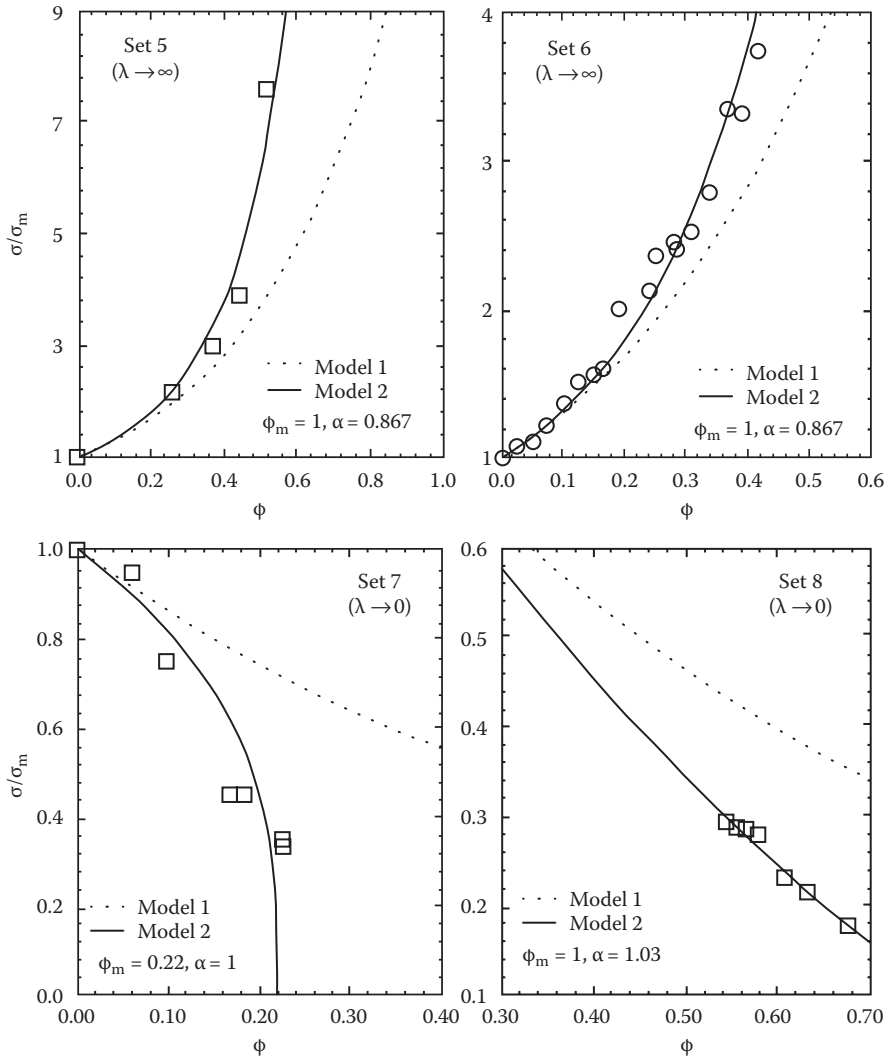

FIGURE 2.3 Comparison between experimental σ/σ_m data of particulate composites and Models 1 and 2. The values of α and ϕ_m used in the models are indicated in the figure. Note that the same value of α is used in Models 1 and 2. (From Pal, R., *J. Composite Mater.* 41: 2499–2511, 2007.)

where

$$\psi = 1 + \left(\frac{1 - \phi_m}{\phi_m^2} \right) \phi \tag{2.39b}$$

Pal [27] has suggested a value of 2 for A. If A = 2, the Lewis–Nielsen model reduces to the Maxwell model when ϕ_m is unity. Equation 2.39a with A = 2 is evaluated

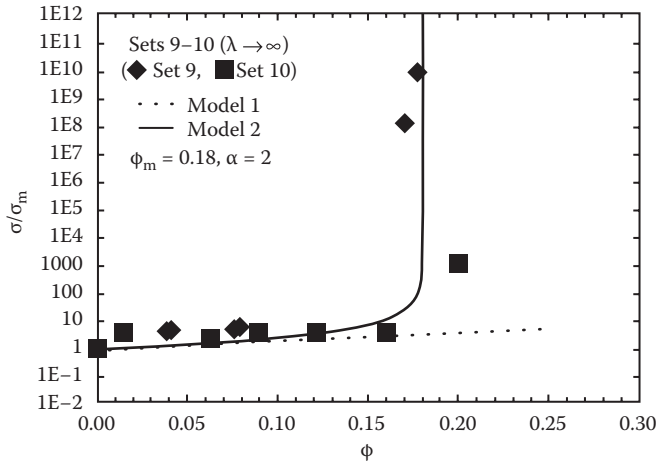

FIGURE 2.4 Comparison between experimental σ/σ_m data of particulate composites and Models 1 and 2. The values of α and ϕ_m used in the models are indicated in the figure. Note that the same value of α is used in Models 1 and 2. (From Pal, R., *J. Composite Mater.* 41: 2499–2511, 2007.)

by Pal [27] using a number of experimental data sets available on the electrical conductivity of particulate composites. The model is found to describe the experimental data reasonably well (see Figures 2.5 and 2.6).

2.3 ELECTRICAL PERCOLATION IN COMPOSITES

Composites of metal particles and insulator matrix exhibit percolation behavior. They act like insulators when the volume fraction of the particles is below a certain value, referred to as percolation threshold. At filler volume fractions below the percolation threshold, the conductor metal particles are either isolated or form small aggregates/clusters. The composite is an insulator, as no electrical conducting path exists connecting the opposite ends of the sample. As the volume fraction of the filler particles is increased, the average size of the clusters increases. At the threshold concentration of filler, a large cluster is formed which connects the opposite ends of the sample and therefore electric current percolates through the composite. With further increase in the filler concentration, the density of the cluster increases and many more conducting paths are formed in the composite. Consequently, the electrical conductivity of composite increases sharply with the increase in filler concentration above the threshold value.

The conductivity models described in the preceding section are inadequate to describe the percolation behavior of composites. The Maxwell and Bruggeman asymmetric models predict percolation threshold of unity. When applied to metal–insulator composites (high λ), these models predict the electrical conductivity of composite to be closer to the matrix conductivity until the composite is completely filled with filler particles where the composite conductivity rapidly approaches the conductivity

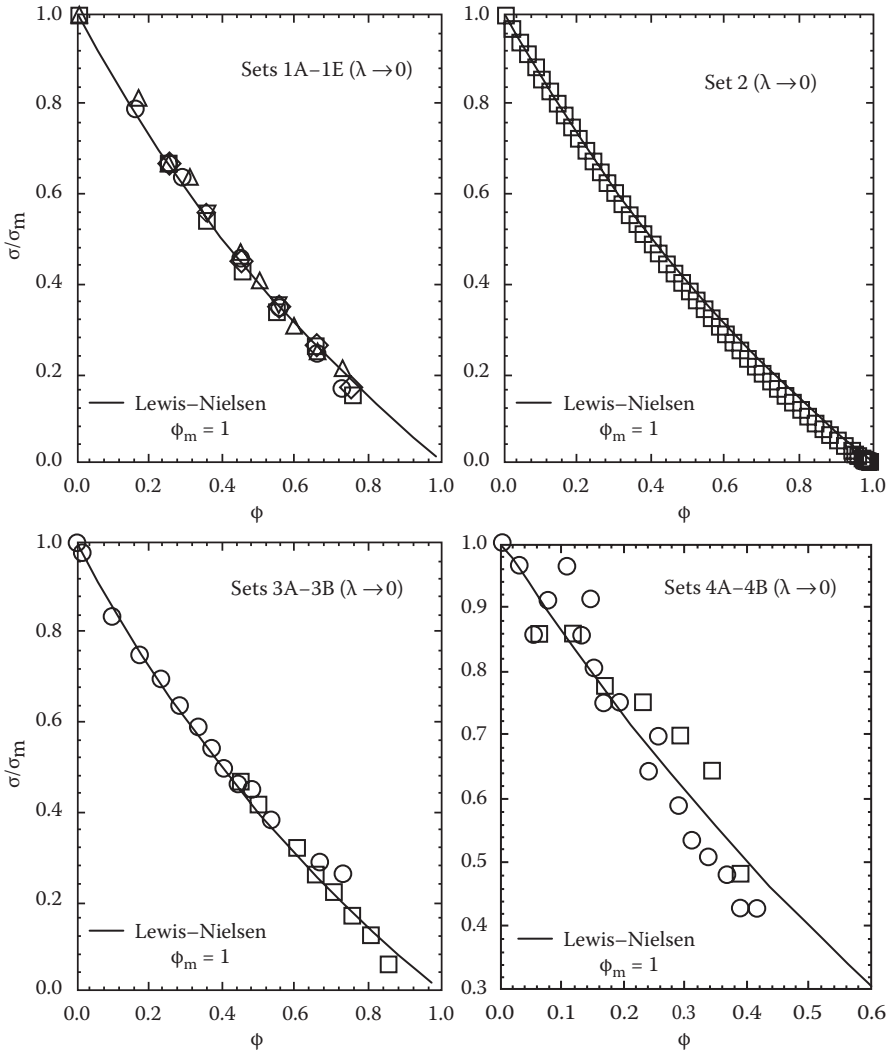

FIGURE 2.5 Comparisons between experimental electrical conductivity data and predictions of the Lewis–Nielsen model. (From Pal, R., *Composites A*. 39: 718–726, 2008.)

of metal filler. The models of Pal and Lewis–Nielsen predict percolation at $\phi \rightarrow \phi_m$. According to these models, the conductivity of metal–insulator composite diverges at $\phi \rightarrow \phi_m$. However, experimental studies indicate that the percolation threshold of composites consisting of interacting particles can be much smaller than ϕ_m, the maximum packing concentration of particles. Thus, these models can be applied to percolating composites only when ϕ_m is interpreted as the percolation threshold concentration of filler particles.

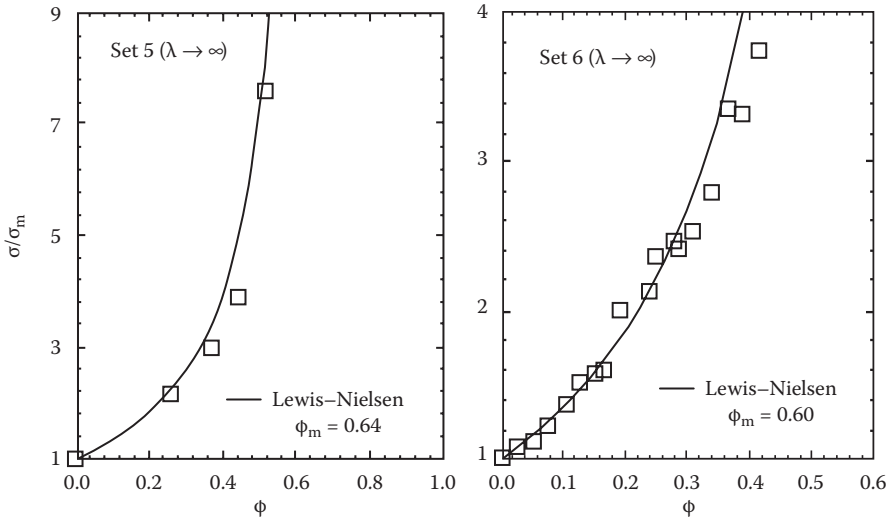

FIGURE 2.6 Comparisons between experimental electrical conductivity data and predictions of the Lewis–Nielsen model. (From Pal, R., *Composites A*. 39: 718–726, 2008.)

Probably the first model capable of describing electrical percolation behavior of composites was developed by Bruggeman [4]. His model, referred to as the Bruggeman symmetric rule, is given as follows:

$$\left(\frac{\sigma_d - \sigma}{\sigma_d + 2\sigma}\right)\phi + \left(\frac{\sigma_m - \sigma}{\sigma_m + 2\sigma}\right)(1-\phi) = 0 \tag{2.40}$$

This equation is quadratic in σ. Of its two solutions, only the following one is physically possible:

$$\sigma = \frac{1}{4}\left(q + \sqrt{q^2 + 8\sigma_m\sigma_d}\right) \tag{2.41}$$

where

$$q = (3\phi - 1)\sigma_d + (2 - 3\phi)\sigma_m \tag{2.42}$$

This solution could be rewritten as

$$\sigma_r = \frac{1}{4}\left(q_r + \sqrt{q_r^2 + 8\lambda}\right) \tag{2.43}$$

where λ is the conductivity ratio σ_d/σ_m and q_r is given as follows:

$$q_r = (3\phi - 1)\lambda + (2 - 3\phi) \tag{2.44}$$

Figures 2.7 and 2.8 show the predictions of the Bruggeman symmetric model for $\lambda = 1000$. For comparison purposes, the predictions of the Bruggeman asymmetric model are also shown. The same data are plotted on semilog and linear scales. The symmetric model predicts a sharp rise in the conductivity when percolation threshold of about 0.33 is reached. The asymmetric model predicts a sharp rise in conductivity only when ϕ is close to unity.

Although the symmetric Bruggeman model predicts the percolation effect in composites with high electrical conductivity contrast, its main drawback is that the percolation threshold predicted is fixed, that is, 0.33. It is well known that the percolation threshold in composites varies from one system to another depending on the nature of particle–particle interactions and particle–matrix interactions and the shape of particles.

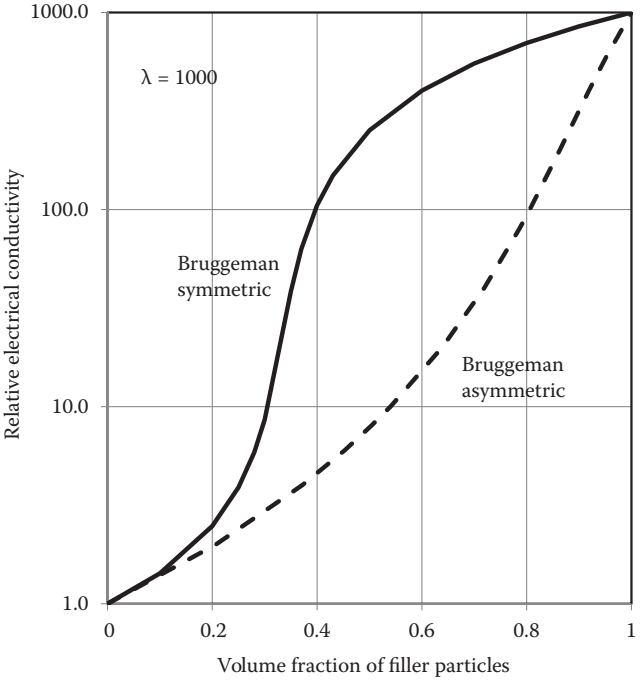

FIGURE 2.7 Predictions of electrical conductivity of composites from the Bruggeman symmetric and asymmetric models for $\lambda = 1000$, on a semilog scale.

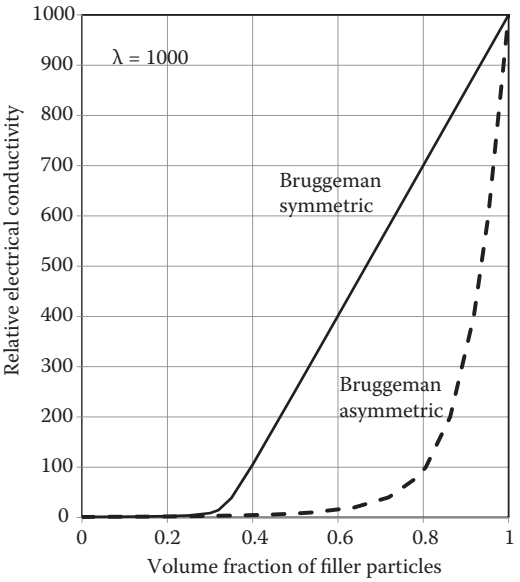

FIGURE 2.8 Predictions of electrical conductivity of composites from the Bruggeman symmetric and asymmetric models for $\lambda = 1000$, on a linear scale.

The following General Effective Media (GEM) model of McLachlan [15, 23–26] is widely used to describe the percolation behavior of conductor–insulator composites:

$$\frac{f\left(\sigma_l^{1/t} - \sigma^{1/t}\right)}{\left(\sigma_l^{1/t} + \left\{f_c/(1-f_c)\right\}\sigma^{1/t}\right)} + \frac{(1-f)\left(\sigma_h^{1/t} - \sigma^{1/t}\right)}{\left(\sigma_h^{1/t} + \left\{f_c/(1-f_c)\right\}\sigma^{1/t}\right)} = 0 \tag{2.45}$$

where f is the volume fraction of low-conductivity component, f_c is the critical volume fraction (percolation threshold) of low-conductivity component, σ_l is the conductivity of low-conductivity component, σ_h is the conductivity of high-conductivity component, σ is the conductivity of the composite, and t is an exponent.

For composites of nonconducting particles and conducting matrix ($\lambda = \sigma_d/\sigma_m < 1.0$), the GEM model (Equation 2.45) reduces to

$$\frac{\phi\left(\lambda^{1/t} - \sigma_r^{1/t}\right)}{\left(\lambda^{1/t} + \left\{\phi_c/(1-\phi_c)\right\}\sigma_r^{1/t}\right)} + \frac{(1-\phi)\left(1 - \sigma_r^{1/t}\right)}{\left(1 + \left\{\phi_c/(1-\phi_c)\right\}\sigma_r^{1/t}\right)} = 0 \tag{2.46}$$

where ϕ is the volume fraction of the dispersed phase (nonconducting particles), ϕ_c is the critical value of ϕ, and σ_r is the relative conductivity of composite, defined as σ/σ_m.

For composites of conducting particles and nonconducting matrix ($\lambda = \sigma_d/\sigma_m > 1.0$), the GEM model (Equation 2.45) reduces to

$$\frac{(1-\phi)\left(1-\sigma_r^{1/t}\right)}{\left(1+\left\{(1-\phi_c)/\phi_c\right\}\sigma_r^{1/t}\right)}+\frac{\phi\left(\lambda^{1/t}-\sigma_r^{1/t}\right)}{\left(\lambda^{1/t}+\left\{(1-\phi_c)/\phi_c\right\}\sigma_r^{1/t}\right)}=0 \tag{2.47}$$

where ϕ is the volume fraction of the dispersed phase (conducting particles in the present case) and ϕ_c is the critical value of ϕ.

The GEM model (Equation 2.45) in its asymptotic form reduces to the following percolation expressions [15,27]:

$$\sigma_r = \left(1-\frac{\phi}{\phi_c}\right)^{-t} \quad (\text{when } \lambda \to \infty) \tag{2.48}$$

$$\sigma_r = \left(1-\frac{\phi}{\phi_c}\right)^{t} \quad (\text{when } \lambda \to 0) \tag{2.49}$$

Interestingly, the Pal model (Equation 2.35) gives similar expressions in the limiting cases of $\lambda \to \infty$ and $\lambda \to 0$ (see Equations 2.36 and 2.37). However, the exponent in the Pal model is not the same in two cases of $\lambda \to \infty$ and $\lambda \to 0$. When $\lambda \to \infty$, the Pal model predicts $t = 3\alpha\,\phi_m$ and when $\lambda \to 0$, the Pal model gives $t = 1.5\,\alpha\,\phi_m$. The GEM model assumes the same value of the exponent "t" in the two cases [15,26].

For the nonpercolating systems ($\phi_c = 1$), the GEM model gives the following expressions for the relative conductivity (σ_r):

$$\sigma_r = \{1-\phi(1-\lambda^{-1/t})\}^t \quad (\text{when } \lambda > 1) \tag{2.50}$$

$$\sigma_r = \{1-\phi(1-\lambda^{1/t})\}^t \quad (\text{when } \lambda < 1) \tag{2.51}$$

2.4 PHASE INVERSION IN COMPOSITES

The phenomenon of phase inversion whereby the dispersed and matrix phases of a composite are interchanged suddenly is encountered in the production, mixing, processing, and handling of emulsion-type composite fluids. For example, a water-in-oil emulsion consisting of water droplets dispersed in a continuum of oil phase can, under certain conditions, invert suddenly into an oil-in-water emulsion consisting of oil droplets dispersed in a continuum of aqueous phase. This phase inversion phenomenon is often observed in oil production and related operations. Phase inversion in emulsions can be induced by increasing the volume fraction of the dispersed phase. According to a simple theory proposed by Ostwald [31,32] based on geometrical grounds, phase inversion in emulsions occurs sharply at a dispersed phase volume fraction of 0.74. This is the volume fraction of dispersed phase corresponding to hexagonal close

packing of uniform spheres. When the dispersed phase volume fraction of an emulsion exceeds 0.74, the emulsion droplets become more densely packed than the closest possible packing of droplets and therefore, inversion of phases takes place. However, it should be noted that when the droplets are not uniform in size, the densest packing volume fraction of droplets can far exceed a value of 0.74. This simple theory of Ostwald is often found to be inaccurate as factors other than the volume fraction of the dispersed phase also play a role in the phase inversion phenomenon. The phase inversion of emulsions could be hastened or delayed by the addition of surfactants and nanoparticles to the emulsion. In the absence of any additives (surfactants, solid particle stabilizers such as interfacially active nanoparticles, etc.), Pal [33] found that the inversion of water-in-oil emulsion (prepared from refined mineral oil of viscosity 2.41 mPa.s at 25°C and tap water) to oil-in-water emulsion occurred at a dispersed phase (water) volume fraction of about 0.42. This value is much lower than the Ostwald value of 0.74. Binks and Lumsdon [34] found that emulsions prepared from *hydrophilic* nanoparticles, initially located in the water phase, were of the oil-in-water type up to an oil volume fraction of about 0.70. The oil-in-water emulsion inverted to water-in-oil emulsion when the oil volume fraction was increased above 0.70. When *hydrophobic* nanoparticles were added to the oil phase, the emulsions were of water-in-oil type up to a water volume fraction of about 0.70. Inversion of water-in-oil emulsion to oil-in-water emulsion occurred above the water volume fraction of 0.70. Thus, phase inversion in the emulsions investigated by Binks and Lumsdon [34] occurred close to the Ostwald value of 0.74.

Upon inversion of emulsions, a sharp change in the electrical conductivity of emulsion occurs. For example, a sharp increase in conductivity occurs upon inversion of water-in-oil emulsion to oil-in-water emulsion as the conductive phase becomes the matrix phase upon inversion. Figure 2.9a shows the electrical conductivity data for emulsions without any additives (surfactants or solid nanoparticle stabilizer). The viscosity of the oil used was 22.9 mPa.s at 25 °C. At low volume fractions of water, the emulsion is of the water-in-oil type. A sharp increase in conductivity occurs at a water volume fraction of about 0.33 due to phase inversion. For water-in-oil emulsions, $\sigma_m = 0$ as the oil phase is nonconductive. Thus, the symmetric Bruggeman expression (Equation 2.41) reduces to

$$\sigma = \frac{q}{2} = \frac{\sigma_d}{2}(3\phi - 1), \quad \phi \geq 1/3 \tag{2.52}$$

where ϕ is the volume fraction of water and σ_d is conductivity of water. The prediction of this equation is shown on the plot. The percolation threshold concentration of water droplets is 1/3. This concentration coincides with the phase inversion concentration. For oil-in-water emulsions, $\sigma_d = 0$ as oil is nonconductive. Thus, Equation 2.41 becomes

$$\sigma = \frac{q}{2} = \sigma_m\left(1 - \frac{3\phi}{2}\right), \quad \phi \leq 2/3 \tag{2.53}$$

where ϕ is the volume fraction of oil and σ_m is conductivity of water. This equation gives the same values of emulsion conductivity as the previous equation. The

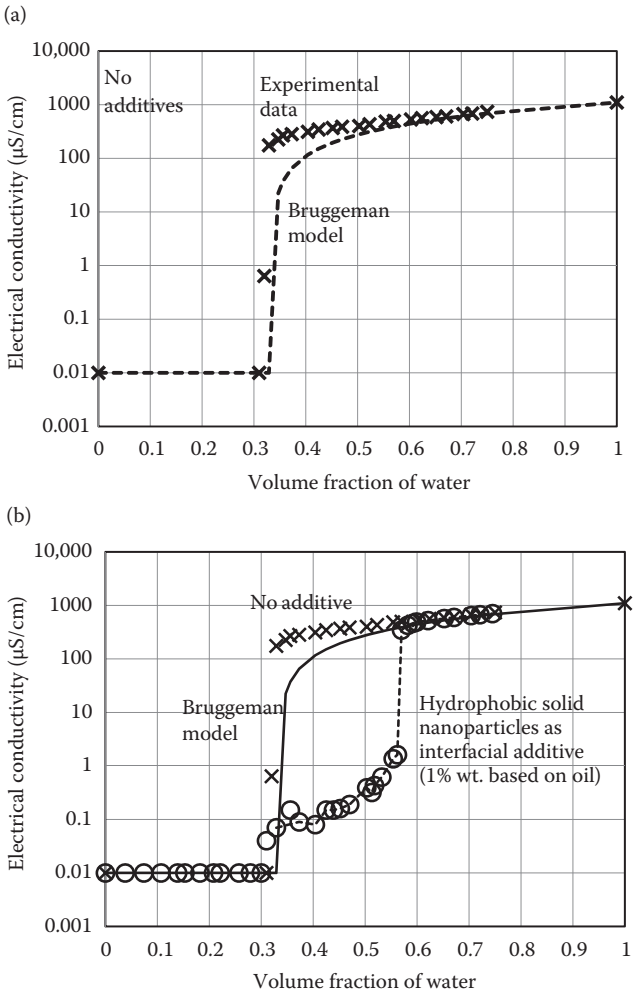

FIGURE 2.9 (a) Phase inversion in composite emulsion-based fluid without any additives (surfactants or solid nanoparticle stabilizer). (b) Influence of hydrophobic nanoparticles on phase inversion of composite emulsion-based fluids.

percolation threshold concentration of oil is 2/3. Thus, the electrical conductivity models for percolating composites could probably be applied to unstable emulsions (no additives) without specifically taking into consideration the inversion of phases. Phase inversion is taken care of by the percolation phenomenon. The concentration of dispersed phase where phase inversion occurs corresponds to the percolation threshold concentration. The conductivity plot generated by the model is the same regardless of whether water droplets are assumed to be the dispersed phase or oil droplets are assumed to be the dispersed phase.

Figure 2.9b compares the electrical conductivity versus dispersed-phase volume fraction plots for emulsions, with and without additive. The additive is hydrophobic

silica nanoparticles, added to the oil phase at a concentration of 1% wt. based on oil. Clearly, the addition of hydrophobic nanoparticles to the oil phase delays the inversion of water-in-oil emulsion to oil-in-water emulsion [35]. In addition, the symmetric Bruggeman model is no longer valid.

REFERENCES

1. Maxwell, J.C. 1881. *A Treatise on Electricity and Magnetism*, 2nd ed., Vol. 1, p. 435, Oxford: Clarendon Press.
2. Wagner, K.W. 1914. Erklärung der Dielektrischen Nachwirkungen auf Grund Maxwellscher Vorstellungen. *Arch Elektrotech. (Berlin)* 2: 371–387.
3. Wiener, O. 1912. Allgemeine Sätze über die Dielektizitatkonstanten der Mischkorper. *Abh. Kgl. Sachs, Ges. Wiss. Math. Physik Klasse* 32: 509–574.
4. Bruggeman, D.A.G. 1935. Berechnung verschiedener physikalischer Konstanten von heterogenen Substanzen. *Ann. Phys. (Leipzig)* 24: 636–679.
5. Meredith, R.E. and C.W. Tobias. 1960. Resistance to potential flow through a cubical array of spheres. *J. Appl. Phys.* 31: 1270–1273.
6. Meredith, R.E. and C.W. Tobias. 1962. Conduction in heterogeneous systems, In: *Advances in Electrochemistry and Electrochemical Engineering*, eds. P. Delahay and C.W. Tobias, Vol. 2, p. 15, New York: Interscience.
7. Rayleigh, L. 1892. On the influence of obstacles arranged in rectangular order on the properties of a medium. *Phil. Mag.* 34: 481.
8. Bottcher, C.J.F. 1952. *Theory of Electric Polarization*, p. 419, New York: Elsevier.
9. Feitosa, K., S. Marze, A. Saint-Jalmes and D.J. Durian. 2005. Electrical conductivity of dispersions: From dry foams to dilute suspensions. *J. Phys. Condens. Matter*. 17: 6301–6305.
10. Zuzovsky, M. and H. Brenner. 1977. Effective conductivities of composite materials composed of cubic arrangements of spherical particles embedded in an isotropic matrix. *J. Appl. Math. Phys*. 28: 979–992.
11. Pal, R. 1987. Emulsions: Pipeline flow behavior, viscosity equations, and flow measurement, PhD thesis, University of Waterloo, Ontario, Canada.
12. Clingerman, M.L., E.H. Weber, J.A. King and K.H. Schulz. 2003. Development of an additive equation for predicting the electrical conductivity of carbon-filled composites. *J. Appl. Poly. Sci*. 88: 2280–2299.
13. Mamunya, Y.P., V.V. Davydenko, P. Pissis and E.V. Lebedev. 2002. Electrical and thermal conductivity of polymers filled with metal powders. *Euro-Poly. J.* 38: 1887–1897.
14. Krupa, I., I. Novak and I. Chodak. 2004. Electrically and thermally conductive polyethylene/graphite composites and their mechanical properties. *Syn. Metals* 145: 245–252.
15. McLachlan, D.S., M. Blaszkiewicz and R.E. Newnham. 1990. Electrical resistivity of composites. *J. Am. Ceram. Soc*., 73: 2187–2203.
16. Peng, H.X., Z. Fan and J.R.G. Evans. 2001. Bi-continuous metal matrix composites, *Mat. Sci. Eng. A* 303: 37–45.
17. Pinto, G. and M.B. Maidana. 2001. Conducting polymer composites of zinc-filled nylon 6. *J. Appl. Poly. Sci.* 82: 1449–1454.
18. Campo, M.A., L.Y. Woo, T.O. Mason and E.J. Garboczi. 2002. Frequency-dependent electrical mixing law behavior in spherical particle composites. *J. Electro Ceram.* 9: 49–56.
19. Weber, L., J. Dorn and A. Mortensen. 2003. On the electrical conductivity of metal matrix composites containing high volume fractions of non-conducting inclusions. *Acta Materialia* 51: 3199–3211.
20. da Rocha, S.R.P., P.A. Psathas, E. Klein and K.P. Johnston. 2001. Concentrated CO_2-in-water emulsions with nonionic polymeric surfactants. *J. Colloid Int. Sci.* 239: 241–253.

21. Dhanuka, V.V., J.L. Dickson, W. Ryoo and K.P. Johnston. 2006. High internal phase CO_2-in-water emulsions stabilized with a branched nonionic hydrocarbon surfactant. *J. Colloid Int. Sci.* 298: 406–418.
22. Pal, R. 2007. On the electrical conductivity of particulate composites. *J. Composite Mater.* 41: 2499–2511.
23. McLachlan, D.S. 1987. An equation for the conductivity of binary mixtures with anisotropic grain structures. *J. Phys. C Solid State Phys.* C20: 865–877.
24. McLachlan, D.S. 1986. Equations for the conductivity of macroscopic mixtures. *J. Phys. C: Solid State Phys.* C19: 1339–1354.
25. McLachlan, D.S. 1987. Equation for the conductivity of heterogeneous binary media. *Jpn. J. Appl. Phys*. 26: 901–902.
26. McLachlan, D.S. 1988. Measurement and analysis of a model dual-conductivity medium using a generalized effective-medium theory. *J. Phys. C Solid State Phys.* C21: 1521–1532.
27. Pal, R. 2008. On the Lewis–Nielsen model for thermal/electrical conductivity of composites. *Composites A* 39: 718–726.
28. Lewis, T. and L. Nielsen. 1970. Dynamic mechanical properties of particulate filled composites. *J. Appl. Poly. Sci.* 14: 1449–1471.
29. Nielsen, L. 1973. Thermal conductivity of particulate filled polymers. *J. Appl. Poly. Sci.* 17: 3819–3820.
30. Nielsen, L. 1974. The thermal and electrical conductivity of two-phase systems. *Ind. Eng. Chem. Fundam.* 13: 17–20.
31. Ostwald, W.O. 1910. Beiträge zur Kenntnis der Emulsionen. *Kolloid-Z.* 6: 103.
32. Becher, P. 1977. *Emulsions: Theory and Practice,* 2nd ed., New York: Robert E. Krieger Publishing Company.
33. Pal, R. 1993. Pipeline flow of unstable and surfactant-stabilized emulsions. *AIChE J.* 39: 1754–1764.
34. Binks, B.P. and S.O. Lumsdon. 2000. Catastrophic phase inversion of water-in-oil emulsions stabilised by hydrophobic silica. *Langmuir* 16: 2539–2547.
35. Malhotra, V. 2009. Effects of mixed stabilizers (nanoparticles and surfactant) on phase inversion and stability of emulsions. M.A.Sc. thesis, University of Waterloo, Ontario, Canada.

3 Dielectric Properties of Composites

Materials with negligible electrical conductivity and high polarizability are referred to as "dielectric materials." Such materials do not possess free charges. However, they become polarized upon the application of an external electric field.

The dielectric properties of composites of nonconductive matrix are important from both practical and theoretical points of view. Two important practical applications where knowledge of the dielectric properties is required include (1) microwave heating of composite materials and (2) measurement of the composition of composite materials. As the dielectric properties of composite materials are dependent on their composition, the composition could be determined by measuring the dielectric constant.

3.1 BACKGROUND

When subjected to an external electric field, the molecules or atoms of a dielectric material undergo charge separation. The electron cloud of a molecule shifts in one direction and the positive ion core shifts in the opposite direction. Consequently, the molecules behave as electric dipoles, and the induced dipole field opposes the applied field. In the case of polar dielectric materials, the molecules or atoms possess a permanent dipole moment. These dipoles are randomly oriented in the absence of the external electric field. Upon the application of the electric field, the permanent dipoles become aligned with the applied field.

The key property of a dielectric material is the absolute dielectric permittivity (ε_{abs}), which is related to electric susceptibility (χ) as follows:

$$\varepsilon_{abs} = (1 + \chi)\varepsilon_o \tag{3.1}$$

where ε_o is vacuum permittivity, equal to 8.854×10^{-12} farad/m. The electric susceptibility χ is a measure of the degree of polarization of a material in response to an electric field ($\chi = 0$ for vacuum).

The key relation describing the dielectric behavior of a material is as follows:

$$\vec{D} = \varepsilon_{abs}\vec{E} \tag{3.2}$$

where $\vec{D}$ is the electric flux density (also known as electric displacement) which has units of coulomb/m^2, and $\vec{E}$ is the electric field strength. The units of ε_{abs} and $\vec{E}$ are farad/m and volt/m, respectively. According to Equation 3.2, the electric flux density

is directly proportional to the electric field strength in the medium. The proportionality constant is the property of the medium called absolute permittivity. As $\varepsilon_{abs} = \varepsilon_o\, \varepsilon$, where ε is the relative permittivity or dielectric constant (dimensionless), one can rewrite the electric flux density equation as

$$\vec{D} = \varepsilon_o \varepsilon \vec{E} \tag{3.3}$$

Equation 3.1 can be interpreted in terms of a parallel plate capacitor. The electric flux density is the amount of free or unbounded charge on the capacitor plates per unit area, that is, $D = \sigma_f$, where σ_f is free charge per unit area of the plate. In the absence of any dielectric material between the plates of a capacitor, the electric field strength between the plates is

$$E_{vacuum} = \sigma_f/\varepsilon_{abs} = \sigma_f/\varepsilon_o \tag{3.4}$$

Note that $\varepsilon = 1$ for vacuum. With the introduction of a dielectric material ($\varepsilon > 1$) between the plates, the electric field strength is reduced (assuming constant free charge density σ_f) as

$$E = D/\varepsilon_{abs} = \sigma_f/\varepsilon_o\varepsilon \tag{3.5}$$

The reduction in the field strength is caused by the polarization of the dielectric. Some of the free charge present on the plates is now neutralized by the induced (bound) charge on the surface of the dielectric.

Combining Equations 3.1 and 3.2 gives

$$\vec{D} = (1+\chi)\varepsilon_o \vec{E} \tag{3.6}$$

For a fixed amount of free charge (fixed $\vec{D}$), $\vec{E}$ is reduced upon the introduction of the dielectric between the capacitor plates as $\chi > 0$ for the dielectric. This equation could also be rewritten as

$$\vec{D} = \varepsilon_o \vec{E} + \vec{P} \tag{3.7}$$

where $\vec{P}$ is the polarization density vector, given as $\vec{P} = \chi\varepsilon_o\vec{E}$. The polarization density is a measure of the average induced dipole moment per unit volume of the dielectric material. It is also given as $\vec{P} = N\vec{p}$ where N is the number of molecules per unit volume and $\vec{p}$ is induced dipole moment of an individual molecule. The polarization vector is parallel to $\vec{E}$ and it points from the negative charge towards the positive charge (this convention is opposite to that used for the electric field).

Finally, it should be noted that if the electric field strength between the parallel plates of a capacitor is kept constant and the free-charge density σ_f is made variable by connecting the capacitor to an external current source of constant voltage, then

the introduction of a dielectric material between the plates will result in an increase in the free charge density or electric displacement (thus increasing the capacitance of the capacitor). Thus for a given electric field strength, higher the dielectric permittivity (or electric susceptibility) of the medium, greater is the free-charge density.

3.2 DIELECTRIC CONSTANT OF COMPOSITES

The dielectric constant or relative permittivity (ε) of composite materials depends on several factors such as composition (volume fractions of individual phases), dielectric constant of matrix, and dielectric constant of filler particles. It also depends on the shape of particles and morphology (aggregated versus uniformly dispersed particles).

A number of empirical and theoretical relations have been developed to predict the dielectric behavior of composites [1]. Several empirical relations can be expressed in the following form:

$$f(\varepsilon) = \phi f(\varepsilon_d) + (1 - \phi) f(\varepsilon_m) \tag{3.8}$$

where $f(\varepsilon)$ is some function of ε, ε is the dielectric constant of composite, ε_d and ε_m are the dielectric constants of dispersed phase and matrix, respectively. Some examples of the form of function $f(\varepsilon)$, and the resulting dielectric constant equation for composite, are given below:

$$f(\varepsilon) = \varepsilon \quad \Rightarrow \quad \varepsilon = \phi\varepsilon_d + (1 - \phi)\varepsilon_m \tag{3.9}$$

$$f(\varepsilon) = \frac{1}{\varepsilon} \quad \Rightarrow \quad \frac{1}{\varepsilon} = \frac{\phi}{\varepsilon_d} + \frac{1-\phi}{\varepsilon_m} \tag{3.10}$$

$$f(\varepsilon) = \log\varepsilon \quad \Rightarrow \quad \log\varepsilon = \phi\log\varepsilon_d + (1 - \phi)\log\varepsilon_m \tag{3.11}$$

The first expression corresponds to the Voigt rule of mixtures, the second one corresponds to the Reuss rule of mixtures, and the last one corresponds to the Lichtenecker logarithmic rule of mixtures.

Rayleigh [2] was probably the first to develop a model theoretically for the dielectric behavior of dispersions of spherical particles. He analyzed the electrostatic field for a simple cubic lattice arrangement of uniform-size spheres and developed the following equation for the dielectric constant of composite:

$$\frac{\varepsilon}{\varepsilon_m} = 1 + \left[\frac{3\phi}{\left(\frac{\varepsilon_d + 2\varepsilon_m}{\varepsilon_d - \varepsilon_m} \right) - \phi - 1.65 \left(\frac{\varepsilon_d - \varepsilon_m}{\varepsilon_d + 4\varepsilon_m/3} \right) \phi^{\frac{10}{3}}} \right] \tag{3.12}$$

The Maxwell theory [3] for the electrical conductivity of particulate composites can be adapted for the dielectric behavior of composites. Consider a cluster of

particles embedded in an infinite matrix of dielectric constant ε_m. The cluster of particles, enclosed by a spherical region of radius R, consists of n spherical particles of radius "a" and dielectric constant ε_d. The system is subjected to an electric field with a uniform potential gradient of −E at $r \to \infty$. Assuming negligible interaction between the particles, the potential at a radial distance r (r >> R) from the center of the spherical cluster region R is

$$V = -Er\cos\theta + E\left(\frac{\varepsilon_d - \varepsilon_m}{\varepsilon_d + 2\varepsilon_m}\right)\left(\frac{a^3}{r^2}\right)n\cos\theta \tag{3.13}$$

Since $\phi = n(a/R)^3$, Equation 3.13 can be rewritten as

$$V = -Er\cos\theta + E\left(\frac{\varepsilon_d - \varepsilon_m}{\varepsilon_d + 2\varepsilon_m}\right)\left(\frac{1}{r^2}\right)\phi R^3\cos\theta \tag{3.14}$$

Now if the cluster of particles is treated as an "effective homogeneous medium" of radius R and dielectric constant ε, suspended in a matrix of dielectric constant ε_m, the potential at any radial location r (>> R) is given as

$$V = -Er\cos\theta + E\left(\frac{\varepsilon - \varepsilon_m}{\varepsilon + 2\varepsilon_m}\right)\left(\frac{R^3}{r^2}\right)\cos\theta \tag{3.15}$$

Since the above two expressions, Equations 3.14 and 3.15, are equivalent, it follows that

$$\left(\frac{\varepsilon - \varepsilon_m}{\varepsilon + 2\varepsilon_m}\right) = \left(\frac{\varepsilon_d - \varepsilon_m}{\varepsilon_d + 2\varepsilon_m}\right)\phi \tag{3.16}$$

This equation (Equation 3.16) is given various different names in the literature, such as Maxwell–Garnett equation, Maxwell–Wagner equation, Clausius–Mossotti equation, Lorentz–Lorentz equation, and Weiner equation. It may be of interest to note that Maxwell–Garnett and Maxwell are not related. Maxwell is famous for his equations of electromagnetism. Maxwell–Garnett worked on dielectric and optical properties of glasses with metallic inclusions [4,5].

The Maxwell–Garnett equation can be rearranged as

$$\frac{\varepsilon}{\varepsilon_m} = \left[\frac{1 + 2\phi\left(\frac{\varepsilon_d - \varepsilon_m}{\varepsilon_d + 2\varepsilon_m}\right)}{1 - \phi\left(\frac{\varepsilon_d - \varepsilon_m}{\varepsilon_d + 2\varepsilon_m}\right)}\right] \tag{3.17}$$

In the limit $\phi \to 0$, Equation 3.17 reduces to the following expression:

$$\frac{\varepsilon}{\varepsilon_m} = 1 + 3\left(\frac{\varepsilon_d - \varepsilon_m}{\varepsilon_d + 2\varepsilon_m}\right)\phi \tag{3.18}$$

Interestingly, the Rayleigh expression reduces to the Maxwell–Garnett equation when the term containing $\phi^{10/3}$ in the denominator of the Rayleigh equation is neglected. Thus, the Maxwell–Garnett equation is valid for dilute to moderately concentrated composites.

The Maxwell–Garnett equation for dilute systems (Equation 3.18) can be extended to concentrated systems using the differential effective medium approach. According to the differential effective medium approach, a concentrated composite is considered to be obtained from an initial matrix phase by successively adding infinitesimally small quantities of particles to the system until the final volume fraction of filler is reached. The incremental change in dielectric constant upon the addition of an infinitesimally small quantity of particles to the system can be determined from Equation 3.18 as

$$d\varepsilon = 3\varepsilon\left[\frac{\varepsilon_d - \varepsilon}{\varepsilon_d + 2\varepsilon}\right]d\phi \tag{3.19}$$

This equation can be rewritten as

$$\frac{1}{3}\left[\frac{1}{\varepsilon} + \frac{3}{\varepsilon_d - \varepsilon}\right]d\varepsilon = d\phi \tag{3.20}$$

Upon integration with the limit $\varepsilon \to \varepsilon_m$ at $\phi \to 0$, Equation 3.20 gives

$$\left[\frac{\varepsilon}{\varepsilon_m}\right]^{\frac{1}{3}}\left(\frac{\varepsilon_d - \varepsilon_m}{\varepsilon_d - \varepsilon}\right) = \exp(\phi) \tag{3.21}$$

Equation 3.21 is expected to describe the dielectric behavior of particulate composites at low to moderate values of ϕ (volume fraction of particles). This is because in the derivation of the differential equation (Equation 3.20) leading to the final expression (Equation 3.21), it is assumed that all the volume of the existing composite, before a differential quantity of new particles are added to the existing composite, is available as free volume to the new particles. In reality, the free volume available to disperse the new particles is significantly less, due to the volume preempted by the particles already present. This means that when a differential quantity of new particles are added to the existing composite the increase in the actual volume fraction

of the dispersed phase is larger than dϕ. The increase in the volume fraction of the dispersed phase is dϕ/(1 − ϕ). Thus, Equation 3.20 should be revised as

$$\frac{1}{3}\left[\frac{1}{\varepsilon}+\frac{3}{\varepsilon_d-\varepsilon}\right]d\varepsilon=\frac{d\phi}{1-\phi} \tag{3.22}$$

Upon integration with the limit $\varepsilon \to \varepsilon_m$ at $\phi \to 0$, Equation 3.22 gives

$$\left(\frac{\varepsilon_m}{\varepsilon}\right)^{\frac{1}{3}}\left(\frac{\varepsilon-\varepsilon_d}{\varepsilon_m-\varepsilon_d}\right)=1-\phi \tag{3.23}$$

This is the well-known asymmetric Bruggeman equation [6].

Bruggeman developed another useful relation for the dielectric constant of percolating composites [6]. His model, referred to as the Bruggeman symmetric rule, is given as follows:

$$\left(\frac{\varepsilon_d-\varepsilon}{\varepsilon_d+2\varepsilon}\right)\phi+\left(\frac{\varepsilon_m-\varepsilon}{\varepsilon_m+2\varepsilon}\right)(1-\phi)=0 \tag{3.24}$$

This equation is quadratic in ε. Of its two solutions, only the following one is physically possible:

$$\varepsilon=\frac{1}{4}\left(q+\sqrt{q^2+8\varepsilon_m\varepsilon_d}\right) \tag{3.25}$$

where

$$q=(3\phi-1)\varepsilon_d+(2-3\phi)\varepsilon_m \tag{3.26}$$

The Bruggeman symmetric rule predicts percolation threshold of $\frac{1}{3}$, that is, a sharp change in the dielectric constant is expected around the dispersed phase volume fraction of $\frac{1}{3}$, assuming large contrast between the dielectric constants of dispersed and matrix phases.

The models discussed thus far do not consider the influence of particle size, particle shape, and particle size distribution on the dielectric behavior of composites. Aggregation or flocculation of particles is also neglected. The Bruggeman symmetric model predicts percolation at a dispersed phase volume fraction of $\frac{1}{3}$. This may not be the case for all composite systems, especially when the particles are nonspherical and the particle size distribution is wide. To overcome some of these problems, Pal [7] proposed the following model for the dielectric behavior of composites:

$$\left(\frac{\varepsilon_m}{\varepsilon}\right)^{\frac{1}{3}}\left(\frac{\varepsilon-\varepsilon_d}{\varepsilon_m-\varepsilon_d}\right)=\left(1-\frac{\phi}{\phi_m}\right)^{\phi_m} \tag{3.27a}$$

where ϕ_m is the maximum packing volume fraction of filler particles. This equation reduces to the Bruggeman asymmetric model when $\phi_m \rightarrow 1$. The Pal model takes into account the effects of particle size distribution and morphology on the dielectric constant through the parameter ϕ_m. The maximum packing volume fraction of filler particles is sensitive to particle size distribution and aggregation of particles. Another useful model, presented here for the first time without proof, which considers the crowding effect of particles on the dielectric constant is as follows:

$$\left(\frac{\varepsilon_m}{\varepsilon}\right)^{\frac{1}{3}} \left(\frac{\varepsilon - \varepsilon_d}{\varepsilon_m - \varepsilon_d}\right) = \exp\left(-\frac{\phi}{1-\frac{\phi}{\phi_m}}\right) \tag{3.27b}$$

As suggested by Pal [7], the Lewis–Nielsen conductivity model [8–11] could also be adapted to describe the dielectric behavior of composites:

$$\frac{\varepsilon}{\varepsilon_m} = \left[\frac{1+2\left(\frac{\varepsilon_d - \varepsilon_m}{\varepsilon_d + 2\varepsilon_m}\right)\phi}{1-\phi\psi\left(\frac{\varepsilon_d - \varepsilon_m}{\varepsilon_d + 2\varepsilon_m}\right)}\right] \tag{3.28}$$

where

$$\psi = 1 + \left(\frac{1-\phi_m}{\phi_m^2}\right)\phi \tag{3.29}$$

The Lewis–Nielsen model is a modification of the Maxwell–Garnett model. When $\phi_m \rightarrow 1$, the Lewis–Nielsen model reduces to the Maxwell–Garnett model.

Figure 3.1 shows the plots of relative dielectric constant $\varepsilon/\varepsilon_m$ versus dielectric ratio λ (= $\varepsilon_d/\varepsilon_m$) predicted from the Lewis–Nielsen model (Equation 3.28) for different values of filler concentration ϕ. The maximum packing volume fraction ϕ_m is taken to be 0.64 corresponding to random close packing of uniform spheres. When the dielectric ratio λ is unity, the relative dielectric constant is unity regardless of the value of filler concentration ϕ. When $\lambda < 1.0$, the relative dielectric constant decreases with the increase in ϕ; a reverse trend is observed when $\lambda > 1.0$; that is, the relative dielectric constant increases with the increase in ϕ.

Figure 3.2 shows the sensitivity of relative dielectric constant to ϕ_m, the maximum packing volume fraction of particles. When $\lambda > 1.0$, the relative dielectric constant of particulate composite is quite sensitive to ϕ_m. The relative dielectric constant at any given volume fraction of filler (ϕ) increases with the decrease in ϕ_m. When $\lambda < 1.0$, the relative dielectric constant of the composite is not as sensitive to ϕ_m. Furthermore, the relative dielectric constant now decreases with the decrease in ϕ_m. As the maximum packing volume fraction of particles (ϕ_m) is a strong function of

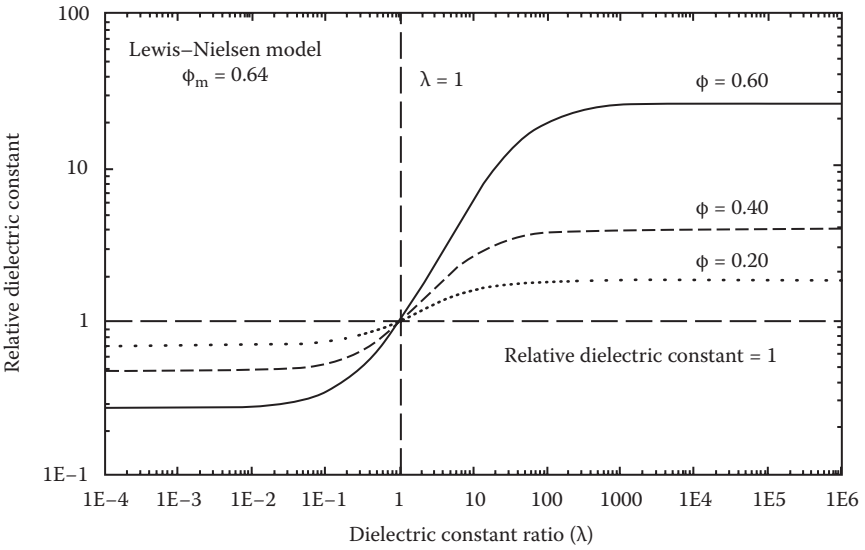

FIGURE 3.1 Relative dielectric constant ε_r (= $\varepsilon/\varepsilon_m$) versus dielectric ratio λ (= $\varepsilon_d/\varepsilon_m$) predicted from the Lewis–Nielsen model for different values of ϕ (volume fraction of filler particles).

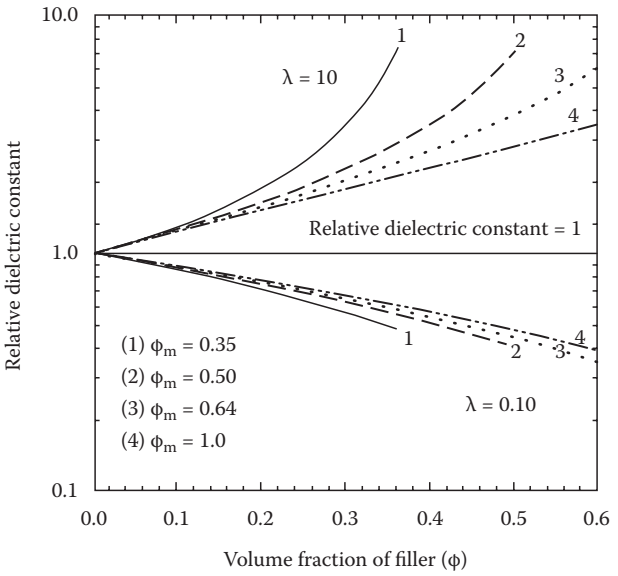

FIGURE 3.2 Relative dielectric constant ε_r (= $\varepsilon/\varepsilon_m$) versus volume fraction of filler particles (ϕ) for different values of ϕ_m, the maximum packing volume fraction of particles.

particle size distribution and shape of particles, the effects of microstructure (size distribution, shape, aggregation of particles) on the relative dielectric constant of composite cannot be ignored.

3.3 INFLUENCE OF INTERPHASE REGION ON DIELECTRIC BEHAVIOR OF COMPOSITES

The dielectric constant of the material in the interphase region adjacent to the surface of the filler particles could be significantly different from that of the matrix due to the presence of additives such as surfactants and coupling agents at the surface of the particles. The covalent bonding of the polymer molecules of the matrix with the surface of the filler particles is another possible reason for the difference in the dielectric constants of the interphase region and bulk matrix. Thus it is important to investigate the influence of interphase region on the dielectric behavior of particle-filled composites.

In order to take into account the influence of the interphase region on the dielectric behavior of composites, the filler particles could be treated as core-and-shell-type particles. Let the dielectric constants of the core, shell, and matrix be ε_3, ε_2, and ε_1, respectively. Let the radius of the core be "a," the thickness of the shell be "d," and the volume fraction of core in the core-shell particle be ϕ_c. Note that $\phi_c = (a/(a + d))^3 = 1/\delta^3$ where δ is the ratio of outer radius of interfacial shell to core radius. Now consider a cluster of core-shell particles embedded in an infinite matrix of dielectric constant ε_1. The cluster of core-shell particles, enclosed by a spherical region of radius R, consists of n spherical core-shell particles. The system is subjected to an electric field with a uniform potential gradient of $-E$ at $r \to \infty$. Assuming negligible interaction between the core-shell particles, the potential at a radial distance r ($r >> R$) from the center of the spherical cluster region R is

$$V = -Er\cos\theta - E\left[\frac{(\varepsilon_1-\varepsilon_2)(2\varepsilon_2+\varepsilon_3)+(\varepsilon_2-\varepsilon_3)(2\varepsilon_2+\varepsilon_1)\phi_c}{(2\varepsilon_1+\varepsilon_2)(2\varepsilon_2+\varepsilon_3)+2(\varepsilon_1-\varepsilon_2)(\varepsilon_2-\varepsilon_3)\phi_c}\right]\left[\frac{(a+d)^3}{r^2}\right]n\cos\theta \tag{3.30}$$

Since the volume fraction of core-shell particles in the dispersion is $\phi = n\,[(a + d)/R]^3$, Equation 3.30 can be rewritten as

$$V = -Er\cos\theta - E\left[\frac{(\varepsilon_1-\varepsilon_2)(2\varepsilon_2+\varepsilon_3)+(\varepsilon_2-\varepsilon_3)(2\varepsilon_2+\varepsilon_1)\phi_c}{(2\varepsilon_1+\varepsilon_2)(2\varepsilon_2+\varepsilon_3)+2(\varepsilon_1-\varepsilon_2)(\varepsilon_2-\varepsilon_3)\phi_c}\right]\left[\frac{R^3}{r^2}\right]\phi\cos\theta \tag{3.31}$$

Now if the cluster of core-shell particles is treated as an "effective homogeneous medium" of radius R and dielectric constant ε, suspended in a matrix of dielectric constant ε_1, the potential at any radial location r ($>> R$) is given as

$$V = -Er\cos\theta - E\left(\frac{\varepsilon_1-\varepsilon}{2\varepsilon_1+\varepsilon}\right)\left(\frac{R^3}{r^2}\right)\cos\theta \tag{3.32}$$

As the above two expressions, Equations 3.31 and 3.32, are equivalent, it follows that

$$\left(\frac{\varepsilon_1-\varepsilon}{2\varepsilon_1+\varepsilon}\right)=\left[\frac{(\varepsilon_1-\varepsilon_2)(2\varepsilon_2+\varepsilon_3)+(\varepsilon_2-\varepsilon_3)(2\varepsilon_2+\varepsilon_1)\phi_c}{(2\varepsilon_1+\varepsilon_2)(2\varepsilon_2+\varepsilon_3)+2(\varepsilon_1-\varepsilon_2)(\varepsilon_2-\varepsilon_3)\phi_c}\right]\phi \tag{3.33}$$

This expression was first developed by Pauly and Schwan [1,12]. Upon rearrangement, this equation could be recast in different forms as shown below:

$$\frac{\varepsilon}{\varepsilon_1}=\left[\frac{(1+2\phi)\varepsilon_2\beta_o+2(1-\phi)\varepsilon_1\gamma_o}{(1-\phi)\varepsilon_2\beta_o+(2+\phi)\varepsilon_1\gamma_o}\right] \tag{3.34}$$

$$\frac{\varepsilon}{\varepsilon_1}=\left[\frac{1+2\left(\frac{\beta-\gamma}{\beta+2\gamma}\right)\phi}{1-\phi\left(\frac{\beta-\gamma}{\beta+2\gamma}\right)}\right] \tag{3.35}$$

where

$$\beta_o=(1+2\phi_c)\varepsilon_3+2(1-\phi_c)\varepsilon_2 \quad \text{and} \quad \gamma_o=(1-\phi_c)\varepsilon_3+(2+\phi_c)\varepsilon_2 \tag{3.36}$$

$$\beta=\beta_o/(\phi_c\varepsilon_1) \quad \text{and} \quad \gamma=\gamma_o/(\phi_c\varepsilon_2) \tag{3.37}$$

The Pauly–Schwan model, Equation 3.35, reduces to the Maxwell–Garnett model when $\phi_c = 1$ (no interfacial shell, $\delta = 1$). However, it is valid only when the volume fraction of core-shell particles ϕ is small to moderate. Furthermore, it does not take into consideration the packing limit of particles and the morphology of composite (particle size distribution, flocculation/aggregation of particles). To overcome these limitations of the Pauly–Schwan model, Pal [7] recently proposed the following model:

$$\frac{\varepsilon}{\varepsilon_1}=\left[\frac{1+2\left(\frac{\beta-\gamma}{\beta+2\gamma}\right)\phi}{1-\phi\psi\left(\frac{\beta-\gamma}{\beta+2\gamma}\right)}\right] \tag{3.38}$$

where β and γ are as defined above in Equation 3.37 and ψ is given by Equation 3.29. This model reduces to the Pauly–Schwan model when $\phi_m \to 1$. When $\phi_c \to 1$, that is, no interfacial shell, this model reduces to the Lewis–Nielsen model. When $\phi_m \to 1$ and $\phi_c \to 1$, the Maxwell–Garnett model is recovered.

According to the Pal model (Equation 3.38), the relative dielectric constant of a composite consisting of particles with interfacial layers can be expressed as

$$\varepsilon_r = \frac{\varepsilon}{\varepsilon_1} = f(\delta, \lambda_{21}, \lambda_{32}, \phi, \phi_m) \tag{3.39}$$

where δ is the ratio of outer radius of interfacial shell to core radius, $\lambda_{21} = \varepsilon_2/\varepsilon_1$ and $\lambda_{32} = \varepsilon_3/\varepsilon_2$. Note that $\lambda_{31} = \lambda_{21}\lambda_{32}$ and $\delta^3 = 1/\phi_c$.

Figure 3.3 shows the relative dielectric constant predicted from the Pal model for different values of ϕ, the volume fraction of core plus shell particles. The plots are generated from Equation 3.38 under the following conditions: $\delta = 4/3$, $\lambda_{32} = 100$, $\phi_m = 0.64$. At a fixed value of ϕ, the relative dielectric constant (ε_r) remains constant initially with the increase in the dielectric ratio λ_{21}. In the range $10^{-2} < \lambda_{21} < 100$, ε_r increases with the increase in λ_{21}. At higher values of λ_{21} ($\lambda_{21} > 100$), ε_r again becomes constant (independent of λ_{21}). Interestingly, ε_r is less than unity for small values of λ_{21} and ε_r is greater than unity when λ_{21} is large. For low values of λ_{21}, ε_r decreases with the increase in ϕ. For large values of λ_{21}, ε_r increases with the increase in ϕ.

Figure 3.4 shows the plots of relative dielectric constant ε_r versus dielectric ratio λ_{21} for different values of radii ratio δ. The plots are generated from Equation 3.38 under the following conditions: $\phi = 0.55$, $\phi_m = 0.64$, $\lambda_{32} = 1000$. The radii ratio δ,

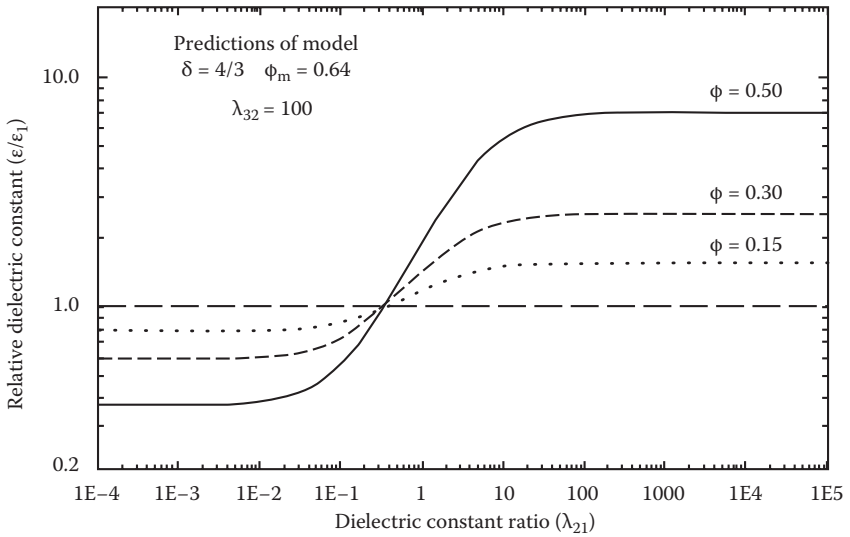

FIGURE 3.3 Relative dielectric constant ε_r ($= \varepsilon/\varepsilon_1$) versus dielectric ratio λ_{21} ($= \varepsilon_2/\varepsilon_1$) behavior predicted by the proposed model (Equation 3.38) under the following conditions: $\delta = 4/3$, $\lambda_{32} = 100$, and $\phi_m = 0.64$. Note that λ_{21} is the ratio of interfacial shell dielectric constant to matrix dielectric constant, λ_{32} is the ratio of filler core-particle dielectric constant to interfacial shell dielectric constant, and δ is the ratio of outer radius of interfacial shell to radius of filler core-particle.

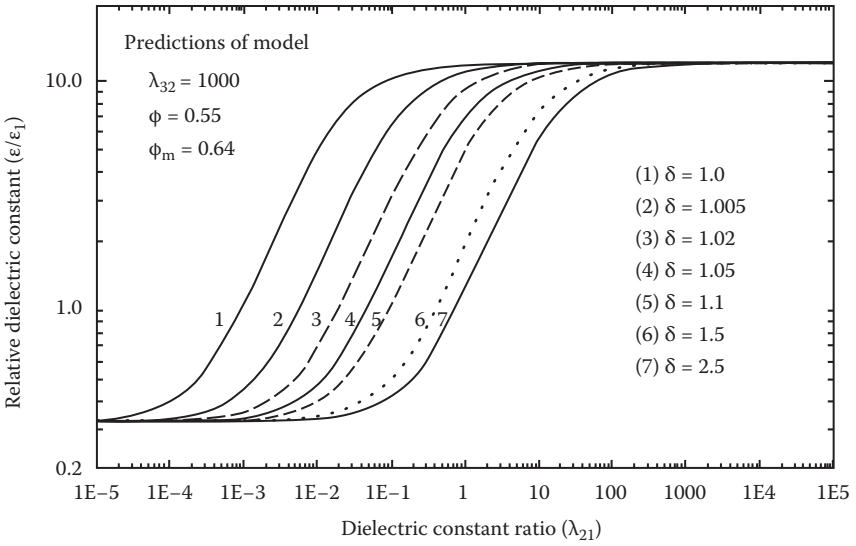

FIGURE 3.4 Relative dielectric constant ε_r (= $\varepsilon/\varepsilon_1$) versus dielectric ratio λ_{21} (= $\varepsilon_2/\varepsilon_1$) plots for different values of radii ratio δ under the following conditions: ϕ = 0.55, ϕ_m = 0.64, and λ_{32} = 1000.

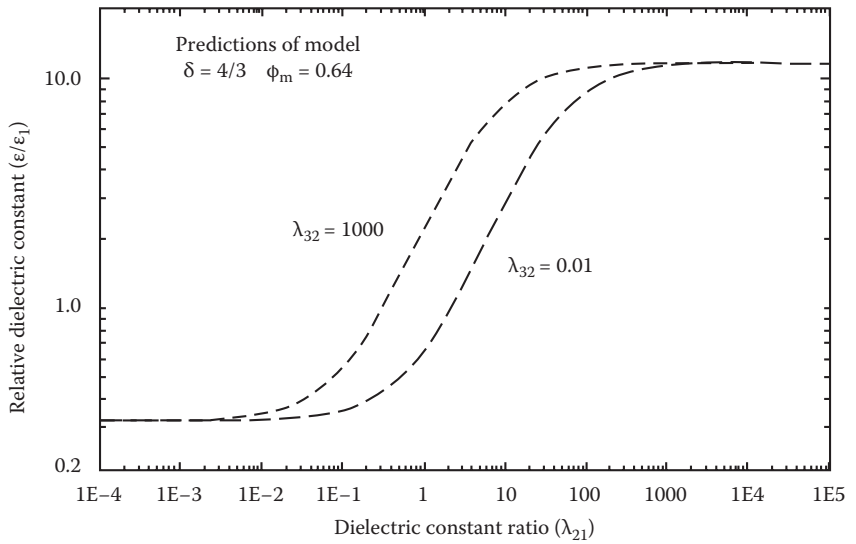

FIGURE 3.5 Effect of dielectric ratio λ_{32} (ratio of filler core-particle dielectric constant to interfacial shell dielectric constant) on the ε_r versus λ_{21} behavior under the following conditions: ϕ_m = 0.64, and δ = 4/3.

and hence the thickness of the interfacial layer, has a strong influence on the relative dielectric constant, especially in the intermediate range of dielectric ratio λ_{21}. At very low and very high values of λ_{21}, ε_r of the composite is independent of the radii ratio δ. In the intermediate range of λ_{21}, ε_r decreases with the increase in δ or the shell thickness of the core-shell particle.

The effect of dielectric ratio λ_{32} on ε_r versus λ_{21} behavior of composite is shown in Figure 3.5, under the following conditions: $\phi = 0.55$, $\phi_m = 0.64$, $\delta = 4/3$. With the increase in λ_{32} (dielectric constant of core material divided by dielectric constant of shell material), the relative dielectric constant ε_r of a composite increases for intermediate values of λ_{21} ($10^{-2} < \lambda_{21} < 100$). However, the effect of λ_{32} on the dielectric constant of composite is moderate.

REFERENCES

1. Hanai, T. 1968. Electrical properties of emulsions. In: *Emulsion Science*, ed. P. Sherman, London: Academic Press.
2. Rayleigh, L. 1892. On the influence of obstacles arranged in rectangular order on the properties of a medium. *Phil. Mag.* 34: 481.
3. Maxwell, J.C. 1881. *A Treatise on Electricity and Magnetism*, 2nd ed., Vol. 1, p. 435, Oxford: Clarendon Press.
4. Maxwell–Garnett, J.C. 1904. Colors in metal glasses and in metallic films. *Philos. Trans. R. Soc. Lond.* 203: 385–420.
5. Landauer, R. 1978. Electrical conductivity in inhomogeneous media. In: *AIP Conference Proceedings—Electrical Transport and Optical Properties of Inhomogeneous Media*. eds. J.C. Garland and D.B. Tanner, Vol. 40, pp. 2–43, New York: American Institute of Physics.
6. Bruggeman, D.A.G. 1935. Berechnung verschiedener physikalischer Konstanten von heterogenen Substanzen. *Ann. Phys. (Leipzig)* 24: 636–679.
7. Pal, R. 2008. Dielectric behavior of double emulsions with core-shell droplet morphology. *J. Colloid Interface Sci.* 325: 500–507.
8. Pal, R. 2008. On the Lewis–Nielsen model for thermal/electrical conductivity of composites. *Composites A* 39: 718–726.
9. Lewis, T. and L. Nielsen. 1970. Dynamic mechanical properties of particulate filled composites. *J. Appl. Poly. Sci.* 14: 1449–1471.
10. Nielsen, L. 1973. Thermal conductivity of particulate filled polymers. *J. Appl. Poly. Sci.* 17: 3819–3820.
11. Nielsen L. 1974. The thermal and electrical conductivity of two-phase systems. *Ind. Eng. Chem. Fundam.* 13: 17–20.
12. Pauly, H. and H.P. Schwan. 1959. Über die Impedanz einer Suspension von kugelformigen Teilchen mit einer Schale. *Z. Naturforsch*. 146: 125–131.

4 Magnetic Properties of Composites

The magnetic properties of composite materials are of interest in many industrial applications dealing with electrical and electronic instruments, electrical power generators and transformers, electric motors, radio, television, telephones, computers, audio and video equipment, and household utensils [1–3].

4.1 BACKGROUND

The bulk magnetic properties of materials are due to magnetic moments associated with the individual electrons [4]. Each electron in an atom possesses a magnetic moment. The magnetic moment of an electron is due to two reasons: (1) orbital rotation and (2) spinning. An electron orbiting around the nucleus produces a magnetic moment along the axis of rotation because an orbiting electron or charge is equivalent to a small current loop. The spinning of an electron around an axis produces a magnetic moment directed along the spin axis. Thus, each electron of an atom is a small magnet with permanent orbital and spin magnetic moments. The net magnetic moment of an atom is the vector sum of the magnetic moments of the constituent electrons, taking into consideration both orbital and spin contributions. In most atoms, electrons occur in pairs. Electrons in a pair spin in opposite directions, and their magnetic fields cancel each other. Likewise, the orbital moments of paired electrons cancel each other as paired electrons orbit in opposite directions. Therefore, atoms consisting of all paired electrons have no net magnetic moment due to total cancellation of orbital and spin moments.

In nonmagnetic (diamagnetic) materials, the electrons of an atom are all paired up, and therefore, there is no net magnetic moment per atom. In paramagnetic materials, the atoms consist of some unpaired electrons. Consequently, the atoms possess a net magnetic moment due to incomplete cancellation of orbital and/or spin magnetic moments. The atoms of a ferromagnetic material also possess permanent magnetic dipole moment, mainly due to uncancelled electron spins. The contribution due to orbital magnetic moments is small in comparison with the spin magnetic moments. However, ferromagnetic materials exhibit a long-range ordering effect at the atomic level meaning that the dipole moments of neighboring atoms align with each other to form domains of intense magnetic field.

The bulk samples of diamagnetic and paramagnetic materials do not possess any net magnetic moments, in the absence of externally imposed magnetic field. This is not unexpected in the case of diamagnetic material, as the atoms of a diamagnetic material have no net dipole moments. The bulk samples of a paramagnetic material, however, do not possess net magnetic moments, as the moments of the

individual atoms are randomly oriented in the absence of an external magnetic field. Likewise, the bulk samples of ferromagnetic materials also do not generally possess a net magnetic moment in the absence of an external magnetic field because of random orientation of magnetic domains. However, different materials respond very differently to externally imposed magnetic field. Diamagnetic materials become only weakly magnetized under the application of the external magnetic field. The induced magnetic moment is rather small and is directed in the direction opposite to the applied magnetic field. The induced moment is caused by a change in the orbital motion of the electrons. Upon the removal of the applied field, the material becomes demagnetized. Paramagnetic materials also become weakly magnetized upon the application of external magnetic field. When magnetic field is imposed, some of the atomic dipoles of the material become aligned with the field, resulting in an increase in the strength of the field. The degree of magnetization is small, as the dipoles of paramagnetic material do not interact with each other to form domains. A large magnetic field is needed to align all the dipoles with the imposed field. The magnetization effect in paramagnetic materials disappears upon removal of the applied field. Ferromagnetic materials, however, become strongly magnetized upon the application of the imposed magnetic field. A large magnetization effect is observed even with application of small magnetic fields due to alignment of magnetic domains of the material. These materials also tend to stay magnetized to some extent even after the imposed magnetic field is removed although all ferromagnetic materials become demagnetized above the Curie temperature due to thermal agitation.

The key magnetic property of a material is its absolute magnetic permeability (μ_{abs}), which is related to magnetic susceptibility (χ_m) as follows:

$$\mu_{abs} = (1 + \chi_m)\mu_o \tag{4.1}$$

where μ_o is vacuum permeability, equal to $4\pi \times 10^{-7}$ henry/m. The magnetic susceptibility χ_m is a measure of the degree of magnetization of a material in response to an external magnetic field. $\chi_m = 0$ for vacuum, χ_m is small but negative for diamagnetic materials ($\chi_m \approx -10^{-5}$), χ_m is small but positive for paramagnetic materials ($\chi_m \approx 10^{-4}$), and χ_m is large and positive for ferromagnetic materials (χ_m is as large as 10^6).

The key relation describing the magnetic behavior of a material is given as

$$\vec{B} = \mu_{abs} \vec{H} \tag{4.2}$$

where $\vec{B}$ is the magnetic flux density (also known as magnetic induction) in the material, which has units of tesla or weber/m^2, and $\vec{H}$ is the applied or external magnetic field (also called magnetic field strength), which has units of amperes/m. Note that the external magnetic field could be generated by passing current through a cylindrical coil (called a solenoid). If the coil consists of N closely spaced turns and its total length is L, then the produced magnetic field strength H is given as

$$H = \frac{NI}{L} \tag{4.3}$$

where I is the current passing through the coil. From this equation, the units of H are as follows: amperes-turn per meter or simply amperes/m.

According to Equation 4.2, the magnetic flux density is directly proportional to the magnetic field strength in the medium. The proportionality constant is the property of the medium called magnetic permeability. As $\mu_{abs} = \mu_o\mu$ where μ is the relative magnetic permeability, one can rewrite the magnetic flux density equation as

$$\vec{B} = \mu_o \mu \vec{H} \tag{4.4}$$

Although $\vec{B}$ is always in the same direction as the applied field $\vec{H}$, its magnitude could be lower or higher depending upon the nature of the material. For example, $|\vec{B}| < |\vec{H}|$ for diamagnetic materials and $|\vec{B}| >> |\vec{H}|$ for ferromagnetic materials.

Combining Equations 4.1 and 4.2 gives

$$\vec{B} = (1 + \chi_m)\mu_o \vec{H} \tag{4.5}$$

This equation could also be rewritten as

$$\vec{B} = \mu_o(\vec{H} + \vec{M}) \tag{4.6}$$

where $\vec{M}$ is the magnetization density vector given as $\vec{M} = \chi_m \vec{H}$. It should be noted that $\vec{H}$ is the magnetic field due to "normal or free electric currents" (normal current is due to motion of free charge). However, the magnetization $\vec{M}$ is due to "bound currents" (bound current is current that is "bound up" in electron orbits and is part of the material), and $\vec{B}$ is magnetic field due to total current, that is, the sum of free and bound currents.

When an external magnetic field is applied, the magnetic moments within a material become aligned with the applied field. The magnetization density, defined as an average induced magnetic moment per unit volume of the material, is a measure of the contribution of induced dipole moments to magnetic flux density $\vec{B}$. If the applied field strength $\vec{H}$ is kept constant (by keeping the current flow through the solenoid constant), then the introduction of a magnetic material in the solenoid will result in an increase in the magnetic flux density (assuming $\chi_m > 0$). Thus for a given magnetic field strength, higher the relative magnetic permeability (or magnetic susceptibility) of the medium, greater is the magnetic flux density.

In what follows, the magnetic properties of composites are discussed. The relative magnetic permeability μ is simply referred to as magnetic permeability in the discussion.

4.2 MAGNETIC PROPERTIES OF COMPOSITES

According to the "Generalized Conductivity Principle" discussed in Chapter 5, the equations used for the calculation of dielectric constant ε of composite could also be used for the calculation of magnetic permeability μ of composite by simply replacing ε with μ. This is possible as the electric- and magnetic-field equations are equivalent in the absence of the electric charge and current sources.

The effective magnetic permeability of a composite material consisting of particles of magnetic material embedded in a polymeric binder (matrix) is a function of the permeabilities of the individual phases and their volume fractions. The key equations for estimating the magnetic permeability of composites are as follows [5]:

Voigt rule of mixtures:

$$\mu = \mu_d \phi + (1 - \phi)\mu_m \tag{4.7}$$

Reuss rule of mixtures:

$$\frac{1}{\mu} = \frac{\phi}{\mu_d} + \frac{1-\phi}{\mu_m} \tag{4.8}$$

Lichtenecker logarithmic rule of mixtures:

$$\log\mu = \phi \log\mu_d + (1 - \phi)\log\mu_m \tag{4.9}$$

Rayleigh equation:

$$\frac{\mu}{\mu_m} = 1 + \left[\frac{3\phi}{\left(\frac{\mu_d + 2\mu_m}{\mu_d - \mu_m} \right) - \phi - 1.65 \left(\frac{\mu_d - \mu_m}{\mu_d + 4\mu_m/3} \right) \phi^{\frac{10}{3}}} \right] \tag{4.10}$$

Maxwell–Garnett equation:

$$\left(\frac{\mu - \mu_m}{\mu + 2\mu_m} \right) = \left(\frac{\mu_d - \mu_m}{\mu_d + 2\mu_m} \right) \phi \tag{4.11}$$

Pal model 1:

$$\left[\frac{\mu}{\mu_m} \right]^{\frac{1}{3}} \left(\frac{\mu_d - \mu_m}{\mu_d - \mu} \right) = \exp(\phi) \tag{4.12}$$

Bruggeman asymmetric model:

$$\left(\frac{\mu_m}{\mu}\right)^{\frac{1}{3}} \left(\frac{\mu-\mu_d}{\mu_m-\mu_d}\right) = (1-\phi) \tag{4.13}$$

Bruggeman symmetric model:

$$\left(\frac{\mu_d-\mu}{\mu_d+2\mu}\right)\phi + \left(\frac{\mu_m-\mu}{\mu_m+2\mu}\right)(1-\phi) = 0 \tag{4.14}$$

Pal model 2:

$$\left(\frac{\mu_m}{\mu}\right)^{\frac{1}{3}} \left(\frac{\mu-\mu_d}{\mu_m-\mu_d}\right) = \left(1-\frac{\phi}{\phi_m}\right)^{\phi_m} \tag{4.15}$$

Pal model 3:

$$\left(\frac{\mu_m}{\mu}\right)^{\frac{1}{3}} \left(\frac{\mu-\mu_d}{\mu_m-\mu_d}\right) = \exp\left(-\frac{\phi}{1-\frac{\phi}{\phi_m}}\right) \tag{4.16}$$

Lewis–Nielsen model:

$$\frac{\mu}{\mu_m} = \left[\frac{1+2\left(\frac{\mu_d-\mu_m}{\mu_d+2\mu_m}\right)\phi}{1-\phi\psi\left(\frac{\mu_d-\mu_m}{\mu_d+2\mu_m}\right)}\right] \tag{4.17a}$$

where

$$\psi = 1+\left(\frac{1-\phi_m}{\phi_m^2}\right)\phi \tag{4.17b}$$

In Equations 4.7 through 4.17, μ is the magnetic permeability of composite, μ_d and μ_m are magnetic permeabilities of dispersed and matrix phases, respectively, ϕ is the volume fraction of the dispersed phase, and ϕ_m is the maximum packing volume fraction of filler particles.

Figure 4.1 compares the predictions of key models for composites with $\mu_d = 10$ and $\mu_m = 1$. The relative magnetic permeability, defined as μ/μ_m, is plotted as a function

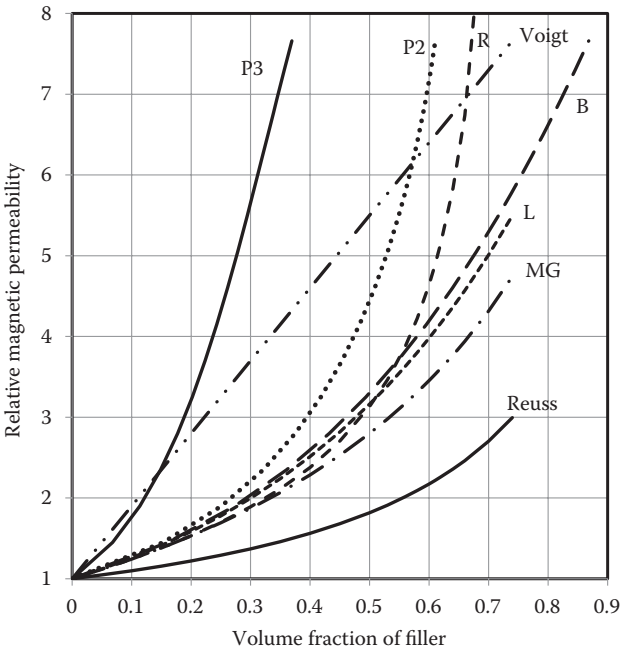

FIGURE 4.1 Comparison of the relative magnetic permeability (μ/μ_m) predicted from different models ($\mu_d = 10$ and $\mu_m = 1$). P3, Pal model 3; P2, Pal model 2; R, Rayleigh model; B, Bruggeman model; L, Lichtenecker logarithmic rule of mixtures; MG, Maxwell–Garnett model.

of the volume fraction of dispersed phase. The Pal model 3 (Equation 4.16) generally predicts the highest value whereas the Reuss ROM (rule of mixtures) predicts the lowest value of the relative permeability. The predictions of other models generally fall in between the predictions of the Pal model 3 and Reuss rule of mixtures. Note that ϕ_m, the maximum packing volume fraction of filler particles, is taken to be 0.637 in the Pal models. Among the three rules of mixtures (Voigt, Reuss, and Lichtenecker), the Voigt ROM predicts the highest value. The predictions of the Lichtenecker logarithmic ROM are close to those of the Bruggeman model and fall in between those of the Voigt and Reuss ROMs.

If the interphase region properties are different from that of the matrix and the composite is not highly concentrated, the Pauly–Schwan model could be applied to predict the magnetic permeability of composites:

$$\frac{\mu}{\mu_1} = \left[\frac{1 + 2\left(\frac{\beta - \gamma}{\beta + 2\gamma}\right)\phi}{1 - \phi\left(\frac{\beta - \gamma}{\beta + 2\gamma}\right)} \right] \tag{4.18}$$

where

$$\beta = \beta_o/(\phi_c\mu_1) \quad \text{and} \quad \gamma = \gamma_o/(\phi_c\mu_2) \tag{4.19}$$

$$\beta_o = (1 + 2\phi_c)\mu_3 + 2(1 - \phi_c)\mu_2 \quad \text{and} \quad \gamma_o = (1 - \phi_c)\mu_3 + (2 + \phi_c)\mu_2 \tag{4.20}$$

ϕ_c is the volume fraction of core in the core-shell particle, μ_1 is the matrix permeability, μ_2 is the shell permeability, and μ_3 is the core magnetic permeability.

For concentrated composites with interphase effect, the following model proposed by Pal [6] could be used to estimate the effective magnetic permeability:

$$\frac{\mu}{\mu_1} = \left[\frac{1 + 2\left(\frac{\beta - \gamma}{\beta + 2\gamma}\right)\phi}{1 - \phi\psi\left(\frac{\beta - \gamma}{\beta + 2\gamma}\right)}\right] \tag{4.21}$$

where the parameters have been defined earlier.

4.3 UPPER AND LOWER BOUNDS ON MAGNETIC PERMEABILITY OF COMPOSITES

Hashin and Shtrikman [7] have presented upper and lower bounds of the magnetic permeability of isotropic composites (regardless of the shape of the filler particles). They used a variational approach to establish the following bounds:

$$\mu_d\left[1 + \frac{3(1-\phi)(\mu_m - \mu_d)}{3\mu_d + \phi(\mu_m - \mu_d)}\right] \le \mu \le \mu_m\left[1 + \frac{3\phi(\mu_d - \mu_m)}{3\mu_m + (1-\phi)(\mu_d - \mu_m)}\right] \quad \text{when } \mu_m > \mu_d \tag{4.22}$$

$$\mu_m\left[1 + \frac{3\phi(\mu_d - \mu_m)}{3\mu_m + (1-\phi)(\mu_d - \mu_m)}\right] \le \mu \le \mu_d\left[1 + \frac{3(1-\phi)(\mu_m - \mu_d)}{3\mu_d + \phi(\mu_m - \mu_d)}\right] \quad \text{when } \mu_d > \mu_m \tag{4.23}$$

where ϕ is the volume fraction of the dispersed phase. Interestingly the same bounds are applicable to other electromagnetic properties such as dielectric constant and electrical conductivity. It should be noted that the Voigt and Reuss rules of mixtures also represent upper and lower bounds, that is,

$$\left[\phi\mu_d^{-1} + (1-\phi)\mu_m^{-1}\right]^{-1} \le \mu \le [\phi\mu_d + (1-\phi)\mu_m] \tag{4.24}$$

However, the Hashin–Shtrikman bounds are much tighter and closer (hence more useful and accurate) in comparison with the Reuss–Voigt bounds.

The Hashin–Shtrikman bounds could be expressed in a more general form as follows:

$$\lambda\alpha_m\left[1+\frac{3(1-\phi)(1-\lambda)}{3\lambda+\phi(1-\lambda)}\right]\le\alpha\le\alpha_m\left[1+\frac{3\phi(\lambda-1)}{3+(1-\phi)(\lambda-1)}\right]\quad\text{when }\alpha_m>\alpha_d \tag{4.25}$$

$$\alpha_m\left[1+\frac{3\phi(\lambda-1)}{3+(1-\phi)(\lambda-1)}\right]\le\alpha\le\lambda\,\alpha_m\left[1+\frac{3(1-\phi)(1-\lambda)}{3\lambda+(1-\phi)(\lambda-1)}\right]\quad\text{when }\alpha_d>\alpha_m \tag{4.26}$$

where $\lambda = \alpha_d/\alpha_m$ and α is any of the following electromagnetic properties: electrical conductivity (σ), dielectric constant (ε), and magnetic permeability (μ). As the bounds give the extreme values of the property, the mean value is often used as

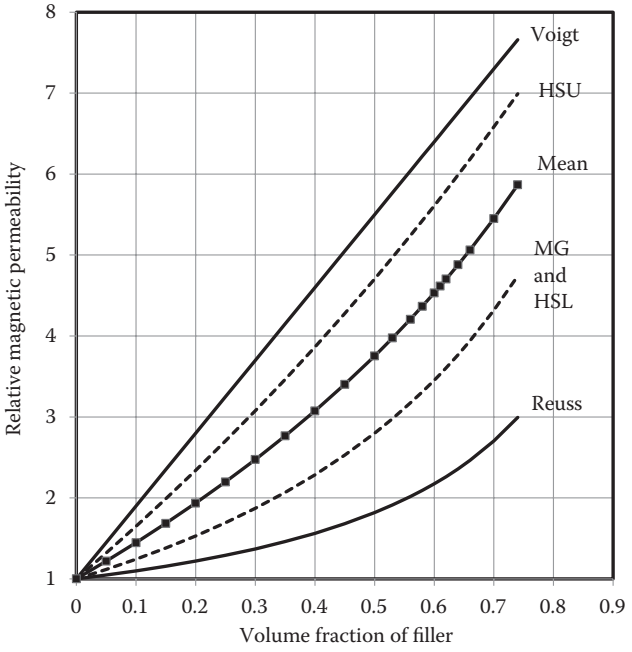

FIGURE 4.2 Comparison of the predictions of Hashin–Shtrikman bounds with the prediction of Reuss–Voigt bounds for composites with $\mu_d = 10$ and $\mu_m = 1$. HSU, Hashin–Shtrikman upper bound; HSL, Hashin–Shtrikman lower bound; MG, Maxwell–Garnett; Mean, arithmetic mean of HSU and HSL.

an estimation of the actual value of the property. Different authors have proposed different types of means [8], such as

Arithmetic mean:

$$\alpha = \frac{\alpha_U + \alpha_L}{2}$$

Geometric mean:

$$\alpha = \sqrt{\alpha_U \alpha_L}$$

where α_U is the upper bound value and α_L is the lower bound value.

Figure 4.2 compares the predictions of Hashin–Shtrikman bounds with the prediction of Reuss–Voigt bounds for composites with $\mu_d = 10$ and $\mu_m = 1$. As expected, the predictions of the Hashin–Shtrikman bounds are close to each other in comparison with the predictions of Reuss–Voigt bounds, which are far apart. The arithmetic mean value of the Hashin–Shtrikman bounds is also shown for comparison purposes. It is interesting to note that the lower Hashin–Shtrikman bound corresponds to the predictions of the Maxwell–Garnett equation (Equation 4.11).

REFERENCES

1. Fiske, T.J., H. Gokturk and D.H. Kaylon. 1997. Enhancement of the relative permeability of polymeric composites with hybrid particulate fillers. *J. Appl. Polym. Sci*. 65: 1371–1377.
2. Bai, Y. 2010. The ferroelectric–ferromagnetic composite ceramics with high permittivity and high permeability in hyper-frequency. In: *Ferroelectrics*, ed. I. Coondoo, Chapter 11, New York: InTech.
3. Koledintseva, M., K.N. Rozanov and J. Drewniak. 2011. Engineering, modeling and testing of composite absorbing materials for EMC applications. In: *Advances in Composite Materials—Ecodesign and Analysis*, ed. B. Attaff, Chapter 13, New York: InTech.
4. Callister, W.D. and D.G. Rethwisch. 2009. *Material Science and Engineering: An Introduction*, 8th ed., Chapter 20, New York: Wiley & Sons.
5. Pal, R. 2014. *Electromagnetic, Mechanical, and Transport Properties of Composite Materials*, Chapter 3, Boca Raton: CRC Press.
6. Pal, R. 2008. Dielectric behavior of double emulsions with core-shell droplet morphology. *J. Colloid Int. Sci*. 325: 500–507.
7. Hashin, Z. and S. Shtrikman. 1962. A variational approach to the theory of the effective magnetic permeability of multiphase materials. *J. Appl. Phys*. 33: 3125–3131.
8. Troschke, B. and H. Burkhardt. 1998. Thermal conductivity models for two-phase systems. *Phys. Chem. Earth* 23: 351–355.

Section II

Electromagnetic Properties of Composites

General Treatment of Electromagnetic Phenomena in Composites

5 Maxwell Equations and the Generalized Conductivity Principle

In this chapter, a general treatment of the electromagnetic phenomena is presented. The Maxwell equations are reviewed, and the generalized conductivity principle is discussed. It is shown that the expressions developed for one stationary electromagnetic property (say static relative permittivity) can be generalized to other static electromagnetic properties. Furthermore, the same expressions could also be extended to complex electromagnetic properties.

5.1 MAXWELL EQUATIONS

When a material medium is subjected to an electromagnetic field, the vectors $\vec{E}$, $\vec{H}$, $\vec{J}$, $\vec{D}$, and $\vec{B}$ obey the following Maxwell equations at every point of the medium:

$$\text{curl}\,\vec{E} = \nabla \times \vec{E} = -\frac{\partial \vec{B}}{\partial t} \tag{5.1}$$

$$\text{curl}\,\vec{H} = \nabla \times \vec{H} = \vec{J} + \frac{\partial \vec{D}}{\partial t} \tag{5.2}$$

$$\text{div}\,\vec{D} = \nabla \bullet \vec{D} = \rho \tag{5.3}$$

$$\text{div}\,\vec{B} = \nabla \bullet \vec{B} = 0 \tag{5.4}$$

where $\vec{E}$ is the electric field intensity (volt/m), $\vec{H}$ is the magnetic field intensity (ampere/m), $\vec{J}$ is the electric current density (free electric current not including polarization current, ampere/m^2), $\vec{D}$ is the electric flux density (coulomb/m^2), $\vec{B}$ is magnetic flux density (weber/m^2), and ρ is free electric charge volume density (coulomb/m^3).

Equation 5.1 is basically the Faraday law of induction, which indicates that the time variation of the magnetic field induces the electric field. Equation 5.2 is the Ampere law (as amended by Maxwell), which indicates that the electric current (including both the free current $\vec{J}$ and the displacement current $\partial\vec{D}/\partial t$) induces the

magnetic field. Equation 5.3 follows from the Gauss law for the electric flux, which states that the flux of $\vec{D}$ through a closed surface is equal to the free charge inside the closed surface. Equation 5.4 follows from the Gauss law for magnetic flux, which states that the flux of $\vec{B}$ through a closed surface is zero. Note that in the field of electromagnetism, flux is defined as the integral of a vector quantity over a finite surface. The vector quantity is referred to as flux density. Thus the fluxes of $\vec{D}$ and $\vec{B}$ are as follows:

$$\text{Flux of } \vec{D} = \int_S \vec{D} \bullet d\vec{S} \tag{5.5}$$

$$\text{Flux of } \vec{B} = \int_S \vec{B} \bullet d\vec{S} \tag{5.6}$$

5.1.1 Constitutive Equations

In addition to the Maxwell equations, the constitutive equations are needed to fully describe the electromagnetic behavior of a given material medium. The constitutive equations are as follows:

$$\vec{J} = \sigma \vec{E} \tag{5.7}$$

$$\vec{D} = \varepsilon_o \varepsilon \vec{E} \tag{5.8}$$

$$\vec{B} = \mu_o \mu \vec{H} \tag{5.9}$$

where σ is electrical conductivity, ε is relative permittivity (dielectric constant), ε_o is vacuum permittivity, μ is relative magnetic permeability, and μ_o is vacuum magnetic permeability.

The Maxwell equations appear to be overdetermined in that they involve only six unknowns (three components of $\vec{E}$ and three components of $\vec{B}$) but eight equations (three components of vector Equation 5.1, three components of vector Equation 5.2, and two scalar laws of Gauss). However, any system that satisfies the Faraday and Ampere laws automatically satisfies the two Gauss laws.

5.1.2 Boundary Conditions

In a two-phase or multiphase system such as composite materials, the Maxwell equations are valid in each of the phases of the system. To solve the Maxwell equations, boundary conditions are required. In composite materials consisting of two phases, the following boundary conditions must be satisfied:

1. The normal components of magnetic flux density $\vec{B}$ across the interface are continuous, that is,

$$\vec{B}_1 \bullet \hat{n}_1 + \vec{B}_2 \bullet \hat{n}_2 = 0 \tag{5.10}$$

where $\hat{n}_1$ is a unit normal vector directed outside phase 1, $\hat{n}_2$ is a unit normal vector directed outside phase 2, $\vec{B}_1$ and $\vec{B}_2$ are magnetic flux densities in phases 1 and 2, respectively.
2. The normal components of electric flux density $\vec{D}$ across an interface of two dielectric mediums are related as follows:

$$\vec{D}_1 \bullet \hat{n}_1 + \vec{D}_2 \bullet \hat{n}_2 = -\sigma_s \tag{5.11}$$

where $\hat{n}_1$ is a unit normal vector directed outside phase 1, $\hat{n}_2$ is a unit normal vector directed outside phase 2, $\vec{D}_1$ and $\vec{D}_2$ are electric flux densities in phases 1 and 2, respectively, and σ_s is the surface density of electric charge. When σ_s is zero, normal components of $\vec{D}$ across an interface are continuous.
3. The normal components of electric current density $\vec{J}$ across an interface of two mediums are related as follows:

$$\vec{J}_1 \bullet \hat{n}_1 + \vec{J}_2 \bullet \hat{n}_2 = \frac{\partial \sigma_s}{\partial t} \tag{5.12}$$

where $\hat{n}_1$ is a unit normal vector directed outside phase 1, $\hat{n}_2$ is a unit normal vector directed outside phase 2, $\vec{J}_1$ and $\vec{J}_2$ are electric current densities in phases 1 and 2, respectively, and σ_s is the surface density of electric charge. In the absence of surface charge σ_s, normal components of $\vec{J}$ across an interface are continuous.
4. The tangential components of $\vec{E}$ and $\vec{H}$ are continuous across an interface of two dielectric mediums:

$$\hat{n}_1 \times (\vec{E}_1 \times \hat{n}_1) = \hat{n}_2 \times (\vec{E}_2 \times \hat{n}_2) \tag{5.13}$$

$$\hat{n}_1 \times (\vec{H}_1 \times \hat{n}_1) = \hat{n}_2 \times (\vec{H}_2 \times \hat{n}_2) \tag{5.14}$$

Equation 5.13 assumes that the surface current density $\vec{J}_s$ (tangential to the surface) is zero.

5.2 TIME-INDEPENDENT ELECTROMAGNETIC PHENOMENA

When there is no time variation, $\partial/\partial t$ is zero in the Maxwell equations and boundary conditions. Thus,

$$\text{curl}\,\vec{E} = \nabla \times \vec{E} = 0 \tag{5.15}$$

$$\text{curl}\,\vec{H} = \nabla \times \vec{H} = \vec{J} \tag{5.16}$$

$$\text{div}\,\vec{D} = \nabla \bullet \vec{D} = \rho \tag{5.17}$$

$$\text{div}\,\vec{B} = \nabla \bullet \vec{B} = 0 \tag{5.18}$$

and the interface boundary conditions are

$$\vec{B}_1 \bullet \hat{n}_1 + \vec{B}_2 \bullet \hat{n}_2 = 0 \tag{5.19}$$

$$\vec{D}_1 \bullet \hat{n}_1 + \vec{D}_2 \bullet \hat{n}_2 = -\sigma_s \tag{5.20}$$

$$\vec{J}_1 \bullet \hat{n}_1 + \vec{J}_2 \bullet \hat{n}_2 = 0 \tag{5.21}$$

$$\hat{n}_1 \times (\vec{E}_1 \times \hat{n}_1) = \hat{n}_2 \times (\vec{E}_2 \times \hat{n}_2) \tag{5.22}$$

$$\hat{n}_1 \times (\vec{H}_1 \times \hat{n}_1) = \hat{n}_2 \times (\vec{H}_2 \times \hat{n}_2) \tag{5.23}$$

5.2.1 Electrostatic Phenomena

The medium is electrically insulating and there is no free electric charge, that is, $\rho = 0$ and $\sigma = 0$ and $\vec{J} = 0$. Thus, the Maxwell equations governing electrostatic phenomena are

$$\text{curl}\,\vec{E} = \nabla \times \vec{E} = 0 \tag{5.24}$$

$$\text{div}\,\vec{D} = \nabla \bullet \vec{D} = 0 \tag{5.25}$$

The interfacial boundary conditions are

$$\vec{D}_1 \bullet \hat{n}_1 + \vec{D}_2 \bullet \hat{n}_2 = 0 \tag{5.26}$$

$$\hat{n}_1 \times (\vec{E}_1 \times \hat{n}_1) = \hat{n}_2 \times (\vec{E}_2 \times \hat{n}_2) \tag{5.27}$$

Since $\vec{D} = \varepsilon_o \varepsilon \vec{E}$, we can rewrite Equations 5.25 and 5.26 as

$$\text{div}\,\vec{E} = \nabla \bullet \vec{E} = 0 \tag{5.28}$$

$$\varepsilon_1(\vec{E}_1 \bullet \hat{n}_1) + \varepsilon_2(\vec{E}_2 \bullet \hat{n}_2) = 0 \tag{5.29}$$

5.2.2 Steady Electrical Phenomena

Now $\vec{J}$ is nonzero and

$$\nabla \bullet \vec{J} = 0 \tag{5.30}$$

Equation 5.30 follows from the following continuity equation based on conservation of electric charge:

$$\nabla \bullet \vec{J} + \frac{\partial \rho}{\partial t} = 0 \tag{5.31}$$

Under steady state condition, $\partial\rho/\partial t = 0$.

Using the constitutive equation $\vec{J} = \sigma \vec{E}$ and assuming constant electrical conductivity σ, Equation 5.30 can be rewritten as

$$\nabla \bullet \vec{E} = 0 \tag{5.32}$$

Under steady state condition, Equation 5.1 reduces to

$$\text{curl}\,\vec{E} = \nabla \times \vec{E} = 0 \tag{5.33}$$

Thus, the equations governing steady electrical phenomena are Equations 5.32 and 5.33.

The interfacial boundary conditions are

$$\hat{n}_1 \times (\vec{E}_1 \times \hat{n}_1) = \hat{n}_2 \times (\vec{E}_2 \times \hat{n}_2) \tag{5.34}$$

$$\sigma_1(\vec{E}_1 \bullet \hat{n}_1) + \sigma_2(\vec{E}_2 \bullet \hat{n}_2) = 0 \tag{5.35}$$

This last boundary condition follows from Equation 5.21 using $\vec{J} = \sigma \vec{E}$.

5.2.3 Magnetostatic Phenomena

Assuming electric current density $\vec{J}$ to be zero (either the medium is electrically insulating with zero electrical conductivity σ, or the current density is negligibly small), the Maxwell equations (Ampere and Gauss laws) under steady state condition become

$$\text{curl}\,\vec{H} = \nabla \times \vec{H} = 0 \tag{5.36}$$

$$\text{div}\,\vec{B} = \nabla \bullet \vec{B} = 0 \tag{5.37}$$

Using the constitutive equation $\vec{B} = \mu_o \mu \vec{H}$, the Gauss law could be written as follows:

$$\text{div}\,\vec{H} = \nabla \bullet \vec{H} = 0 \tag{5.38}$$

The relevant interfacial boundary conditions between the two phases are

$$\hat{n}_1 \times (\vec{H}_1 \times \hat{n}_1) = \hat{n}_2 \times (\vec{H}_2 \times \hat{n}_2) \tag{5.39}$$

$$\vec{B}_1 \bullet \hat{n}_1 + \vec{B}_2 \bullet \hat{n}_2 = 0 \tag{5.40}$$

Using the constitutive equation $\vec{B} = \mu_o \mu \vec{H}$, the second boundary condition expressed in Equation 5.40 can be rewritten as

$$\mu_1(\vec{H}_1 \bullet \hat{n}_1) + \mu_2(\vec{H}_2 \bullet \hat{n}_2) = 0 \tag{5.41}$$

5.2.4 Summary

In summary, Equations 5.24 and 5.27 through 5.29 govern the electrostatic phenomena, Equations 5.32 through 5.35 govern the steady electrical phenomena, and Equations 5.36, 5.38, 5.39, and 5.41 govern the magnetostatic phenomena. Table 5.1

TABLE 5.1
Governing Equations for Three Types of Electromagnetic Phenomena

Electrostatic Phenomena	Steady Electrical Phenomena	Magnetostatic Phenomena
$\text{curl}\,\vec{E} = \nabla \times \vec{E} = 0$	$\text{curl}\,\vec{E} = \nabla \times \vec{E} = 0$	$\text{curl}\,\vec{H} = \nabla \times \vec{H} = 0$
$\text{div}\,\vec{E} = \nabla \bullet \vec{E} = 0$	$\nabla \bullet \vec{E} = 0$	$\text{div}\,\vec{H} = \nabla \bullet \vec{H} = 0$
$\hat{n}_1 \times (\vec{E}_1 \times \hat{n}_1) = \hat{n}_2 \times (\vec{E}_2 \times \hat{n}_2)$	$\hat{n}_1 \times (\vec{E}_1 \times \hat{n}_1) = \hat{n}_2 \times (\vec{E}_2 \times \hat{n}_2)$	$\hat{n}_1 \times (\vec{H}_1 \times \hat{n}_1) = \hat{n}_2 \times (\vec{H}_2 \times \hat{n}_2)$
$\varepsilon_1(\vec{E}_1 \bullet \hat{n}_1) + \varepsilon_2(\vec{E}_2 \bullet \hat{n}_2) = 0$	$\sigma_1(\vec{E}_1 \bullet \hat{n}_1) + \sigma_2(\vec{E}_2 \bullet \hat{n}_2) = 0$	$\mu_1(\vec{H}_1 \bullet \hat{n}_1) + \mu_2(\vec{H}_2 \bullet \hat{n}_2) = 0$

lists these governing equations for the three types of electromagnetic phenomena. There exists a close analogy between the governing equations and boundary conditions for electrostatic, steady electrical, and magnetostatic phenomena. The equations describing electrostatic, stationary electrical, and magnetostatic phenomena for LHI (linear, homogeneous, and isotropic) media are basically the same with $\vec{H}$ taking over the role of $\vec{E}$ in magnetostatics. The only difference is the property of the media (ε for electrostatic phenomena, σ for electrical phenomena, and μ for magnetostatic phenomena). Consequently, the solutions describing one type of phenomena are applicable to the other two types of phenomena using the corresponding material property. This fact is referred to as the "Generalized Conductivity Principle." Thus, the forms of the expressions for material electromagnetic properties (relative permittivity, electrical conductivity, and relative magnetic permeability) are the same. For example, the expression for relative permittivity can be transformed into an expression for electrical conductivity by replacing ε with σ.

5.3 TIME-HARMONIC ELECTRIC AND MAGNETIC FIELDS

In the preceding section, the steady electromagnetic phenomena, where the electric and magnetic fields are time-invariant, were considered. This section considers sinusoidal time variation of electric and magnetic fields (sinusoidal time varying fields are referred to as *harmonic* fields). Time-harmonic electric and magnetic fields can be expressed in complex notation as

$$\vec{E}(\vec{r},t) = \text{Re}\left\{\vec{E}_o^*(\vec{r})\,e^{j\omega t}\right\} \tag{5.42}$$

$$\vec{H}(\vec{r},t) = \text{Re}\left\{\vec{H}_o^*(\vec{r})\,e^{j\omega t}\right\} \tag{5.43}$$

where $\vec{E}$ is the harmonic electric field, $\vec{H}$ is the harmonic magnetic field, $\vec{E}_o^*$ is the vector phasor of instantaneous electric field $\vec{E}$, $\vec{H}_o^*$ is the vector phasor of instantaneous magnetic field $\vec{H}$, j is imaginary number $\sqrt{-1}$, ω is the frequency of oscillation,

t is time, $\vec{r}$ is the position vector, and Re refers to the "real part" of the quantity. Note that the phasor of an instantaneous quantity ($\vec{E}$ or $\vec{H}$) is a complex quantity independent of time, whose amplitude and phase are the amplitude and initial phase of the instantaneous quantity.

As an example, consider the following time-harmonic electric field:

$$\vec{E}(\vec{r},t) = \vec{E}_o(\vec{r})\cos(\omega t + \varphi(\vec{r})) \tag{5.44}$$

where $\vec{E}_o(\vec{r})$ is the vector amplitude of the field and $\varphi(\vec{r})$ is the initial phase of the field at t = 0. Using the Euler formula,

$$e^{j\omega t} = \cos \omega t + j\sin \omega t \tag{5.45}$$

one can reexpress the instantaneous field as

$$\vec{E}(\vec{r},t) = \mathrm{Re}\left\{\vec{E}_o^*(\vec{r})\, e^{j\omega t}\right\} \tag{5.46}$$

where $\vec{E}_o^*(\vec{r})$ is vector phasor of instantaneous electric field $\vec{E}$, given as

$$\vec{E}_o^*(\vec{r}) = \vec{E}_o(\vec{r})\, e^{j\varphi(\vec{r})} \tag{5.47}$$

Thus, the phasor of an instantaneous quantity ($\vec{E}$) is a complex quantity independent of time, whose amplitude and phase are the amplitude and initial phase of the instantaneous quantity.

When all *instantaneous* quantities in an equation are expressed in terms of phasors defined above, then the "Re" term, referring to the real part of a quantity, is often dropped from all parts of the equation and the equation is expressed in terms of the complex quantities. Thus the complex forms of instantaneous electric and magnetic fields are

$$\vec{E}^*(\vec{r},t) = \vec{E}_o^*(\vec{r})\, e^{j\omega t} \tag{5.48}$$

$$\vec{H}^*(\vec{r},t) = \vec{H}_o^*(\vec{r})\, e^{j\omega t} \tag{5.49}$$

Also note that $\partial e^{j\omega t}/\partial t$ is equal to $j\omega e^{j\omega t}$ and therefore, the partial time derivative $\partial/\partial t$ can be replaced by $j\omega$ in the equations. Thus, the Maxwell equations in terms of the complex quantities can be expressed as

$$\nabla \times \vec{E}^* = -j\omega\vec{B}^* \tag{5.50}$$

$$\nabla \times \vec{H}^* = \vec{J}^* + j\omega\vec{D}^* \tag{5.51}$$

$$\nabla \bullet \vec{D}^* = \rho \tag{5.52}$$

$$\nabla \bullet \vec{B}^* = 0 \tag{5.53}$$

where $\vec{J}^*$, $\vec{D}^*$, and $\vec{B}^*$ are now complex quantities.

The constitutive equations for $\vec{D}^*$ and $\vec{J}^*$ can be written as

$$\vec{D}^* = \varepsilon_o \varepsilon^* \vec{E}^* \tag{5.54}$$

$$\vec{J}^* = \sigma \vec{E}^* \tag{5.55}$$

where ε^* is complex relative permittivity and σ is static electrical conductivity of the material. The complex relative permittivity ε^* is given as

$$\varepsilon^* = \varepsilon' - j\varepsilon'' \tag{5.56}$$

where ε' and ε'' are the real and imaginary parts of the relative permittivity. For *dispersive* material, ε' and ε'' are functions of frequency.

Using the constitutive equations, Equation 5.51 could be rewritten as

$$\nabla \times \vec{H}^* = (\sigma + j\omega \varepsilon_o \varepsilon^*) \vec{E}^* \tag{5.57}$$

The effective complex conductivity σ_e^* of a material is defined through the following form of the Maxwell equation:

$$\nabla \times \vec{H}^* = \sigma_e^* \vec{E}^* \tag{5.58}$$

This equation is obtained from Maxwell equation (Equation 5.51) by dropping off the displacement current term and taking care of it through the effective conductivity, which reflects both "free" and "displacement" currents.

Likewise, the effective complex permittivity (relative) ε_e^* of a material is defined through the following form of the Maxwell equation:

$$\nabla \times \vec{H}^* = j\omega \varepsilon_o \varepsilon_e^* \vec{E}^* \tag{5.59}$$

This equation is obtained from Maxwell equation (Equation 5.51) by dropping off the "free" current term and taking care of it through the effective permittivity, which reflects both "free" and "displacement" charges.

Upon comparison of Equations 5.58 and 5.59 with Equation 5.57, the following expressions of effective complex properties σ_e^* and ε_e^* are obtained:

$$\sigma_e^* = \sigma + j\omega \varepsilon_o \varepsilon^* = (\sigma + \omega \varepsilon_o \varepsilon'') + j\omega \varepsilon_o \varepsilon' \tag{5.60}$$

$$\varepsilon_e^* = \varepsilon^* + \frac{\sigma}{j\omega\varepsilon_o} = \varepsilon' - j\left(\varepsilon'' + \frac{\sigma}{\omega\varepsilon_o}\right) \tag{5.61}$$

Note that the effective complex properties σ_e^* and ε_e^* are related to each other as follows:

$$\sigma_e^* = j\omega\varepsilon_o\varepsilon_e^* \tag{5.62}$$

For LHI (linear, homogeneous, isotropic) medium, substitution of the constitutive equation $\vec{D}^* = \varepsilon_o\varepsilon^*\vec{E}^*$ into Gauss's law (assuming charge-free medium, $\rho = 0$) gives

$$\nabla \bullet \vec{E}^* = 0 \tag{5.63}$$

In summary, the Maxwell equations for time-harmonic electric and magnetic fields in electric charge-free LHI material medium are

$$\nabla \times \vec{H}^* = \sigma_e^* \vec{E}^* \tag{5.58}$$

or

$$\nabla \times \vec{H}^* = j\omega\varepsilon_o\varepsilon_e^* \vec{E}^* \tag{5.59}$$

$$\nabla \times \vec{E}^* = -j\omega\vec{B}^* \tag{5.50}$$

$$\nabla \bullet \vec{E}^* = 0 \tag{5.63}$$

$$\nabla \bullet \vec{B}^* = 0 \tag{5.53}$$

5.3.1 Quasistationary Approximation

As the divergence of $\vec{B}^*$ is zero, $\vec{B}^*$ can be expressed as a curl of some vector $\vec{A}^*$:

$$\vec{B}^* = \text{curl}\,\vec{A}^* \tag{5.64}$$

Consequently, the Maxwell Equation 5.50 can be rewritten as

$$\nabla \times (\vec{E}^* + j\omega\vec{A}^*) = 0 \tag{5.65}$$

Under quasistationary condition, $j\omega\vec{A}^* << \vec{E}^*$, and therefore,

$$\nabla \times \vec{E}^* = 0 \tag{5.66}$$

A similar analysis could be carried out for $\vec{E}^*$ as divergence of $\vec{E}^*$ is zero. Writing $\vec{E}^*$ as a curl of some vector $\vec{A}^*$,

$$\vec{E}^* = \text{curl}\,\vec{A}^* \tag{5.67}$$

The Maxwell Equation 5.59 could be rewritten as

$$\nabla \times \vec{H}^* = j\omega\varepsilon_o\varepsilon_e^*\vec{E}^* = j\omega\varepsilon_o\varepsilon_e^*\nabla \times \vec{A}^* \tag{5.68}$$

that is,

$$\nabla \times (\vec{H}^* - j\omega\varepsilon_o\varepsilon_e^*\vec{A}^*) = 0 \tag{5.69}$$

Under quasistationary condition, $j\omega\varepsilon^*\vec{A}^* << \vec{H}^*$, and therefore,

$$\nabla \times \vec{H}^* = 0 \tag{5.70}$$

5.3.2 Boundary Conditions

The interfacial boundary conditions are

$$\vec{J}_1^* \bullet \hat{n}_1 + \vec{J}_2^* \bullet \hat{n}_2 = \frac{\partial\sigma_s}{\partial t} \tag{5.71}$$

$$\vec{D}_1^* \bullet \hat{n}_1 + \vec{D}_2^* \bullet \hat{n}_2 = -\sigma_s \tag{5.72}$$

$$\vec{B}_1^* \bullet \hat{n}_1 + \vec{B}_2^* \bullet \hat{n}_2 = 0 \tag{5.73}$$

$$\hat{n}_1 \times (\vec{E}_1^* \times \hat{n}_1) = \hat{n}_2 \times (\vec{E}_2^* \times \hat{n}_2) \tag{5.74}$$

$$\hat{n}_1 \times (\vec{H}_1^* \times \hat{n}_1) = \hat{n}_2 \times (\vec{H}_2^* \times \hat{n}_2) \tag{5.75}$$

Replacing ∂/∂t with jω and combining Equations 5.71 and 5.72 result in the following equation:

$$\hat{n}_1 \bullet (\vec{J}_1^* + j\omega\vec{D}_1^*) + \hat{n}_2 \bullet (\vec{J}_2^* + j\omega\vec{D}_2^*) = 0 \tag{5.76}$$

This equation can be rewritten in terms of the total current density $\vec{J}_t^*(= \vec{J}^* + j\omega\vec{D}^*)$ as

$$\hat{n}_1 \bullet \vec{J}_{t,1}^* + \hat{n}_2 \bullet \vec{J}_{t,2}^* = 0 \tag{5.77}$$

where the total current density is the sum of conduction current density and displacement current density. Upon substitution of $\vec{J}_t^* = (\sigma + j\omega\varepsilon_o\varepsilon^*)\vec{E}^* = \sigma_e^*\vec{E}^*$ into Equation 5.77,

$$\sigma_{1e}^*(\vec{E}_1^* \bullet \hat{n}_1) + \sigma_{2e}^*(\vec{E}_2^* \bullet \hat{n}_2) = 0 \tag{5.78}$$

where $\sigma_e^* = \sigma + j\omega\varepsilon_o\varepsilon_e^*$. Since $\sigma_e^* = j\omega\varepsilon_o\varepsilon_e^*$, this boundary condition could be rewritten as

$$\varepsilon_{1e}^*(\vec{E}_1^* \bullet \hat{n}_1) + \varepsilon_{2e}^*(\vec{E}_2^* \bullet \hat{n}_2) = 0 \tag{5.79}$$

Using $\vec{B}^* = \mu_o\mu^*\vec{H}^*$, the boundary condition given by Equation 5.73 could be reexpressed as

$$\mu_1^*(\vec{H}_1^* \bullet \hat{n}_1) + \mu_2^*(\vec{H}_2^* \bullet \hat{n}_2) = 0 \tag{5.80}$$

where μ* is complex relative permeability, defined as

$$\mu^* = \mu' - j\mu'' \tag{5.81}$$

5.3.3 Comparison of Governing Equations

Table 5.2 compares the governing equations and boundary conditions of time-harmonic electric and magnetic fields. Once again, the equations are of the same form and the only difference is the property of the media. It should also be noted that these equations and boundary conditions are of the same form as those describing the stationary electromagnetic phenomena (see Table 5.1).

Consequently, the expressions developed for any one stationary electromagnetic property (say static relative permittivity) can be extended to dynamic electromagnetic

TABLE 5.2
Comparison of Governing Equations and Boundary Conditions for Time-Harmonic Electric and Magnetic Fields

Electric Field ($\vec{E}^*$) with σ_e^*	Electric Field ($\vec{E}^*$) with ε_e^*	Magnetic Field, $\vec{H}^*$
$\text{curl}\,\vec{E}^* = \nabla \times \vec{E}^* = 0$	$\text{curl}\,\vec{E}^* = \nabla \times \vec{E}^* = 0$	$\text{curl}\,\vec{H}^* = \nabla \times \vec{H}^* = 0$
$\text{div}\,\vec{E}^* = \nabla \bullet \vec{E}^* = 0$	$\text{div}\,\vec{E}^* = \nabla \bullet \vec{E}^* = 0$	$\text{div}\,\vec{H}^* = \nabla \bullet \vec{H}^* = 0$
$\hat{n}_1 \times (\vec{E}_1^* \times \hat{n}_1) = \hat{n}_2 \times (\vec{E}_2^* \times \hat{n}_2)$	$\hat{n}_1 \times (\vec{E}_1^* \times \hat{n}_1) = \hat{n}_2 \times (\vec{E}_2^* \times \hat{n}_2)$	$\hat{n}_1 \times (\vec{H}_1^* \times \hat{n}_1) = \hat{n}_2 \times (\vec{H}_2^* \times \hat{n}_2)$
$\sigma_{1e}^* (\vec{E}_1^* \bullet \hat{n}_1) + \sigma_{2e}^* (\vec{E}_2^* \bullet \hat{n}_2) = 0$	$\varepsilon_{1e}^* (\vec{E}_1^* \bullet \hat{n}_1) + \varepsilon_{2e}^* (\vec{E}_2^* \bullet \hat{n}_2) = 0$	$\mu_1^* (\vec{H}_1^* \bullet \hat{n}_1) + \mu_2^* (\vec{H}_2^* \bullet \hat{n}_2) = 0$

properties by replacing the stationary electromagnetic property with the complex electromagnetic property (σ_e^*, ε_e^*, or μ^*). This is called the *Generalized Conductivity Principle*.

SUPPLEMENTAL READING

Clausse, M. 1983. Dielectric properties of emulsions and related systems. In: *Encyclopedia of Emulsion Technology*, ed., P. Becher, Vol. 1, Chapter 9, pp. 483–715, New York: Marcel Dekker.

Maxwell's equations. Wikipedia, http://en.wikipedia.org/wiki/Maxwell's_equations.

6 Complex Electromagnetic Properties of Composites

In Chapters 2 through 4, the *static* electromagnetic properties (conductivity, permittivity, and permeability) of composite materials were discussed. In this chapter, the *dynamic* electromagnetic properties of composites subjected to sinusoidal time-varying electric and magnetic fields are discussed. The electromagnetic properties of interest are effective complex relative permittivity (ε_e^*) and complex relative permeability (μ^*). As effective complex conductivity (σ_e^*) is related to effective complex relative permittivity (ε_e^*), it is not considered separately. The most interesting feature of the complex electromagnetic properties is their dependence on the frequency of the applied alternating field. The variation of electromagnetic properties with frequency is referred to as *dispersion* in the literature. Both "dielectric dispersion" and "magnetic dispersion" are discussed in this chapter.

6.1 COMPLEX PERMITTIVITY OF COMPOSITES

The complex relative permittivity ε^* is defined according to the following constitutive relation for the complex electric flux density $\vec{D}^*$:

$$\vec{D}^* = \varepsilon_o \varepsilon^* \vec{E}^* \tag{6.1}$$

where ε_o is the permittivity of vacuum (= 8.854×10^{-12} farads/m) and $\vec{E}^*$ is the complex electric field intensity. The complex relative permittivity ε^* can be expressed as follows:

$$\varepsilon^* = \varepsilon' - j\varepsilon'' \tag{6.2}$$

where ε' and ε'' are the real and imaginary parts of the relative complex permittivity. For *dispersive* material, ε' and ε'' are functions of frequency. The real part ε' reflects the polarization property of the material. The imaginary part ε'' is called "polarization loss" as it reflects energy loss in the dielectric material caused by a delay in the material's response to the applied field. The complex relative permittivity ε^*, as defined above, considers only "displacement charges." It is assumed that the static electrical conductivity of the material is negligible. To consider both "free" and "displacement" charges, the effective (complex) relative permittivity ε_e^* is defined as follows:

$$\varepsilon_e^* = \varepsilon^* + \frac{\sigma}{j\omega\varepsilon_o} = \varepsilon' - j\left(\varepsilon'' + \frac{\sigma}{\omega\varepsilon_o}\right) \tag{6.3}$$

where σ is the static (d.c.) electrical conductivity of the material. Now the loss term (imaginary part) includes both polarization loss and energy loss due to d.c. electric conductivity. The effective loss factor ε''_{eff} that takes into account energy losses due to polarization as well as static conductivity is defined by expressing ε^*_e as

$$\varepsilon^*_e = \varepsilon' - j\varepsilon''_{eff} \tag{6.4}$$

where ε''_{eff} is

$$\varepsilon''_{eff} = \left(\varepsilon'' + \frac{\sigma}{\omega \varepsilon_o} \right) \tag{6.5}$$

Alternatively, the effective electrical conductivity σ'_{eff} that takes into account energy losses due to polarization as well as static conductivity could be defined as follows:

$$\sigma^*_e = j\omega \varepsilon_o \varepsilon^*_e = \sigma'_{eff} + j\sigma'' \tag{6.6}$$

where

$$\sigma'_{eff} = (\sigma + \omega \varepsilon_o \varepsilon'') \tag{6.7}$$

$$\sigma'' = \omega \varepsilon_o \varepsilon' \tag{6.8}$$

The dielectric properties of composites vary with frequency. The key mechanisms responsible for dielectric relaxation, that is, a decrease in the real part of the complex permittivity ε′ with the increase in frequency are interfacial polarization, orientational polarization, and electronic polarization. Interfacial polarization, also referred to as Maxwell–Wagner–Sillars (MWS) effect, is almost always present in composite materials composed of two or more phases [1–3]. Due to the difference in conductivities and permittivities of the constituent phases, buildup of electric charge takes place at the interfaces leading to the MWS effect. The dielectric relaxation related to interfacial polarization effect usually appears at moderate frequencies of the order of MHz. The orientational polarization occurs due to alignment/orientation of electric dipoles of polar molecules with the applied field. The dielectric relaxation related to orientational polarization (also referred to as Debye-type dipolar relaxation) usually appears at frequencies of the order of GHz. The electronic polarization (also referred to as distortion polarization)

occurs due to displacement of electron cloud in an atom. The dielectric relaxation related to distortion polarization appears at very high frequencies of the order of terahertz (>1 THz).

As an example, Figure 6.1 shows the dielectric behavior of a 47% by volume water-in-oil (W/O) emulsion at 296 K [1,2]. Emulsions are basically composite materials in liquid form, consisting of droplets of one liquid phase dispersed in a continuum of another immiscible liquid phase. The figure shows the plots of real permittivity ε' and effective loss factor ε'' (note that the effective loss factor $\varepsilon''_{\text{eff}}$ is denoted as simply ε'' here and in the remainder of the chapter) as functions of frequency. As the frequency range covered is approximately 10 kHz–10 MHz, only interfacial polarization effect is expected. The real permittivity ε' is initially constant up to frequency of about 200 kHz but it decreases rapidly with further increase in frequency and it becomes constant again at high frequencies. The observed dielectric relaxation in W/O emulsion, around frequencies of 100 kHz to 10 MHz, is due to "interfacial" or "migration" polarization (also called MWS effect). The presence of free charge or ions in the dispersed water droplets is responsible for interfacial polarization [1–3]. Figure 6.2 shows another set of experimental data obtained by Hanai et al. [3] for W/O emulsions at a fixed ϕ of 0.60. Once again, only interfacial polarization (MWS effect) is observed in the frequency range covered in the experiments. The plots of real

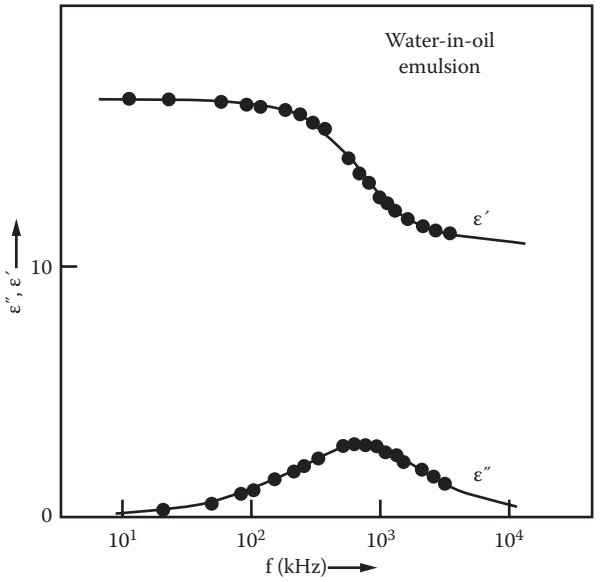

FIGURE 6.1 Dielectric behavior of a 47% by volume water-in-vaseline oil emulsion. (From Clausse, M., Dielectric properties of emulsions and related systems. In: *Encyclopedia of Emulsion Technology*, ed., P. Becher, Vol. 1, Chapter 9, pp. 483–715, New York: Marcel Dekker, 1983; Pal, R., *Colloids Surf.* 84: 141–193, 1994.)

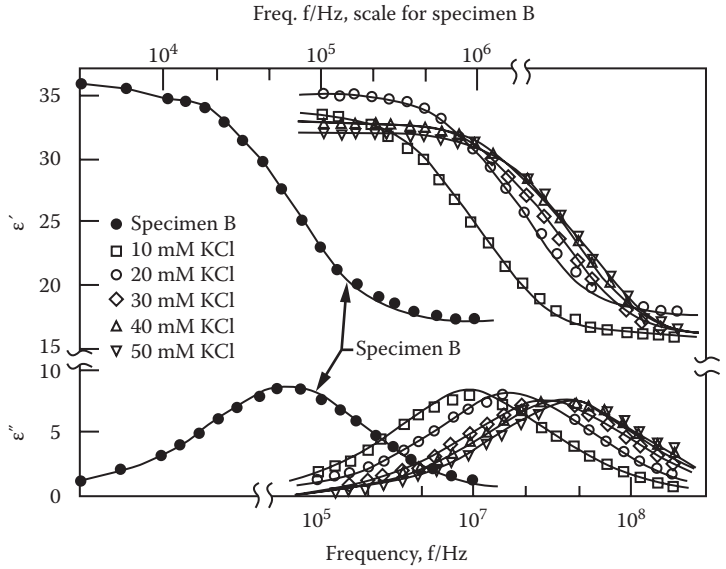

FIGURE 6.2 Influence of salt concentration on the dielectric behavior of water-in-oil (W/O) emulsions at a fixed ϕ of 0.60. Specimen B has zero salt concentration. (From Pal, R., *Colloids Surf.* 84: 141–193, 1994; Hanai, T. et al., *Colloid Polym. Sci.* 260: 1029–1034, 1982.)

permittivity ε′ and effective loss factor ε″ versus frequency shift towards higher frequencies with the increase in the salt content of the dispersed water droplets, indicating an increase in the relaxation frequency. The relaxation frequency, which is defined as the frequency corresponding to the half-value point of the entire domain of interfacial polarization relaxation, generally depends on the following factors: dispersed phase (water) concentration, water conductivity or salinity, and temperature.

Figure 6.3 exhibits the dielectric behavior of an emulsion of core-shell droplets of oil-in-water-in-oil (O/W/O) type over a broad range of frequencies [4]. Such emulsions are also referred to as "O/W/O double emulsions." A schematic diagram of the core-shell droplet is shown in Figure 6.4. The core and the matrix phase of the emulsion was oil of dielectric constant 2.5 (independent of the frequency). The shell of the core-shell droplets was aqueous phase of electrical conductivity 1 S/m. The ratio of outer radius of interfacial shell to core radius (δ) was 1.1 and the volume fraction of the core-shell droplets (ϕ) was 0.50. The top portion of Figure 6.3 shows the plots of real permittivity (ε′) and effective loss factor (ε″) as functions of frequency. The bottom portion of Figure 6.3 shows the Cole–Cole plot in terms of effective loss factor ε″ versus real permittivity ε′ (once again, it should be pointed out that the effective loss factor $\varepsilon''_{\text{eff}}$ is denoted as simply ε″). Clearly, the emulsion of core-shell droplets composed of oil core

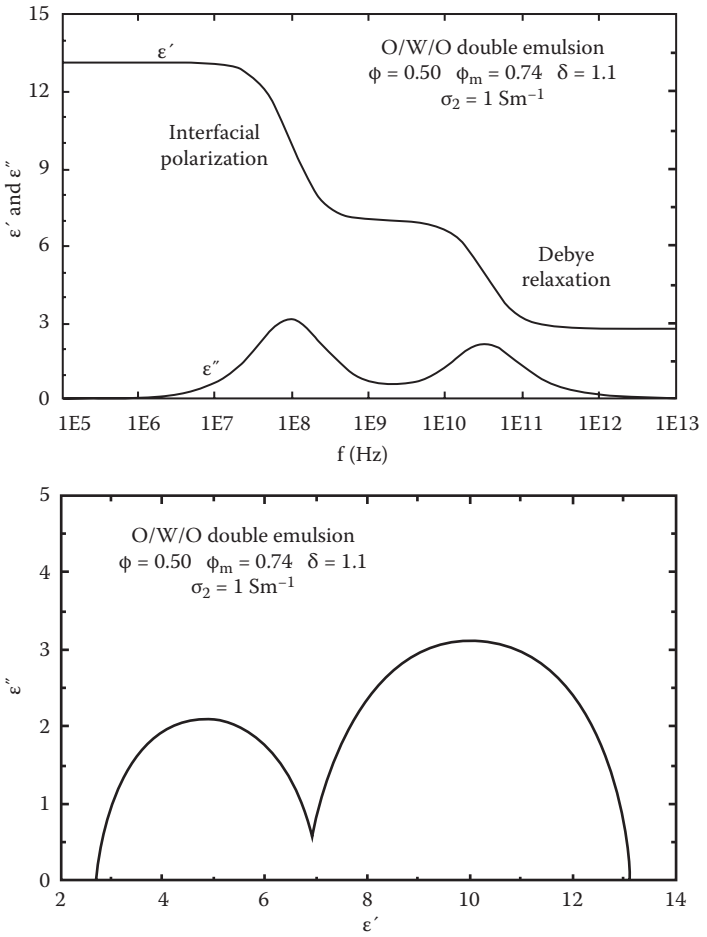

FIGURE 6.3 The dielectric behavior of an emulsion of core-shell droplets of oil-in-water-in-oil (O/W/O) type over a broad range of frequencies. (From Pal, R., *J. Colloid Int. Sci.* 325: 500–507, 2008.)

and matrix, and conductive aqueous phase as shell, exhibits two dielectric relaxations, one due to interfacial polarization at intermediate frequencies (around 10–100 MHz) and the other due to Debye-type dipolar relaxation of water molecules at microwave frequencies (around 10–100 GHz). The Cole–Cole diagram shows two frequency domains: the right-hand side semicircle corresponds to dielectric relaxation due to interfacial polarization at intermediate frequencies and the left-hand semicircle corresponds to Debye-type dipolar relaxation at high frequencies.

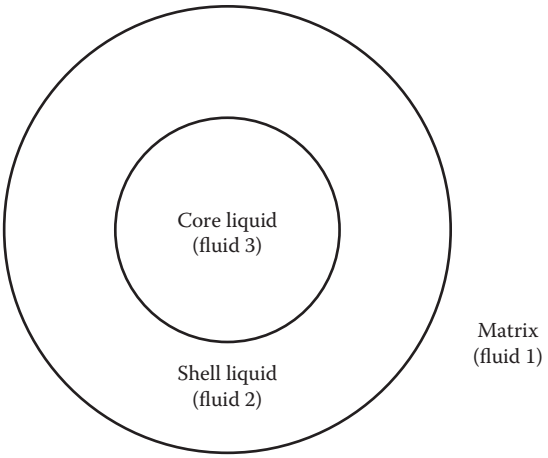

FIGURE 6.4 Schematic diagram of core-shell emulsion droplet.

6.1.1 Models for Complex Permittivity of Composites

According to the "Generalized Conductivity Principle" discussed in the preceding chapter, all the expressions developed for a stationary property (static relative permittivity) can be extended to a corresponding complex property (effective relative permittivity ε_e^*). In what follows the key models for the effective complex relative permittivity of composites, denoted as simply $\varepsilon^* (= \varepsilon' - j\varepsilon'')$, are given.

Maxwell–Garnett model:

$$\frac{\varepsilon^*}{\varepsilon_m^*} = \left[\frac{1 + 2\left(\dfrac{\varepsilon_d^* - \varepsilon_m^*}{\varepsilon_d^* + 2\varepsilon_m^*} \right)\phi}{1 - \left(\dfrac{\varepsilon_d^* - \varepsilon_m^*}{\varepsilon_d^* + 2\varepsilon_m^*} \right)\phi} \right] \tag{6.9}$$

Bruggeman–Hanai model:

$$\left(\frac{\varepsilon^* - \varepsilon_d^*}{\varepsilon_m^* - \varepsilon_d^*} \right) \left(\frac{\varepsilon_m^*}{\varepsilon^*} \right)^{1/3} = 1 - \phi \tag{6.10}$$

Lewis–Nielsen model (as suggested by Pal [4]):

$$\frac{\varepsilon^*}{\varepsilon_m^*} = \left[\frac{1 + 2\left(\frac{\varepsilon_d^* - \varepsilon_m^*}{\varepsilon_d^* + 2\varepsilon_m^*} \right)\phi}{1 - \left(\frac{\varepsilon_d^* - \varepsilon_m^*}{\varepsilon_d^* + 2\varepsilon_m^*} \right)\phi\psi} \right] \tag{6.11a}$$

where

$$\psi = 1 + \left(\frac{1 - \phi_m}{\phi_m^2} \right)\phi \tag{6.11b}$$

Pal model 1:

$$\left(\frac{\varepsilon^*}{\varepsilon_m^*} \right)^{1/3} \left(\frac{\varepsilon_d^* - \varepsilon_m^*}{\varepsilon_d^* - \varepsilon^*} \right) = \left(1 - \frac{\phi}{\phi_m} \right)^{-\phi_m} \tag{6.12}$$

Pal model 2:

$$\left(\frac{\varepsilon^*}{\varepsilon_m^*} \right)^{1/3} \left(\frac{\varepsilon_d^* - \varepsilon_m^*}{\varepsilon_d^* - \varepsilon^*} \right) = \exp\left(\frac{\phi}{1 - \frac{\phi}{\phi_m}} \right) \tag{6.13}$$

Bruggeman symmetric model:

$$\left(\frac{\varepsilon_d^* - \varepsilon^*}{\varepsilon_d^* + 2\varepsilon^*} \right)\phi + \left(\frac{\varepsilon_m^* - \varepsilon^*}{\varepsilon_m^* + 2\varepsilon^*} \right)(1 - \phi) = 0 \tag{6.14}$$

In these models, ε^*, ε_d^*, and ε_m^* are the effective complex relative permittivities of composite, dispersed phase, and matrix, respectively, ϕ is the volume fraction of the dispersed phase, and ϕ_m is the maximum packing volume fraction of dispersed phase. These models could be recast in terms of the effective complex conductivity using the following relation: $\sigma^* = j\omega\varepsilon_o\varepsilon^*$. For example, the Bruggeman–Hanai model for the effective complex conductivity is as follows:

$$\left(\frac{\sigma^* - \sigma_d^*}{\sigma_m^* - \sigma_d^*} \right)\left(\frac{\sigma_m^*}{\sigma^*} \right)^{1/3} = 1 - \phi \tag{6.15}$$

where σ^*, σ_d^*, and σ_m^* are the effective complex conductivities of composite, dispersed phase, and matrix, respectively (note that the effective complex conductivity σ^* was denoted as σ_e^* in the preceding sections).

In order to use the models to predict the dielectric behavior of composites, knowledge of the effective permittivity of the individual phases is needed. For the individual phases of the composite, the Debye model could be used to describe the dielectric behavior:

$$\varepsilon^* = \varepsilon_\infty + \frac{\varepsilon_\ell - \varepsilon_\infty}{1 + j\omega\tau} \tag{6.16}$$

where ε_ℓ and ε_∞ are the limiting values of the real permittivity ε' at low and high frequencies, respectively, and ω is the frequency in rad/s. The Debye model consists of a single relaxation time τ, corresponding to dipolar relaxation. For water at 25°C, the approximate values of the parameters in the Debye model are $\varepsilon_\infty = 4.2$, $\varepsilon_\ell = 78.5$, $\tau = 8.25 \times 10^{-12}$ s. An ohmic term can be incorporated into the loss factor to take into account the effect of static or d.c. conductivity on the dielectric behavior. Thus, the effective relative permittivity of an individual phase can be expressed as

$$\varepsilon^* = \varepsilon_\infty + \frac{\varepsilon_\ell - \varepsilon_\infty}{1 + j\omega\tau} + \frac{\sigma}{j\omega\varepsilon_o} \tag{6.17}$$

where σ is the static electrical conductivity of the material.

Upon substituting the expressions for the effective relative permittivity ε^* of individual phases into the models for composites, one can, in principle, solve for the effective relative permittivity ε^* of composites and express it in the following form:

$$\varepsilon^* = \varepsilon_\infty + \frac{\varepsilon_\ell - \varepsilon_i}{1 + j\omega\tau_1} + \frac{\varepsilon_i - \varepsilon_\infty}{1 + j\omega\tau_2} + \frac{\sigma_\ell}{j\omega\varepsilon_o} \tag{6.18}$$

where ε_ℓ, ε_i, and ε_∞ are the three plateau values of real permittivity corresponding to low, intermediate, and high frequencies. Now there are two relaxation times: τ_1 corresponds to relaxation related to interfacial polarization and τ_2 corresponds to dipolar relaxation. σ_ℓ is the low frequency or static electrical conductivity of the composite.

Alternatively, one can obtain an expression for the effective complex conductivity σ^* of composite from the model and express it in the following form:

$$\sigma^* = \sigma_\ell + \frac{j\omega\tau_1(\sigma_i - \sigma_\ell)}{1 + j\omega\tau_1} + \frac{j\omega\tau_2(\sigma_\infty - \sigma_i)}{1 + j\omega\tau_2} + j\omega\varepsilon_o\varepsilon_\infty \tag{6.19}$$

where σ_ℓ, σ_i, and σ_∞ are the three plateau values of electrical conductivity corresponding to low, intermediate, and high frequencies.

6.1.2 Comparison of Model Predictions with Experimental Data

Figures 6.5 and 6.6 compare the predictions of models with experimental data for clay-in-water suspensions and O/W emulsions. The plots show relative dielectric constant $\varepsilon'_r (= \varepsilon'/\varepsilon'_m)$ and relative loss factor $\varepsilon''_r (= \varepsilon''/\varepsilon''_m)$ as functions of dispersed-phase volume fraction. The experimental data were measured at a frequency of 9.36 GHz [5]. As the dielectric constant of the dispersed phase (clay particles and oil droplets) can be neglected in comparison with that of matrix (water), the complex permittivity models discussed in the preceding section simplify to the following expressions:

Maxwell–Garnett model:

$$\frac{\varepsilon^*}{\varepsilon^*_m} = \left[\frac{2(1-\phi)}{2+\phi}\right] \tag{6.20}$$

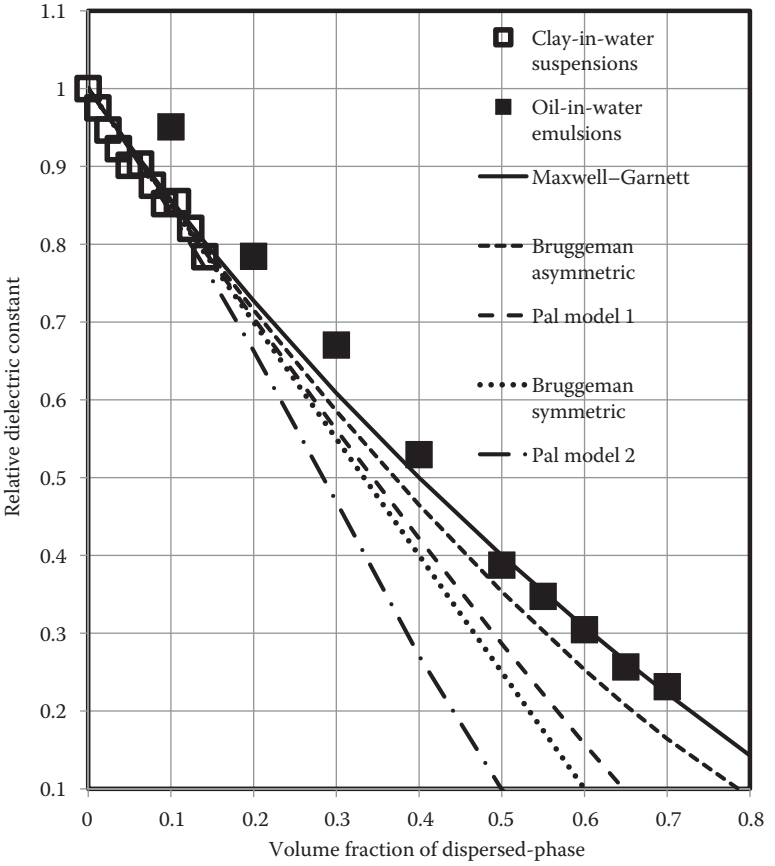

FIGURE 6.5 Comparison of relative dielectric constant predicted from models with experimental data obtained for clay-in-water suspensions and oil-in-water emulsions.

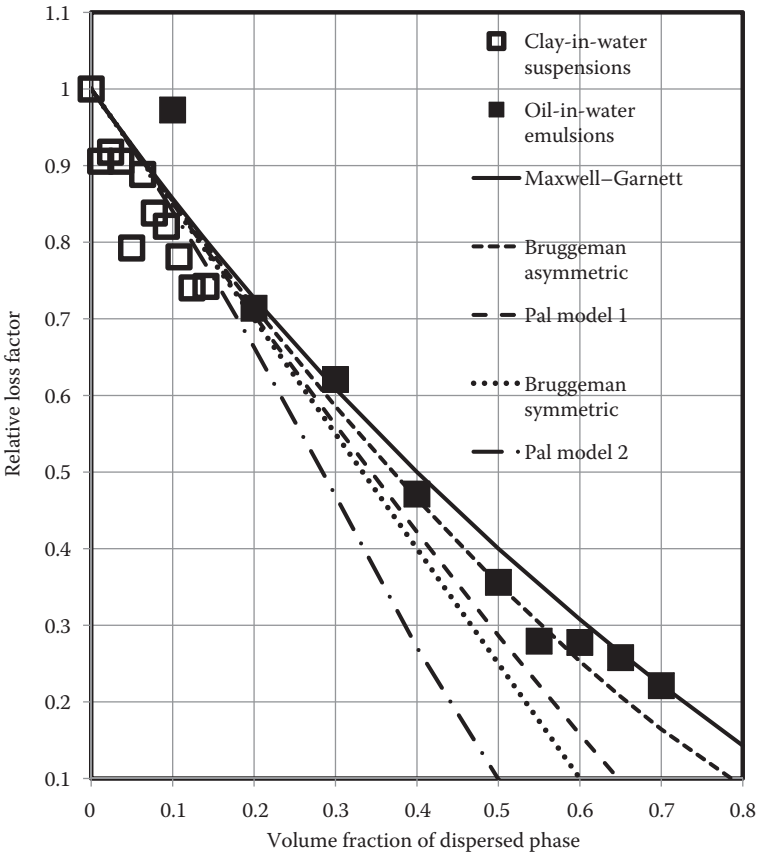

FIGURE 6.6 Comparison of relative loss factor predicted from models with experimental data obtained for clay-in-water suspensions and oil-in-water emulsions.

Bruggeman–Hanai model:

$$\frac{\varepsilon^*}{\varepsilon_m^*} = (1-\phi)^{3/2} \tag{6.21}$$

Lewis–Nielsen model:

$$\frac{\varepsilon^*}{\varepsilon_m^*} = \left[\frac{2(1-\phi)}{2+\phi\psi}\right] \tag{6.22a}$$

where

$$\psi = 1 + \left(\frac{1 - \phi_m}{\phi_m^2} \right) \phi \tag{6.22b}$$

Pal model 1:

$$\frac{\varepsilon^*}{\varepsilon_m^*} = \left(1 - \frac{\phi}{\phi_m} \right)^{3\phi_m/2} \tag{6.23}$$

Pal model 2:

$$\frac{\varepsilon^*}{\varepsilon_m^*} = \exp\left(- \frac{3\phi/2}{1 - \dfrac{\phi}{\phi_m}} \right) \tag{6.24}$$

Bruggeman symmetric model:

$$\frac{\varepsilon^*}{\varepsilon_m^*} = 1 - \frac{3}{2}\phi \tag{6.25}$$

According to these expressions, the relative dielectric constant $\varepsilon_r' (= \varepsilon'/\varepsilon_m')$ and relative loss factor $\varepsilon_r'' (= \varepsilon''/\varepsilon_m'')$ are equal and are independent of frequency. They are dependent only on the volume fraction of the dispersed phase and are given as follows:

$$\frac{\varepsilon'}{\varepsilon_m'} = \frac{\varepsilon''}{\varepsilon_m''} = \left[\frac{2(1-\phi)}{2+\phi} \right] \qquad \text{(Maxwell–Garnett)} \tag{6.26}$$

$$\frac{\varepsilon'}{\varepsilon_m'} = \frac{\varepsilon''}{\varepsilon_m''} = (1-\phi)^{3/2} \qquad \text{(Bruggeman–Hanai)} \tag{6.27}$$

$$\frac{\varepsilon'}{\varepsilon_m'} = \frac{\varepsilon''}{\varepsilon_m''} = \left[\frac{2(1-\phi)}{2+\phi\psi} \right] \qquad \text{(Lewis–Nielsen)} \tag{6.28}$$

$$\frac{\varepsilon'}{\varepsilon'_m} = \frac{\varepsilon''}{\varepsilon''_m} = \left(1 - \frac{\phi}{\phi_m}\right)^{3\phi_m/2} \quad \text{(Pal model 1)} \qquad (6.29a)$$

$$\frac{\varepsilon'}{\varepsilon'_m} = \frac{\varepsilon''}{\varepsilon''_m} = \exp\left(-\frac{3\phi/2}{1 - \frac{\phi}{\phi_m}}\right) \quad \text{(Pal model 2)} \qquad (6.29b)$$

$$\frac{\varepsilon'}{\varepsilon'_m} = \frac{\varepsilon''}{\varepsilon''_m} = 1 - \frac{3}{2}\phi \quad \text{(Bruggeman)} \qquad (6.30)$$

According to Figures 6.5 and 6.6, the Maxwell–Garnett model describes the experimental data reasonably well. Other models tend to underpredict the relative dielectric constant $\varepsilon'_r (= \varepsilon'/\varepsilon'_m)$ and relative loss factor $\varepsilon''_r (= \varepsilon''/\varepsilon''_m)$ at high volume fractions of dispersed phase.

6.1.3 Influence of Interphase Region on the Complex Permittivity of Composites

As noted in Chapter 3, the dielectric properties of the material in the interphase region, adjacent to the surface of the filler particles, could be significantly different from those of the matrix due to (a) covalent bonding of the matrix molecules with the surface of the filler particles, and (b) the presence of additives such as surfactants and coupling agents at the surface of the particles. Composite systems with interphase effects could be modeled as suspensions of core-shell type particles with the shell portion representing the interphase between core filler particles and the matrix. The suspensions of core-shell particles are not only suitable models for interphase effects but they are also of direct importance in many practical applications. For example, emulsions of core-shell droplets, also referred to as "double emulsions" or "multiple emulsions," have many direct applications. Due to their special morphology, double emulsions are highly suited for a variety of applications in the pharmaceutical, food and cosmetic industries. They have also shown significant promise in waste water treatment and separation of hydrocarbons. As double emulsions are able to entrap important substances in their internal droplets, they are particularly suited for applications where controlled release (slow and prolonged) of important ingredients is desired.

Pal [4] proposed the following model for the effective complex relative permittivity of composites of core-shell-type particles:

$$\frac{\varepsilon^*}{\varepsilon_1^*} = \left[\frac{1 + 2\left(\frac{\beta^* - \gamma^*}{\beta^* + 2\gamma^*}\right)\phi}{1 - \left(\frac{\beta^* - \gamma^*}{\beta^* + 2\gamma^*}\right)\phi\psi}\right] \qquad (6.31)$$

where β* and γ* are given as

$$\beta^* = (2+\delta^3)(\varepsilon_3^*/\varepsilon_1^*) - 2(1-\delta^3)(\varepsilon_2^*/\varepsilon_1^*) \tag{6.32}$$

$$\gamma^* = 1 + 2\delta^3 - (1-\delta^3)(\varepsilon_3^*/\varepsilon_2^*) \tag{6.33}$$

$$\psi = 1 + \left(\frac{1-\phi_m}{\phi_m^2}\right)\phi \tag{6.34}$$

In these equations, ϕ is the volume fraction of core-shell particles, δ is the ratio of outer radius of interfacial shell to core radius, ε_1^* is the complex relative permittivity of matrix, ε_3^* is the complex relative permittivity of core material, ε_2^* is the complex relative permittivity of shell material (see Figure 6.4), and ϕ_m is the maximum packing volume fraction of core-shell particles.

In what follows, the predictions of Equation 6.31 are discussed for emulsions of core-shell droplets [4]. Two types of double emulsions are discussed, namely, (1) O/W/O type double emulsion consisting of oil core, water shell, and oil matrix, and (2) W/O/W type double emulsion consisting of water core, oil shell, and water matrix.

The following modified Debye model is used to describe the dielectric behavior of the aqueous phase:

$$\varepsilon^* = \varepsilon_\infty + \frac{\varepsilon_\ell - \varepsilon_\infty}{1 + j\omega\tau} + \frac{\sigma}{j\omega\varepsilon_o} \tag{6.35}$$

where $\varepsilon_\infty = 4.2$, $\varepsilon_\ell = 78.5$, $\tau = 8.25 \times 10^{-12}$ s. The oil phase is assumed to have a dielectric constant of 2.5, independent of the frequency.

Figure 6.7 compares the dielectric behavior of O/W/O double emulsion with that of a simple W/O emulsion at the same volume fraction of water. A simple W/O emulsion is a special case of an O/W/O double emulsion with $\delta \to \infty$. Both simple and double emulsions exhibit two dielectric relaxations (interfacial and Debye types). However, the relaxation effects in the case of O/W/O double emulsion are much stronger. The effect of aqueous-phase conductivity on the dielectric behavior of O/W/O double emulsion is shown in Figure 6.8. With the increase in aqueous phase conductivity σ_2, the relaxation frequency of interfacial polarization increases. However, the dipolar relaxation behavior of O/W/O double emulsion is unaffected by the aqueous phase conductivity.

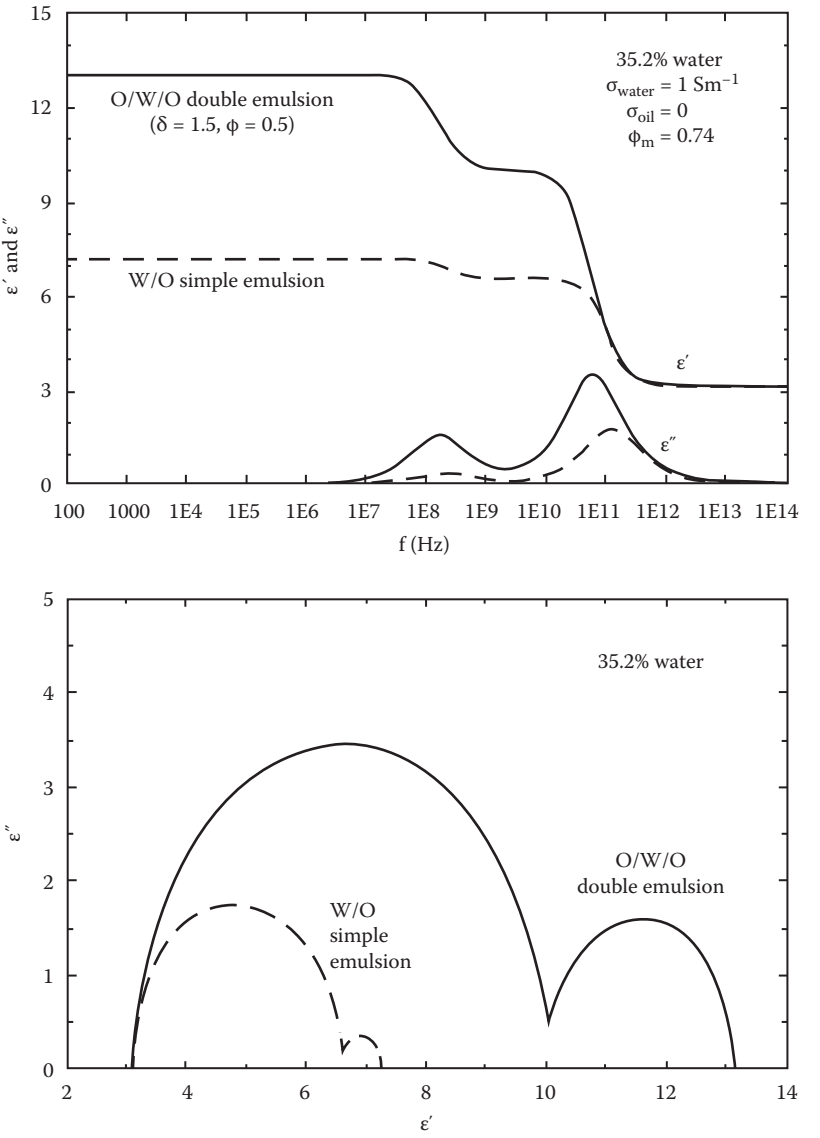

FIGURE 6.7 Comparison of the dielectric behaviors of O/W/O double emulsion and W/O simple emulsion at the same water content. (From Pal, R., *J. Colloid Int. Sci.* 325: 500–507, 2008.)

Figure 6.9 shows the effect of shell-to-core radii ratio δ on the dielectric behavior of O/W/O double emulsion. Note that the volume fraction of internal droplet (core) within a single core-shell droplet (ϕ_c) is related to δ as

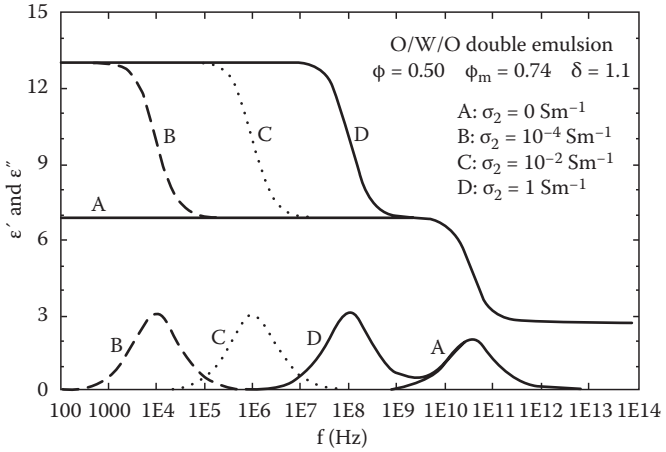

FIGURE 6.8 Effect of aqueous phase conductivity σ_2 on the dielectric behavior of O/W/O double emulsion. (From Pal, R., *J. Colloid Int. Sci.* 325: 500–507, 2008.)

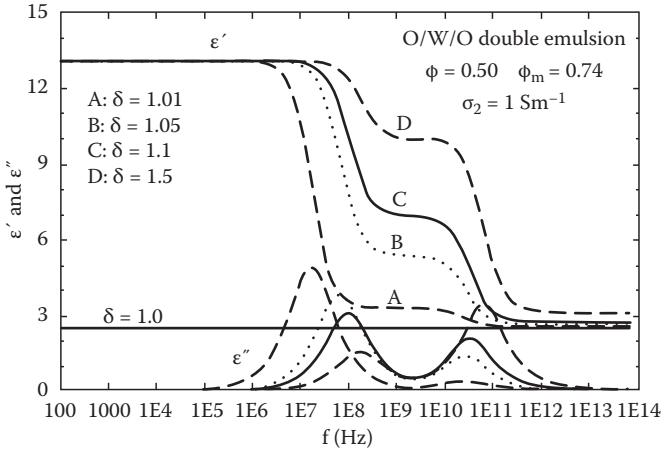

FIGURE 6.9 Effect of shell-to-core radii ratio δ on the dielectric behavior of O/W/O double emulsion. (From Pal, R., *J. Colloid Int. Sci.* 325: 500–507, 2008.)

$$\phi_c = \frac{(4/3)\pi R_c^3}{(4/3)\pi R_s^3} = \frac{1}{\delta^3} \tag{6.36}$$

where R_c is radius of the core (internal droplet) and R_s is the outer radius of the shell. For O/W/O double emulsion, an increase in δ at a fixed ϕ implies an increase in the thickness of water layer surrounding the internal oil droplets. According to Figure 6.9, the plateau values of permittivity (ε′) at intermediate frequencies and at high frequencies are affected by the value of δ. With the increase in δ, the plateau

values of ε' increase. This is to be expected as the water content of the double emulsion increases with the increase in δ (at a fixed value of ϕ). In addition, the double emulsion becomes more lossy (ε'' increases) with the increase in δ at high frequencies (microwave range around 10–100 GHz). However, at intermediate frequencies, an opposite effect is observed in that the double emulsion becomes less lossy (ε'' decreases) with the increase in δ.

The effect of volume fraction of core-shell droplets (ϕ) on the dielectric behavior of O/W/O double emulsion is shown in Figure 6.10. With the increase in ϕ at a constant δ, the permittivity ε' and loss factor ε'' both are affected strongly. The plateau values of ε' at low and intermediate frequencies increase with the increase in ϕ. The increase in ε' is negligible at high frequencies ($\omega > 100$ GHz). The effective loss factor ε'' increases with the increase in ϕ at intermediate and microwave frequencies. The increases in ε' and ε'' with ϕ at a fixed δ are due to an increase in water content of the double emulsion.

Figure 6.11 exhibits the dielectric behavior of W/O/W double emulsion under the following conditions: $\sigma_1 = 0$, $\sigma_3 = 1.0$ Sm^{-1}, $\phi = 0.50$, $\phi_m = 0.74$, and $\delta = 1.1$. Thus, the internal water droplets were conductive and the external water phase was nonconductive. The Cole–Cole plot (bottom portion of Figure 6.11) is also shown. The W/O/W double emulsion exhibits two dielectric relaxations—relaxation due to interfacial polarization at intermediate frequencies and dipolar relaxation at microwave frequencies. However, the interfacial polarization effect is not strong under the given conditions.

Figure 6.12 compares the dielectric behavior of a W/O/W double emulsion with that of a simple O/W emulsion at the same volume fraction of water. A simple O/W emulsion is a special case of a W/O/W double emulsion with $\delta \to \infty$. The dielectric behaviors of simple and double emulsions are similar in that they both exhibit only a single Debye-type relaxation.

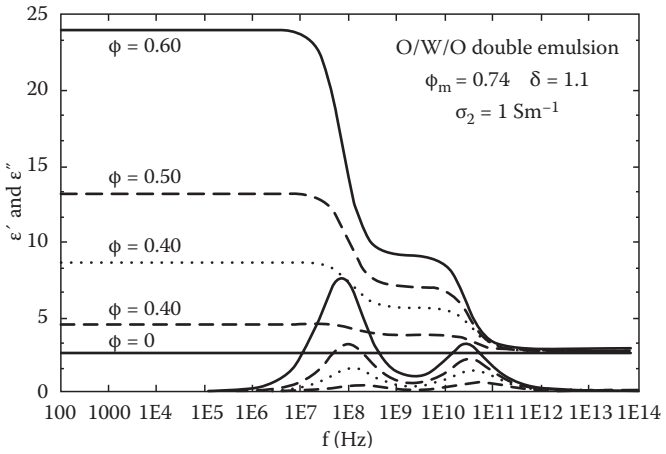

FIGURE 6.10 Effect of volume fraction of core-shell droplets (ϕ) on the dielectric behavior of O/W/O double emulsion. (From Pal, R., *J. Colloid Int. Sci.* 325: 500–507, 2008.)

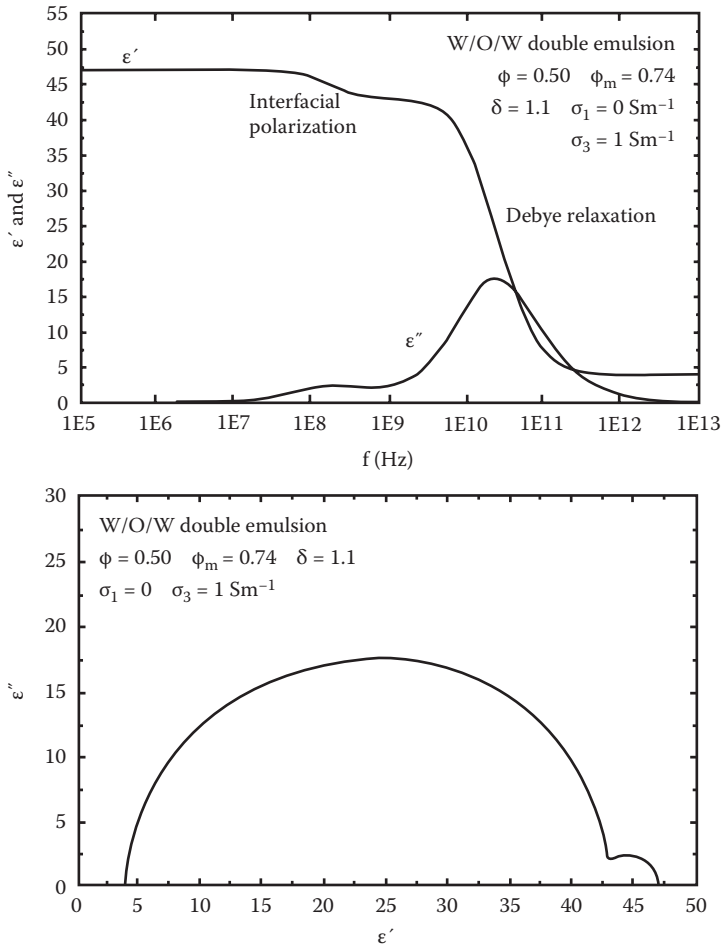

FIGURE 6.11 Dielectric behavior of W/O/W double emulsion under the conditions $\sigma_1 = \sigma_2 = 0$, $\sigma_3 = 1$ Sm^{-1}, $\phi = 0.50$, $\phi_m = 0.74$, $\delta = 1.1$. (From Pal, R., *J. Colloid Int. Sci.* 325: 500–507, 2008.)

The effect of internal droplet conductivity (σ_3) on the dielectric behavior of W/O/W double emulsion is shown in Figure 6.13. With the increase in σ_3, the relaxation frequency of interfacial polarization shifts to a higher value. The dipolar relaxation behavior at microwave frequencies is unaffected by σ_3.

Figure 6.14 shows the effect of shell-to-core radii ratio δ on the dielectric behavior of W/O/W double emulsion. An increase in δ at a fixed ϕ implies a decrease in the volume fraction of water within core-shell droplets (ϕ_c decreases). The plateau values of permittivity (ε') at low frequencies and at intermediate frequencies decrease with the increase in δ. The decrease in ε' is due to a decrease in water content of the double emulsion. In addition, the double emulsion becomes less lossy (ε'' decreases) with the increase in δ.

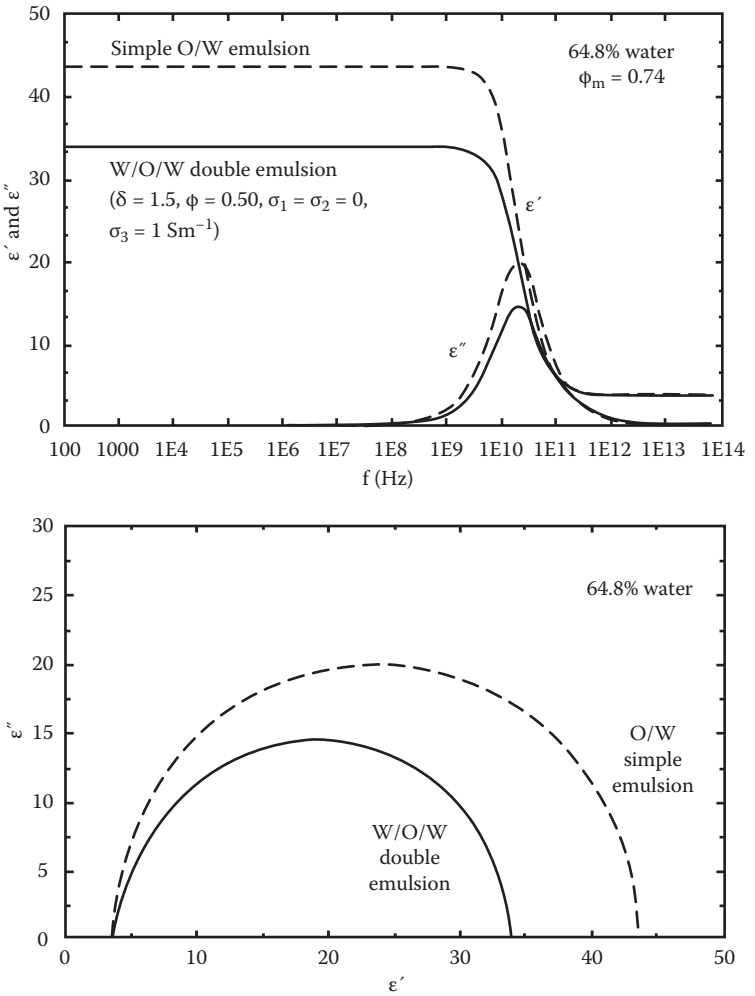

FIGURE 6.12 Comparison of the dielectric behaviors of W/O/W double emulsion and O/W simple emulsion at the same water content. (From Pal, R., *J. Colloid Int. Sci.* 325: 500–507, 2008.)

The effect of volume fraction of core-shell droplets (ϕ) on the dielectric behavior of W/O/W double emulsion is shown in Figure 6.15. With the increase in ϕ at a constant δ, the permittivity (ε′) and effective loss factor (ε″) both decrease due to a decrease in the water content of the double emulsion.

The dielectric behaviors of O/W/O and W/O/W double emulsions are compared in Figures 6.16 and 6.17 for the same water content. For the same water content, there exist more than one combination of ϕ (volume fraction of core-shell droplets) and δ values. Thus, comparisons are made either at the same ϕ but different δ (Figure 6.16) or at the same δ but different ϕ (Figure 6.17). An important point to note is that the interfacial polarization effect is absent in the case of W/O/W double emulsion. The

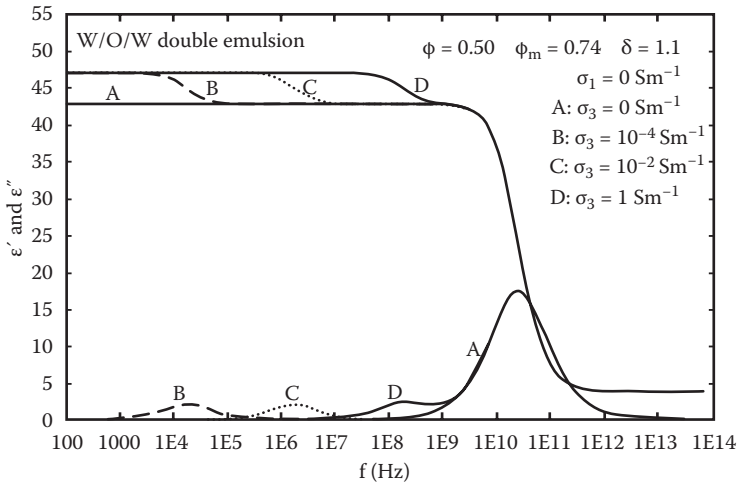

FIGURE 6.13 Effect of aqueous phase conductivity σ_3 on the dielectric behavior of W/O/W double emulsion. (From Pal, R., *J. Colloid Int. Sci.* 325: 500–507, 2008.)

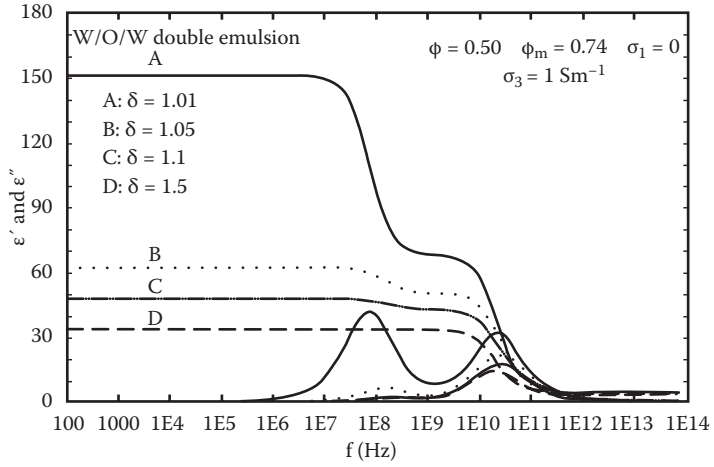

FIGURE 6.14 Effect of shell-to-core radii ratio δ on the dielectric behavior of W/O/W double emulsion. (From Pal, R., *J. Colloid Int. Sci.* 325: 500–507, 2008.)

W/O/W double emulsion exhibits only Debye relaxation whereas the O/W/O double emulsion exhibits both interfacial and Debye relaxations.

In summary, the dielectric behavior of composites with interphase effects could be modeled by treating the particles and their surrounding interphase region as core-shell-type particles. The complex relative permittivity model proposed by Pal [4] for dispersions of core-shell particles is discussed and applied to double emulsions of O/W/O and W/O/W types. The O/W/O double emulsions with conductive aqueous

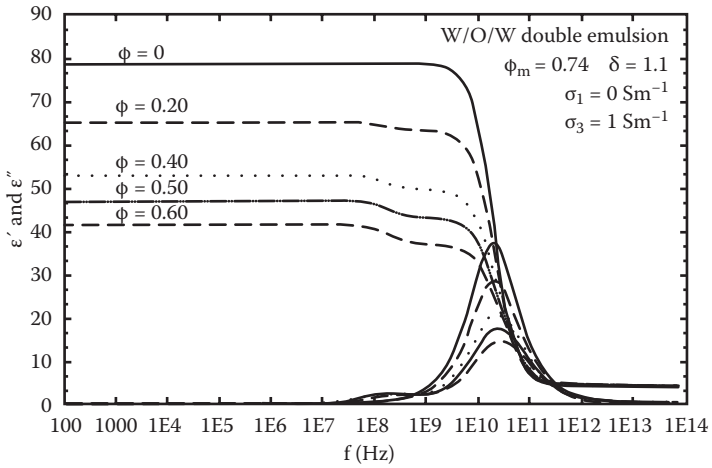

FIGURE 6.15 Effect of volume fraction of core-shell droplets (ϕ) on the dielectric behavior of W/O/W double emulsion.

phase exhibit two dielectric relaxations—relaxation due to interfacial polarization and Debye-type dipolar relaxation of water molecules. The W/O/W double emulsions also exhibit two dielectric relaxations (interfacial and Debye types) when the internal aqueous phase is conductive; however, the interfacial polarization effect in W/O/W double emulsions is much weaker. The factors that affect the dielectric behavior of double emulsions are volume fraction of core-shell droplets, shell-to-core radii ratio, aqueous phase conductivity, and type of double emulsion (O/W/O or W/O/W).

6.2 COMPLEX MAGNETIC PERMEABILITY OF COMPOSITES

The complex relative permeability μ* is defined according to the following constitutive relation for the complex magnetic flux density $\vec{B}^*$:

$$\vec{B}^* = \mu_o \mu^* \vec{H}^* \tag{6.37}$$

where $\vec{H}^*$ is the complex magnetic field intensity. The complex relative permeability μ* can be expressed as follows:

$$\mu^* = \mu' - j\mu'' \tag{6.38}$$

where μ′ and μ″ are the real and imaginary parts of the relative permeability. For *dispersive* material, μ′ and μ″ are functions of frequency. The real part μ′ reflects the polarization property of the material. It is a measure of the amount of magnetic moments that become aligned with the applied magnetic field. It also reflects the amount of energy stored by the magnetic moments upon the application of the external magnetic field. The imaginary part μ″ is called "polarization loss" as it reflects

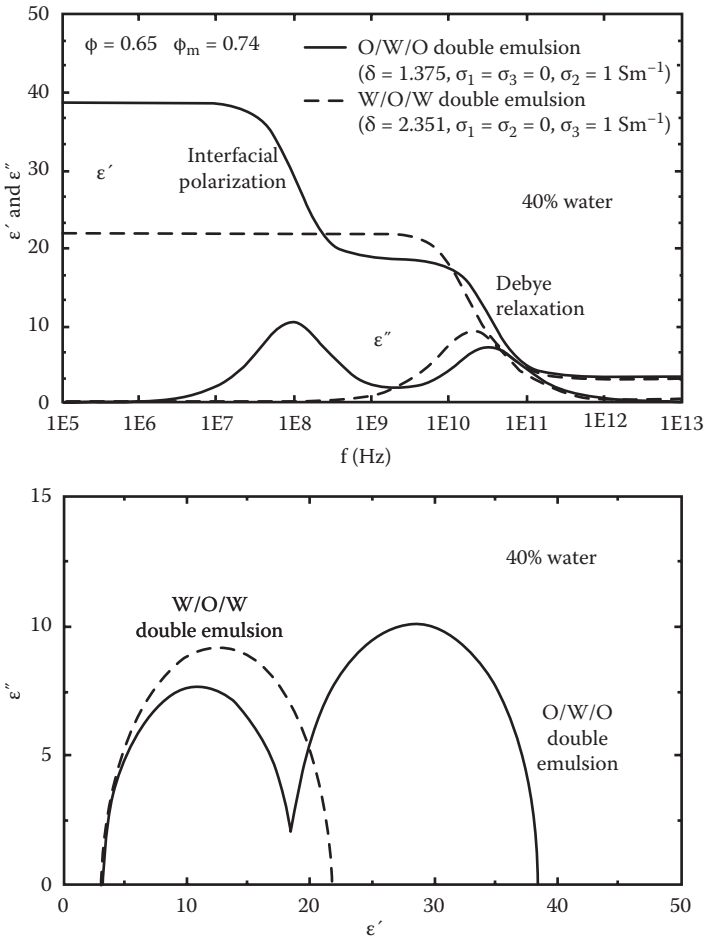

FIGURE 6.16 Comparison of the dielectric behaviors of O/W/O and W/O/W double emulsions at the same water content and ϕ (volume fraction of core-shell droplets). (From Pal, R., *J. Colloid Int. Sci.* 325: 500–507, 2008.)

energy loss in the magnetic material caused by a delay in the material's response to the applied field.

The magnetic dispersion, that is, frequency dependence of permeability, appears when the frequency of oscillation of the external magnetic field is too high for the magnetic moments to orient with the field.

The key mechanisms responsible for magnetic dispersion are domain wall displacement, domain rotation, detrital rotation, spin magnetic-moment orientation, and orbital magnetic-moment orientation [6]. Relaxation of spin magnetic moments occurs at high frequencies. The spin magnetic dipole moments cannot stay aligned with the external filed when frequencies are higher than 10 GHz. Thus, the magnetic

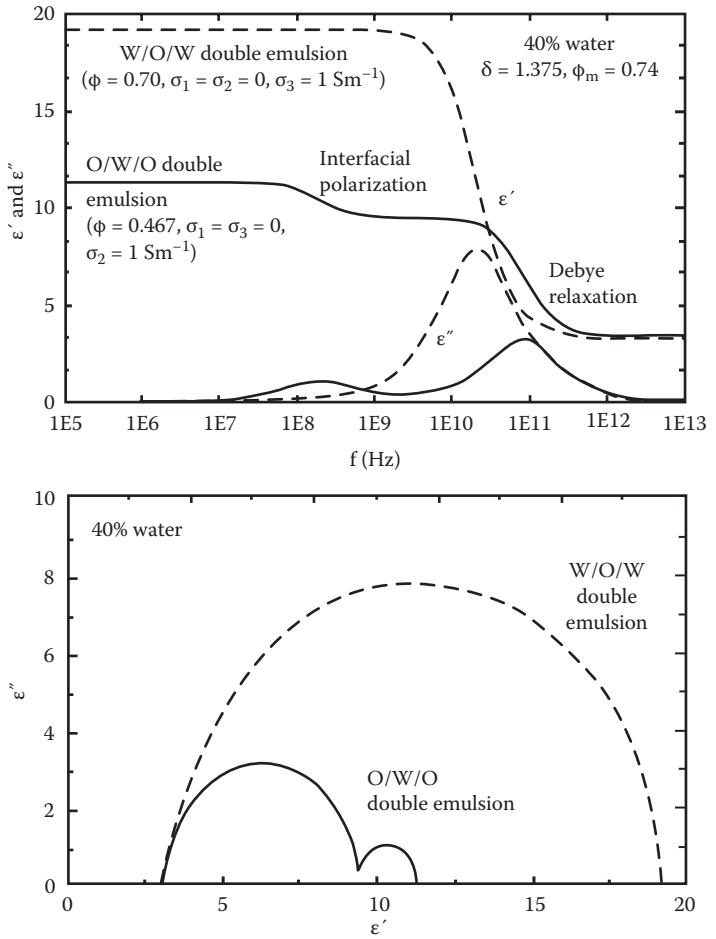

FIGURE 6.17 Comparison of the dielectric behaviors of O/W/O and W/O/W double emulsions at the same water content and δ (shell-to-core radii ratio). (From Pal, R., *J. Colloid Int. Sci.* 325: 500–507, 2008.)

permeability of materials at such high frequencies corresponds to that of free space due to the absence of any polarization effect. Relaxation of orbital magnetic dipole moments occurs at frequencies lower than that of spin relaxation. Domain wall displacement occurs in grains or particles consisting of magnetic multidomains. The magnetic domain wall, also called the Bloch wall, is the boundary region between two neighboring magnetic domains oriented in opposite directions. In this transition region, the sublattice magnetic moments rotate from a direction corresponding to one magnetic domain to an opposite direction corresponding to the neighboring domain. When an external magnetic field is applied, the magnetic domains oriented in the direction of the applied field undergo expansion whereas the magnetic domains oriented in the opposite direction shrink. The expansion and shrinking of

neighboring magnetic domains takes place by the movement of the magnetic domain walls. When the frequency of oscillation of the external field is high enough that the magnetic domain walls are not able to move to the extent to cause full expansion or shrinking of the neighboring domains, frequency dependence of permeability appears. When the grain or particle size is small, the number of magnetic domains in a grain decreases. Below a certain critical size, only one magnetic domain is present in a grain. The magnetic moment of a single domain particle is usually oriented along the easy axes of the crystal. When a single domain particle is subjected to an external magnetic field, the magnetic moment of the particle tends to align with the external field either by rotation of the magnetic domain (called domain rotation) or by rotation of the entire grain (called detrital rotation). Magnetic dispersion due to domain wall movement occurs in the lower-frequency radiofrequency (RF) band (1 MHz–1 GHz) whereas dispersion due to domain rotation occurs in the higher-frequency microwave band (1–100 GHz) [7].

6.2.1 Models for Complex Magnetic Permeability of Composites

According to the "Generalized Conductivity Principle" discussed in Chapter 5, the models developed for the static magnetic permeability μ of composites could be applied to complex magnetic permeability μ* by simply replacing μ with μ*. Thus, the key equations for estimating the relative magnetic permeability of composites are as follows [8]:

Voigt rule of mixtures:

$$\mu^* = \mu_d^* \phi + (1-\phi)\mu_m^* \tag{6.39}$$

Reuss rule of mixtures:

$$\frac{1}{\mu^*} = \frac{\phi}{\mu_d^*} + \frac{1-\phi}{\mu_m^*} \tag{6.40}$$

Lichtenecker logarithmic rule of mixtures:

$$\log \mu^* = \phi \log \mu_d^* + (1-\phi)\log \mu_m^* \tag{6.41}$$

Rayleigh equation:

$$\frac{\mu^*}{\mu_m^*} = 1 + \left[\frac{3\phi}{\left(\frac{\mu_d^* + 2\mu_m^*}{\mu_d^* - \mu_m^*} \right) - \phi - 1.65 \left(\frac{\mu_d^* - \mu_m^*}{\mu_d^* + 4\mu_m^*/3} \right) \phi^{10/3}} \right] \tag{6.42}$$

Maxwell–Garnett equation:

$$\left(\frac{\mu^* - \mu_m^*}{\mu^* + 2\mu_m^*}\right) = \left(\frac{\mu_d^* - \mu_m^*}{\mu_d^* + 2\mu_m^*}\right)\phi \tag{6.43}$$

Pal model 1:

$$\left(\frac{\mu^*}{\mu_m^*}\right)^{1/3}\left(\frac{\mu_d^* - \mu_m^*}{\mu_d^* - \mu^*}\right) = \exp(\phi) \tag{6.44}$$

Bruggeman asymmetric model:

$$\left(\frac{\mu_m^*}{\mu^*}\right)^{1/3}\left(\frac{\mu^* - \mu_d^*}{\mu_m^* - \mu_d^*}\right) = (1 - \phi) \tag{6.45}$$

Bruggeman symmetric model:

$$\left(\frac{\mu_d^* - \mu^*}{\mu_d^* + 2\mu^*}\right)\phi + \left(\frac{\mu_m^* - \mu^*}{\mu_m^* + 2\mu^*}\right)(1 - \phi) = 0 \tag{6.46}$$

Pal model 2:

$$\left(\frac{\mu_m^*}{\mu^*}\right)^{1/3}\left(\frac{\mu^* - \mu_d^*}{\mu_m^* - \mu_d^*}\right) = \left(1 - \frac{\phi}{\phi_m}\right)^{\phi_m} \tag{6.47a}$$

Pal model 3:

$$\left(\frac{\mu_m^*}{\mu^*}\right)^{1/3}\left(\frac{\mu^* - \mu_d^*}{\mu_m^* - \mu_d^*}\right) = \exp\left(-\frac{\phi}{1 - \frac{\phi}{\phi_m}}\right) \tag{6.47b}$$

Lewis-Nielsen model:

$$\frac{\mu^*}{\mu_m^*} = \left[\frac{1 + 2\left(\frac{\mu_d^* - \mu_m^*}{\mu_d^* + 2\mu_m^*} \right)\phi}{1 - \phi\psi\left(\frac{\mu_d^* - \mu_m^*}{\mu_d^* + 2\mu_m^*} \right)} \right] \tag{6.48}$$

where ψ is defined in Equation 6.34.

6.2.2 Experimental Observations on Complex Magnetic Permeability of Composites

A number of experimental studies [7,9–14] have been published on frequency dispersion of magnetic permeability of composites consisting of magnetic filler particles (such as Mn–Zn and Ni–Zn ferrites, carbonyl iron) and polymeric binder (matrix). According to Tsutaoka [14], the frequency dispersion of magnetic permeability of polycrystalline materials and their composites can be characterized by a superposition of two types of magnetic resonance mechanisms: domain wall motion and gyromagnetic spin motion. Consequently, one can describe the frequency dispersion of magnetic permeability by the following two-component formula of complex magnetic permeability:

$$\mu^* = 1 + \frac{\omega_d^2 \chi_{do}}{\omega_d^2 - \omega^2 + j\omega\beta} + \frac{(\omega_s + j\omega\alpha)\omega_s \chi_{so}}{(\omega_s + j\omega\alpha)^2 - \omega^2} \tag{6.49}$$

where ω_d and ω_s are resonance frequencies of domain-wall and spin components, respectively, χ_{do} and χ_{so} are the static magnetic susceptibilities of domain-wall and spin components, α and β are damping factors, ω is the frequency of external magnetic field. The second term of Equation 6.49 is the domain-wall component and the third term is the spin component of the complex magnetic permeability. The real and imaginary parts of Equation 6.49 are as follows:

$$\mu' = 1 + \frac{\omega_d^2 \chi_{do}(\omega_d^2 - \omega^2)}{(\omega_d^2 - \omega^2)^2 + \omega^2\beta^2} + \frac{\chi_{so}\omega_s^2[\omega_s^2 + \omega^2 + \omega^2\alpha^2]}{[\omega_s^2 - \omega^2(1+\alpha^2)]^2 + 4\omega^2\omega_s^2\alpha^2} \tag{6.50}$$

$$\mu'' = \frac{\omega_d^2 \chi_{do}\omega\beta}{(\omega_d^2 - \omega^2)^2 + \omega^2\beta^2} + \frac{\chi_{so}\omega\alpha\omega_s[\omega_s^2 + \omega^2 + \omega^2\alpha^2]}{[\omega_s^2 - \omega^2(1+\alpha^2)]^2 + 4\omega^2\omega_s^2\alpha^2} \tag{6.51}$$

In Equation 6.50, the second term is the contribution of domain-wall motion to μ' and the third term is the contribution of spin motion to μ'. In Equation 6.51, the

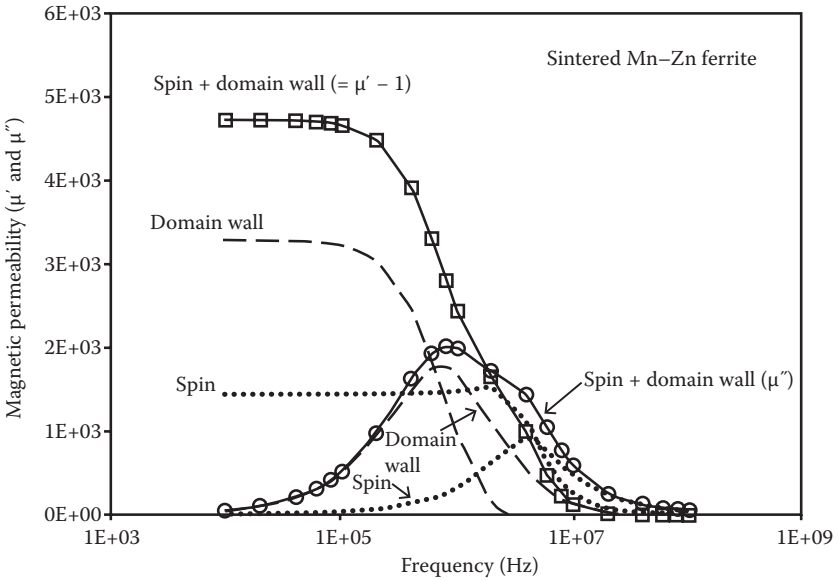

FIGURE 6.18 Magnetic permeability spectra of sintered Mn–Zn ferrite. (Based on Tsutaoka, T., *J. Appl. Phys*. 93: 2789–2796, 2003.)

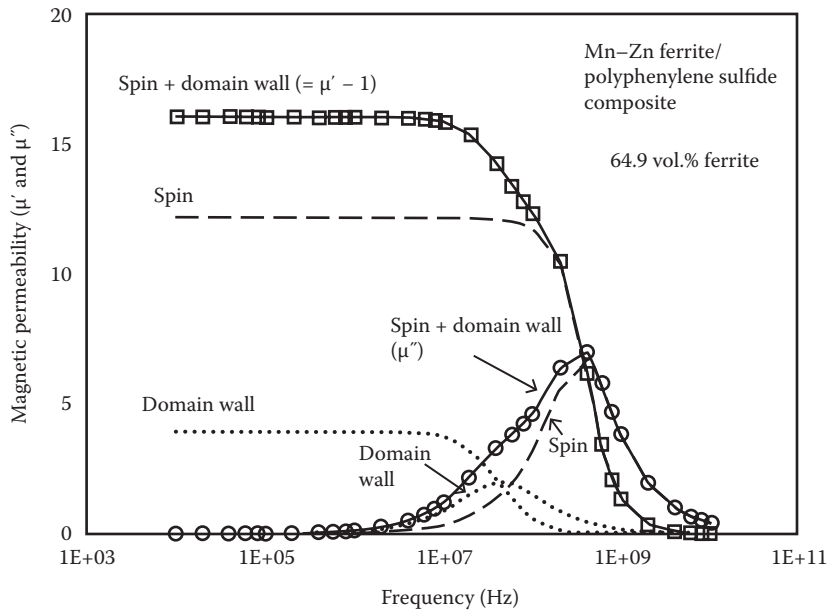

FIGURE 6.19 The magnetic permeability spectra of composite of sintered Mn–Zn ferrite particles and polymeric binder (polyphenylene sulfide). (Based on Tsutaoka, T., *J. Appl. Phys*. 93: 2789–2796, 2003.)

first term is the contribution of domain-wall motion to μ'' and the second term is the contribution of spin motion to μ''.

As an example, Figure 6.18 shows the magnetic permeability spectra of sintered Mn–Zn ferrite obtained experimentally by Tsutaoka [14]. The figure also shows the curves generated from the above equations using the following values of the parameters: $\chi_{do} = 3282$, $\omega_d = 2.5$ MHz, $\beta = 9.3 \times 10^6$, $\chi_{so} = 1438$, $\omega_s = 6.3$ MHz, $\alpha = 1.28$. Clearly, the domain wall contribution is dominant in this system. Also note that spin resonance occurs at a higher frequency than domain-wall resonance, as expected. The permeability spectra of composite of sintered Mn–Zn ferrite particles and polymeric binder (polyphenylene sulfide) is shown in Figure 6.19. The filler (Mn–Zn ferrite particles) content of the composite is 64.9 vol.%. The figure shows the experimental observations as well as the curves generated from Equations 6.50 and 6.51 using the following values of the parameters: $\chi_{do} = 3.9$, $\omega_d = 296$ MHz, $\beta = 2 \times 10^9$, $\chi_{so} = 12.2$, $\omega_s = 875$ MHz, $\alpha = 2.31$. Now the domain wall contribution is less important than the spin contribution. In the composite material, the domain wall contribution is diminished due to a decrease in the domain walls.

Figure 6.20 shows variation of the real part of complex permeability (μ') as a function of filler concentration for carbonyl iron-filled polymer composites at a fixed

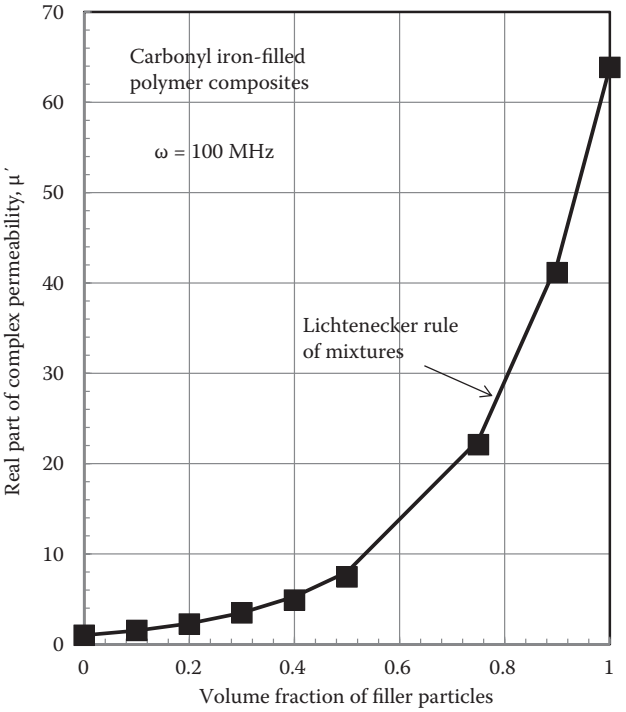

FIGURE 6.20 Variation of real part of complex permeability (μ') as a function of filler concentration for carbonyl iron-filled polymer composites at a fixed frequency of 100 MHz. (Based on Abshinova, M. et al., *Composites A* 38: 2471–2785, 2007.)

frequency of 100 MHz [7]. The experimental data can be described adequately with the Lichtenecker logarithmic rule of mixtures (Equation 6.41).

REFERENCES

1. Clausse, M. 1983. Dielectric properties of emulsions and related systems. In: *Encyclopedia of Emulsion Technology*, ed., P. Becher, Vol. 1, Chapter 9, pp. 483–715, New York: Marcel Dekker.
2. Pal, R. 1994. Techniques for measuring the composition (oil and water content) of emulsions—a state of the art review. *Colloids Surf.* 84: 141–193.
3. Hanai, T., T. Imakita, and N. Koizumi. 1982. Analysis of dielectric relaxations of W/O emulsions in the light of theories of interfacial polarization. *Colloid Polym. Sci.* 260: 1029–1034.
4. Pal, R. 2008. Dielectric behavior of double emulsions with core-shell droplet morphology. *J. Colloid Int. Sci.* 325: 500–507.
5. Yuan, F. 1995. Composition measurement of suspensions and emulsions using a microwave technique. M.A.Sc. thesis. University of Waterloo, Canada.
6. Stillman, D.E. 2006. Frequency and temperature dependence in electromagnetic properties of Martian analog minerals, PhD thesis (geophysics), Colorado School of Mines, USA.
7. Abshinova, M., A. Lopatin, N. Kazantseva, J. Vilcakova, and P. Saha. 2007. Correlation between the microstructure and the electromagnetic properties of carbonyl iron filled composites. *Composites A* 38: 2471–2785.
8. Pal, R. 2014. *Electromagnetic, Mechanical, and Transport Properties of Composite Materials*, Chapter 4, Boca Raton: CRC Press.
9. Anhalt, M. and B. Weidenfeller. 2007. Magnetic properties of polymer bonded soft magnetic particles for various filler fractions. *J. Appl. Phys*. 101: 023907-1.
10. Gokturk, H.S., T.J. Fiske, and D.M. Kalyon. 1993. Electric and magnetic properties of a thermoplastic elastomer incorporated with ferromagnetic powders. *IEEE Trans. Magnet*. 29: 4170–4176.
11. Choi, H.D., K.S. Moon, I.S. Jeon, W. S. Kim, and T.J. Moon, 1997. Frequency dispersion model of the complex permeability of the epoxy–ferrite composite. *J. Appl. Polym. Sci*. 66: 477–482.
12. Tsutaoka, T., M. Ueshima, T. Tokunaga, T. Nakamura, and K. Hatakeyama. 1995. Frequency dispersion and temperature variation of complex permeability of Ni–Zn ferrite composite materials. *J. Appl. Phys.* 78: 3983–3991.
13. Kasagi, T., T. Tsutaoka, and K. Hatakeyama. 1999. Particle size effect on the complex permeability for permalloy composite materials. *IEEE Trans. Magnet*. 35: 3424–3426.
14. Tsutaoka, T. 2003. Frequency dispersion of complex permeability in Mn–Zn and Ni–Zn spinel ferrites and their composite materials. *J. Appl. Phys*. 93: 2789–2796.

Section III

Mechanical Properties of Composites

7 Mechanical Properties of Dilute Particulate-Filled Composites

Knowledge of the mechanical properties of composites is required in the analysis and design of structures made from composite materials. They also play a vital role in the development of new composite materials that meet specific strength or stiffness requirements. In order to develop tailor-made composites with specific mechanical properties, models are needed to predict the mechanical properties of composites from the properties and volume fractions of the individual components.

7.1 BACKGROUND

The key mechanical properties of composite solids are shear modulus (G), Young's modulus (E), Poisson's ratio (υ), and bulk modulus (K). When a shear stress is applied to a material, it undergoes shear strain (angular deformation). For a given shear stress, the shear strain depends on the material property called shear modulus (G), which is the ratio of shear stress (τ) to shear strain (γ):

$$\tau = G\gamma \text{ or } G = \tau/\gamma \tag{7.1}$$

When a tensile stress (elongational stress) is applied to a material, the material undergoes extension (elongational strain). For a given tensile stress, the elongational strain depends on the material property called Young's modulus (E), which is the ratio of tensile stress (σ) to elongational strain (ε_x):

$$\sigma = E\varepsilon_x \text{ or } E = \sigma/\varepsilon_x \tag{7.2}$$

When a material is stretched in the axial direction, it shrinks in the transverse or lateral direction. The Poisson ratio is defined to be the ratio of lateral strain to longitudinal strain with a negative sign. Thus,

$$\nu = -\varepsilon_y/\varepsilon_x \tag{7.3}$$

In principle, $-1 \le \nu \le 0.5$, but usually, ν is positive. For most common materials, $0 < \nu \le 0.5$. For incompressible materials, ν is 0.5.

When the pressure acting on a material is increased, it shrinks (undergoes compression). K is a measure of the compressibility of material. It is the ratio of pressure increase to negative of volumetric strain:

$$K = \frac{\Delta P}{-\left(\frac{\Delta V}{V}\right)} = -V\frac{dP}{dV} = \rho\frac{dP}{d\rho} \tag{7.4}$$

where ρ is density. For incompressible materials, $K \to \infty$.

In *isotropic* materials (that is, no directional dependence of properties), only two of the four mechanical properties (elastic constants) are independent. If two properties are fixed, the remaining two are automatically fixed. Suppose that G and K (shear and bulk moduli) are known. Then the other two constants can be determined from the following fundamental relations [1]:

$$E = \frac{9KG}{3K + G} \tag{7.5}$$

$$\nu = \frac{3K - 2G}{6K + 2G} = \frac{1}{2}\left(1 - \frac{E}{3K}\right) = \frac{E}{2G} - 1 \tag{7.6}$$

Over the past several decades, a number of empirical and theoretical studies have been published in the literature on the mechanical properties of particulate composite materials. In what follows, the key empirical and theoretical models describing the mechanical properties of particulate composites are discussed. However, the discussion is focused on the mechanical properties of *dilute* composites in this chapter. Concentrated composites with large volume fractions of filler particles are dealt with in the following chapters.

7.2 EMPIRICAL RULES OF MIXTURES

7.2.1 Voigt Rule of Mixtures

The Voigt rule of mixture (ROM) gives the *upper* bound of the property. It is based on *action in parallel* approach. It is assumed that each component of the composite undergoes the same strain (*isostrain*) and that each component contributes to the stress to an extent depending on the volume fraction of that component. Thus, $\varepsilon = \varepsilon_m = \varepsilon_d$ and $\tau = (1 - \phi)\tau_m + \phi\tau_d$, where ε, ε_d, and ε_m are the strains in composite, dispersed phase, and matrix, respectively; τ, τ_d, and τ_m are the stresses in the composite, dispersed phase, and matrix, respectively; and ϕ is volume fraction of the dispersed phase. Substituting the stress–strain relations $\tau = L\varepsilon$, $\tau_m = L_m\varepsilon_m$, and $\tau_d = L_d\varepsilon_d$ into $\tau = (1 - \phi)\tau_m + \phi\tau_d$ and equating the strains, one can readily arrive at the following result:

$$L = \phi L_d + (1 - \phi)L_m \tag{7.7}$$

where L is the composite property, L_d is the corresponding property of the dispersed phase, and L_m is the corresponding property of the matrix. Equation 7.7 is referred to as the Voigt ROM.

7.2.2 Reuss Rule of Mixtures

The Reuss ROM gives the *lower* bound of the property. It is based on *action in series* approach. It is assumed that each component of the composite undergoes the same stress (*isostress*) and that each component contributes to the strain to an extent depending on the volume fraction of that component. Thus, $\tau = \tau_m = \tau_d$ and $\varepsilon = (1 - \phi)\varepsilon_m + \phi\varepsilon_d$. Also, $\tau = L\varepsilon$, $\tau_m = L_m\varepsilon_m$, and $\tau_d = L_d\varepsilon_d$. Thus, it can be readily shown that

$$\frac{1}{L} = \frac{\phi}{L_d} + \frac{(1-\phi)}{L_m} \tag{7.8}$$

Equation 7.8 is referred to as the Reuss ROM.

The Voigt and Reuss ROMs give a crude estimate of the property. The actual value usually falls in between these two bounds.

7.3 THEORETICAL MODELS

7.3.1 Dilute Composites with Spherical Particles

For dilute composites of solid (not necessarily rigid) spherical particles, the exact theoretical expressions for shear modulus (G) and its intrinsic value [G] are given as follows [1]:

$$\frac{G}{G_m} = 1 + \left[\frac{15(1-\nu_m)(G_d - G_m)}{2G_d(4-5\nu_m) + G_m(7-5\nu_m)}\right]\phi \tag{7.9}$$

$$[G] = \lim_{\phi \to 0} \frac{G/G_m - 1}{\phi} = \frac{15(1-\nu_m)(\lambda_G - 1)}{2\lambda_G(4-5\nu_m) + (7-5\nu_m)} \tag{7.10}$$

where G_d and G_m are shear moduli of dispersed phase and matrix, respectively, ν_m is the Poisson ratio of matrix, and λ_G is the shear modulus ratio G_d/G_m.

The exact theoretical expression for bulk modulus (K) of dilute composites of solid spherical particles is given as follows [1]:

$$\frac{K}{K_m} = 1 + \left[\left(\frac{3K_m + 4G_m}{3K_m}\right)\left(\frac{3K_d - 3K_m}{3K_d + 4G_m}\right)\right]\phi \tag{7.11}$$

where K_d and K_m are bulk moduli of dispersed phase and matrix, respectively. Since $G/K = [3(1 - 2\nu)]/[2(1 + \nu)]$ for isotropic materials, Equation 7.11 can be rewritten as

$$\frac{K}{K_m} = 1 - \left[\frac{3(1-\nu_m)(K_m - K_d)}{2K_m(1-2\nu_m) + K_d(1+\nu_m)}\right]\phi \tag{7.12}$$

The intrinsic bulk modulus [K] is given as

$$[K] = \lim_{\phi \to 0} \frac{K/K_m - 1}{\phi} = -\left[\frac{3(1-\nu_m)(1-\lambda_K)}{2(1-2\nu_m) + \lambda_K(1+\nu_m)}\right] \tag{7.13}$$

where λ_K is the bulk modulus ratio K_d/K_m.

With the results obtained for the shear and bulk moduli (G and K), the other two elastic constants, namely, Young's modulus (E) and Poisson's ratio (ν) can be obtained from the standard relations for isotropic materials, that is, Equations 7.5 and 7.6.

It can be readily shown that for a dilute dispersion of spherical solid particles in a solid matrix, Young's modulus (E) is given by the following expression [2]:

$$\frac{E}{E_m} = 1 + \left\{\left[\frac{10(1-\nu_m^2)(1+\nu_m)E_d - 10(1-\nu_m^2)(1+\nu_d)E_m}{2(4-5\nu_m)(1+\nu_m)E_d + (7-5\nu_m)(1+\nu_d)E_m}\right] + \left[\frac{(1-\nu_m)(1-2\nu_m)E_d - (1-\nu_m)(1-2\nu_d)E_m}{(1+\nu_m)E_d + 2E_m(1-2\nu_d)}\right]\right\}\phi \tag{7.14}$$

where E_d and E_m are Young's moduli of the dispersed phase and the matrix phase, respectively, ν_d and ν_m are the Poisson ratios of the dispersed and matrix phases, respectively.

The intrinsic Young's modulus [E] is given by

$$[E] = \lim_{\phi \to 0} \frac{E/E_m - 1}{\phi} = \left\{\left[\frac{10(1-\nu_m^2)(1+\nu_m)\lambda_E - 10(1-\nu_m^2)(1+\nu_d)}{2(4-5\nu_m)(1+\nu_m)\lambda_E + (7-5\nu_m)(1+\nu_d)}\right] + \left[\frac{(1-\nu_m)(1-2\nu_m)\lambda_E - (1-\nu_m)(1-2\nu_d)}{(1+\nu_m)\lambda_E + 2(1-2\nu_d)}\right]\right\} \tag{7.15}$$

where λ_E is Young's modulus ratio defined as E_d/E_m.

Figure 7.1 shows the intrinsic shear modulus [G] plots generated from Equation 7.10. For a given shear modulus ratio λ_G, [G] generally increases with the increase in ν_m (matrix Poisson's ratio). For a given ν_m, [G] increases with the increase in λ_G.

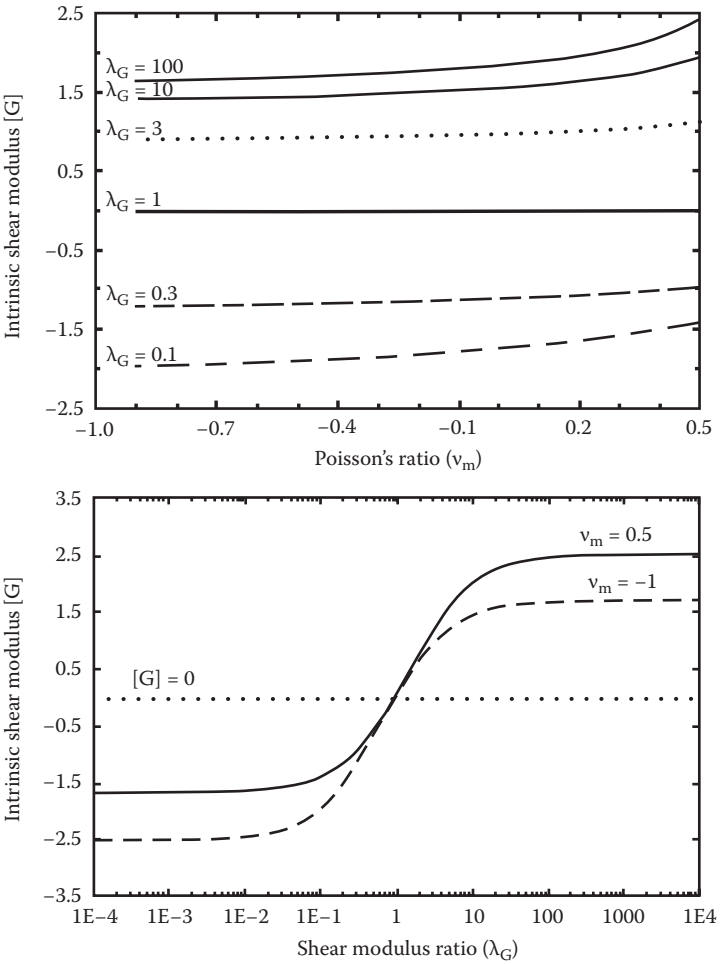

FIGURE 7.1 Intrinsic shear modulus [G] plots of particulate composite with spherical particles. (From Pal, R., *Rheology of Particulate Dispersions and Composites*, Chapter 12, Boca Raton: CRC Press, 2007.)

At $\lambda_G = 1$, [G] is zero regardless of the value of ν_m. When $\lambda_G < 1$, [G] is negative and when $\lambda_G > 1$, [G] is positive.

Figure 7.2 shows the intrinsic bulk modulus [K] plots generated from Equation 7.13. For a given bulk modulus ratio λ_K, [K] generally decreases with the increase in ν_m. For a given ν_m, [K] increases with the increase in λ_K. At $\lambda_K = 1$, [K] is zero regardless of the value of ν_m. When $\lambda_K < 1$, [K] is negative and when $\lambda_K > 1$, [K] is positive.

Figure 7.3 shows the intrinsic Young's modulus [E] plots generated from Equation 7.15. For the top graph of Figure 7.3, the matrix is taken to be incompressible

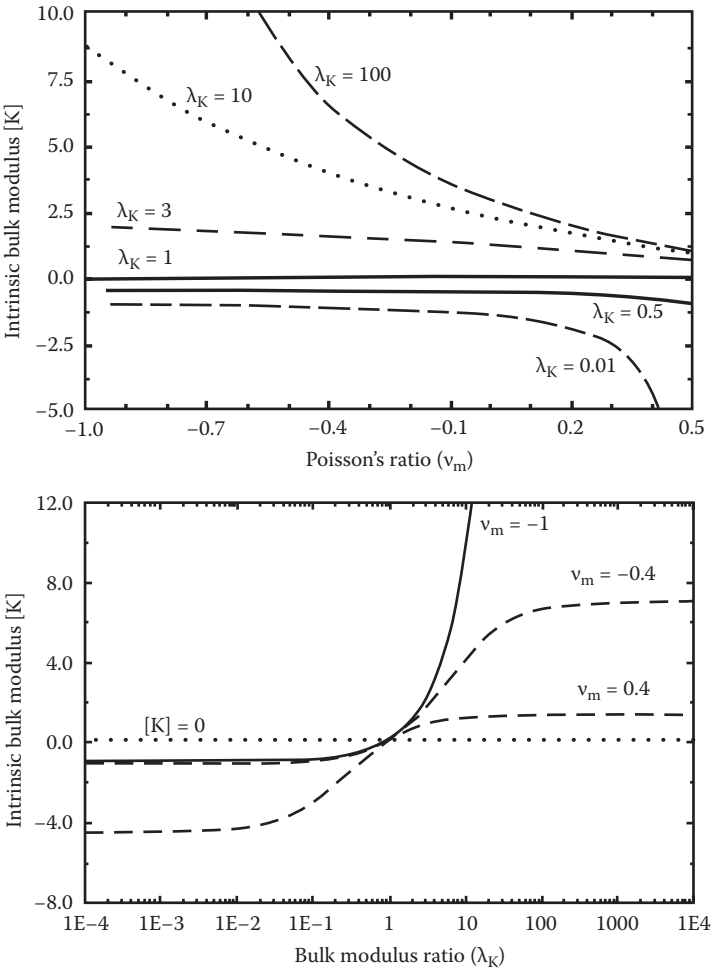

FIGURE 7.2 Intrinsic bulk modulus [K] plots of particulate composite with spherical particles. (From Pal, R., *Rheology of Particulate Dispersions and Composites*, Chapter 12, Boca Raton: CRC Press, 2007.)

(ν_m = 0.5) and for the bottom graph of Figure 7.3, the particles are taken to be incompressible (ν_d = 0.5). For a given ν_d (particle Poisson's ratio), the intrinsic Young's modulus [E] of composite with incompressible matrix (ν_m = 0.5) increases with the increase in λ_E, the Young's modulus ratio. In addition, [E] decreases with the increase in ν_d in the intermediate range of λ_E ($10^{-2} < \lambda_E < 100$). The crossover value of the modulus ratio λ_E where [E] crosses from the region of [E] > 0 to the region [E] < 0, increases with the increase in ν_d. The crossover value of λ_E is unity

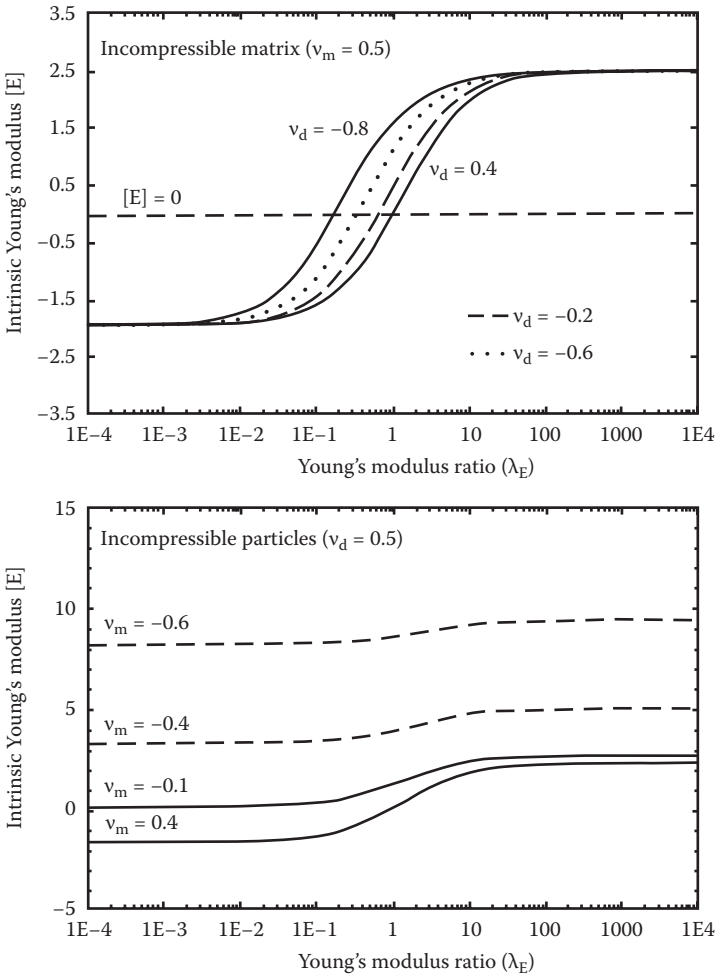

FIGURE 7.3 Intrinsic Young's modulus [E] plots of particulate composite with spherical particles. (From Pal, R., *Rheology of Particulate Dispersions and Composites*, Chapter 12, Boca Raton: CRC Press, 2007.)

only when ν_d is near 0.5. For a given ν_m, [E] increases with the increase λ_E when the particles are incompressible ($\nu_d = 0.5$).

7.3.1.1 Composites with Rigid Spherical Particles

For particulate composite reinforced by rigid particles ($\nu_d \to 0.5$, $K_d \to \infty$, $G_d \to \infty$, $E_d \to \infty$), the equations for the shear, bulk, and Young's moduli reduce to the following expressions:

$$\frac{G}{G_m} = 1 + \left[\frac{15(1-\nu_m)}{2(4-5\nu_m)}\right]\phi \tag{7.16}$$

$$\frac{K}{K_m} = 1 + \left[\frac{3(1-\nu_m)}{(1+\nu_m)}\right]\phi \tag{7.17}$$

$$\frac{E}{E_m} = 1 + \left[\frac{3(1-\nu_m)(5\nu_m^2 - \nu_m + 3)}{(1+\nu_m)(4-5\nu_m)}\right]\phi \tag{7.18}$$

If, in addition to rigid particles, the composite matrix is incompressible ($\nu_m \to 0.5$, $K_m \to \infty$), the expressions for the relative shear and Young's moduli become identical, that is,

$$\frac{G}{G_m} = \frac{E}{E_m} = 1 + \frac{5}{2}\phi \tag{7.19}$$

7.3.1.2 Composites with Incompressible Matrix

For particulate composites with incompressible matrix ($\nu_m = 0.5$), the equations for the effective elastic properties G, K, and E reduce to the following:

$$\frac{G}{G_m} = 1 + \left[\frac{5(G_d - G_m)}{2(G_d + 1.5G_m)}\right]\phi \tag{7.20}$$

$$K = \frac{3K_d + 4G_m}{3\phi} \tag{7.21}$$

$$\frac{E}{E_m} = 1 + \left[\left\{\frac{15(E_d/E_m) - 10(1+\nu_d)}{6(E_d/E_m) + 6(1+\nu_d)}\right\} - \left\{\frac{1-2\nu_d}{3(E_d/E_m) + 4(1-2\nu_d)}\right\}\right]\phi \tag{7.22}$$

If both dispersed and matrix phases are incompressible, that is, $\nu_m = 0.5$ and $\nu_d = 0.5$, the expression for G remains the same as Equation 7.20, but K becomes infinite and E is given by

$$\frac{E}{E_m} = 1 + \left[\frac{5(E_d - E_m)}{2(E_d + 1.5E_m)}\right]\phi \tag{7.23}$$

7.3.1.3 Composites with Pores

Composites with pores (pore-solid composite materials) find many engineering applications ranging from acoustic absorption to heat shields in reentry vehicles.

Pore-solid composites are of interest in biomedical applications as well [3–5]. Even in nature many of the solids are porous.

For pore-solid composites, the equations for the shear, bulk, and Young's moduli (Equations 7.9, 7.12, and 7.14) simplify to the following expressions:

$$\frac{G}{G_m} = 1 - \left[\frac{15(1-\nu_m)}{7-5\nu_m}\right]\phi \tag{7.24}$$

$$\frac{K}{K_m} = 1 - \left[\frac{3(1-\nu_m)}{2(1-2\nu_m)}\right]\phi \tag{7.25}$$

$$\frac{E}{E_m} = 1 - \left[\frac{3(1-\nu_m)(9+5\nu_m)}{2(7-5\nu_m)}\right]\phi \tag{7.26}$$

The moduli of the dispersed phase (voids) are taken to be zero, that is, $G_d \to 0$, $E_d \to 0$, and $K_d \to 0$. It is interesting to note that while the effective shear and bulk moduli (G and K) of porous materials are strongly dependent on the matrix Poisson ratio, ν_m, the effective Young's modulus E of pore-solid composites is insensitive to ν_m [6], especially when $0 \le \nu_m \le 0.5$.

7.3.2 Dilute Composites with Disk-Shaped Particles

For *dilute* particulate composites with *disk-shaped* particles, the elastic properties K and G are given as follows [7]:

$$\frac{K}{K_m} = 1 + \phi\left[\frac{(K_d - K_m)(3K_m + 4G_d)}{K_m(3K_d + 4G_d)}\right] \tag{7.27}$$

$$\frac{G}{G_m} = 1 + \phi\left[\frac{(G_d - G_m)(G_m + G_g)}{G_m(G_g + G_d)}\right] \tag{7.28}$$

where

$$G_g = \frac{G_d(9K_d + 8G_d)}{6(K_d + 2G_d)} \tag{7.29}$$

Equations 7.27 and 7.28 could be recast in the following forms:

$$\frac{K}{K_m} = 1 + \phi(\lambda_K - 1)\left[\frac{(1+\nu_d) + 2\lambda_K(1-2\nu_d)}{3\lambda_K(1-\nu_d)}\right] \tag{7.30}$$

$$\frac{G}{G_m} = 1 + \phi(\lambda_G - 1)\left[\frac{(8 - 10\nu_d) + \lambda_G(7 - 5\nu_d)}{15\lambda_G(1 - \nu_d)}\right] \tag{7.31}$$

where λ_K is the bulk moduli ratio and λ_G is the shear moduli ratio.

Figure 7.4 compares the relative shear modulus G_r (defined as G/G_m) of composites with disks and spheres as filler particles. When shear modulus ratio λ_G is 100, the relative shear modulus is larger than one and G_r of composite with disk-shaped

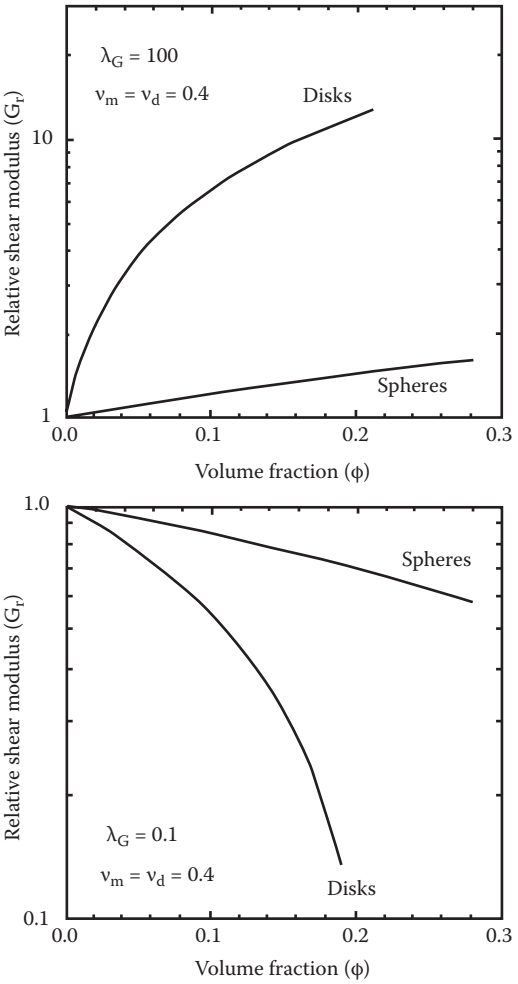

FIGURE 7.4 Relative shear modulus of composites with disks and spheres as particles. (From Pal, R., *Rheology of Particulate Dispersions and Composites*, Chapter 12, Boca Raton: CRC Press, 2007.)

particles is much larger than the G_r of composite with spherical particles at the same volume fraction of particles (ϕ). When $\lambda_G = 0.1$, an opposite effect is observed. Now $G_r < 1$ and spherical particles give a larger value of G_r.

Figure 7.5 compares the relative bulk modulus K_r (defined as K/K_m) of composites with disks and spheres as filler particles. The relative bulk modulus exhibits a behavior similar to that exhibited by G_r. When λ_K is 100, $K_r > 1$ and K_r of composite with disk shaped particles is much larger than the K_r of composite with

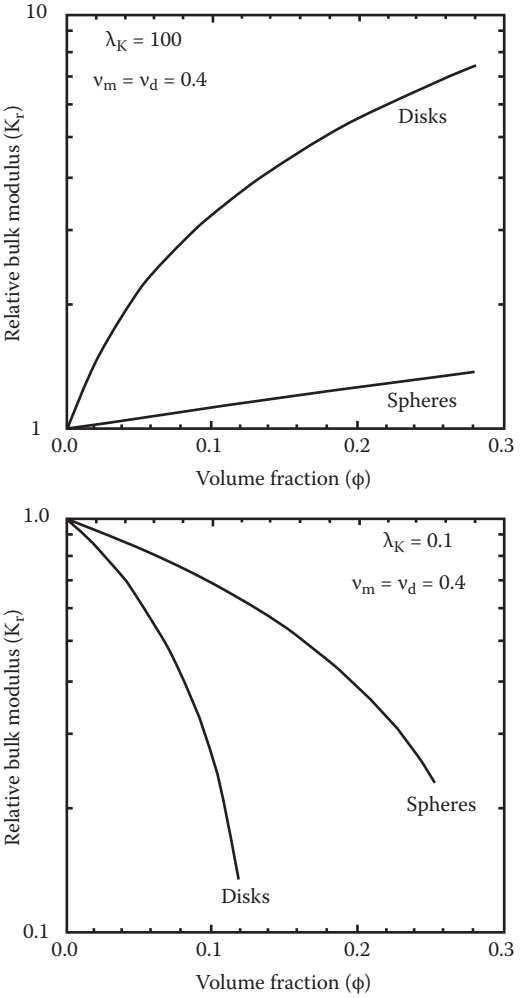

FIGURE 7.5 Relative bulk modulus of composites with disks and spheres as particles. (From Pal, R., *Rheology of Particulate Dispersions and Composites*, Chapter 12, Boca Raton: CRC Press, 2007.)

spherical particles. When $\lambda_K = 0.1$, $K_r < 1$ and spherical particles result in a larger value of K_r.

7.4 BOUNDS FOR THE EFFECTIVE ELASTIC PROPERTIES OF PARTICULATE COMPOSITES

The equations for the effective elastic properties of particulate composites given in the preceding section are valid for *dilute* composites with *spherical* or *disk-shaped* inclusions (particles). Interestingly, the elastic properties of isotropic two-phase composites are restricted by definite lower and upper bounds [8–22], regardless of the geometry of the inclusions (spherical or nonspherical). Such bounds depend only on the volume fractions of the components and the properties of the components. The effective elastic property of the composite lies somewhere in the interval between the lower and upper bounds.

A composite material composed of isotropic dispersed phase (unknown geometry) distributed randomly in an isotropic matrix has isotropic effective properties. Assuming that the composite is linearly elastic, it has two independent elastic constants (properties) such as bulk modulus (K) and shear modulus (G). Thus, the bounds for bulk modulus and shear modulus are reported simultaneously.

The elementary bounds for bulk modulus (K) and shear modulus (G) of isotropic two-phase composites are known as the Voigt–Reuss bounds [21,22] as they are based on the Voigt and Reuss ROMs discussed earlier. The Voigt ROM represents the upper bound on modulus (K or G) and the Reuss ROM represents the lower bound on modulus. The Voigt (upper) bounds for the effective bulk and shear moduli of isotropic composite are as follows [21]:

$$K \le \phi\, K_d + (1 - \phi)\, K_m \tag{7.32}$$

$$G \le \phi\, G_d + (1 - \phi)\, G_m \tag{7.33}$$

The Reuss (lower) bounds for the effective bulk and shear moduli of isotropic composite are given as follows [22]:

$$K \ge \frac{1}{\left(\dfrac{\phi}{K_d} + \dfrac{1-\phi}{K_m}\right)} \tag{7.34}$$

$$G \ge \frac{1}{\left(\dfrac{\phi}{G_d} + \dfrac{1-\phi}{G_m}\right)} \tag{7.35}$$

The actual effective moduli of isotropic composite are expected to lie somewhere in the interval between the Voigt and Reuss bounds, regardless of the geometry of inclusions. The upper and lower bounds given by Equations 7.32 through 7.35 are generally not close enough to provide a good estimate of the effective moduli of composite.

Hashin and Shtrikman [13] and Walpole [16] employed a variational theorem to obtain improved (and much tighter) upper and lower bounds for the effective bulk and shear moduli of isotropic composites. The Hashin–Shtrikman–Walpole (HSW) bounds are given as follows [8,13,16]:

$$\left[\frac{(K_m + K_\ell)\phi}{K_m + K_\ell + (K_d - K_m)(1-\phi)}\right] \le \left(\frac{K - K_m}{K_d - K_m}\right) \le \left[\frac{(K_m + K_g)\phi}{K_m + K_g + (K_d - K_m)(1-\phi)}\right] \tag{7.36}$$

$$\left[\frac{(G_m + G_\ell)\phi}{G_m + G_\ell + (G_d - G_m)(1-\phi)}\right] \le \left(\frac{G - G_m}{G_d - G_m}\right) \le \left[\frac{(G_m + G_g)\phi}{G_m + G_g + (G_d - G_m)(1-\phi)}\right] \tag{7.37}$$

where K_ℓ, K_g, G_ℓ, and G_g are given in terms of the matrix and dispersed-phase properties as follows:

When $(G_d - G_m)(K_d - K_m) \ge 0$,

$$K_\ell = \frac{4}{3}G_m, \quad K_g = \frac{4}{3}G_d \tag{7.38}$$

$$G_\ell = \frac{3}{2}\left[\frac{1}{G_m} + \frac{10}{9K_m + 8G_m}\right]^{-1}, \quad G_g = \frac{3}{2}\left[\frac{1}{G_d} + \frac{10}{9K_d + 8G_d}\right]^{-1} \tag{7.39}$$

When $(G_d - G_m)(K_d - K_m) \le 0$,

$$K_\ell = \frac{4}{3}G_d, \quad K_g = \frac{4}{3}G_m \tag{7.40}$$

$$G_\ell = \frac{3}{2}\left[\frac{1}{G_m} + \frac{10}{9K_d + 8G_m}\right]^{-1}, \quad G_g = \frac{3}{2}\left[\frac{1}{G_d} + \frac{10}{9K_m + 8G_d}\right]^{-1} \tag{7.41}$$

Note that when $G_m = G_d$, the lower and upper bounds for shear modulus coincide and the composite shear modulus is identical to the matrix shear modulus, that is,

$G = G_m$. The lower and upper bounds for bulk modulus also coincide when $G_m = G_d$ and the composite K is given by

$$K = K_m + \left[\frac{(K_d - K_m)(3K_m + 4G_m)\phi}{(3K_d + 4G_m) - (3K_d - 3K_m)\phi} \right] \tag{7.42}$$

Figures 7.6 through 7.9 compare the Voigt–Reuss bounds with the HSW bounds under different conditions: $\lambda_K > 1$, $\lambda_G > 1$ in Figure 7.6; $\lambda_K < 1$, $\lambda_G < 1$ in Figure 7.7;

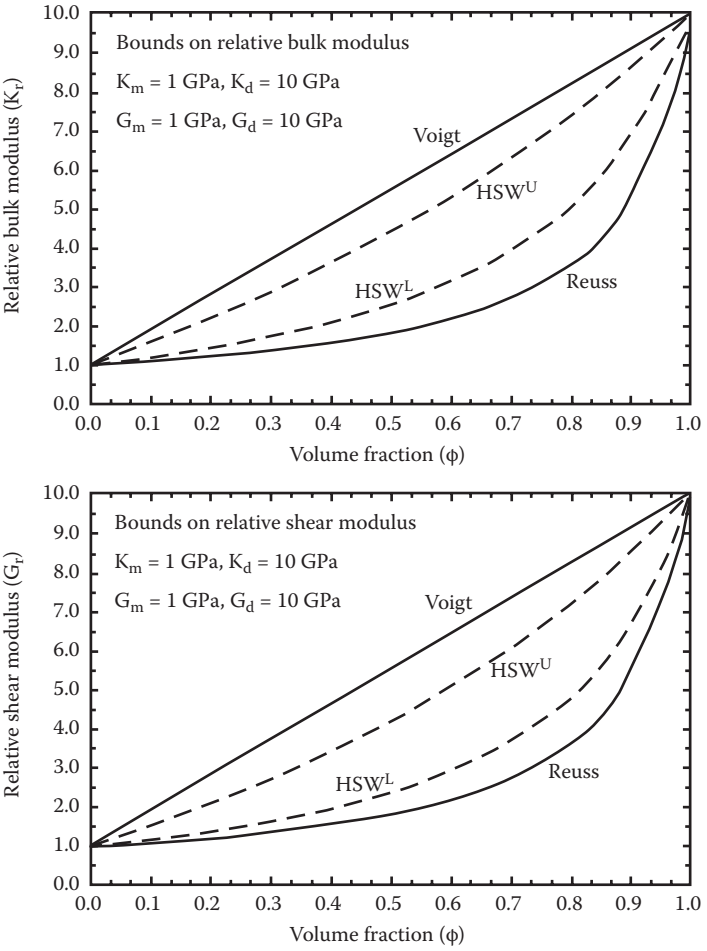

FIGURE 7.6 Voigt, Reuss, and Hashin–Shtrikman–Walpole (HSW) bounds for the relative bulk and shear moduli of isotropic composites under the conditions $\lambda_K > 1$ and $\lambda_G > 1$ (note that $\lambda_K = K_d/K_m$ and $\lambda_G = G_d/G_m$). (From Pal, R., *Rheology of Particulate Dispersions and Composites*, Chapter 12, Boca Raton: CRC Press, 2007.)

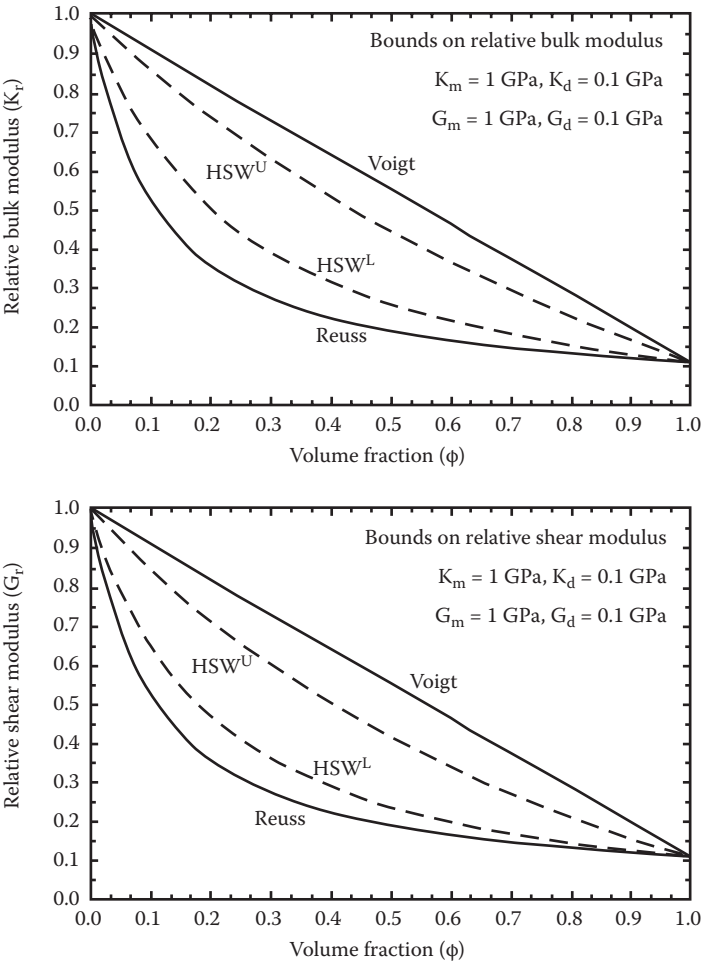

FIGURE 7.7 Voigt, Reuss, and Hashin–Shtrikman–Walpole (HSW) bounds for the relative bulk and shear moduli of isotropic composites under the conditions $\lambda_K < 1$ and $\lambda_G < 1$ (where $\lambda_K = K_d/K_m$ and $\lambda_G = G_d/G_m$). (From Pal, R., *Rheology of Particulate Dispersions and Composites*, Chapter 12, Boca Raton: CRC Press, 2007.)

$\lambda_K < 1$, $\lambda_G > 1$ in Figure 7.8; and $\lambda_K > 1$, $\lambda_G < 1$ in Figure 7.9. Clearly, the HSW bounds are much tighter, and hence better, as compared with the Voigt–Reuss bounds.

The HSW bounds, although better than the Voigt–Reuss bounds, yield satisfactory estimates for the effective moduli, in that the upper and lower bounds are close, only when the ratios between the corresponding moduli of the two phases are close to unity. When the moduli of the two phases are very different, the bounds become too wide to be of any practical value.

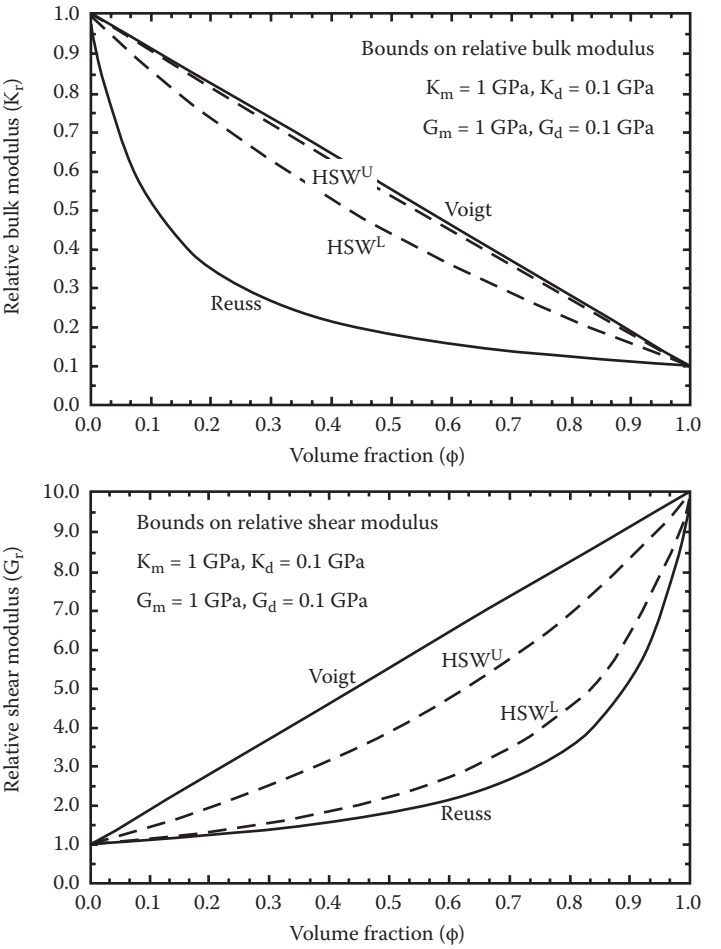

FIGURE 7.8 Voigt, Reuss, and Hashin–Shtrikman–Walpole (HSW) bounds for the relative bulk and shear moduli of isotropic composites under the conditions $\lambda_K < 1$ and $\lambda_G > 1$ (where $\lambda_K = K_d/K_m$ and $\lambda_G = G_d/G_m$). (From Pal, R., *Rheology of Particulate Dispersions and Composites*, Chapter 12, Boca Raton: CRC Press, 2007.)

It is interesting to note that for dilute particulate composites under the condition $(G_d - G_m)(K_d - K_m) \geq 0$, the lower HSW bounds for effective bulk and shear moduli correspond to the formulae for composites of spherical filler particles and the upper HSW bounds correspond to the formulae for composites of disk-shaped particles. This indicates that when $(G_d - G_m)(K_d - K_m) \geq 0$, the spherical particles provide the minimum reinforcing effect whereas the disk-shaped filler particles provide the maximum reinforcing effect [7].

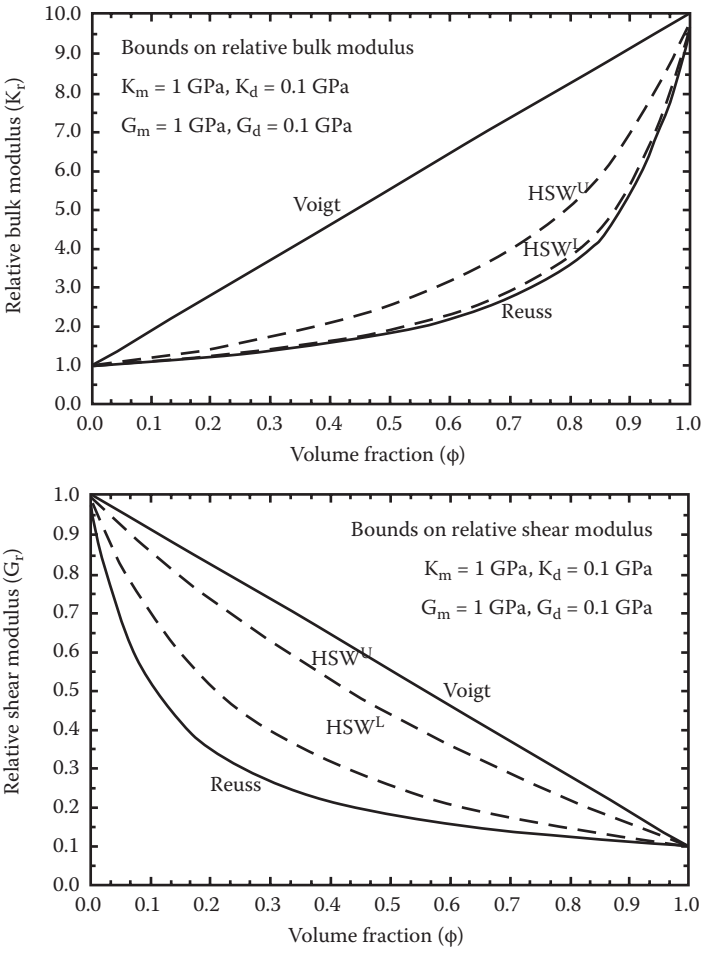

FIGURE 7.9 Voigt, Reuss, and Hashin–Shtrikman–Walpole (HSW) bounds for the relative bulk and shear moduli of isotropic composites under the conditions $\lambda_K > 1$ and $\lambda_G < 1$ (where $\lambda_K = K_d/K_m$ and $\lambda_G = G_d/G_m$). (From Pal, R., *Rheology of Particulate Dispersions and Composites*, Chapter 12, Boca Raton: CRC Press, 2007.)

REFERENCES

1. Pal, R. 2007. *Rheology of Particulate Dispersions and Composites*, Chapter 12, Boca Raton: CRC Press.
2. Pal, R. 2005. New models for effective Young's modulus of particulate composites. *Composites B* 36: 513–523.
3. Zhang, K., Y. Wang, M.A. Hillmyer, and L.F. Francis. 2004. Processing and properties of poly(L-lactide)/bioactive glass composites. *Biomaterials* 25: 2489–2500.
4. Zhang, K., Y. Ma, and L.F. Francis. 2002. Porous polymer/bioactive glass composites for soft-to-hard tissue interfaces. *J. Biomed. Mater. Res.* 61: 551–563.

5. Milosevski, M., J. Bossert, D. Milosevski, and N. Gruevska. 1999. Preparation and properties of dense and porous calcium phosphate. *Ceram. Int.* 25: 693–696.
6. Christensen, R.M. 1993. Effective properties of composite materials containing voids. *Proc. R. Soc. Lond. A* 440: 461–473.
7. Boucher., S. 1974. On the effective moduli of isotropic two-phase elastic composites. *J. Comp. Mater.* 8: 82–89.
8. Chen, H.S. and A. Acrivos. 1978. The effective elastic moduli of composite materials containing spherical inclusions at non-dilute concentrations. *Int. J. Solids Struct.* 14: 349–364.
9. Hashin, Z. 1970. Theory of composite materials. In: *Mechanics of Composite Materials*, eds, F.W. Wendt, H. Liebowitz, and N. Perrone, pp. 201–242, Oxford: Pergamon Press.
10. Christensen, R.M. 1979. *Mechanics of Composite Materials*, New York: John Wiley & Sons.
11. Christensen, R.M. 1982. Mechanical properties of composite materials. In: *Mechanics of Composite Materials—Recent Advances*, eds., Z. Hashin and C.T. Herakovich, pp. 1–16, New York: Pergamon Press.
12. Hashin, Z. 1962. The elastic moduli of heterogeneous materials. *J. Appl. Mech*. 29: 143–150.
13. Hashin, Z. and S. Shtrikman. 1963. A variational approach to the theory of the behavior of multiphase materials. *J. Mech. Phys. Solids*. 11: 127–140.
14. Hill, R. 1963. Elastic properties of reinforced solids: Some theoretical principles. *J. Mech. Phys. Solids.* 11: 357–372.
15. Hashin, Z. 1964. Theory of mechanical behaviour of heterogeneous media. *Appl. Mech. Rev.* 17: 1–9.
16. Walpole, L.J. 1966. On the bounds for the overall elastic moduli of inhomogeneous systems. *J. Mech. Phys. Solids.* 14: 151–162, 289–301.
17. Roscoe, R. 1973. Isotropic composites with elastic or viscoelastic phases: General bounds for the moduli and solutions for special geometries. *Rheol. Acta.* 12: 404–411.
18. Milton, C.W. and N. Phan-Thien. 1982. New bounds on effective elastic moduli of two-component materials. *Proc. R. Soc. Lond. A* 380: 305–331.
19. Chinh, P.D. 1998. Bounds on the effective properties of some multiphase matrix mixtures of coated-sphere geometry. *Mech. Mater*. 27: 249–260.
20. Gibiansky, L.V. and O. Sigmund. 2000. Multiphase composites with extremal bulk modulus. *J. Mech. Phys. Solids.* 48: 461–498.
21. Voigt, W. 1928. *Lehrbuch der Kristallphysik*, Leipzig: Teubner-Verlag.
22. Reuss, A. 1929. Berechnung der Fliessgrenze von Mischkristallen auf Grund der Plastizitätsbedingung für Einkristalle. *Z. Angew. Math. Mech.* 9: 49–58.

8 Mechanical Properties of Concentrated Pore-Solid Composites

8.1 INTRODUCTION

Porous solids could be considered as composite materials consisting of pores and solid matrix. Such composite materials are utilized in many engineering applications ranging from acoustic absorption to heat shields in reentry vehicles. Porous ceramics are widely used as filters, catalyst supports, low dielectric substances, thermal insulators, and lightweight structural components. Porous-solid materials are of interest in biomedical applications as well [1–3]. Many industrial materials such as wood, carbon, ceramics, foams, and bricks are also porous in nature.

A number of experimental and theoretical studies have been reported on the mechanical properties of pore-solid composites [4–31]. The presence of pores decreases the mechanical properties, such as the Young's and shear moduli, of the material. For an *infinitely dilute* dispersion of spherical pores in an *incompressible matrix*, the exact expressions for the effective Young's and shear moduli are given as follows [4,5,32]:

$$E = E_m\left(1 - \frac{23}{12}\phi\right) \tag{8.1}$$

$$G = G_m\left(1 - \frac{5}{3}\phi\right) \tag{8.2}$$

where E and G are the effective Young's and shear moduli of the pore-solid composite, respectively; E_m and G_m are the Young's and shear moduli of the solid matrix, respectively; and ϕ is the porosity (volume fraction of pores). These equations follow from Equations 7.24 and 7.26 of Chapter 7, assuming incompressible matrix (Poisson ratio of matrix equal to 0.5).

Equations 8.1 and 8.2 cannot be applied at finite concentration of pores, as the interaction between the pores is not considered in their derivation. For concentrated systems, a number of empirical expressions for the relationship between elastic moduli (E and G) and porosity (ϕ) have been proposed in the literature. Some of them are listed below [25]:

$$M = M_m\exp(-a\phi) \tag{8.3}$$

$$M = M_m(1 - b\phi)^n \tag{8.4}$$

$$M = M_m(1 - c_1\phi + c_2\phi^2) \tag{8.5}$$

$$M = M_m(1 - \phi)/(1 + d\phi) \tag{8.6}$$

where M is the effective modulus (E or G) of the pore-solid composite; M_m is the modulus (E_m or G_m) of the solid matrix; and a, b, c_1, c_2, d, and n are constants determined from experimental results by data fitting. The constants a, b, c_1, c_2, d, and n are different for Young's modulus and shear modulus.

The empirical equations such as those listed above (Equations 8.3 through 8.6) are good for data fitting. They cannot be used to predict the elastic moduli unless the constants involved in the equations are known for a given material. Furthermore, the empirical equations offer little insight into the underlying principles governing the elastic behavior of composites.

Pal [33] has recently developed new models for the elastic moduli of concentrated pore-solid composites. The models developed are consistent with the exact expressions for dilute systems (Equations 8.1 and 8.2). The models were evaluated using published data on the Young's and shear moduli of porous composites. The expressions for the bulk modulus (K) and Poisson ratio (ν) of pore-solid composites were also derived using the models developed for the Young's and shear moduli.

8.2 PAL MODELS FOR ELASTIC MODULI OF CONCENTRATED PORE-SOLID COMPOSITES

Pal [33] developed the equations for elastic moduli of concentrated pore-solid composites using the differential effective medium approach (DEMA). According to this approach, a concentrated pore-solid composite can be obtained from an initial solid matrix by successively adding infinitesimally small quantities of pores to the system while the final volume fraction of the pores is reached. At any arbitrary stage (i) of the process, the addition of an infinitesimal amount of pores leads to the next stage (i + 1). The pore-solid composite of stage (i) is then treated as an equivalent "effective medium," which is homogenous with respect to the new set of pores added to reach stage (i + 1). The solution of a dilute system is then applied to determine the increment change in moduli in going from stage (i) to stage (i + 1). The differential equation derived in this manner is integrated to obtain the final solution for a concentrated pore-solid composite. This approach was utilized by Bruggeman [34] to develop an equation for the dielectric constant of a concentrated solids-in-liquid suspension.

Now consider a pore-solid composite with porosity ϕ (volume fraction of pores). Into this composite, an infinitesimally small amount of new pores is added. The increment changes in the Young's and shear moduli (dE and dG) resulting from the addition of the new pores can be calculated from Equations 8.1 and 8.2 by treating the pore-solid composite into which new pores are added as an equivalent "effective medium" of Young's modulus E and shear modulus G. Thus,

$$dE = -\frac{23}{12}Ed\phi \tag{8.7}$$

$$dG = -\frac{5}{3}Gd\phi \tag{8.8}$$

Upon integration with the limits $E \to E_m$ and $G \to G_m$ at $\phi \to 0$, Equations 8.7 and 8.8 give

$$E = E_m \exp\left(-\frac{23}{12}\phi\right) \tag{8.9}$$

$$G = G_m \exp\left(-\frac{5}{3}\phi\right) \tag{8.10}$$

Equations 8.9 and 8.10, referred to as model 1, reduce to Equations 8.1 and 8.2 in the limit $\phi \to 0$.

Model 1 is expected to describe the moduli of pore-solid composites at low to moderate values of porosity ϕ. This is because in the derivation of the differential equations (Equations 8.7 and 8.8) leading to model 1 (Equations 8.9 and 8.10), it is assumed that the whole volume of the pore-solid composite before new pores are added is available as free volume to the new pores. In reality, the free volume available to disperse the new pores is significantly less due to the volume preempted by the pores already present. The increase in the actual volume fraction of pores when new pores are added to the system is $d\phi/(1 - \phi)$. Thus, Equations 8.7 and 8.8 become

$$dE = -\frac{23}{12} E \frac{d\phi}{1-\phi} \tag{8.11}$$

$$dG = -\frac{5}{3} G \frac{d\phi}{1-\phi} \tag{8.12}$$

Upon integration with the limits $E \to E_m$ and $G \to G_m$ at $\phi \to 0$, Equations 8.11 and 8.12 give

$$E = E_m(1 - \phi)^{23/12} \tag{8.13}$$

$$G = G_m(1 - \phi)^{5/3} \tag{8.14}$$

Equations 8.13 and 8.14, referred to as model 2, reduce to Equations 8.1 and 8.2 in the limit $\phi \to 0$.

One serious limitation of models 1 and 2 is that they fail to account for the so-called crowding effect of pores at high values of porosity ϕ. For example, Equations 8.13 and 8.14 predict nonzero values of the elastic moduli for all $\phi < 1$; the moduli are zero only at $\phi = 1$. In reality, the moduli values become zero at $\phi = \phi_m$, the maximum packing volume fraction of inclusions (pores) where the inclusions touch each other. For random close packing of monosized spherical inclusions (pores, particles), ϕ_m is 0.637 (well below unity). Due to entrapment of some of the matrix material in the interstitial region between the existing pores, the free volume of the matrix available to disperse the new pores is significantly less than $(1 - \phi)$. If we take the incremental increase in the volume fraction of the pores when infinitesimal amount of new pores are added to an existing pore-solid composite of porosity ϕ as $d[\phi/(1 - \phi/\phi_m)]$ rather than $d\phi/(1 - \phi)$ as used in the derivation of model 2, Equations 8.7 and 8.8 become [33]

$$dE = \left(\frac{-23}{12}E\right) d\left[\frac{\phi}{1-\frac{\phi}{\phi_m}}\right] \tag{8.15}$$

$$dG = \left(\frac{-5}{3}G\right) d\left[\frac{\phi}{1-\frac{\phi}{\phi_m}}\right] \tag{8.16}$$

Upon integration with the limits $E \to E_m$ and $G \to G_m$ at $\phi \to 0$, Equations 8.15 and 8.16 give

$$E = E_m \exp\left[\frac{\frac{-23}{12}\phi}{1-\frac{\phi}{\phi_m}}\right] \tag{8.17}$$

$$G = G_m \exp\left[\frac{\frac{-5}{3}\phi}{1-\frac{\phi}{\phi_m}}\right] \tag{8.18}$$

Equations 8.17 and 8.18, referred to as model 3, reduce to Equations 8.1 and 8.2 in the limit $\phi \to 0$.

Another way to account for the crowding effect of pores [33] is to take the incremental increase in the volume fraction of the inclusions (particles or pores as in the present case) when infinitesimal amount of new inclusions are added to an existing inclusions-matrix composite as $d\phi/(1 - \phi/\phi_m)$ rather than $d[\phi/(1 - \phi/\phi_m)]$ as used in the derivation of model 3. Thus,

$$dE = \left(\frac{-23}{12}E\right) \frac{d\phi}{\left(1-\frac{\phi}{\phi_m}\right)} \tag{8.19}$$

$$dG = \left(\frac{-5}{3}G\right) \frac{d\phi}{\left(1-\frac{\phi}{\phi_m}\right)} \tag{8.20}$$

Upon integration with the limits $E \to E_m$ and $G \to G_m$ at $\phi \to 0$, Equations 8.19 and 8.20 give

$$E = E_m \left(1-\frac{\phi}{\phi_m}\right)^{\frac{23}{12}\phi_m} \tag{8.21}$$

$$G = G_m\left(1 - \frac{\phi}{\phi_m}\right)^{\frac{5}{3}\phi_m} \tag{8.22}$$

Equations 8.21 and 8.22, referred to as model 4, reduce to Equations 8.1 and 8.2 in the limit $\phi \to 0$ as expected.

As ϕ_m, the maximum packing volume fraction of pores, is sensitive to the pore size distribution, models 3 and 4 are capable of taking into account the effect of the pore size distribution on the elastic properties of pore-solid composites. An increase in ϕ_m occurs when a composite with monosized pore distribution is changed to a composite with polydisperse pore size distribution.

8.3 COMPARISON OF MODEL PREDICTIONS WITH EXPERIMENTAL DATA

Sixteen sets of experimental data on pore-solid composites covering a broad range of porosity are considered to evaluate the models. Table 8.1 gives a summary of the various pore-solid composite systems considered [33].

TABLE 8.1
Summary of Various Pore-Solid Composites Considered in Evaluating the Models

Set No.	Range of ϕ (Volume Fraction of Pores)	Ref. No.	Comments
1	0–0.41	[7]	Young's modulus of porous polycrystalline alumina
2	0–0.12	[13]	Young's modulus of porous polycrystalline mullite
3	0–0.36	[14]	Elastic properties (Young's and shear moduli) of porous polycrystalline monoclinic gadolinium oxide
4	0–0.40	[15]	Elastic properties (Young's and shear moduli) of porous polycrystalline monoclinic samarium oxide
5	0–0.32	[16]	Elastic properties (Young's and shear moduli) of porous polycrystalline cubic lutetium oxide
6	0–0.28	[17]	Elastic properties (Young's and shear moduli) of porous polycrystalline monoclinic hafnium oxide
7A–7G	0–0.40	[18]	Elastic moduli of porous refractory spinels (seven sets of data)
8	0–0.36	[19]	Elastic properties (Young's and shear moduli) of porous stabilized hafnium oxide
9A–9B	0–0.18	[20]	Elastic properties (Young's and shear moduli) of porous hafnium and zirconium oxides stabilized with praseodymium or terbium oxide (two sets of data)

Source: Pal, R., *J. Comp. Mater*. 39: 1147–1158, 2005.

Figure 8.1 shows a comparison between model predictions of Young's modulus and experimental data. The data are plotted as E_r versus ϕ. As can be seen, the experimental Young's modulus data can be described reasonably well with model 3 (Equation 8.17) using a single ϕ_m value of 0.58. Models 1, 2, and 4 generally overpredict the relative Young's modulus of pore-solid composites, especially when $\phi > 0.1$. The scatter in experimental data observed in Figure 8.1 is likely due to variations in porosity structure (size, shape, orientation of pores) from one set of

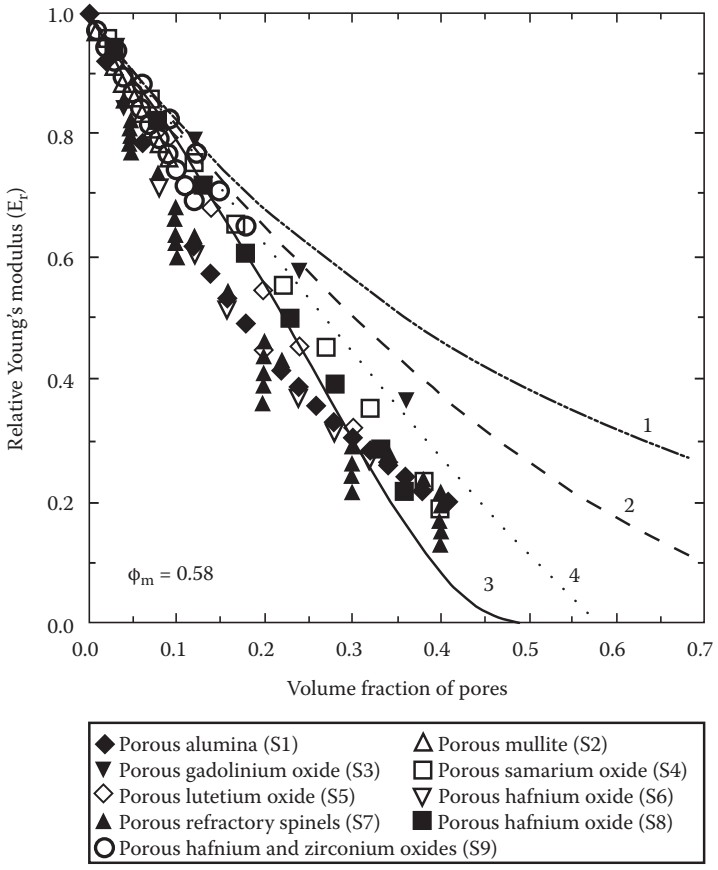

FIGURE 8.1 Comparison between published experimental data and predictions of various models for the relative Young's modulus of pore-solid composites. The numbers shown on the curves refer to the corresponding model number. (From Pal, R., *J. Comp. Mater.* 39: 1147–1158, 2005.)

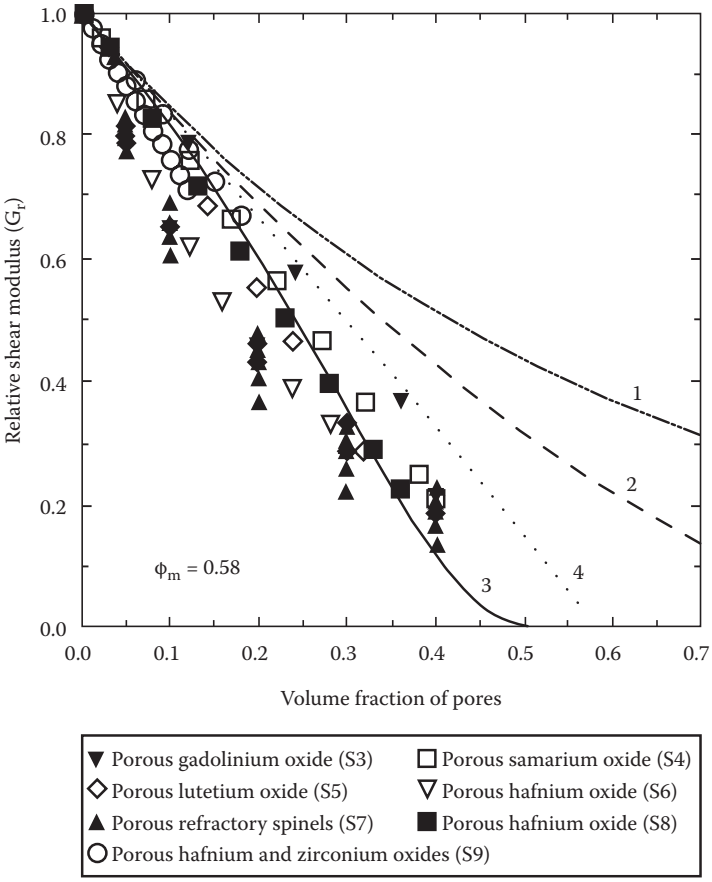

FIGURE 8.2 Comparison between published experimental data and predictions of various models for the relative shear modulus of pore-solid composites. The numbers shown on the curves refer to the corresponding model number. (From Pal, R., *J. Comp. Mater.* 39: 1147–1158, 2005.)

experimental data to another. It should also be noted that the solid matrix of the experimental pore-solid composites was not strictly incompressible as assumed in the models.

Figure 8.2 shows a comparison between model predictions of shear modulus and experimental data. The data are plotted as relative shear modulus G_r versus porosity ϕ. Once again, model 3 (Equation 8.18) describes the experimental data satisfactorily using a single ϕ_m value of 0.58. Models 1, 2, and 4 generally overpredict G_r, especially when $\phi > 0.1$.

8.4 BULK MODULUS AND POISSON'S RATIO OF CONCENTRATED PORE-SOLID COMPOSITES

From the Young's and shear moduli, the bulk modulus (K) of pore-solid composite can be obtained using the following standard relation for isotropic materials:

$$K = EG/[3(3G - E)] \tag{8.23}$$

Assuming that the solid matrix is incompressible, Equation 8.23 can be rewritten as

$$K_r = K/G_m = E_rG_r/[3(G_r - E_r)] \tag{8.24}$$

where K_r is the relative bulk modulus, defined as the ratio of bulk modulus of pore-solid composite to the shear modulus of the matrix. Note that the bulk modulus of the matrix (K_m) is infinite as matrix is assumed to be incompressible.

The Poisson ratio (ν) of isotropic materials is related to the Young's and shear moduli as

$$\nu = [1 - (2G/E)]/(2G/E) \tag{8.25}$$

TABLE 8.2
Equations for E_r, G_r, K_r, and ν

Model No.	$E_r = E/E_m$	$G_r = G/G_m$	$K_r = K/G_m$	ν
1	$\exp\left(\frac{-23}{12}\phi\right)$	$\exp\left(\frac{-5}{3}\phi\right)$	$\frac{\exp\left(\frac{-43}{12}\phi\right)}{3\left[\exp\left(\frac{-5}{3}\phi\right)-\exp\left(\frac{-23}{12}\phi\right)\right]}$	$\frac{[1-(2/3)\exp(\phi/4)]}{(2/3)\exp(\phi/4)}$
2	$(1-\phi)^{\frac{23}{12}}$	$(1-\phi)^{\frac{5}{3}}$	$\frac{(1-\phi)^{43/12}}{3((1-\phi)^{5/3}-(1-\phi)^{23/12})}$	$\frac{(1-(2/3)(1-\phi)^{-0.25})}{(2/3)(1-\phi)^{-0.25}}$
3	$\exp\left[\frac{\frac{-23}{12}\phi}{1-\frac{\phi}{\phi_m}}\right]$	$\exp\left[\frac{\frac{-5}{3}\phi}{1-\frac{\phi}{\phi_m}}\right]$	$\frac{\exp\left[\frac{\frac{-43}{12}\phi}{1-\phi/\phi_m}\right]}{3\left[\exp\left(\frac{\frac{-5}{3}\phi}{1-\phi/\phi_m}\right)-\exp\left(\frac{\frac{-23}{12}\phi}{1-\phi/\phi_m}\right)\right]}$	$(2/3)\exp\left(\frac{\phi/4}{1-\phi/\phi_m}\right)$
4	$\left(1-\frac{\phi}{\phi_m}\right)^{\frac{23}{12}\phi_m}$	$\left(1-\frac{\phi}{\phi_m}\right)^{\frac{5}{3}\phi_m}$	$\frac{\left(1-\frac{\phi}{\phi_m}\right)^{\frac{43}{12}\phi_m}}{3\left[\left(1-\frac{\phi}{\phi_m}\right)^{\frac{5}{3}\phi_m}-\left(1-\frac{\phi}{\phi_m}\right)^{\frac{23}{12}\phi_m}\right]}$	$\frac{\left[1-(2/3)\left(1-\frac{\phi}{\phi_m}\right)^{-0.25\phi_m}\right]}{(2/3)\left(1-\frac{\phi}{\phi_m}\right)^{-0.25\phi_m}}$

For incompressible solid matrix, Equation 8.25 can be expressed as

$$\nu = [1 - (2G_r/3E_r)]/(2G_r/3E_r) \tag{8.26}$$

Using Equations 8.24 and 8.26, the expressions for relative bulk modulus (K_r) and Poisson's ratio (ν) of pore-solid composites are determined from models 1 through 4. The expressions are summarized in Table 8.2.

Figure 8.3 shows the model predictions of relative bulk modulus as a function of porosity ϕ. As $\phi \to 0$, the relative bulk modulus approaches infinity as expected for incompressible matrix. All models predict a decrease in K_r with an increase in ϕ. The predictions of K_r from different models at any given ϕ are in the following order: K_r (model 1) > K_r (model 2) > K_r (model 4) > K_r (model 3).

The Poisson ratio of pore-solid composites predicted from the models is plotted as a function of porosity in Figure 8.4. As $\phi \to 0$, the Poisson ratio approaches 0.5 as expected for an incompressible matrix. With an increase in porosity ϕ, all models predict a decrease in the Poisson ratio. The predictions of ν from different models at any given ϕ are in the following order: ν (model 1) > ν (model 2) > ν (model 4) > ν (model 3). Interestingly, ν approaches a value of –1 when $\phi \to \phi_m$ in the case of models 3 and 4 (see Table 8.2). Model 2 also predicts a ν value of –1 when $\phi \to 1.0$. Model 1 predicts the Poisson ratio of pore-solid composite to be positive ($\mu > 0$) over the full range of porosity ($0 \le \phi \le 1$).

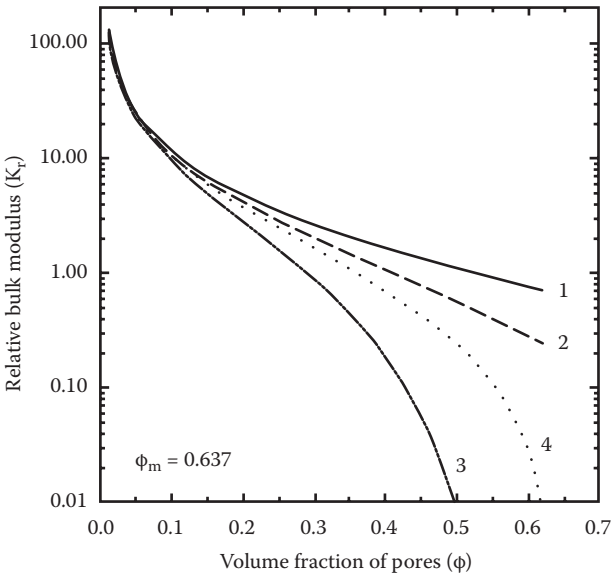

FIGURE 8.3 Relative bulk modulus K_r of pore-solid composite as a function of porosity ϕ, as predicted by the models. The numbers shown on the curves refer to the corresponding model number. (From Pal, R., *J. Comp. Mater.* 39: 1147–1158, 2005.)

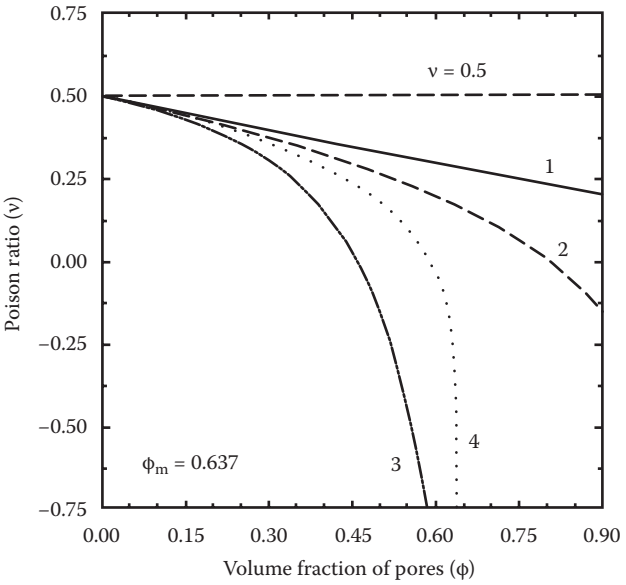

FIGURE 8.4 Poisson's ratio of pore-solid composite as a function of porosity ϕ, as predicted by the models. The numbers shown on the curves refer to the corresponding model number. (From Pal, R., *J. Comp. Mater.* 39: 1147–1158, 2005.)

REFERENCES

1. Zhang, K., Y. Wang, M.A. Hillmyer, and L.F. Francis. 2004. Processing and properties of porous poly(L-lactide)/bioactive glass composites. *Biomaterials* 25: 2489–2500.
2. Zhang, K., Y. Ma, and L.F. Francis. 2002. Porous polymer/bioactive glass composites for soft-to-hard tissue interfaces. *J. Biomed. Mater. Res*. 61: 551–563.
3. Milosevski, M., J. Bossert, D. Milosevski, and N. Gruevska. 1999. Preparation and properties of dense and porous calcium phosphate. *Ceram. Int.* 25: 693–696.
4. Dewey, J.M. 1947. The elastic constants of materials loaded with non-rigid fillers. *J. Appl. Phys.* 18: 578–581.
5. Mackenzie, J.K. 1950. The elastic constants of a solid containing spherical holes. *Proc. Phys. Soc. London B* 63: 2–11.
6. Coble, R.L. and W.D. Kingery. 1956. Effect of porosity on physical properties of sintered alumina. *J. Am. Ceram. Soc*. 39: 377–385.
7. Knudsen, F.P. 1962. Effect of porosity on Young's modulus of alumina. *J. Am. Ceram. Soc.* 45: 94–95.
8. Hashin, Z. 1964. Theory of mechanical behavior of heterogeneous media. *Appl. Mech. Rev.* 17: 1–9.
9. Smith, C.F. and W.B. Crandall. 1964. Calculated high-temperature elastic constants for zero porosity monoclinic zirconia. *J. Am. Ceram. Soc.* 47: 624–627.
10. Piatasik, R.S. and D.P.H. Hasselman. 1964. Effect of open and closed pores on Young's modulus of polycrystalline ceramics. *J. Am. Ceram. Soc.* 47: 50–51.
11. Hasselman, D.P.H. and R.M. Fulrath. 1964. Effect of small fraction of spherical porosity on elastic moduli of glass. *J. Am. Ceram. Soc.* 47: 52–53.

12. Manning, W.R., O. Hunter, and B.R. Powell. 1969. Elastic properties of polycrystalline yttrium oxide, dysprosium oxide, holmium oxide, and erbium oxide: Room temperature measurements. *J. Am. Ceram. Soc.* 52: 436–442.
13. Penty, R.A., D.P.H. Hasselman, and R.M. Spriggs. 1972. Young's modulus of high density polycrystalline mullite. *J. Am. Ceram. Soc.* 55: 169–170.
14. Haglund, J.A. and O. Hunter. 1973. Elastic properties of polycrystalline monoclinic Gd_2O_3. *J. Am. Ceram. Soc.* 56: 327–330.
15. Hunter, O., H.J. Korklam, and R.R. Suchomel. 1974. Elastic properties of polycrystalline monoclinic Sm_2O_3. *J. Am. Ceram. Soc.* 57: 267–268.
16. Hunter, O. and G.E. Graddy. 1976. Porosity dependence of elastic properties of polycrystalline cubic Lu_2O_3. *J. Am. Ceram. Soc.* 59: 82.
17. Dole, S.L., O. Hunter, and C.J. Wooge. 1977. Elastic properties of monoclinic Hafnium oxide at room temperature. *J. Am. Ceram. Soc.* 60: 488–490.
18. Porter, D.F., J.S. Reed, and D. Lewis. 1977. Elastic moduli of refractory spinels. *J. Am. Ceram. Soc.* 60: 345–349.
19. Dole, S.L., O. Hunter, and F.W. Calderwood. 1980. Elastic properties of stabilized HfO_2 compositions. *J. Am. Ceram. Soc.* 63: 136–139.
20. Dole, S.L. and O. Hunter. 1983. Elastic properties of hafnium and zirconium oxides stabilized with praseodymium or terbium oxide. *Commun. Am. Ceram. Soc.* March: C-47–C-49.
21. Ramakrishnan, N. and V.S. Arunachalam. 1990. Effective elastic moduli of porous solids. *J. Mat. Sci.* 25: 3930–3937.
22. Christensen, R.M. 1993. Effective properties of composite materials containing voids. *Proc. R. Soc. Lond. A* 440: 461–473.
23. Dunn, M.L. and H. Ledbetter. 1995. Poisson's ratio of porous and microcracked solids: Theory and application to oxide superconductors. *J. Mater. Res.* 10: 2715–2722.
24. Boccaccini, A.R. and Z. Fan. 1997. A new approach for the Young's modulus–porosity correlation of ceramic materials. *Ceram. Int.* 23: 239–245.
25. Luo, J. and R. Stevens. 1999. Porosity dependence of elastic moduli and hardness of 3Y-TZP ceramics. *Ceram. Int.* 25: 281–286.
26. Lu, G., G.Q. Lu, and Z.M. Xiao. 1999. Mechanical properties of porous materials. *J. Porous Mat.* 6: 359–368.
27. Boccaccini, A.R. 1999. Fabrication, microstructural characterization and mechanical properties of glass compacts containing controlled porosity of spheroidal shape. *J. Porous Mat.* 6: 369–379.
28. Roberts, A.P. and E.J. Garboczi. 2000. Elastic properties of model porous ceramics. *J. Am. Ceram. Soc.* 83: 3044–3048.
29. Nakamura, T., G. Qian, and C.C. Berndt. 2000. Effects of pores on mechanical properties of plasma-sprayed ceramic coatings. *J. Am. Ceram. Soc.* 83: 578–584.
30. Deng, Z.Y., T. Fukasawa, and M. Ando. 2001. Microstructure and mechanical properties of porous alumina ceramics fabricated by the decomposition of aluminum hydroxide. *J. Am. Ceram. Soc.* 84: 2638–2644.
31. Dorey, R.A., J.A. Yeomans, and P.A. Smith. 2002. Effect of pore clustering on the mechanical properties of ceramics. *J. Euro. Ceram. Soc.* 22: 403–409.
32. Christensen, R.M. 2000. Mechanics of cellular and other low-density materials. *Int. J. Solids Struct.* 37: 93–104.
33. Pal, R. 2005. Porosity-dependence of effective mechanical properties of pore-solid composite materials. *J. Comp. Mater*. 39: 1147–1158.
34. Bruggeman, D.A.G. 1935. Berechung verschieder physikalischer Konstanten von heterogenen Substanzen I. Dielekrizitätskonstanen und Leifähigkeiten der Mischkörper aus isotropen Substanzen. *Ann. Phys.* 24: 636–679.

9 Effective Young's Modulus of Concentrated Composites

9.1 INTRODUCTION

As discussed in Chapter 7, the key mechanical properties of composite solids are shear modulus (G), Young's modulus (E), Poisson's ratio (υ), and bulk modulus (K). In *isotropic* materials (that is, no directional dependence of properties), only two of the four mechanical properties are independent. If two properties are fixed, the remaining two are automatically fixed. In Chapter 7, models for the mechanical properties of *dilute* composites were presented. In this chapter and the next (Chapter 10), the models for the mechanical properties of *concentrated* particulate composites are discussed in detail. The two mechanical properties chosen are Young's modulus (E) and shear modulus (G). The present chapter deals with the Young's modulus, and the following Chapter 10 focuses on the shear modulus of particulate composites.

The Young's modulus, also referred to as tensile modulus, is needed to estimate the extension of a material under tension or the shortening of a material under compression. Depending upon the ratio of filler-particle Young's modulus (E_d) to matrix Young's modulus (E_m), two-phase particulate composites can be divided into three major classes [1]: (1) composites with high filler-to-matrix modulus ratio ($E_d/E_m > 20$), which include most filled or reinforced polymer composites; (2) composites with low filler-to-matrix modulus ratio ($1 < E_d/E_m < 5$), which include most cement concretes and metal matrix composites—note that concrete is a composite material consisting of cement paste matrix and particles of various sizes ranging from sand grains of diameter 100 μm to large rock particles of diameter 10 to 20 mm [2]; and (3) composites with soft particles ($0 < E_d/E_m \leq 1$) and composites with voids ($E_d/E_m = 0$).

9.2 BACKGROUND

Over the past 50 years or so, a number of experimental and theoretical studies have been published on the mechanical properties of particulate composites [3–37]. However, the exact micromechanical models are available only for *infinitely dilute* systems. In concentrated systems where particle–particle interactions are important, it is difficult to solve the fundamental equations of mechanics and hence no *exact* analytical solutions exist for the effective properties of concentrated particulate composites. Only approximate micromechanical models are available for the concentrated

systems. Based on different modeling approaches, a number of expressions have been proposed to describe the elastic properties of concentrated particulate composites.

As already noted in Chapter 7, one approach to predict the effective mechanical properties of a two-phase composite is to apply the *rules of mixtures*. According to the rules of mixtures, each of the constituent phases of the composite contributes to the effective mechanical property to an extent depending on the volume fraction of the constituent phase. If it is assumed that each component of the composite undergoes the same strain (isostrain or action-in-parallel situation), the effective mechanical property can be calculated from the Voigt rule of mixtures [31]. If it is assumed that the each component of the composite experiences the same stress (isostress or action-in-series situation), then the Reuss rule of mixtures [32] can be used to estimate the effective mechanical property of the composite. The rules of mixtures for the effective mechanical properties of composite materials provide only crude estimates. The actual value of the mechanical property shows large deviation from the rule of mixtures.

Several researchers have applied the *variational theorems* of the theory of elasticity to obtain upper and lower bounds for the effective modulus. A composite material composed of isotropic components distributed randomly in the material space will have isotropic effective properties, which are restricted by definite lower and upper bounds. Regardless of the geometry of the inclusions (dispersed phase), the effective property of the composite lies somewhere in the interval between the lower and upper bounds. Such bounds depend only on the volume fractions of the components and the properties of the components. This approach was utilized by Hashin and Shtrikman [6] and Walpole [13]. However, the Hashin–Shtrikman–Walpole bounds yield satisfactory estimates for the effective moduli (in that the upper and lower bounds are close) only when the particles and the matrix material have similar moduli. When the moduli of the two phases are very different, the bounds become too wide to be of any practical value.

Another well-known method to determine the effective mechanical properties of concentrated composites is the "self-consistent scheme." This approach involves embedding the particle in a homogeneous infinite medium that has the effective mechanical properties of the composite. The bond between the particle and the surrounding infinite medium is assumed to be perfect so that there occur displacement and traction continuity across the interface between phases. The system is subjected to uniform strain or stress at infinity and the stress and strain fields in the particle are determined. From the relationship between the far-field stresses and strains and the stresses and strains in the particle, the elastic properties of the infinite homogeneous medium (composite) are determined. This self-consistent scheme was first utilized by Hill [8] and Budiansky [9] to develop the equations for the elastic moduli of particulate composites. The self-consistent scheme does not give accurate predictions of the moduli especially when there is a large mismatch in the properties of the dispersed phase and matrix. Furthermore, this scheme gives unrealistic results in the limiting cases.

In order to overcome the limitations of the self-consistent scheme, the "generalized self-consistent scheme" was proposed to determine the effective mechanical properties of concentrated composites [23]. According to the generalized self-consistent scheme, the composite is first treated as an equivalent "effective medium" which is homogeneous and has the same macroscopic mechanical properties as that of the composite.

Then a small portion of the effective homogeneous medium is replaced by the actual components of the composite. The mechanical properties of the effective medium are then determined by insisting that if a small portion of the effective homogeneous medium is replaced by the actual components of the dispersion, no difference in mechanical properties could be detected by macroscopic observations. This approach was utilized by Kerner [10], van der Poel [12], Smith [15,16], and others [23,36]. The equations developed on the basis of the generalized self-consistent scheme give reasonable predictions at low to moderate concentrations of the particulate phase. At high concentrations of the particulate phase, a large deviation between the experimental and predicted values is generally observed. Furthermore, the equations predict the modulus of the particulate composite to be independent of the particle size distribution.

Pal [38] has recently developed *new* equations for Young's modulus of concentrated particulate composites using a *differential scheme* along with the exact solution of an infinitely dilute system. The key features of the Pal models are (1) they are closed form expressions, (2) they are valid over the full range of the particle concentration, (3) they take into consideration the effects of the particulate (dispersed) phase compressibility (Poisson's ratio) on the Young's modulus of the composite, (4) they consider the effect of the modulus ratio (defined as the ratio of the dispersed phase Young's modulus to matrix Young's modulus) on the Young's modulus of the composite and are valid over the full range of the modulus ratio, and (5) they include the effect of the particle size distribution on the Young's modulus of the composite through the parameter ϕ_m, the maximum packing volume fraction of the particles. The ϕ_m value for any composite depends on the particle size distribution of the particulate phase. The equations are evaluated using seven sets of experimental data on Young's modulus of particulate composites.

In what follows, the Pal models for Young's modulus of concentrated composites are discussed in detail.

9.3 PAL MODELS FOR YOUNG'S MODULUS OF CONCENTRATED COMPOSITES

For infinitely dilute particulate composites, the Young's modulus is given as follows:

$$E_r = \frac{E}{E_m} = 1 + \left\{ \left[\frac{15(E_d/E_m) - 10(1+\nu_d)}{6(E_d/E_m) + 6(1+\nu_d)} \right] - \left[\frac{1-2\nu_d}{3(E_d/E_m) + 4(1-2\nu_d)} \right] \right\} \phi \quad (9.1)$$

where E_r is the relative Young's modulus, defined as the ratio of composite Young's modulus (E) to matrix-phase Young's modulus (E_m), ν_d is the dispersed-phase Poisson ratio, and ϕ is the volume fraction of filler particles. This equation is an exact expression valid for infinitely dilute composites of spherical filler particles and incompressible matrix phase. Equation 9.1 cannot be applied at finite concentrations of dispersed phase as the interaction between the particles is ignored in its derivation.

Pal [38] utilized the differential effective medium approach to extend the dilute system micromechanical model to concentrated composites. Consider a particulate composite with a volume fraction of particles ϕ. Into this composite, an infinitely

small number of new particles are added. The increment increase in Young's modulus, dE, resulting from the addition of new particles can be calculated from the dilute system result (Equation 9.1) by treating the composite into which the new particles are added as an equivalent effective medium of Young's modulus E. Thus,

$$dE = E\left[\frac{15E_d - 10E(1+\nu_d)}{6E_d + 6E(1+\nu_d)} - \frac{(1-2\nu_d)E}{3E_d + 4E(1-2\nu_d)}\right]d\phi \tag{9.2}$$

This equation is separable, since we can write it as

$$\frac{dE}{E\left[\frac{15E_d - 10E(1+\nu_d)}{6E_d + 6E(1+\nu_d)} - \frac{(1-2\nu_d)E}{3E_d + 4E(1-2\nu_d)}\right]} = d\phi \tag{9.3}$$

After considerable algebra and integration with the limit $E \to E_m$ at $\phi \to 0$, Equation 9.3 gives

$$\left(\frac{E}{E_m}\right)\left[\frac{ME_m - 3E_d(P+Q)}{ME - 3E_d(P+Q)}\right]^{N+\frac{53}{46}}\left[\frac{ME - 3E_d(P-Q)}{ME_m - 3E_d(P-Q)}\right]^{N-\frac{53}{46}} = \exp(2.5\phi) \tag{9.4}$$

where

$$M = 46(1 + \nu_d)(1 - 2\nu_d) \tag{9.5}$$

$$P = 4 - 23\nu_d \tag{9.6}$$

$$Q = \sqrt{3(23\nu_d^2 - 138\nu_d + 82)} \tag{9.7}$$

$$N = (833 - 736\nu_d)/(46Q) \tag{9.8}$$

Equation 9.4, referred to as model 1, reduces to the following equation for particulate composite of incompressible spherical particles ($\nu_d = 0.5$):

$$\left(\frac{E}{E_m}\right)\left(\frac{E - E_d}{E_m - E_d}\right)^{-2.5} = \exp(2.5\phi) \tag{9.9}$$

Model 1 (Equation 9.4) is expected to describe Young's modulus of particulate composites of incompressible matrix at low to moderate values of ϕ. This is because in the derivation of the differential equation, Equation 9.2, leading to model 1 (Equation 9.4), it is assumed that all the volume of the composite before new particles are added is available as free volume to the new particles. In reality, the free volume available to disperse the new particles is significantly less, due to the volume

preempted by the particles already present. The increase in the actual volume fraction of the dispersed phase when new particles are added to the composite is $d\phi/(1-\phi)$. Thus, Equation 9.3 becomes

$$\frac{dE}{E\left[\frac{15E_d-10E(1+\nu_d)}{6E_d+6E(1+\nu_d)}-\frac{(1-2\nu_d)E}{3E_d+4E(1-2\nu_d)}\right]}=\frac{d\phi}{1-\phi} \tag{9.10}$$

Upon integration with the limit $E \to E_m$ at $\phi \to 0$, Equation 9.10 gives

$$\left(\frac{E}{E_m}\right)\left[\frac{ME_m-3E_d(P+Q)}{ME-3E_d(P+Q)}\right]^{N+\frac{53}{46}}\left[\frac{ME-3E_d(P-Q)}{ME_m-3E_d(P-Q)}\right]^{N-\frac{53}{46}}=(1-\phi)^{-2.5} \tag{9.11}$$

Equation 9.11, referred to as model 2, reduces to the following equation for particulate composite of incompressible spherical particles ($\nu_d = 0.5$):

$$\left(\frac{E}{E_m}\right)\left(\frac{E-E_d}{E_m-E_d}\right)^{-2.5}=(1-\phi)^{-2.5} \tag{9.12}$$

According to models 1 and 2 (Equations 9.4 and 9.11), it is possible for the volume fraction of the dispersed phase to reach unity as more and more particles are added to the composite. This is physically unrealistic, especially for composite systems of rigid particles. In reality, there exists an upper limit for ϕ, referred to as maximum packing volume fraction of particles (ϕ_m). The value of ϕ_m varies with the type of packing arrangement of particles and the shape of filler particles. For example, it is 0.637 for random close packing of monosized spherical particles. For hexagonal close packing of uniform spheres, ϕ_m is 0.74.

To account for the packing limit of particles, the incremental increase in the volume fraction of the dispersed phase, when infinitesimal amount of new particles are added to an existing suspension of dispersed phase volume fraction ϕ, is taken to be $d[\phi/(1-\phi/\phi_m)]$ rather than $d\phi/(1-\phi)$ as used in the derivation of model 2 [38]. Thus, Equation 9.3 becomes

$$\frac{dE}{E\left[\frac{15E_d-10E(1+\nu_d)}{6E_d+6E(1+\nu_d)}-\frac{(1-2\nu_d)E}{3E_d+4E(1-2\nu_d)}\right]}=d\left[\frac{\phi}{1-\frac{\phi}{\phi_m}}\right] \tag{9.13}$$

Upon integration, Equation 9.13 gives

$$\left(\frac{E}{E_m}\right)\left[\frac{ME_m-3E_d(P+Q)}{ME-3E_d(P+Q)}\right]^{N+\frac{53}{46}}\left[\frac{ME-3E_d(P-Q)}{ME_m-3E_d(P-Q)}\right]^{N-\frac{53}{46}}=\exp\left[\frac{2.5\phi}{1-\frac{\phi}{\phi_m}}\right] \tag{9.14}$$

Equation 9.14, referred to as model 3, reduces to the following equation for particulate composite of incompressible spherical particles ($\nu_d = 0.5$):

$$\left(\frac{E}{E_m}\right)\left(\frac{E-E_d}{E_m-E_d}\right)^{-2.5} = \exp\left[\frac{2.5\phi}{1-\frac{\phi}{\phi_m}}\right] \tag{9.15}$$

Another way to account for the packing limit of particles is to take the incremental increase in the volume fraction of the dispersed phase, when infinitesimal amount of new particles are added to an existing suspension of concentration ϕ, as $d\phi/(1 - \phi/\phi_m)$ rather than $d[\phi/(1 - \phi/\phi_m)]$ as used in the derivation of model 3 [38]. Hence,

$$\frac{dE}{E\left[\frac{15E_d-10E(1+\nu_d)}{6E_d+6E(1+\nu_d)}-\frac{(1-2\nu_d)E}{3E_d+4E(1-2\nu_d)}\right]} = \frac{d\phi}{\left(1-\frac{\phi}{\phi_m}\right)} \tag{9.16}$$

Upon integration, Equation 9.16 gives

$$\left(\frac{E}{E_m}\right)\left[\frac{ME_m-3E_d(P+Q)}{ME-3E_d(P+Q)}\right]^{N+\frac{53}{46}}\left[\frac{ME-3E_d(P-Q)}{ME_m-3E_d(P-Q)}\right]^{N-\frac{53}{46}} = \left(1-\frac{\phi}{\phi_m}\right)^{-2.5\phi_m} \tag{9.17}$$

Equation 9.17, referred to as model 4, reduces to the following equation for particulate composite of incompressible spherical particles ($\nu_d = 0.5$):

$$\left(\frac{E}{E_m}\right)\left(\frac{E-E_d}{E_m-E_d}\right)^{-2.5} = \left(1-\frac{\phi}{\phi_m}\right)^{-2.5\phi_m} \tag{9.18}$$

9.3.1 Model Predictions of Young's Modulus

According to the models discussed in the preceding section, the Young's modulus of a particulate composite of incompressible matrix can be expressed as

$$E_r = f(\nu_d, \lambda, \phi, \phi_m) \tag{9.19}$$

where E_r is relative Young's modulus (defined as E/E_m), ν_d is Poisson's ratio of the dispersed phase, λ is the ratio of dispersed-phase Young's modulus (E_d) to matrix-phase Young's modulus (E_m), ϕ is volume fraction of particles, and ϕ_m is maximum packing volume fraction of filler particles.

Figure 9.1 shows the comparison between the predictions of different models for two different values of λ: in one case $\lambda = 5$, that is, greater than unity, and in the other case, $\lambda = 0.1$, that is, less than unity. Poisson's ratio of the dispersed phase is

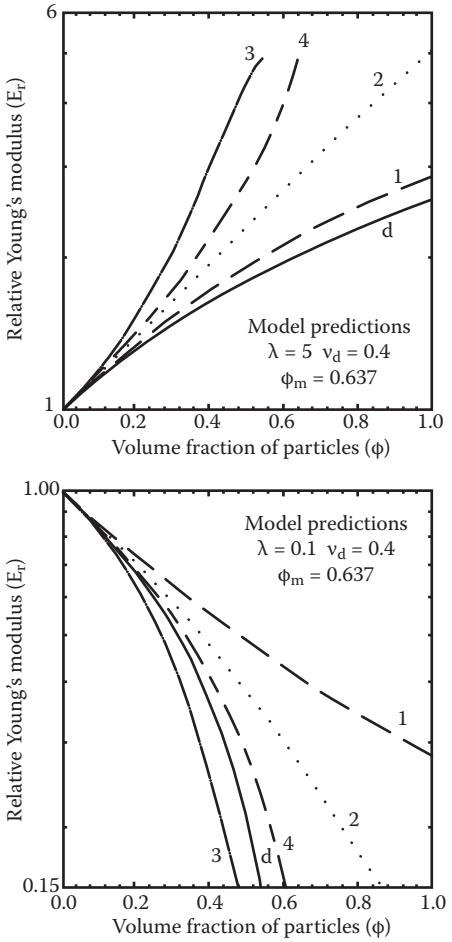

FIGURE 9.1 Relative Young's modulus (E_r) as a function of volume fraction of particles (ϕ) predicted by the models. The numbers shown on the curves refer to the corresponding model number. The letter "d" on the curve refers to the dilute system model (Equation 9.1). (From Pal, R., *Composites B* 36: 513–523, 2005.)

kept the same in both cases, that is, $\nu_d = 0.4$. The maximum packing volume fraction of particles (ϕ_m) is taken to be 0.637 (corresponding to random close packing of uniform spheres) in the calculations for models 3 and 4. The number shown on the curve refers to the corresponding model number. The letter "d" on the curve refers to dilute system model, that is, Equation 9.1.

When $\lambda = 5$, all models predict an increase in relative Young's modulus (E_r) with the increase in the volume fraction of the particles (ϕ). The predictions of E_r from different models at any given ϕ are in the following order: E_r (model 3) > E_r (model 4) > E_r (model 2) > E_r (model 1) > E_r (dilute system model).

At a low λ value of 0.1, all models predict a decrease in relative Young's modulus with the increase in the volume fraction of the particles. The predictions of E_r from

different models at any given ϕ are now in the following order: E_r (model 1) > E_r (model 2) > E_r (model 4) > E_r (dilute system model) > E_r (model 3).

Figure 9.2 shows the effect of dispersed-phase Poisson's ratio (ν_d) on E_r versus ϕ behavior at different values of modulus ratio λ. The calculations are based on model 4 (Equation 9.17) with ϕ_m value of 0.637. When λ is high, there is little effect of ν_d

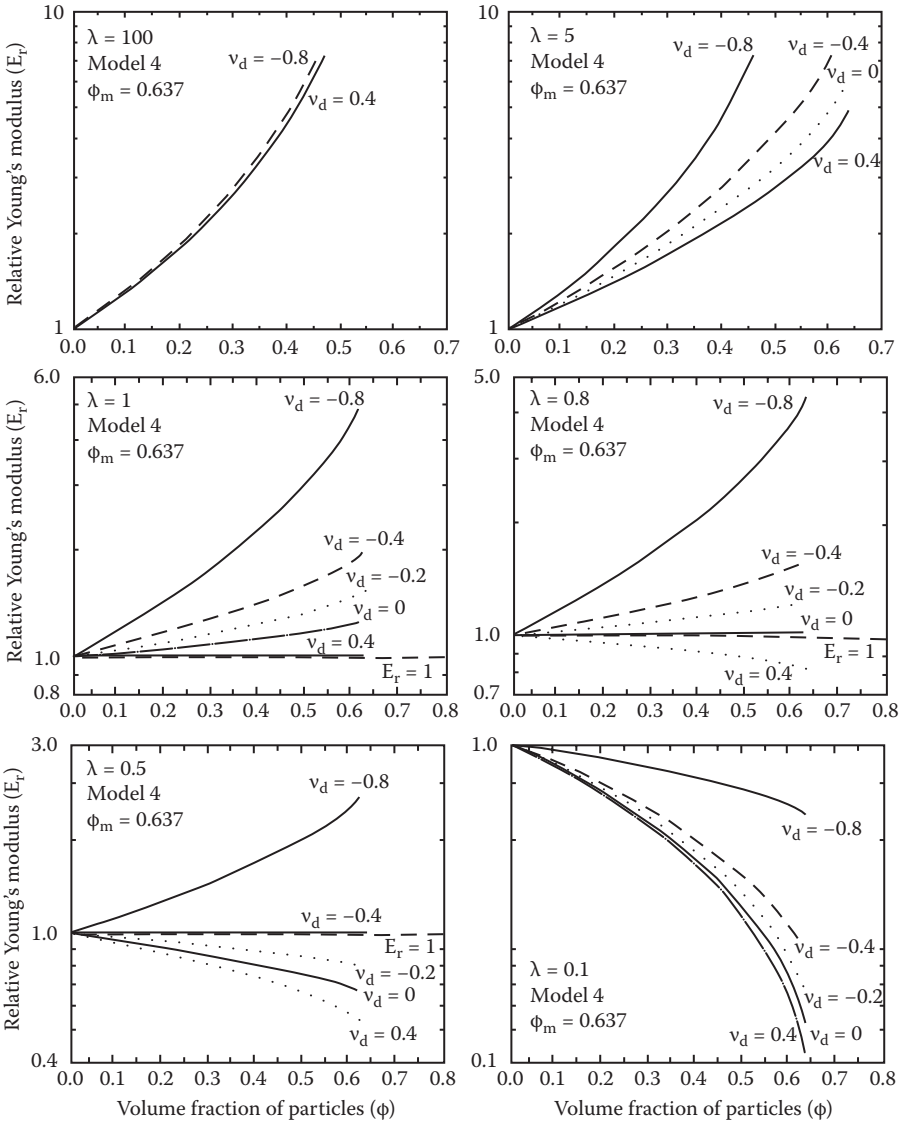

FIGURE 9.2 Effect of dispersed-phase Poisson's ratio (ν_d) on E_r versus ϕ behavior, as predicted from model 4 (Equation 9.17) for different values of modulus ratio λ. (From Pal, R., *Composites B* 36: 513–523, 2005.)

on E_r versus ϕ behavior of particulate composites. However, at moderate values of λ ($\lambda < 100$), the effect of ν_d on E_r versus ϕ behavior is significant; with the increase in ν_d from –1 to +0.5, relative Young's modulus of a particulate composite decreases at any given value of ϕ. It is interesting to note that for negative values of dispersed-phase Poisson's ratio (ν_d), relative Young's modulus (E_r) can be larger than unity even when the modulus ratio λ is less than unity. Thus, the widely held belief that when $\lambda < 1$, E_r is less than unity and that E_r decreases with the increase in ϕ, is valid only for positive values of dispersed-phase Poisson's ratio ($\nu_d > 0$).

The effect of modulus ratio λ on relative Young's modulus E_r for different values of dispersed-phase Poisson's ratio ν_d is shown in Figure 9.3. The calculations are based on model 4 (Equation 9.17) with ϕ_m value of 0.637. The volume fraction of the particles (ϕ) is fixed at 0.50. The following points should be noted from Figure 9.3: (1) At low values of λ ($\lambda < 10^{-3}$), ν_d has no effect on relative Young's modulus of particulate composites; (2) at high values of λ ($\lambda > 1000$), ν_d has no effect on E_r; (3) Poisson's ratio of the dispersed phase (ν_d) has a significant effect on E_r in the intermediate range of λ, that is, $10^{-3} < \lambda < 10^3$; (4) at any given value of λ in the intermediate range ($10^{-3} < \lambda < 10^3$), E_r decreases with the increase in ν_d; and (5) the cross-over value of the modulus ratio λ where relative Young's modulus of the particulate

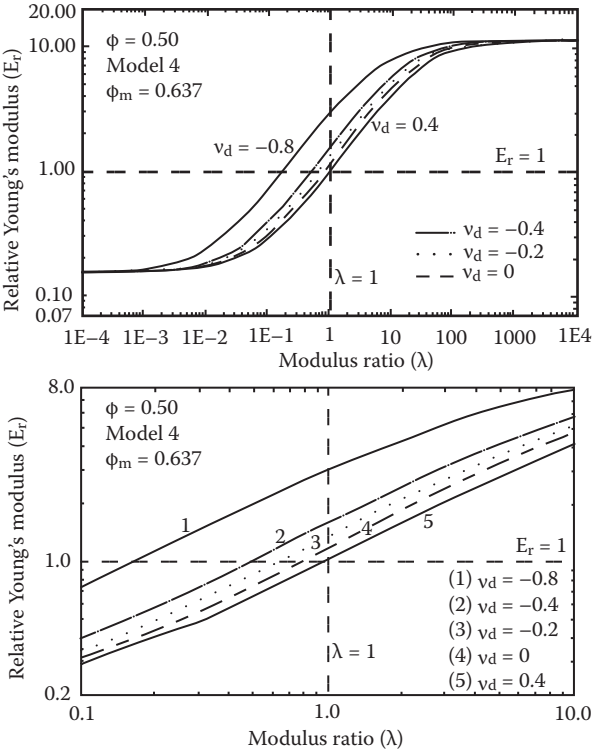

FIGURE 9.3 Effect of modulus ratio λ on E_r for different values of dispersed-phase Poisson's ratio (ν_d), at a fixed ϕ of 0.50. (From Pal, R., *Composites B* 36: 513–523, 2005.)

composite crosses from the region $E_r > 1$ to the region $E_r < 1$ increases with the increase in Poisson's ratio ν_d. The crossover value of λ is unity only when $\nu_d = 0.50$.

9.3.2 Comparison of Model Predictions with Experimental Data

Seven sets of experimental data on Young's modulus of particulate composites covering a wide range of particle volume fraction ϕ and a wide range of modulus ratio λ are considered to evaluate the models. Table 9.1 gives a summary of the various particulate composite systems considered to evaluate the models.

TABLE 9.1
Summary of Various Particulate Composites Considered in Evaluating Models

Set No.	Range of ϕ	Modulus Ratio (λ)	Ref. No.	Comments
1	0–0.524	0.254	[28]	Rubber-toughened poly(methyl methacrylate) (PMMA) composites; $\nu_d = 0.40$
2	0–0.706	19.3	[39]	Dental restorative composites, a total of 55 composites of varying filler volume fraction were investigated; $\nu_d = 0.20$
3	0–0.552	32	[40]	Dental composites of varying filler volume fraction; $\nu_d = 0.20$
4	0–0.68	Rigid filler—high λ	[41]	The composite systems investigated were (1) polyisobutylene filled with 8.7, 20.3, and 36.7% by volume of glass beads about 40 μm in diameter; (2) two castable polyurethane rubbers containing 54% by volume of similar glass beads; (3) propellant A containing 55, 61, and 68% solids by volume; (4) propellant B containing 38, 43, 48, 53, and 59% solids by volume; $\nu_d = 0.50$
5	0–0.625	Rigid filler—high λ	[25]	Crosslinked polyurethane rubber filled with glass beads ranging from 60 to 90 μm in diameter; $\nu_d = 0.50$
6	0–0.235	Rigid filler—high λ	[3]	Reinforced-rubber composites; the fillers investigated were (1) carbon black, (2) Kadox, (3) XX Zinc oxide, and (4) Catalpo clay; $\nu_d = 0.50$
7	0–0.206	Rigid filler—high λ	[3]	Reinforced-rubber composites; the fillers investigated were (1) Thermax, (2) Gilder's whiting, and (3) P-33; $\nu_d = 0.50$

Source: Pal, R., *Composites B* 36: 513–523, 2005.

Figures 9.4 through 9.10 show comparisons between experimental data and predictions of various models. Except for set 1 data, all other sets of data have $E_r > 1$. Note that set 1 data has a modulus ratio λ of less than one. The experimental data of set 1 (Figure 9.4) on rubber-toughened PMMA composites can be described adequately by model 2 (Equation 9.11). Model 1 (Equation 9.4) overpredicts E_r whereas other models (models 3 and 4 and the dilute system) underpredict E_r. The experimental data of set 2 (Figure 9.5) involves 55 commercial and experimental dental composites. While the data exhibits significant scatter, it can be described reasonably

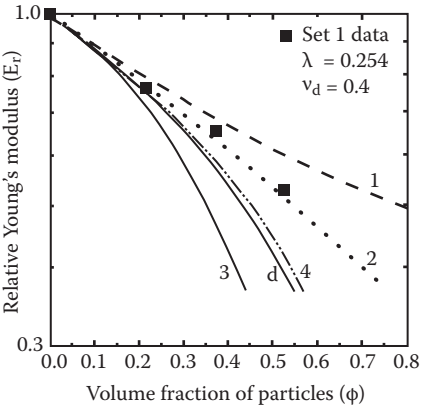

FIGURE 9.4 Comparison between experimental data of set 1 particulate composites and predictions of various models. The numbers shown on the curves refer to the corresponding model number. The letter "d" on the curve refers to the dilute system model (Equation 9.1). For models 3 and 4, ϕ_m is taken to be 0.637. (From Pal, R., *Composites B* 36: 513–523, 2005.)

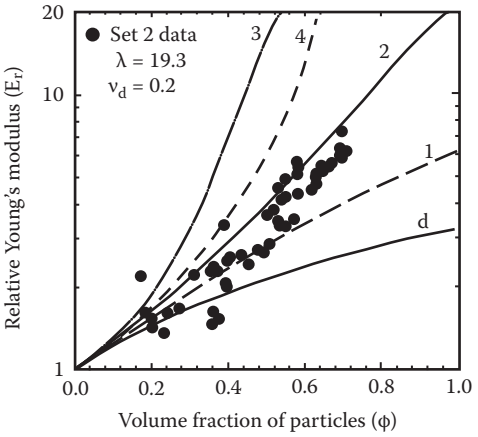

FIGURE 9.5 Comparison between experimental data of set 2 particulate composites and predictions of various models. The numbers shown on the curves refer to the corresponding model number. The letter "d" on the curve refers to the dilute system model (Equation 9.1). For models 3 and 4, ϕ_m is taken to be 0.637. (From Pal, R., *Composites B* 36: 513–523, 2005.)

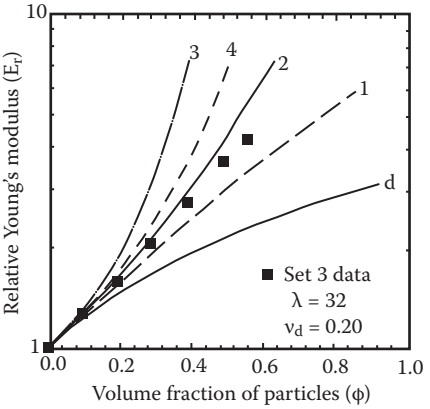

FIGURE 9.6 Comparison between experimental data of set 3 particulate composites and predictions of various models. The numbers shown on the curves refer to the corresponding model number. The letter "d" on the curve refers to the dilute system model (Equation 9.1). For models 3 and 4, ϕ_m is taken to be 0.637. (From Pal, R., *Composites B* 36: 513–523, 2005.)

well by model 2 (Equation 9.11). Set 3 data on dental composites (Figure 9.6) can also be described adequately by model 2 (Equation 9.11). The experimental data of set 4 (Figure 9.7) on Young's modulus of composite propellants and filled elastomers fits well with model 4 (Equation 9.17) using a ϕ_m value of 0.85. Set 5 data on glass beads-reinforced-rubber composites (Figure 9.8) can be described very well by model 4 (Equation 9.17) using a ϕ_m value of 0.637. The experimental data of set 6 (Figure 9.9) on Young's modulus of various filler-reinforced-rubber composites can also be described reasonably well by model 4 (Equation 9.17); however, the ϕ_m

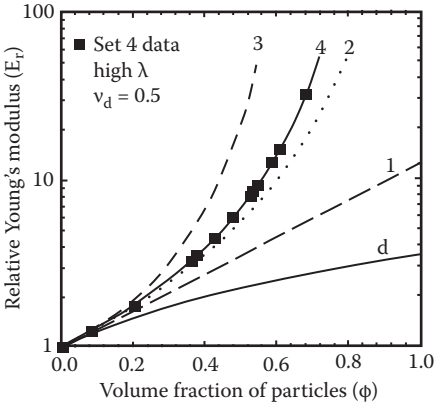

FIGURE 9.7 Comparison between experimental data of set 4 particulate composites and predictions of various models. The numbers shown on the curves refer to the corresponding model number. The letter "d" on the curve refers to the dilute system model (Equation 9.1). For models 3 and 4, ϕ_m is taken to be 0.85. (From Pal, R., *Composites B* 36: 513–523, 2005.)

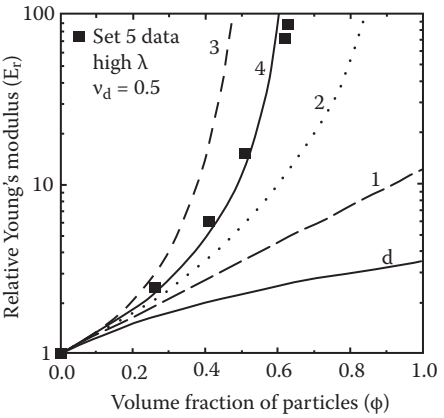

FIGURE 9.8 Comparison between experimental data of set 5 particulate composites and predictions of various models. The numbers shown on the curves refer to the corresponding model number. The letter "d" on the curve refers to the dilute system model (Equation 9.1). For models 3 and 4, ϕ_m is taken to be 0.637. (From Pal, R., *Composites B* 36: 513–523, 2005.)

value used in model 4 is now much lower, that is, $\phi_m = 0.25$. A low value of ϕ_m is indicative of flocculation of particulate filler present in the composite. Indeed, fillers like carbon black are known to exhibit flocculation in rubber [3]. Set 7 data on reinforced-rubber composites, shown in Figure 9.10, can be described well by model 2 (Equation 9.11).

Based on comparisons between experimental data (seven sets) and predictions of the models, model 4 (Equation 9.17) appears superior to other models. Model 2 (Equation 9.11) is simply a special case of model 4 with $\phi_m = 1.0$.

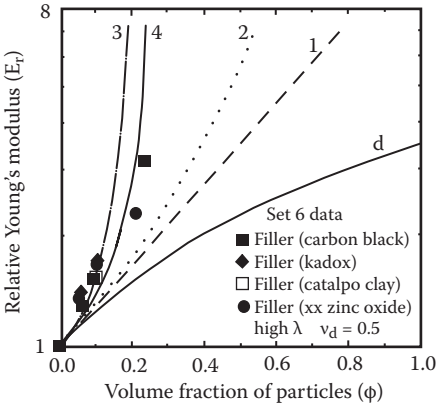

FIGURE 9.9 Comparison between experimental data of set 6 particulate composites and predictions of various models. The numbers shown on the curves refer to the corresponding model number. The letter "d" on the curve refers to the dilute system model (Equation 9.1). For models 3 and 4, ϕ_m is taken to be 0.25. (From Pal, R., *Composites B* 36: 513–523, 2005.)

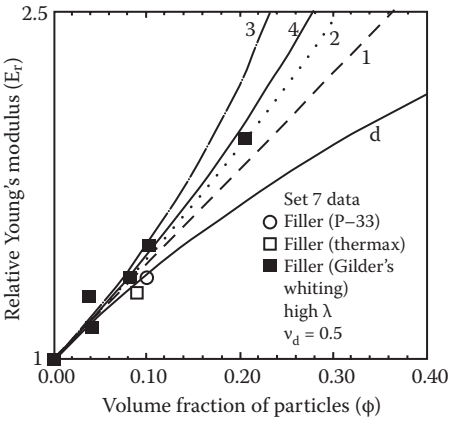

FIGURE 9.10 Comparison between experimental data of set 7 particulate composites and predictions of various models. The numbers shown on the curves refer to the corresponding model number. The letter "d" on the curve refers to the dilute system model (Equation 9.1). For models 3 and 4, ϕ_m is taken to be 0.637. (From Pal, R., *Composites B* 36: 513–523, 2005.)

9.4 CONCLUDING REMARKS

Models are discussed for the Young's modulus of concentrated particulate composites. According to the models, the relative Young's modulus (E_r) of concentrated particulate composites of incompressible matrix is a function of the following variables: modulus ratio λ (ratio of dispersed-phase modulus to the matrix-phase modulus), dispersed-phase Poisson's ratio ν_d, volume fraction of particles ϕ, and maximum packing volume fraction of particles ϕ_m. For positive values of ν_d ($0 < \nu_d < 0.5$), all models predict an increase in E_r with the increase in ϕ provided that the modulus ratio λ is greater than unity ($\lambda > 1$); when the modulus ratio λ is less than unity, all models predict a decrease in E_r with the increase in ϕ. At low values of λ ($\lambda < 10^{-3}$), dispersed-phase Poisson's ratio ν_d has negligible effect on E_r. Also, at high values of λ ($\lambda > 10^3$), ν_d has negligible effect on E_r. Only in the intermediate range of λ ($10^{-3} < \lambda < 10^3$), relative Young's modulus decreases with the increase in ν_d from –1 to 0.5.

The models are evaluated using seven sets of experimental data on Young's modulus of concentrated particulate composites. Model 4 (Equation 9.17) appears to be somewhat superior to other models (models 1 through 3) when comparisons are made with the experimental data. Model 4 is quite capable of predicting the effect of particle size distribution on Young's modulus of particulate composites. The maximum packing volume fraction of particles (ϕ_m), present as a parameter in the model, is known to be sensitive to particle size distribution; the ϕ_m value for particulate composite of uniform particles is expected to be significantly smaller than the ϕ_m value for polydisperse composite.

REFERENCES

1. Cohen, L.J. and O. Ishai. 1967. The elastic properties of three-phase composites. *J. Composite Mater.* 1: 390–403.
2. Garboczi, E.J. and J.G. Berryman. 2001. Elastic moduli of a material containing composite inclusions: Effective medium theory and finite element computations. *Mech. Mater*. 33: 455–470.
3. Smallwood, H.M. 1944. Limiting law of the reinforcement of rubber. *J. Appl. Phys*. 15: 758–766.
4. Eshelby, J.D. 1957. The determination of the field of an ellipsoidal inclusion and related problems. *Proc. Roy. Soc. London A* 241: 376–396.
5. Hashin, Z. 1962. The elastic moduli of heterogeneous materials. *J. Appl. Mech*. 29: 143–150.
6. Hashin, Z and S. Shtrikman. 1962. A variational approach to the theory of the elastic behavior of multiphase materials. *J. Mech. Phys. Solids* 11: 127–140.
7. Hashin, Z. 1964. Theory of mechanical behavior of heterogeneous media. *Appl. Mech. Rev*. 17: 1–9.
8. Hill, R. 1965. A self consistent mechanics of composite materials. *J. Mech. Phys. Solids* 13: 213–222.
9. Budiansky, B. 1965. On the elastic moduli of some heterogeneous materials. *J. Mech. Phys. Solids* 13: 223–227.
10. Kerner, E.H. 1956. The elastic and thermoelastic properties of composite media. *Proc. Phys. Soc. London B* 69: 808–813.
11. Hill, R. 1963. Elastic properties of reinforced solids: Some theoretical principles. *J. Mech. Phys. Solids* 11: 357–372.
12. Van der Poel, C. 1958. On the rheology of concentrated dispersions. *Rheol. Acta* 1: 198–205.
13. Walpole, L.J. 1972. The elastic behavior of a suspension of spherical particles. *Quart. J. Mech. Appl. Math.* 25: 153–160.
14. Roscoe, R. 1973. Isotropic composites with elastic or viscoelastic phases: General bounds for the moduli and solutions for special geometrics. *Rheol. Acta* 12: 404–411.
15. Smith, J.C. 1974. Correction and extension of van der Poel's method for calculating the shear modulus of a particulate composite. *J. Res. Nat. Burr. Stand. (U.S.)* 78A: 355–361.
16. Smith, J.C. 1975. Simplification of van der Poel's formula for the shear modulus of a particulate composite. *J. Res. Nat. Burr. Stand. (U.S.)* 79A: 419–423.
17. McLaughlin, R. 1977. A study of the differential scheme for composite materials. *Int. J. Eng Sci.* 15: 237–244.
18. Chen, H.S. and A. Acrivos. 1978. The effective elastic moduli of composite materials containing spherical inclusions at nondilute concentrations. *Int. J. Solids Struct*. 14: 349–364.
19. Christensen, R.M. 1979. *Mechanics of Composite Materials*, New York: John Wiley & Sons.
20. Christensen, R.M. 1982. Mechanical properties of composite materials. In: *Mechanics of Composite Materials—Recent Advances*, eds, Z. Hashin and C.T. Herakovich, pp. 1–16, New York: Pergamon Press.
21. Hashin, Z. 1962. Analysis of composite materials: A survey. *J. Appl. Mech.* 50: 481–504.
22. Norris, A.N. 1985. A differential scheme for the effective moduli of composites. *Mech. Mater.* 4: 1–16.
23. Christensen, R.M. 1990. A critical evaluation for a class of micromechanics models. *J. Mech. Phys. Solids* 38: 379–404.

24. Phan-Thien, N. and D.C. Pham. 1997. Differential multiphase models for polydispersed suspensions and particulate solids. *J. Non-Newtonian Fluid Mech.* 72: 305–318.
25. Bills, K.W., K.H. Sweeney, and F.S. Salcedo. 1960. The tensile properties of highly filled polymers—Effect of filler concentrations. *J. Appl. Polym. Sci.* 4: 259–268.
26. Munstedt, H. 1981. Rheology of rubber-modified polymer melts. *Poly. Eng. Sci*. 21: 259–269.
27. Chantler, P.M., X. Hu, and N.M. Boyd. 1999. An extension of a phenomenological model for dental composites. *Dental Mater.* 15: 144–149.
28. Biwa, S., N. Ito, and N. Ohno. 2001. Elastic properties of rubber particles in toughened PMMA: Ultrasonic and micromechanical evaluation. *Mech. Mater.* 33: 717–728.
29. Luo, J.J. and I.M. Daniel. 2003. Characterization and modeling of mechanical behavior of polymer/clay nanocomposites. *Composites Sci. Tech.* 63: 1607–1616.
30. Ji, S. 2004. Generalized means of an approach for predicting Young's moduli of multiphase materials. *Mat. Sci. Eng*. A366: 195–201.
31. Voigt, W. 1928. *Lehrbuch der Kristallphysik*, Leipzig: Teubner-Verlag.
32. Reuss, A. 1929. Berechnung der Fliessgrenze von Mischkristallen auf Grund der Plastizitätsbedingung für Einkristalle. *Z. Angew. Math. Mech.* 9: 49–58.
33. Agarwal, B.D. and J.J. Broutman. 1990. *Analysis and Performance of Fiber Composites*, New York: John Wiley & Sons.
34. Chawla, K.K. 1998. *Composite Materials*, New York: Springer.
35. Herakovich, C.T. 1998. *Mechanics of Fibrous Composites*, New York: John Wiley & Sons.
36. Halpin, J.C. and J.L. Kardos. 1976. The Halpin–Tsai equations: A review. *Poly. Eng. Sci.* 16: 344–352.
37. Christensen, R.M. and K.H. Lo. 1979. Solutions for the effective shear properties in three phase sphere and cylinder models. *J. Mech. Phys. Solids* 27: 315–331.
38. Pal, R. 2005. New models for effective Young's modulus of particulate composites. *Composites B* 36: 513–523.
39. Braem, M., V.E. Van Doren, P. Lambrechts, and G. Vanherle. 1987. Determination of Young's modulus of dental composites: A phenomenological model. *J. Mater. Sci.* 22: 2037–2042.
40. Braem, M., W. Finger, V.E. Van Doren, P. Lambrechts, and G. Vanherle. 1989. Mechanical properties and filler fraction of dental composites. *Dental Mater.* 5: 346–349.
41. Landel, R.F. and T.L. Smith. 1961. Viscoelastic properties of rubber-like composite propellants and filled elastomers. *ARS J.* 31: 599–608.

10 Effective Shear Modulus of Concentrated Composites

10.1 INTRODUCTION

As noted in Chapter 7, a composite material composed of isotropic components distributed randomly in the material space will have isotropic effective properties, which are restricted by definite lower and upper bounds [1–13]. Regardless of the geometry of the inclusions (dispersed phase), the effective property of the composite lies somewhere in the interval between the lower and upper bounds. Such bounds depend only on the volume fractions of the components and the properties of the components.

The upper bound for the effective shear modulus (G) of an isotropic composite, referred to as the Voigt rule of mixtures, is given as [14]

$$G \le \phi\, G_d + (1 - \phi) G_m \tag{10.1}$$

where G_m and G_d are shear moduli of the matrix and the dispersed phase, respectively, and ϕ is volume fraction of the dispersed phase.

The lower bound for the effective shear modulus of an isotropic composite, referred to as the Reuss rule of mixtures, is given as [15]

$$G \ge \frac{1}{\left(\dfrac{\phi}{G_d} + \dfrac{1-\phi}{G_m}\right)} \tag{10.2}$$

The actual effective shear modulus of the isotropic composite is expected to lie somewhere in the interval between the Voigt and Reuss bounds, regardless of the geometry of the inclusions. The bounds given by Equations 10.1 and 10.2 are generally not close enough to provide a good estimate of the effective shear modulus of the composite.

Hashin and Shtrikman [5] and Walpole [8] employed a variational theorem to obtain the following improved bounds for the effective shear modulus of isotropic composites [5,8,10]:

$$\left[\frac{(G_m + G_\ell)\phi}{G_m + G_\ell + (G_d - G_m)(1-\phi)}\right] \le \left(\frac{G - G_m}{G_d - G_m}\right) \le \left[\frac{(G_m + G_g)\phi}{G_m + G_g + (G_d - G_m)(1-\phi)}\right] \tag{10.3}$$

where G_ℓ and G_g depend on the properties of the matrix and dispersed phase.

When $(G_d - G_m)(K_d - K_m) \geq 0$,

$$G_\ell = \frac{3}{2}\left[\frac{1}{G_m} + \frac{10}{9K_m + 8G_m}\right]^{-1} \quad , \quad G_g = \frac{3}{2}\left[\frac{1}{G_d} + \frac{10}{9K_d + 8G_d}\right]^{-1} \tag{10.4}$$

When $(G_d - G_m)(K_d - K_m) \leq 0$,

$$G_\ell = \frac{3}{2}\left[\frac{1}{G_m} + \frac{10}{9K_d + 8G_m}\right]^{-1} \quad , \quad G_g = \frac{3}{2}\left[\frac{1}{G_d} + \frac{10}{9K_m + 8G_d}\right]^{-1} \tag{10.5}$$

where K_m and K_d are the bulk moduli of matrix and dispersed phase, respectively.

For composites with incompressible components ($K_d \to \infty$, $K_m \to \infty$), the Hashin–Shtrikman–Walpole bounds reduce to

$$\left[\frac{\left(G_m + \frac{3}{2}G_m\right)\phi}{\left(G_m + \frac{3}{2}G_m\right) + (G_d - G_m)(1-\phi)}\right] \leq \left(\frac{G - G_m}{G_d - G_m}\right) \leq \left[\frac{\left(G_m + \frac{3}{2}G_d\right)\phi}{\left(G_m + \frac{3}{2}G_d\right) + (G_d - G_m)(1-\phi)}\right] \tag{10.6}$$

when $\lambda = G_d/G_m > 1.0$, and

$$\left[\frac{\left(G_m + \frac{3}{2}G_d\right)\phi}{\left(G_m + \frac{3}{2}G_d\right) + (G_d - G_m)(1-\phi)}\right] \leq \left(\frac{G - G_m}{G_d - G_m}\right) \leq \left[\frac{\left(G_m + \frac{3}{2}G_m\right)\phi}{\left(G_m + \frac{3}{2}G_m\right) + (G_d - G_m)(1-\phi)}\right] \tag{10.7}$$

when $\lambda = G_d/G_m < 1.0$.

Figure 10.1 compares the Voigt–Reuss bounds for effective shear modulus of particulate composites with the Hashin–Shtrikman–Walpole bounds for two different values of λ (ratio of dispersed phase to continuous phase moduli). The dispersed and continuous phases are assumed to be incompressible ($K_d \to \infty$, $K_m \to \infty$). As expected, the Hashin–Shtrikman–Walpole (HSW) bounds are much closer as compared with the Voigt–Reuss bounds, which are far apart.

The obvious drawback of the bounds is that they do not give the precise value of the property. They only provide a range or interval of values. Thus, it is important to develop models for the direct estimation of the property (rather than its bounds). However, this is possible only for the known geometry inclusions. In what follows, the shear modulus equations for particulate composites consisting of spherical or nearly spherical filler particles are described in details.

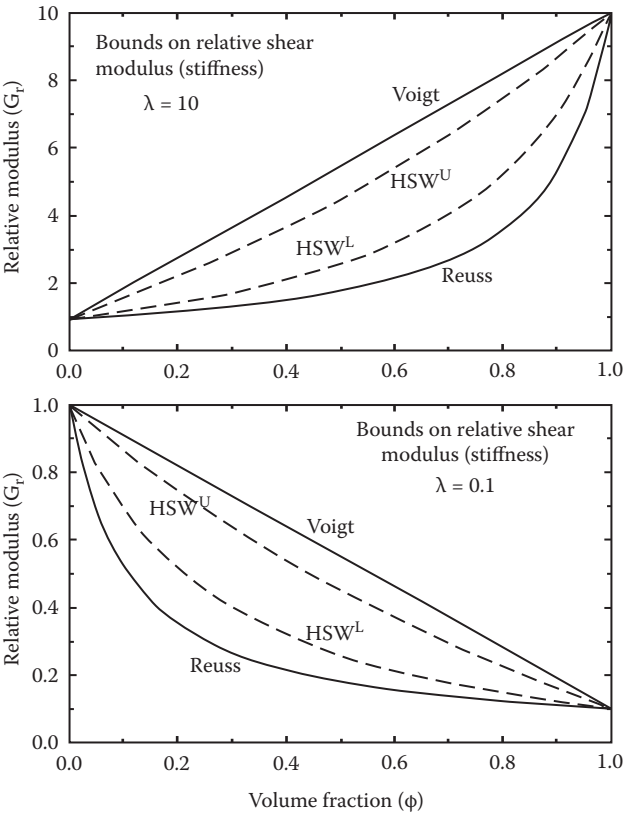

FIGURE 10.1 Comparison of Voigt–Reuss bounds with Hashin–Shtrikman–Walpole (HSW) bounds for effective shear modulus of particulate composites at two different values of modulus ratio λ (HSW^U refers to upper HSW bound and HSW^L refers to lower HSW bound).

10.2 SINGLE-PARAMETER SHEAR MODULUS EQUATIONS FOR COMPOSITES

For an *infinitely dilute* dispersion of solid spherical particles in an incompressible solid matrix, the exact expression for the shear modulus is given as [2,10,16,17]

$$\frac{G}{G_m} = 1 + \frac{5}{2}\left[\frac{2G_d - 2G_m}{2G_d + 3G_m}\right]\phi \tag{10.8}$$

The intrinsic shear modulus [G] is defined as

$$[G] = \lim_{\phi \to \theta}\left(\frac{G/G_m - 1}{\phi}\right) \tag{10.9}$$

Using Equation 10.8, the intrinsic shear modulus [G] is found to be

$$[G] = \frac{5}{2}\left[\frac{2\lambda - 2}{2\lambda + 3}\right] \tag{10.10}$$

where λ is the modulus ratio G_d/G_m. [G] is less than unity when $\lambda < 1$. At $\lambda = 1$, [G] is unity. [G] is greater than unity when $\lambda > 1$. When $\lambda \to \infty$, [G] becomes 2.5 and when $\lambda \to 0$, [G] becomes negative with a value of −5/3.

Equation 10.8 can be expressed in terms of the relative shear modulus, (defined as G/G_m) and λ as follows:

$$G_r = 1 + \frac{5}{2}\left[\frac{2\lambda - 2}{2\lambda + 3}\right]\phi \tag{10.11}$$

According to Equation 10.11, the relative shear modulus of different composites is the same when comparison is made at the same volume fraction of the dispersed-phase and the same modulus ratio λ. Thus, Equation 10.11 is a single-parameter G_r versus ϕ equation with λ as a parameter.

In the derivation of Equation 10.11, the interaction between the neighboring particles is not considered, as the composite is very dilute. However, at finite concentrations of the dispersed phase, the interaction between the particles is significant. Consequently, the shear modulus of a concentrated particulate composite is significantly different from that predicted by Equation 10.11.

Chen and Acrivos [10] considered particle–pair interactions within the composite and developed the following expression for the effective shear modulus of particulate composites:

$$G_r = 1 + \frac{5}{2}\left[\frac{2\lambda - 2}{2\lambda + 3}\right]\phi + \frac{5}{2}\left[\frac{2\lambda - 2}{2\lambda + 3}\right]^2 H\phi^2 \tag{10.12}$$

where H is a function of modulus ratio λ (assuming that the matrix and dispersed phases are incompressible). For composites of rigid particles ($\lambda \to \infty$), H = 2.004.

The Chen and Acrivos equation (Equation 10.12) cannot be applied at particle concentrations where three-particle or higher-order particle interactions are present. The higher-order particle interactions are generally important when $\phi > 0.10$.

Several authors [9,10,18–22] have developed shear modulus equations for concentrated particulate composites using different approaches. However, all these equations are single-parameter G_r versus ϕ equations with λ as the parameter (assuming that the matrix is incompressible). They can be expressed as

$$G_r = f(\lambda, \phi) \tag{10.13}$$

Kerner [18] utilized the generalized self-consistent method to develop the following expression for G_r:

$$G_r = \left[\frac{1 + \frac{3}{2}\phi\gamma}{1 - \phi\gamma} \right] \tag{10.14}$$

where γ is given as

$$\gamma = \left[\frac{2(\lambda - 1)}{2\lambda + 3} \right] \tag{10.15}$$

In the limit $\phi \to 0$, Equation 10.14 reduces to Equation 10.11.

Equation 10.14 upon expansion as a power series in ϕ gives

$$G_r = 1 + \frac{5}{2}\left[\frac{2\lambda - 2}{2\lambda + 3} \right]\phi + \frac{5}{2}\left[\frac{2\lambda - 2}{2\lambda + 3} \right]^2 \phi^2 \tag{10.16}$$

The coefficient of ϕ^2 in Equation 10.16 is about one-half of the actual theoretical value determined by Chen and Acrivos [10] (see Equation 10.12) when $\lambda \to \infty$. Therefore, the Kerner equation (Equation 10.14) is expected to give a reasonable estimate of G_r only at low to moderate values of filler concentration.

Smith [21] has proposed an improvement of the Kerner equation. The improved Kerner formula for shear modulus of particulate composites, developed by Smith [21], is given as follows:

$$G_r = 1 + X_K + \left[\frac{126P\left(1 - \phi^{2/3}\right)^2 X_K^3}{\frac{525}{4}P + \frac{15}{2}RX_K - 252P\left(1 - \phi^{2/3}\right)^2 X_K^2} \right] \tag{10.17}$$

where $X_K = G_r - 1$ is estimated from the Kerner equation (Equation 10.14), and P and R are given as follows:

$$P = \frac{19}{2}\lambda + 8 \tag{10.18}$$

$$R = 76\lambda + 64 - 76(\lambda - 1)\phi^{7/3} \tag{10.19}$$

Using the self-consistent method [17], Budiansky [20] and Hill [19] also developed shear modulus equations for concentrated particulate composites. The equation of Budiansky [20] is somewhat different from the one developed by Hill [19]. The Budiansky equation is as follows:

$$G_r = \frac{3 + 2\lambda - 5\phi}{3 + \lambda(2 - 5\phi)} \tag{10.20}$$

One problem with the Budiansky equation is that it predicts G_r to be infinite at $\phi = 0.40$ for particulate composites of rigid particles ($\lambda \to \infty$). In addition, for porous composites Equation 10.20 predicts G_r to be zero, at a void fraction of 0.60.

Hill [19] developed the following equation:

$$\frac{G_r - \lambda}{1 - \lambda} = \frac{1 - \phi}{\left[1 + \frac{2}{5}\left(\frac{1}{G_r} - 1\right)\right]} \tag{10.21}$$

The Hill equation suffers from the same problems as the Budiansky equation. It predicts $G_r \to \infty$ at $\phi = 0.40$ when $\lambda \to \infty$. For porous composites, Equation 10.21 predicts $G_r \to 0$ when $\phi = 0.60$.

Roscoe [9] utilized a differential scheme to extend the result of dilute systems (Equation 10.8) to concentrated systems. His equation is given as follows:

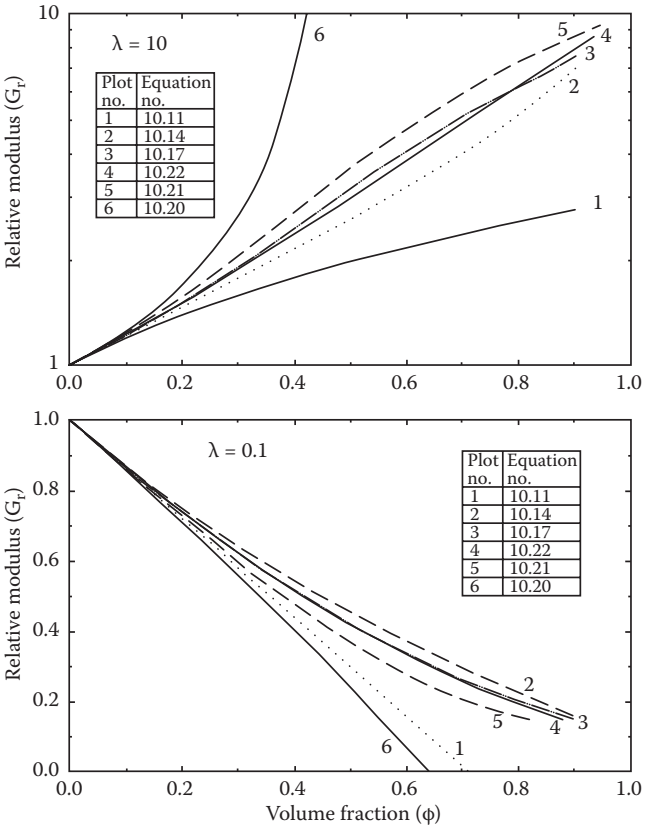

FIGURE 10.2 Relative shear modulus (G_r) predicted by single-parameter G_r versus ϕ equations for two different values of the parameter λ ($\lambda = 10$ and $\lambda = 0.10$).

$$G_r\left[\frac{G_r-\lambda}{1-\lambda}\right]^{-2.5}=(1-\phi)^{-2.5} \tag{10.22}$$

Figure 10.2 compares the predictions of various equations for two different values of modulus ratio λ (λ = 10 and λ = 0.10). For a high λ value of 10, all equations predict the relative shear modulus G_r to be greater than unity and G_r increases with the increase in particle concentration ϕ. For a low λ value of 0.1, all equations predict G_r to be less than unity and G_r decreases with the increase in ϕ.

In summary, the single-parameter G_r versus ϕ equations for particulate composites (assuming incompressible matrix) predict that the relative shear modulus is a function of modulus ratio λ and volume fraction of the dispersed-phase ϕ.

10.3 TWO-PARAMETER SHEAR MODULUS EQUATIONS FOR COMPOSITES

One serious limitation of the single-parameter G_r versus ϕ equations, with λ as a parameter, is that they predict the shear modulus of particulate composite to be independent of the particle size distribution. The particle size distribution does not appear in any of the equations discussed in Section 10.2. Furthermore, for composites of rigid particles ($\lambda \to \infty$), the single-parameter equations either predict finite values of shear modulus over the entire ϕ range or predict divergence of shear modulus at ϕ = 0.40 (see Budiansky equation, Equation 10.20, and Hill equation, Equation 10.21) and at ϕ = 1.0 (see Roscoe equation, Equation 10.22). This is in contradiction with the experimental fact that the G_r of particulate composites (rigid particles, incompressible matrix) diverges at $\phi = \phi_m$, the maximum packing volume fraction of particles. For random close packing of monosized spherical particles, ϕ_m is 0.637 [23].

To account for the effects of particle size distribution and divergence of shear modulus, the correct form of the shear modulus versus filler concentration equation for particulate composites (incompressible matrix) is a two-parameter equation:

$$G_r = f(\lambda, \phi_m, \phi) \tag{10.23}$$

where ϕ_m is a function of the particle size distribution.

Pal [24] recently derived the following two-parameter shear modulus equations for concentrated particulate composites of spherical particles using a differential scheme along with the solution of an infinitely dilute system:

$$G_r\left[\frac{G_r-\lambda}{1-\lambda}\right]^{-2.5}=\exp\left[\frac{2.5\,\phi}{1-\dfrac{\phi}{\phi_m}}\right] \tag{10.24}$$

$$G_r\left[\frac{G_r-\lambda}{1-\lambda}\right]^{-2.5}=\left[1-\frac{\phi}{\phi_m}\right]^{-2.5\,\phi_m} \tag{10.25}$$

The salient features of these two-parameter (λ and ϕ_m) G_r versus ϕ equations are: (1) they take into account the effect of modulus ratio λ, (2) they exhibit divergence of G_r at $\phi = \phi_m$ when $\lambda \to \infty$, and (3) they take into account the effect of particle size distribution through the parameter ϕ_m.

Figure 10.3 shows comparison between the predictions of Equations 10.24 and 10.25 at a fixed ϕ value of 0.5. The value of the maximum packing volume fraction ϕ_m is taken to be 0.637, corresponding to random close packing volume fraction of uniform spheres. When $\lambda < 1.0$, both equations predict $G_r < 1.0$; however, the values predicted by Equation 10.25 are higher than those predicted by Equation 10.24. When $\lambda = 1.0$, both equations predict $G_r = 1.0$. When $\lambda > 1.0$, both equations predict $G_r > 1.0$; however, the values predicted by Equation 10.24 are higher than the values predicted by Equation 10.25.

Figure 10.4 shows the effect of particle size distribution on the relative shear modulus of particulate composites for two values of modulus ratio λ: $\lambda = 0$ and $\lambda = \infty$. Composites with bimodal particle size distribution are considered. The relative shear modulus of composite containing a mixture of large and small particles is plotted as a function of the volume fraction of small particles, with total volume fraction of particles as a parameter. The particle size ratio is 5:1. The relative shear modulus is calculated from Equation 10.25 using ϕ_m values predicted from the Ouchiyama and Tanaka formula [25–27]:

$$\phi = \frac{\sum D_i^3 f_i}{\sum (D_i \sim \bar{D})^3 f_i + \frac{1}{\beta}\sum [(D_i + \bar{D})^3 - (D_i \sim \bar{D})^3] f_i} \tag{10.26}$$

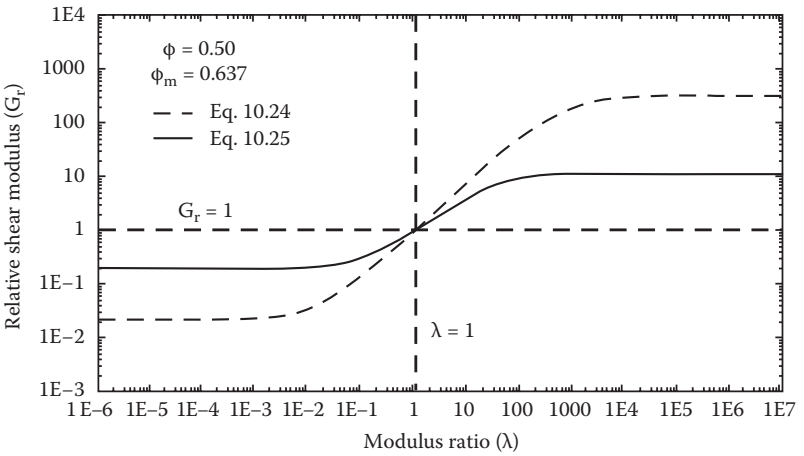

FIGURE 10.3 Comparison between the predictions of different two-parameter G_r versus ϕ equations (Equations 10.24 and 10.25) for particulate composites with $\phi = 0.50$. ϕ_m is taken to be 0.637, corresponding to random close packing of uniform spheres.

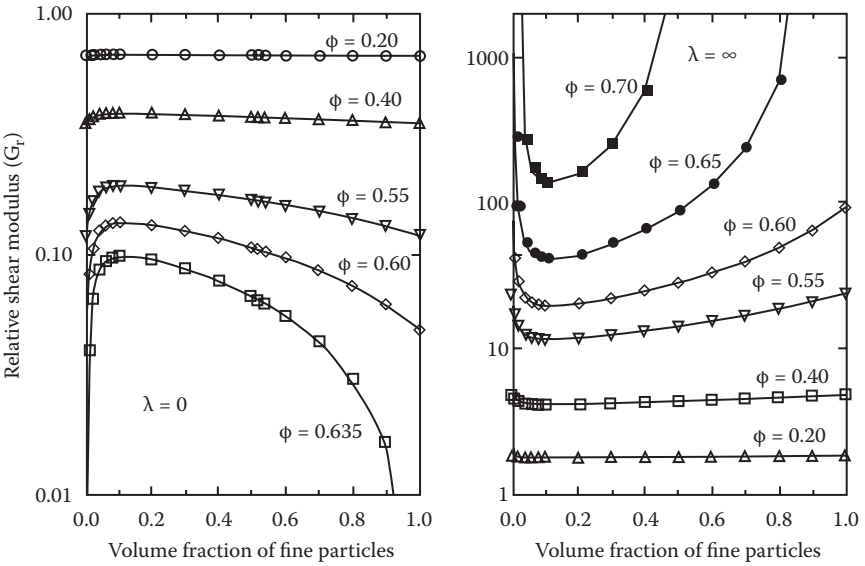

FIGURE 10.4 The effect of particle size distribution on the relative shear modulus of bimodal composites for two different values of modulus ratio λ (λ = 0 and λ = ∞). The particle size ratio between large and small particles is 5:1.

where

$$\beta = 1 + \frac{4}{13}\left(8\phi_m^o - 1\right)\bar{D}\,\frac{\sum (D_i + \bar{D})^2 \left[1 - \dfrac{(3/8)\bar{D}}{(D_i + \bar{D})}\right] f_i}{\sum \left[D_i^3 - (D_i \sim \bar{D})^3\right] f_i} \tag{10.27}$$

$$\bar{D} = \sum D_i f_i . \tag{10.28}$$

Here ϕ_m^o is the maximum packing volume fraction of a particulate composite of uniform (same size) particles, f_i is the number fraction of particles of diameter D_i, $\bar{D}$ is the number-average diameter of the composite, and the abbreviation $(D_i \sim \bar{D})$ is defined as

$$(D_i \sim \bar{D}) = 0 \quad \text{for} \quad D_i \le \bar{D} \tag{10.29}$$

$$= D_i - \bar{D} \quad \text{for} \quad D_i > \bar{D} \tag{10.30}$$

The maximum packing concentration of a composite with uniform particles, that is ϕ_m^o, is taken to be 0.637. The Ouchiyama and Tanaka formula has been used by several investigators [28,29] to predict the value of ϕ_m. The experimentally measured values of ϕ_m are found to agree reasonably well with those predicted from the Ouchiyama and Tanaka formula.

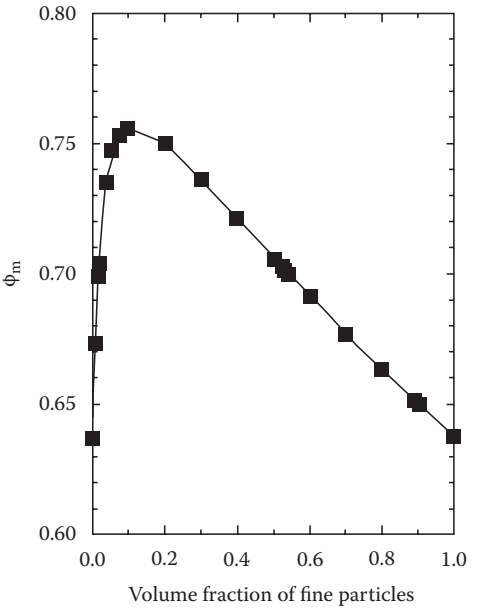

FIGURE 10.5 The effect of particle size distribution on ϕ_m, the maximum packing volume fraction of particles.

Figure 10.5 shows the plot of ϕ_m predicted from the Ouchiyama and Tanaka formula as a function of volume fraction of fine particles. With the increase in the proportion of fine particles in a bimodal composite, the value of ϕ_m increases initially, reaches a maximum value of approximately 0.76 at a fine particle proportion of about 10%, and then decreases. The ϕ_m values shown in Figure 10.5 were used to generate the relative shear modulus plots of Figure 10.4.

At low λ, Figure 10.4 reveals the following information: (1) a large increase in relative shear modulus occurs when a monosized composite is changed to a bimodal composite—this effect is negligible when $\phi \leq 0.40$ and (2) the plots of relative shear modulus versus volume fraction of fine particles, at high values of ϕ, exhibit a maximum at a fine particle volume fraction of about 0.1 (where a maximum in ϕ_m occurs). At high λ, Figure 10.4 shows a very different behavior: (1) the relative shear modulus now exhibits an opposite effect, that is, it decreases when a concentrated ($\phi \geq 0.55$) monosized composite is changed to a bimodal composite—this effect is negligible when $\phi \leq 0.40$ and (2) the plots of relative shear modulus versus volume fraction of fine particles, at high values of ϕ, exhibit a minimum at a fine particle volume fraction of about 0.10 (where a maximum in ϕ_m occurs).

10.4 ANALOGY BETWEEN SHEAR MODULUS OF COMPOSITES AND VISCOSITY OF SUSPENSIONS

There exists a close analogy between the shear modulus of particulate composites and the viscosity of suspensions of rigid particles in Newtonian liquids. The relative

viscosity (η_r) of suspensions of rigid spherical particles in Newtonian liquids is often expressed by the following equations:

$$\eta_r = \exp\left[\frac{2.5\phi}{1-\frac{\phi}{\phi_m}}\right] \tag{10.31}$$

$$\eta_r = \left(1-\frac{\phi}{\phi_m}\right)^{-2.5\phi_m} \tag{10.32}$$

where the relative viscosity (η_r) is defined as the ratio of suspension viscosity to continuous-phase viscosity. Equation 10.31 is the Mooney equation [30] and Equation 10.32 is the Krieger and Dougherty equation [31] for the relative viscosity of solids-in-liquid suspensions.

An important point to note is that the right-hand sides of the relative viscosity equations, Equations 10.31 and 10.32, are identical to the right-hand sides of the relative shear modulus equations, Equations 10.24 and 10.25. This implies that one can transform a suspension viscosity equation to a shear modulus equation for particulate composite by replacing η_r with $G_r\,(G_r - \lambda)^{-2.5}\,(1-\lambda)^{2.5}$, that is,

$$G_r\left[\frac{G_r-\lambda}{1-\lambda}\right]^{-2.5} = \eta_r \tag{10.33}$$

when comparison is made at the same ϕ and ϕ_m. On the basis of this analogy, Pal [32] proposed the following two-parameter equations for concentrated particulate composites:

$$G_r\left[\frac{G_r-\lambda}{1-\lambda}\right]^{-2.5} = \left[1+\frac{1.25\phi}{1-\frac{\phi}{\phi_m}}\right]^2 \tag{10.34}$$

$$G_r\left[\frac{G_r-\lambda}{1-\lambda}\right]^{-2.5} = \left[1-\frac{\phi}{\phi_m}\right]^{-a} \tag{10.35}$$

$$G_r\left[\frac{G_r-\lambda}{1-\lambda}\right]^{-2.5} = \frac{9}{8}\left[\frac{(\phi/\phi_m)^{1/3}}{1-(\phi/\phi_m)^{1/3}}\right] \tag{10.36}$$

$$G_r\left[\frac{G_r-\lambda}{1-\lambda}\right]^{-2.5} = \left[1+\frac{0.75(\phi/\phi_m)}{1-(\phi/\phi_m)}\right]^2 \tag{10.37}$$

$$G_r\left[\frac{G_r-\lambda}{1-\lambda}\right]^{-2.5} = 1+2.5\phi+\left[\frac{2.25}{\alpha\left(1+\frac{\alpha}{2}\right)(1+\alpha)^2}\right] \tag{10.38}$$

where α is given by

$$\alpha = 2\left[1-(\phi/\phi_m)^{1/3}\right]\Big/(\phi/\phi_m)^{1/3} \tag{10.39}$$

Equations 10.34 through 10.38 exhibit features similar to those of Equations 10.24 and 10.25. When the left-hand side term $G_r\,(G_r-\lambda)^{-2.5}\,(1-\lambda)^{2.5}$ is replaced by η_r in Equations 10.34 through 10.38, they reduce to the corresponding relative viscosity equations for solids-in-liquid suspensions. For example, Equation 10.34 reduces to the Eilers [33] equation, Equation 10.35 reduces to the Roscoe [34] equation if a = 2.5, Equation 10.35 reduces to the Maron and Pierce [35] equation if a = 2, Equation 10.36 reduces to the Frankel and Acrivos [36] equation, Equation 10.37 reduces to the Chong et al. [37] equation, and Equation 10.38 reduces to the Graham [38] equation.

10.5 COMPARISON OF EXPERIMENTAL DATA WITH PREDICTIONS OF SHEAR MODULUS EQUATIONS

Fifteen sets of experimental data [39–46] are considered to evaluate the shear modulus equations. Table 10.1 gives a summary of the various composite systems considered in evaluating the equations.

Figures 10.6 through 10.9 show comparisons between the experimental data and predictions of various two-parameter shear modulus–concentration equations. The experimental data are plotted as $G_r(G_r-\lambda)^{-2.5}\,(1-\lambda)^{2.5}$ versus volume fraction ϕ. The value of the maximum packing volume fraction (ϕ_m) of inclusions (particles or

TABLE 10.1
Summary of Various Composite Systems Considered to Evaluate Models

Set No.	Range of ϕ	Ref. No.	Comments
1	0–0.36	[39]	Pore-solid composites (porous polycrystalline monoclinic gadolinium oxide), $\lambda \to 0$
2	0–0.40	[40]	Pore-solid composites (porous polycrystalline monoclinic samarium oxide), $\lambda \to 0$
3	0–0.32	[41]	Pore-solid composites (porous polycrystalline cubic lutetium oxide), $\lambda \to 0$
4	0–0.28	[42]	Pore-solid composites (porous polycrystalline monoclinic hafnium oxide), $\lambda \to 0$
5A–5G	0–0.40	[43]	Pore-solid composites (porous refractory spinels, seven sets of data), $\lambda \to 0$
6	0–0.36	[44]	Pore-solid composites (porous stabilized hafnium oxide), $\lambda \to 0$
7A–7B	0–0.18	[45]	Pore-solid composites (porous hafnium and zirconium oxides stabilized with praseo-dymium or terbium oxide, two sets of data), $\lambda \to 0$
8	0–0.449	[46]	Suspensions of rigid particles in polymeric matrix, $\lambda \to \infty$

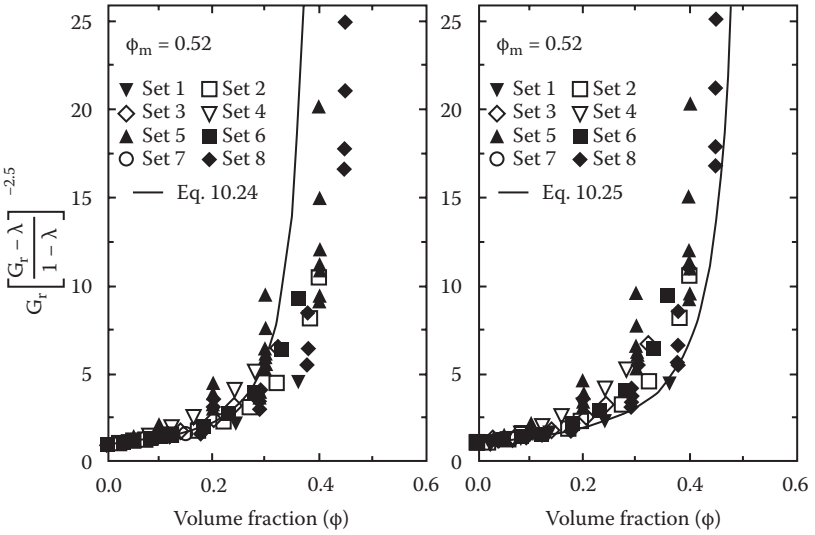

FIGURE 10.6 Comparison between the experimental data and the predictions of Equations 10.24 and 10.25.

voids) in the equations is taken as 0.52, corresponding to simple cubic packing of spherical inclusions.

Equation 10.24 gives good prediction of the relative shear modulus only when $\phi \leq 0.30$. At higher values of ϕ, Equation 10.24 overpredicts the $G_r(G_r - \lambda)^{-2.5}(1 - \lambda)^{2.5}$ values. Equation 10.25 generally underpredicts the $G_r(G_r - \lambda)^{-2.5}(1 - \lambda)^{2.5}$ values

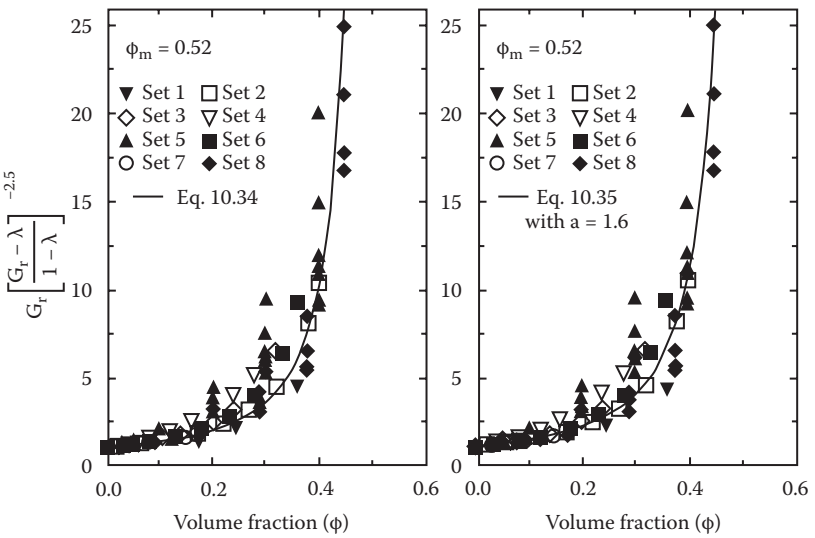

FIGURE 10.7 Comparison between the experimental data and predictions of Equations 10.34 and 10.35.

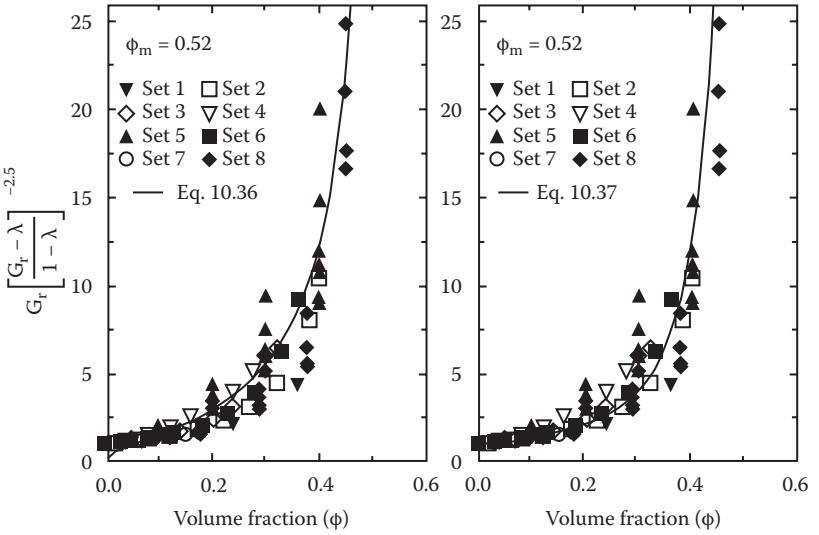

FIGURE 10.8 Comparison between the experimental data and predictions of Equations 10.36 and 10.37.

although the deviation between the experimental and predicted values is not large. Equations 10.34 and 10.36 give good predictions of data over the full range of ϕ covered (in Equation 10.36, "a" is taken to be 1.6). Equations 10.37 and 10.38 give good predictions of data over the full range of ϕ covered. It should be noted that some scatter of experimental data is expected as the systems are not mono disperse. Furthermore, the size distribution of inclusions is not the same for different sets.

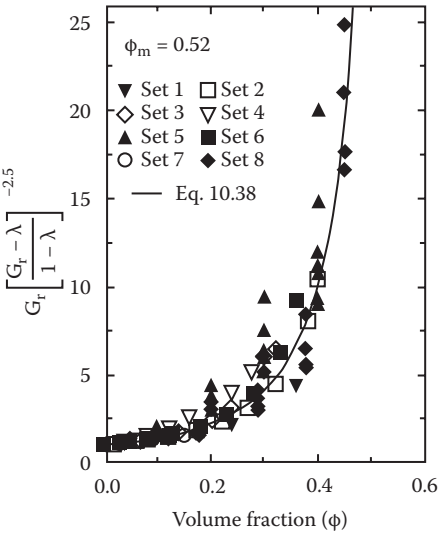

FIGURE 10.9 Comparison between the experimental data and predictions of Equation 10.38.

10.6 CONCLUDING REMARKS

The relative shear modulus G_r versus volume fraction ϕ equations for particulate composites of spherical particles and incompressible matrix are reviewed. Some of the available G_r versus ϕ equations are single-parameter equations with modulus ratio λ as the only parameter. One serious limitation of the single-parameter G_r versus ϕ equations is that they predict G_r to be independent of the particle size distribution. Furthermore, these equations fail to predict divergence in G_r at $\phi = \phi_m$ (maximum packing volume fraction of particles) for particulate composites of rigid ($\lambda \to \infty$) particles. To account for the effects of particle size distribution and divergence of shear modulus, the correct form of the shear modulus versus particle concentration equation for particulate composites (incompressible matrix) is a two-parameter equation with modulus ratio λ and ϕ_m as the parameters. A number of such two-parameter equations are presented.

REFERENCES

1. Hashin, Z. 1970. In: *Mechanics of Composite Materials*, eds., F.W. Wendt, H. Liebowitz, and N. Perrone, pp. 201–242, Oxford: Pergamon Press.
2. Christensen, R.M. 1979. *Mechanics of Composite Materials*, New York: John Wiley & Sons.
3. Christensen, R.M. 1982. In: *Mechanics of Composite Materials—Recent Advances*, eds., Z. Hashin and C.T. Herakovich, pp. 1–16, New York: Pergamon Press.
4. Hashin, Z. 1962. The elastic moduli of heterogeneous materials. *J. Appl. Mech*. 29: 143–150.
5. Hashin, Z. and S. Shtrikman. 1963. A variational approach to the theory of the behavior of multiphase materials. *J. Mech. Phys. Solids* 11: 127–140.
6. Hill, R. 1963. Elastic properties of reinforced solids: some theoretical principles. *J. Mech. Phys. Solids* 11: 357–372.
7. Hashin, Z. 1964. Theory of mechanical behaviour of heterogeneous media. *Appl. Mech. Rev.* 17: 1–9.
8. Walpole, L.J. 1966. On the bounds for the overall elastic moduli of inhomogeneous systems. *J. Mech. Phys. Solids* 14: 151–162, 289–301.
9. Roscoe, R. 1973. Isotropic composites with elastic or viscoelastic phases: General bounds for the moduli and solutions for special geometries. *Rheol. Acta* 12: 404–411.
10. Chen, H.S. and A. Acrivos. 1978. The effective elastic moduli of composite materials containing spherical inclusions at non-dilute concentrations. *Int. J. Solids Struct.* 14: 349–364.
11. Milton, C.W. and N. Phan-Thien. 1982. New bounds on effective elastic moduli of two-component materials. *Proc. R. Soc. Lond. A* 380: 305–331.
12. Chinh, P.D. 1998. Bounds on the effective properties of some multiphase matrix mixtures of coated-sphere geometry. *Mech. Mater*. 27: 249–260.
13. Gibiansky, L.V. and O. Sigmund. 2000. Multiphase composites with extremal bulk modulus. *J. Mech. Phys. Solids* 48: 461–498.
14. Voigt, W. 1928. *Lehrbuch der Kristallphysik*, Leipzig: Teubner-Verlag.
15. Reuss, A. 1929. Berechnung der Fliessgrenze von Mischkristallen auf Grund der Plastizitätsbedingung für Einkristalle. *Z. Angew. Math. Mech.* 9: 49–58.
16. Walpole, L.J. 1972. The elastic behavior of a suspension of spherical particles. *Quart. J. Mech. Appl. Math.* 25: 153–160.
17. Christensen, R.M. 1990. A critical evaluation for a class of micromechanics models. *J. Mech. Phys. Solids* 38: 379–404.

18. Kerner, E.H. 1956. The elastic and thermoelastic properties of composite media. *Proc. Phys. Soc. Lond. B*. 69: 808–813.
19. Hill, R. 1965. A self consistent mechanics of composite materials. *J. Mech. Phys. Solids* 13: 213–222.
20. Budiansky, B. 1965. On the elastic moduli of some heterogeneous materials. *J. Mech. Phys. Solids* 13: 223–227.
21. Smith, J.C. 1975. Simplification of van der Poel's formula for the shear modulus of a particulate composite. *J. Res. Nat. Burr. Stand. (U.S.)* 79A: 419–423.
22. Halpin, J.C. and J.L. Kardos. 1976. The Halpin–Tsai equations: A review. *Poly. Eng. Sci.* 16: 344–352.
23. Barnes, H.A., J.F. Hutton, and K. Walters. 1989. *An Introduction to Rheology,* Amsterdam: Elsevier.
24. Pal, R. 2002. Novel shear modulus equation for concentrated emulsions of two immiscible elastic liquids with interfacial tension. *J. Non-Newtonian Fluid Mech.* 105: 21–33.
25. Ouchiyama, N. and T. Tanaka. 1980. Estimation of the average number of contacts between randomly mixed solid particles. *Ind. Eng. Chem. Fundam*. 19: 338–340.
26. Ouchiyama, N. and T. Tanaka. 1981. Porosity of a mass of solid particles having a range of sizes. *Ind. Eng. Chem. Fundam* 20: 66–71.
27. Ouchiyama, N. and T. Tanaka. 1984. Porosity estimation for random packings of spherical particles. *Ind. Eng. Chem. Fundam*. 23: 490–493.
28. Gupta, R.K. and S.G. Seshadri. 1986. Maximum loading levels in filled liquid systems *J. Rheol*. 30: 503–508.
29. Poslinski, A.J., M.E. Ryan, R.K. Gupta, S.G. Seshadri, and F.J. Frechette. 1988. Rheological behavior of filled polymeric systems. II. The effect of a bimodal size distribution of particulates. *J. Rheol.* 32: 751–771.
30. Mooney, M. 1951. The viscosity of a concentrated suspension of spherical particles. *J. Colloid Sci.* 6: 162–170.
31. Krieger, I.M. and T.J. Dougherty. 1959. A mechanism for non-Newtonian flow in suspensions of rigid particles. *Trans. Soc. Rheol*. 3: 137–152.
32. Pal, R. 2004. Single-parameter and two-parameter equations for the effective shear-modulus of particulate composites. In: *Recent Advances in Composite Materials,* eds., V.K. Srivastava and M. Singh, New Delhi: Allied Publishers.
33. Eilers, V.H. 1943. Die Viskosität-Konzentrationsabhängigkeit kolloider Systeme in organischen Lösungsmitteln. *Kolloid Z.* 102: 154–169.
34. Roscoe, R. 1952. The viscosity of suspensions of rigid spheres. *Br. J. Appl. Phys*. 3: 267–269.
35. Maron, S.H. and P.E. Pierce. 1956. Application of Ree–Eyring generalized flow theory to suspensions of spherical particles. *J. Colloid Sci.* 11: 80–95.
36. Frankel, N.A. and A. Acrivos. 1967. On the viscosity of a concentrated suspension of solid particles. *Chem. Eng. Sci.* 22: 847–853.
37. Chong, J.S., E.B. Christianen, and A.D. Baer. 1971. Rheology of concentrated suspensions. *J. Appl. Polym. Sci.* 15: 2007–2021.
38. Graham, A.L. 1981. On the viscosity of a suspension of solid particles. *Appl. Sci. Res.* 37: 275–286.
39. Haglund, J.A. and O. Hunter. 1973. Elastic properties of polycrystalline monoclinic Gd_2O_3. *J. Am. Ceram. Soc.* 56: 327–330.
40. Hunter, O., H.J. Korklam, and R.R. Suchomel. 1974. Elastic properties of polycrystalline monoclinic Sm_2O_3. *J. Am. Ceram. Soc.* 57: 267–268.
41. Hunter, O. and G.E. Graddy. 1976. Porosity dependence of elastic properties of polycrystalline cubic Lu_2O_3. *J. Am. Ceram. Soc.* 59: 82.
42. Dole, S.L., O. Hunter, and C.J. Wooge. 1977. Elastic properties of monoclinic hafnium oxide at room temperature. *J. Am. Ceram. Soc.* 60: 488–490.

43. Porter, D.F., J.S. Reed, and D. Lewis. 1977. Elastic moduli of refractory spinels. *J. Am. Ceram. Soc.* 60: 345–349.
44. Dole, S.L., O. Hunter, and F.W. Calderwood. 1980. Elastic properties of stabilized HfO_2 compositions. *J. Am. Ceram. Soc.* 63: 136–139.
45. Dole, S.L. and O. Hunter. 1983. Elastic properties of hafnium and zirconium oxides stabilized with praseodymium or terbium oxide. *Commun. Am. Ceram. Soc.* March: C-47–C-49.
46. Pal, R. 2002. Complex shear modulus of concentrated suspensions of solid spherical particles. *J. Colloid Inter. Sci.* 245: 171–177.

11 Mechanical Properties of Concentrated Composites of Randomly Oriented Platelets

11.1 INTRODUCTION

Nanocomposites of polymer and clay are a rapidly growing class of nano-engineered materials [1–11]. They consist of clay platelets (single clay layers) dispersed in a continuum of polymeric matrix. The thickness of the platelet or disk-shaped clay nanofillers is approximately 1 nm, and their aspect ratio (ratio of diameter to thickness) ranges from 10 to 1000. In their natural form, clays consist of aggregates (stacks) of primary platelike particles. These stacks are exfoliated and the individual primary platelets are dispersed uniformly in the polymer matrix to produce polymer–clay nanocomposites. The dispersion of single clay layers in a polymeric matrix is known to dramatically enhance the mechanical and other physical properties. Although significant advances have been made in the development of polymer–clay nanocomposites in the recent past, the understanding of the relationship between the macroscopic mechanical behavior and the microstructural properties (such as volume fraction of clay) is far from satisfactory.

The exact micromechanical models for the effective elastic properties of composites are available only for the *infinitely dilute* systems, where the volume fraction of the dispersed phase is very small. For infinitely dilute isotropic composite of randomly oriented platelets, the exact expressions for the bulk modulus (K) and shear modulus (G) are given as follows [12,13]:

$$\frac{K}{K_m} = 1 + \phi\left[\frac{(K_d - K_m)(3K_m + 4G_d)}{K_m(3K_d + 4G_d)}\right] \tag{11.1}$$

$$\frac{G}{G_m} = 1 + \phi\left[\frac{(G_d - G_m)(G_m + G_g)}{G_m(G_g + G_d)}\right] \tag{11.2}$$

where

$$G_g = \left[\frac{G_d(9K_d + 8G_d)}{6(K_d + 2G_d)}\right] \tag{11.3}$$

Here K_m and K_d are bulk moduli of matrix and dispersed phase (filler), G_m and G_d are shear moduli of the matrix and the dispersed phase, and ϕ is the volume fraction of the dispersed phase (disk shaped particles).

As noted in Chapter 7, the isotropic materials are fully characterized by two independent elastic constants [13], such as bulk modulus (K) and shear modulus (G). Once the bulk modulus (K) and shear modulus (G) of a composite are known, the Young's modulus (E) and Poisson's ratio (ν) can be determined from the following standard relations for isotropic materials:

$$E = \left(\frac{9KG}{3K + G} \right) \tag{11.4}$$

$$\nu = \left(\frac{3K - 2G}{6K + 2G} \right) \tag{11.5}$$

Equations 11.1 and 11.2 are restricted to *infinitely dilute* dispersions of thin platelets having random orientation in a continuous matrix phase. They cannot be applied at finite concentrations of dispersed phase (platelets), as the interaction between the particles is ignored in their derivation. Pal [14] has recently developed models for the moduli of *concentrated* composite solids of thin platelets having random orientation in a continuous matrix phase. The models are derived using a differential scheme along with the exact solution of an infinitely dilute composite. The models are closed-form expressions valid over the full range of the filler concentration.

11.2 PAL MODELS FOR CONCENTRATED COMPOSITES OF RANDOMLY ORIENTED PLATELETS

Equations for the moduli (bulk and shear) of concentrated composite solids of thin platelets (having random orientation in a matrix) can be derived using the differential effective medium approach [14]. A concentrated composite is considered to be obtained from an initial matrix phase by successively adding differential (infinitesimally small) quantities of disk-shaped filler particles to the system until the final volume fraction of the filler is reached. The increment change in moduli, resulting from the addition of a differential amount of filler particles to a composite with volume fraction of particles ϕ, is calculated from the dilute-system equations (Equations 11.1 and 11.2) by treating the existing composite as an effective medium with respect to the added particles. Thus,

$$dK = \left[\frac{(K_d - K)(3K + 4G_d)}{(3K_d + 4G_d)} \right] d\phi \tag{11.6}$$

$$dG = \left[\frac{(G_d - G)(G + G_g)}{(G_g + G_d)} \right] d\phi \tag{11.7}$$

These equations can be rewritten as

$$\frac{dK}{(K_d - K)} + \frac{3dK}{(3K + 4G_d)} = d\phi \tag{11.8}$$

$$\frac{dG}{(G_d - G)} + \frac{dG}{(G + G_g)} = d\phi \tag{11.9}$$

Upon integration with the limits $K \to K_m$ and $G \to G_m$ as $\phi \to 0$, Equations 11.8 and 11.9 yield

$$\left[\frac{3K + 4G_d}{3K_m + 4G_d}\right]\left[\frac{K_d - K_m}{K_d - K}\right] = \exp(\phi) \tag{11.10}$$

$$\left[\frac{G + G_g}{G_m + G_g}\right]\left[\frac{G_d - G_m}{G_d - G}\right] = \exp(\phi) \tag{11.11}$$

where G_g is defined in Equation 11.3. Equations 11.10 and 11.11, referred to as *model 1*, are expected to describe the mechanical properties composites at low to moderate values of ϕ. At high values of ϕ, model 1 is expected to deviate from the actual behavior. This is because in the development of the differential equations, Equations 11.8 and 11.9, leading to model 1 (Equations 11.10 and 11.11), it is assumed that all the volume of the composite, before a differential quantity of new particles is added, is available as free volume to the new particles. In reality, the free volume available to disperse the new particles is significantly less, due to the volume preempted by the particles already present. The increase in the actual volume fraction of the dispersed phase when new particles are added to the composite is $d\phi/(1 - \phi)$. Thus, Equations 11.8 and 11.9 become

$$\frac{dK}{(K_d - K)} + \frac{3dK}{(3K + 4G_d)} = \frac{d\phi}{1 - \phi} \tag{11.12}$$

$$\frac{dG}{(G_d - G)} + \frac{dG}{(G + G_g)} = \frac{d\phi}{1 - \phi} \tag{11.13}$$

Upon integration with the limits $K \to K_m$ and $G \to G_m$ as $\phi \to 0$, Equations 11.12 and 11.13 yield

$$\left[\frac{3K + 4G_d}{3K_m + 4G_d}\right]\left[\frac{K_d - K_m}{K_d - K}\right] = (1 - \phi)^{-1} \tag{11.14}$$

$$\left[\frac{G + G_g}{G_m + G_g}\right]\left[\frac{G_d - G_m}{G_d - G}\right] = (1 - \phi)^{-1} \tag{11.15}$$

Equations 11.14 and 11.15, referred to as *model 2,* fail to account for the "crowding effect" of particles at high values of ϕ. Due to immobilization of some of the matrix material in the interstitial region between the existing particles, the free volume of the matrix available to disperse the new particles is significantly less than $(1 - \phi)$. If the incremental increase in the volume fraction of the particles, when the differential amount of new particles are added to an existing composite of particle volume fraction ϕ, is taken to be $d[\phi/(1 - \phi/\phi_m)]$ rather than $d\phi/(1 - \phi)$ as used in the derivation of model 2, Equations 11.8 and 11.9 become [14]

$$\frac{dK}{(K_d - K)} + \frac{3dK}{(3K + 4G_d)} = d\left[\frac{\phi}{1 - \frac{\phi}{\phi_m}}\right] \tag{11.16}$$

$$\frac{dG}{(G_d - G)} + \frac{dG}{(G + G_g)} = d\left[\frac{\phi}{1 - \frac{\phi}{\phi_m}}\right] \tag{11.17}$$

where ϕ_m is the maximum packing volume fraction or percolation threshold of particles. Upon integration with the limits $K \to K_m$ and $G \to G_m$ as $\phi \to 0$, Equations 11.16 and 11.17 give

$$\left[\frac{3K + 4G_d}{3K_m + 4G_d}\right]\left[\frac{K_d - K_m}{K_d - K}\right] = \exp\left[\frac{\phi}{1 - \frac{\phi}{\phi_m}}\right] \tag{11.18}$$

$$\left[\frac{G + G_g}{G_m + G_g}\right]\left[\frac{G_d - G_m}{G_d - G}\right] = \exp\left[\frac{\phi}{1 - \frac{\phi}{\phi_m}}\right] \tag{11.19}$$

Equations 11.18 and 11.19 together are referred to as *model 3.*

Another way to account for the packing limit of particles is to take the incremental increase in the volume fraction of particles, when differential amount of new particles are added to an existing composite of particle volume fraction ϕ, as $d\phi/(1 - \phi/\phi_m)$ rather than $d[\phi/(1 - \phi/\phi_m)]$ as used in the derivation of model 3 [14]. Thus, Equations 11.8 and 11.9 become

$$\frac{dK}{(K_d - K)} + \frac{3dK}{(3K + 4G_d)} = \frac{d\phi}{\left(1 - \frac{\phi}{\phi_m}\right)} \tag{11.20}$$

$$\frac{dG}{(G_d - G)} + \frac{dG}{(G + G_g)} = \frac{d\phi}{\left(1 - \frac{\phi}{\phi_m}\right)} \tag{11.21}$$

Upon integration with the limits $K \to K_m$ and $G \to G_m$ as $\phi \to 0$, Equations 11.20 and 11.21 yield

$$\left[\frac{3K + 4G_d}{3K_m + 4G_d}\right]\left[\frac{K_d - K_m}{K_d - K}\right] = \left(1 - \frac{\phi}{\phi_m}\right)^{-\phi_m} \tag{11.22}$$

$$\left[\frac{G + G_g}{G_m + G_g}\right]\left[\frac{G_d - G_m}{G_d - G}\right] = \left(1 - \frac{\phi}{\phi_m}\right)^{-\phi_m} \tag{11.23}$$

Equations 11.22 and 11.23 together are referred to as *model 4*.

Note that models 1 to 4 could be recast as

$$K = \left[\frac{4G_d(K_m - K_d) + fK_d(3K_m + 4G_d)}{3(K_d - K_m) + f(3K_m + 4G_d)}\right] \tag{11.24}$$

$$G = \left[\frac{G_g(G_m - G_d) + fG_d(G_m + G_g)}{(G_d - G_m) + f(G_m + G_g)}\right] \tag{11.25}$$

where f is given as

$$f = \exp(\phi) \quad \text{Model 1} \tag{11.26}$$

$$f = (1 - \phi)^{-1} \quad \text{Model 2} \tag{11.27}$$

$$f = \exp\left[\frac{\phi}{1 - \frac{\phi}{\phi_m}}\right] \quad \text{Model 3} \tag{11.28}$$

$$f = \left(1 - \frac{\phi}{\phi_m}\right)^{-\phi_m} \quad \text{Model 4} \tag{11.29}$$

11.2.1 Model Predictions

According to Equations 11.24 and 11.25, the relative moduli of particulate composites of thin randomly oriented platelets are functions of four variables:

$$K_r = \frac{K}{K_m} = F(\nu_d, \lambda_K, \phi, \phi_m) \tag{11.30}$$

$$G_r = \frac{G}{G_m} = F(\nu_d, \lambda_G, \phi, \phi_m) \tag{11.31}$$

where K_r is the relative bulk modulus, G_r is the relative shear modulus, λ_K is the bulk moduli ratio K_d/K_m, and λ_G is the shear moduli ratio G_d/G_m. Note that $G_d/K_d = [3(1 - 2\nu_d)]/[2(1 + \nu_d)]$.

Figure 11.1 shows the relative bulk modulus (K_r) plots for different values of particle Poisson's ratio (ν_d). The plots are generated from model 4 (Equations 11.24 and 11.29) under the following conditions: $\phi = 0.20$ and $\phi_m = 0.82$. Note that for thin inert disks, the random close packing volume fraction (ϕ_m) is approximately 0.82 [15]. At a given value of ν_d, the relative modulus K_r versus moduli ratio (K_d/K_m) plot exhibits three distinct regions: at low values of K_d/K_m, K_r increases nearly linearly with moduli ratio K_d/K_m on a log–log scale; at intermediate values of moduli ratio (K_d/K_m around unity), the relative bulk modulus tends to level off; and at high values of K_d/K_m, K_r once again increases with the increase in K_d/K_m (almost linearly on a log–log scale). With the increase in the particle Poisson's ratio, the relative bulk modulus (K_r) decreases at a given value of moduli ratio K_d/K_m. The effect of ν_d on K_r is significantly larger when $K_d/K_m > 1.0$. Also note that at $K_d/K_m = 1.0$, the relative bulk modulus is unity regardless of the value of ν_d.

Figure 11.2 shows the relative shear modulus (G_r) as a function of shear moduli ratio (G_d/G_m) for two different values of particle Poisson's ratio (ν_d). The plots are generated

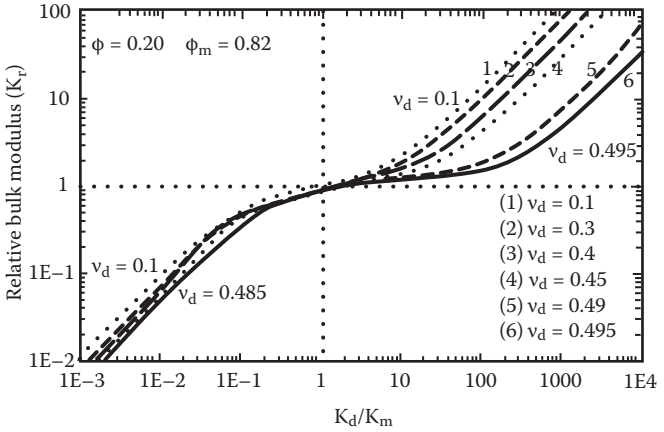

FIGURE 11.1 Relative bulk modulus (K_r) as a function of bulk moduli ratio (K_d/K_m) for different values of particle Poisson's ratio (ν_d). The plots are generated from model 4 under the conditions $\phi = 0.20$ and $\phi_m = 0.82$. (From Pal, R., *Composites A* 39: 1496–1502, 2008.)

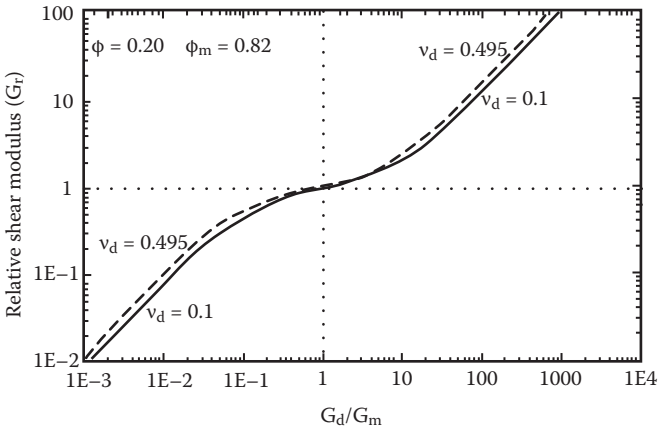

FIGURE 11.2 Relative shear modulus (G_r) as a function of shear moduli ratio (G_d/G_m) for two different values of particle Poisson's ratio (ν_d). The plots are generated from model 4 under the conditions $\phi = 0.20$ and $\phi_m = 0.82$. (From Pal, R., *Composites A* 39: 1496–1502, 2008.)

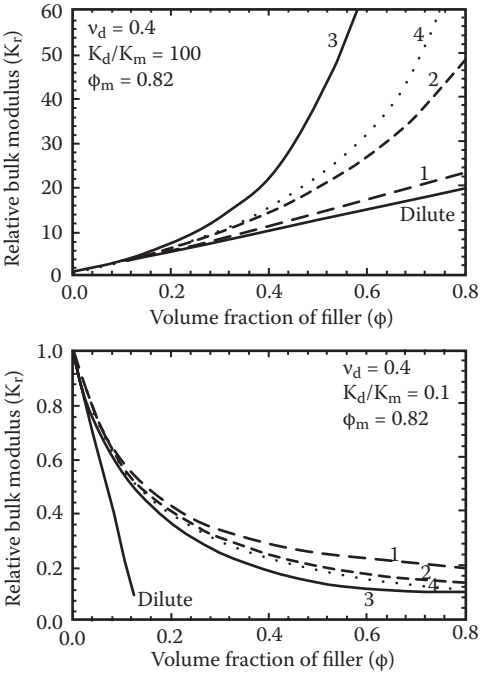

FIGURE 11.3 Comparison of relative bulk modulus (K_r) predicted by different models. The numbers shown on the plots refer to the model number. (From Pal, R., *Composites A* 39: 1496–1502, 2008.)

from model 4 (Equations 11.25 and 11.29) for $\phi = 0.20$ and $\phi_m = 0.82$. The G_r versus G_d/G_m plot at a given value of ν_d appears similar to the K_r versus K_d/K_m plot (see Figure 11.1). However, the effect of Poisson's ratio (ν_d) on G_r is negligibly small. Also note that the relative shear modulus increases (unlike K_r, which decreases) with the increase in ν_d.

Figure 11.3 compares the predictions of various models. The relative bulk modulus is plotted as a function of ϕ for two different values of K_d/K_m: $K_d/K_m = 100$ for the top figure and $K_d/K_m = 0.1$ for the bottom figure. The particle Poisson's ratio is taken to be 0.4 and ϕ_m is 0.82. When $K_d/K_m = 100$, the predicted relative modulus K_r is always greater than unity; at a given ϕ, the predictions of K_r from various models are in the following order: model 3 > model 4 > model 2 > model 1 > dilute-system model (Equation 11.1). Note that for low values of ϕ, all models give the same predictions. When $K_d/K_m = 0.1$, the predicted K_r values are always less than unity; at a given ϕ, the K_r predictions by various models are in the following order: model 1 > model 2 > model 4 > model 3 > dilute-system model.

The relative shear modulus (G_r) predicted by different models is shown in Figure 11.4 where G_r is plotted as a function of ϕ for two different values of moduli ratio G_d/G_m: $G_d/G_m = 100$ for the top figure and $G_d/G_m = 0.1$ for the bottom figure. The particle Poisson's ratio is 0.4 and ϕ_m is 0.82. When $G_d/G_m = 100$, G_r is always greater than unity; at a given ϕ, the G_r predictions by various models are in the following order: model 3 > model 4 > model 2 > dilute-system model (Equation 11.2) > model 1. For

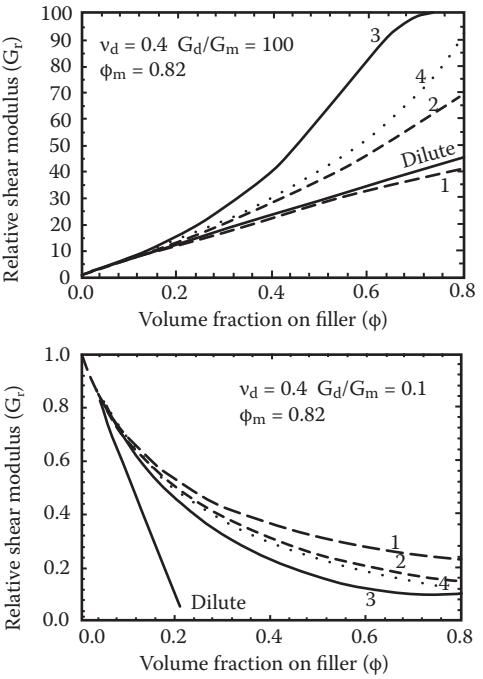

FIGURE 11.4 Comparison of relative shear modulus (G_r) predicted by different models. The numbers shown on the plots refer to the model number. (From Pal, R., *Composites A* 39: 1496–1502, 2008.)

low values of G_d/G_m ($G_d/G_m = 0.1$), the relative shear modulus is always less than unity and the order of predictions is as follows: model 1 > model 2 > model 4 > model 3 > dilute system model.

11.2.2 Comparison of Model Predictions with Experimental Data

Four sets of experimental data on the relative Young's modulus of polymer–clay nanocomposites are considered to evaluate the models. Table 11.1 gives a brief description of the experimental systems.

Figures 11.5 through 11.8 show comparisons between model predictions and experimental Young's modulus data of polymer–clay nanocomposites. The relative Young's modulus (E_r) is estimated from the bulk and shear moduli models using the following relationship:

$$E_r = \frac{E}{E_m} = \left[\frac{9G_rK_r}{6(1+\nu_m)K_r + 3(1-2\nu_m)G_r}\right] \tag{11.32}$$

where E is Young's modulus of composite, E_m is Young's modulus of the continuous phase (matrix) and ν_m is Poisson's ratio of the continuous phase. Equation 11.32 follows from Equation 11.4, the standard relation for isotropic materials. The predictions of the following well-known rules of mixtures (ROM) are also shown:

$$E = \phi E_d + 1(1 - \phi)E_m \tag{11.33a}$$

TABLE 11.1
Brief Description of Polymer–Clay Nanocomposites Considered in Evaluating Models

Set No.	Clay Type	Polymer Type	Wt% Clay	Vol% Clay	Reference No.
1	Organoclay (bis (hydroxy ethyl)-(methyl)-rapeseed quaternary ammonium organoclay)	High molecular weight nylon 6	0–7.2	0–3.03	[2]
2	Na-montmorillonite	SBR (styrene butadiene rubber)	0–25	0–8.45	[3]
3	Na-montmorillonite	NBR (nitrile rubber)	0–30	0–10.05	[3]
4	Na-montmorillonite	CNBR (carboxylated acrylonitrile butadiene rubber)	0–30	0–10.34	[3]

Source: Pal, R., *Composites A* 39: 1469–1502, 2008.

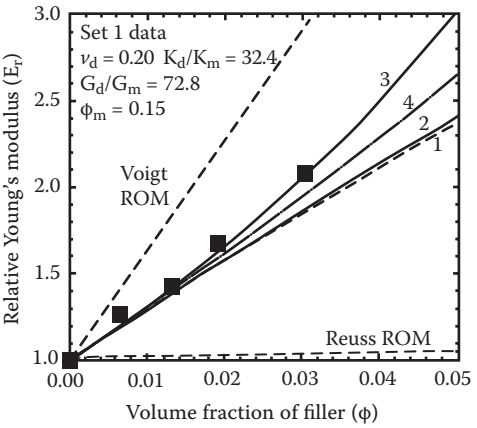

FIGURE 11.5 Comparison of model predictions and experimental data (set 1) for relative Young's modulus of organoclay–nylon 6 nanocomposites. The numbers shown on the plots refer to the model number. (From Pal, R., *Composites A* 39: 1496–1502, 2008.)

$$\frac{1}{E} = \frac{\phi}{E_d} + \frac{(1-\phi)}{E_m} \tag{11.33b}$$

where E_d is Young's modulus of the dispersed phase (filler). Equation 11.33a is the Voigt ROM and Equation 11.33b is the Reuss ROM.

According to Figures 11.5 through 11.8, the experimental data can be described reasonably well with model 3 (Equations 11.24 and 11.25 with f given by Equation

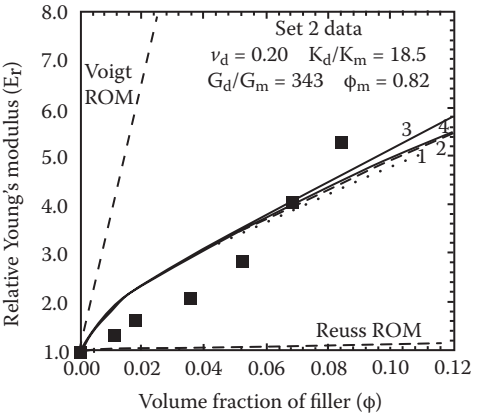

FIGURE 11.6 Comparison of model predictions and experimental data (set 2) for relative Young's modulus of clay–SBR nanocomposites. The numbers shown on the plots refer to the model number. (From Pal, R., *Composites A* 39: 1496–1502, 2008.)

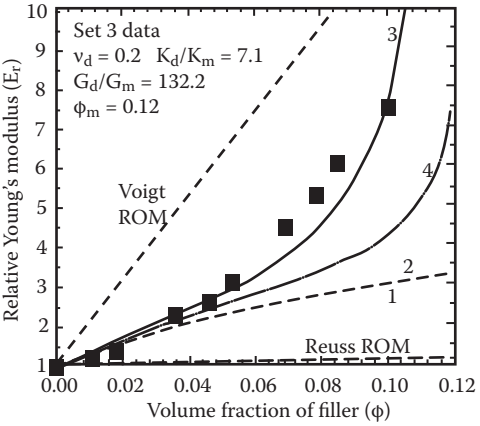

FIGURE 11.7 Comparison of model predictions and experimental data (set 3) for relative Young's modulus of clay–NBR nanocomposites. The numbers shown on the plots refer to the model number. (From Pal, R., *Composites A* 39: 1496–1502, 2008.)

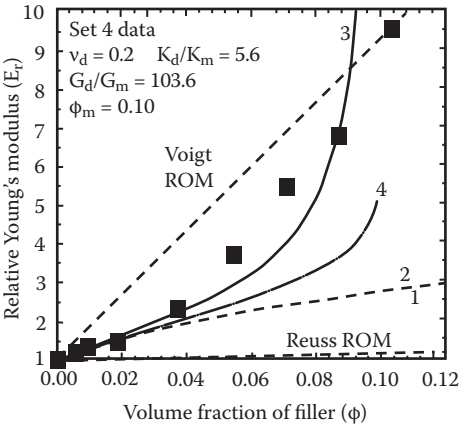

FIGURE 11.8 Comparison of model predictions and experimental data (set 4) for relative Young's modulus of clay–CNBR nanocomposites. The numbers shown on the plots refer to the model number. (From Pal, R., *Composites A* 39: 1496–1502, 2008.)

11.28). Models 1, 2, and 4 generally underpredict the relative Young's modulus of polymer–clay nanocomposites, especially for large ϕ. Also note that the value of ϕ_m is generally much smaller than the random close-packing concentration of inert disks ($\phi_m \approx 0.82$) as clay platelets are not inert particles. Composites of clay platelets are expected to have a low percolation-threshold concentration due to interactions between the platelets. The Voigt ROM, Equation 11.33a, overpredicts and the Reuss ROM, Equation 11.33b, underpredicts the relative Young's modulus of polymer–clay nancomposites.

11.3 COMPOSITES OF THREE-PHASE CORE-SHELL-TYPE PLATELETS

Due to the interaction of the polymer molecules with the surface of the clay platelets, the properties of the matrix material in the interphase region surrounding the clay platelets are expected to be different from the bulk polymer matrix. According to some studies the interphase-to-matrix moduli ratio could be 2 or more [10], indicating that the polymer molecules in direct contact with the filler surface become somewhat rigidified in comparison to the bulk polymer molecules. In such situations, the platelets should be treated as three-phase core-shell-type particles (the three phases being bulk matrix, interfacial layer, and clay platelets).

The mechanical properties of three-phase polymer–clay nanocomposites consisting of core-shell platelets can be modeled using a two-step approach. In the first step, the model equations developed in the preceding section (Equations 11.24 and 11.25) are applied to determine the mechanical properties of a single core-shell particle consisting of clay platelet as core and interfacial layer as shell. The interfacial layer is treated as matrix with respect to the clay platelet. In the second step, the core-shell composite particles are treated as "homogeneous" particles (disk-shaped) of mechanical properties obtained from the first step. The model equations (Equations 11.24 and 11.25) are applied once again to determine the mechanical properties of three-phase polymer–clay nanocomposites. Thus,

$$K_p = \left[\frac{4G_3(K_2 - K_3) + f_p K_3(3K_2 + 4G_3)}{3(K_3 - K_2) + f_p(3K_2 + 4G_3)} \right] \tag{11.34a}$$

where K_p is the bulk modulus of a single core-shell particle (disk-shaped), subscripts "2" and "3" refer to interphase (shell) and core of a core-shell particle, respectively, f_p is a function of the volume fraction of core (ϕ_c) in the combined volume of core and interfacial shell. Equation 11.34a follows from Equation 11.24. Using model 3 (see Equation 11.28), f_p can be expressed as

$$f_p = \exp\left[\frac{\phi_c}{1 - \phi_c} \right] \tag{11.34b}$$

As the volume fraction of core in the combined volume of core and shell can vary from 0 to 1 ($0 \le \phi_c \le 1$), ϕ_m in model 3 is taken to be unity. Using the two-step approach, the effective bulk modulus (K) of a composite consisting of disk-shaped core-shell particles is given as follows:

$$K = \left[\frac{4G_p(K_1 - K_p) + fK_p(3K_1 + 4G_p)}{3(K_p - K_1) + f(3K_1 + 4G_p)} \right] \tag{11.35}$$

where subscript "1" refers to external phase (matrix), f is a function of the volume fraction of core-shell particles (ϕ) given by Equation 11.28, and G_p is the shear modulus of a single core-shell particle, given by Equation 11.38 described below.

Following the two-step approach, the effective shear modulus (G) of a composite consisting of disk-shaped core-shell particles can be expressed as

$$G = \left[\frac{G_{g1}(G_1 - G_p) + fG_p(G_1 + G_{g1})}{(G_p - G_1) + f(G_1 + G_{g1})} \right] \tag{11.36}$$

where

$$G_{g1} = \left[\frac{G_p(9K_p + 8G_p)}{6(K_p + 2G_p)} \right] \tag{11.37}$$

and G_p, the shear modulus of a single core-shell particle, is

$$G_p = \left[\frac{G_{g2}(G_2 - G_3) + f_p G_3(G_2 + G_{g2})}{(G_3 - G_2) + f_p(G_2 + G_{g2})} \right] \tag{11.38}$$

where

$$G_{g2} = \left[\frac{G_3(9K_3 + 8G_3)}{6(K_3 + 2G_3)} \right] \tag{11.39}$$

where f_p is given by Equation 11.34b and f is given by Equation 11.28 with ϕ as a volume fraction of core-shell particles. Note that the subscripts "1," "2," and "3" refer to matrix, interphase, and core, respectively.

According to the model (Equations 11.34 through 11.39) for the mechanical properties of composites of three-phase core-shell-type platelets, the relative moduli can be expressed as

$$K_r = \frac{K}{K_1} = F(\nu_2, \nu_3, K_3/K_2, K_2/K_1, G_3/G_2, \phi_c, \phi) \tag{11.40}$$

$$G_r = \frac{G}{G_1} = F(\nu_2, \nu_3, G_3/G_2, G_2/G_1, K_3/K_2, \phi_c, \phi) \tag{11.41}$$

Figure 11.9 shows the relative bulk and shear moduli predicted from the model, as a function of ϕ (volume fraction of core-shell particles). The plots are generated from Equations 11.34 through 11.39 with f given by Equation 11.28. At a fixed value of ϕ, the relative moduli (K_r and G_r) decrease with the decrease in ϕ_c (volume fraction of core in a single core-shell particle). A decrease in ϕ_c at fixed ϕ implies an increase

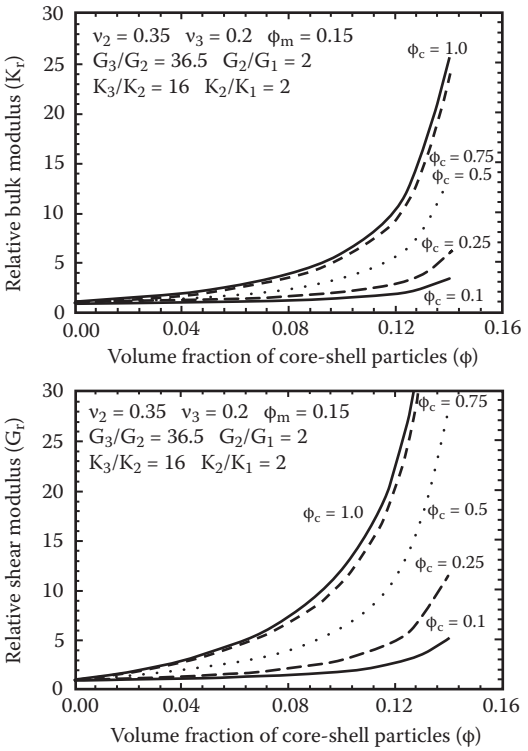

FIGURE 11.9 Relative bulk and shear moduli predicted from the model, as functions of ϕ (volume fraction of core-shell particles), for different values of ϕ_c (volume fraction of core in a single core-shell particle). (From Pal, R., *Composites A* 39: 1496–1502, 2008.)

in the thickness of the shell of the core-shell particles. An increase in the interphase thickness results in a decrease in moduli as stiffer core material (clay platelet) is being replaced by softer interphase. However, an opposite behavior is observed (see Figure 11.10) when relative moduli are plotted as function of volume fraction of core particles in the composite; note that the volume fraction of core particles in a composite is given as the product of ϕ_c and ϕ. At a fixed volume fraction of core particles in a composite, the relative moduli increase with the decrease in ϕ_c because the softer matrix material is being replaced by stiffer interphase.

In summary, the relative modulus (bulk or shear) of concentrated composites of platelets (randomly oriented in the matrix) is a function of four variables: particle Poisson's ratio, particle-to-matrix moduli ratio, volume fraction of particles, and maximum packing volume fraction of particles. Model 3 (Equations 11.24, 11.25, and 11.28) appears to be somewhat superior to other models (models 1, 2, and 4) when comparisons are made with experimental Young's modulus data of polymer–clay nanocomposites. The mechanical properties of composites are significantly affected by the presence of an interfacial layer (with properties different from that

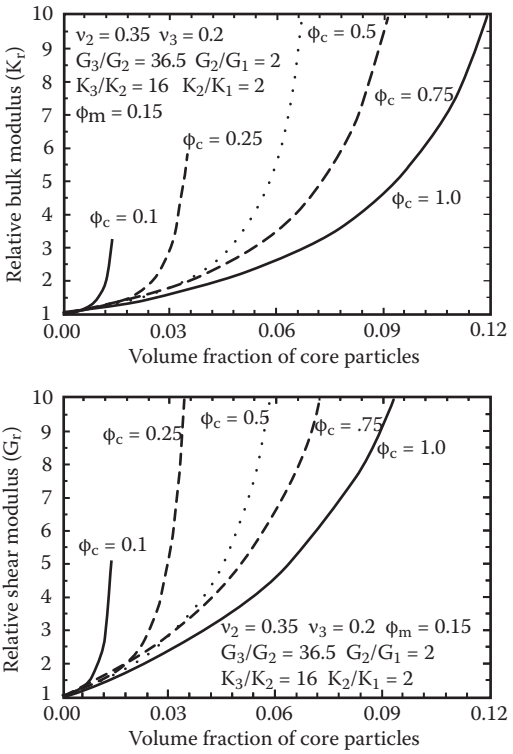

FIGURE 11.10 Relative bulk and shear moduli predicted from the model, as functions of the volume fraction of core particles, for different values of ϕ_c (volume fraction of core in a single core-shell particle). (From Pal, R., *Composites A* 39: 1496–1502, 2008.)

of the bulk matrix) around the particles. The two-phase models can be extended to three-phase composites of platelets, interphase, and matrix.

REFERENCES

1. Yung, K.C., J. Wang, and T.M. Yue. 2006. Modeling Young's modulus of polymer-layered silicate nanocomposites using a modified Halpin–Tsai micromechanical model. *J. Reinf. Plast. Composites* 25: 847–861.
2. Fornes, T.D. and D.R. Paul. 2003. Modeling properties of nylon 6/clay nanocomposites using composite theories. *Polymer* 44: 4993–5013.
3. Wu, Y.P., Q.X. Jia, D.S. Yu, and L.Q. Zhang. 2004. Modeling Young's modulus of rubber–clay nanocomposites using composite theories. *Polym. Test.* 23: 903–909.
4. Wu, Y.P., Q.X. Jia, D.S. Yu, and L.Q. Zhang. 2003. Structure and properties of nitrile rubber (NBR)–clay nanocomposites by coagulating NBR latex and clay aqueous suspension. *J. Appl. Poly. Sci*. 89: 3855–3858.
5. Brune, D.A. and J. Bicerano. 2002. Micromechanics of nanocomposites: Comparison of tensile and compressive elastic moduli, and prediction of effects of incomplete exfoliation and imperfect alignment on modulus. *Polymer* 43: 369–387.

6. Lee, K.Y. and L.A. Goettler. 2004. Structure–property relationships in polymer blend nanocomposites. *Poly. Eng. Sci.* 44: 1103–1111.
7. Chen, L., S.C. Wong, and S. Pisharath. 2003. Fracture properties of nanoclay-filled polypropylene. *J. Appl. Poly. Sci*. 88: 3298–3305.
8. Yoon, P.J., D.L. Hunter, and D.R. Paul. 2003. Polycarbonate nanocomposites. Part 1. Effect of organoclay structure on morphology and properties. *Polymer* 44: 5323–5339.
9. Xu, Y., W.J. Brittain, R.A. Vaia, and G. Price. 2006. Improving the physical properties of PEA/PMMA blends by the uniform dispersion of clay platelets. *Polymer* 47: 4564–4570.
10. Fertig, R.S. and M.R. Garrnich. 2004. Influence of constituent properties and microstructural parameters on the tensile modulus of a polymer/clay nanocomposite. *Composites Sci. Tech*. 64: 2577–2588.
11. Sheng, N., M.C. Boyce, D.M. Parks, G.C. Rutledge, J.I. Abes, and R.E. Cohen. 2004. Multiscale micromechanical modeling of polymer/clay nanocomposites and the effective clay particle. *Polymer* 45: 487–506.
12. Boucher, S. 1974. On the effective moduli of isotropic two-phase elastic composites. *J. Composite Mater.* 8: 82–89.
13. Pal R. 2007. *Rheology of Particulate Dispersions and Composites*, Boca Raton: CRC Press.
14. Pal, R. 2008. Mechanical properties of composites of randomly oriented platelets. *Composites A* 39: 1496–1502.
15. Berryman, J.G. 1983. Random close packing of hard spheres and disks. *Phys. Rev. A* 27: 1053–1061.

12 Interfacial and Interphase Effects on Mechanical Properties of Composites

12.1 BACKGROUND

Composite solids can be treated as isotropic materials so long as the filler particles are positioned randomly in the matrix. The isotropic materials are fully characterized by two independent elastic constants, namely, bulk modulus (K) and shear modulus (G). The Young's modulus (E) and Poisson's ratio (ν) are related to K and G as follows:

$$E = \frac{9GK}{3K + G} \tag{12.1}$$

$$\nu = \frac{3K - 2G}{6K + 2G} \tag{12.2}$$

For isotropic composites consisting of spherical fillers embedded in a matrix, the bulk and shear moduli at low filler concentration are given as [1]

$$\frac{K}{K_m} = 1 + \left[\left(\frac{3K_m + 4G_m}{3K_m} \right) \left(\frac{3K_d - 3K_m}{3K_d + 4G_m} \right) \right] \phi \tag{12.3}$$

$$\frac{G}{G_m} = 1 + \left[\frac{15(1 - \nu_m)(G_d - G_m)}{2G_d(4 - 5\nu_m) + G_m(7 - 5\nu_m)} \right] \phi \tag{12.4}$$

where K and G are bulk and shear moduli of the composite, K_m and G_m are bulk and shear moduli of matrix, K_d and G_d are bulk and shear moduli of the dispersed phase (filler particles), ν_m is the Poisson's ratio of the matrix, and ϕ is the volume fraction of the dispersed phase.

Equations 12.3 and 12.4 cannot be applied at high concentrations of filler particles, as the interaction between the particles is ignored in their derivation. Kerner [2] was probably the first to develop equations for nondilute composites using the generalized self-consistent scheme (GSCS). According to the GSCS, the composite is first treated as an equivalent "effective medium," which is homogeneous and has the same macroscopic mechanical properties as that of the composite. Then a small portion of the effective homogeneous medium is replaced by the actual components of the composite. The mechanical properties of the effective medium are then determined by insisting that if a small portion of the effective homogeneous medium is replaced by the actual components of the dispersion, no difference in mechanical properties could be detected by macroscopic observations.

The Kerner equations are described below in terms of relative bulk modulus (K_r) and relative shear modulus (G_r), where K_r is defined as the ratio of bulk modulus of composite (K) to the bulk modulus of matrix (K_m) and G_r is defined as the ratio of shear modulus of composite (G) to the shear modulus of matrix (G_m).

$$K_r = \frac{K}{K_m} = \left[\frac{1 + \left(\frac{4}{3} \frac{G_m}{K_m} \right) k\phi}{1 - k\phi} \right] \tag{12.5}$$

$$G_r = \frac{G}{G_m} = \left[\frac{1 + \left(\frac{7 - 5\nu_m}{8 - 10\nu_m} \right) h\phi}{1 - h\phi} \right] \tag{12.6}$$

In Equations 12.5 and 12.6, k and h are parameters defined as

$$k = \left[\frac{\frac{K_d}{K_m} - 1}{\frac{K_d}{K_m} + \frac{4}{3} \frac{G_m}{K_m}} \right] \tag{12.7}$$

$$h = \left[\frac{(8 - 10\nu_m)\left(\frac{G_d}{G_m} - 1 \right)}{(8 - 10\nu_m)\left(\frac{G_d}{G_m} \right) + (7 - 5\nu_m)} \right] \tag{12.8}$$

The parameters k and h describe the effect of differences in matrix and filler properties on the overall properties of composite. When there is no difference in matrix and filler properties ($K_d = K_m$ and $G_d = G_m$), the parameters k and h are both zero, and the composite and component properties are the same ($K = K_d = K_m$ and

$G = G_d = G_m$). When there exists a difference in matrix and filler properties, the parameters k and h deviate from zero. For example, k and h are both unity when $K_d/K_m \to \infty$ and $G_d/G_m \to \infty$. Also note that in the limit $\phi \to 0$, Equations 12.5 and 12.6 reduce to Equations 12.3 and 12.4, respectively.

The Kerner equations, Equations 12.5 and 12.6, describe the mechanical properties of particulate composites well when ϕ is less than about 0.2. At higher values of ϕ, significant deviations occur between the predictions of Kerner equations and actual values. In addition, the Kerner equations fail to predict the correct behavior at $\phi \to \phi_m$, where ϕ_m is the maximum packing volume fraction of filler particles. At $\phi \to \phi_m$, the relative moduli (K_r and G_r) are expected to diverge, especially for composites with $K_d/K_m \to \infty$ and $G_d/G_m \to \infty$. Furthermore, the Kerner equations do not account for the particle size distribution, particle shape, and aggregation of particles.

Lewis and Nielsen [3] modified the Kerner equation for shear modulus (Equation 12.6) as follows:

$$G_r = \frac{G}{G_m} = \left[\frac{1 + \left(\frac{7 - 5\nu_m}{8 - 10\nu_m} \right) h\phi}{1 - h\psi\phi} \right] \tag{12.9}$$

where the function ψ is given as

$$\psi = \left[1 - \exp\left\{ \frac{-\phi}{1 - (\phi/\phi_m)} \right\} \right] \Big/ \phi \tag{12.10}$$

The factor ψ takes into account the packing limit of particles (ϕ_m). Note that according to the Kerner equation for shear modulus (Equation 12.6), it is possible for the volume fraction of particles to reach a value of unity. However, this is physically unrealistic. Only in special cases may it be possible for the volume fraction of particles to reach a value close to unity. For example, when the particle size distribution is extremely wide or when the particles are highly deformable, the maximum packing volume fraction of particles may be close to unity. In general, however, the maximum packing volume fraction of particles (ϕ_m) is expected to be significantly less than unity. For random close packing of spherical particles, ϕ_m is about 0.64. Thus, $\psi\phi$ in Equation 12.9 can be considered as an effective concentration of particles that approaches a value of unity at $\phi = \phi_m$, rather than at $\phi = 1.0$. The other boundary conditions imposed upon $\psi\phi$ are as follows: $\psi\phi = 0$ at $\phi = 0$ and $d(\psi\phi)/d\phi = 1$ at $\phi = 0$.

The Lewis–Nielsen equation (Equation 12.9) is certainly an improvement over the unmodified Kerner equation (Equation 12.6). However, the analysis of a large amount of experimental data carried out by Pal [4] indicated that the shear modulus,

as well as the bulk modulus, of particulate composites can be described better by the following equations:

$$K_r = \frac{K}{K_m} = \left[\frac{1+\left(\frac{4}{3}\frac{G_m}{K_m}\right)k\psi\phi}{1-k\psi\phi}\right] \tag{12.11}$$

$$G_r = \frac{G}{G_m} = \left[\frac{1+\left(\frac{7-5\nu_m}{8-10\nu_m}\right)h\psi\phi}{1-h\psi\phi}\right] \tag{12.12}$$

where ψ is given by Equation 12.10. Note that Lewis and Nielsen modified the Kerner equation by incorporating the function ψ in the denominator term only whereas the equations proposed by Pal (Equations 12.11 and 12.12) include ψ in both the numerator and denominator terms. It is not unreasonable to replace ϕ by effective volume fraction of particles $\psi\phi$ in both numerator and denominator terms.

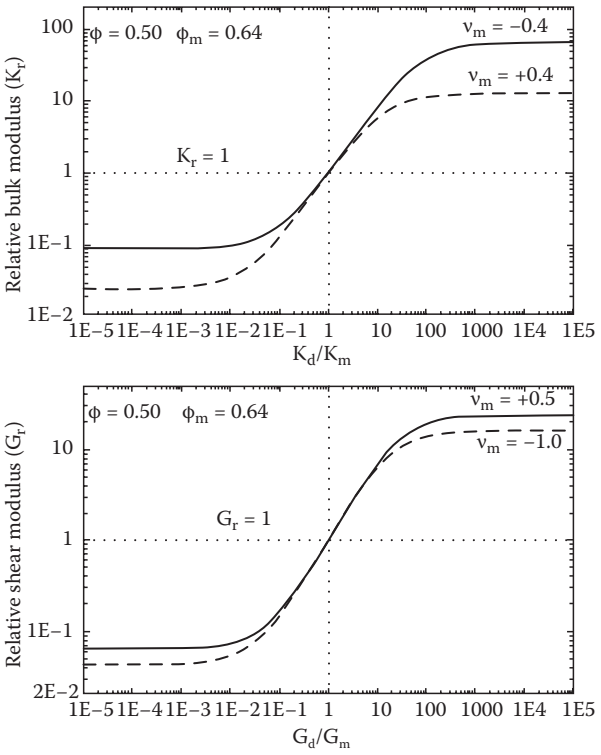

FIGURE 12.1 Variation of relative modulus (bulk and shear) with moduli ratio for two different values of matrix Poisson's ratio. (From Pal, R., *Polym. Composites* 30: 451–459, 2009.)

Figure 12.1 shows the plots of relative bulk modulus (K_r) and relative shear modulus (G_r) as functions of moduli ratio (bulk moduli ratio K_d/K_m in the case of relative bulk modulus and shear moduli ratio G_d/G_m in the case of relative shear modulus). The plots are shown for two different values of matrix Poisson's ratio. Equations 12.11 and 12.12 are used to generate the plots shown in Figure 12.1. At low values of moduli ratio (K_d/K_m or G_d/G_m), the relative modulus is constant independent of the moduli ratio; at intermediate values of moduli ratio, the relative modulus increases with the increase in moduli ratio, and at high values of moduli ratio, the relative modulus again becomes constant independent of the moduli ratio. With the increase in matrix Poisson's ratio, the relative bulk modulus decreases at high and low values of moduli ratio. However, the relative shear modulus shows an opposite behavior in that it increases with the increase in matrix Poisson's ratio at high and low values of moduli ratio.

12.2 POOR ADHESION BETWEEN PARTICLES AND MATRIX

The models discussed in the preceding section assume perfect adhesion between the filler particles and matrix. The matrix obeys the no-slip boundary condition at the filler surface. However, the bonding between the particles and matrix is often poor. When the adhesion between the filler particles and matrix is poor in filled polymeric composites, the polymer chains tend to pull away from the filler surface to create interfacial void space around the particles [5–12]. Consequently, the matrix does not obey the no-slip condition (it slips by the filler particles) and the filler particles behave more like cavities (void space) with moduli values of zero, that is, $K_d \to 0$ and $G_d \to 0$. Thus, the relative bulk and shear moduli of particulate composites, when the adhesion between particles and matrix is poor, can be described by the following equations:

$$K_r = \frac{K}{K_m} = \left[\frac{1-\psi\phi}{1+\left(\frac{3K_m}{4G_m}\right)\psi\phi}\right] \tag{12.13}$$

$$G_r = \frac{G}{G_m} = \left[\frac{1-\psi\phi}{1+\left(\frac{8-10\nu_m}{7-5\nu_m}\right)\psi\phi}\right] \tag{12.14}$$

Equations 12.13 and 12.14 follow from Equations 12.11 and 12.12 with $k = -(3K_m/4G_m)$ and $h = -(8 - 10\nu_m)/(7 - 5\nu_m)$.

Figure 12.2 shows the effect of adhesion between the filler particles and matrix. The plots shown in Figure 12.2 are generated from Equations 12.11 through 12.14. When adhesion between the particles and matrix is perfect (no slippage of matrix occurs at the particle surface), the addition of filler to the matrix has the reinforcement

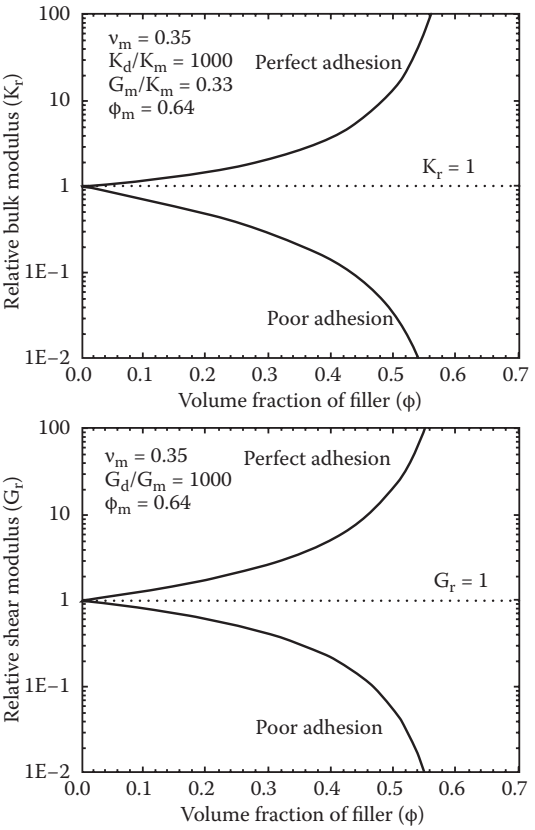

FIGURE 12.2 The effect of adhesion between the filler particles and matrix on the mechanical properties of particulate composites. (From Pal, R., *Polym. Composites* 30: 451–459, 2009.)

effect in that the moduli (K and G) increase with the increase in filler volume fraction. When adhesion between the particles and matrix is poor (matrix slips by the filler particles) an opposite effect is seen, that is, the moduli (K and G) decrease with the increase in filler concentration; in addition, the values of the relative moduli K_r and G_r are less than unity.

12.3 EFFECT OF INTERPHASE LAYER

In order to promote adhesion between filler particles and matrix (assumed to be some polymeric material), suitable compatibilizer or coupling agents are used. The coupling agent promotes interfacial adhesion by bridging the two phases (filler particle and polymer matrix) together through chemical bonding. However, the presence of a compatibilizer at the interface complicates the mechanical behavior of particulate composites, as the mechanical properties of a thin layer surrounding the particles are no longer the same as that of the bulk matrix (polymer). Even in the absence of a coupling agent, the mechanical properties of a thin layer of material surrounding the

particles are expected to be somewhat different from the mechanical properties of matrix. The mobility of polymer chains in the thin region surrounding the particles is severely limited compared to the mobility of polymer chains in the bulk matrix.

The presence of a thin interphase layer around the particles can have a significant influence on the overall mechanical properties of the particulate composites. The mechanical properties of three-phase particulate composites (the three phases being bulk matrix, interphase layer, and filler particles) can be modeled using a two-step approach [4] discussed earlier in Chapter 11 in relation to disk-shaped particles (here we are dealing with spherical inclusions). In the first step, the moduli equations for two-phase composites (Equations 12.11 and 12.12) are applied to determine the mechanical behavior of a single core-shell particle consisting of filler as core and interfacial layer as shell. The interfacial layer is treated as matrix with respect to the filler core-particle. In the second step, the core-shell particles are treated as "homogeneous" particles of mechanical properties obtained from the first step. The moduli equations for two-phase composites (Equations 12.11 and 12.12) are applied once again to determine the mechanical behavior of three-phase composites. Thus,

$$\frac{K_{cs}}{K_s} = \left[\frac{1+\left(\frac{4}{3}\frac{G_s}{K_s}\right)k_1\phi_c}{1-k_1\phi_c}\right] \tag{12.15}$$

$$K_r = \frac{K}{K_m} = \left[\frac{1+\left(\frac{4}{3}\frac{G_m}{K_m}\right)k_2\psi\phi}{1-k_2\psi\phi}\right] \tag{12.16}$$

where K_{cs} is bulk modulus of a core-shell composite particle, K_s is bulk modulus of interfacial shell, G_s is shear modulus of shell, ϕ_c is volume fraction of filler core-particle in the combined volume of core and interfacial shell, K is the bulk modulus of the three-phase composite, K_m and G_m are moduli of the matrix, ϕ is the volume fraction of total dispersed phase (filler core particles plus interfacial layers), and k_1 and k_2 are given as

$$k_1 = \left[\frac{\frac{K_c}{K_s}-1}{\frac{K_c}{K_s}+\frac{4}{3}\left(\frac{G_s}{K_s}\right)}\right] \tag{12.17}$$

$$k_2 = \left[\frac{\frac{K_{cs}}{K_m}-1}{\frac{K_{cs}}{K_m}+\frac{4}{3}\left(\frac{G_m}{K_m}\right)}\right] \tag{12.18}$$

where K_c is the bulk modulus of the filler core particle. Note that ψ is taken to be unity for the calculation of the bulk modulus of a core-shell composite particle (K_{cs}) in Equation 12.15 as ϕ_c (the volume fraction of filler core particle in the combined volume of core and interfacial shell) can vary from zero to unity depending on the thickness of the interfacial shell. In addition, ϕ_c is related to δ, the ratio of outer radius of interfacial shell (R_s) to radius of core particle (R_c), as follows:

$$\phi_c = \frac{\frac{4}{3}\pi R_c^3}{\frac{4}{3}\pi R_s^3} = \left(\frac{R_c}{R_s}\right)^3 = \frac{1}{\delta^3} \tag{12.19}$$

The equations for the shear modulus of a three-phase composite can be derived in a similar manner using the two-step approach. Thus,

$$\frac{G_{cs}}{G_s} = \left[\frac{1+\left(\frac{7-5\nu_s}{8-10\nu_s}\right)h_1\phi_c}{1-h_1\phi_c}\right] \tag{12.20}$$

$$G_r = \frac{G}{G_m} = \left[\frac{1+\left(\frac{7-5\nu_m}{8-10\nu_m}\right)h_2\psi\phi}{1-h_2\psi\phi}\right] \tag{12.21}$$

where G_{cs} is shear modulus of a core-shell composite particle, G_s is shear modulus of interfacial shell, ν_s is Poisson's ratio of shell material, G is shear modulus of the three-phase composite, ν_m is Poisson's ratio of matrix material, and h_1 and h_2 are given as

$$h_1 = \left[\frac{(8-10\nu_s)\left(\frac{G_c}{G_s}-1\right)}{(8-10\nu_s)\left(\frac{G_c}{G_s}\right)+(7-5\nu_s)}\right] \tag{12.22}$$

$$h_2 = \left[\frac{(8-10\nu_m)\left(\frac{G_{cs}}{G_m}-1\right)}{(8-10\nu_m)\left(\frac{G_{cs}}{G_m}\right)+(7-5\nu_m)}\right] \tag{12.23}$$

where G_c is shear modulus of the filler core particle.

The effect of interfacial layer on the mechanical properties (bulk and shear moduli) of composites is shown in Figure 12.3. The relative bulk modulus plots are generated from Equations 12.15 through 12.18 and the relative shear modulus plots are generated from Equations 12.20 through 12.23. The plots show relative modulus (bulk and shear) as a function of shell-to-matrix moduli ratio (K_s/K_m in the case of bulk modulus and G_s/G_m in the case of shear modulus) for different values of δ (shell-to-core radii ratio, see Equation 12.19). For a given value of δ, the modulus increases with the increase in shell-to-matrix moduli ratio from some low limiting value to a high limiting value. The low limiting value corresponds to soft shell whereas the high limiting value corresponds to hard shell. For the limiting cases of soft and hard shells, the effect of δ (and hence shell thickness) on the mechanical properties of composites is negligible. However, in the intermediate range of shell-to-matrix moduli ratio, the mechanical properties of composites are strongly influenced by δ. For a given value of shell-to-matrix moduli ratio in the intermediate range of 10^{-4} to 100, the bulk modulus as well as the shear modulus

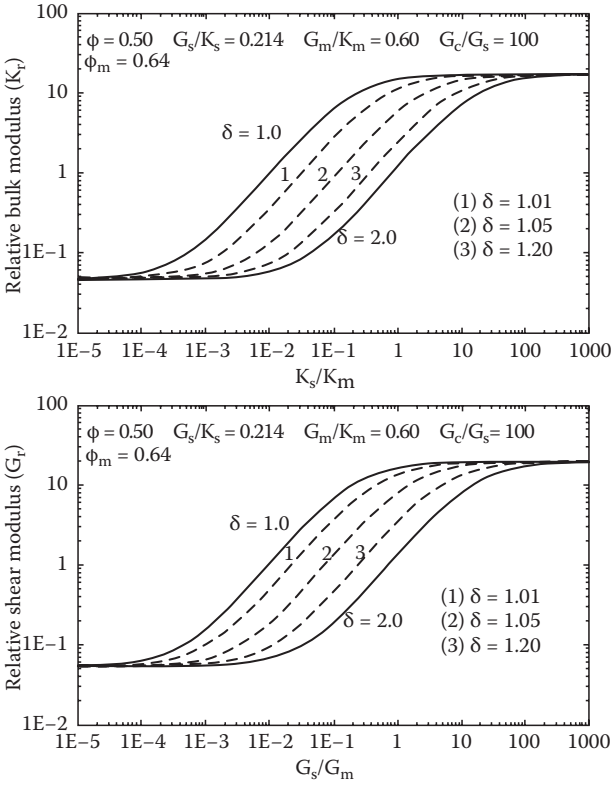

FIGURE 12.3 The effect of interfacial layer on the mechanical properties (relative bulk and shear moduli) of particulate composites. (From Pal, R., *Polym. Composites* 30: 451–459, 2009.)

of composite decrease with the increase in δ. An increase in δ at a given ϕ implies an increase in the shell thickness. Thus for intermediate values of shell-to-matrix moduli ratio where the shell material is neither too hard nor too soft (compared to the matrix), an increase in the shell thickness reduces the reinforcement effect of the filler particles.

Figure 12.4 shows the effect of core-to-shell moduli ratio (K_c/K_s in the case of bulk modulus and G_c/G_s in the case of shear modulus) on the relative modulus versus shell-to-matrix moduli ratio behavior of composites. At low and high values of shell-to-matrix moduli ratio, the mechanical properties of composites are unaffected by the core-to-shell moduli ratio. However, in the intermediate range of shell-to-matrix moduli ratio, the core-to-shell moduli ratio exerts a strong influence on the mechanical properties of composites; the relative modulus (bulk or shear) increases with the increase in core-to-shell moduli ratio. Thus, the material properties of the core are significant only when the shell material is neither too hard nor too soft compared to the matrix material.

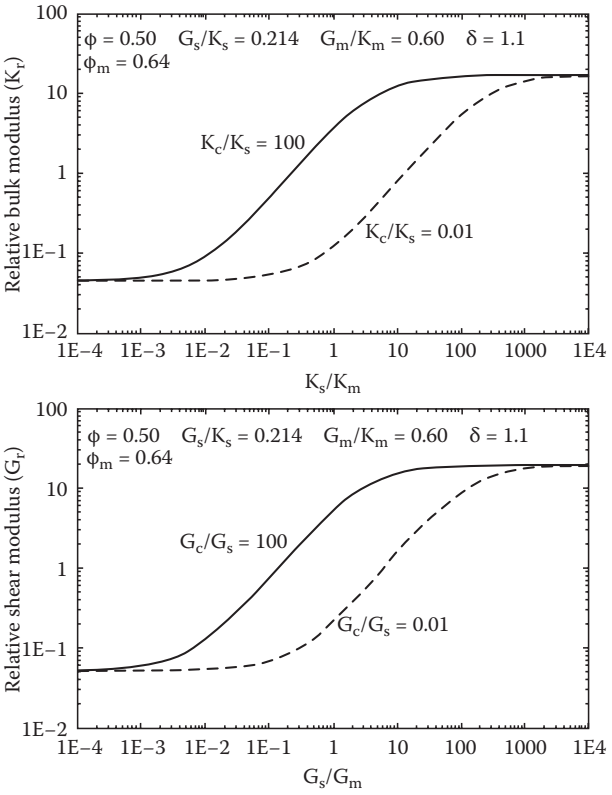

FIGURE 12.4 The effect of core-to-shell moduli ratio on the mechanical properties of particulate composites. (From Pal, R., *Polym. Composites* 30: 451–459, 2009.)

12.4 COMPARISON OF MODEL PREDICTIONS WITH EXPERIMENTAL DATA

The experimental data on the mechanical properties of three different particulate composite systems are considered to verify the models (see Table 12.1 for a summary of

TABLE 12.1
Summary of Various Composite Systems Considered to Evaluate Models

Set No.	Range of ϕ (Volume Fraction of Inclusions)	Ref. No.	Comments
1	0–0.41	[13]	Young's modulus of porous polycrystalline alumina
2	0–0.12	[14]	Young's modulus of porous polycrystalline mullite
3	0–0.36	[15]	Elastic properties (Young's and shear moduli) of porous polycrystalline monoclinic gadolinium oxide
4	0–0.40	[16]	Elastic properties (Young's and shear moduli) of porous polycrystalline monoclinic samarium oxide
5	0–0.32	[17]	Elastic properties (Young's and shear moduli) of porous polycrystalline cubic lutetium oxide
6	0–0.28	[18]	Elastic properties (Young's and shear moduli) of porous polycrystalline monoclinic hafnium oxide
7	0–0.40	[19]	Elastic properties (Youngs's and shear moduli) of porous refractory spinels
8	0–0.36	[20]	Elastic properties (Young's and shear moduli) of porous stabilized hafnium oxide
9	0–0.18	[21]	Elastic properties (Young's and shear moduli) of porous hafnium and zirconium oxides stabilized with praseodymium or terbium oxide
10	0–0.524	[22]	Elastic properties (Young's and shear moduli) of rubber-toughened poly(methyl methacrylate) composites
11	0–0.706	[23]	Young's modulus of dental restorative composites, a total of 55 composites of varying filler volume fraction
12	0–0.552	[24]	Young's modulus of dental composites of varying filler volume fraction
13	0–0.68	[25]	Young's modulus of particulate composites
14	0–0.625	[26]	Young's modulus of crosslinked polyurethane rubber filled with glass beads ranging from 60 to 90 μm in diameter
15	0–0.65	[27,28]	Elastic properties (bulk and shear moduli) of sand particles/cement paste composites. The sand particles (850 μm in diameter) were covered with an interphase of thickness 25 μm

Source: Pal, R., *Polym. Composites* 30: 451–459, 2009.

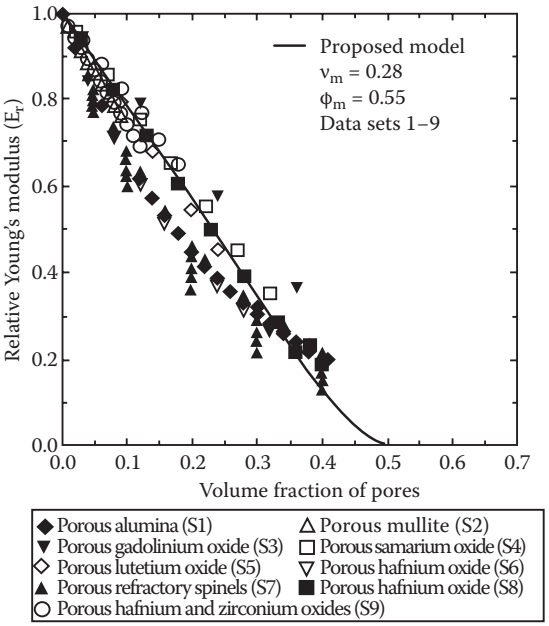

FIGURE 12.5 Comparison between model prediction and experimental relative Young's modulus data for pore-solid composites. (From Pal, R., *Polym. Composites* 30: 451–459, 2009.)

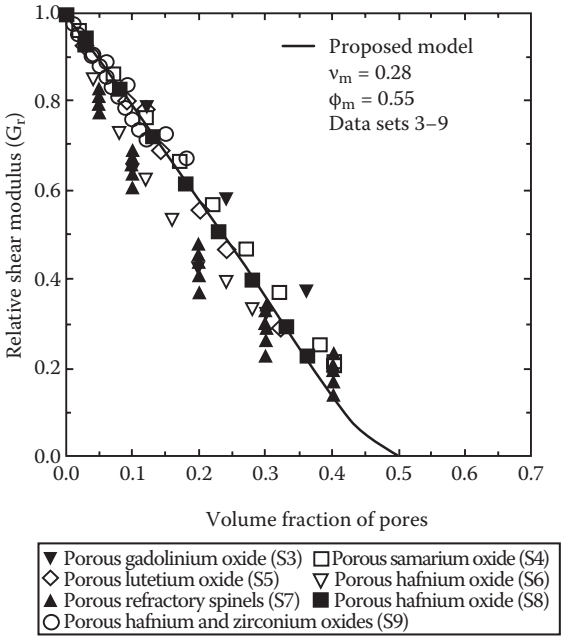

FIGURE 12.6 Comparison between model prediction and experimental relative shear modulus data for pore-solid composites. (From Pal, R., *Polym. Composites* 30: 451–459, 2009.)

the various composite systems considered here). The systems considered are as follows: (1) composites with cavities (pores) as inclusions and solid material as matrix (data sets 1 through 9) [13–21]—these pore-solid composites are considered to evaluate the model (Equations 12.13 and 12.14) for mechanical properties of composites with poor adhesion between inclusions and matrix; (2) particulate composites with good particle–matrix adhesion (data sets 10 through 14) [22–26]—these composites are considered to evaluate the model (Equations 12.11 and 12.12) for mechanical properties of composites with good adhesion between particles and composites; and (3) particulate composites with core-shell particles as inclusions (data set 15) [27,28]—these composites are considered to evaluate the model (Equations 12.16 and 12.21) for mechanical properties of composites with interphase layer around the particles.

Figures 12.5 and 12.6 compare the predictions of Equations 12.13 and 12.14 with experimental data for composites with cavities or pores as inclusions. The relative

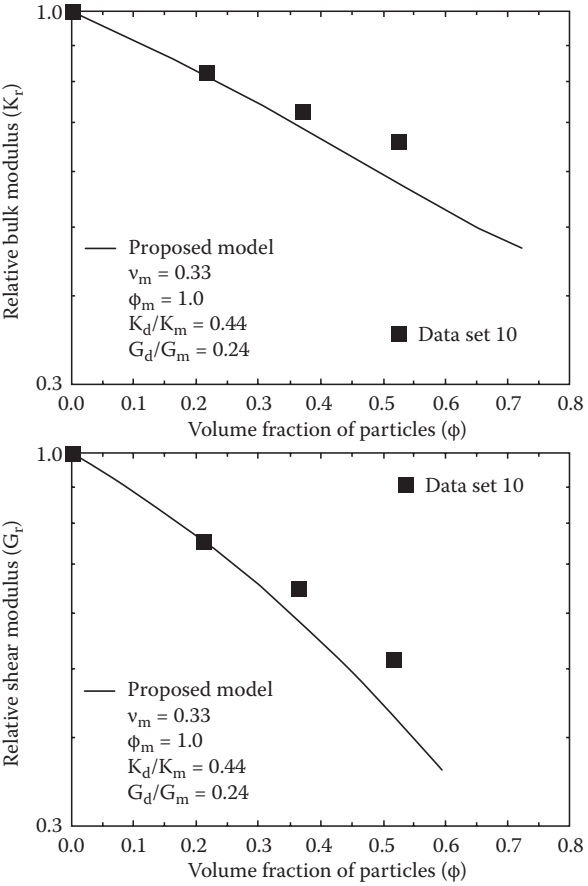

FIGURE 12.7 Comparison between model predictions and experimental relative moduli (bulk and shear) for particulate composites with good particle–matrix contact. (From Pal, R., *Polym. Composites* 30: 451–459, 2009.)

Young's modulus (E_r) is estimated from the bulk and shear moduli models using the following relation:

$$E_r = \frac{9G_rK_r}{\left[6(1+\nu_m)K_r + 3(1-2\nu_m)G_r\right]} \tag{12.24}$$

The experimental relative moduli data (Young's modulus and shear modulus) are in good agreement with the predictions of the model.

Figures 12.7 through 12.9 compare the predictions of Equations 12.11 and 12.12 with experimental data for particulate composites having good particle–matrix adhesion. The predictions of the model are in a reasonably good agreement with experimental data.

The predictions of Equations 12.16 and 12.21 are compared with experimental data for particulate composites composed of core-shell particles in Figure 12.10. Once again, the predictions of the model show a reasonably good agreement with the experimental data.

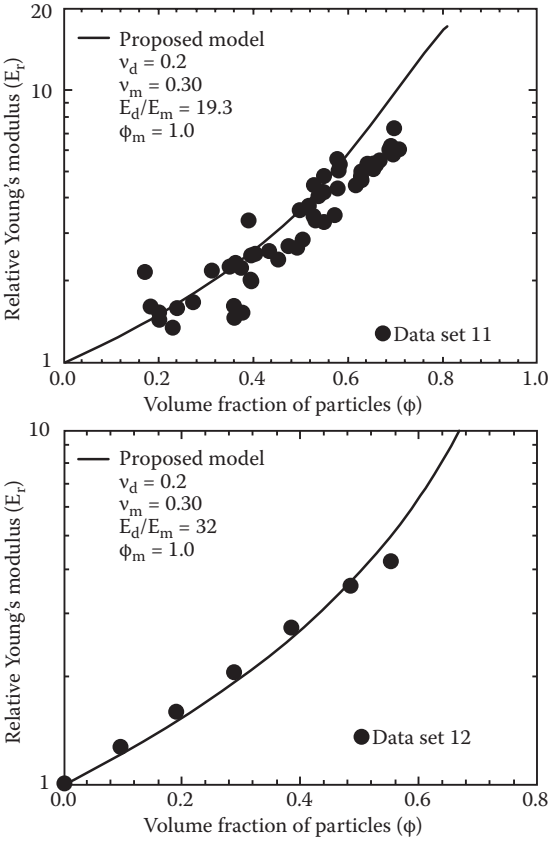

FIGURE 12.8 Comparison between model predictive and experimental relative Young's modulus for particulate composites with good particle–matrix contact. (From Pal, R., *Polym. Composites* 30: 451–459, 2009.)

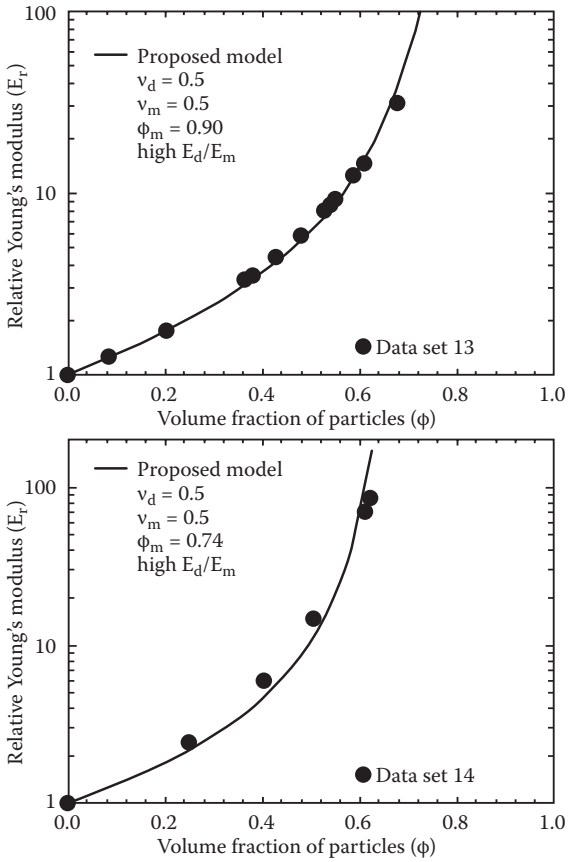

FIGURE 12.9 Comparison between model predictions and experimental relative Young's modulus for particulate composites with good particle–matrix contact. (From Pal, R., *Polym. Composites* 30: 451–459, 2009.)

12.5 CONCLUDING REMARKS

Models describing the effects of interfacial and interphase phenomena on the mechanical properties of particulate composites are discussed. Based on model predictions, the following conclusions can be made:

1. The addition of filler to the matrix improves the mechanical properties of composites only if adhesion between the particles and matrix is good. The mechanical properties of composites deteriorate with the increase in filler concentration if adhesion between the particles and matrix is poor.
2. The mechanical properties of composites are strongly affected by the presence of interphase (interfacial layer or shell) around the particles. With the increase in interphase-to-matrix moduli ratio, the mechanical properties of composites show a strong improvement. The thickness of the interphase

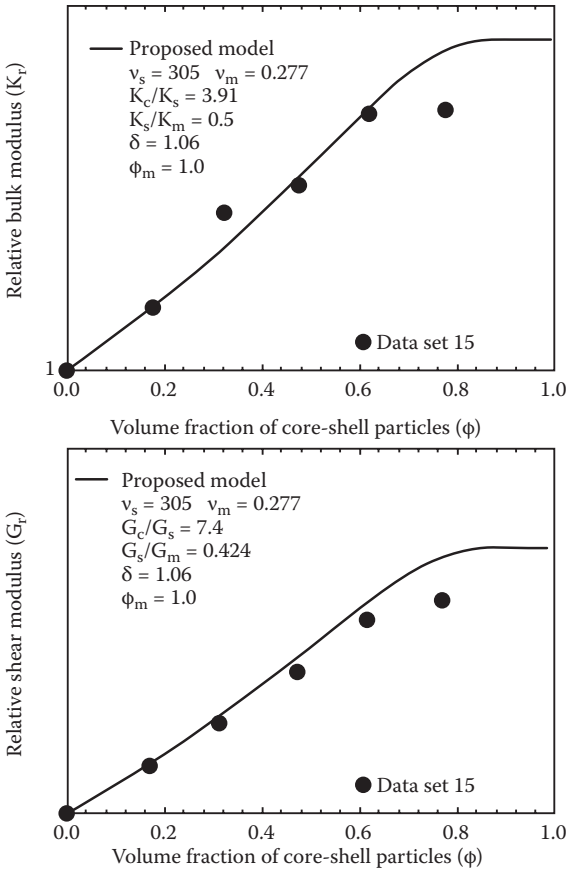

FIGURE 12.10 Comparison between model predictions and experimental relative moduli (bulk and shear) for composites of core-shell particles. (From Pal, R., *Polym. Composites* 30: 451–459, 2009.)

layer and the core-to-shell moduli ratio also exert significant influence on the mechanical properties of composites, especially in the intermediate range of interphase-to-matrix moduli ratio.

3. The models are evaluated using 15 sets of experimental data on the mechanical properties of particulate composites. The models describe the experimental data reasonably well.

REFERENCES

1. Pal, R. 2007. *Rheology of Particulate Dispersions and Composites.* Boca Raton: CRC Press.
2. Kerner, E.H. 1956. The elastic and thermoelastic properties of composite media. *Proc. Phys. Soc. Lond. B* 69: 808–813.
3. Lewis, T. and L. Nielsen. 1970. Dynamic mechanical properties of particulate filled composites. *J. Appl. Poly. Sci.* 14: 1449–1471.

4. Pal, R. 2009. Influence of interfacial phenomena on the mechanical properties of particulate composite membranes. *Polym. Composites* 30: 451–459.
5. Chung, T.S., L.Y. Jiang, and S. Kulprathipanja. 2007. Mixed matrix membranes comprising organic polymers with dispersed inorganic fillers for gas separation. *Prog. Polym. Sci.* 32: 483–507.
6. Mahajan, R., W.J. Koros, and M. Thundyil. 1999. Mixed matrix membranes: Important and challenging! *Membr. Tech*. 105: 6–8.
7. Moore, T.T., R. Mahajan, D.Q. Vu, and W.J. Koros. 2004. Hybrid membrane materials comprising organic polymers with rigid dispersed phases. *AIChE J*. 50: 311–321.
8. Vu, D.Q., W.J. Koros, and S.J. Miller. 2003. Mixed matrix membranes using carbon molecular sieves II. Modeling permeation behavior. *J. Membr. Sci.* 211: 335–348.
9. Mahajan, R. and W.J. Koros. 2000. Factors controlling successful formation of mixed-matrix gas separation materials. *Ind. Eng. Chem. Res.* 39: 2692–2696.
10. Mahajan, R. and W.J. Koros. 2002. Mixed matrix membrane materials with glassy polymers. Part 1. *Poly. Eng. Sci.* 42: 1420–1431.
11. Sen, D., H. Kalipcilar, and L. Yilmaz, 2006. Development of zeolite filled polycarbonate mixed matrix gas separation membranes. *Desalination* 200: 222–224.
12. Bliznakov, E.D., C.C. White, and M.T. Shaw. 2000. Mechanical properties of blends of HDPE and recycled urea–formaldehyde resin. *J. Appl. Poly. Sci*. 77: 3220–3227.
13. Knudsen, F.P. 1962. Effect of porosity on Young's modulus of alumina. *J. Am. Ceram. Soc*. 45: 94–95.
14. Penty, R.A., D.P.H. Hasselman, and R.M. Spriggs. 1972. Young's modulus of high density polycrystalline mullite. *J. Am. Ceram. Soc.* 55: 169–170.
15. Haglund, J.A. and O. Hunter. 1973. Elastic properties of polycrystalline monoclinic Gd_2O_3. *J. Am. Ceram. Soc.* 56: 327–330.
16. Hunter, O., H.J. Korklam, and R.R. Suchomel. 1974. Elastic properties of polycrystalline monoclinic Sm_2O_3. *J. Am. Ceram. Soc.* 57: 267–268.
17. Hunter, O. and G.E. Graddy. 1976. Porosity dependence of elastic properties of polycrystalline cubic Lu_2O_3. *J. Am. Ceram. Soc.* 59: 82.
18. Dole, S.L., O. Hunter, and C.J. Wooge. 1977. Elastic properties of monoclinic hafnium oxide at room temperature. *J. Am. Ceram. Soc.* 60: 488–490.
19. Porter, D.F., J.S. Reed, and D. Lewis. 1977. Elastic moduli of refractory spinels. *J. Am. Ceram. Soc.* 60: 345–349.
20. Dole, S.L., O. Hunter, and F.W. Calderwood. 1980. Elastic properties of stabilized HfO_2 compositions. *J. Am. Ceram. Soc.* 63: 136–139.
21. Dole, S.L. and O. Hunter. 1983. Elastic properties of hafnium and zirconium oxides stabilized with praseodymium or terbium oxide. *Commun. Am. Ceram. Soc.* March: C-47–C-49.
22. Biwa, S., N. Ito, and N. Ohno. 2001. Elastic properties of rubber particles in toughened PMMA: Ultrasonic and micromechanical evaluation. *Mech. Mater.* 33: 717–728.
23. Braem, M., V.E. Van Doren, P. Lambrechts, and G. Vanherle. 1987. Determination of Young's modulus of dental composites: A phenomenological model. *J. Mater. Sci.* 22: 2037–2042.
24. Braem, M., W. Finger, V.E. Van Doren, P. Lambrechts, and G. Vanherle. 1989. Mechanical properties and filler fraction of dental composites. *Dental Mater.* 5: 346–349.
25. Landel, R.F. and T.L. Smith. 1961. Viscoelastic properties of rubber-like composite propellants and filled elastomers. *ARS J.* 31: 599–608.
26. Bills, K.W., K.H. Sweeney, and F.S. Salcedo. 1960. The tensile properties of highly filled polymers—Effect of filler concentrations. *J. Appl. Polym. Sci.* 4: 259–268.
27. Wang, J.A., J. Lubliner, and P.J.M. Monteiro. 1988. Effect of ice formation on the elastic moduli of cement paste and mortar. *Cem. Concr. Res.* 18: 874–885.
28. Hashin, Z. and P.J.M. Monteiro. 2002. An inverse method to determine the elastic properties of the interphase between the aggregate and the cement paste. *Cem. Concr. Res.* 32: 1291–1300.

13 Viscoelastic Behavior of Composites

13.1 INTRODUCTION

A purely elastic material (for example, Hookean solid) differs widely in its deformational characteristics from a purely viscous material (for example, Newtonian fluid). The stress in a purely elastic material is a function only of the instantaneous magnitude of deformation (strain) whereas in a purely viscous material, the stress is a function only of the instantaneous rate of deformation. Also, purely elastic materials return to their natural or undeformed state upon removal of applied loads whereas purely viscous materials possess no tendency at all for deformational recovery. The term "viscoelastic" implies the simultaneous existence of viscous and elastic characteristics in a material. Thus, a material behavior that incorporates a blend of both viscous and elastic characteristics is called viscoelastic behavior.

Many materials, including composites, exhibit viscoelastic behavior. They flow under the influence of applied stresses, unlike purely elastic materials, which exhibit a constant strain and no flow. Upon removal of the applied stress, some of their deformation is gradually recovered; that is, they exhibit elastic recovery unlike purely viscous materials, which exhibit no recovery at all. The term "linear viscoelasticity" implies the study of viscoelastic effects in a small strain region where strain varies linearly with stress (doubling the stress will double the strain). Among the various techniques available to study the linear viscoelastic behavior of materials, oscillatory testing at small strain amplitudes is very popular. The material is subjected to oscillatory strain, and its stress response is monitored. The material could be subjected to either oscillatory normal strain or oscillatory shear strain. For purely elastic materials, stress is in phase with the strain. For viscoelastic materials, there occurs a lag between the stress and strain.

Particulate composites often contain polymeric material as one of the two phases (dispersed phase and matrix phase). The polymeric phase imparts a viscoelastic behavior to the composite [1]. For example, the ethylene–propylene–diene monomer (EPDM) rubber is being increasingly used in many applications due to its excellent oxidation resistance and electrical properties [2]. As the EPDM, like many other polymeric materials, is viscoelastic in nature, the composites prepared from EPDM as one of the phases are also viscoelastic. Therefore, a good understanding of the effective properties of viscoelastic composites is of great industrial interest [3–14].

In this chapter, the viscoelastic behavior of dilute and concentrated composites is described in terms of the effective complex moduli.

13.2 ELASTIC–VISCOELASTIC CORRESPONDENCE PRINCIPLE

The "elastic–viscoelastic correspondence principle" states that the expressions for the effective *complex moduli* of a viscoelastic heterogeneous material can be obtained from the corresponding expressions for the effective *elastic moduli* of an associated heterogeneous elastic material (with identical phase geometry) simply by replacement of phase elastic moduli by phase complex moduli [6,15,16]. This correspondence principle is based on the fact that the governing equations and the boundary conditions for elastic and viscoelastic problems are the same; only the stress–strain relations in the two cases are different.

13.3 COMPLEX MODULI OF DILUTE COMPOSITES

Using the "elastic–viscoelastic correspondence principle," the expressions for the effective elastic moduli of dilute particulate composites (given in Chapter 7) can be converted into the corresponding expressions for the complex moduli of viscoelastic particulate composites.

For *dilute* composites of spherical particles, the results are as follows:

$$\frac{G^*}{G_m^*} = 1 + \left[\frac{15(1-\nu_m^*)(G_d^* - G_m^*)}{2G_d^*(4-5\nu_m^*) + G_m^*(7-5\nu_m^*)} \right] \phi \tag{13.1}$$

$$\frac{K^*}{K_m^*} = 1 + \left[\left(\frac{3K_m^* + 4G_m^*}{3K_m^*} \right) \left(\frac{3K_d^* - 3K_m^*}{3K_d^* + 4G_m^*} \right) \right] \phi \tag{13.2}$$

where G^*, G_m^*, and G_d^* are the complex shear moduli of the composite, the continuous phase, and the dispersed phase, respectively; ν_m^* is the complex Poisson ratio of the continuous phase; and K^*, K_m^*, and K_d^* are the complex bulk moduli of the composite, the continuous phase, and the dispersed phase, respectively. The definitions of complex shear modulus, complex Poisson's ratio, and complex bulk modulus are

$$G^* = G' + jG'' \tag{13.3}$$

$$\nu^* = \nu' + j\nu'' \tag{13.4}$$

$$K^* = K' + jK'' \tag{13.5}$$

where single-primed quantities are the storage components, double-primed quantities are the loss components, and j is the imaginary number ($\sqrt{-1}$).

For the case where (1) the particles are purely elastic and (2) the matrix is elastic in dilation and viscoelastic in shear, one can write

$$G_d^* = G_d \tag{13.6}$$

$$K_d^* = K_d \tag{13.7}$$

$$K_m^* = K_m \tag{13.8}$$

$$G_m^* = G_m' + jG_m'' \tag{13.9}$$

Introducing the above expressions for G_d^*, K_d^*, K_m^*, and G_m^* into Equations 13.1 and 13.2, and making an additional assumption that $\tan^2 \delta_{Gm} = \left(\frac{G_m''}{G_m'}\right)^2 \ll 1$, the following results are obtained for the bulk moduli [6]:

$$K' = K_m + \frac{(K_d - K_m)(4G_m' + 3K_m)}{(4G_m' + 3K_d)}\phi \tag{13.10a}$$

$$K'' = 12\left[\frac{K_d - K_m}{4G_m' + 3K_d}\right]^2 G_m''\phi \tag{13.10b}$$

where K' and K'' are storage and loss bulk moduli, respectively, of the composite. Interestingly, the composite is viscoelastic in dilation (K' and K'' are nonzero) even though the dispersed phase and matrix are purely elastic in dilation. The shear viscoelasticity of the matrix introduces dilational viscoelasticity in the composite.

For the case where (1) the particles are elastic, and (2) the matrix is incompressible and viscoelastic in shear, the following expressions for the complex bulk and shear moduli are obtained from Equations 13.1 and 13.2:

$$K^* = K' + jK'' = \frac{3K_d + 4(G_m' + jG_m'')}{3\phi} \tag{13.11}$$

$$\frac{G^*}{G_m^*} = 1 + \frac{5}{2}\left[\frac{G_d - G_m^*}{G_d + \frac{3}{2}G_m^*}\right]\phi \tag{13.12}$$

From Equation 13.11, the expressions for the bulk storage (K′) and loss (K″) moduli are as follows:

$$K' = \frac{3K_d + 4G'_m}{3\phi} \tag{13.13a}$$

$$K'' = \frac{4G''_m}{3\phi} \tag{13.13b}$$

Figure 13.1 shows the shear moduli of matrix and dilational (bulk) moduli of composite. The dilational moduli are calculated from Equations 13.13a and 13.13b. The matrix is assumed to follow the Maxwell model, that is,

$$G'_m = G_m \omega^2 \tau_{gm}^2 / (1 + \omega^2 \tau_{gm}^2) \tag{13.14}$$

$$G''_m = G_m \omega \tau_{gm} / (1 + \omega^2 \tau_{gm}^2) \tag{13.15}$$

where G_m is the high frequency limiting value of shear modulus, ω is the frequency, and τ_{gm} is the shear relaxation time of the matrix. An important point to note is that shear viscoelasticity of matrix results in dilational viscoelasticity of composite.

When the particles are viscoelastic in both shear and dilation, and the matrix is incompressible and viscoelastic in shear, the expressions for the complex bulk and shear moduli of the composite become

$$K^* = \frac{3K_d^* + 4G_m^*}{3\phi} \tag{13.16}$$

$$\frac{G^*}{G_m^*} = 1 + \frac{5}{2}\left[\frac{G_d^* - G_m^*}{G_d^* + \frac{3}{2}G_m^*}\right]\phi \tag{13.17}$$

From Equation 13.16, the expressions for the bulk storage (K′) and loss (K″) moduli are as follows:

$$K' = \frac{3K'_d + 4G'_m}{3\phi} \tag{13.18}$$

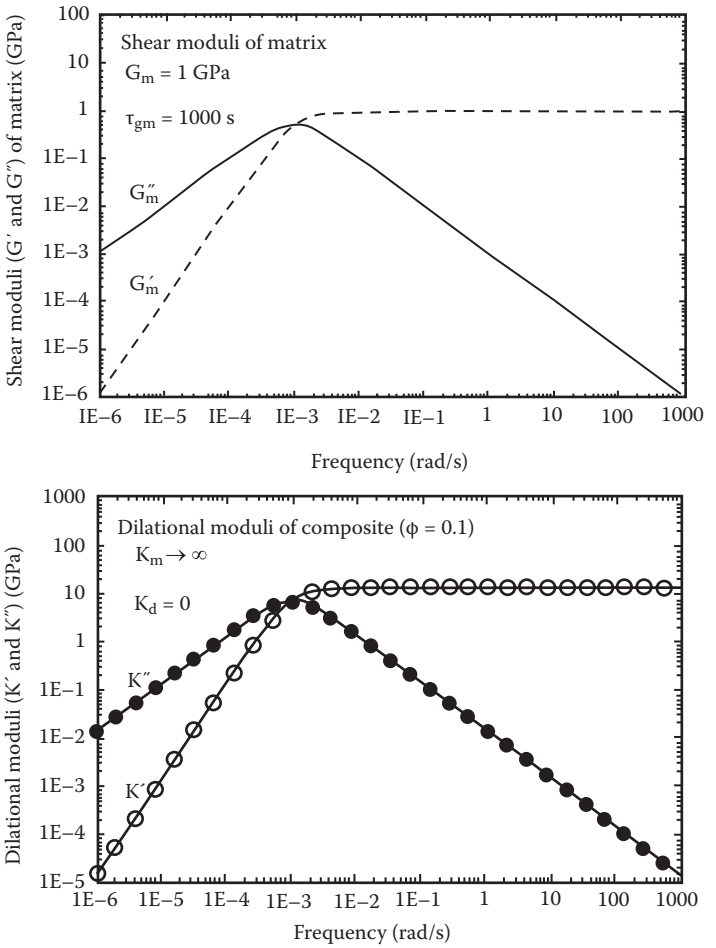

FIGURE 13.1 Shear viscoelasticity of matrix results in dilational viscoelasticity of composite. (From Pal, R., *Rheology of Particulate Dispersions and Composites*. Boca Raton: CRC Press, 2007.)

$$K'' = \frac{3K''_d + 4G''_m}{3\phi} \tag{13.19}$$

From Equation 13.17, the expressions for the storage and loss shear moduli (G′ and G″) of the composite can be obtained as follows:

$$G' = (1 + \phi A_1)G'_m - \phi A_2 G''_m \tag{13.20}$$

$$G'' = \phi A_2 G'_m + (1 + \phi A_1)G''_m \tag{13.21}$$

where A_1 and A_2 are given as

$$A_1 = 5\left[\frac{ac + bd}{c^2 + d^2}\right] \tag{13.22}$$

$$A_2 = 5\left[\frac{bc - ad}{c^2 + d^2}\right] \tag{13.23}$$

$$a = G'_d - G'_m, \quad b = G''_d - G''_m \tag{13.24}$$

$$c = 2G'_d + 3G'_m, \quad d = 2G''_d + 3G''_m \tag{13.25}$$

Figures 13.2a and b show the plots of bulk moduli of composite calculated from Equations 13.18 and 13.19. The shear moduli of the matrix phase and the bulk moduli of the dispersed phase are assumed to follow the Maxwell model. When the shear relaxation time of the matrix (τ_{gm}) and dilational relaxation time of the particles (τ_{kd}) are equal, the composite exhibits a single relaxation time (see Figure 13.2a). When the shear relaxation time of the matrix and dilational relaxation time of the particles are different, the composite exhibits two relaxation times as can be seen in Figure 13.2b. The Cole–Cole plot (K″ versus K′ plot) clearly shows two frequency domains.

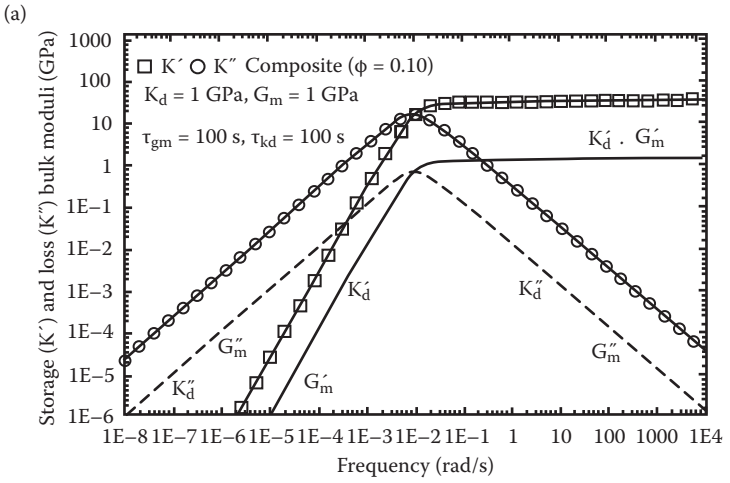

FIGURE 13.2 (a) Bulk moduli of composite when the shear relaxation time of the matrix (τ_{gm}) is equal to the dilational relaxation time of the particles (τ_{kd}). (From Pal, R., *Rheology of Particulate Dispersions and Composites*. Boca Raton: CRC Press, 2007.)

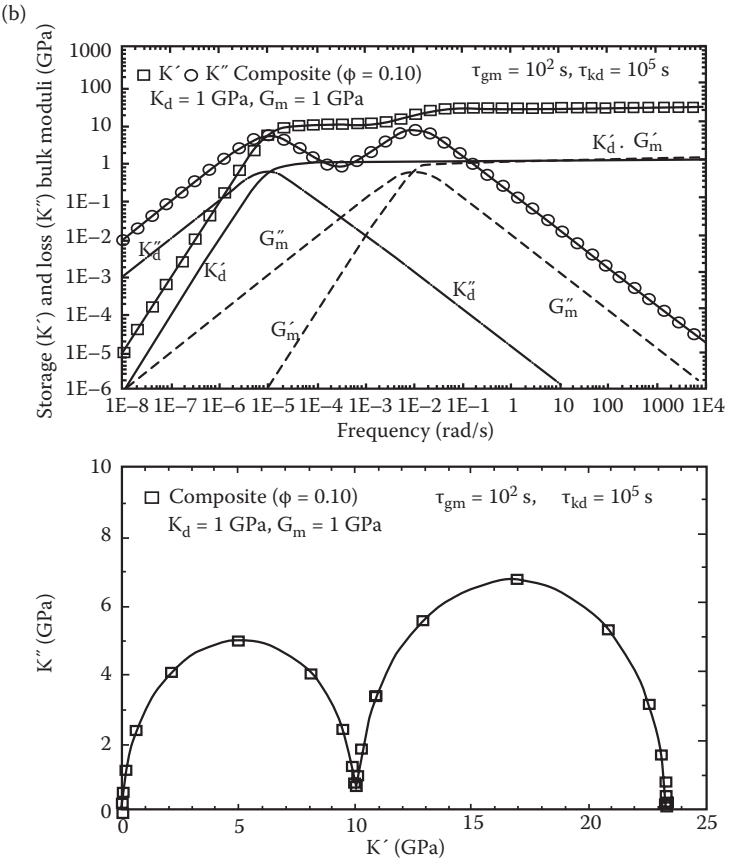

FIGURE 13.2 (Continued) (b) Bulk moduli and Cole–Cole diagram for composite when the shear relaxation time of the matrix and dilational relaxation time of the particles are different. (From Pal, R., *Rheology of Particulate Dispersions and Composites.* Boca Raton: CRC Press, 2007.)

Figure 13.3 shows the effects of K_d (high frequency limiting value of dispersed phase bulk modulus) and G_m (high frequency limiting value of matrix shear modulus) on the bulk moduli of composite. The shear relaxation time of the matrix is taken to be equal to the dilational relaxation time of the particulate phase. With the increase in K_d, K′ and K″ of the composite increase as shown in the top portion of Figure 13.3. The bulk moduli of the composite (K′ and K″) also increase with the increase in shear modulus of the matrix G_m as can be seen in the bottom portion of Figure 13.3.

Figure 13.4 shows the plots of storage and loss shear moduli of viscoelastic composite of Maxwellian components obtained from Equation 13.17 under the following conditions: $\phi = 0.10$, $G_m = 10^{10}$ Pa, $G_d = 10^7$ Pa, $\tau_{gm} = 100$ s, and $\tau_{gd} = 10^{-5}$ s. Clearly, the composite response is dominated by the matrix material

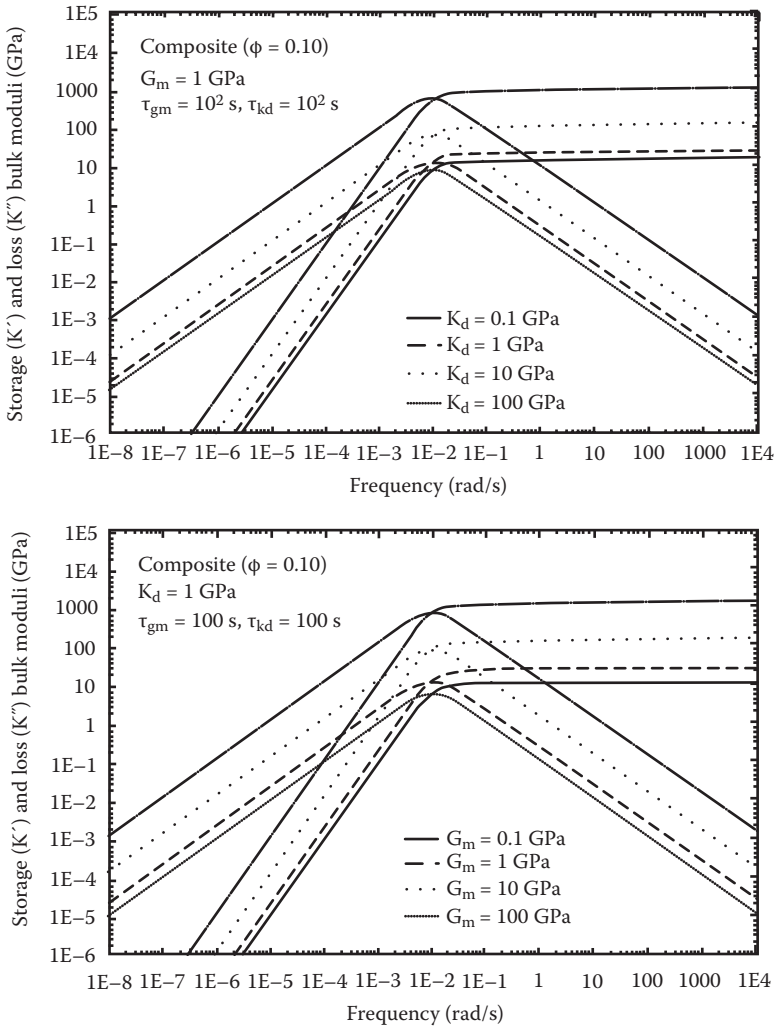

FIGURE 13.3 The effects of K_d (dispersed phase bulk modulus at high frequency) and G_m (matrix shear modulus at high frequency) on the bulk moduli of composite. (From Pal, R., *Rheology of Particulate Dispersions and Composites*. Boca Raton: CRC Press, 2007.)

properties; the storage modulus values are closer to that of the matrix. However, the loss modulus of the composite is dominated by the matrix only at low to moderate frequencies; at high frequencies, the composite loss modulus is dominated by the loss modulus of the softer material (dispersed phase in the present situation).

Figure 13.5 shows the effect of dispersed-phase shear relaxation time τ_{gd} on the shear moduli of composite. The data are generated from Equation 13.17 under the following conditions: $\phi = 0.10$, $G_m = G_d = 10^8$ Pa, $\tau_{gm} = 1$ s. The storage shear

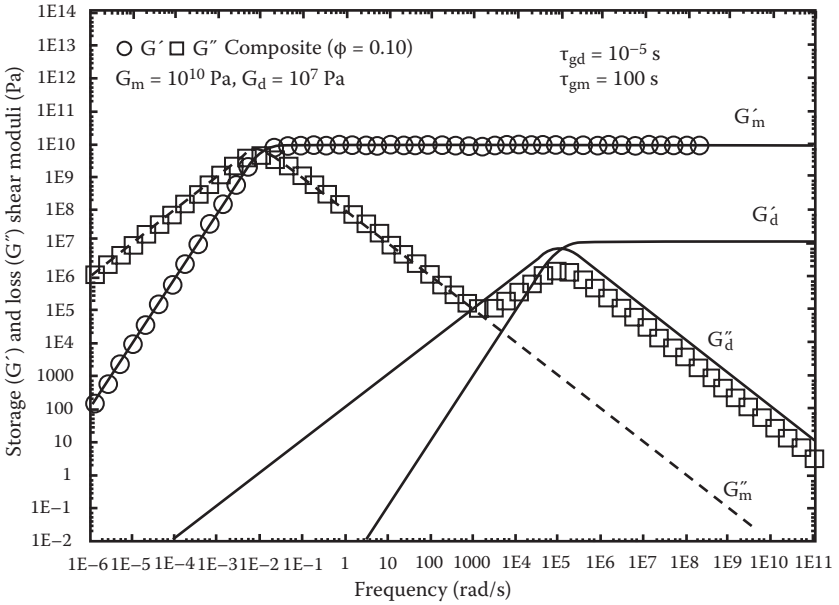

FIGURE 13.4 Shear moduli of composite composed of Maxwellian components. (From Pal, R., *Rheology of Particulate Dispersions and Composites*. Boca Raton: CRC Press, 2007.)

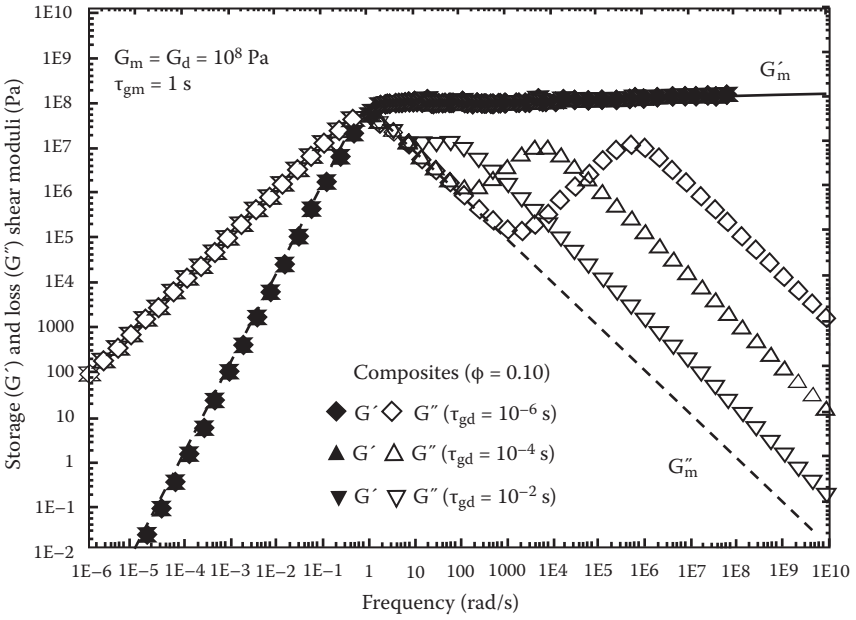

FIGURE 13.5 The effect of dispersed-phase relaxation time (τ_{gd}) on the shear moduli of composite. (From Pal, R., *Rheology of Particulate Dispersions and Composites*. Boca Raton: CRC Press, 2007.)

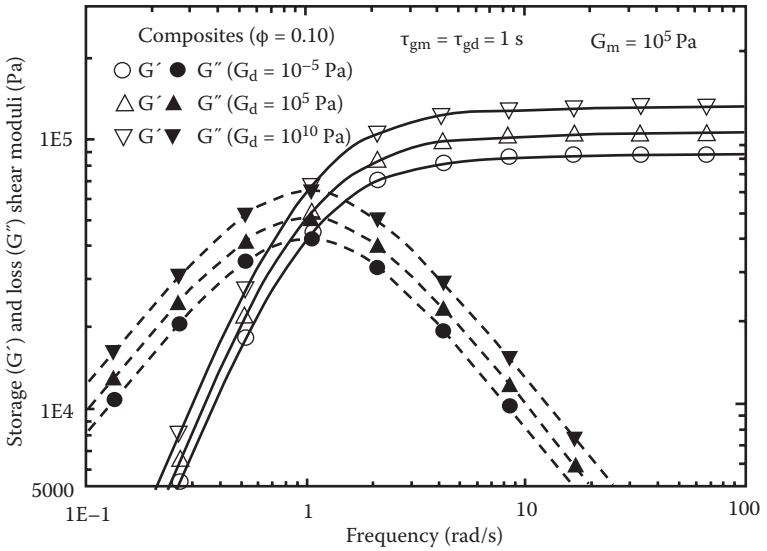

FIGURE 13.6 Effect of dispersed phase shear modulus (G_d) on the shear moduli of composite. (From Pal, R., *Rheology of Particulate Dispersions and Composites*. Boca Raton: CRC Press, 2007.)

modulus versus frequency behavior of the composite is dominated by the matrix phase for all values of τ_{gd}. At high frequencies, the loss shear modulus of the composite deviates from the loss shear modulus of the matrix phase. With the decrease in τ_{gd}, the deviation of composite loss modulus from the matrix loss modulus increases; the frequency at which the deviation occurs also increases with the decrease in τ_{gd}.

The effect of G_d (dispersed phase shear modulus) on the shear moduli of composite is shown in Figure 13.6 under the following conditions: $\phi = 0.10$, $G_m = 10^5$ Pa, $\tau_{gm} = \tau_{gd} = 1$ s. With the increase in G_d, the storage shear modulus versus frequency plot shifts toward higher modulus values. The loss modulus versus frequency plot also shifts toward higher modulus values. Thus, both storage and loss shear moduli increase with the increase in G_d.

13.4 COMPLEX MODULI OF CONCENTRATED COMPOSITES

In the preceding section, the models for complex moduli of *dilute* composites were discussed. In this section, the models are developed for the complex moduli of *concentrated* composites. For isotropic materials, only two out of the four mechanical properties or elastic constants (G, K, E, and ν) are independent. If two properties are fixed, the remaining two are automatically fixed. In the following discussion, complex shear modulus and complex Young's modulus are chosen to be independent. The dispersed phase and matrix of the composite are treated as viscoelastic materials.

13.4.1 Complex Shear Modulus of Concentrated Composites

For a *dilute* composite solid of spherical filler particles and incompressible matrix, the complex shear modulus (G*) in the linear viscoelastic region is given as [17]

$$G^* = G_m^* \left[1 + \frac{5}{2}\phi H \right] \tag{13.26}$$

in which H is given by

$$H = \frac{2(G_d^* - G_m^*)}{2G_d^* + 3G_m^*} \tag{13.27}$$

For *rigid* spherical particles $(G_d^* \to \infty)$, H is unity, and Equation 13.26 reduces to

$$G^* = G_m^* \left[1 + \frac{5}{2}\phi \right] \tag{13.28}$$

The dilute composite equation (Equation 13.26) can be extended to concentrated composites using a self-consistent treatment similar to the Lorentz sphere method in electricity [17]. The equation for nondilute composites is given as

$$G^* = G_m^* \left[\frac{1 + \frac{3}{2}\phi H}{1 - \phi H} \right] \tag{13.29}$$

where H is defined by Equation 13.27. In the limit $\phi \to 0$, Equation 13.29 reduces to Equation 13.28. Equation 13.29 is often referred to as the Palierne model. It follows from the Kerner equations (Equations 12.6 and 12.8) under the restriction of incompressible matrix ($\nu_m = 0.5$). Equation 13.29 generally underpredicts the values of the storage and loss moduli at high concentrations of dispersed phase. Furthermore, it does not show divergence of the modulus as $\phi \to \phi_m$, where ϕ_m is the maximum packing concentration of particles. At $\phi = \phi_m$, the shear modulus of composite of rigid particles is expected to become infinite.

Equations for the complex shear modulus of concentrated composites of spherical filler particles can be derived using the differential effective medium approach as follows [18]: A concentrated composite is considered to be obtained from an initial matrix by successively adding infinitesimally small quantities of filler particles to the system until the final volume fraction of dispersed phase is reached. At any arbitrary stage (i) of the process, the addition of an infinitesimal amount of particles leads to the next stage (i + 1). The composite of stage (i) is then treated as an equivalent effective medium which is homogeneous with respect to the new set of particles

added to reach stage (i + 1). The solution of a dilute composite system, that is, Equation 13.26), is applied to determine the incremental increase in complex shear modulus in going from stage (i) to stage (i + 1). The differential equation derived in this manner is integrated to obtain the final solution. A similar approach was utilized by Brinkman [19] and Roscoe [20] in derivation of a viscosity equation for solids-in-liquid suspensions. At stage (i) in the process of dispersed-phase addition, let the total volume of the composite be V_t, the dispersed-phase (particles) volume be V_d, the dispersed-phase volume fraction be ϕ, and the complex shear modulus of the composite be G*. Upon addition of dV_d to the stage (i) composite, the stage (i + 1) is reached where the dispersed-phase volume is $V_d + dV_d$, the total volume of the composite is $V_t + dV_d$, the dispersed-phase volume fraction is $\phi + d\phi$, and the complex shear modulus is G* + dG*. One can now apply Equation 13.26 to calculate the complex shear modulus of stage (i + 1) composite by treating the composite into which the new particles are added as an equivalent effective medium of complex shear modulus G*. Therefore,

$$G^* + dG^* = G^*\left[1 + \frac{5}{2}\left(\frac{dV_d}{V_t + dV_d}\right)\left(\frac{2G_d^* - 2G^*}{2G_d^* + 3G^*}\right)\right] \tag{13.30}$$

The change in the dispersed-phase volume fraction, $d\phi$, from stage (i) to stage (i + 1) can be written as

$$d\phi = \frac{\phi V_t + dV_d}{V_t + dV_d} - \phi \tag{13.31}$$

Equation 13.31, upon rearrangement gives

$$\frac{dV_d}{V_t + dV_d} = \frac{d\phi}{1 - \phi} \tag{13.32}$$

From Equations 13.30 and 13.32, one obtains

$$\frac{dG^*}{G^*\left[\dfrac{2G_d^* - 2G^*}{2G_d^* + 3G^*}\right]} = \frac{5}{2}\left(\frac{d\phi}{1 - \phi}\right) \tag{13.33}$$

Upon integrating Equation 13.33 with the limit $G^* \to G_m^*$ at $\phi = 0$, the following result is obtained

$$\ell n\left(\frac{G^*}{G_m^*}\right)-\frac{5}{2}\ell n\left(\frac{G_d^*-G^*}{G_d^*-G_m^*}\right)=-\frac{5}{2}\ell n(1-\phi) \tag{13.34}$$

Thus,

$$\left(\frac{G^*}{G_m^*}\right)\left(\frac{G^*-G_d^*}{G_m^*-G_d^*}\right)^{-2.5}=(1-\phi)^{-2.5} \tag{13.35}$$

This equation, referred to as model 1, reduces to the following equation for composites of rigid filler particles ($G_d^* \to \infty$):

$$G^*=G_m^*(1-\phi)^{-2.5} \tag{13.36}$$

Model 1 (Equation 13.35) assumes that the volume fraction of dispersed phase can reach unity as more and more particles are added to the composite. This is physically impossible, especially for composites of rigid filler particles. In reality, there exists an upper limit for ϕ, referred to as ϕ_m (maximum packing volume fraction of particles). The value of ϕ_m varies with the type of packing arrangement of particles. For example, it is 0.52 for simple cubic packing of uniform spheres; it is approximately 0.64 for random close packing and 0.74 for hexagonal close packing of uniform hard spheres. At $\phi = \phi_m$, the complex shear modulus of composite of rigid particles ($G_d^* \to \infty$) is expected to exhibit divergence. However, model 1 exhibits divergence in G* only at $\phi = 1.0$.

One possible way to account for the divergence in complex shear modulus at $\phi = \phi_m$ is to equate $dV_d/(V_t + dV_d)$ in Equation 13.32 to $d[\phi/(1 - \phi/\phi_m)]$, that is,

$$\frac{dV_d}{V_t+dV_d}=d\left[\frac{\phi}{1-\frac{\phi}{\phi_m}}\right] \tag{13.37}$$

Mooney [21] made a similar assumption in the derivation of his equation for the viscosity of concentrated suspensions. Thus,

$$\frac{dG^*}{G^*\left[\frac{2G_d^*-2G^*}{2G_d^*+3G^*}\right]}=\frac{5}{2}d\left[\frac{\phi}{1-\frac{\phi}{\phi_m}}\right] \tag{13.38}$$

Upon integration, Equation 13.38 gives

$$\left(\frac{G^*}{G_m^*}\right)\left(\frac{G^* - G_d^*}{G_m^* - G_d^*}\right)^{-2.5} = \exp\left[\frac{2.5\phi}{1 - \frac{\phi}{\phi_m}}\right] \tag{13.39}$$

This equation, referred to as model 2, reduces to the following equation for composite solids of rigid filler particles ($G_d^* \to \infty$):

$$G^* = G_m^* \exp\left[\frac{2.5\phi}{1 - \frac{\phi}{\phi_m}}\right] \tag{13.40}$$

Another way to account for divergence in G^* at $\phi = \phi_m$ for composites of rigid particles is to modify Equation 13.31 as

$$d\phi = \frac{\frac{\phi}{\phi_m} V_t + dV_d}{V_t + dV_d} - \frac{\phi}{\phi_m} \tag{13.41}$$

The justification for this modification is that the effective volume fraction of particles at stage (i), before new particles are added to reach stage (i + 1), is ϕ/ϕ_m (instead of ϕ), as some of the continuous phase fluid is immobilized between the particles when they are crowded. In other words, the free volume of continuous phase fluid available before new particles are added is only $(1 - \phi/\phi_m)$, instead of $1 - \phi$. Krieger and Dougherty [22], in the derivation of their equation for the viscosity of concentrated suspensions, made an equivalent assumption.

Equation 13.41, upon rearrangement, gives

$$\frac{dV_d}{V_t + dV_d} = \frac{d\phi}{1 - \frac{\phi}{\phi_m}} \tag{13.42}$$

Thus,

$$\frac{dG^*}{G^*\left[\frac{2G_d^* - 2G^*}{2G_d^* + 3G^*}\right]} = \frac{5}{2}\frac{d\phi}{\left(1 - \frac{\phi}{\phi_m}\right)} \tag{13.43}$$

Upon integrating Equation 13.43 with the limit $G^* \to G_m^*$ at $\phi = 0$, the following equation is obtained:

$$\left(\frac{G^*}{G_m^*}\right)\left(\frac{G^* - G_d^*}{G_m^* - G_d^*}\right)^{-2.5} = \left(1 - \frac{\phi}{\phi_m}\right)^{-2.5\phi_m} \tag{13.44}$$

This equation, referred to as model 3, reduces to the following equation for solid composites of rigid particles ($G_d^* \to \infty$):

$$G^* = G_m^*\left(1 - \frac{\phi}{\phi_m}\right)^{-2.5\phi_m} \tag{13.45}$$

It is interesting to note that in the case of composites of rigid spherical particles, models 1 to 3 (Equations 13.35, 13.39, and 13.44) predict the phase lag angle (δ) between stress and strain to be independent of ϕ, that is,

$$\tan\delta = \frac{G''}{G'} = \frac{G_m''}{G_m'} \tag{13.46}$$

Thus, the phase lag angle δ for composites is the same as that of the matrix.

Figures 13.7 through 13.10 compare model predictions with experimental data of Pal [18] obtained for composites of spherical glass beads and polymeric liquid. The experimental data consisting of phase-lag angle and complex shear modulus as functions of oscillation frequency of stress are plotted and compared with model predictions at various volume fractions of the dispersed phase. Further details regarding the nature and composition of composites and experimental measurements can be found in the original reference [18].

Equation 13.29 (Palierne equation) gives good predictions of the complex modulus only at low volume fractions of the dispersed phase ($\phi \le 0.176$). At higher values of ϕ, this equation underpredicts the complex modulus and the deviation increases with the increase in ϕ value.

Model 1 (Equation 13.35) is a slight improvement over Equation 13.29. At low volume fractions of the dispersed phase ($\phi \le 0.176$), model 1 gives good predictions of the complex modulus. At higher values of ϕ, model 1 under predicts the complex modulus although the predictions are somewhat better than those of Equation 13.29.

Model 2 (Equation 13.39) gives excellent predictions of the complex modulus over the full range of ϕ investigated in this work ($0 \le \phi \le 0.449$) provided that ϕ_m value of 0.74 is used.

Model 3 (Equation 13.44) also gives excellent predictions of the complex modulus over the full range of ϕ investigated, when ϕ_m value of 0.50 is used. While model 2 gives a high ϕ_m value of 0.74, corresponding to hexagonal close-packed arrangement

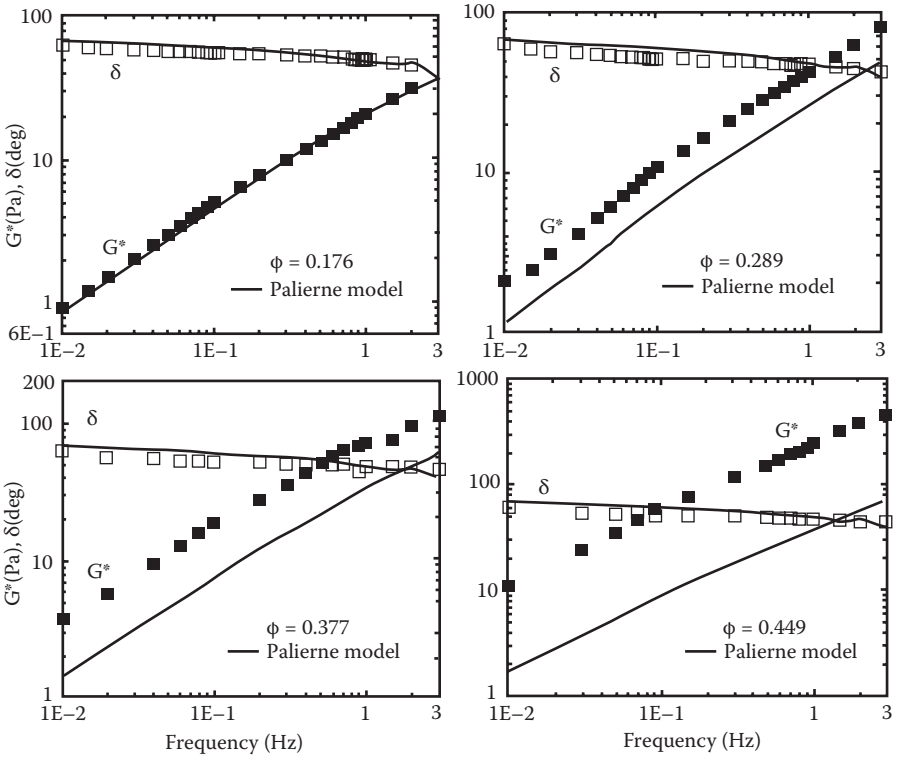

FIGURE 13.7 Comparison of complex shear modulus/phase lag angle data of suspensions with predictions of the Palierne model (Equation 13.29). (From Pal, R., *J. Colloid Interface Sci.* 245: 171–177, 2002.)

of uniform spheres, model 3 gives a significantly lower value of ϕ_m, corresponding to simple cubic packing of uniform spheres.

Interestingly, all models give good prediction of the phase lag angle (δ). As expected from the models, δ for composites is nearly the same as that of the matrix.

13.4.2 Complex Young's Modulus of Concentrated Composites

For an *infinitely dilute* dispersion of elastic solid particles (spherical in shape) in an elastic solid matrix, the exact expression for the Young's modulus is given as [23]

$$\frac{E}{E_m} = 1 + \left\{ \left[\frac{10(1-\nu_m^2)(1+\nu_m)E_d - 10(1-\nu_m^2)(1+\nu_d)E_m}{2(4-5\nu_d)(1+\nu_m)E_d + (7-5\nu_m)(1+\nu_d)E_m} \right] + \left[\frac{(1-\nu_m)(1-2\nu_m)E_d - (1-\nu_m)(1-2\nu_d)E_m}{(1+\nu_m)E_d + 2E_m(1-2\nu_d)} \right] \right\} \phi \qquad (13.47)$$

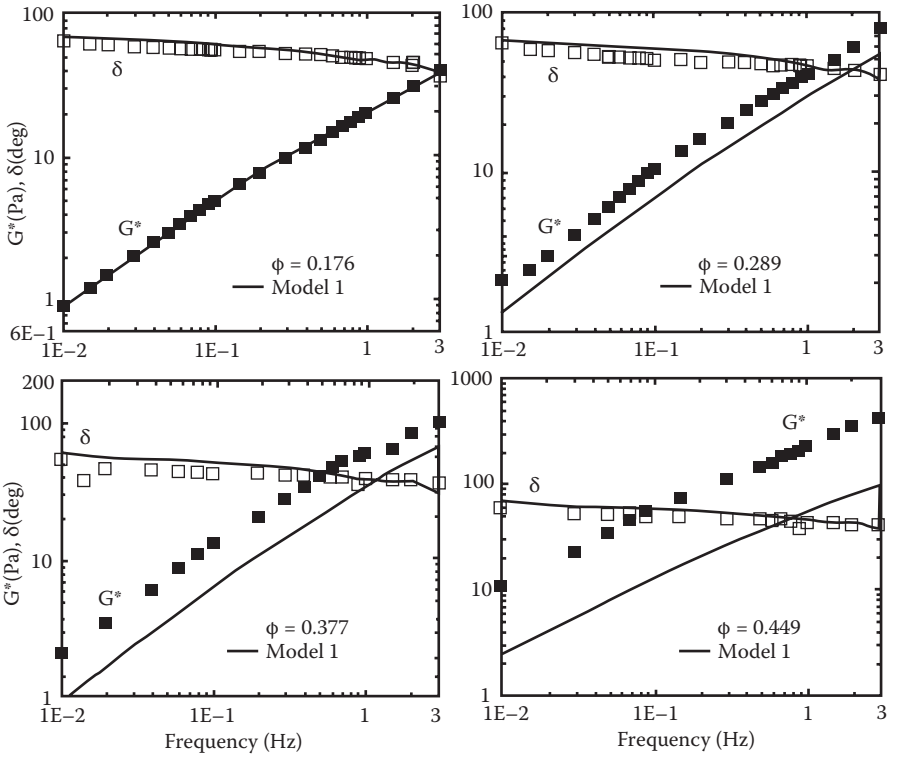

FIGURE 13.8 Comparison of complex shear modulus/phase lag angle data of suspensions with predictions of model 1 (Equation 13.35). (From Pal, R., *J. Colloid Interface Sci.* 245: 171–177, 2002.)

where E is Young's modulus of the composite, E_m is Young's modulus of the matrix, E_d is Young's modulus of the dispersed phase (particles), ν_m and ν_d are Poisson ratios of matrix and dispersed phase, respectively, and ϕ is the volume fraction of particles.

For incompressible composites ($\nu_m = 0.5$, $\nu_d = 0.5$), Equation 13.47 can be written as

$$E_r = \frac{E}{E_m} = 1 + \frac{5}{2}\left[\frac{2E_d - 2E_m}{2E_d + 3E_m}\right]\phi \tag{13.48}$$

Equation 13.47 is restricted to elastic composites (both dispersed phase and matrix as purely elastic materials). Using the elastic–viscoelastic correspondence principle, the complex Young's modulus of *dilute* viscoelastic composites of incompressible matrix and dispersed phases can be expressed as follows:

$$E^* = E_m^*\left[1 + \frac{5}{2}\left(\frac{2E_d^* - 2E_m^*}{2E_d^* + 3E_m^*}\right)\phi\right] \tag{13.49}$$

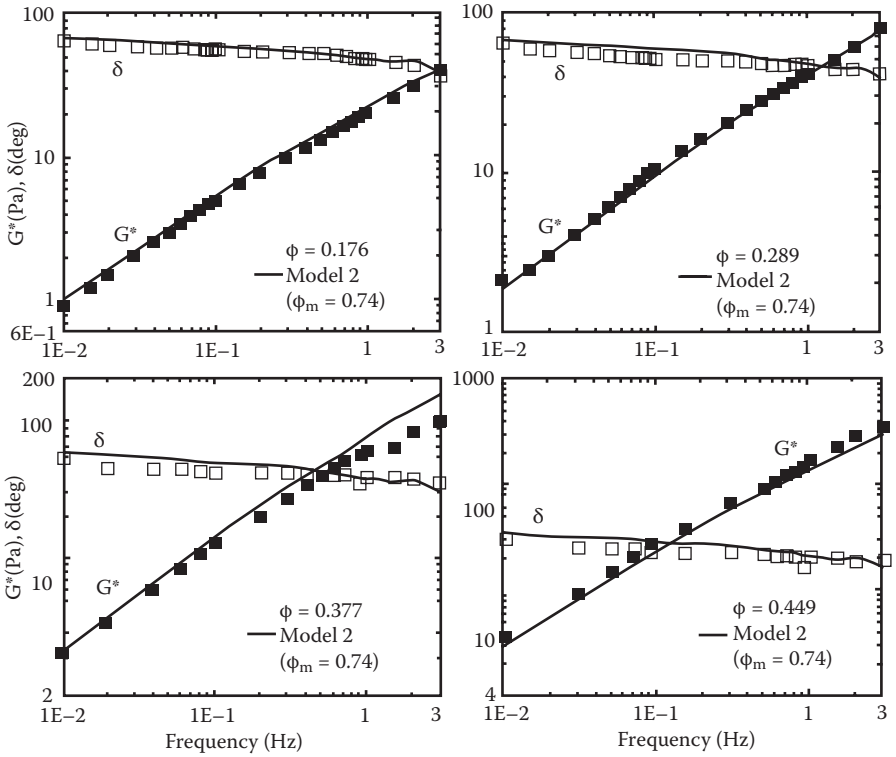

FIGURE 13.9 Comparison of complex shear modulus/phase lag angle data of suspensions with predictions of model 2 (Equation 13.39). (From Pal, R., *J. Colloid Interface Sci.* 245: 171–177, 2002.)

where E* is the complex Young's modulus of the composite, E_d^* is the complex Young's modulus of the dispersed phase, and E_m^* is the complex Young's modulus of the matrix. Note that the complex Young's modulus (E*) is defined as $E^* = E' + jE''$ where E′ is the storage Young's modulus, E″ is the loss Young's modulus, and j is the imaginary number $\left(\sqrt{-1}\right)$.

For composites of Maxwellian matrix and dispersed phase, E_d^* and E_m^* are given as

$$E_d^* = \frac{j\omega\tau_d E_d}{1 + j\omega\tau_d} = E_d' + jE_d'' \tag{13.50}$$

$$E_m^* = \frac{j\omega\tau_m E_m}{1 + j\omega\tau_m} = E_m' + jE_m'' \tag{13.51}$$

where τ_d and τ_m are the relaxation times of dispersed phase and matrix, respectively, E_d and E_m are the high-frequency limiting values of the Young's moduli of

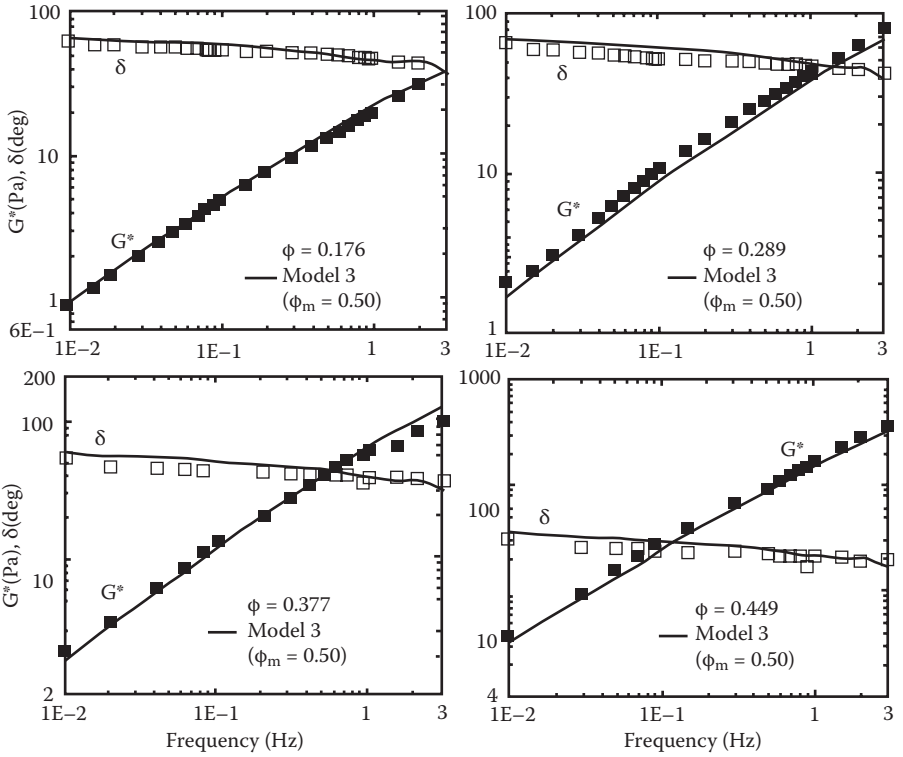

FIGURE 13.10 Comparison of complex shear modulus/phase lag angle data of suspensions with predictions of model 3 (Equation 13.44). (From Pal, R., *J. Colloid Interface Sci*. 245: 171–177, 2002.)

dispersed phase and matrix, respectively, ω is frequency of oscillation of stress or strain, E'_d and E'_m are the storage Young's moduli of the dispersed phase and matrix, respectively, and E''_d and E''_m are the loss Young's moduli of the dispersed phase and matrix, respectively.

While Equation 13.49 describes all the important features of the viscoelastic behavior of composites very well, it is restricted to infinitely dilute systems. It fails to predict the correct values of storage and loss Young's moduli at finite concentrations of dispersed phase. The expressions for the complex Young's modulus (E*) of concentrated composites can be developed using a differential scheme along with the solution of an infinitely dilute system, that is, Equation 13.49. Using this differential scheme, Pal [24] developed the following four equations for the complex Young's modulus (E*) of concentrated composites:

$$\left(\frac{E^*}{E_m^*}\right)\left(\frac{E^* - E_d^*}{E_m^* - E_d^*}\right)^{-2.5} = \exp(2.5\phi) \tag{13.52}$$

$$\left(\frac{E^*}{E_m^*}\right)\left(\frac{E^*-E_d^*}{E_m^*-E_d^*}\right)^{-2.5}=(1-\phi)^{-2.5} \tag{13.53}$$

$$\left(\frac{E^*}{E_m^*}\right)\left(\frac{E^*-E_d^*}{E_m^*-E_d^*}\right)^{-2.5}=\exp\left[\frac{2.5\,\phi}{1-\dfrac{\phi}{\phi_m}}\right] \tag{13.54}$$

$$\left(\frac{E^*}{E_m^*}\right)\left(\frac{E^*-E_d^*}{E_m^*-E_d^*}\right)^{-2.5}=\left(1-\frac{\phi}{\phi_m}\right)^{-2.5\phi_m} \tag{13.55}$$

13.5 CONCLUDING REMARKS

The linear viscoelastic behavior of composites is presented. Complex shear and Young's moduli models for dilute and concentrated composites are developed and discussed. Where possible, the model predictions are compared with the available experimental data.

REFERENCES

1. Christensen, R.M. 1979. *Mechanics of Composite Materials*. New York: John Wiley & Sons.
2. Sohn, M.S., K.S. Kim, S.H. Hong, and J.K. Kim. 2003. Dynamic mechanical properties of particle-reinforced EPDM composites. *J. Appl. Polym. Sci.* 87: 1595–1601.
3. Brinson, L.C. and W.S. Lin. 1998. Comparison of micromechanics methods for effective properties of multiphase viscoelastic composites. *Composite Struct.* 41: 353–367.
4. Landel, R.F. and T.L. Smith. 1961. Viscoelastic properties of rubberlike composite propellants and filled elastomers. *ARS J.* 31: 599–608.
5. Hashin, Z. 1965. Viscoelastic behavior of heterogeneous media. *Appl. Mech. Trans. ASME* 32E: 630–636.
6. Hashin, Z. 1970. Complex moduli of viscoelastic composites—I. General theory and application to particulate composites. *Int. J. Solids Struct.* 6: 539–552.
7. Lewis, T. and L. Nielsen. 1970. Dynamic mechanical properties of particulate filled composites. *J Appl. Poly. Sci.* 14: 1449–1471.
8. Mete, P. and N.D. Alberola. 1996. Prediction of the viscoelastic behaviour of particulate composites: Effect of mechanical coupling. *Composites Sci. Tech.* 56: 849–853.
9. Gibiansky, L.V. and R. Lakes. 1997. Bounds on the complex bulk and shear moduli of a two-phase viscoelastic composite. *Mech. Mat.* 25: 79–95.
10. Nikkeski, S., M. Kudo, and T. Masuki. 1998. Dynamic viscoelastic properties and thermal properties of powder-epoxy resin composites. *J. Appl. Poly. Sci.* 69: 2593–2598.
11. Liang, J.Z., R.K.Y. Li, and S.C. Tjong. 1999. Effects of glass bead content and surface treatment on viscoelasticity of filled polypropylene/elastomer hybrid composites. *Polym. Inter.* 48: 1068–1072.

12. Drozdov, A.D. 1999. Modeling viscoelastic response of particulate polymeric composites with high volume fractions of fillers. *Math. Comp. Model.* 29: 11–25.
13. Liang, J.Z., R.K.Y. Li, and S.C. Tjong. 2000. Effects of glass bead size and content on the viscoelasticity of filled polypropylene composites. *Polym. Testing* 19: 213–220.
14. Privalko, V.P., V.F. Shumsky, E.G. Privalko, V.M. Karaman, R. Walter, K. Friedrich, M.Q. Zhang, and M.Z. Rong. 2002. Viscoelasticity and flow behavior of irradiation grafted nano-inorganic particle filled polypropylene composites in the melt state. *Sci. Tech. Adv. Mater.* 3: 111–116.
15. Hashin, Z. 1970. Complex moduli of viscoelastic composites. II: Fiber reinforced materials. *Int. J. Solids Struct.* 6: 797–807.
16. Pal, R. 2007. *Rheology of Particulate Dispersions and Composites*. Boca Raton: CRC Press.
17. Palierne, J.F. 1990. Linear rheology of viscoelastic emulsions with interfacial-tension. *Rheol. Acta* 29: 204–214.
18. Pal, R. 2002. Complex shear modulus of concentrated suspensions of solid spherical particles. *J. Colloid Interface Sci.* 245: 171–177.
19. Brinkman, H.C. 1952. The viscosity of concentrated suspensions and solutions. *J. Chem. Phys.* 20: 571.
20. Roscoe, R. 1952. The viscosity of suspensions of rigid spheres. *Br. J. Appl. Phys*. 3: 267–269.
21. Mooney, M. 1951. The viscosity of a concentrated suspension of spherical particles. *J. Colloid Sci.* 6: 162–170.
22. Krieger, I.M. and T.J. Dougherty. 1959. A mechanism for non-Newtonian flow in suspensions of rigid particles. *Trans. Soc. Rheol*. 3: 137–152.
23. Pal, R. 2005. New models for effective Young's modulus of particulate composites. *Composites B* 36: 513–523.
24. Pal, R. 2005. Modeling viscoelastic behavior of particulate composites with high volume fraction of filler. *Mater. Sci. Eng. A* 412: 71–77.

Section IV

Transport Properties of Composites

Heat Transfer in Composites

14 General Introduction to Heat Transfer

When two objects at different temperatures are brought in thermal contact (not necessarily physical contact) with each other, energy flows from one object to the other. This energy, which flows by virtue of temperature difference between the two objects or due to temperature gradient within the same object, is called "heat." Thus, heat is a form of energy that comes into play only in the presence of temperature gradient. Heat has meaning only during the transfer process. Once it has flowed into a body, it manifests as internal energy of the body. Because heat is relevant only during the transfer process, it is often referred to as "energy in transit" (energy in the process of being transferred). In accordance with the second law of thermodynamics, heat flows in the direction of decreasing temperature (from high temperature to low temperature). A good understanding of heat transfer is important in a number of applications involving composite materials.

14.1 DIFFERENT MODES OF HEAT TRANSFER

Heat transfer from one body to another (or from one location to another within the same medium) can take place by conduction, convection, radiation, or any combination of these three modes of heat transfer.

14.1.1 Conductive Heat Transfer

The flow of heat in a stationary medium (solid or fluid) when there exists a temperature gradient in the medium is referred to as "heat conduction" or "conductive heat transfer." As an example, heat transfer in a plane solid wall when the two sides of the wall are exposed to different temperatures is due to conduction. The important features of conductive heat transfer are as follows: presence of material medium, the material medium is stationary (no bulk motion of matter is involved), and there exists a temperature gradient in the medium.

14.1.1.1 Rate Equation for Heat Conduction

For one-dimensional heat conduction in the x-direction, the rate of heat transfer per unit area perpendicular to the direction of heat flow is given by the following Fourier law of heat conduction:

$$q_x'' = -k\frac{dT}{dx} \tag{14.1}$$

TABLE 14.1
Thermal Conductivity (W/m.K) of Some Materials at Room Temperature

Material	k (W/m.K)
Metallic solids	Silver: 420
	Copper: 390
Nonmetallic solids	Glass: 1
	Limestone: 1.5
Liquids	Water: 0.6
	Engine oil: 0.15
Gases	Air: 0.026
	Steam: 0.018

where q_x'' is the heat flux (W/m^2) defined as the rate of heat transfer per unit area perpendicular to the direction of heat transfer, dT/dx is the temperature gradient (K/m), and k is the material property called thermal conductivity (W/m.K). The thermal conductivity is a measure of the ability of the material to conduct heat. For a prescribed temperature gradient, the conduction heat flux increases with the increase in thermal conductivity. Thus, good conductors of heat have high values of k.

The total rate of heat transfer q is given by

$$q = -kA\frac{dT}{dx} \tag{14.2}$$

where A is the area of heat transfer, area perpendicular to the direction of heat flow. The unit of q is W or J/s.

The thermal conductivity varies widely from one material to another (see Table 14.1). Gases are poor conductors of heat with low values of k whereas metallic solids are excellent conductors of heat with high values of k. In general, the thermal conductivity of a solid is larger than that of a liquid, which in turn has a larger k than that of a gas. The thermal conductivity of a solid may be four orders of magnitude larger than that of a gas.

The thermal conductivity of materials (solids, liquids, and gases) varies significantly with temperature. For example, the thermal conductivity of gases is proportional to the square root of temperature. However, the pressure dependence of thermal conductivity is usually weak.

14.1.1.2 Mechanisms of Heat Conduction

In gases, heat is conducted by random motion and collision of molecules. The molecules of a gas are in ceaseless random motion even though there is no bulk motion. In a high-temperature region, the gas molecules possess higher kinetic energy as compared with the molecules in a low-temperature region. Due to random motion of molecules, some molecules from a high-temperature region reach a region of low temperature and give up part of their kinetic energy through collisions with lower energy molecules. In a similar random process, some molecules from

a low-temperature region reach a region of high temperature and receive energy through collisions with high-energy molecules. Thus, there occurs a net transfer of energy from a high-temperature region to a low-temperature region due to a *diffusion process* (random motion and collision of molecules). The mechanism of heat conduction in liquids is similar to that of gases, that is, random motion and collision of molecules. However, the molecules in liquids are more closely spaced, and as a result, intermolecular forces exert a strong influence on random motion and energy exchange in the collision process.

Heat conduction in solids occurs by two different mechanisms: (1) random motion and collision of free electrons and (2) transmission of vibrational energy in the lattice structure. The "free" electrons (also called "electron gas") are electrons loosely bound to the atoms and are relatively free to move through the lattice structure of the solid. In the high-temperature region, the free electrons possess higher kinetic energy as compared with electrons in a low-temperature region. The free electrons transfer energy from a high-temperature region to a low-temperature region much like the gas molecules, that is, by random motion and collisions. This mechanism of heat conduction is dominant in metals (solids and liquid). In nonmetallic solids, heat conduction occurs mainly due to lattice vibrations. The atoms or molecules of a solid are bound to each other by a number of bonds that act like springs. The atoms/molecules in the high-temperature region of the solid vibrate more vigorously as compared with the atoms/molecules in the low-temperature region. The vibrations are passed from the high-temperature region to a low-temperature region of the lattice structure through the springlike motion of the bonds. The energy associated with lattice vibrations (lattice waves) is quantized, and the quantized unit of vibrational energy is called "phonons." Thus, one can consider lattice waves as a continuous stream of packets of energy called phonons.

The thermal conductivity of isotropic solids can be expressed as

$$k = k_e + k_{ph} \tag{14.3}$$

where k_e is the contribution of electron gas and k_{ph} is the contribution of lattice vibrations (phonons). In metallic solids, the dominant mechanism of heat conduction is electron gas and $k \approx k_e$. In nonmetallic solids, heat conduction is mainly due to transmission of phonons through the lattice and $k \approx k_{ph}$.

14.1.2 Convective Heat Transfer

Convective heat transfer involves fluid motion in or around a solid object that is at a temperature different from that of the fluid. Thus, the flow of heat between a solid surface and a fluid moving adjacent to the solid surface, when the solid surface and the fluid are at different temperatures, is referred to as "heat convection" or "convective heat transfer."

Heat transfer by convection involves two mechanisms operating simultaneously—energy transfer due to random motion and collision of molecules (diffusion of energy) and superimposed upon the molecular motion is energy transfer by advection (advection means transport of a quantity, which, in the present case, is energy,

by bulk fluid motion). Near the contact (solid) surface, the fluid is nearly stationary. Consequently, the heat is transferred by conduction only (random motion and collision of molecules). Away from the solid boundary, both mechanisms are important; that is, energy transfer occurs due to bulk motion (advection) as well as molecular phenomenon (diffusion).

Convection heat transfer can be classified into two broad groups based on the driving means for fluid flow. When the fluid motion is caused by external means, such as by a fan or a pump, we speak of *forced convection*. When fluid flow is induced by buoyancy forces, which arise from density differences caused by temperature variations in the fluid, we have "free" or "natural" convection.

Convection heat transfer could further involve *external* and *internal* flows. In external flows, fluid flows around a body that is completely submerged in it. The flow is unbounded flow. In internal flows, fluid flows in tubes or channels. Fluid is confined within the channel boundaries. The flow is bounded flow, surrounded by the solid channel boundaries.

14.1.2.1 Rate Equation for Convection

The rate equation for convective heat transfer is known as *Newton's law of cooling*. For *external* flows, the Newton law of cooling is given as

$$q_s'' = h(T_s - T_\infty) \tag{14.4}$$

where q_s'' is the local heat flux normal to the solid surface (also called surface heat flux), h is the local heat transfer coefficient (W/m^2.K), T_s is the local surface (solid) temperature, and T_∞ is the free stream temperature of the fluid. The heat transfer coefficient depends on several factors such as geometry of the solid surface, nature of flow, and thermodynamic properties.

For *internal* flows, the Newton law of cooling is given as

$$q_s'' = h(T_s - T_m) \tag{14.5}$$

where T_m is the mean or average temperature of the fluid (averaged over the cross section at any axial location).

The total rate of heat transfer q may be obtained by integrating the local flux over the entire surface as

$$q = \int_{A_s} q_s'' dA_s = \int_{A_s} h(T_s - T_c)\, dA_s \tag{14.6}$$

where T_c is characteristic temperature of the fluid (T_∞ in the case of external flow and T_m in the case of internal flow) and A_s is the area of heat transfer (contact area between the fluid and solid).

The typical values of the heat transfer coefficient h (W/m^2.K) are summarized in Table 14.2.

TABLE 14.2
Typical Values of Heat Transfer Coefficient

Free Convection, Typical h Values ($W/m^2.K$)	Forced Convection, Typical h Values ($W/m^2.K$)	Boiling/Condensation (Convection with Phase Change), Typical h Values ($W/m^2.K$)
Gases 2–25	Gases 25–250	2500–100,000
Liquids 50–100	Liquids 50–20,000	

14.1.3 Radiative Heat Transfer

14.1.3.1 Nature of Thermal Radiation

All matter emits energy by virtue of having a nonzero absolute temperature. This energy, emitted in the form of electromagnetic waves or photons due to nonzero absolute temperature, is called *thermal radiation*. Thermal radiation is emitted by matter due to changes in the vibrational, rotational, and electronic states of constituent molecules or atoms.

Thermal radiation covers a broad range of wavelengths: approximately 0.1 to 1000 μm. It includes part of the UV region (0.1 to 0.38 μm), visible region (0.38 to 0.76 μm), and infrared region (0.76 to 1000 μm). Thermal radiation follows the Planck law of electromagnetic radiation:

$$e = h\,\upsilon = h\,c/\lambda \tag{14.7}$$

where e is the energy associated with photon, h is Planck's constant ($= 6.626 \times 10^{-34}$ J.s), and υ is the frequency of radiation ($\upsilon = c/\lambda$, where λ is the wave length and c is the speed of light, 3×10^8 m/s in vacuum). The higher the temperature of the object, the smaller is the wave length of the emitted thermal radiation and the more energetic is the radiation. Thus, thermal radiation effect is important at high temperatures.

The rate at which energy is emitted by a surface per unit area is called the emissive power (E). The emissive power of an ideal (black) surface is given by the Stefan–Boltzmann law:

$$E_b = \sigma T_s^4 \tag{14.8}$$

where E_b is the emissive power of a black surface, T_s is the absolute temperature of the surface, and σ is the Stefan–Boltzmann constant ($= 5.67 \times 10^{-8}$ $W/(m^2.K^4)$. Note that E_b is the total emissive power of a black surface, integrated over all the wavelengths.

Black surfaces are surfaces that absorb all of the incident thermal radiation (none of the incident radiation is reflected or transmitted; all is absorbed). Thus, black surfaces are perfect absorbers of thermal radiation. Any material that absorbs visible light appears as "visually black." However, this concept is extended to a much broader thermal band in heat transfer. A "thermally black" surface is one that absorbs all of the incident thermal radiation. A surface that appears black to the eye may not

be thermally black. For example, a surface may absorb all visible radiation and may reflect thermal radiation outside the visible band. Interestingly, snow is considered to be thermally black, as it absorbs a major portion of the thermal radiation band and reflects the visible band.

Black surfaces are also perfect emitters of thermal radiation. The emissive power of a black surface is the highest as compared with any nonblack surface at the same temperature. No real surface behaves like an ideal black surface. The emissivity (ε) of a real surface is defined as

$$\varepsilon = E/E_b \tag{14.9}$$

where E is the emissive power of the real surface and E_b is the emissive power of a black (ideal) surface. For an ideal (black) surface, ε = 1.

14.1.3.2 Thermal Radiation Exchange

When two objects (surfaces) at different temperatures are placed in view of each other, net transfer of energy occurs between the objects due to exchange of thermal radiation. The object at a higher temperature cools down, and the object at a lower temperature gets heated up. This phenomenon whereby energy transfer between objects at different temperatures occurs due to exchange of thermal radiation is called radiative heat transfer.

As an example, consider two large black parallel surfaces of equal area (A) facing each other. Let the absolute temperature of surface 1 be T_1 and the absolute temperature of surface 2 be T_2. Let the rate at which energy *leaving* surface 1 and *intercepted* (seen) by surface 2 be $q_{1\to2}$. In general, the radiation leaving surface 1 will include both emitted and reflected radiations. Also, not all the radiation leaving surface 1 will reach surface 2. However, in the present example, the radiation leaving surface 1 includes only the emitted radiation (black surface), and all the radiation leaving surface 1 is intercepted by surface 2 (parallel surfaces). From the Stefan–Boltzmann law,

$$q_{1\to2} = \sigma T_1^4 A \tag{14.10}$$

The rate at which energy *leaving* surface 2 and *intercepted* (seen) by surface 1; that is, $q_{2\to1}$, can be determined in a similar manner. It is given as

$$q_{2\to1} = \sigma T_2^4 A \tag{14.11}$$

Thus, the net rate of radiation heat transfer *from* black surface 1 to black surface 2 is

$$q_{1\to2,\text{net}} = q_{1\to2} - q_{2\to1} = \sigma\left(T_1^4 - T_2^4\right)A \tag{14.12}$$

14.1.4 Summary

In summary, Table 14.3 compares the key features of the three modes of heat transfer. Convection is generally considered to be the most efficient mode of heat transfer.

TABLE 14.3
Comparison of the Three Modes of Heat Transfer

Conduction	Convection	Radiation
Needs matter	Needs matter	Does not need matter
Energy transfer a molecular phenomenon (diffusion process)	Energy transfer by bulk motion (advection) as well as diffusion	Energy transfer by photons (electromagnetic waves)
No bulk motion of matter	Bulk motion of matter needed	No bulk motion of matter
Temperature difference/gradient needed	Temperature difference/ gradient needed	Temperature difference between surfaces needed

It is followed by conduction whereas radiation is considered to be the least efficient and slowest among the three modes of heat transfer.

14.2 ENERGY BALANCE

In engineering problems, it is often necessary to apply energy balance to a control volume. Control volume (CV) is a region of space (within the material medium) bounded by a control surface. For *nonflow* systems, only energy and no mass can enter or leave the control volume. Energy can enter the control volume through the control surface in two ways: heat transfer and work transfer. However, for *flow* systems, both mass and energy can enter or leave the control volume. Now in addition to heat and work transfer, energy can enter or leave the control volume in a direct manner by *advection* process whereby the mass entering and leaving the control volume carries energy with it.

Consider a *stationary* medium with nonuniform temperature distribution where only heat enters or leaves the control volume through *conduction* and there is no work transfer involved. For a cubical control volume, heat enters the control volume through the x, y, and z faces and leaves through the $x + \Delta x$, $y + \Delta y$, and $z + \Delta z$ faces. Heat is also generated inside the control volume through means such as passage of electric current through the medium. Thus, energy balance can be written as

$$\left\{\begin{matrix}\text{Rate at which heat}\\ \text{enters the CV}\end{matrix}\right\} - \left\{\begin{matrix}\text{Rate at which heat}\\ \text{leaves the CV}\end{matrix}\right\} + \left\{\begin{matrix}\text{Rate at which heat is generated}\\ \text{within the CV}\end{matrix}\right\}$$
$$= \left\{\begin{matrix}\text{Rate at which internal energy is stored or}\\ \text{accumulated inside the CV}\end{matrix}\right\} \tag{14.13}$$

Let us now determine each term of the energy balance equation:

$$\left\{\begin{matrix}\text{Rate at which heat}\\ \text{enters the CV}\end{matrix}\right\} = q''_x\big|_x(\Delta y)(\Delta z) + q''_y\big|_y(\Delta x)(\Delta z) + q''_z\big|_z(\Delta y)(\Delta x) \quad (14.14)$$

$$\left\{\begin{matrix}\text{Rate at which heat}\\ \text{leaves the CV}\end{matrix}\right\} = q''_x\big|_{x+\Delta x}(\Delta y)(\Delta z) + q''_y\big|_{y+\Delta y}(\Delta x)(\Delta z) + q''_z\big|_{z+\Delta z}(\Delta y)(\Delta x) \quad (14.15)$$

$$\left\{\begin{matrix}\text{Rate at which heat is generated}\\ \text{within the CV}\end{matrix}\right\} = \dot{q}(\Delta x\Delta y\Delta z) \quad (14.16)$$

$$\left\{\begin{matrix}\text{Rate at which internal energy is stored or}\\ \text{accumulated inside the CV}\end{matrix}\right\} = \rho(\Delta x\Delta y\Delta z)\frac{\partial U}{\partial t} \quad (14.17)$$

where q''_x, q''_y, and q''_z are the x, y, and z components of heat flux vector; $\dot{q}$ is the rate of heat generation per unit volume; ρ is density of the medium; and U is internal energy per unit mass.

Thus, the energy balance could be written as

$$\begin{aligned}&-\left[\left(q''_x\big|_{x+\Delta x} - q''_x\big|_x\right)(\Delta y)(\Delta z)\right] - \left[\left(q''_y\big|_{y+\Delta y} - q''_y\big|_y\right)(\Delta x)(\Delta z)\right]\\ &-\left[\left(q''_z\big|_{z+\Delta z} - q''_z\big|_z\right)(\Delta y)(\Delta x)\right] + [\dot{q}(\Delta x\Delta y\Delta z)] = \rho(\Delta x\Delta y\Delta z)\frac{\partial U}{\partial t}\end{aligned} \quad (14.18)$$

If we divide this equation by $(\Delta x\Delta y\Delta z)$ and take the limits $\Delta x\to 0$, $\Delta y\to 0$, $\Delta z\to 0$, the following result is obtained:

$$-\left[\frac{\partial q''_x}{\partial x} + \frac{\partial q''_y}{\partial y} + \frac{\partial q''_z}{\partial z}\right] + \dot{q} = \rho\frac{\partial U}{\partial t} \quad (14.19)$$

This energy balance is applicable to stationary systems, with or without chemical reactions. In the absence of chemical reactions (constant composition) and assuming constant density (incompressible material), one can express the time derivative of U as

$$\frac{\partial U}{\partial t} = c_v\frac{\partial T}{\partial t} = c_p\frac{\partial T}{\partial t} \quad (14.20)$$

where c_p and c_v are constant-pressure and constant-volume heat capacities, respectively. Note that $c_p = c_v$ for incompressible materials. Thus, the energy balance gives

$$-\nabla \cdot \vec{q}'' + \dot{q} = \rho c_p \frac{\partial T}{\partial t} \tag{14.21}$$

where $\vec{q}''$ is the heat flux vector.

SUPPLEMENTAL READING

Bejan, A. 1993. *Heat Transfer*, New York: John Wiley & Sons.

Bergman, T.L., A.S. Levine, F.P. Incropera, and D.P. Dewitt. 2011. *Fundamentals of Heat and Mass Transfer*, 7th Edition, New York: John Wiley & Sons.

Bird, R.B., W.E. Stewart, and E.N. Lightfoot. 2007. *Transport Phenomena*, 2nd Edition, New York: John Wiley & Sons.

Cengel, Y.A. 2007. *Heat and Mass Transfer*, 3rd Edition, New York: McGraw-Hill.

Holman, J.P. 2009. *Heat Transfer*, 10th Edition, New York: McGraw-Hill.

Keith, F. and M.S. Bohn. 1993. *Principles of Heat Transfer*, 5th Edition, St. Paul: West Publishing Co.

Welty, J.R., C.E. Wicks, R.E. Wilson, and G.L. Rorrer, 2008. *Fundamentals of Momentum, Heat, and Mass Transfer*, 5th Edition, New York: John Wiley & Sons.

15 Fundamentals of Conductive Heat Transfer

Conductive heat transfer is commonly encountered in engineering applications of composite materials. In some applications, the objective is to reduce the rate of conductive heat loss and in others the aim is to enhance the rate of conductive heat transfer. Thus a good understanding of conductive heat transfer is required in the design and applications of composite materials. In this chapter, the fundamental aspects of conductive heat transfer are reviewed.

15.1 HEAT FLUX VECTOR AND TEMPERATURE GRADIENT

The heat flux vector $\vec{q}''$ gives the rate of heat transfer per unit area (W/m^2) perpendicular to the direction of heat flow. It is expressed as

$$\vec{q}'' = q_x''\hat{i} + q_y''\hat{j} + q_z''\hat{k} \tag{15.1}$$

where q_x'', q_y'', q_z'' are the components of heat flux vector in x, y, and z directions, respectively. q_x'' is the rate of heat transfer in the x-direction per unit area normal to x, q_y'' is the rate of heat transfer in the y-direction per unit area normal to y, and q_z'' is the rate of heat transfer in the z-direction per unit area normal to z.

The temperature gradient ∇T at any point in the medium can be expressed as

$$\nabla T = \frac{\partial T}{\partial x}\hat{i} + \frac{\partial T}{\partial y}\hat{j} + \frac{\partial T}{\partial z}\hat{k} \tag{15.2}$$

where $\partial T/\partial x$ is the temperature gradient in the x-direction, $\partial T/\partial y$ is the temperature gradient in the y-direction, and $\partial T/\partial z$ is the temperature gradient in the z-direction.

For one-dimensional heat conduction in the x-direction,

$$\begin{aligned} &q_x'' \neq 0; \quad q_y'' = 0; \quad q_z'' = 0 \\ &T = T(x); \quad \frac{\partial T}{\partial x} \neq 0; \quad \frac{\partial T}{\partial y} = 0; \quad \frac{\partial T}{\partial z} = 0 \end{aligned} \tag{15.3}$$

For two-dimensional heat conduction in the x- and y-directions,

$$\begin{aligned} &q_z'' = 0; \quad q_x'' \neq 0; \quad q_y'' \neq 0 \\ &T = T(x, y); \quad \frac{\partial T}{\partial x} \neq 0; \quad \frac{\partial T}{\partial y} \neq 0; \quad \frac{\partial T}{\partial z} = 0 \end{aligned} \tag{15.4}$$

For three-dimensional heat conduction, temperature is a function of all three space coordinates and all three heat flux components are nonzero.

$$q''_x \neq 0; \quad q''_y \neq 0; \quad q''_z \neq 0$$
$$T = T(x,y,z); \quad \frac{\partial T}{\partial x} \neq 0; \quad \frac{\partial T}{\partial y} \neq 0; \quad \frac{\partial T}{\partial z} \neq 0 \tag{15.5}$$

15.2 FOURIER'S LAW OF HEAT CONDUCTION

Fourier's law of heat conduction states that the local heat flux vector $\vec{q}''$ at any point in the material is proportional to the local temperature gradient ∇T and is given as

$$\vec{q}'' = -\bar{\bar{k}} \cdot \nabla T \tag{15.6}$$

where $\bar{\bar{k}}$ is the thermal conductivity tensor of the material. The minus sign in Fourier's law of heat conduction is a consequence of the second law of thermodynamics which requires that heat must flow in the direction of decreasing temperature. The thermal conductivity tensor is given as

$$\bar{\bar{k}} = \sum_i \sum_j k_{ij} \hat{\delta}_i \hat{\delta}_j = \begin{pmatrix} k_{11} & k_{12} & k_{13} \\ k_{21} & k_{22} & k_{23} \\ k_{31} & k_{32} & k_{33} \end{pmatrix} \tag{15.7}$$

In the case of an isotropic medium, $k_{ij} = 0$ if $i \neq j$ and $k_{ii} = k$, that is, the nondiagonal components are zero and the diagonal components are all equal. Thus, for isotropic media, $\bar{\bar{k}} = k\bar{\bar{\delta}}$ ($\bar{\bar{\delta}}$ is a unit tensor) and Fourier's law of heat conduction simplifies to

$$\vec{q}'' = -k\bar{\bar{\delta}} \cdot \nabla T = -k\nabla T \tag{15.8}$$

where k is the thermal conductivity of the material. Note that for isotropic materials, the heat flux vector $\vec{q}''$ at any location is parallel to ∇T and hence, normal to the isothermal surface passing through that location. In the case of anisotropic materials, $\vec{q}''$ at any location is not parallel to ∇T and therefore, the direction of $\vec{q}''$ is not generally normal to the isothermal surface passing through that location. Table 15.1 presents Fourier's law of heat conduction in rectangular, cylindrical, and spherical coordinate systems.

TABLE 15.1
Fourier's Law of Heat Conduction in Different Coordinate Systems

Coordinate System	General Form	Component Form (For the Given Coordinate System)
Cartesian	$\vec{q}'' = -k\nabla T$	$\vec{q}'' = q_x''\hat{i} + q_y''\hat{j} + q_z''\hat{k} = -k\left[\left(\frac{\partial T}{\partial x}\right)\hat{i} + \left(\frac{\partial T}{\partial y}\right)\hat{j} + \left(\frac{\partial T}{\partial z}\right)\hat{k}\right]$
Cylindrical	$\vec{q}'' = -k\nabla T$	$\vec{q}'' = q_r''\hat{r} + q_\theta''\hat{\theta} + q_z''\hat{z} = -k\left[\left(\frac{\partial T}{\partial r}\right)\hat{r} + \frac{1}{r}\left(\frac{\partial T}{\partial \theta}\right)\hat{\theta} + \left(\frac{\partial T}{\partial z}\right)\hat{z}\right]$
Spherical	$\vec{q}'' = -k\nabla T$	$\vec{q}'' = q_r''\hat{r} + q_\theta''\hat{\theta} + q_\phi''\hat{\phi} = -k\left[\left(\frac{\partial T}{\partial r}\right)\hat{r} + \frac{1}{r}\left(\frac{\partial T}{\partial \theta}\right)\hat{\theta} + \frac{1}{r\sin\theta}\left(\frac{\partial T}{\partial \phi}\right)\hat{\phi}\right]$

15.3 GENERAL HEAT CONDUCTION EQUATION

The energy balance in a stationary medium gives the following equation (see Chapter 14):

$$-\nabla \cdot \vec{q}'' + \dot{q} = \rho c_p \frac{\partial T}{\partial t} \tag{15.9}$$

where $\dot{q}$ is the rate of heat generation per unit volume, ρ is the density, and c_p is the heat capacity. Substitution of the expression for heat flux vector $\vec{q}''$ from Fourier's law of heat conduction into this equation gives

$$\nabla \cdot (k\nabla T) + \dot{q} = \rho c_p \frac{\partial T}{\partial t} \tag{15.10}$$

$$\frac{\partial}{\partial x}\left(k\frac{\partial T}{\partial x}\right) + \frac{\partial}{\partial y}\left(k\frac{\partial T}{\partial y}\right) + \frac{\partial}{\partial z}\left(k\frac{\partial T}{\partial z}\right) + \dot{q} = \rho c_p \frac{\partial T}{\partial t} \tag{15.11}$$

where it is assumed that the medium is isotropic. This is the most general form of the heat conduction equation. It describes the temperature variation with space coordinates and time. When the thermal conductivity k is constant, this equation further simplifies to

$$\nabla^2 T + \frac{\dot{q}}{k} = \frac{1}{\alpha}\frac{\partial T}{\partial t} \tag{15.12}$$

where α is the thermal diffusivity (m^2/s) of material, defined as $k/(\rho c_p)$. In the absence of thermal energy generation, the heat conduction reduces to

$$\nabla^2 T = \frac{1}{\alpha}\frac{\partial T}{\partial t} \tag{15.13}$$

Table 15.2 presents the heat conduction equation in rectangular, cylindrical, and spherical coordinate systems.

15.3.1 Boundary and Initial Conditions

In order to solve the heat conduction equation, the boundary and initial conditions that characterize the given heat transfer configuration must be specified. Because the heat conduction equation is second order in spatial coordinates, two boundary conditions are required for each coordinate. Only one initial condition is required as the equation is first order in time. Some examples of the boundary conditions in one-dimensional heat conduction problems are as follows:

1. The temperature at the boundary (located at $x = x_o$) of the conducting medium is held constant, that is, at $x = x_o$, $T = T_o$. This type of boundary condition is called *Dirichlet* boundary condition or boundary condition of *first kind.*
2. The heat flux at the boundary (located at $x = x_o$) of the conducting medium is held constant, that is, at $x = x_o$, $q''_x\big|_{x=x_o} = q''_o$. This type of boundary condition is called *Newmann* boundary condition or boundary condition of *second kind*. A special case of this boundary condition is $q''_x\big|_{x=x_o} = q''_o = 0$. No heat passes through the boundary surface located at $x = x_o$. This type of boundary condition is often referred to as *adiabatic* boundary condition.
3. Convection occurs at the boundary (located at $x = x_o$) of the conducting medium. Thus

$$-k\left(\frac{\partial T}{\partial x}\right)_{x=0} = h\left(T_\infty - T\big|_{x=0}\right) \tag{15.14}$$

where h is the heat transfer coefficient and T_∞ is the free stream temperature of the fluid. This type of boundary condition is called boundary condition of *third kind.*

An example of the *initial condition* is the specification of temperature of the medium at the start of the time interval of interest, such as at $t = t_o$, $T = T_i$. Another initial condition of interest is the specification of heat flux at the boundary of the medium at the start of the time interval of interest.

TABLE 15.2
Heat Conduction Equation in Rectangular, Cylindrical, and Spherical Coordinate Systems

Coordinate System	Heat Diffusion Equation (General Form)	Heat Diffusion Equation (For the Given Coordinate System)
Cartesian	$\nabla\cdot(k\nabla T)+\dot{q}=\rho C_P\dfrac{\partial T}{\partial t}$	$\dfrac{\partial}{\partial x}\left(k\dfrac{\partial T}{\partial x}\right)+\dfrac{\partial}{\partial y}\left(k\dfrac{\partial T}{\partial y}\right)+\dfrac{\partial}{\partial z}\left(k\dfrac{\partial T}{\partial z}\right)+\dot{q}=\rho C_P\dfrac{\partial T}{\partial t}$
	When k = constant	When k = constant
	$\nabla^2 T+\dfrac{\dot{q}}{k}=\dfrac{1}{\alpha}\left(\dfrac{\partial T}{\partial t}\right)$	$\dfrac{\partial^2 T}{\partial x^2}+\dfrac{\partial^2 T}{\partial y^2}+\dfrac{\partial^2 T}{\partial z^2}+\dfrac{\dot{q}}{k}=\dfrac{1}{\alpha}\dfrac{\partial T}{\partial t}$
Cylindrical	$\nabla\cdot(k\nabla T)+\dot{q}=\rho C_P\dfrac{\partial T}{\partial t}$	$\dfrac{1}{r}\dfrac{\partial}{\partial r}\left(kr\dfrac{\partial T}{\partial r}\right)+\dfrac{1}{r^2}\dfrac{\partial}{\partial\theta}\left(k\dfrac{\partial T}{\partial\theta}\right)+\dfrac{\partial}{\partial z}\left(k\dfrac{\partial T}{\partial z}\right)+\dot{q}=\rho C_P\dfrac{\partial T}{\partial t}$
	When k = constant	When k = constant
	$\nabla^2 T+\dfrac{\dot{q}}{k}=\dfrac{1}{\alpha}\left(\dfrac{\partial T}{\partial t}\right)$	$\dfrac{1}{r}\dfrac{\partial}{\partial r}\left(r\dfrac{\partial T}{\partial r}\right)+\dfrac{1}{r^2}\dfrac{\partial^2 T}{\partial\theta^2}+\dfrac{\partial^2 T}{\partial z^2}+\dfrac{\dot{q}}{k}=\dfrac{1}{\alpha}\dfrac{\partial T}{\partial t}$
Spherical	$\nabla\cdot(k\nabla T)+\dot{q}=\rho C_P\dfrac{\partial T}{\partial t}$	$\dfrac{1}{r^2}\dfrac{\partial}{\partial r}\left(kr^2\dfrac{\partial T}{\partial r}\right)+\dfrac{1}{r^2\sin^2\theta}\dfrac{\partial}{\partial\phi}\left(k\dfrac{\partial T}{\partial\phi}\right)+\dfrac{1}{r^2\sin\theta}\dfrac{\partial}{\partial\theta}\left(k\sin\theta\dfrac{\partial T}{\partial\theta}\right)+\dot{q}=\rho C_P\dfrac{\partial T}{\partial t}$
	When k = constant	When k = constant
	$\nabla^2 T+\dfrac{\dot{q}}{k}=\dfrac{1}{\alpha}\left(\dfrac{\partial T}{\partial t}\right)$	$\dfrac{1}{r^2}\dfrac{\partial}{\partial r}\left(r^2\dfrac{\partial T}{\partial r}\right)+\dfrac{1}{r^2\sin^2\theta}\dfrac{\partial^2 T}{\partial\phi^2}+\dfrac{1}{r^2\sin\theta}\dfrac{\partial}{\partial\theta}\left(\sin\theta\dfrac{\partial T}{\partial\theta}\right)+\dfrac{\dot{q}}{k}=\dfrac{1}{\alpha}\dfrac{\partial T}{\partial t}$

15.4 STEADY-STATE HEAT CONDUCTION

Under steady-state condition, the temperature distribution in an isotropic medium of constant k is governed by the following Poisson equation:

$$\nabla^2 T + \frac{\dot{q}}{k} = 0 \tag{15.15}$$

In the absence of thermal energy generation, this equation reduces to the following Laplace equation:

$$\nabla^2 T = 0 \tag{15.16}$$

15.4.1 One-Dimensional Steady-State Heat Conduction

Assuming no thermal energy generation and the material to be isotropic of constant k, the Laplace equation can be expressed in the three coordinate systems as follows:

Cartesian coordinates: For heat flow in the x-direction, the Laplace equation gives

$$\frac{d^2T}{dx^2} = 0 \tag{15.17}$$

Cylindrical coordinates: For heat flow in the radial direction, the Laplace equation gives

$$\frac{d}{dr}\left(r\frac{dT}{dr}\right) = 0 \tag{15.18}$$

Spherical coordinates: For heat flow in the radial direction, the Laplace equation gives

$$\frac{d}{dr}\left(r^2\frac{dT}{dr}\right) = 0 \tag{15.19}$$

For a slab (solid wall) of uniform thickness, Equation 15.17 gives the following linear temperature profile:

$$\frac{T - T_1}{T_2 - T_1} = \frac{x}{L} \tag{15.20}$$

where T_1 is the temperature of the slab at x = 0, T_2 is the temperature of the slab at x = L, and L is the slab thickness. The heat flux and the heat transfer rate through the slab are given as follows:

$$q''_x = -k\frac{dT}{dx} = \frac{k}{L}(T_1 - T_2) \tag{15.21}$$

$$q = q''_x A = \frac{kA}{L}(T_1 - T_2) \tag{15.22}$$

For a cylindrical shell with boundary conditions, $T = T_1$ at $r = r_1$ (inner cylindrical surface) and $T = T_2$ at $r = r_2$ (outer cylindrical surface), Equation 15.18 gives the following temperature profile:

$$\frac{T - T_1}{T_2 - T_1} = \frac{\ln(r/r_1)}{\ln(r_2/r_1)} \tag{15.23}$$

Thus, the temperature distribution is logarithmic in cylindrical shells. The heat flux and the heat transfer rate through the cylindrical shell are given as follows:

$$q''_r = -k\frac{dT}{dr} = -\frac{k}{r}\frac{(T_2 - T_1)}{\ln(r_2/r_1)} \tag{15.24}$$

$$q = q''_r(2\pi rL) = \frac{2\pi kL}{\ln(r_2/r_1)}(T_1 - T_2) \tag{15.25}$$

where L is the length of the cylindrical shell. Note that the heat flux in a cylindrical shell is not constant. The heat flux decreases with the increase in the radial position r as the area of heat transfer increases.

For a spherical shell with boundary conditions, $T = T_1$ at $r = r_1$ (inner spherical surface) and $T = T_2$ at $r = r_2$ (outer spherical surface), Equation 15.19 gives the following temperature profile:

$$\frac{T - T_1}{T_2 - T_1} = \frac{1}{\left(\frac{1}{r_2} - \frac{1}{r_1}\right)}\left(\frac{1}{r} - \frac{1}{r_1}\right) \tag{15.26}$$

The heat flux and the heat transfer rate through the spherical shell are given as follows:

$$q_r'' = -k\frac{dT}{dr} = -\frac{k}{r^2}\frac{(T_2 - T_1)}{\left(\frac{1}{r_1} - \frac{1}{r_2}\right)} \tag{15.27}$$

$$q = q_r''(4\pi r^2) = \frac{4\pi k}{\left(\frac{1}{r_2} - \frac{1}{r_1}\right)}(T_2 - T_1) \tag{15.28}$$

Note that at steady state, the total heat transfer rate is constant but the heat flux decreases with the increase in the radial position r due to an increase in the heat transfer area. Table 15.3 summarizes the results for one-dimensional steady-state heat conduction in different geometries.

TABLE 15.3
One-Dimensional Steady-State Heat Conduction in Different Geometries

Boundary Conditions	Temperature Distribution	Heat Flux (q'')	Heat Transfer Rate (q)
	Plane Wall		
at $x = x_1$, $T = T_1$	$T = c_1x + c_2$	$q_x'' =$ constant	$q =$ constant
at $x = x_2$, $T = T_2$	$\frac{T - T_1}{T_2 - T_1} = \frac{x - x_1}{x_2 - x_1}$	$q_x'' = -k\frac{(T_2 - T_1)}{(x_2 - x_1)}$	$q = -kA\frac{(T_2 - T_1)}{(x_2 - x_1)}$
	Cylindrical Shell		
at $r = r_1$, $T = T_1$	$T = c_1 \ln r + c_2$	q_r'' decreases with r	$q =$ constant
at $r = r_2$, $T = T_2$	$\frac{T - T_1}{T_2 - T_1} = \frac{\ln\left(\frac{r}{r_1}\right)}{\ln\left(\frac{r_2}{r_1}\right)}$	$q_r'' = -\frac{k}{r}\frac{(T_2 - T_1)}{\ln\left(\frac{r_2}{r_1}\right)}$	$q = -\frac{2\pi kL(T_2 - T_1)}{\ln\left(\frac{r_2}{r_1}\right)}$
	Spherical Shell		
at $r = r_1$, $T = T_1$	$T = \frac{c_1}{r} + c_2$	q_r'' decreases with r	$q =$ constant
at $r = r_2$, $T = T_2$	$\frac{T - T_1}{T_2 - T_1} = \frac{\left(\frac{1}{r} - \frac{1}{r_1}\right)}{\left(\frac{1}{r_2} - \frac{1}{r_1}\right)}$	$q_r'' = -\frac{k}{r^2}\frac{(T_2 - T_1)}{\left(\frac{1}{r_1} - \frac{1}{r_2}\right)}$	$q = -\frac{4\pi k(T_2 - T_1)}{\left(\frac{1}{r_1} - \frac{1}{r_2}\right)}$

15.4.2 Analogy between Heat Flow and Electric Current Flow

There exists a close analogy between one-dimensional steady-state heat conduction (without thermal energy generation) and electric current flow. According to Ohm's law,

$$\frac{I}{A} = \sigma\left(\frac{\Delta V}{L}\right) \tag{15.29}$$

where I is current, A is cross-section area of conductor, σ is electrical conductivity, ΔV is voltage drop across the conductor, and L is the length/thickness of the conductor. Compare this Ohm's law with the following Fourier's law of heat conduction for planar objects:

$$\frac{q}{A} = k\left(\frac{\Delta T}{L}\right) \tag{15.30}$$

Thus, the heat flow rate q is analogous to electric current I, thermal conductivity k is analogous to electric conductivity σ, and temperature drop ΔT is analogous to voltage drop ΔV. The two laws could also be expressed in terms of resistances as

$$I = \frac{\Delta V}{R} \quad \text{where } R = L/(\sigma A) \tag{15.31}$$

$$q = \frac{\Delta T}{R} \quad \text{where } R = L/(kA) \tag{15.32}$$

Thus, thermal resistance of an object is given as follows:

$$R = \frac{\text{thickness}}{(\text{thermal conductivity})(\text{characteristic area of heat transfer})} \tag{15.33}$$

For *cylindrical* shells, the thickness is $(r_2 - r_1)$ and the characteristic area of heat transfer is the log mean area of inner and outer cylindrical surfaces, given as

$$A_{lm} = \frac{A_2 - A_1}{\ln\left(\frac{A_2}{A_1}\right)} = \frac{2\pi L(r_2 - r_1)}{\ln\left(\frac{r_2}{r_1}\right)} \tag{15.34}$$

Therefore, the thermal resistance of cylindrical shells is

$$R = \frac{\ln\left(\frac{r_2}{r_1}\right)}{2\pi kL} \tag{15.35}$$

For *spherical* shells, the thickness is $(r_2 - r_1)$ and the characteristic area of heat transfer is the geometric mean area of inner and outer surfaces, given as

$$A_{gm} = \sqrt{A_1 A_2} = 4\pi r_1 r_2 \tag{15.36}$$

Therefore, the thermal resistance of spherical shells is

$$R = \frac{(r_2 - r_1)}{4\pi k r_1 r_2} \tag{15.37}$$

15.4.3 Temperature-Dependent Thermal Conductivity

The thermal conductivity of a material is generally a weak function of pressure but can vary significantly with temperature. Thus, we need to account for temperature variation of k. As k is not constant, the appropriate heat conduction equation is as follows:

$$\nabla \cdot (k\nabla T) + \dot{q} = \rho c_p \frac{\partial T}{\partial t} \tag{15.38}$$

Assuming steady state and no thermal energy generation, this equation simplifies to

$$\nabla \cdot (k\nabla T) = 0 \tag{15.39}$$

Consider one-dimensional steady-state heat conduction in a planar object in the x direction. The above equation reduces to

$$\frac{d}{dx}\left(k\frac{dT}{dx}\right) = 0 \tag{15.40}$$

Upon integration,

$$k\frac{dT}{dx} = C_1 \tag{15.41}$$

With further integration,

$$\int_{T_1}^{T_2} k(T)\, dT = C_1 \int_{x_1}^{x_2} dx \tag{15.42}$$

$$C_1 = \frac{\int_{T_1}^{T_2} k(T)\,dT}{(x_2 - x_1)} \tag{15.43}$$

Thus, the heat flux becomes

$$q''_x = -k\frac{dT}{dx} = -\frac{\int_{T_1}^{T_2} k(T)\,dT}{(x_2 - x_1)} \tag{15.44}$$

For constant k case, the heat flux is

$$q''_x = -k\frac{dT}{dx} = -\frac{k(T_2 - T_1)}{(x_2 - x_1)} \tag{15.45}$$

Upon comparing the above two expressions, one can define a mean thermal conductivity as

$$k_m = \frac{\int_{T_1}^{T_2} k(T)\,dT}{(T_2 - T_1)} \tag{15.46}$$

The heat flux in terms of mean k is

$$q''_x = -k\frac{dT}{dx} = -\frac{k_m(T_2 - T_1)}{(x_2 - x_1)} \tag{15.47}$$

This is the same expression as that obtained in the constant k case, with k replaced by k_m. Thus, one can apply the same formulae for heat flux and thermal resistance obtained earlier for one-dimensional steady-state heat conduction in different coordinate systems provided that the mean thermal conductivity (as defined in Equation 15.46) is used. However, the temperature distribution expressions obtained for constant k cases are no longer valid. For example, the temperature distribution in a planar object with constant k is linear but with variable k (say, k = a + bT) it is nonlinear as shown below:

$$aT + (b/2)T^2 = C_1x + C_2 \tag{15.48}$$

where C_1 and C_2 are integration constants.

15.4.4 Composite Systems with and without Contact Resistance

In many applications involving conductive heat transfer, conduction takes place in a multilayer composite system consisting of several parallel layers of different materials joined together. If thermal contact between two layers of different materials is *perfect*, the interfacial boundary conditions are

(1) Continuity of temperature at the interface, that is,

$$T_I = T_{II} \text{ at the interface} \tag{15.49}$$

(2) Continuity of heat flux at the interface, that is,

$$q_I'' = q_{II}'' \text{ at the interface} \tag{15.50}$$

$$-k_I \frac{dT_I}{dx}\bigg|_{\text{interface}} = -k_{II} \frac{dT_{II}}{dx}\bigg|_{\text{interface}} \tag{15.51}$$

The total thermal resistance for two layers in series with perfect thermal contact is given as follows:

$$R_{\text{total}} = R_I + R_{II} = \frac{L_I}{k_I A} + \frac{L_{II}}{k_{II} A} \tag{15.52}$$

where L_I and L_{II} are the thicknesses of the layers. The thermal contact between two layers of different materials is *imperfect* when the materials do not fit tightly together. As a consequence, some voids or pockets of air/gas are formed at the interface between the two layers. An imperfect contact results in an interfacial resistance to heat transfer called "thermal contact resistance, R_C''," defined as

$$R_C'' = \frac{T_I - T_{II}}{q''_{\text{interface}}} \tag{15.53}$$

where $T_I - T_{II}$ is the temperature drop across the interface and $q''_{\text{interface}}$ is the heat flux at interface. Note that the temperature distribution is not continuous at the interface although the heat flux is still continuous, that is

$$T_I \neq T_{II} \text{ at the interface} \tag{15.54}$$

$$q_I'' = q_{II}'' = q''_{\text{interface}} \text{ at the interface} \tag{15.55}$$

The interfacial or contact resistance is mainly a function of surface roughness, pressure keeping the two surfaces in contact, interfacial fluid material, and interface temperatures. At the interface, heat transfer occurs through conduction at the contact points and through convection and radiation across the trapped interfacial fluid.

The contact resistance R_C'' is defined on a unit interfacial-area basis. It has the SI units of m^2.K/W and is typically of the order of 10^{-4} m^2.K/W. The total contact resistance R_C is defined as

$$R_C = \frac{R_C''}{A_{interface}} \tag{15.56}$$

where $A_{interface}$ is the interface area and R_C has SI units of K/W.

The total thermal resistance for two layers in series with *imperfect* thermal contact is as follows:

$$R_{total} = R_I + R_C + R_{II} = \frac{L_I}{k_I A} + \frac{R_C''}{A_{interface}} + \frac{L_{II}}{k_{II} A} \tag{15.57}$$

15.4.5 Conduction with Convection at the Boundaries

Consider a solid plane wall of thickness L and thermal conductivity k. On one side of the wall, there is present a hot fluid with a free stream temperature of $T_{\infty,1}$, and on other side of the wall, there is present a cold fluid with free stream temperature of $T_{\infty,2}$. This problem has three thermal resistances in series: convective resistance on the hot fluid side ($1/h_1A$), conductive wall resistance (L/kA), and convective resistance on the cold fluid side ($1/h_2A$). Thus, the total thermal resistance is

$$R_{total} = \frac{1}{h_1 A} + \frac{L}{kA} + \frac{1}{h_2 A} \tag{15.58}$$

where A is the heat transfer area normal to the direction of heat flow, and h_1 and h_2 are heat transfer coefficients on the two sides. The heat transfer rate q through this system is as follows:

$$q = \frac{T_{\infty,1} - T_{\infty,2}}{R_{total}} = \frac{T_{\infty,1} - T_{\infty,2}}{\frac{1}{h_1 A} + \frac{L}{kA} + \frac{1}{h_2 A}} \tag{15.59}$$

The surface temperatures at the two sides of the solid wall are given by

$$T_{\infty,1} - T_{s,1} = q\left(\frac{1}{h_1 A}\right) \tag{15.60}$$

$$T_{s,2} - T_{\infty,2} = q\left(\frac{1}{h_2 A}\right) \tag{15.61}$$

In such combined conductive–convective problems, one can define an overall heat transfer coefficient (U) as

$$q = UA(T_{\infty,1} - T_{\infty,2}) = \frac{T_{\infty,1} - T_{\infty,2}}{R_{total}} \tag{15.62}$$

Thus, the overall heat transfer coefficient is given as

$$U = \frac{1}{R_{total}A} = \frac{1}{\left(\frac{1}{h_1} + \frac{L}{k} + \frac{1}{h_2}\right)} \tag{15.63}$$

As another example, consider a hot fluid flowing in a pipe. Let the pipe wall be a composite consisting of two layers in perfect thermal contact, the inner layer of metal with $k = k_I$ and the outer layer of insulating material with $k = k_{II}$. The mean temperature of the fluid inside the pipe at any given axial position is T_m. The free stream temperature of the cold fluid outside the composite pipe wall is T_∞. Now, there are four thermal resistors in series: inside convective resistance, conductive metal-wall resistance, conductive insulation resistance, and outside convective resistance. Thus, the total resistance is

$$R_{total} = \frac{1}{h_i A_i} + \frac{\ln(r_2/r_1)}{2\pi k_I L} + \frac{\ln(r_3/r_2)}{2\pi k_{II} L} + \frac{1}{h_o A_o} \tag{15.64}$$

where h_i and h_o are the inside and outside heat transfer coefficients, respectively, A_i is the inside area of the cylindrical geometry (equal to $2\pi r_1 L$), and A_o is the outside area of the cylindrical geometry (equal to $2\pi r_3 L$). The heat transfer rate q for this system is

$$q = \frac{T_m - T_\infty}{R_{total}} = \frac{T_m - T_\infty}{\frac{1}{h_i A_i} + \frac{\ln(r_2/r_1)}{2\pi k_I L} + \frac{\ln(r_3/r_2)}{2\pi k_{II} L} + \frac{1}{h_o A_o}} \tag{15.65}$$

For a planar geometry, there is no ambiguity about the heat transfer area in the definition of the overall heat transfer coefficient. For radial geometries (cylindrical or spherical), however, one has to specify the area on which the overall heat transfer coefficient is based. One can define the overall heat transfer coefficient either on the basis of inside heat transfer area (U_i) or on the basis of outside heat transfer area (U_o). Thus,

$$q = \frac{T_m - T_\infty}{R_{total}} = U_i A_i (T_m - T_\infty) = U_o A_o (T_m - T_\infty) \tag{15.66}$$

Upon comparison of different terms of the above expression,

$$U_o A_o = U_i A_i = \frac{1}{R_{total}} \tag{15.67}$$

Thus,

$$U_o = \frac{1}{\frac{1}{h_i}\left(\frac{A_o}{A_i}\right) + A_o \frac{\ln(r_2/r_1)}{2\pi k_I L} + A_o \frac{\ln(r_3/r_2)}{2\pi k_{II} L} + \frac{1}{h_o}} \tag{15.68}$$

$$U_i = \frac{1}{\frac{1}{h_i} + A_i \frac{\ln(r_2/r_1)}{2\pi k_I L} + A_i \frac{\ln(r_3/r_2)}{2\pi k_{II} L} + \frac{1}{h_o}\left(\frac{A_i}{A_o}\right)} \tag{15.69}$$

15.4.6 Heat Conduction with Thermal Energy Generation

Heat conduction with thermal energy generation is important industrially. In many applications, thermal energy is generated by passage of electric current through the medium.

Consider a plane solid wall of thickness 2L, maintained at same temperatures on both sides, that is,

$$T = T_S \text{ at } x = +L \tag{15.70}$$

$$T = T_S \text{ at } x = -L \tag{15.71}$$

where x is the distance from the center of the wall. The rate of thermal energy generation within the wall per unit volume is $\dot{q}$. The temperature distribution in the wall can be obtained by solving the following Poisson equation (assuming k is constant):

$$\frac{d^2T}{dx^2} + \frac{\dot{q}}{k} = 0 \tag{15.72}$$

The solution of this equation subject to the given boundary conditions is

$$T - T_S = \frac{\dot{q}L^2}{2k}\left(1 - \left(\frac{x}{L}\right)^2\right) \tag{15.73}$$

The temperature distribution is symmetric about the midplane with a maximum temperature at x = 0 (midplane). The maximum temperature is

$$T_{max} = \frac{\dot{q}L^2}{2k} + T_S \tag{15.74}$$

Thus, the temperature distribution can be expressed in dimensionless form as

$$\frac{T - T_S}{T_{max} - T_S} = 1 - \left(\frac{x}{L}\right)^2 \tag{15.75}$$

The heat flux at any location is

$$q''_x = -k\frac{dT}{dx} = k\left(\frac{2x}{L^2}(T_{max} - T_S)\right) \tag{15.76}$$
$$= \dot{q}x$$

The heat transfer rates at the two sides of the wall are

$$q\big|_{x=-L} = -\dot{q}\left(\frac{V}{2}\right) \tag{15.77}$$

$$q\big|_{x=+L} = \dot{q}\left(\frac{V}{2}\right) \tag{15.78}$$

where V is the volume of the wall. Thus the total heat generated within the wall leaves the wall from the two sides equally.

A similar analysis could be carried out for radial systems with heat generation. For example, consider a long, solid cylinder with heat generation. Heat generation in the cylinder could be due to passage of current. Heat generation within a solid cylindrical object is also encountered in nuclear reactors consisting of cylindrical fuel elements.

The Poisson equation for this case of heat conduction in radial direction is as follows:

$$\frac{1}{r}\frac{d}{dr}\left(r\frac{dT}{dr}\right) + \frac{\dot{q}}{k} = 0 \tag{15.79}$$

This equations needs to be solved subject to the following boundary conditions:

$$T = T_S \text{ at } r = R \tag{15.80}$$

$$\frac{dT}{dr}\Big|_{r=0} = 0 \tag{15.81}$$

where R is the radius of the cylinder. The solution to this problem is as follows:

$$T - T_S = \frac{\dot{q}R^2}{4k}\left(1 - \left(\frac{r}{R}\right)^2\right) \tag{15.82}$$

The temperature distribution is symmetric about the center line with a maximum temperature at r = 0 (center line). The maximum temperature is

$$T_{max} = \frac{\dot{q}R^2}{4k} + T_S \tag{15.83}$$

Thus, the temperature distribution can be expressed in dimensionless form as

$$\frac{T - T_S}{T_{max} - T_S} = 1 - \left(\frac{r}{R}\right)^2 \tag{15.84}$$

The heat flux at any radial location is

$$\begin{aligned} q_r'' &= -k\frac{dT}{dr} = k\left(\frac{2r}{R^2}(T_{max} - T_S)\right) \\ &= \dot{q}r/2 \end{aligned} \tag{15.85}$$

Thus,

$$\begin{aligned} q\big|_{r=R} &= (2\pi RL)q_r''\big|_{r=R} \\ &= (\pi R^2 L)\dot{q} = V\dot{q} \end{aligned} \tag{15.86}$$

where V is the volume of the cylinder.

15.4.7 Heat Transfer from Extended Surfaces

Extended surfaces are used to enhance heat transfer between a solid surface and a fluid moving adjacent to the solid surface. For example, consider a plane solid wall at a uniform temperature T_b. The adjoining fluid is moving at a free stream velocity of V_∞ with a free stream temperature of T_∞. Assuming $T_b > T_\infty$, heat will flow from the solid surface to the fluid. The heat flow rate q is given by

$$q = hA(T_b - T_\infty) \tag{15.87}$$

where h is the heat transfer coefficient and A is the heat transfer area (area in contact with the moving fluid).

There are three ways to increase the rate of heat transfer between the plane solid surface and the moving fluid: (1) increase the fluid velocity to increase the heat transfer coefficient, (2) increase the temperature difference $T_b - T_\infty$ by reducing the fluid free stream temperature, and (3) increase the contact area A between the fluid and the solid across which convection is taking place. In many practical applications, one has little or no control on fluid velocity and fluid temperature. The only viable option to enhance the heat transfer rate in such applications is to increase the fluid/solid contact area across which convection occurs. The surface area exposed to the fluid can be "extended" by employing *fins*. Fins are protrusions from the base surface into the cooling fluid. They are made from high thermal conductivity material in order to provide maximum possible enhancement of heat transfer. Fins come in a variety of shapes and forms, such as straight or longitudinal fins with different shape profiles (rectangular, trapezoidal, and parabolic), annular fins, and cylindrical pin fins.

To analyze heat transfer from a fin, consider a long cylindrical pin fin of constant cross-section attached to a plane wall at a uniform surface temperature T_b. Let x be the axial coordinate of the fin. The surrounding fluid is at a free stream temperature of T_∞ and the heat transfer coefficient is h. Assuming that the transverse temperature gradients in the fin are negligible (the temperature at any given cross-section of the fin is uniform), the temperature in the fin is a function of x only.

Energy balance on a small cylindrical element (length Δx) of the fin at steady state can be expressed as follows:

$$\left\{\begin{matrix}\text{Rate at which heat enters}\\ \text{the element by conduction}\end{matrix}\right\} = \left\{\begin{matrix}\text{Rate at which heat leaves}\\ \text{the element by conduction}\end{matrix}\right\} + \left\{\begin{matrix}\text{Rate at which heat leaves}\\ \text{the element by convection}\end{matrix}\right\} \tag{15.88}$$

Each term of the energy balance (Equation 15.88) is now determined.

$$\left\{\begin{matrix}\text{Rate at which heat}\\ \text{enters by conduction}\end{matrix}\right\} = q''_x\big|_x A_c \tag{15.89}$$

$$\left\{\begin{matrix}\text{Rate at which heat}\\ \text{leaves by conduction}\end{matrix}\right\} = q''_x\big|_{x+\Delta x} A_c \tag{15.90}$$

$$\left\{\begin{matrix}\text{Rate at which heat}\\ \text{leaves by convection}\end{matrix}\right\} = h(T - T_\infty)P\Delta x \tag{15.91}$$

where A_c is the cross-sectional area and P is the perimeter of the fin. Thus, energy balance could be written as

$$\frac{q''_x\big|_{x+\Delta x} - q''_x\big|_x}{\Delta x} = -\frac{h(T - T_\infty)P}{A_c} \tag{15.92a}$$

In the limit $\Delta x \to 0$, this gives

$$\frac{dq''_x}{dx} = \frac{-h(T - T_\infty)P}{A_c} \tag{15.92b}$$

Using Fourier's law of heat conduction, this equation can be rewritten as

$$\frac{d^2T}{dx^2} - \frac{hP(T - T_\infty)}{kA_c} = 0 \tag{15.93}$$

The boundary conditions are

$$x = 0,\ T = T_b \tag{15.94}$$

$$x = L,\quad \left.\frac{dT}{dx}\right|_{x=L} = 0 \tag{15.95}$$

where L is the length of the fin. The second boundary condition follows from the assumption of adiabatic tip. As the tip area of the fin is small, we can neglect heat transfer from the tip. The solution of this problem is as follows:

$$\frac{T - T_\infty}{T_b - T_\infty} = \frac{\cosh m(L - x)}{\cosh mL} \tag{15.96}$$

where m is defined as

$$m = \sqrt{\frac{hP}{kA_c}} \tag{15.97}$$

The heat transfer rate from the fin can be determined by noting that all the heat lost by the fin must be conducted into the fin at the root or base (x = 0). Thus,

$$q = A_c q''_x\big|_{x=0} = -kA_c\left(\frac{dT}{dx}\right)_{x=0} = kA_c m(T_b - T_\infty)\tanh mL \tag{15.98}$$

The *effectiveness* (ε) of a fin is defined as the ratio of heat transfer rate from the fin to heat transfer rate without fin. Heat transfer without fin refers to heat transfer that would have occurred from the base area in the absence of the fin. Thus,

$$\varepsilon = \frac{q_{fin}}{A_c h(T_b - T_\infty)} \tag{15.99}$$

The effectiveness must be larger than unity for fin to provide additional heat transfer. For a cylindrical pin fin with adiabatic tip, ε is given as

$$\varepsilon = \sqrt{\frac{kP}{hA_c}} \tanh mL \tag{15.100}$$

For long fins with $T \to T_\infty$ at the tip, this expression reduces to

$$\varepsilon = \sqrt{\frac{kP}{hA_c}} \tag{15.101}$$

Fins are more effective if k of fin is high, diameter of fin is small (P/A_c is large), and the convection coefficient h is low (fins are more effective when the fluid is gas).

Another important measure of fin performance is the *fin efficiency*, defined as the ratio of actual rate of heat transfer from the fin to maximum possible rate of heat transfer from the fin:

$$\eta = \frac{q_{fin,actual}}{q_{fin,maximum}} \tag{15.102}$$

The heat transfer rate from the fin is maximum when the entire surface of the fin is at the base temperature T_b. Therefore,

$$\eta = \frac{q_{fin,actual}}{hA_f(T_b - T_\infty)} \tag{15.103}$$

where A_f is the surface area of the fin exposed to the fluid. The efficiency of a fin depends on several factors. It increases with the increase in thermal conductivity of the fin material. It decreases with the increase in fin length. It also depends on the geometry of the fin.

For cylindrical pin fin with adiabatic tip,

$$\eta = \frac{\tanh mL}{mL} \tag{15.104}$$

In most practical applications involving the use of fins, an *array* of fins is used to increase the heat transfer area. Let A_t be the total surface area in contact with the fluid. If there are N fins and the exposed surface area of each fin is A_f, then

$$A_t = NA_f + A_b \tag{15.105}$$

where A_b is the exposed portion of the base area (area not occupied by the fins). Thus, the total rate of heat transfer (q_t) from an array of fins is

$$\begin{aligned} q_t &= Nq_{fin} + A_b h(T_b - T_\infty) \\ &= N\eta h A_f (T_b - T_\infty) + A_b h(T_b - T_\infty) \end{aligned} \tag{15.106}$$

Upon substitution of A_t and rearrangement, this expression can be rewritten as

$$q_t = hA_t \left[1 - \frac{NA_f}{A_t}(1-\eta)\right](T_b - T_\infty) \tag{15.107}$$

The overall efficiency of an array of fins is defined as

$$\eta_o = \frac{q_t}{q_{max}} = \frac{q_t}{hA_t(T_b - T_\infty)} \tag{15.108}$$

where q_{max} is the maximum possible rate of heat transfer from the array assembly. Upon substitution of the expression for q_t, the overall efficiency can be written as

$$\eta_o = \left[1 - \frac{NA_f}{A_t}(1-\eta)\right] \tag{15.109}$$

15.5 TRANSIENT HEAT CONDUCTION

When a solid body is suddenly subjected to a change in thermal environment, the temperature inside the body varies with both location and time. Such unsteady or transient heat conduction problems are commonly encountered in engineering applications. To obtain time dependence of the temperature distribution within an object, one needs to solve the heat conduction equation subject to the given initial and boundary conditions. As an example, consider transient heat conduction in a semi-infinite solid. Such a solid has a single plane surface and extends to infinity in all but one direction. The heat conduction equation for this situation can be written as

$$\frac{\partial^2 T}{\partial x^2} = \frac{1}{\alpha}\frac{\partial T}{\partial t} \tag{15.110}$$

The object is initially at a uniform temperature of T_i. The exposed surface is suddenly subjected to a constant temperature of T_S. Thus, the boundary conditions are

$$T(0, t) = T_S \text{ and } T(\infty, t) = T_i \tag{15.111}$$

and the initial condition is

$$T(x, 0) = T_i \tag{15.112}$$

This problem can be solved by two different techniques: similarity technique and Laplace transform technique. According to the similarity technique, the two independent variables (x and t) are combined into a single variable η (called the similarity variable) such that the original partial differential equation is converted into an ordinary differential equation. This technique usually works if the T versus x profiles are similar at different times. For the problem at hand, the similarity variable is

$$\eta = \frac{x}{2\sqrt{\alpha t}} \tag{15.113}$$

The partial differential equation (Equation 15.110) can now be converted into an ordinary differential equation using η. Thus, Equation 15.110 becomes

$$\frac{d^2T}{d\eta^2} = -2\eta\frac{dT}{d\eta} \tag{15.114}$$

and the new boundary conditions are

$$T|_{\eta=0} = T_S \text{ and } T|_{\eta=\infty} = T_i \tag{15.115}$$

The solution of Equation 15.114 subjected to the given boundary conditions is as follows:

$$\frac{T - T_i}{T_S - T_i} = 1 - \text{erf}\left(\frac{x}{2\sqrt{\alpha t}}\right) \tag{15.116}$$

where erf(z) is the error function defined as

$$\text{erf}(z) = \frac{2}{\sqrt{\pi}}\int_0^z \exp(-u^2)\,du \tag{15.117}$$

The Laplace transform technique could also be applied to solve this problem. The Laplace transform of any function f(t) is defined as

$$£[f(t)] = \int_0^\infty f(t)e^{-st}\,dt \tag{15.118}$$

where s is the Laplace variable. The given partial differential equation can be converted into an ordinary differential equation using Laplace transformation. Thus,

$$\alpha \frac{d^2T}{dx^2} - sT = -T_i \tag{15.119}$$

where T is now a function of x and s. The new boundary conditions are

$$T(x = 0, s) = \frac{T_S}{s} \text{ and } T(x = \infty, s) = \frac{T_i}{s} \tag{15.120}$$

The solution of Equation 15.119 subjected to the given boundary conditions is

$$T(x,s) = \frac{T_i}{s} + \left(\frac{T_S - T_i}{s}\right)e^{-\left(\sqrt{s/\alpha}\right)x} \tag{15.121}$$

The same solution (Equation 15.116) is obtained upon taking the inverse Laplace transform of Equation (15.121).

From the solution of T(x, t), one can easily determine the instantaneous heat flux at the surface as

$$q''_x(t) = -k\left(\frac{\partial T}{\partial x}\right)_{x=0} = \frac{k(T_S - T_i)}{\sqrt{\pi\alpha t}} \tag{15.122}$$

15.5.1 Lumped Capacity Analysis

In many transient heat conduction problems of practical interest, the object is initially at a uniform temperature. It is suddenly immersed in a fluid with a different temperature. Heat transfer occurs between the object and the fluid. This problem involves both conduction and convection, conduction within the object and convection at the boundaries of the object.

In general, the temperature of the object varies with both spatial coordinates and time. However, the problem is easy to solve if there is no spatial variation of temperature, that is, the temperature of the object is uniform spatially but varies with time. This can occur if the internal conductive resistance is negligible in comparison

with the external convective resistance. The ratio of internal conductive resistance to external convective resistance is called the Biot number (Bi):

$$\mathrm{Bi} = \frac{(L_c/kA)}{(1/hA)} = \frac{hL_c}{k} \tag{15.123}$$

where L_c is the characteristic length of the object.

The lumped capacity analysis assumes that the temperature of the object is uniform spatially but varies with time. This is a safe assumption when Bi < 0.1. For low Bi, the internal conductive resistance is quite small compared with the external convective resistance.

From energy balance,

Rate of heat loss by convection = Rate of decrease of internal energy (15.124)

$$hA(T - T_\infty) = -mc_p \frac{dT}{dt} \tag{15.125}$$

where m is the mass of the object, A is its surface area, c_p is the heat capacity, T is the temperature at any time t, and T_∞ is the free-stream temperature of the fluid.

Upon integration, Equation 15.125 gives

$$\frac{T - T_\infty}{T_i - T_\infty} = \exp\left(-\frac{hA}{\rho V c_p} t\right) \tag{15.126}$$

where T_i is the initial temperature of the object and V is its volume. The instantaneous rate of heat transfer is

$$q = hA(T - T_\infty) \tag{15.127}$$

The total amount of heat transferred to the fluid from t = 0 to time t is

$$Q = mc_p(T_i - T) \tag{15.128}$$

The maximum amount of heat that can be transferred to the fluid is

$$Q_{max} = mc_p(T_i - T_\infty) \tag{15.129}$$

15.5.2 Transient Conduction with Nonnegligible Internal Resistance

The lumped capacity analysis assumes negligible internal conductive resistance. It can only be applied if the Biot number is less than 0.1. When Bi is larger than 0.1, the internal conductive resistance is significant in comparison with the external

convective resistance. Both spatial and time variations of temperature become important. In such situations, one needs to solve the heat conduction equation subject to the given initial and boundary conditions.

Consider transient heat conduction in a rectangular slab of thickness 2L. The slab is initially at a uniform temperature of T_i. It is suddenly immersed in a cold fluid with a free stream temperature of T_∞. The internal conductive resistance is nonnegligible as compared with external convective resistance. For this problem, the heat conduction equation along with the initial and boundary conditions are as follows:

$$\frac{\partial T}{\partial t} = \alpha \frac{\partial^2 T}{\partial x^2} \tag{15.130}$$

Initial condition

$$T(x, t = 0) = T_i \tag{15.131}$$

Boundary conditions

$$-k\left(\frac{\partial T}{\partial x}\right)_{x=L} = h\left(T\Big|_{x=L} - T_\infty\right) \tag{15.132}$$

$$\left(\frac{\partial T}{\partial x}\right)_{x=0} = 0 \tag{15.133}$$

Note that at midplane (x = 0), the temperature gradient is zero due to symmetry of the problem.

This mathematical problem can be solved using the separation of variables technique. The solution T(x, t) turns out to be an infinite series that can be expressed as

$$\frac{T(x,t) - T_\infty}{T_i - T_\infty} = f\left(\frac{x}{L}, Fo, Bi\right) \tag{15.134}$$

where Fo is the Fourier number, defined as

$$Fo = \frac{t}{(L^2/\alpha)} = \frac{\alpha t}{L^2} \tag{15.135}$$

The solution is available in the literature in the form of charts, referred to as "Heisler Charts." The Heisler charts are often presented in two parts. The first chart gives the dimensionless temperature at the center or midplane (x = 0) of the object $(T_c - T_\infty)/(T_i - T_\infty)$, as a function of Fo and Bi. Once the midplane temperature T_c is determined, the second chart is read to obtain the temperature T(x, t) at any other

location. The second chart presents T(x, t) in dimensionless form as $(T(x, t) - T_\infty)/(T_c - T_\infty)$, as a function of Bi and x/L. The solutions to transient heat conduction problems involving radial geometries (cylindrical and spherical objects) are also available in the literature in the form of Heisler charts.

SUPPLEMENTAL READING

Bejan, A. 1993. *Heat Transfer*, New York: John Wiley & Sons.

Bergman, T.L., A.S. Levine, F.P. Incropera, and D.P. Dewitt. 2011. *Fundamentals of Heat and Mass Transfer*, 7th Edition. New York: John Wiley & Sons.

Bird, R.B., W.E. Stewart, and E.N. Lightfoot. 2007. *Transport Phenomena*, 2nd Edition, New York: John Wiley & Sons.

Cengel, Y.A. 2007. *Heat and Mass Transfer*, 3rd Edition, New York: McGraw-Hill.

Holman, J.P. 2009. *Heat Transfer*, 10th Edition, New York: McGraw-Hill.

Keith, F. and M.S. Bohn. 1993. *Principles of Heat Transfer*, 5th Edition, St. Paul: West Publishing Co.

Welty, J.R., C.E. Wicks, R.E. Wilson, and G.L. Rorrer. 2008. *Fundamentals of Momentum, Heat, and Mass Transfer*, 5th Edition, New York: John Wiley & Sons.

16 Thermal Conductivity of Composites

New applications in the electronics industry, with major emphasis on miniaturization and increasing power of electronic devices, require materials which are good conductors of heat so that the heat generated in the devices is dissipated away as quickly as possible in order to maintain the temperature of the device at the desired level. To that end, polymer–matrix composites (PMCs) consisting of highly thermally conductive filler are considered to be good candidates. The heat conducting ability of the plastic material (polymer) is enhanced greatly by dispersing thermally conductive filler in the polymer matrix.

In order to design and manufacture two-phase composite materials of controlled thermal conductivity, it is important to know the variations of thermal conductivity with the kind and concentration of filler materials. Over the past several decades, a number of experimental and theoretical studies have been published in the literature on the thermal conductivity of particulate composites [1–15]. In what follows, the key empirical and theoretical models describing the thermal conductivity of particulate composites are discussed.

16.1 EMPIRICAL RULES OF MIXTURES

According to the *Voigt* rule of mixture (ROM), the thermal conductivity of a composite material is given as

$$k = \phi k_d + (1 - \phi)k_m \tag{16.1}$$

where k, k_d, and k_m are the thermal conductivities of composite, dispersed phase and matrix, respectively, and ϕ is the volume fraction of filler particles. This formula can be derived by considering two thermal conductors, matrix and dispersed phase, in parallel with the same temperature gradients but with composite heat flux proportional to the content of the individual phases, that is,

$$\left(\frac{dT}{dx}\right) = \left(\frac{dT}{dx}\right)_m = \left(\frac{dT}{dx}\right)_d \tag{16.2}$$

$$q'' = (1 - \phi)q''_m + \phi q''_d \tag{16.3}$$

where (dT/dx), $(dT/dx)_m$, and $(dT/dx)_d$ are the temperature gradients in composite, matrix, and dispersed phase, respectively, and q'', q''_m, and q''_d are the heat fluxes in composite, matrix, and dispersed phase, respectively. Note that the heat fluxes are additive due to parallel arrangement of the matrix and dispersed phase. From Fourier's law of heat conduction,

$$q'' = -k\left(\frac{dT}{dx}\right), \quad q''_m = -k_m\left(\frac{dT}{dx}\right)_m, \quad q''_d = -k_d\left(\frac{dT}{dx}\right)_d \tag{16.4}$$

Upon substituting the expressions for fluxes from Equation 16.4 into Equation 16.3 and realizing that the temperature gradients are the same, one can readily arrive at the Voigt ROM (Equation 16.1).

According to another ROM, namely the *Reuss* ROM, the thermal conductivity of a composite material is given as

$$1/k = [\phi/k_d] + [(1 - \phi)/k_m] \tag{16.5}$$

This formula can be derived by considering two thermal conductors, matrix and dispersed phase, in series with the same heat fluxes but with composite temperature gradient proportional to the content of individual phases, that is,

$$q'' = q''_m = q''_d \tag{16.6}$$

$$\left(\frac{dT}{dx}\right) = (1-\phi)\left(\frac{dT}{dx}\right)_m + \phi\left(\frac{dT}{dx}\right)_d \tag{16.7}$$

Note that the temperature gradients are additive due to series arrangement of the matrix and dispersed phase. From Fourier's law of heat conduction,

$$\left(\frac{dT}{dx}\right) = -\frac{q''}{k}, \quad \left(\frac{dT}{dx}\right)_m = -\frac{q''_m}{k_m}, \quad \left(\frac{dT}{dx}\right)_d = -\frac{q''_d}{k_d} \tag{16.8}$$

Upon substituting the expressions for temperature gradients from Equation 16.8 into Equation 16.7 and realizing that the heat fluxes are the same, one can readily arrive at the Reuss ROM (Equation 16.5).

It should be noted that Voigt and Reuss rules of mixtures represent the upper and the lower bounds, respectively of the thermal conductivity of two-phase isotropic composites, regardless of the shape of the filler particles.

The other useful bounds, namely the Hashin–Shtrikman [16] bounds on the thermal conductivity of isotropic composites, are given as follows:

$$\phi k_d + (1-\phi)k_m - \left[\frac{(k_d - k_m)^2\phi(1-\phi)}{\phi k_m + (1-\phi)k_d + 2k_{min}}\right] \le k \le \phi k_d + (1-\phi)k_m - \left[\frac{(k_d - k_m)^2\phi(1-\phi)}{\phi k_m + (1-\phi)k_d + 2k_{max}}\right] \tag{16.9}$$

where

$$k_{min} = \text{Min}(k_d, k_m), \quad k_{max} = \text{Max}(k_d, k_m) \tag{16.10}$$

The Hashin–Shtrikman bounds are much tighter and closer (hence more useful and accurate) in comparison with the Voigt–Reuss bounds.

16.2 THEORETICAL MODELS

The thermal conductivity bounds discussed in the preceding section give the extreme values of the thermal conductivity. The Hashin–Shtrikman bounds, although better than the Voigt–Reuss bounds, yield satisfactory estimates for the effective thermal conductivity, in that the upper and lower bounds are close, only when the ratio between the thermal conductivities of the two phases is not too different from unity. When the thermal conductivities of the two phases are very different, the bounds become too wide to be of any practical value. To overcome this difficulty, a number of theoretical and semitheoretical models have been developed for the thermal conductivity of composites of filler particles of specific shape (usually spherical).

For an *infinitely dilute* composite of spherical particles, the exact expression for the thermal conductivity is given as

$$\frac{k}{k_m} = 1 + 3\left(\frac{k_d - k_m}{k_d + 2k_m}\right)\phi \tag{16.11}$$

This equation could be rewritten as

$$k_r = 1 + 3\left(\frac{\lambda - 1}{\lambda + 2}\right)\phi \tag{16.12}$$

where k_r is the relative thermal conductivity defined as k/k_m and λ is the thermal conductivity ratio defined as k_d/k_m.

Equation 16.11 is good only for very dilute composites. For *nondilute* composites of spherical particles, one can derive an equation for thermal conductivity using Maxwell's approach [17]. Consider a single spherical particle of radius "a" and thermal conductivity k_d, embedded in an infinite matrix of thermal conductivity k_m. Let the system be subjected to a temperature field with uniform temperature gradient α far away from the particle.

For any given boundary and initial conditions, the temperature distribution in the particle and surrounding matrix is governed by the heat diffusion equation (see Chapter 15), expressed as follows in spherical polar coordinates (r, θ, ϕ) with origin at the centre of the particle:

$$\frac{1}{r^2}\frac{\partial}{\partial r}\left(r^2\frac{\partial T}{\partial r}\right)+\frac{1}{r^2\sin^2\theta}\frac{\partial^2 T}{\partial \phi^2}+\frac{1}{r^2\sin\theta}\frac{\partial}{\partial\theta}\left(\sin\theta\frac{\partial T}{\partial\theta}\right)+\frac{\dot{q}}{k}=\frac{1}{\alpha}\frac{\partial T}{\partial t} \tag{16.13}$$

Assuming steady state, no heat generation, and temperature to be independent of ϕ (that is, axisymmetric temperature distribution), Equation 16.13 simplifies to

$$\frac{\partial}{\partial r}\left(r^2\frac{\partial T}{\partial r}\right)+\frac{1}{\sin\theta}\frac{\partial}{\partial\theta}\left(\sin\theta\frac{\partial T}{\partial\theta}\right)=0 \tag{16.14}$$

At $r \to \infty$, the temperature distribution is given as

$$T(r,\theta)=\alpha z \text{ where } z=r\cos\theta \tag{16.15}$$

At the particle–matrix interface, the temperature and the normal heat flux are continuous, that is,

$$\text{at } r=a,\ T_d=T_m,\ k_d\frac{\partial T_d}{\partial r}=k_m\frac{\partial T_m}{\partial r} \tag{16.16}$$

The temperature distributions in the particle and matrix, satisfying Equations 16.14 through 16.16, are given as [18]

$$T_d(r,\theta)=\frac{3k_m}{k_d+2k_m}\alpha r\cos\theta \quad (0<r<a) \tag{16.17}$$

$$T_m(r,\theta)=\alpha r\cos\theta+\left(\frac{3k_m}{k_d+2k_m}-1\right)\frac{\alpha a^3\cos\theta}{r^2} \quad (a<r<\infty) \tag{16.18}$$

Consider now a cluster of particles embedded in an infinite matrix of thermal conductivity k_m. The cluster of particles, enclosed by a spherical region of radius R, consists of n spherical particles of radius "a" and thermal conductivity k_d. Let the system be subjected to a temperature field with uniform temperature gradient α at $r \to \infty$. At $r \to \infty$, the temperature distribution is given by Equation 16.15. Assuming negligible interaction between the particles, the temperature at a radial distance r ($r \gg R$) from the centre of the spherical cluster region R can be determined from Equation 16.18 as

$$T(r,\theta) = \left(\alpha r + n\beta \frac{1}{r^2}\right)\cos\theta \tag{16.19}$$

where the constant β is given by

$$\beta = \left(\frac{k_m - k_d}{k_d + 2k_m}\right) a^3 \alpha \tag{16.20}$$

Since $\phi = n(a/R)^3$, Equation 16.19 can be rewritten as

$$T(r,\theta) = \alpha\left[r + \phi R^3 \left(\frac{k_m - k_d}{k_d + 2k_m}\right)\frac{1}{r^2}\right]\cos\theta \tag{16.21}$$

Now if the cluster of particles is treated as an "effective homogeneous medium" of radius R and thermal conductivity k, suspended in a matrix of conductivity k_m, the temperature at any radial location r (≫ R) is given as

$$T(r,\theta) = \alpha\left[r + R^3 \left(\frac{k_m - k}{k + 2k_m}\right)\frac{1}{r^2}\right]\cos\theta \tag{16.22}$$

Since the two expressions, Equations 16.21 and 16.23, are equivalent, it follows that

$$\left(\frac{k - k_m}{k + 2k_m}\right) = \left(\frac{k_d - k_m}{k_d + 2k_m}\right)\phi \tag{16.23}$$

Equation 16.23 is often referred to as the Maxwell–Eucken equation in the literature as Eucken [19] was probably the first to adapt Maxwell's approach to thermal conductivity of particulate composites.

The Maxwell–Eucken equation can be rearranged as

$$k_r = \frac{k}{k_m} = \left[\frac{1 + 2\phi\left(\frac{\lambda - 1}{\lambda + 2}\right)}{1 - \phi\left(\frac{\lambda - 1}{\lambda + 2}\right)}\right] \tag{16.24}$$

In the limit $\phi \to 0$, Equation 16.24 reduces to Equation 16.12. Interestingly the thermal conductivity of composite predicted by the Maxwell–Eucken equation can be expressed as the sum of Voigt ROM estimate and a correction term as follows:

$$k = \phi k_d + (1-\phi)k_m - \left[\frac{(k_d - k_m)^2 \phi(1-\phi)}{\phi k_m + (1-\phi)k_d + 2k_m}\right] \tag{16.25}$$

It should also be noted that this Maxwell–Eucken equation (Equation 16.25) coincides with the lower Hashin–Shtrikman bound (see Equation 16.9) when $k_m < k_d$ and with the upper Hashin–Shtrikman bound when $k_d < k_m$.

Pal [13] has recently developed a series of models for the thermal conductivity of concentrated particulate composites using the differential effective medium approach. Consider a particulate composite with volume fraction of particles ϕ. Into this composite, a differential quantity of new particles is added. The increment change in thermal conductivity dk resulting from the addition of new particles can be calculated from Equation 16.11 by replacing $k_m \rightarrow k$, $k \rightarrow k + dk$, and $\phi \rightarrow d\phi$. Thus,

$$\left[\frac{k_d + 2k}{3k(k_d - k)}\right] dk = d\phi \tag{16.26}$$

Upon integration with the limit $k \rightarrow k_m$ at $\phi = 0$, Equation 16.26 gives

$$\left(\frac{k}{k_m}\right)^{1/3} \left(\frac{k_d - k_m}{k_d - k}\right) = \exp(\phi) \tag{16.27}$$

or

$$(k_r)^{1/3} \left(\frac{\lambda - 1}{\lambda - k_r}\right) = \exp(\phi) \tag{16.28}$$

where k_r is relative thermal conductivity defined as k/k_m and λ is the thermal conductivity ratio defined as k_d/k_m. Equation 16.27 or 16.28 will be referred to as Model 1.

Model 1 (Equation 16.28) assumes that all the volume of the composite before new particles are added is available as free volume to the new particles. In reality, the free volume available to disperse the new particles is significantly less, due to the volume preempted by the particles already present. This means that when new particles are added to the composite, the increase in the actual volume fraction of the dispersed phase is larger than $d\phi$. To account for the "crowding effect" of particles, the increase in the volume fraction can be taken as $d[\phi/(1 - \phi/\phi_m)]$, where ϕ_m is the maximum packing volume fraction of particles [13]. Thus, Equation 16.26 should be revised as

$$\left[\frac{k_d + 2k}{3k(k_d - k)}\right] dk = d\left[\frac{\phi}{1 - \frac{\phi}{\phi_m}}\right] \tag{16.29}$$

Upon integration, Equation 16.29 gives

$$\left(\frac{k}{k_m}\right)^{1/3}\left(\frac{k_d - k_m}{k_d - k}\right) = \exp\left[\frac{\phi}{1-\frac{\phi}{\phi_m}}\right] \tag{16.30}$$

or

$$(k_r)^{1/3}\left(\frac{\lambda - 1}{\lambda - k_r}\right) = \exp\left[\frac{\phi}{1-\frac{\phi}{\phi_m}}\right] \tag{16.31}$$

Equation 16.30 or 16.31 will be referred to as Model 2.

Another way to account for the "crowding effect" of particles is to take the increase in the volume fraction of the dispersed phase, when new particles are added, as $d\phi/(1 - \phi/\phi_m)$, instead of $d[\phi/(1 - \phi/\phi_m)]$ as done in the derivation of Model 2 [13]. Thus, Equation 16.26 can be rewritten as

$$\left[\frac{k_d + 2k}{3k(k_d - k)}\right]dk = \frac{d\phi}{\left(1-\frac{\phi}{\phi_m}\right)} \tag{16.32}$$

Upon integration with the limit $k \to k_m$ at $\phi = 0$, Equation 16.32 gives

$$\left(\frac{k}{k_m}\right)^{1/3}\left(\frac{k_d - k_m}{k_d - k}\right) = \left(1-\frac{\phi}{\phi_m}\right)^{-\phi_m} \tag{16.33}$$

or

$$(k_r)^{1/3}\left(\frac{\lambda - 1}{\lambda - k_r}\right) = \left(1-\frac{\phi}{\phi_m}\right)^{-\phi_m} \tag{16.34}$$

Equation 16.33 or 16.34 will be referred to as Model 3. Model 3 reduces to the following Bruggeman-type equation [20] for thermal conductivity when ϕ_m is taken to be equal to unity.

$$\left(\frac{k_d - k}{k_d - k_m}\right)\left(\frac{k_m}{k}\right)^{1/3} = (1-\phi) \tag{16.35}$$

Figure 16.1 shows the relative thermal conductivities predicted from Models 1 through 3 (Equations 16.28, 16.31, and 16.34). All the three models predict that at a fixed value of ϕ, the relative thermal conductivity (k_r) initially remains constant with the increase in the thermal conductivity ratio (λ). In the range $10^{-2} < \lambda < 10^4$, k_r increases with the increase in λ. At higher values of λ ($\lambda > 10^4$), k_r again becomes constant (independent of λ). Interestingly, k_r is less than unity when $\lambda < 1.0$ and k_r is greater than unity when $\lambda > 1.0$. For $\lambda < 1.0$, the values of k_r predicted by different models are as follows: Model 1 (Equation 16.28) > Model 3 (Equation 16.34) > Model 2 (Equation 16.31). For $\lambda > 1.0$, the order is reversed and the values of k_r predicted by different models are as follows: Model 2 > Model 3 > Model 1.

Figure 16.2 shows the effect of dispersed phase volume fraction (ϕ) on the relative thermal conductivity (k_r). The plots are generated from Model 3 (Equation 16.34);

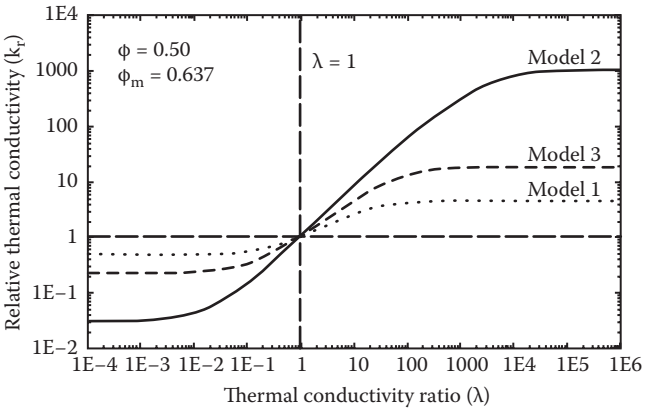

FIGURE 16.1 Relative thermal conductivity (k_r) of particulate composite predicted from the models. (From Pal, R., *J. Reinforced Plastics and Composites* 26: 643–651, 2007.)

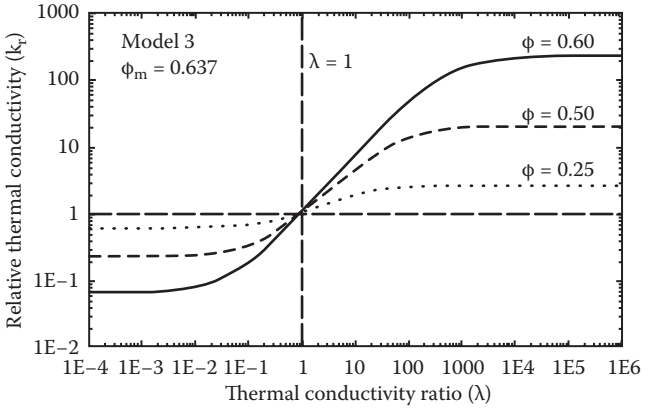

FIGURE 16.2 Effect of volume fraction of filler (ϕ) on the relative thermal conductivity of particulate composite. (From Pal, R., *J. Reinforced Plastics and Composites* 26: 643–651, 2007.)

the value of ϕ_m is taken to be 0.637 corresponding to random packing of uniform spheres. When the thermal conductivity ratio λ is unity, k_r is unity for all values of ϕ. For $\lambda < 1.0$, k_r decreases with the increase in ϕ. For $\lambda > 1.0$, k_r increases with the increase in ϕ.

Figures 16.3 through 16.5 show comparisons between the experimental data and predictions of various models. Model 1 (Equation 16.28) generally underpredicts the values of relative thermal conductivity, especially at high values of ϕ. The experimental data can be described very well using Model 3 (Equation 16.34) with reasonable values of ϕ_m, the maximum packing volume fraction of particles. For the same ϕ_m, Model 2 (Equation 16.31) overpredicts the values of k_r. Note that not all sets of data could be described by the same value of ϕ_m. This is expected as the particle size

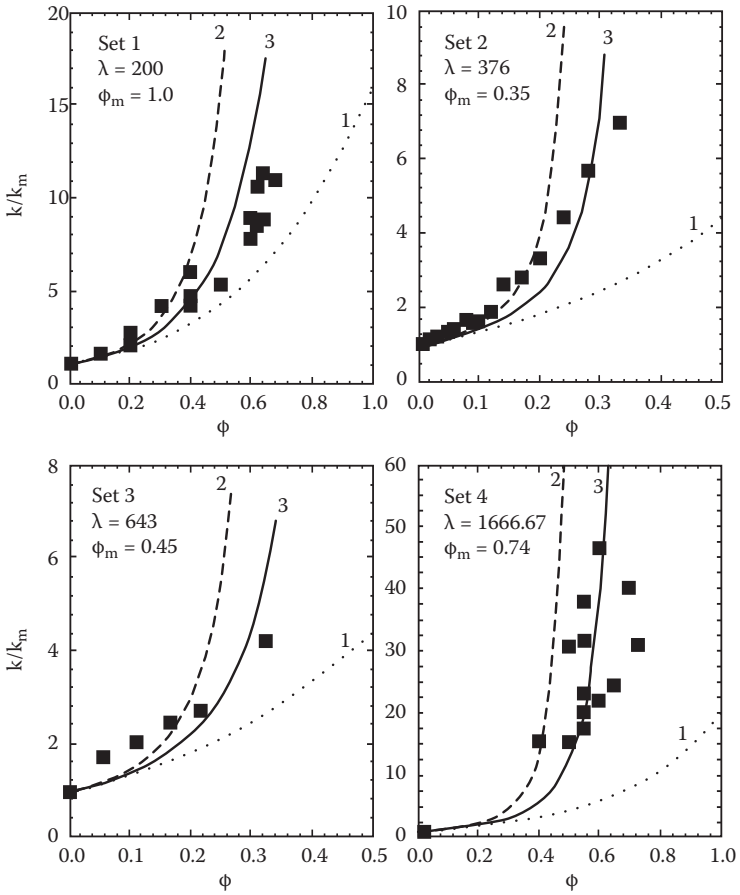

FIGURE 16.3 Comparisons between experimental thermal conductivity data of particulate composites and predictions of various models. (From Pal, R., *J. Reinforced Plastics and Composites* 26: 643–651, 2007.)

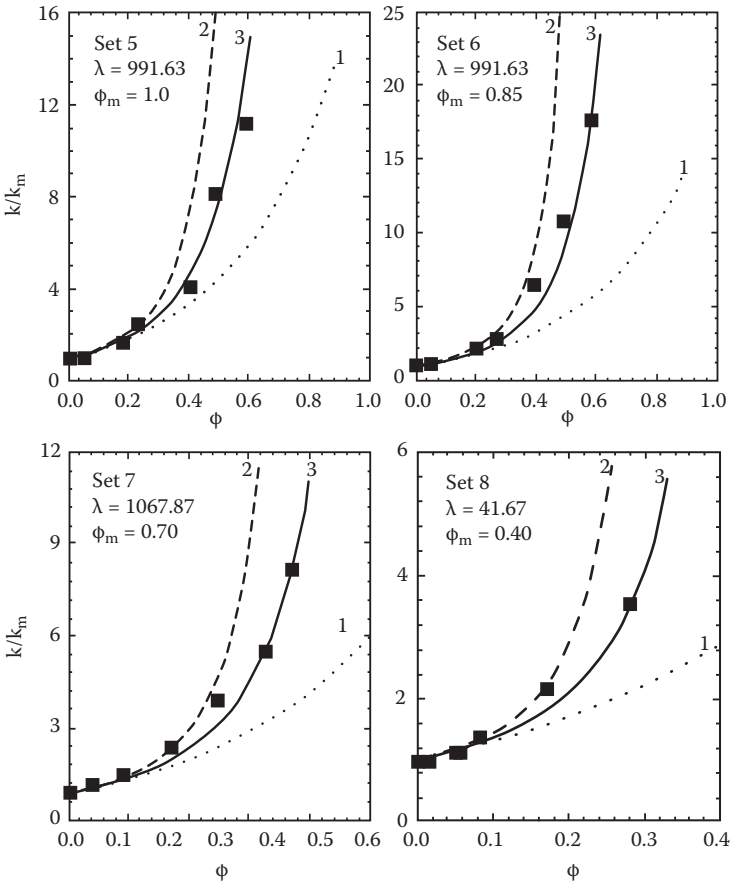

FIGURE 16.4 Comparisons between experimental thermal conductivity data of particulate composites and predictions of various models. (From Pal, R., *J. Reinforced Plastics and Composites* 26: 643–651, 2007.)

distribution and degree of aggregation of particles are different for different sets of experimental data. The value of ϕ_m ranges from 0.32 to 1.0.

The Pal models just described are implicit in nature. There are other useful models available in the literature, which are explicit but empirical in nature. Some of them are given below:

Cheng–Vachon model [11]

$$\frac{1}{k} = \frac{1}{MN}\ell n\left[\frac{2N + PM}{2N - PM}\right] + \left(\frac{1 - P}{k_m}\right) \tag{16.36}$$

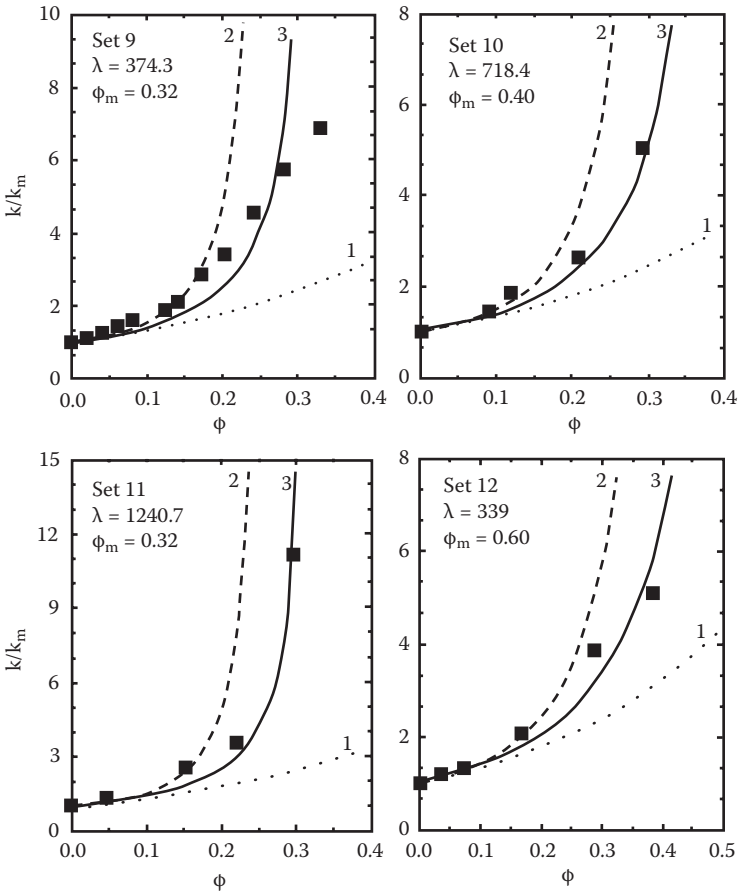

FIGURE 16.5 Comparisons between experimental thermal conductivity data of particulate composites and predictions of various models. (From Pal, R., *J. Reinforced Plastics and Composites* 26: 643–651, 2007.)

where M, N, and P are defined as

$$M = \sqrt{[2/(3\phi)]^{1/2}(k_d - k_m)} \tag{16.37}$$

$$N = \sqrt{k_m + P(k_d - k_m)} \tag{16.38}$$

$$P = \sqrt{3\phi/2} \tag{16.39}$$

Agari–Uno model [9]

$$k = \left[\frac{k_d^{C_2}}{C_1 k_m}\right]^{\phi} (C_1 k_m) \tag{16.40}$$

or

$$\ell n\, k = \phi C_2\, \ell n(k_d) + (1 - \phi)\ell n(C_1 k_m) \tag{16.41}$$

where C_1 and C_2 in Equations 16.40 and 16.41 are empirical constants of order unity.

Another useful semiempirical model is due to Lewis and Nielsen [14,15,21]. Lewis and Nielsen [14,15,21] modified and adapted the Halpin–Tsai equation for elastic moduli of composite materials to thermal conductivity of filled composites. The Lewis–Nielsen model is given as

$$k_r = \frac{k}{k_m} = \frac{1 + AB\phi}{1 - B\,\psi\phi} \tag{16.42}$$

where

$$B = \left(\frac{\lambda - 1}{\lambda + A}\right) \tag{16.43}$$

$$A = k_E - 1 \tag{16.44}$$

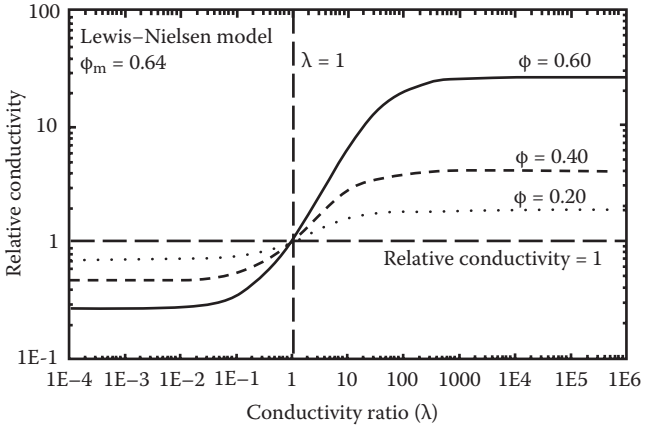

FIGURE 16.6 Relative conductivity versus conductivity ratio predicted from the Lewis–Nielsen model for different values of ϕ (volume fraction of filler particles). (From Pal, R., *Composites: Part A* 39: 718–726, 2008.)

$$\psi = 1 + \left(\frac{1 - \phi_m}{\phi_m^2} \right) \phi \tag{16.45}$$

k_E is the Einstein coefficient (k_E = 2.5 for rigid spheres suspended in a matrix with Poisson's ratio of 0.5), and ϕ_m is the maximum packing volume fraction of particles. However, Pal [22] suggested that the constant "A" in the Lewis–Nielsen model (see Equation 16.44) should be 2.0 (instead of 1.5) for spherical particles. If A = 2.0, the Lewis–Nielsen model reduces to the Maxwell–Eucken equation (Equation 16.24) when ϕ_m = 1.0. Thus, for composites of isometric particles the Lewis–Nielsen model is

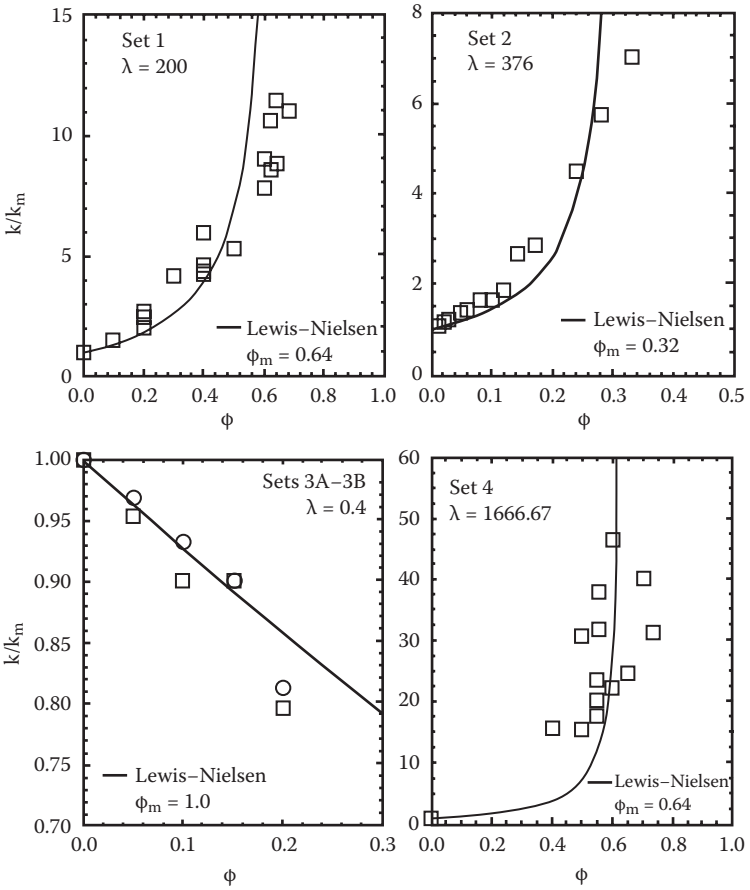

FIGURE 16.7 Comparisons between experimental thermal conductivity data (Sets 1 through 4) and predictions of the Lewis–Nielsen model. (From Pal, R., *Composites: Part A* 39: 718–726, 2008.)

$$k_r = \left[\frac{1+2\left(\frac{\lambda-1}{\lambda+2}\right)\phi}{1-\phi\psi\left(\frac{\lambda-1}{\lambda+2}\right)}\right] \tag{16.46}$$

where k_r is the relative thermal conductivity and λ is the thermal conductivity ratio (k_d/k_m). The expression for ψ is given by Equation 16.45.

Figure 16.6 shows the plots of relative thermal conductivity versus thermal conductivity ratio λ predicted from the Lewis–Nielsen model (Equation 16.46) for

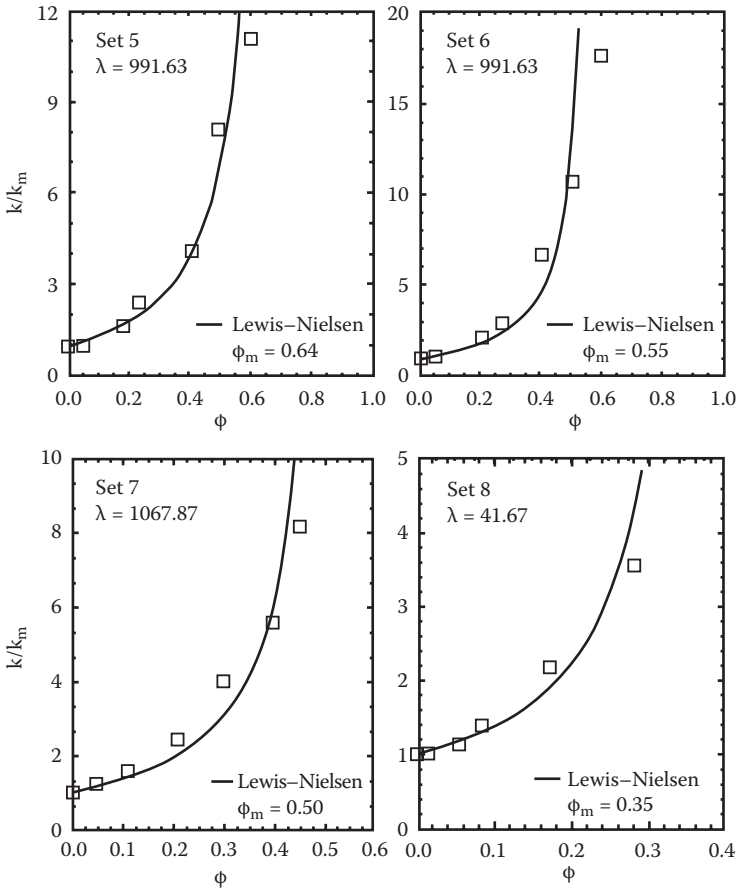

FIGURE 16.8 Comparisons between experimental thermal conductivity data (Sets 5 through 8) and predictions of the Lewis–Nielsen model. (From Pal, R., *Composites: Part A* 39: 718–726, 2008.)

different values of filler concentration ϕ. The maximum packing volume fraction ϕ_m is taken to be 0.64 corresponding to random close packing of uniform spheres. The predictions of the Lewis–Nielsen model are similar to those of the Pal models (see Figure 16.2). When the conductivity ratio λ is unity, the relative conductivity is unity regardless of the value of filler concentration ϕ. When $\lambda < 1.0$, the relative conductivity decreases with the increase in ϕ; a reverse trend is observed when $\lambda > 1.0$, that is, the relative conductivity increases with the increase in ϕ.

Figures 16.7 through 16.10 draw comparisons between the experimental thermal conductivity data and predictions of the Lewis–Nielsen model (Equation 16.46). The Lewis–Nielsen model describes the experimental data reasonably well [22].

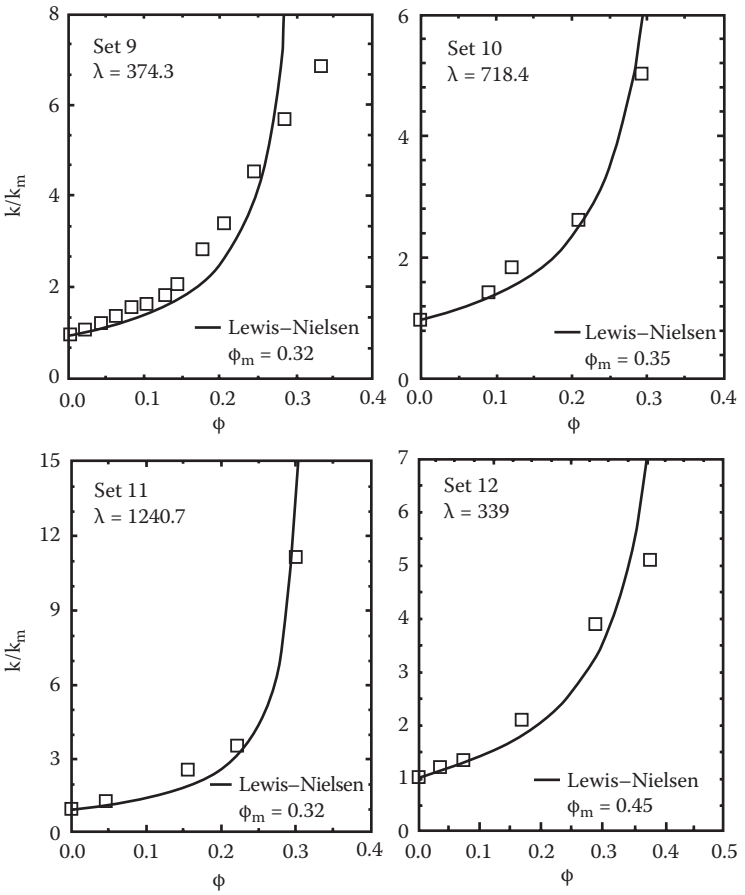

FIGURE 16.9 Comparisons between experimental thermal conductivity data (Sets 9 through 12) and predictions of the Lewis–Nielsen model. (From Pal, R., *Composites: Part A* 39: 718–726, 2008.)

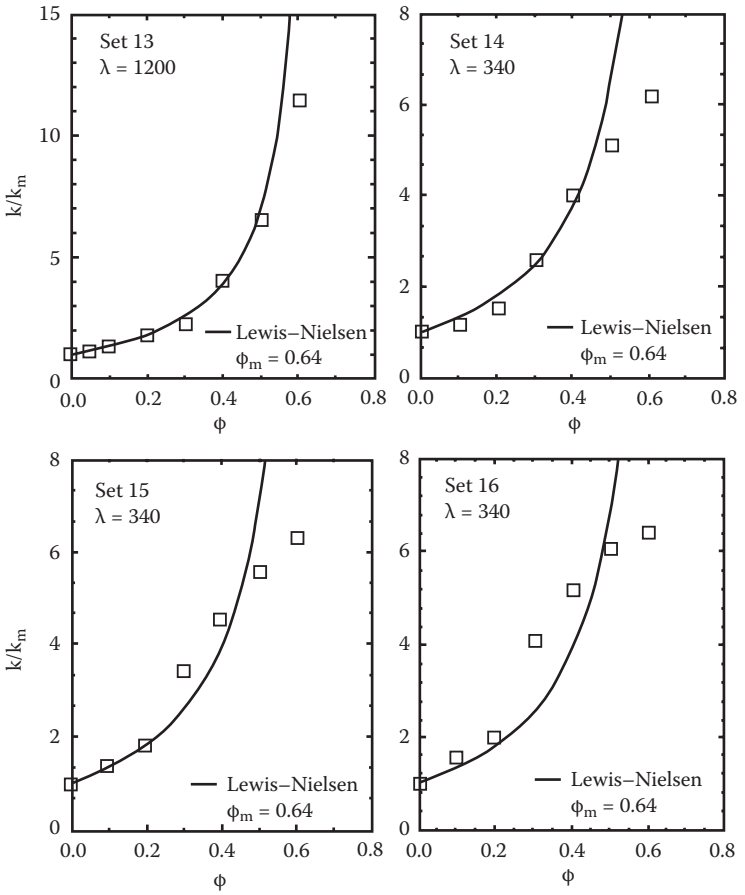

FIGURE 16.10 Comparisons between experimental thermal conductivity data (Sets 13 through 16) and predictions of the Lewis–Nielsen model. (From Pal, R., *Composites: Part A* 39: 718–726, 2008.)

REFERENCES

1. Progelhof, R.C., J.L. Throne, and R.R. Ruetsch. 1976. Methods for predicting the thermal conductivity of composite systems: A review. *Poly. Eng. & Sci.* 16: 615–625.
2. Rajaiah, J., G. Andrews, E. Ruckenstein, and R.K. Gupta. 1992. Thermal conductivity of concentrated, sterically stabilized suspensions. *Chem. Eng. Sci*. 47: 3863–3868.
3. Kumlutas, D., I.H. Tavman, and M.T. Coban. 2003. Thermal conductivity of particle filled polyethylene composite materials. *Composites Sci. & Tech*. 63: 113–117.
4. Yin, Y. and S.T. Tu. 2002. Thermal conductivities of PTFE composites with random distributed graphite particles. *J. Reinforced Plastics & Composites* 21: 1619–1627.
5. Xu, Y., D.D.L. Chung, and C. Mroz. 2001. Thermally conducting aluminum nitride polymer–matrix composites. *Composites Part A* 32: 1749–1757.

6. Boudenne, A., L. Ibos, M. Fois, M., E. Gehin, and J.C. Majeste. 2004. Thermophysical properties of polypropylene/aluminum composites. *J. Appl. Poly. Sci.* 42: 722–732.
7. Lin, F., G.S. Bhatia, and J.D. Ford. 1993. Thermal conductivities of powder-filled resins. *J. Appl. Poly. Sci.* 49: 1901–1908.
8. Tavman, I.H. 1996. Thermal and mechanical properties of aluminum powder-filled high-density polyethylene composites. *J. Appl. Poly. Sci*. 62: 2161–2167.
9. Agari, Y. and T. Uno. 1985. Thermal conductivity of polymer filled with carbon materials: Effect of conductive particle chains on thermal conductivity. *J. Appl. Poly. Sci.* 30: 2225–2235.
10. Krupa, I., I. Novak, and I. Chodak. 2004. Electrically and thermally conductive polyethylene/graphite composites and their mechanical properties. *Synthetic Metals* 145: 245–252.
11. Cheng, S.C. and R.I. Vachon. 1969. The prediction of the thermal conductivity of two and three phase solid heterogeneous mixtures. *Int. J. Heat Mass Transfer* 12: 249–264.
12. Agari, Y. and T. Uno. 1986. Estimation on thermal conductivities of filled polymers. *J. Appl. Poly. Sci.* 32: 5705–5712.
13. Pal, R. 2007. New models for thermal conductivity of particulate composites. *J. Reinforced Plastics and Composites* 26: 643–651.
14. Nielsen, L. 1973. Thermal conductivity of particulate filled polymers. *J. Appl. Poly. Sci.* 17: 3819–3820.
15. Nielsen, L. 1974. The thermal and electrical conductivity of two-phase systems. *Ind. Eng. Chem. Fundam.* 13: 17–20.
16. Hashin, Z. and S. Shtrikman. 1962. A variational approach to the theory of effective magnetic permeability of multiphase materials. *J. Appl. Phys.* 33: 3125–3131.
17. Maxwell, J. 1873. *Electricity and Magnetism*. Oxford: Clarendon.
18. McCartney, L.N. and A. Kelly. 2008. Maxwell's far-field methodology applied to the prediction of properties of multi-phase isotropic particulate composites. *Proc. Roy. Soc. A* 464: 423–446.
19. Eucken, A. 1932. Warmeleitfähigkeit keramischer feuerfester Stoffe: Berechnung aus der Wärmeleitfähigkeit der Bestandteile. *Forsch. Gebiete Ingenieurw, B3 Forschungsheft* 353.
20. Bruggeman, D.A.G. 1935. Berechnung verschiedener physikalischer Konstanten von heterogenen Substanzen. *Ann. Phys. (Leipzig)* 24: 636–679.
21. Lewis, T. and L. Nielsen. 1970. Dynamic mechanical properties of particulate-filled composites. *J. Appl. Poly. Sci.* 14: 1449–1471.
22. Pal, R. 2008. On the Lewis–Nielsen model for thermal/electrical conductivity of composites. *Composites: Part A* 39: 718–726.

17 Thermal Conductivity of Composites of Core-Shell Particles

Composite materials consisting of core-shell particles randomly distributed in a continuous medium (matrix) are of importance in many industrial applications [1–5]. The core-shell-type particles consist of a homogeneous core surrounded by a homogeneous shell of a different material. The encapsulation of core with shell is desirable for many reasons: to improve the thermal and/or mechanical properties, to modify the surface properties of particles, and to improve the dispersibility of particles in the matrix. One practical example of composites of core-shell-type particles is "syntactic foam" [6]. Syntactic foam consists of core-shell particles with gas core and glass shell (hollow glass microspheres) dispersed in a plastic resin.

In this chapter, the thermal conductivity of three-component composites consisting of core-shell type filler particles is discussed.

17.1 DILUTE COMPOSITES OF CORE-SHELL PARTICLES

For an *infinitely dilute* composite (volume fraction of filler → 0) of core-shell particles, the exact expression for the relative thermal conductivity is given as [1]

$$k_r = \frac{k}{k_1} = 1 + 3\left(\frac{(B/A)-1}{(B/A)+2}\right)\phi \tag{17.1}$$

where k_r is the relative thermal conductivity of composite, k is the effective thermal conductivity of composite, k_1 is the thermal conductivity of the matrix (continuous phase), ϕ is the volume fraction of the filler (core-shell particles), B and A are given as

$$B = (2+\delta^3)\frac{k_3}{k_1} - 2(1-\delta^3)\frac{k_2}{k_1} \tag{17.2}$$

$$A = 1 + 2\delta^3 - (1-\delta^3)\frac{k_3}{k_2} \tag{17.3}$$

In Equations 17.2 and 17.3, δ is the ratio of outer radius of shell to core radius, k_2 is the thermal conductivity of shell material, and k_3 is the thermal conductivity of the core material.

17.2 NONDILUTE COMPOSITES OF CORE-SHELL PARTICLES

Equation 17.1 is valid for infinitely dilute systems ($\phi \to 0$) and therefore, it cannot be applied at finite concentration of particles as the interaction between the particles is not considered in its derivation. One can derive a thermal conductivity expression for nondilute composites of core-shell particles using the Maxwell approach.

Consider a single core-shell particle embedded in an infinite matrix of thermal conductivity k_1. Let the radius of the core be "a," the thickness of the shell be "d," and the volume fraction of core in the core-shell particle be ϕ_c. Note that $\phi_c = (a/(a + d))^3 = 1/\delta^3$, where δ is the ratio of outer radius of interfacial shell to core radius. The system is subjected to a temperature field with uniform temperature gradient α far away from the particle. The temperature in the matrix at a radial distance r ($r > a + d$) from the centre of the particle is

$$T(r,\theta) = \alpha r\cos\theta + \alpha\left[\frac{(k_1 - k_2)(2k_2 + k_3) + (k_2 - k_3)(2k_2 + k_1)\phi_c}{(2k_1 + k_2)(2k_2 + k_3) + 2(k_1 - k_2)(k_2 - k_3)\phi_c}\right]\left[\frac{(a+d)^3}{r^2}\right]\cos\theta \tag{17.4}$$

Now consider a cluster of core-shell particles embedded in an infinite matrix of thermal conductivity k_1. The cluster of core-shell particles, enclosed by a spherical region of radius R, consists of n spherical core-shell particles. The system is subjected to a temperature field with uniform temperature gradient α at large values of r. Assuming negligible interaction between the core-shell particles, the temperature at a radial distance r ($r \gg R$) from the centre of the spherical cluster region R is

$$T(r,\theta) = \alpha r\cos\theta + \alpha\left[\frac{(k_1 - k_2)(2k_2 + k_3) + (k_2 - k_3)(2k_2 + k_1)\phi_c}{(2k_1 + k_2)(2k_2 + k_3) + 2(k_1 - k_2)(k_2 - k_3)\phi_c}\right]\left[\frac{(a+d)^3}{r^2}\right]n\cos\theta \tag{17.5}$$

Since the volume fraction of core-shell particles in the dispersion is $\phi = n\,[(a + d)/R]^3$, Equation 17.5 can be rewritten as

$$T(r,\theta) = \alpha r\cos\theta + \alpha\left[\frac{(k_1 - k_2)(2k_2 + k_3) + (k_2 - k_3)(2k_2 + k_1)\phi_c}{(2k_1 + k_2)(2k_2 + k_3) + 2(k_1 - k_2)(k_2 - k_3)\phi_c}\right]\left[\frac{R^3}{r^2}\right]\phi\cos\theta \tag{17.6}$$

Now if the cluster of core-shell particles is treated as an "effective homogeneous medium" of radius R and thermal conductivity k, suspended in a matrix of thermal conductivity k_1, the potential at any radial location r ($\gg R$) is given as

$$T(r,\theta) = \alpha r\cos\theta + \alpha\left(\frac{k_1 - k}{2k_1 + k}\right)\left(\frac{R^3}{r^2}\right)\cos\theta \tag{17.7}$$

As the above two expressions, Equations 17.6 and 17.7, are equivalent, it follows that

$$\left(\frac{k_1 - k}{2k_1 + k}\right) = \left[\frac{(k_1 - k_2)(2k_2 + k_3) + (k_2 - k_3)(2k_2 + k_1)\phi_c}{(2k_1 + k_2)(2k_2 + k_3) + 2(k_1 - k_2)(k_2 - k_3)\phi_c}\right]\phi \tag{17.8}$$

This equation could be recast as follows:

$$k_r = \frac{k}{k_1} = \left[\frac{2(1-\phi) + (1+2\phi)(B/A)}{(2+\phi) + (1-\phi)(B/A)}\right] \tag{17.9}$$

where B and A are defined in Equations 17.2 and 17.3. This expression was recently derived by Felske [1]. Interestingly, the same expression (Equation 17.9) was derived earlier by Pauly and Schwan [7] for the dielectric constant of particulate dispersions of core-shell particles. In the limit $\phi \to 0$, Equation 17.9 reduces to Equation 17.1.

Equation 17.9 generally describes the thermal conductivity data well when ϕ is less than about 0.2. At higher values of ϕ, significant deviation occurs between the predictions of Equation 17.9 and the actual values. Furthermore, the equation fails to exhibit divergence in thermal conductivity k at $\phi \to \phi_m$, where ϕ_m is the maximum packing volume fraction of particles. Note that at $\phi = \phi_m$, k is expected to diverge especially for composites with $k_3 \to \infty$ and $k_2 \to \infty$.

Pal [8] has recently developed a series of models for the relative thermal conductivity of concentrated composites of core-shell particles using the differential effective medium approach. Consider a composite with a volume fraction of core-shell particles ϕ. Into this composite, add a small differential quantity of new core-shell particles. The increment change in thermal conductivity dk resulting from the addition of the new core-shell particles can be calculated from Equation 17.1 by treating the composite into which the new core-shell particles are added as an equivalent effective medium of thermal conductivity k. Therefore,

$$dk = 3k\left[1 - \frac{3A}{2A + Bk_1/k}\right]d\phi \tag{17.10}$$

This equation could be rewritten as

$$\frac{dk}{3k} + \frac{A\,dk}{(Bk_1 - Ak)} = d\phi \tag{17.11}$$

Upon integration with the limit $k \to k_1$ at $\phi \to 0$, Equation 17.11 gives

$$(k_r)^{1/3}\left[\frac{\beta - 1}{\beta - k_r}\right] = \exp(\phi) \tag{17.12}$$

where k_r is the relative thermal conductivity (k/k_1) and β is given as

$$\beta = \frac{B}{A} = \frac{(2+\delta^3)\lambda_{31} - 2(1-\delta^3)\lambda_{21}}{(1+2\delta^3) - (1-\delta^3)\lambda_{32}} \tag{17.13}$$

In Equation 17.13, λ_{21} is the ratio of shell material thermal conductivity (k_2) to matrix thermal conductivity (k_1), λ_{31} is the ratio of core-to-matrix thermal conductivities (k_3/k_1), and λ_{32} is the ratio of core-to-shell thermal conductivities (k_3/k_2). Note that $\lambda_{31} = \lambda_{21}\lambda_{32}$.

Equation 17.12, referred to as Model 1, is expected to describe the relative thermal conductivity of composites only at low to moderate concentrations of core-shell particles. At high values of ϕ, Model 1 is expected to deviate from the actual thermal conductivity because in the derivation of Equation 17.12, it is assumed that the entire volume of the existing composite before new core-shell particles are added is available as free volume to the new core-shell particles. In reality, the free volume to disperse the new particles is significantly less, due to the volume preempted by the particles already present. When new particles are added to the composite, the increase in the actual volume fraction of the dispersed phase (core-shell particles) is $d\phi/(1 - \phi)$. Therefore,

$$\frac{dk}{3k} + \frac{Adk}{(Bk_1 - Ak)} = \frac{d\phi}{1-\phi} \tag{17.14}$$

Upon integration with the limit $k \to k_1$ at $\phi \to 0$, Equation 17.14 gives

$$(k_r)^{1/3}\left[\frac{\beta - 1}{\beta - k_r}\right] = (1-\phi)^{-1} \tag{17.15}$$

This equation, referred to as Model 2, assumes that the volume fraction of dispersed phase (core-shell particles) can reach unity as more and more core-shell particles are added to the composite. In reality, there exists an upper limit for ϕ, referred to as ϕ_m (maximum packing volume fraction of core-shell particles in the composite), where the particles just touch each other. To account for the packing limit of particles the incremental increase in the volume fraction of the dispersed phase, when small differential quantity of new particles are added to an existing suspension of dispersed phase volume fraction ϕ, is taken to be $d[\phi/(1 - \phi/\phi_m)]$ rather than $d\phi/(1 - \phi)$ [8]. Thus, Equation 17.14 is revised as

$$\frac{dk}{3k} + \frac{Adk}{(Bk_1 - Ak)} = d\left(\frac{\phi}{1 - \frac{\phi}{\phi_m}}\right) \tag{17.16}$$

Upon integration with the limit $k \to k_1$ at $\phi \to 0$, Equation 17.16 gives

$$(k_r)^{1/3}\left[\frac{\beta-1}{\beta-k_r}\right]=\exp\left(\frac{\phi}{1-\frac{\phi}{\phi_m}}\right) \tag{17.17}$$

This equation is referred to as Model 3.

Another way to account for the packing limit of particles [8] is to take the incremental increase in the volume fraction of the dispersed phase, when a small quantity of new particles are added to an existing suspension of concentration ϕ, as $d\phi/(1 - \phi/\phi_m)$ rather than $d[\phi/(1 - \phi/\phi_m)]$. Thus, Equation 17.14 should be revised as

$$\frac{dk}{3k}+\frac{Adk}{(Bk_1-Ak)}=\left(\frac{d\phi}{1-\frac{\phi}{\phi_m}}\right) \tag{17.18}$$

Upon integration with the limit $k \to k_1$ at $\phi \to 0$, Equation 17.18 gives

$$(k_r)^{1/3}\left[\frac{\beta-1}{\beta-k_r}\right]=\left(1-\frac{\phi}{\phi_m}\right)^{-\phi_m} \tag{17.19}$$

This equation is referred to as Model 4.

17.3 MODEL PREDICTIONS

Based on the models just discussed in the preceding section, the relative thermal conductivity of a composite of core-shell particles can be expressed as

$$k_r = f(\delta, \lambda_{21}, \lambda_{32}, \phi, \phi_m) \tag{17.20}$$

Figure 17.1 shows the relative thermal conductivity predicted from the models under the conditions $\delta = 4/3$, $\lambda_{32} = 10$, $\phi = 0.45$, $\phi_m = 0.637$. The models predict that at a fixed value of ϕ, the relative thermal conductivity (k_r) initially remains constant with the increase in the thermal conductivity ratio λ_{21}. In the range $10^{-2} < \lambda_{21} < 10^3$, k_r increases with the increase in λ_{21} as the shell material becomes more conductive. At higher values of $\lambda_{21}(\lambda_{21} > 10^3)$, k_r again becomes constant (independent of λ_{21}). Interestingly, k_r is less than unity for small values of $\lambda_{21}(\lambda_{21} < 0.4)$ and k_r is greater than unity when λ_{21} is large ($\lambda_{21} > 0.4$). For low values of $\lambda_{21}(\lambda_{21} < 0.4)$, the values of k_r predicted by different models are as follows: Model 1 (Equation 17.12) > Model 2 (Equation 17.15) > Model 4 (Equation 17.19) > Model 3 (Equation 17.17). For large $\lambda_{21}(\lambda_{21} > 0.4)$, the order is reversed and the values of k_r predicted by different models are as follows: Model 3 > Model 4 > Model 2 > Model 1.

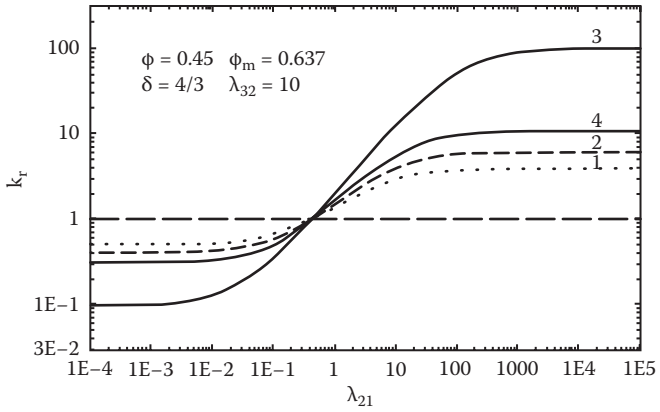

FIGURE 17.1 Relative thermal conductivity (k_r) of composite of core-shell particles predicted from the models. (From Pal, R., *Mat. Sci. Eng. A*. 498: 135–141, 2008.)

Figure 17.2 shows the effect of filler volume fraction (ϕ) on the relative thermal conductivity (k_r). The plots are generated from Model 4 (Equation 17.19) under the conditions $\delta = 4/3$, $\lambda_{32} = 10$, $\phi_m = 0.637$. Note that a ϕ_m value of 0.637 corresponds to random packing of uniform spheres. For low values of $\lambda_{21}(\lambda_{21} < 0.4)$, k_r decreases with the increase in ϕ. For large values of $\lambda_{21}(\lambda_{21} > 0.4)$, k_r increases with the increase in ϕ.

Figure 17.3 shows relative thermal conductivity k_r versus thermal conductivity ratio λ_{21} plots for different values of radii ratio δ. The plots are generated from Model 4 (Equation 17.19) under the conditions: $\phi = 0.50$, $\phi_m = 0.637$, and $\lambda_{32} = 10$. The radii ratio δ affects the relative thermal conductivity of composite only in the intermediate range of λ_{21}. At very low and very high values of $\lambda_{21}(\lambda_{21} < 10^{-3}$ and $\lambda_{21} > 10^3$, respectively), k_r of composite is independent of the radii ratio δ. In the intermediate range of $\lambda_{21}(10^{-3} <$

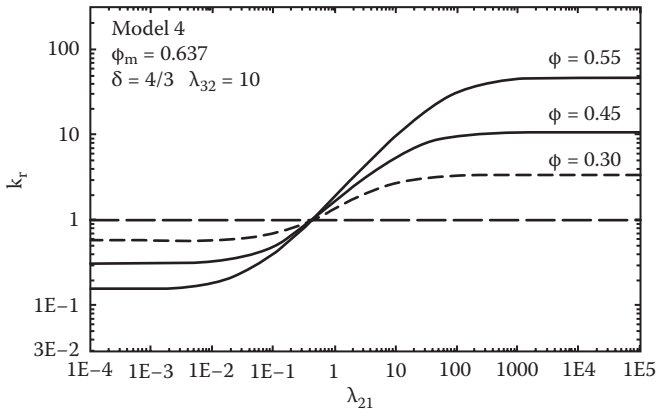

FIGURE 17.2 Effect of filler volume fraction (ϕ) on the relative thermal conductivity of composite of core-shell particles. (From Pal, R., *Mat. Sci. Eng. A*. 498: 135–141, 2008.)

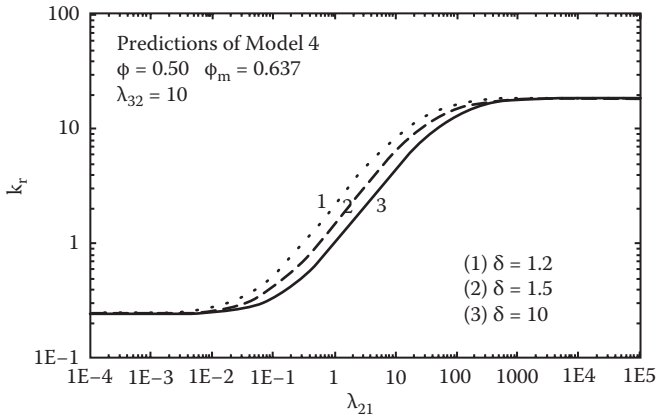

FIGURE 17.3 Effect of shell-to-core radii ratio (δ) on the relative thermal conductivity of composite of core-shell particles. (From Pal, R., *Mat. Sci. Eng. A*. 498: 135–141, 2008.)

$\lambda_{21} < 10^3$), the relative thermal conductivity of a composite decreases with the increase in δ. An increase in the ratio δ implies an increase in the shell thickness of the core-shell particle of a composite. Thus, the relative thermal conductivity of a composite of core-shell particles decreases with an increase in the shell thickness.

Figure 17.4 shows relative thermal conductivity versus λ_{21} plots for two different values of thermal conductivity ratio λ_{32} (thermal conductivity of core material divided by thermal conductivity of shell material). The plots are generated from Model 4 (Equation 17.19) under the conditions: $\phi = 0.50$, $\phi_m = 0.637$, and $\delta = 4/3$. With the increase in λ_{32}, the core material becomes more conductive and the relative thermal conductivity of a composite increases for intermediate values of $\lambda_{21}(10^{-3} < \lambda_{21} < 10^3)$.

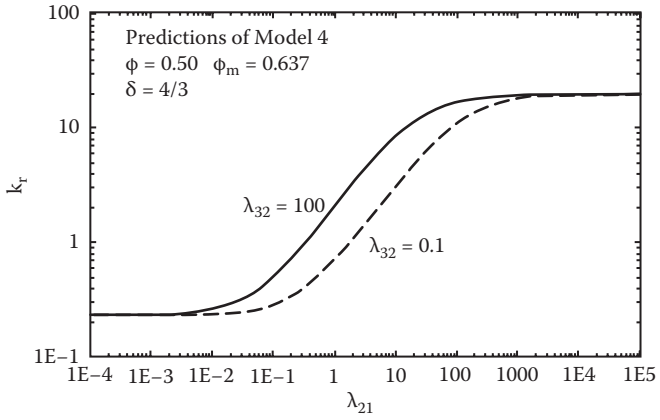

FIGURE 17.4 Effect of core-to-shell thermal conductivities ratio (λ_{32}) on the relative thermal conductivity of composite of core-shell particles. (From Pal, R., *Mat. Sci. Eng. A*. 498: 135–141, 2008.)

Figures 17.5 and 17.6 show the plots of relative thermal conductivity of composite (k_r) as a function of the volume fraction of core-shell particles (ϕ) for thermally *nonconducting core* ($k_3 \to 0$). The plots are generated from Model 4 (Equation 17.19). With the increase in thermal conductivity ratio λ_{21} (see Figure 17.5) for a fixed radii ratio δ, the relative thermal conductivity of the composite increases at a given volume fraction of particles ϕ. The increase in k_r with the increase in λ_{21} (for fixed δ and ϕ) is expected as the shell material becomes more thermally conductive. With the increase in radii ratio δ for a fixed λ_{21} of 10 (see Figure 17.6), the relative thermal conductivity at a given volume fraction of particles increases. The increase in k_r with

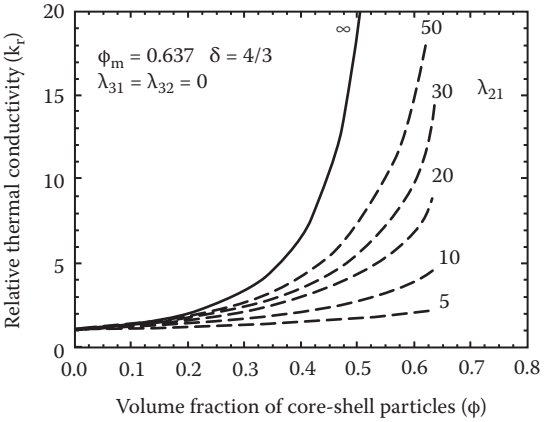

FIGURE 17.5 Relative thermal conductivity of composite as a function of filler volume fraction for different values of λ_{21} when the core is *thermally nonconducting* ($k_3 \to 0$). (From Pal, R., *Mat. Sci. Eng. A*. 498: 135–141, 2008.)

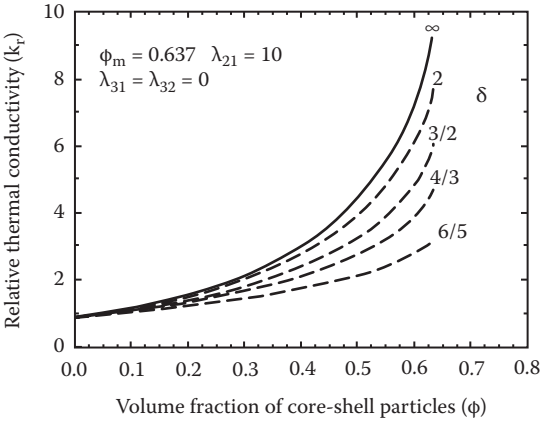

FIGURE 17.6 Relative thermal conductivity of composite as a function of filler volume fraction for different values of shell-to-core radii ratio (δ) when the core is *thermally nonconducting* ($k_3 \to 0$). (From Pal, R., *Mat. Sci. Eng. A*. 498: 135–141, 2008.)

the increase in radii ratio δ (for fixed λ_{21} and ϕ) is expected as the nonconductive core material ($k_3 \to 0$) is replaced by conductive shell material ($\lambda_{21} = 10$).

Figures 17.7 and 17.8 show the plots of relative thermal conductivity (k_r) as a function of the volume fraction of core-shell particles (ϕ) for *highly conducting core* ($k_3 \to \infty$). The plots are generated from Model 4 (Equation 17.19). With the increase in λ_{21} (see Figure 17.7) for a fixed δ (fixed shell thickness), k_r of the composite at a given volume fraction of particle increases. The increase in k_r with the increase in λ_{21} (for fixed δ and ϕ) is expected as the shell material becomes more thermally conductive. With the increase in radii ratio δ (that is, increase in shell thickness) at a fixed λ_{21} of 2.5 (Figure 17.8), the relative conductivity of the composite decreases at

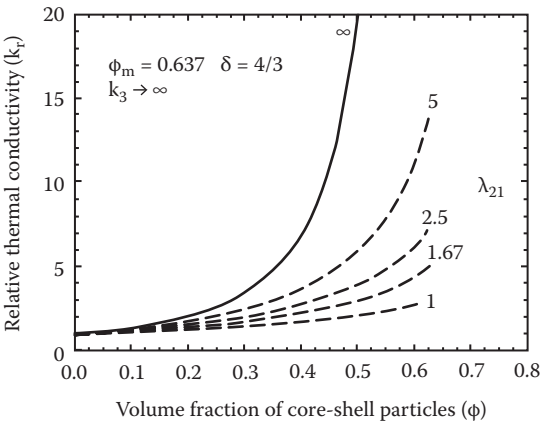

FIGURE 17.7 Relative thermal conductivity of composite as a function of filler volume fraction for different values of λ_{21} when the core is *thermally highly conducting* ($k_3 \to \infty$). (From Pal, R., *Mat. Sci. Eng. A*. 498: 135–141, 2008.)

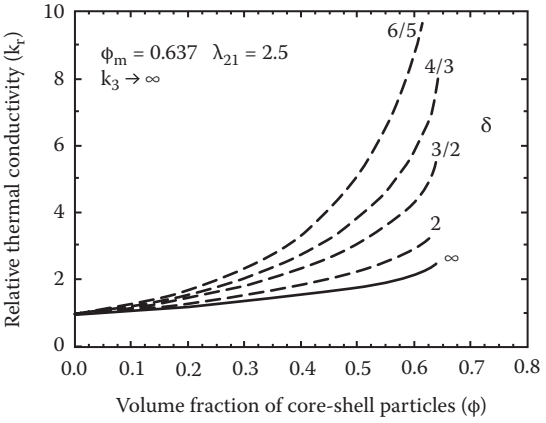

FIGURE 17.8 Relative thermal conductivity of composite as a function of filler volume fraction for different values of shell-to-core radii ratio (δ) when the core is *thermally highly conducting* ($k_3 \to \infty$). (From Pal, R., *Mat. Sci. Eng. A*. 498: 135–141, 2008.)

a given volume fraction of dispersed phase. The decrease in k_r with the increase in radii ratio δ (for fixed λ_{21} and ϕ) is expected as the highly conductive core material ($k_3 \to \infty$) is replaced by less conductive shell material ($\lambda_{21} = 2.5$).

17.4 COMPARISON OF MODEL PREDICTIONS WITH EXPERIMENTAL DATA

The experimental data considered for comparison are of two types [8]. One type of data (Sets 1 through 13) deals with the situation where $\delta = 1$, that is, the particles are without any shell. In this case, the composite consists of simple homogeneous particles with $\beta = \lambda_{31}$. These data are used to select the best model among the four Pal models discussed in Section 17.2. The other type of data (Sets 14 through 17) deals with composites of nanoparticles where $\delta > 1$, that is, the nanoparticles are of core-shell type with nonzero shell thickness. These data are used to evaluate the model selected on the basis of homogeneous particle data (Sets 1 through 13).

The comparisons of experimental data with the predictions of the models for the case where $\delta = 1$ (that is, particles without shells) revealed that Model 4 (Equation 17.19) is the best among the models discussed in the preceding section. The experimental data could be described adequately with Model 4 using reasonable values of ϕ_m, the maximum packing volume fraction of particles. Model 1 (Equation 17.12) generally underpredicts the values of relative thermal conductivity, especially at high values of ϕ, whereas Model 3 (Equation 17.17) generally overpredicts the values of k_r. Model 2 (Equation 17.15) is just a special case of model 4 with a fixed ϕ_m of 1.0.

Figure 17.9 shows all thirteen sets of experimental data on thermal conductivity of particulate composites with $\delta = 1$. The data are compared with Model 4 (Equation

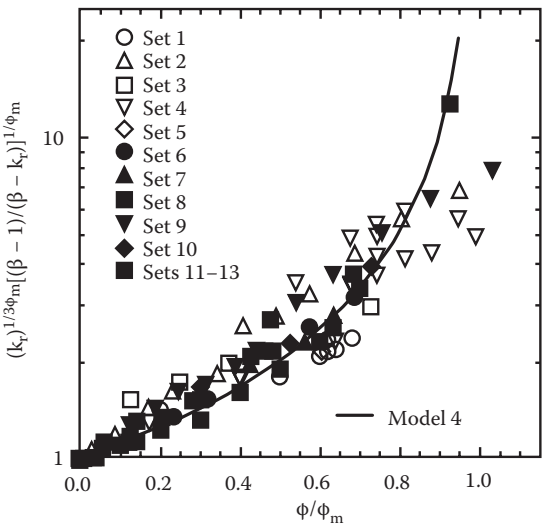

FIGURE 17.9 Comparison between experimental thermal conductivity data (13 sets) and prediction of Model 4 (Equation 17.19). (From Pal, R., *Mat. Sci. Eng. A*. 498: 135–141, 2008.)

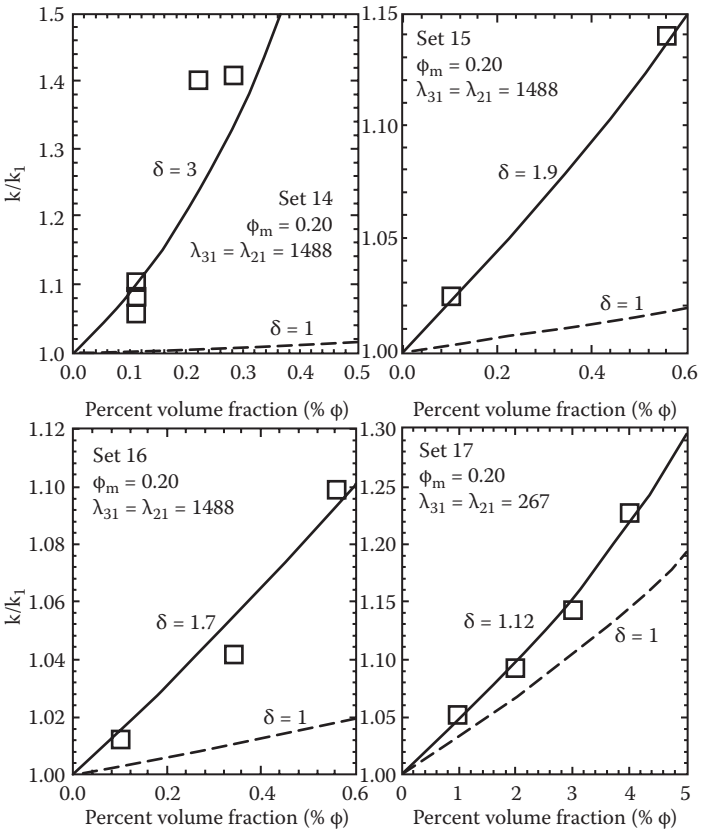

FIGURE 17.10 Comparisons between experimental thermal conductivity data and predictions of Model 4 (Equation 17.19) for composite systems with $\delta > 1.0$. (From Pal, R., *Mat. Sci. Eng. A*. 498: 135–141, 2008.)

17.19) predictions. The experimental data are plotted as $(k_r)^{1/3\phi_m}[(\beta-1)/(\beta-k_r)]^{1/\phi_m}$ versus ϕ/ϕ_m. As can be seen, Model 4 describes the experimental data adequately.

The experimental thermal conductivity data for composites with $\delta > 1$ (Sets 14 through 17) are compared with the predictions of Model 4 (Equation 17.19) in Figure 17.10. For comparison purposes, the predictions of Model 4 for the case where δ is unity (particles without shell) are also shown. The experimental data are plotted as relative thermal conductivity (k/k_1) versus percent volume fraction of core particles. The data can be described very well by Model 4 using $\phi_m = 0.20$, $\lambda_{21} = \lambda_{31}$ (shell conductivity is equal to core particle conductivity), and δ values as follows: $\delta = 3$ (Set 14), $\delta = 1.9$ (Set 15), $\delta = 1.7$ (Set 16), and $\delta = 1.12$ (Set 17).

17.5 CONCLUDING REMARKS

The relative thermal conductivity (k_r) of composites of core-shell filler particles is a function of five variables, that is, $k_r = f(\delta, \lambda_{21}, \lambda_{32}, \phi, \phi_m)$, where δ is the ratio of

shell-to-core radii, λ_{21} is the ratio of shell-to-matrix thermal conductivities, λ_{32} is the ratio of core-to-shell thermal conductivities, ϕ is the volume fraction of filler, and ϕ_m is the maximum packing volume fraction of filler (core-shell particles). When the core is thermally nonconducting ($\lambda_{31} \to 0$, $\lambda_{32} \to 0$), k_r is greater than unity and it increases with the increase in ϕ provided that λ_{21} is large ($\lambda_{21} \gg 1.0$). The relative thermal conductivity increases with the increase in λ_{21} for any given ϕ and δ. The k_r also increases with the increase in δ for any given ϕ provided that $\lambda_{21} > 1.0$. When the core is highly thermally conducting ($\lambda_{31} \to \infty$, $\lambda_{32} \to \infty$), k_r is greater than unity and it increases with the increase in ϕ provided that $\lambda_{21} > 1.0$. Even when λ_{21} is less than, but close to, unity, the relative thermal conductivity of the composite is larger than unity. The relative thermal conductivity increases with the increase in λ_{21} for any given ϕ and δ. However, k_r decreases with the increase in δ at any given ϕ for intermediate values of $\lambda_{21}(10^{-3} < \lambda_{21} < 10^3)$. At very low and very high values of λ_{21} ($\lambda_{21} < 10^{-3}$ and $\lambda_{21} > 10^3$, respectively), k_r is independent of the film thickness. Model 4 (Equation 17.19) describes the thermal conductivity data for composites of homogeneous and core-shell filler particles reasonably well.

REFERENCES

1. Felske, J.D. 2004. Effective thermal conductivity of composite spheres in a continuous medium with contact resistance. *Int. J. Heat Mass. Tran.* 47: 3453–3461.
2. Huber, G. and T.A. Vilgis. 2002. On the mechanism of hydrodynamic reinforcement in elastic composites. *Macromolecules.* 35: 9204–9210.
3. Luzinov, I., C. Pagnoulle, and R. Jerome. 2000. Ternary polymer blend with core-shell dispersed phases: Effect of the core-forming polymer on phase morphology and mechanical properties. *Polymer.* 41: 7099–7109.
4. Garboczi, E.J. and J.G. Berryman. 2001. Elastic moduli of a material containing composite inclusions: Effective medium theory and finite element computations. *Mech. Mater.* 33: 455–470.
5. Oksman, K. and C. Clemons. 1998. Mechanical properties and morphology of impact modified polypropylene–wood flour composites. *J. Appl. Polym. Sci.* 67: 1503–1513.
6. Gupta, N. and D. Pinisetty. 2013. A review of thermal conductivity of polymer matrix syntactic foams–effect of hollow particle wall thickness and volume fraction. *JOM.* 65: 234–245.
7. Pauly, H. and H.P. Schwan. 1959. Über die Impedanz einer Suspension von kugelformigen Teilchen mit einer Schale. *Z. Naturforsch.* 146: 125–131.
8. Pal, R. 2008. Thermal conductivity of three-component composites of core-shell particles. *Mat. Sci. Eng. A.* 498: 135–141.

18 Influence of Interfacial Contact Resistance on Thermal Conductivity of Composites

18.1 INTRODUCTION

In the preceding chapters, the thermal contact resistance between the filler particles and the matrix was neglected. The temperatures were assumed to be continuous across the filler–matrix interfaces. Thermal contact resistance arises in situations where there is poor adherence between the particles and the matrix [1–7]. Also, when the coefficients of thermal expansion of dispersed phase and matrix are significantly different from each other, voids or gap may develop between the two phases resulting in contact resistance.

As noted in Chapter 15, the interfacial resistance to heat transfer or thermal contact resistance, R_C'', is defined as

$$R_C'' = \frac{T_I - T_{II}}{q''_{interface}} \tag{18.1}$$

where $T_I - T_{II}$ is the temperature drop across the interface and $q''_{interface}$ is the heat flux at interface. The temperature distribution is not continuous at the interface although the heat flux is still continuous, that is,

$$T_I \neq T_{II} \text{ at the interface} \tag{18.2}$$

$$q_I'' = q_{II}'' = q''_{interface} \text{ at the interface} \tag{18.3}$$

The effective thermal conductivity of a composite is expected to be low in the presence of interfacial contact resistance between the filler particles and matrix. In the extreme case of high contact resistance, the filler particles are expected to be thermally nonconducting, regardless of their thermal conductivity.

18.2 THERMAL CONDUCTIVITY MODELS FOR COMPOSITES WITH CONTACT RESISTANCE

18.2.1 Spherical Filler Particles

Consider a single spherical particle of radius "a" and thermal conductivity k_d, embedded in an infinite matrix of thermal conductivity k_m. The system is subjected to a temperature field with uniform temperature gradient α far away from the particle. At $r \to \infty$, the temperature distribution is given as

$$T(r,\theta) = \alpha z \text{ where } z = r\cos\theta \tag{18.4}$$

At the particle–matrix interface (r = a), the boundary conditions to be satisfied are as follows:

$$k_d \frac{\partial T_d}{\partial r} = k_m \frac{\partial T_m}{\partial r} \tag{18.5}$$

$$T_d - T_m = q''_{interface} R''_C = -R''_C k_d \frac{\partial T_d}{\partial r} \tag{18.6}$$

As noted earlier, the heat flux is taken as continuous and the temperature as discontinuous at the interface.

The temperature distributions in the particle and matrix are given as follows:

$$T_d(r,\theta) = Ar\cos\theta \quad (0 < r < a) \tag{18.7}$$

$$T_m(r,\theta) = \alpha r\cos\theta + B\frac{\cos\theta}{r^2} \quad (a < r < \infty) \tag{18.8}$$

The constants A and B can be determined from the two boundary conditions at the interface, that is, Equations 18.5 and 18.6. The boundary condition corresponding to the continuity of heat flux at the interface (Equation 18.5) gives

$$k_d A = k_m \alpha - \frac{2B}{a^3} k_m \tag{18.9}$$

From the other boundary condition corresponding to a jump in temperature at the interface (Equation 18.6), the following result is obtained:

$$Aa - \alpha a - \frac{B}{a^2} = -R''_C k_d A \tag{18.10}$$

Equations 18.9 and 18.10 give the following expressions for B and A:

$$B = \left[\frac{k_m - k_d + \dfrac{k_d k_m R_C''}{a}}{k_d + 2k_m + \dfrac{2k_d k_m R_C''}{a}} \right] \alpha a^3 = \alpha a^3 \left[\frac{k_m}{k_d} + \frac{k_m R_C''}{a} - 1 \right] \left[1 + \frac{2k_m}{k_d} \left(1 + \frac{R_C'' k_d}{a} \right) \right]^{-1} \tag{18.11}$$

$$A = \left[\frac{B + \alpha a^3}{a^3 + a^2 R_C'' k_d} \right] = \left[\frac{1 + \left(\dfrac{k_m}{k_d} + \dfrac{k_m R_C''}{a} - 1 \right) \left[1 + \dfrac{2k_m}{k_d} \left(1 + \dfrac{R_C'' k_d}{a} \right) \right]^{-1}}{\left(1 + \dfrac{R_C'' k_d}{a} \right)} \right] \alpha \tag{18.12}$$

Upon substituting for B and A into the temperature distribution equations (Equations 18.7 and 18.8), the following expressions for temperature distributions are obtained:

$$T_d(r,\theta) = \left[\frac{1 + \left(\dfrac{k_m}{k_d} + \dfrac{k_m R_C''}{a} - 1 \right) \left[1 + \dfrac{2k_m}{k_d} \left(1 + \dfrac{R_C'' k_d}{a} \right) \right]^{-1}}{\left(1 + \dfrac{R_C'' k_d}{a} \right)} \right] \alpha r \cos\theta \quad (0 < r < a) \tag{18.13}$$

$$T_m(r,\theta) = \alpha r \cos\theta + \frac{\cos\theta}{r^2} \alpha a^3 \left[\frac{k_m}{k_d} + \frac{k_m R_C''}{a} - 1 \right] \left[1 + \frac{2k_m}{k_d} \left(1 + \frac{R_C'' k_d}{a} \right) \right]^{-1} \quad (a < r < \infty) \tag{18.14}$$

When thermal contact resistance R_C'' is negligible, the temperature distributions simplify to

$$T_d(r,\theta) = \left[\frac{3k_m}{k_d + 2k_m} \right] \alpha r \cos\theta \quad (0 < r < a) \tag{18.15}$$

$$T_m(r,\theta) = \alpha r \cos\theta + \frac{\cos\theta}{r^2} \alpha a^3 \left[\frac{k_m - k_d}{k_d + 2k_m} \right] \quad (a < r < \infty) \tag{18.16}$$

Now that the temperature distribution in a single-particle system is known, the thermal conductivity equation for composites can be derived using the Maxwell approach. Consider a cluster of particles embedded in an infinite matrix of thermal conductivity k_m. The cluster of particles, enclosed by a spherical region of radius R, consists of n spherical particles of radius "a" and thermal conductivity k_d. The system is subjected to a temperature field with uniform temperature gradient α at large values of r. At $r \to \infty$, the temperature distribution is given by Equation 18.4. Assuming negligible interaction between the particles, the temperature at a radial distance r ($r \gg R$) from the center of the spherical cluster region R can be determined from Equation 18.14 as

$$T_m(r,\theta) = \alpha r\cos\theta + n\frac{\cos\theta}{r^2}\alpha a^3\left[\frac{k_m}{k_d} + \frac{k_m R_C''}{a} - 1\right]\left[1 + \frac{2k_m}{k_d}\left(1 + \frac{R_C'' k_d}{a}\right)\right]^{-1} \quad (a < r < \infty) \tag{18.17}$$

Since $\phi = n(a/R)^3$, Equation 18.17 can be rewritten as

$$T_m(r,\theta) = \alpha r\cos\theta + \phi\frac{\cos\theta}{r^2}\alpha R^3\left[\frac{k_m}{k_d} + \frac{k_m R_C''}{a} - 1\right]\left[1 + \frac{2k_m}{k_d}\left(1 + \frac{R_C'' k_d}{a}\right)\right]^{-1} \quad (a < r < \infty) \tag{18.18}$$

Now, if the cluster of particles is treated as an "effective homogeneous medium" of radius R and thermal conductivity k, suspended in a matrix of conductivity k_m, the temperature at any radial location r ($\gg R$) is given as

$$T_m(r,\theta) = \alpha r\cos\theta + \frac{\cos\theta}{r^2}\alpha R^3\left[\frac{k_m}{k} + \frac{k_m R_C''}{R} - 1\right]\left[1 + \frac{2k_m}{k}\left(1 + \frac{R_C'' k}{R}\right)\right]^{-1} \quad (a < r < \infty) \tag{18.19}$$

Since the two expressions, Equations 18.18 and 18.19, are equivalent, it follows that

$$\phi\left[\frac{k_m}{k_d} + \frac{k_m R_C''}{a} - 1\right]\left[1 + \frac{2k_m}{k_d}\left(1 + \frac{R_C'' k_d}{a}\right)\right]^{-1} = \left[\frac{k_m}{k} + \frac{k_m R_C''}{R} - 1\right]\left[1 + \frac{2k_m}{k}\left(1 + \frac{R_C'' k}{R}\right)\right]^{-1} \tag{18.20}$$

As R is large, we can simplify this equation to

$$\phi\left[\frac{k_m}{k_d} + \frac{k_m R_C''}{a} - 1\right]\left[1 + \frac{2k_m}{k_d}\left(1 + \frac{R_C'' k_d}{a}\right)\right]^{-1} = \left[\frac{k_m}{k} - 1\right]\left[1 + \frac{2k_m}{k}\right]^{-1} \tag{18.21}$$

Upon rearrangement, Equation 18.21 results in the following expression for the effective thermal conductivity of composite:

$$\frac{k}{k_m} = \frac{1 + 2\phi\left[\dfrac{(k_d/k_m) - (R_C'' k_d/a) - 1}{2 + 2(R_C'' k_d/a) + (k_d/k_m)}\right]}{1 - \phi\left[\dfrac{(k_d/k_m) - (R_C'' k_d/a) - 1}{2 + 2(R_C'' k_d/a) + (k_d/k_m)}\right]} \tag{18.22}$$

This equation was first derived by Hasselman and Johnson [1]. When the interfacial contact resistance R_C'' is negligible, Equation 18.22 reduces to the Maxwell–Eucken equation (Chapter 16, Equation 16.24). Note that the relative thermal conductivity of composites in the presence of thermal contact resistance is not only a function of filler volume fraction (ϕ) and thermal conductivity ratio λ ($= k_d/k_m$), it also depends on the size of the filler particles.

Figure 18.1 shows the predictions of thermal conductivity of composites using Equation 18.22 for different values of the contact resistance term $R_C'' k_d/a$. The relative thermal conductivity of the composite decreases with the increase in the contact resistance at any given volume fraction of filler particles. Also, note from Figure 18.1 that although the conductivity ratio λ ($= k_d/k_m$) is large, the relative thermal conductivity of the composite decreases with the increase in filler concentration when the thermal contact resistance is large.

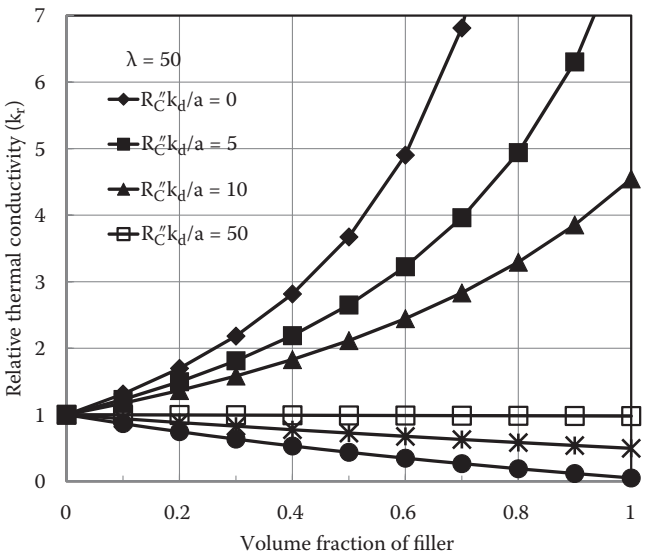

FIGURE 18.1 Relative thermal conductivity of composite versus volume fraction of filler for different values of thermal contact resistance term $R_C'' k_d/a$.

18.2.2 Nonspherical Filler Particles

Using the Maxwell approach discussed in the preceding section, Hasselman and Johnson [1] developed the following expression for the thermal conductivity of composites of *cylindrical particles* with cylinder axis oriented perpendicular to the direction of heat flow:

$$\frac{k}{k_m} = \frac{1+\phi\left[\dfrac{(k_d/k_m)-(R''_C k_d/a)-1}{1+(R''_C k_d/a)+(k_d/k_m)}\right]}{1-\phi\left[\dfrac{(k_d/k_m)-(R''_C k_d/a)-1}{1+(R''_C k_d/a)+(k_d/k_m)}\right]} \tag{18.23}$$

where "a" is the radius of the cylindrical particles.

For composites of *flat plate*-type filler particles oriented perpendicular to the direction of heat flow (that is, heat flow is perpendicular to the plane of the plate), Hasselman and Johnson [1] proposed the following Reuss-type mixing rule:

$$\frac{1}{k} = \frac{\phi}{k_d} + \frac{1-\phi}{k_m} + \frac{2\phi R''_C}{a} \tag{18.24}$$

where "a" is the thickness of the plate-type particles. It is interesting to note that when the thermal contact resistance is large, the thermal conductivity of composite of flat plate-type filler particles becomes negligibly small. Thus, the flat plate-type filler particles with interfacial thermal resistance are most effective in lowering the thermal conductivity of composite.

REFERENCES

1. Hasselman, D.P.H. and L.F. Johnson. 1987. Effective thermal conductivity of composites with interfacial thermal barrier resistance. *J. Compos. Mater*. 21: 508–515.
2. Nan, C.-W., R. Birringer, D.R. Clarke, and H. Gleiter. 1997. Effective thermal conductivity of particulate composites with interfacial thermal resistance. *J. Appl. Phys*. 81: 6692–6699.
3. Hasselman, D.P.H., K.Y. Donaldson, and A.L. Geiger. 1992. Effect of reinforcement particle size on the thermal conductivity of a particulate-silicon carbide-reinforced aluminum matrix composite. *J. Am. Ceram. Soc*. 75: 3137–3140.
4. Geiger, A.L., D.P.H. Hasselman, and K.Y. Donaldson. 1993. Effect of reinforcement particle size on the thermal conductivity of a particulate silicon carbide-reinforced aluminium-matrix composite. *J. Mater. Sci. Lett*. 12: 420–423.
5. Every, A.G., Y. Tzou, D.P.H. Hasselman, and R. Raj. 1992. The effect of particle size on the thermal conductivity of ZnS/diamond composites: Theory and experiment. *Acta. Metall. Mater*. 40: 123–129.
6. Hasselman, D.P.H., K.Y. Donaldson, J. Liu, L.J. Gauckler, and P.D. Ownby. 1994. Thermal conductivity of a particulate-diamond-reinforced cordierite matrix composite. *J. Am. Ceram. Soc*. 77: 1757–1760.
7. Bai, G., W. Jiang, and L. Chen. 2006. Effect of interfacial thermal resistance on effective thermal conductivity of $MoSi_2$/SiC composites. *Mater. Trans*. 47: 1247–1249.

19 Thermal Diffusivity and Coefficient of Thermal Expansion of Composites

19.1 THERMAL DIFFUSIVITY OF COMPOSITES

The thermal diffusivity (α') of a material is defined as

$$\alpha' = \frac{k}{\rho C_p} \tag{19.1}$$

where k is the thermal conductivity, ρ is the density, and C_p is the heat capacity of the material. Thermal diffusivity is a key material property involved in transient heat conduction. It appears in the following heat diffusion equation derived in Section 15.3 of Chapter 15:

$$\frac{\partial T}{\partial t} = \alpha' \nabla^2 T \tag{19.2}$$

The thermal diffusivity of an isotropic composite can be determined from the knowledge of thermal conductivity, density, and heat capacity of the composite. The thermal conductivity of the composite can be estimated from the models discussed in the previous chapters. Assuming composite to be a pseudo-homogeneous mixture of dispersed phase and matrix, the density and heat capacity of the composite could be estimated from the following relations [1]:

$$\frac{1}{\rho} = \frac{x}{\rho_d} + \frac{1-x}{\rho_m} \tag{19.3}$$

or

$$\rho = \phi\rho_d + (1 - \phi)\rho_m \tag{19.4}$$

$$C_p = (\rho_d C_{p,d}\, \phi + \rho_m (1 - \phi) C_{p,m})/\rho \tag{19.5}$$

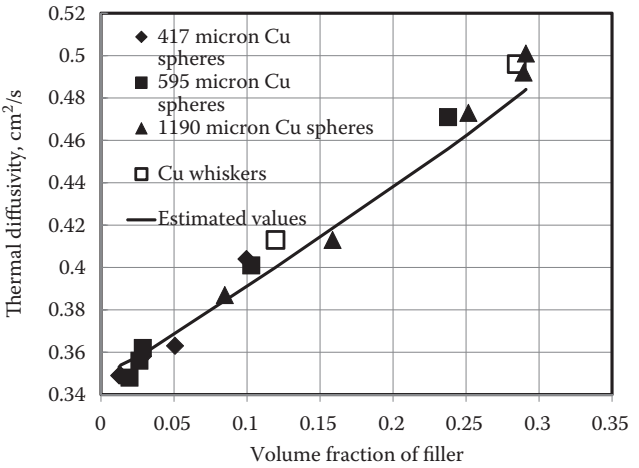

FIGURE 19.1 Comparison of experimental and estimated values of thermal diffusivity of composites of copper spheres and copper whiskers. (From Lee, H.J. and R.E. Taylor, *J. App. Phys*. 47: 148–151, 1976.)

or

$$C_p = xC_{p,d} + (1 - x)C_{p,m} \tag{19.6}$$

where subscript "d" refers to dispersed phase property and "m" refers to matrix property, ϕ is the volume fraction of filler, and x is the mass fraction of filler. Note that ϕ and x are related as follows:

$$x = \frac{\rho_d}{\rho}\phi \tag{19.7}$$

Figure 19.1 shows the plot of experimental values of thermal diffusivity of composites of copper spheres and copper whiskers [1]. The data are plotted as a function of filler volume fraction. The estimated values of thermal diffusivity, using the above equations in conjunction with the Maxwell–Eucken equation (Equation 16.24 of Chapter 16), are also shown as a solid curve. Clearly there is a good agreement between the experimental and estimated values.

19.2 COEFFICIENT OF THERMAL EXPANSION OF COMPOSITES

Another important thermal property of a composite is coefficient of thermal expansion (CTE). CTE is important in determining the dimensional changes of the composite resulting from temperature variations. CTE is defined as

$$\alpha = \frac{1}{V}\left(\frac{\partial V}{\partial T}\right)_P \tag{19.8}$$

where α is CTE, V is volume, T is temperature, and P is pressure. The CTE is generally positive for most materials, including composites. However, this is not always true as some materials do exhibit negative CTE [2]. For example, zirconium tungstate is a metal oxide which exhibits a large negative CTE.

In many applications, it is important to minimize the degree of thermal expansion. For example, composite materials used in the manufacture of aircrafts and space vehicles are subjected to extreme weather conditions. In order for the structure to be stable, it is necessary that the composite materials used in the construction to have low CTE. One example of composite material with low CTE is zirconium tungstate filled polymer composite. The CTE is an important parameter in the design and manufacture of electronic packaging for microelectronic devices. Also in many applications, it is necessary to match the CTEs of different materials of a composite to avoid build-up of internal stresses caused by temperature changes.

A number of experimental and theoretical studies have been carried out on the CTE of composites [3–18]. In what follows, the key models for the estimation of CTE of composites are presented and discussed.

19.2.1 Models for CTE of Composites

The simplest models for the thermal expansion coefficient of composites are the Voigt–Reuss rules of mixtures:

$$\alpha = \phi\alpha_d + (1 - \phi)\alpha_m \quad \text{Voigt ROM} \tag{19.9}$$

$$\frac{1}{\alpha} = \frac{\phi}{\alpha_d} + \frac{1-\phi}{\alpha_m} \quad \text{Reuss ROM} \tag{19.10}$$

where α, α_d, and α_m are CTEs of composite, dispersed phase, and matrix, respectively.

The Voigt rule of mixture (ROM) is often referred to as an iso-strain model as each phase is assumed to undergo the same strain whereas the Reuss ROM is called an iso-stress model as each phase is assumed to experience the same stress. These simple ROMs for thermal expansion of composites do not account for the shear and bulk stiffness of the component phases.

Thomas [4] proposed the following empirical model for CTE of composites:

$$\alpha = \left[\phi\alpha_d^m + (1-\phi)\alpha_m^m\right]^{1/m} \tag{19.11}$$

where m varies from −1 to +1. When m = 1, Equation 19.11 becomes the Voigt ROM (Equation 19.9). When m = −1, the Reuss ROM (Equation 19.10) is obtained. For small values of m, Equation 19.11 becomes equivalent to the following equation:

$$\log \alpha = \phi \log \alpha_d + (1 - \phi)\log \alpha_m \tag{19.12}$$

This is basically the Lichtenecker logarithmic rule of mixtures for CTE of composites.

Turner [5] derived the following equation for the CTE of composites, taking into consideration the bulk stiffness of components:

$$\alpha = \frac{\alpha_d \phi K_d + \alpha_m (1-\phi) K_m}{\phi K_d + (1-\phi) K_m} \tag{19.13}$$

where K_d and K_m are the bulk moduli of dispersed and matrix phases, respectively. All phases of the composite were assumed to undergo the same change in dimension with the change in temperature. However, the shear deformation of phases was neglected. According to the Turner model, CTE is independent of the size and shape of filler particles. When $K_m = K_d$, the Turner model simplifies to the Voigt ROM.

Kerner [6] developed the following model for CTE of composites assuming particles to be spherical in shape and wetted by the matrix and taking into account the shear effects at the boundaries between the phases [7]:

$$\alpha = \bar{\alpha} + \phi(1-\phi)(\alpha_d - \alpha_m)\left[\frac{K_d - K_m}{(1-\phi)K_m + \phi K_d + \frac{3K_d K_m}{4G_m}}\right] \tag{19.14}$$

where G_m is the shear modulus of matrix and $\bar{\alpha}$ is defined as follows:

$$\bar{\alpha} = \phi\alpha_d + (1-\phi)\alpha_m \tag{19.15}$$

Thus, the term in addition to $\bar{\alpha}$ present in Equation 19.14 denotes deviation of the Kerner equation from the Voigt ROM.

The Kerner model could be recast in the following form:

$$\alpha = \frac{\frac{\phi K_d \alpha_d}{K_d + (4/3)G_m} + \frac{(1-\phi)K_m \alpha_m}{K_m + (4/3)G_m}}{\frac{\phi K_d}{K_d + (4/3)G_m} + \frac{(1-\phi)K_m}{K_m + (4/3)G_m}} \tag{19.16}$$

Equation 19.16 is valid for one type of inclusions. It could be further generalized to N multiple types of inclusions present in the same composite as follows [8]:

$$\alpha = \frac{\sum_{i=1}^{N} \frac{\phi_i K_{d,i} \alpha_{d,i}}{K_{d,i} + (4/3)G_m} + \frac{(1-\phi)K_m \alpha_m}{K_m + (4/3)G_m}}{\sum_{i=1}^{N} \frac{\phi_i K_{d,i}}{K_{d,i} + (4/3)G_m} + \frac{(1-\phi)K_m}{K_m + (4/3)G_m}} \tag{19.17}$$

where ϕ_i is the volume fraction of type-i inclusion and ϕ is the total volume fraction of inclusions. When N = 1, Equation 19.17 reduces to Equation 19.16.

Several CTE models proposed in the literature for composite materials are expressed in terms of the Young's moduli of the individual phases. Examples are the Blackburn [3] and Tummala and Friedberg [9] models. The Blackburn model is as follows:

$$\alpha = \alpha_m - \phi\theta(\alpha_m - \alpha_d) \tag{19.18}$$

where θ is given in terms of the Young's moduli as

$$\theta = \frac{3E_d(1-\nu_m)}{[(1+\nu_m)+2\phi(1-2\nu_m)]E_d + [2(1-\phi)E_m(1-2\nu_m)]} \tag{19.19}$$

The Tummala and Friedberg model [9] is given by Equation 19.18 with the following expression for θ:

$$\theta = \frac{E_d(1+\nu_m)}{[(1+\nu_m)]E_d + [E_m(1-2\nu_m)]} \tag{19.20}$$

where E_d and E_m are Young's moduli of dispersed phase and matrix, respectively and ν_m is the Poisson's ratio of matrix.

Figure 19.2 compares the CTEs predicted from different models for following filler and matrix properties: $E_d = 70 \times 10^9$ Pa, $K_d = 73 \times 10^9$ Pa, $G_d = 26.12 \times 10^9$ Pa,

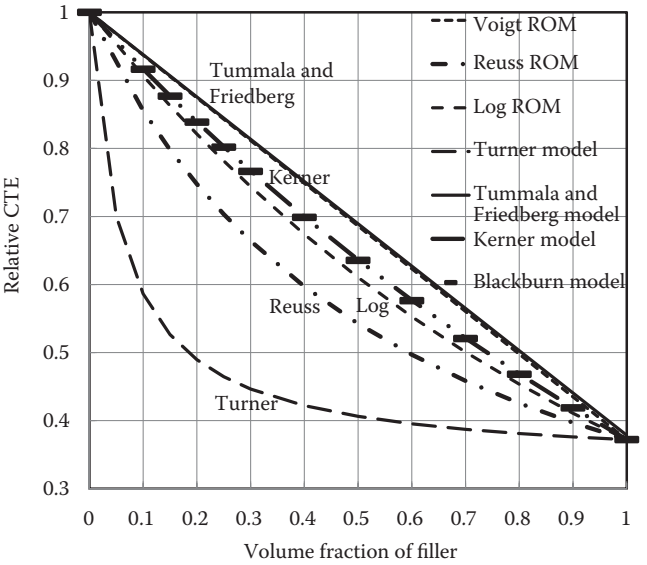

FIGURE 19.2 Comparison of the predictions of various models for relative CTE of particulate composites.

$\nu_d = 0.34$, $\alpha_d = 22.4 \times 10^{-6}$ deg^{-1}, $E_m = 3.5 \times 10^9$ Pa, $K_m = 4.2 \times 10^9$ Pa, $G_m = 1.287 \times 10^9$ Pa, $\nu_m = 0.36$, $\alpha_m = 60.26 \times 10^{-6}$ deg^{-1}. Based on the figure, the following points could be made: (1) the relative CTE, defined as α/α_m, decreases with the increase in filler concentration as the filler CTE is much smaller than that of the matrix; (2) the Turner model gives the lowest values whereas the Tummala and Friedberg model predicts the highest values of composite CTE; (3) the predictions of the Tummala and Friedberg model are only slightly higher than those of the Voigt model (they almost overlap); (4) the predictions of the Kerner and Blackburn models overlap; and (5) the predictions of the logarithmic rule of mixture (Equation 19.12) fall in between the predictions of Voigt–Reuss rules of mixtures.

19.2.2 Upper and Lower Bounds of CTE of Composites

Schapery [10] used the variation principles to develop the following lower and upper bounds of CTE of composites, regardless of the shape of the filler particles:

$$\alpha^l = \alpha_m + \left(\frac{K_d}{K^u}\right)\frac{(K_m - K^u)(\alpha_d - \alpha_m)}{(K_m - K_d)} = \alpha_m + (\alpha_d - \alpha_m)\left[\frac{\dfrac{1}{K^u} - \dfrac{1}{K_m}}{\dfrac{1}{K_d} - \dfrac{1}{K_m}}\right] \tag{19.21}$$

$$\alpha^u = \alpha_m + \left(\frac{K_d}{K^l}\right)\frac{(K_m - K^l)(\alpha_d - \alpha_m)}{(K_m - K_d)} = \alpha_m + (\alpha_d - \alpha_m)\left[\frac{\dfrac{1}{K^l} - \dfrac{1}{K_m}}{\dfrac{1}{K_d} - \dfrac{1}{K_m}}\right] \tag{19.22}$$

where α^l and α^u are lower and upper bounds of CTE, respectively and K^l and K^u are lower and upper bounds of the bulk modulus of composite, respectively. Note that the Schapery bounds do not contain ϕ or $(1 - \phi)$ terms as the volume fraction of the phases is taken into account through the bulk modulus K of the composite.

The lower and upper bounds of the bulk modulus of composite are given as

$$K^l = K_m + \frac{\phi}{\dfrac{1}{(K_d - K_m)} + \dfrac{1-\phi}{K_m + (4/3)G_m}} \tag{19.23}$$

$$K^u = K_d + \frac{1-\phi}{\dfrac{1}{(K_m - K_d)} + \dfrac{\phi}{K_d + (4/3)G_d}} \tag{19.24}$$

where G_d and G_m are shear moduli of dispersed phase and matrix, respectively. These bounds are the same as Hashin–Shtrikman–Walpole (HSW) bounds, discussed in Chapter 7.

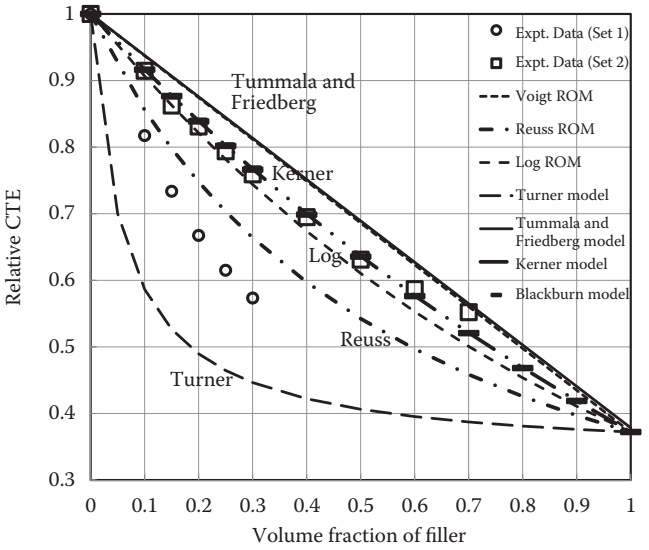

FIGURE 19.3 Comparison of model predictions with two sets of experimental data on composites of aluminium filler particles and epoxy resin matrix. (Data from Lombado, N., *Compos. Sci. Technol*. 65: 2118–2128, 2005; Holliday, L. and J. Robinson, *J. Mater. Sci*. 8: 301–311, 1973; Siderides, E. and G.C. Papanicolaou, *Rheol. Acta*. 27: 608–616, 1988.)

19.2.3 Comparison of Model Predictions with Experimental Data

Figure 19.3 compares the model predictions with two sets of experimental data on composites of aluminium filler particles and epoxy resin matrix [11–13]. The mechanical properties and CTEs of filler and matrix were as follows: $E_d = 70 \times 10^9$ Pa, $K_d = 73 \times 10^9$ Pa, $G_d = 26.12 \times 10^9$ Pa, $\nu_d = 0.34$, $\alpha_d = 22.4 \times 10^{-6}$ deg^{-1}, $E_m = 3.5 \times 10^9$ Pa, $K_m = 4.2 \times 10^9$ Pa, $G_m = 1.287 \times 10^9$ Pa, $\nu_m = 0.36$, $\alpha_m = 60.26 \times 10^{-6}$ deg^{-1}. The experimental data for Set 1 fall in between the predictions of the Reuss and Turner models. The experimental data for Set 2 nearly overlaps with the predictions of the Kerner and Blackburn models. The predictions of the logarithmic rule of mixtures fall only slightly below the experimental data of Set 2 when the filler volume fraction is less than 0.6. The thermal expansion coefficients of Set 1 data were significantly smaller than the corresponding values of Set 2 data due to a high degree of agglomeration of filler particles in Set 1 data.

REFERENCES

1. Lee, H.J. and R.E. Taylor. 1976. Thermal diffusivity of dispersed composites. *J. App. Phys.* 47: 148–151.
2. Jakubinek, M.B., C.A. Whitman, and M.A. White. 2010. Negative thermal expansion materials. *J. Therm. Anal. Calorim.* 99: 165–172.
3. Sevostianov, I. 2011. On the thermal expansion of composite materials and cross-property connection between thermal expansion and thermal conductivity. *Mech. Mater*. 45: 20–33.

4. Thomas, J.P. 1960. Effect of inorganic fillers on coefficient of thermal expansion of polymeric materials. General Dynamics, Fort Worth, TX, AD0287826.
5. Turner, P.S. 1946. Thermal expansion stresses in reinforced plastics. *J. Res.* (*Nat. Bur. Stand.*) 37: 239–250.
6. Kerner, E.H. 1956. The elastic and thermoelastic properties of composite media. *Proc. Phys. Soc. B*: 808–813.
7. Chan, K.C. and J. Liang. 2001. Thermal expansion and deformation behavior of aluminium-matrix composites in laser forming. *Compos. Sci. and Technol*. 61: 1265–1270.
8. McCartney, L.N. and A. Kelly. 2008. Maxwell's far-field methodology applied to the prediction of properties of multiphase isotropic particulate composites. *Proc. Roy. Soc. A.* 464: 423–446.
9. Tummala, R.R. and A.L. Friedberg. 1970. Thermal expansion of composite materials. *J. Appl. Phys*. 41: 5104–5107.
10. Schapery, R.A. 1968. Thermal expansion coefficients of composite materials based on energy principles. *J. Compos. Mater*. 2: 380–404.
11. Lombado, N. 2005. Effect of an inhomogeneous interphase on the thermal expansion coefficient of a particulate composite. *Compos. Sci. Technol*. 65: 2118–2128.
12. Holliday, L. and J. Robinson. 1973. Review: The thermal expansion of composites based on polymers. *J. Mater. Sci.* 8: 301–311.
13. Siderides, E. and G.C. Papanicolaou. 1988. A theoretical model for the prediction of thermal expansion behavior of particulate composites. *Rheol. Acta*. 27: 608–616.
14. Wong, C.P. and R.S. Bollampally. 1999. Thermal conductivity, elastic modulus, and coefficient of thermal expansion of polymer composites filled with ceramic particles for electronic packaging. *J. Appl. Poly. Sci.* 74: 3396–3403.
15. Elomari, S., M.D. Skibo, A. Sundarrajan, and H. Richards. 1998. Thermal expansion behavior of particulate metal-matrix composites. *Compos. Sci. Technol.* 58: 369–376.
16. Fridlyander, I.N., N.S. Klyagina, I.D. Tykachinskii, E.P. Dain, and G.D. Gordeeva. 1974. Composite materials with a low coefficient of thermal expansion. *Met. Sci. Heat. Treat.* 16: 495–497.
17. Yoshida, K. and H. Morigami. 2004. Thermal properties of diamond/copper composite material. *Microelectron. Reliab*. 44: 303–308.
18. Sun, Q. and O.T. Inal. 1996. Fabrication and characterization of diamond/copper composites for thermal management substrate applications. *Mat. Sci. Eng. B.* 41: 261–266.

20 Radiative Heat Transfer and Radiative Properties of Composites

Knowledge of the radiative properties of composite materials is important in a number of practical applications [1–9]. Coatings of composite materials are widely used to enhance or to reduce radiative heat loss from a variety of systems. For example, heat loss from a furnace can be reduced significantly by applying high thermal emissivity ceramic-composite coating on the interior surface of the furnace chamber [8]. The energy that is absorbed by the surface from hot gases is reemitted back to the furnace. High thermal emissivity composite coatings are also used in space applications. The spacecraft surfaces exposed to the space environment are coated with high-emissivity composite coatings to enhance the loss of heat generated due to high friction between the space vehicle surface and atmosphere [2]. In several applications, the composite coatings are designed to have low thermal emissivity. For example, low-emissivity composite coatings are used on the under roof of the houses to help keep the attic area cool during summer. The heat from the sun is reflected back to the atmosphere.

In this chapter, the fundamentals of radiative heat transfer are first reviewed and then the key radiative property of composite materials, namely, the thermal emissivity, is discussed.

20.1 FUNDAMENTALS OF RADIATIVE HEAT TRANSFER

When two bodies or surfaces at different temperatures are placed in view of each other and are separated by vacuum, the sole mechanism of heat transfer between them is the exchange of thermal radiation.

20.1.1 Nature of Thermal Radiation

Thermal radiation is a stream of electromagnetic radiation emitted by a body as a result of its finite absolute temperature. All forms of matter at finite absolute temperature emit thermal radiation as a result of atomic and molecular scale motions, such as translational, vibrational and rotational movement of molecules, vibration of atoms, and certain electronic transitions.

Thermal radiation is a part of the electromagnetic spectrum confined to wavelengths in the range 0.1 to 1000 μm. It includes a portion of ultraviolet region (0.1 to 0.38 μm), all of the visible (0.38 to 0.76 μm) and infrared (0.76 to 1000 μm) regions.

The wavelength (λ) of thermal radiation is related to frequency (ν) and speed of light (c) as

$$\lambda = c/\nu \tag{20.1}$$

While the propagation velocity and wavelength of electromagnetic waves are affected by the medium in which they are travelling, the frequency is independent of the medium and depends only on the radiating source.

Interestingly, electromagnetic radiation including thermal radiation has both a particulate and wavelike nature. Thus, thermal radiation can be thought of as a stream of discrete packets of energy called photons or quanta. Each photon or quantum has energy of

$$e = h\nu \tag{20.2}$$

where h is Planck's constant (= 6.625×10^{-34} J·s).

The thermal radiation emitted by a surface at a finite absolute temperature is not monochromatic (single wavelength). It covers a range of wavelengths and is emitted in all directions. The intensity of the radiation varies with the wavelength and with the direction of the emission. The variation of intensity with λ is called spectral distribution, and the variation of intensity with direction is called directional distribution.

20.1.1.1 Emissive Power, Irradiation, and Radiosity

The total (hemispherical) emissive power E (W/m^2) of the radiation emitted by a surface is defined as

$$E = \int_0^\infty E_\lambda \, d\lambda \tag{20.3}$$

where E_λ (W/m^3) is the spectral (hemispherical) emissive power of radiation. It is the rate at which radiation energy is emitted by a surface per unit wavelength interval about λ in *all directions* per unit surface area. As a hemisphere placed above the emitting surface intercepts all the radiation rays emitted by the surface, E_λ is called spectral hemispherical emissive power of radiation and E is called total hemispherical emissive power.

The total (hemispherical) irradiation G (W/m^2) is defined as

$$G = \int_0^\infty G_\lambda \, d\lambda \tag{20.4}$$

where G_λ (W/m^3) is the spectral (hemispherical) irradiation. It is the rate at which radiation energy is incident on a surface per unit wavelength interval about λ from *all directions* per unit surface area.

The total (hemispherical) radiosity J (W/m^2) is defined as

$$J = \int_0^\infty J_\lambda \, d\lambda \tag{20.5}$$

where J_λ (W/m^3) is the spectral (hemispherical) radiosity. It is the rate at which radiation energy leaves a surface per unit wavelength interval about λ from *all directions* per unit surface area. It includes the reflected portion of the irradiation as well as direct emission.

20.1.1.2 Absorptivity, Reflectivity, and Transmissivity

When radiation falls on a surface, some of it is absorbed, some of it is reflected, and the remaining part is transmitted. Let the total incident radiation flux on a surface from all directions and over all wavelengths be G.

The total absorptivity (α) is the fraction of G absorbed by the surface, that is,

$$\alpha = \frac{G_{abs}}{G} \tag{20.6}$$

where G_{abs} is the absorbed portion of incident radiation G.

The total reflectivity (ρ) is the fraction of G reflected by the surface, that is,

$$\rho = \frac{G_{ref}}{G} \tag{20.7}$$

where G_{ref} is the reflected portion of incident radiation G.

The total transmissivity (τ) is the fraction of G transmitted through the surface, that is,

$$\tau = \frac{G_{trans}}{G} \tag{20.8}$$

where G_{trans} is the transmitted portion of incident radiation G.

Using energy balance

$$G_{abs} + G_{ref} + G_{trans} = G \tag{20.9}$$

or

$$\alpha + \rho + \tau = 1 \tag{20.10}$$

In the case of opaque surfaces, $\tau = 0$ and therefore,

$$\alpha + \rho = 1 \tag{20.11}$$

20.1.1.3 Black Bodies

A black body is one which absorbs all incident radiation, regardless of wavelength and direction. Black bodies are not only perfect absorbers of radiation, they are also the best emitters of radiation. At any given temperature, radiation emitted from a black body has the maximum possible value of spectral emissive power. No surface can emit radiation with spectral emissive power higher than that of a black surface when comparison is made at the same temperature. Furthermore, black bodies are diffuse emitters of radiation, that is, the spectral emissive power is independent of direction and depends only on wavelength and temperature.

It should be noted that a surface that appears black to the eye absorbs radiation in the narrow band of the visible portion of the electromagnetic spectrum (approximately 0.38 to 0.76 μm), whereas a black body absorbs all incident radiation of all wavelengths. For example, snow appears white to the eye but it is essentially black with respect to long wavelength (infrared) thermal radiation.

The spectral emissive power emitted by a black body is given by Planck's radiation law

$$E_{\lambda,b}(\lambda, T) = \frac{2\pi hc_o^2}{\lambda^5\left[\exp(hc_o/\lambda kT) - 1\right]} \tag{20.12}$$

where h is Planck's constant ($= 6.6256 \times 10^{-34}$ J·s), k is Boltzmann constant ($= 1.3805 \times 10^{-23}$ J/K), c_o is the speed of light in vacuum ($= 2.998 \times 10^8$ m/s) and T is the absolute temperature. The Planck's radiation law indicates that: (a) the spectral emissive power of a black body is continuous function of wavelength (λ) at any given temperature, (b) the spectral emissive power increases with the increase in temperature at any given wavelength, and (c) the wavelength at which the spectral emissive power has its maximum value decreases with the increase in temperature.

The wavelength at which the spectral emissive power is maximum can be obtained from Planck's law by setting $dE_\lambda/d\lambda = 0$. Thus,

$$\lambda_{max} T = 2.898 \times 10^{-3}\ \text{mK} \tag{20.13}$$

where λ_{max} is the value of λ where $E_{\lambda,b}$ is maximum. This equation is referred to as Wien's displacement law.

The total emissive power of a black body is given by the Stefan–Boltzmann law

$$E_b = \sigma T^4 \tag{20.14}$$

where σ is the Stefan–Boltzmann constant (= 5.67 × 10^{-8} W/m^2·K^4). The Stefan–Boltzmann law follows from the Planck distribution, Equation 20.12:

$$E_b = \int_0^\infty \frac{2\pi hc_o^2 d\lambda}{\lambda^5\left[\exp(hc_o/\lambda kT)-1\right]} = \sigma T^4 \tag{20.15}$$

In practice, it is often required to estimate the *band emission* from a radiating body. Band emission is a fraction of the total emission that is in a certain wavelength interval (band) at a given temperature. One can easily calculate band emission from a black body using the Planck distribution and Stefan–Boltzmann law. Thus, the band emission $F_{(\lambda_1\to\lambda_2)}$ over the wavelength band of ($\lambda_1 \to \lambda_2$) is

$$F_{(\lambda_1\to\lambda_2)} = F_{(0\to\lambda_2)} - F_{(0\to\lambda_1)} = \frac{\int_0^{\lambda_2} E_{\lambda,b}\, d\lambda - \int_0^{\lambda_1} E_{\lambda,b}\, d\lambda}{\sigma T^4} \tag{20.16}$$

20.1.1.4 Real Bodies

Real surfaces are not perfect absorbers of incident radiation. They absorb only a fraction of the incident radiation. Some of the incident radiation is reflected and some of it is transmitted. Real surfaces emit less radiation energy at any given temperature as compared with black surfaces at the same temperature.

The total hemispherical emissivity (ε) of a real surface is defined as the ratio of total hemispherical emissive power of a real surface (E) to total hemispherical emissive power of a black surface at the same temperature, that is,

$$\varepsilon = \frac{E}{E_b} \tag{20.17}$$

Note that the emissivity of a real surface can be defined in different ways. For example, the spectral or monochromatic hemispherical emissivity ε_λ is defined as the ratio of spectral hemispherical emissive power of a real surface to spectral hemispherical power of a black surface at the same temperature

$$\varepsilon_\lambda = \frac{E_\lambda}{E_{\lambda,b}} \tag{20.18}$$

The total hemispherical emissivity is related to spectral hemispherical emissivity as follows:

$$\varepsilon = \frac{E}{E_b} = \frac{\int_0^\infty \varepsilon_\lambda E_{\lambda,b}\, d\lambda}{\sigma T^4} \tag{20.19}$$

20.1.1.5 Some More Definitions

Diffuse Emitter: A diffuse emitter is one whose emissivity is independent of the direction, that is, the radiation is emitted isotropically (equally in all directions).

Diffuse Reflector: A diffuse reflector is one which reflects incident radiation equally in all directions. There is no directional dependence of reflected radiation. Rough surfaces give diffuse reflection.

Diffuse Surface: A diffuse surface is one which reflects and emits radiation in a diffuse manner.

Gray Surface: In general, the radiation properties of the material (emissivity, reflectivity, absorptivity, transmissivity) are functions of wavelength of the radiation. Gray surface is one whose radiation properties are independent of the wavelength.

Diffuse Gray Surface: A surface whose radiation properties are independent of both direction and wavelength (diffuse implies directional independence and gray implies wavelength independence).

20.1.1.6 Kirchhoff's Radiation Law

Kirchhoff's radiation law states that the monochromatic directional emissivity ($\varepsilon_{\lambda,\theta}$) of a surface is equal to the monochromatic directional absorptivity ($\alpha_{\lambda,\theta}$) of the surface, when comparison is made at the same temperature. Thus,

$$\varepsilon_{\lambda,\theta} = \alpha_{\lambda,\theta} \tag{20.20}$$

Note that, in general, $\varepsilon_{\lambda,\theta}$ and $\alpha_{\lambda,\theta}$ are both functions of direction and wavelength. This form of Kirchhoff's radiation law is very general as $\varepsilon_{\lambda,\theta}$ and $\alpha_{\lambda,\theta}$ are inherent surface properties.

Another form of Kirchhoff's law that is less general is as follows:

$$\varepsilon = \alpha \tag{20.21}$$

where ε and α are total hemispherical emissivity and absorptivity of the surface. This form of Kirchhoff's law is valid under the condition that the surface is in thermal equilibrium with its surroundings.

For *diffuse gray surface*, the emissivity and absorptivity are equal and are independent of direction and wavelength. This is true whether or not the surface is in thermal equilibrium with its surroundings.

20.1.2 Radiative Heat Transfer between Surfaces

Thus far, thermal radiation and thermal radiation properties of bodies have been described. In what follows, radiative heat exchange among the surfaces is described.

The exchange of radiation energy between two surfaces depends on their view factors. The view factor F_{ij} is the fraction of radiant energy leaving surface i that is intercepted by surface j, that is,

$$F_{ij} = \frac{q_{i\to j}}{A_i J_i} \tag{20.22}$$

where $q_{i\to j}$ is radiation energy leaving surface i and being intercepted by surface j, J_i is the radiosity of surface i, and A_i is area of the surface through which radiation is being emitted. Note that the total radiation leaving the surface i is the sum of emitted radiation and reflected radiation. The radiosity J_i of a surface is the sum of emitted radiation (E_i) and reflected irradiation ($\rho_i G_i$)

$$J_i = E_i + \rho_i G_i \tag{20.23}$$

The view factor F_{ji} is the fraction of radiant energy leaving surface j that is intercepted by surface i, that is,

$$F_{ji} = \frac{q_{j\to i}}{A_j J_j} \tag{20.24}$$

where $q_{j\to i}$ is radiation energy leaving surface j and being intercepted by surface i, J_j is the radiosity of surface j, and A_j is area of the surface through which radiation is being emitted.

The net rate of radiative heat transfer from surface i to surface j is given by

$$q_{ij} = q_{i\to j} - q_{j\to i} = A_i J_i F_{ij} - A_j J_j F_{ji} \tag{20.25}$$

Also note that

$$q_{ji} = -q_{ij} = q_{j\to i} - q_{i\to j} = A_j J_j F_{ji} - A_i J_i F_{ij} \tag{20.26}$$

The view factors F_{ij} and F_{ji} are purely geometric quantities. They depend only on size, orientation and relative positions of surfaces i and j.

It can be readily shown that

$$A_i F_{ij} = A_j F_{ji} \tag{20.27}$$

This equation is called the *reciprocity relation* for view factors and is applicable to any pair of radiating surfaces provided that they emit and reflect radiation diffusively.

Most radiative heat transfer problems of practical interest involve enclosed spaces (enclosures). As the total radiation leaving any surface i of an enclosure must be intercepted by the surfaces of the enclosures (including surface i itself), the energy balance gives

$$\sum_{j=1}^{N} F_{ij} = \sum_{j=1}^{N} \frac{q_{i\to j}}{A_i J_i} = 1 \tag{20.28}$$

where N is the number of surfaces forming the enclosure. This equation is referred to as the summation rule. The summation rule can be applied to each surface present in the enclosure. If there are N surfaces present in an enclosure, N^2 view factors are

required. For example, in a two surface enclosure, the four view factors required are as follows: F_{11}, F_{22}, F_{12}, and F_{21}. As the summation rule is applicable to each surface of the enclosure, it leads to N equations. The reciprocity relation gives additional $N(N-1)/2$ equations. Thus, the number of view factors that must be obtained from geometric considerations is $N(N-1)/2$.

Consider now a single surface i (not necessarily in an enclosure) which is receiving radiation from other surfaces and is emitting radiation. Assume that the surface is opaque, diffuse, and gray (radiation properties are independent of λ and direction and $\alpha = \varepsilon = 1 - \rho$). The surface is irradiated with incident radiation energy rate of G_iA_i. The surface is emitting and reflecting radiation energy at a rate of J_iA_i. Thus, the net rate of radiation energy leaving surface i is

$$q_i = A_i(J_i - G_i) \tag{20.29}$$

The radiosity J_i of the surface is the sum of emitted radiation (E_i) and reflected irradiation (ρ_iG_i):

$$J_i = E_i + \rho_iG_i \tag{20.30}$$

Since $E_i = \varepsilon_iE_{b,i}$ and $\rho_i = 1 - \varepsilon_i$, the above equation gives

$$G_i = \frac{J_i - \varepsilon_iE_{b,i}}{1-\varepsilon_i} \tag{20.31}$$

Elimination of G_i from Equation 20.29 gives

$$q_i = \frac{E_{b,i} - J_i}{\left[\frac{1-\varepsilon_i}{\varepsilon_iA_i}\right]} \tag{20.32}$$

This equation can be interpreted in terms of electrical analog as follows: q_i, the net radiative heat transfer rate from a surface, is the "current" through the surface, $E_{b,i} - J_i$, the difference in the radiosities of a black surface and actual surface, is the "driving potential" for the current, and $(1 - \varepsilon_i)/(\varepsilon_iA_i)$ is the "resistance" to current flow through the surface. When the radiosity of the actual surface is less than the radiosity of the surface if it was black, the driving potential for net radiative heat transfer is positive, and there occurs a net radiation heat transfer from the surface. When the radiosity of the actual surface is more than the radiosity of the surface if it was black, there occurs a net radiation heat transfer to the surface. The larger the difference in radiosities, the greater is the net radiative heat transfer rate. The resistance term $(1 - \varepsilon_i)/(\varepsilon_iA_i)$ is also called "surface resistance". If the actual surface is a black surface, the surface resistance is zero and $E_{b,i} = J_i$. In this case, $q_i = A_i (E_{b,i} - G_i)$.

Consider another example where a real surface at constant temperature is just emitting radiation. No radiation is falling on the surface, and hence, there is no

reflected radiation. The surface has an emissivity of ε_i. In this case, the radiosity J_i is just $\varepsilon_i E_{b,i}$ as there is no reflected radiation present. Thus, the net rate of radiative heat transfer from the surface is given as

$$q_i = \frac{E_{b,i} - \varepsilon_i E_{b,i}}{\left[\frac{1-\varepsilon_i}{\varepsilon_i A_i}\right]} = \varepsilon_i E_{b,i} A_i \tag{20.33}$$

Consider now radiation exchange between two surfaces. As noted earlier, the net rate of radiative heat transfer from surface i to surface j is given by

$$q_{ij} = q_{i\to j} - q_{j\to i} = A_i J_i F_{ij} - A_j J_j F_{ji} \tag{20.34}$$

Using the reciprocity relation and rearranging Equation 20.34, the following result is obtained:

$$q_{ij} = \frac{J_i - J_j}{\left(\frac{1}{A_i F_{ij}}\right)} \tag{20.35}$$

Thus, the driving potential for net radiative heat transfer between two surfaces is the difference in the radiosities of the two surfaces, and the resistance to radiative heat transfer between two surfaces is $1/(A_i F_{ij})$.

If surface i is in an enclosure, it will exchange radiation with each of the N surfaces present in the enclosure. The net rate of radiative heat transfer from surface i in an enclosure is equal to the sum of the net rates of radiative heat transfer from surface i to N surfaces:

$$q_i = \sum_{j=1}^{N} q_{ij} = \sum_{j=1}^{N} \frac{J_i - J_j}{\left(\frac{1}{A_i F_{ij}}\right)} \tag{20.36}$$

It should be noted that in radiative heat transfer between surfaces, two different types of resistances are encountered: the surface resistance given by $(1 - \varepsilon_i)/(\varepsilon_i A_i)$ and space or view resistance given as $1/(A_i F_{ij})$. If surface i is a black surface and is exchanging radiation with surface j, the surface resistance is zero but the space resistance between surfaces i and j is not zero.

20.1.2.1 Radiation Heat Exchange between Two Real Surfaces

Open systems: Consider two real surfaces maintained at constant temperatures T_1 and T_2. Assume that the surfaces are diffuse and gray and their emissivities are ε_1 and ε_2. The surfaces are open in that they do not form an enclosure. The surfaces

may be exchanging thermal radiation with other surfaces present in the surroundings. The net rate of radiative heat transfer from surface 1 to surface 2 is as follows:

$$q_{12} = \frac{J_1 - J_2}{\left(\frac{1}{A_1 F_{12}}\right)} \tag{20.37}$$

It is important to realize that q_{12} is not equal to q_1, the net rate of radiative heat transfer from surface 1 to all the surrounding surfaces (including surface 2). If the surfaces 1 and 2 are black surfaces, the above expression simplifies to

$$q_{12} = \frac{E_{b,1} - E_{b,2}}{\left(\frac{1}{A_1 F_{12}}\right)} = \frac{\sigma\left(T_1^4 - T_2^4\right)}{\left(\frac{1}{A_1 F_{12}}\right)} \tag{20.38}$$

Enclosures: Consider two real surfaces which together form an enclosure such that the two surfaces exchange radiation only with each other. As there are only two surfaces exchanging radiation with each other, it follows that

$$q_1 = -q_2 = q_{12} = -q_{21} \tag{20.39}$$

Now there are three radiative resistances in series: surface resistance corresponding to surface 1, space resistance between the two surfaces, and surface resistance corresponding to surface 2. Thus,

$$R_{total} = \frac{1-\varepsilon_1}{\varepsilon_1 A_1} + \frac{1}{A_1 F_{12}} + \frac{1-\varepsilon_2}{\varepsilon_2 A_2} \tag{20.40}$$

The overall driving potential for radiative heat transfer from surface 1 to surface 2 is $E_{b,1} - E_{b,2}$. Thus,

$$q_1 = \frac{E_{b,1} - E_{b,2}}{\frac{1-\varepsilon_1}{\varepsilon_1 A_1} + \frac{1}{A_1 F_{12}} + \frac{1-\varepsilon_2}{\varepsilon_2 A_2}} = \frac{\sigma\left(T_1^4 - T_2^4\right)}{\frac{1-\varepsilon_1}{\varepsilon_1 A_1} + \frac{1}{A_1 F_{12}} + \frac{1-\varepsilon_2}{\varepsilon_2 A_2}} \tag{20.41}$$

If the two surfaces are infinitely large parallel surfaces maintained at temperatures T_1 and T_2, $A_1 = A_2 = A$, $F_{12} = 1$, and Equation 20.41 simplifies to

$$q_1 = \frac{\sigma A\left(T_1^4 - T_2^4\right)}{\frac{1-\varepsilon_1}{\varepsilon_1} + 1 + \frac{1-\varepsilon_2}{\varepsilon_2}} = \frac{\sigma A\left(T_1^4 - T_2^4\right)}{\frac{1}{\varepsilon_1} + \frac{1}{\varepsilon_2} - 1} \tag{20.42}$$

For systems such as two long concentric cylinders or two concentric spheres, $F_{12} = 1$ and $F_{21} = A_1/A_2$. In this case, the net rate of radiative heat transfer from surface 1 to surface 2 as given by Equation 20.41 is as follows:

$$q_1 = \frac{\sigma A_1 \left(T_1^4 - T_2^4\right)}{\frac{1}{\varepsilon_1} + \frac{A_1}{A_2}\left(\frac{1}{\varepsilon_2} - 1\right)} \tag{20.43}$$

In the special case of a small convex body enclosed in a large enclosure, A_1/A_2 is approximately zero. Thus,

$$q_1 = \sigma A_1 \varepsilon_1 \left(T_1^4 - T_2^4\right) \tag{20.44}$$

This same result is obtained if a small convex body is enclosed in a black enclosure. Consequently, a large enclosure can be approximately treated as a black surface.

20.1.3 Radiation Shielding

In many practical situations, it is desired to reduce radiative heat transfer between two surfaces. This can be achieved by inserting a thin sheet of high reflectivity and low-emissivity material between the two surfaces. Such thin sheets of highly reflective material are called "radiation shields". The radiation shield adds another resistance in the path of heat flow so that the overall rate of radiative heat transfer is reduced. Insertion of any surface (regardless of its surface radiative properties) that intercepts the radiation path always reduces the net radiative heat transfer rate. However, the higher the reflectivity (that is, smaller the emissivity) of the shield, the greater is the resistance associated with the shield.

Consider two infinitely large parallel surfaces maintained at temperatures T_1 and T_2 exchanging thermal radiation with each other. In the absence of any radiation shield, there are three radiative resistances in series (two surface resistances and one space resistance) and the net rate of radiative heat transfer from surface 1 to surface 2 is as follows:

$$q_1 = \frac{\sigma A \left(T_1^4 - T_2^4\right)}{\frac{1}{\varepsilon_1} + \frac{1}{\varepsilon_2} - 1} \tag{20.45}$$

When a radiation shield (large parallel sheet) is inserted between the two parallel surfaces, two additional surface resistances (corresponding to two sides of the shield) come into play. The net rate of radiative heat transfer from surface 1 to surface 2 now becomes

$$q_1 = \frac{\sigma \left(T_1^4 - T_2^4\right)}{\frac{1-\varepsilon_1}{\varepsilon_1 A_1} + \frac{1}{A_1 F_{13}} + \frac{1-\varepsilon_{3(1)}}{\varepsilon_{3(1)} A_3} + \frac{1-\varepsilon_{3(2)}}{\varepsilon_{3(2)} A_3} + \frac{1}{A_3 F_{32}} + \frac{1-\varepsilon_2}{\varepsilon_2 A_2}} \tag{20.46}$$

where $\varepsilon_{3(1)}$ is emissivity of radiation shield facing surface 1, $\varepsilon_{3(2)}$ is emissivity of radiation shield facing surface 2, and A_3 is surface area of the shield (same on both sides). Assuming $A_1 = A_2 = A_3 = A$ and $\varepsilon_{3(1)} = \varepsilon_{3(2)} = \varepsilon_s$, this expression simplifies to

$$q_1 = \frac{\sigma A\left(T_1^4 - T_2^4\right)}{\frac{1}{\varepsilon_1} + \frac{1}{\varepsilon_2} + 2\left(\frac{1}{\varepsilon_s} - 1\right)} \tag{20.47}$$

Note that $F_{13} = 1$ and $F_{32} = 1$. In the special case of emissivities of all surfaces being equal ($\varepsilon_1 = \varepsilon_2 = \varepsilon_s = \varepsilon$), the net rates of radiative heat transfer from surface 1 to surface 2 with and without shield are given as

$$q_1 = \frac{\sigma A\left(T_1^4 - T_2^4\right)}{2\left(\frac{2}{\varepsilon} - 1\right)} \quad \text{(with shield)} \tag{20.48}$$

$$q_1 = \frac{\sigma A\left(T_1^4 - T_2^4\right)}{\left(\frac{2}{\varepsilon} - 1\right)} \quad \text{(without shield)} \tag{20.49}$$

Thus, the insertion of a radiation shield reduces the net heat transfer rate to one half the rate that prevails when the shield is not present.

20.1.4 Radiative Heat Transfer Coefficient

Thus far, radiative heat transfer is treated as an isolated phenomenon. In many practical problems, radiation and convection occur simultaneously. In such situations, it is convenient to express the net radiative heat transfer in terms of Newton's law of cooling. Assuming a two-surface enclosure, the net radiative heat transfer rate from surface 1 to surface 2 can be expressed as

$$q_1 = h_r(T_1 - T_2)A_1 \tag{20.50}$$

where h_r is the radiative heat transfer coefficient, given as

$$h_r = \frac{\sigma(T_1 + T_2)\left(T_1^2 + T_2^2\right)}{\frac{1-\varepsilon_1}{\varepsilon_1} + \frac{1}{F_{12}} + \left(\frac{A_1}{A_2}\right)\frac{1-\varepsilon_2}{\varepsilon_2}} \tag{20.51}$$

For a small body in a large enclosure ($F_{12} = 1$ and $A_1/A_2 = 0$), this expression reduces to

$$h_r = \sigma\varepsilon_1(T_1 + T_2)\left(T_1^2 + T_2^2\right) \tag{20.52}$$

Note that the radiation heat transfer coefficient h_r is a strong function of temperature whereas convective heat transfer coefficient depends only weakly on temperature (through temperature dependence of properties).

When radiation and convection occur in parallel, the total rate of heat transfer can be expressed as

$$q_{total} = q_{radiation} + q_{convection} = \frac{(T_1 - T_2)}{\left(\frac{1}{h_r A_1}\right)} + \frac{(T_1 - T_2)}{\left(\frac{1}{h_c A_1}\right)} \tag{20.53}$$

where h_c is the convective heat transfer coefficient.

20.2 RADIATIVE PROPERTIES OF COMPOSITES

As noted in the preceding sections, thermal emissivity of a material is the key property involved in radiative heat transfer calculations. Some applications require that the thermal emissivity of the material be as low as possible whereas other applications require a high thermal emissivity. It is well known that metals have low values of thermal emissivity whereas polymers exhibit high values of thermal emissivity due to the presence of certain functional groups [1,4,5]. Therefore, by mixing these two materials (metals and polymers) in different proportions, one can generate materials of any desired thermal emissivity. It is for this reason that composites of metal

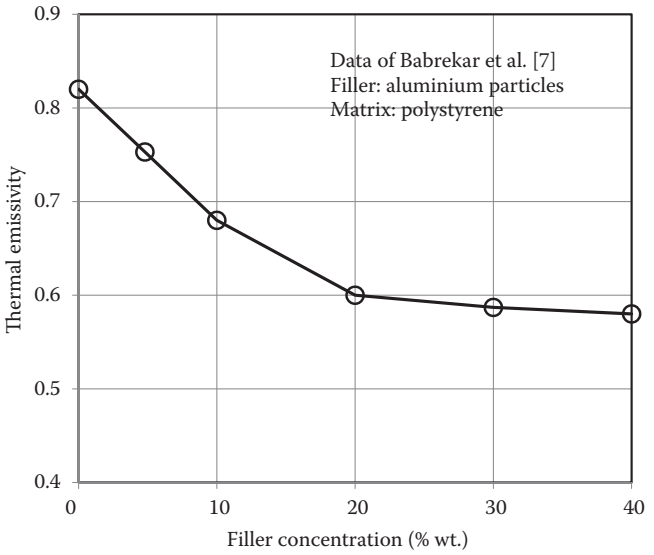

FIGURE 20.1 Thermal emissivity of composites of aluminum particles/polystyrene matrix as a function of filler concentration (wt.% aluminum particles). (Based on Babrekar, H.A. et al., *Mater Sci Eng B*. 168: 40–44, 2010.)

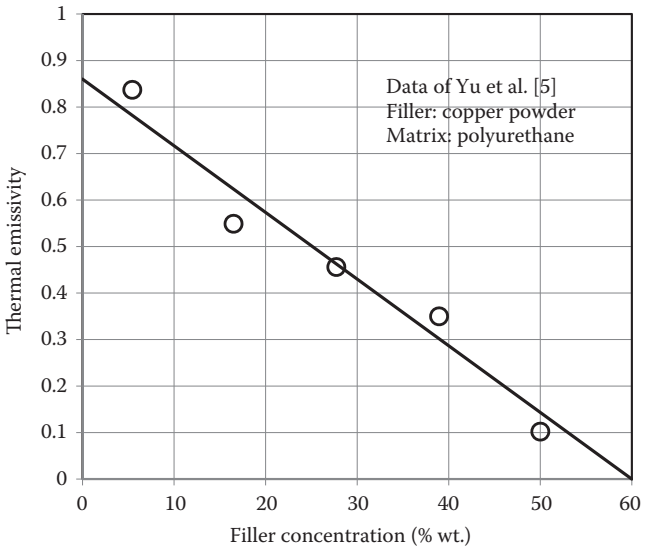

FIGURE 20.2 Thermal emissivity of composites of copper particles/polyurethane matrix as a function of filler concentration (wt.% copper particles). (Based on Yu, H. et al., *Appl Surf Sci*. 255: 6077–6081, 2009.)

filler particles and polymer matrix are used widely as coating materials of designed thermal emissivity.

Figure 20.1 shows the plot of thermal emissivity of composites of aluminum particles/polystyrene matrix as a function of filler concentration (wt.% aluminum particles) [7]. As expected, the thermal emissivity decreases with the increase in low-emissivity filler concentration. A similar behavior is seen in composites of copper particles/polyurethane matrix [5] (see Figure 20.2).

20.2.1 Estimation of Thermal Emissivity of Composites

Assuming transmittivity to be negligible, the absorptivity and reflectivity are related to each other as

$$\alpha + \rho = 1 \tag{20.11}$$

From Kirchoff's law,

$$\varepsilon = \alpha \tag{20.21}$$

From Equations 20.11 and 20.21,

$$\varepsilon = 1 - \rho \tag{20.54}$$

Thus, one can calculate emissivity once reflectivity of a material is known. According to Equation 20.54, a high reflectivity means low emissivity.

The reflectivity of a material is related to the refractive index via the Fresnel equations. For normal incidence of radiation on the surface, the Fresnel equation is given as follows [10]:

$$\rho = \left[\frac{n-1}{n+1}\right]^2 \tag{20.55}$$

where n is the refractive index of the material which is related to dielectric constant and magnetic permeability as follows:

$$n = \sqrt{\epsilon \mu} \tag{20.56}$$

Here ϵ is the dielectric constant (relative permittivity) and μ is the relative magnetic permeability.

For nonmagnetic materials, $\mu = 1$ and therefore,

$$n = \sqrt{\epsilon} \tag{20.57}$$

From Equations 20.55 and 20.57, we get

$$\rho = \frac{\left(\sqrt{\epsilon}-1\right)^2}{\left(\sqrt{\epsilon}+1\right)^2} \tag{20.58}$$

Thus, the emissivity of the material is related to dielectric constant as follows [1,7]:

$$\varepsilon = 1 - \frac{\left(\sqrt{\epsilon}-1\right)^2}{\left(\sqrt{\epsilon}+1\right)^2} \tag{20.59}$$

The dielectric constant of a composite material can be estimated from the expressions discussed in Chapter 3. As an example, the Maxwell–Garnett model is given below:

$$\left(\frac{\epsilon-\epsilon_m}{\epsilon+2\epsilon_m}\right) = \left(\frac{\epsilon_d-\epsilon_m}{\epsilon_d+2\epsilon_m}\right)\phi \tag{20.60}$$

where ϵ_m and ϵ_d are the dielectric constants of matrix and dispersed phase, respectively.

It should be noted that the dielectric constant is a bulk property whereas the emissivity is a surface property. Hence, Equation 20.59 may not be very accurate when the composite is heterogeneous in the sense that bulk composition is different from the surface composition.

REFERENCES

1. Nagar, H., R.M.A. Abdul Majeed, V.N. Bhoraskar, and S.V. Bhorasker. 2008. Radiation-assisted phosphorous diffused polyimide as low thermal emissivity material. *Nucl Instrum Meth B* 266: 781.
2. He, X., Y. Li, L. Wang, Y. Sun, and S. Zhang. 2009. High emissivity coatings for high temperature: Progress and prospect. *Thin Solid Films* 517: 5120–5129.
3. Ye, X., Y. Zhou, Y. Sun, J. Chen, and Z. Wang. 2008. Structure and infrared emissivity of collagen/SiO_2 composite. *Appl Surf Sci* 254: 5975–5980.
4. Yu, H., G. Xu, X. Shen, X. Yan, C. Shao, and C. Hu. 2009. Effects of size, shape and floatage of Cu particles on the low infrared emissivity coatings. *Prog Org Coat* 66: 161–166.
5. Yu, H., G. Xu, X. Shen, X. Yan, and C. Cheng. 2009. Low infrared emissivity of polyurethane/Cu composite coatings. *Appl Surf Sci* 255: 6077–6081.
6. Chou, K.S. and Y.C. Lu. 2007. The applications of nanosized silver colloids in far infrared low-emissive coating. *Thin Solid Films* 515: 7217–7221.
7. Babrekar, H.A., N.V. Kulkarni, J.P. Jog, V.L. Mathe, and S.V. Bhoraskar. 2010. Influence of filler size and morphology in controlling the thermal emissivity of aluminium/polymer composites for space applications. *Mater Sci Eng B* 168: 40–44.
8. Chauhan, D.V., S.N. Misra, and R.N. Shukla. 2012. Study of high emissivity coating of ceramic material for energy conservation. *Der Chemica Sinica* 3: 621–627.
9. Mauer, M., P. Kalenda, M. Honner, and P. Vacikova. 2012. Composite fillers and their influence on emissivity. *J Phys Chem Solids* 73: 1550–1555.
10. http://en.wikipedia.org/wiki/Refractive_index.

SUPPLEMENTAL READING

Bejan, A. 1993. *Heat Transfer*, New York: John Wiley & Sons.

Bergman, T.L., A.S. Levine, F.P. Incropera, and D.P. Dewitt. 2011. *Fundamentals of Heat and Mass Transfer*, 7th Edition, New York: John Wiley & Sons.

Holman, J.P. 2009. *Heat Transfer*, 10th Edition, New York: McGraw-Hill.

Kreith, F. and M.S. Bohn. 1993. *Principles of Heat Transfer*, St. Paul: West Publishing Company.

Thomas, L.C. 1992. *Heat Transfer*. Englewood Cliffs, NJ: Prentice-Hall.

Section V

Transport Properties of Composites

Mass Transfer in Composites

21 Fundamentals of Diffusion Mass Transfer

There are many applications of composite materials where diffusion mass transfer plays an important role. Composite membranes are used extensively in the separation of gas mixtures. In the packaging industry, composite membranes are used as barrier films. In the design and application of composite membranes, a good understanding of diffusion mass transfer is required. In this chapter, the key concepts and equations governing diffusion mass transfer are reviewed.

21.1 INTRODUCTION

Consider a binary mixture of species A and B. Let the mass concentration of species A, ρ_A, be nonuniform in the mixture and let the mixture as a whole be at rest without any macroscopic (bulk) motion, that is, the mixture velocity $\vec{V} = 0$. The presence of a concentration gradient $d\rho_A/dx$ in the system gives rise to a diffusional mass flux j_A ($kg/m^2.s$) whose magnitude is proportional to the concentration gradient. According to Fick's law of diffusion, the mass flux j_A is given as

$$j_A = -D_{AB}\frac{d\rho_A}{dx} \tag{21.1}$$

where D_{AB} (m^2/s) is the diffusion coefficient of species A in B. Equation 21.1 is a simplified one-dimensional form of Fick's law of diffusion. A more general vector form of Fick's law is presented in the Section 21.2.

When the system as a whole is in motion ($\vec{V} \neq 0$), then an advective mass flux of species A, given as $\rho_A\vec{V}$, is present in addition to the diffusional mass flux $\vec{j}_A$ at any given point in the system. Thus, the total mass flux of species A at any given point in the system consists of two parts:

$$\vec{n}_A = \vec{j}_A + \rho_A\vec{V} \tag{21.2}$$

where $\vec{n}_A$ and $\vec{j}_A$ are the vectorial total and diffusional mass fluxes of species A, respectively, and $\rho_A\vec{V}$ is the advective mass flux of species A. Note that $\vec{n}_A$ is the absolute mass flux of species A relative to a stationary observer whereas $\vec{j}_A$ is the relative mass flux of species A relative to an observer moving with mass average velocity $\vec{V}$ of the system.

The bulk or macroscopic motion in mixtures of different species can be caused either by external means such as a pump or by molecular-level diffusion process

itself. In the latter case, the advective mass flux of species A (given as $\rho_A \vec{V}$) is often referred to as "bulk diffusion flux."

21.2 FICK'S LAW OF DIFFUSION

The general vector form of Fick's law of diffusion for a binary system is given as

$$\vec{j}_A = -\rho D_{AB} \nabla \omega_A \tag{21.3}$$

where the mass flux $\vec{j}_A$ is the rate of diffusional mass transfer of A per unit area perpendicular to the direction of transfer, ρ is the total mass concentration of the mixture ($\rho = \rho_A + \rho_B$), D_{AB} is the binary diffusion coefficient or mass diffusivity of A in B, and ω_A is the mass fraction of species A given as ρ_A/ρ.

When the total mass concentration of the mixture is constant (ρ = constant), Fick's law reduces to

$$\vec{j}_A = -D_{AB} \nabla \rho_A \tag{21.4}$$

Fick's law of diffusion could also be stated in terms of the molar flux of species A ($\vec{J}_A$) as

$$\vec{J}_A = -C D_{AB} \nabla x_A \tag{21.5}$$

where the molar flux $\vec{J}_A$ is the rate of diffusional mass transfer of species A in moles per unit time per unit area perpendicular to the direction of transfer, C is the total molar concentration of the mixture ($C = C_A + C_B$), and x_A is the mole fraction of species A given as C_A/C. Note that $\vec{J}_A$ is the molar flux relative to coordinates that move with the molar average velocity $\vec{V}^*$ of the mixture.

When the total concentration of the mixture is constant (C = constant), Fick's law reduces to

$$\vec{J}_A = -D_{AB} \nabla C_A \tag{21.6}$$

21.3 SOME DEFINITIONS AND CONCEPTS

21.3.1 Velocities

The mass average velocity $\vec{V}$ of a multicomponent mixture is defined as

$$\vec{V} = \frac{\sum_i \rho_i \vec{V}_i}{\rho} \tag{21.7}$$

where ρ_i is the mass concentration of species i (mass per unit volume of mixture), ρ is the total concentration of the mixture $\left(\rho = \sum_i \rho_i\right)$, and $\vec{V}_i$ is the absolute velocity of species i (relative to a stationary observer). Note that $\vec{V}_i$ at any point in the mixture is the average velocity of all the species i molecules contained in a small volume about the point.

For a binary mixture of species A and B, the mass average velocity becomes

$$\vec{V} = \frac{\rho_A \vec{V}_A + \rho_B \vec{V}_B}{\rho} \tag{21.8}$$

where $\vec{V}_A$ and $\vec{V}_B$ are absolute velocities of species A and B, respectively.

The molar average velocity ($\vec{V}^*$) of a multicomponent mixture is defined as

$$\vec{V}^* = \frac{\sum_i C_i \vec{V}_i}{C} \tag{21.9}$$

where C_i is the molar concentration of species i (moles per unit volume of mixture), and C is the total molar concentration of the mixture $\left(C = \sum_i C_i\right)$. For a binary mixture

$$\vec{V}^* = \frac{C_A \vec{V}_A + C_B \vec{V}_B}{C} \tag{21.10}$$

21.3.2 Fluxes

As already noted, mass transfer flux could be defined in terms of either mass or moles and it is a vector quantity. In any given direction, it is the amount (either mass or molar units) of a particular species that passes through a unit area normal to the given direction per unit time.

Flux may be defined either with reference to coordinates fixed in space (stationary coordinates) or with reference to coordinates moving with either $\vec{V}$ (mass average velocity of the system) or $\vec{V}^*$ (molar average velocity of the system).

The absolute mass flux of species i with respect to stationary coordinates, $\vec{n}_i$, is defined as

$$\vec{n}_i = \rho_i \vec{V}_i \tag{21.11}$$

The diffusional mass flux of species i with respect to mass average velocity ($\vec{V}$) of the system is given as

$$\vec{j}_i = \rho_i (\vec{V}_i - \vec{V}) \tag{21.12}$$

where $\vec{V}_i$ is the absolute velocity of species i.

The absolute molar flux of species i, $\vec{N}_i$, and diffusional molar flux of species i, $\vec{J}_i$, are defined as

$$\vec{N}_i = C_i \vec{V}_i \tag{21.13}$$

$$\vec{J}_i = C_i(\vec{V}_i - \vec{V}^*) \tag{21.14}$$

21.4 RELATIONSHIP BETWEEN FLUXES

21.4.1 Mass Fluxes

From Equations 21.7, 21.11, and 21.12, it follows that

$$\vec{j}_i = \rho_i(\vec{V}_i - \vec{V}) = \rho_i \vec{V}_i - \rho_i \sum_{j=1}^{N} \frac{\rho_j \vec{V}_j}{\rho} = \vec{n}_i - \omega_i \sum_{j=1}^{N} \vec{n}_j \tag{21.15}$$

where N is the total number of species in the multicomponent mixture and ω_i is the mass fraction of species i. Equation 21.15 can be rewritten as

$$\vec{n}_i = \vec{j}_i + \omega_i \sum_{j=1}^{N} \vec{n}_j \tag{21.16}$$

For a binary mixture of species A and B, Equation 21.16 can be expressed as

$$\vec{n}_A = \vec{j}_A + \omega_A \left(\vec{n}_A + \vec{n}_B\right) \tag{21.17}$$

$$\vec{n}_B = \vec{j}_B + \omega_B \left(\vec{n}_A + \vec{n}_B\right) \tag{21.18}$$

Using Fick's law of diffusion (Equation 21.3), Equations 21.17 and 21.18 become

$$\vec{n}_A = -\rho D_{AB} \nabla \omega_A + \omega_A \left(\vec{n}_A + \vec{n}_B\right) \tag{21.19}$$

$$\vec{n}_B = -\rho D_{BA} \nabla \omega_B + \omega_B \left(\vec{n}_A + \vec{n}_B\right) \tag{21.20}$$

Interestingly,

$$\sum_{i=1}^{N} \vec{j}_i = 0 \tag{21.21}$$

that is, the sum of mass diffusional fluxes of all species present in the mixture is always zero. This result simply follows from Equation 21.15 when it is summed over N species:

$$\sum_{i=1}^{N} \vec{j}_i = \sum_{i=1}^{N} \vec{n}_i - \left(\sum_{j=1}^{N} \vec{n}_j \right) \left(\sum_{i=1}^{N} \omega_i \right) = 0 \tag{21.22}$$

Note that

$$\left(\sum_{i=1}^{N} \omega_i \right) = 1 \text{ and } \left(\sum_{i=1}^{N} \vec{n}_i \right) = \left(\sum_{j=1}^{N} \vec{n}_j \right) \tag{21.23}$$

Thus, in a binary mixture of species A and B, $\vec{j}_A$ is always equal to $-\vec{j}_B$:

$$\vec{j}_A = -\vec{j}_B \tag{21.24}$$

The addition of Equations 21.19 and 21.20 leads to another interesting result, that is,

$$D_{AB} = D_{BA} \tag{21.25}$$

21.4.2 Molar Fluxes

From Equations 21.9, 21.13, and 21.14, it follows that

$$\vec{J}_i = C_i \vec{V}_i - C_i \vec{V}^* = \vec{N}_i - \frac{C_i}{C} \sum_{j=1}^{N} C_j \vec{V}_j = \vec{N}_i - x_i \sum_{j=1}^{N} \vec{N}_j \tag{21.26}$$

or,

$$\vec{N}_i = \vec{J}_i + x_i \sum_{j=1}^{N} \vec{N}_j \tag{21.27}$$

where x_i is the mole fraction of species i in the mixture. For a binary mixture of species A and B, Equation 21.27 gives

$$\vec{N}_A = \vec{J}_A + x_A \left(\vec{N}_A + \vec{N}_B \right) \tag{21.28}$$

$$\vec{N}_B = \vec{J}_B + x_B \left(\vec{N}_A + \vec{N}_B \right) \tag{21.29}$$

Using Fick's law of diffusion (Equation 21.5), Equations 21.28 and 21.29 can be rewritten as

$$\vec{N}_A = -CD_{AB}\nabla x_A + x_A\left(\vec{N}_A + \vec{N}_B\right) \tag{21.30}$$

$$\vec{N}_B = -CD_{BA}\nabla x_B + x_B\left(\vec{N}_A + \vec{N}_B\right) \tag{21.31}$$

The addition of Equations 21.30 and 21.31 leads to $D_{AB} = D_{BA}$. Furthermore, Equation 21.27 when summed over N species gives

$$\sum_{i=1}^{N} \vec{J}_i = 0 \tag{21.32}$$

For a binary mixture, Equation 21.32 implies that

$$\vec{J}_A = -\vec{J}_B \tag{21.33}$$

21.5 DIFFERENTIAL MASS BALANCE EQUATIONS

Consider a differential control volume $\Delta x\Delta y\Delta z$ through which a multicomponent mixture of different chemical species is flowing (see Figure 21.1). Let the mass flux components of species i in the x, y, and z directions be $n_{i,x}$, $n_{i,y}$, and $n_{i,z}$, respectively. We can derive the differential equation of mass transfer by carrying out a mass balance on species i over the differential control volume. Thus,

$$\left\{\begin{array}{l}\text{Rate at which mass of species i}\\ \text{enters the control volume}\end{array}\right\} - \left\{\begin{array}{l}\text{Rate at which mass of species i}\\ \text{leaves the control volume}\end{array}\right\} + \left\{\begin{array}{l}\text{Rate at which mass of species i}\\ \text{is generated inside the control volume}\end{array}\right\} = \left\{\begin{array}{l}\text{Rate at which mass of species i}\\ \text{accumulates inside the control volume}\end{array}\right\} \tag{21.34}$$

$$\left\{\begin{array}{l}\text{Rate at which mass of species i}\\ \text{enters the control volume}\end{array}\right\} = n_{i,x}\Big|_x \Delta y\Delta z + n_{i,y}\Big|_y \Delta x\Delta z + n_{i,z}\Big|_z \Delta x\Delta y \tag{21.35}$$

$$\left\{\begin{array}{l}\text{Rate at which mass of species i}\\ \text{leaves the control volume}\end{array}\right\} = n_{i,x}\Big|_{x+\Delta x} \Delta y\Delta z + n_{i,y}\Big|_{y+\Delta y} \Delta x\Delta z + n_{i,z}\Big|_{z+\Delta z} \Delta x\Delta y \tag{21.36}$$

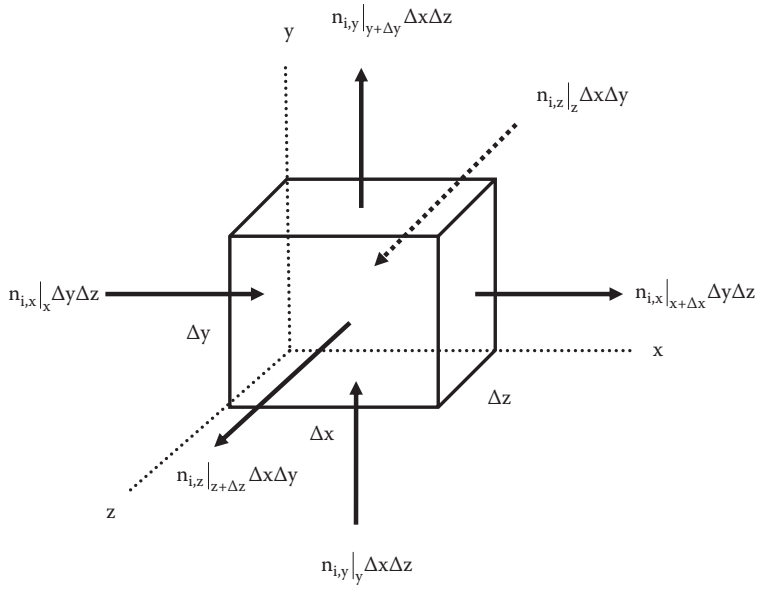

FIGURE 21.1 Mass flux components of species i entering and leaving a differential control volume.

$$\left\{\begin{array}{l}\text{Rate at which mass of species i}\\ \text{is generated inside the control volume}\end{array}\right\} = r_i(\Delta x\Delta y\Delta z) \tag{21.37}$$

$$\left\{\begin{array}{l}\text{Rate at which mass of species i}\\ \text{accumulates inside the control volume}\end{array}\right\} = (\Delta x\Delta y\Delta z)\frac{\partial \rho_i}{\partial t} \tag{21.38}$$

where r_i is the rate of production of species i in units of mass of i produced per unit volume of the mixture per unit time. Upon substitution of the above expressions into the mass balance relation and rearranging with the limits Δx, Δy, and Δz all going to zero, the following partial differential equation is obtained:

$$-\nabla\cdot\vec{n}_i + r_i = \frac{\partial \rho_i}{\partial t} \tag{21.39}$$

This is the continuity equation for species i. Upon substitution of the relation $\vec{n}_i = \vec{j}_i + \rho_i\vec{V}$ into the above equation, we obtain

$$\frac{D\rho_i}{Dt} = -\rho_i(\nabla\cdot\vec{V}) - \nabla\cdot\vec{j}_i + r_i \tag{21.40}$$

where $D\rho_i/Dt$ is the substantial derivative of ρ_i, defined as

$$\frac{D\rho_i}{Dt} = \frac{\partial \rho_i}{\partial t} + \vec{V} \cdot \nabla \rho_i \tag{21.41}$$

It should be noted that

$$\sum_{i=1}^{N} r_i = 0 \tag{21.42}$$

This result follows from the principle of conservation of mass.

In terms of molar units, the continuity equations corresponding to Equations 21.39 and 21.40 are as follows:

$$-\nabla \cdot \vec{N}_i + R_i = \frac{\partial C_i}{\partial t} \tag{21.43}$$

$$\frac{DC_i}{Dt} = -C_i(\nabla \cdot \vec{V}^*) - \nabla \cdot \vec{J}_i + R_i \tag{21.44}$$

where R_i is the rate of production of species i in units of moles of i produced per unit volume of the mixture per unit time and DC_i/Dt is substantial derivative of C_i, defined as

$$\frac{DC_i}{Dt} = \frac{\partial C_i}{\partial t} + \vec{V}^* \cdot \nabla C_i \tag{21.45}$$

Note that $\sum_i R_i$ is not generally zero (unlike $\sum_i r_i = 0$) as the number of moles is not conserved in general. For a binary mixture of species A and B, $R_A + R_B$ is equal to zero only if one mole of A is produced for every mole of B consumed (or one mole of B is produced for every mole of A consumed).

Thus, mass transfer in a nonstationary medium ($\vec{V} \neq 0$, $\vec{V}^* \neq 0$) requires the solution of the general forms of the governing equations, summarized below:

$$\vec{n}_i = -\rho D_{im} \nabla \omega_i + \omega_i \sum_j \vec{n}_j \tag{21.46}$$

$$\frac{\partial \rho_i}{\partial t} + \nabla \cdot \vec{n}_i - r_i = 0 \tag{21.47}$$

In terms of molar units, the corresponding equations are

$$\vec{N}_i = -CD_{im}\nabla x_i + x_i \sum_j \vec{N}_j \tag{21.48}$$

$$\frac{\partial C_i}{\partial t} + \nabla \cdot \vec{N}_i - R_i = 0 \tag{21.49}$$

The macroscopic or bulk motion of the medium can be either due to molecular-level diffusion process itself or due to external means such as a pump or gravity.

In a *stationary* medium ($\vec{V} = 0,\ \vec{V}^* = 0$), it follows that

$$\vec{n}_i = \vec{j}_i = -\rho D_{im}\nabla \omega_i \tag{21.50}$$

$$\frac{\partial \rho_i}{\partial t} = -\nabla \cdot \vec{j}_i + r_i \tag{21.51}$$

$$\vec{N}_i = \vec{J}_i = -CD_{im}\nabla x_i \tag{21.52}$$

$$\frac{\partial C_i}{\partial t} = -\nabla \cdot \vec{J}_i + R_i \tag{21.53}$$

where D_{im} is diffusion coefficient of species i in the mixture.

If the mass density (mass concentration) of the mixture ρ and diffusion coefficient D_{im} are constant, Equations 21.50 and 21.51 lead to the following result:

$$\frac{\partial \rho_i}{\partial t} = D_{im}\nabla^2 \rho_i + r_i \tag{21.54}$$

In the absence of a chemical reaction ($r_i = 0$), Equation 21.54 gives

$$\frac{\partial \rho_i}{\partial t} = D_{im}\nabla^2 \rho_i \tag{21.55}$$

If the total concentration of the mixture (C) and diffusion coefficient (D_{im}) are constant, Equations 21.52 and 21.53 lead to the following result:

$$\frac{\partial C_i}{\partial t} = D_{im}\nabla^2 C_i + R_i \tag{21.56}$$

In the absence of a chemical reaction ($R_i = 0$), Equation 21.56 gives

$$\frac{\partial C_i}{\partial t} = D_{im}\nabla^2 C_i \tag{21.57}$$

21.6 SPECIAL CASES

21.6.1 Equimolar Counter Diffusion

Consider equimolar counter diffusion in a binary mixture of nonreacting gases. In equimolar counter diffusion, 1 mole of species A diffuses in a given direction for each mole of species B diffusing in the opposite direction. This type of behavior is often observed in a binary distillation process where a mole of species A diffuses to the gas/liquid interface and condenses for every mole of species B that evaporates and moves away from the interface. In such cases, $\vec{N}_A = -\vec{N}_B$ and the molar average velocity ($\vec{V}^*$) of the mixture is zero. From Equation 21.52

$$\vec{N}_A = -CD_{AB}\nabla x_A \tag{21.58}$$

Let y be the direction of mass transfer. Assuming steady-state and constant C and D_{AB}, Equation 21.58 gives

$$N_{A,y} = \frac{D_{AB}}{L}(C_{A,1} - C_{A,2}) \tag{21.59}$$

where $C_{A,1} - C_{A,2}$ is the concentration difference over the diffusion zone of thickness L. At low to moderate pressures, the ideal gas law can be applied to calculate the concentrations. Thus,

$$N_{A,y} = \frac{D_{AB}}{RT}(p_{A,1} - p_{A,2}) \tag{21.60}$$

where R is the gas constant, T the absolute temperature, and p_A the partial pressure of species A.

21.6.2 Diffusion of Species A through Stagnant B (Dilute Binary System without Chemical Reaction)

Consider the diffusion of nonreacting species A through a stationary B. In this case, $\vec{n}_B = 0$ but $\vec{n}_A$ is not zero. Provided that the concentration of the diffusing species A is small ($\omega_A \ll 1$), the bulk or advective effects of mass transfer can be neglected and the stationary medium results can be applied. Thus

$$\vec{n}_A = \vec{j}_A = -\rho D_{AB}\nabla\omega_A \tag{21.61}$$

$$\frac{\partial \rho_A}{\partial t} = \nabla \cdot [\rho D_{AB} \nabla \omega_A] \tag{21.62}$$

As $\omega_A \ll 1$, $\rho = \rho_A + \rho_B \approx \rho_B$ = constant. If we further assume that D_{AB} is constant, it follows that

$$\vec{n}_A = \vec{j}_A = -D_{AB} \nabla \rho_A \tag{21.63}$$

$$\frac{\partial \rho_A}{\partial t} = D_{AB} \nabla^2 \rho_A \tag{21.64}$$

In terms of molar units, the corresponding equations are as follows:

$$\vec{N}_A = \vec{J}_A = -D_{AB} \nabla C_A \tag{21.65}$$

$$\frac{\partial C_A}{\partial t} = D_{AB} \nabla^2 C_A \tag{21.66}$$

Equations 21.63 and 21.64 or Equations 21.65 and 21.66 form the basis for solving many diffusional mass transfer problems of practical interest.

21.6.2.1 Steady-State Diffusion in Planar Geometry

Consider a plane solid wall of material B through which species A (say gaseous) is diffusing. Let the mass concentration of species A be $\rho_{A,1}$ within the material B at $x = x_1$ and let the mass concentration of species A be $\rho_{A,2}$ within the material B at $x = x_2$. At steady state, the concentration distribution of A within the material B is given by Equation 21.64 as

$$\frac{d^2 \rho_A}{dx^2} = 0 \tag{21.67}$$

$$\rho_A = \rho_{A,1} + \frac{\rho_{A,2} - \rho_{A,1}}{x_2 - x_1}(x - x_1) \tag{21.68}$$

From Equation 21.63, the mass flux of species A within the material B is given as

$$j_{A,x} = -D_{AB} \frac{d\rho_A}{dx} = -\frac{D_{AB}(\rho_{A,2} - \rho_{A,1})}{x_2 - x_1} \tag{21.69}$$

Thus, the concentration distribution of species A is linear and the mass flux of A is constant. Similar results can be obtained in terms of molar units. From Equation 21.66

$$\frac{d^2C_A}{dx^2} = 0 \tag{21.70}$$

$$C_A = C_{A,1} + \frac{C_{A,2} - C_{A,1}}{x_2 - x_1}(x - x_1) \tag{21.71}$$

where $C_{A,1}$ is the molar concentration of species A within the material B at $x = x_1$ and $C_{A,2}$ is the molar concentration of species A within the material B at $x = x_2$. The molar flux of species A is given as

$$J_{A,x} = -D_{AB}\frac{dC_A}{dx} = -\frac{D_{AB}(C_{A,2} - C_{A,1})}{x_2 - x_1} \tag{21.72}$$

The resistance to diffusional mass transfer can be defined as

$$R_m = \frac{\Delta\rho_A}{\dot{m}_A} = \frac{\Delta C_A}{\dot{M}_A} \tag{21.73}$$

where $\Delta\rho_A = \rho_{A,1} - \rho_{A,2}$, $\Delta C_A = C_{A,1} - C_{A,2}$, $\dot{m}_A$ is the mass transfer rate of species A in units of mass/time and $\dot{M}_A$ is the mass transfer rate of species A in units of moles/time. Note that $\dot{m}_A = j_A A$ and $\dot{M}_A = J_A A$, where A is the area of mass transfer (area normal to the direction of mass transfer). From Equations 21.72 and 21.73, the resistance to diffusional mass transfer for plane objects is

$$R_m = \frac{L}{D_{AB}A} \tag{21.74}$$

where L is the thickness of the planar object.

It should be pointed out that in practical problems involving diffusion of gaseous species A through a stationary solid material B, the concentration of species A in the solid at the gas/solid interface is not known. The concentration of gaseous species A in the solid at the gas/solid interface can be determined from the following equilibrium relationship:

$$C_{A,\text{ solid side}} = Sp_{A,\text{ gas side}} \tag{21.75}$$

where S is the solubility of A in the solid material B, units of mol/(m^3.Pa), and p_A is the partial pressure of species A in the gas. Thus, the molar flux of species A through material B can be expressed as

$$J_{A,x} = \frac{p_{A,1} - p_{A,2}}{\left(\frac{L}{SD_{AB}}\right)} \tag{21.76}$$

or,

$$\dot{M}_A = \frac{A(p_{A,1} - p_{A,2})}{\left(\frac{L}{SD_{AB}}\right)} = \frac{\Delta p_A}{\left(\frac{L}{SAD_{AB}}\right)} \tag{21.77}$$

Equation 21.77 indicates that the resistance to diffusional mass transfer is $L/(SAD_{AB})$ if the driving force is taken to be difference in partial pressures. The product of solubility (S) and diffusion coefficient (D_{AB}) is referred to as permeability or permeability coefficient (P), that is

$$P = SD_{AB} \tag{21.78}$$

The permeability is the flux per unit pressure gradient, often expressed in units of Barrers (1 Barrer = 10^{-10} cm^3 (STP)/[(cm^2.s)(cmHg/cm)]). It reflects the combination of solubility and diffusion characteristics of species A in material B. The resistance to diffusional mass transfer can now be expressed as L/PA provided that the driving force for mass transfer is taken to be the difference in partial pressures of species A on the two sides of material B.

21.6.2.2 Steady-State Diffusion in Cylindrical Geometry

Consider a solid cylindrical shell of material B with inner and outer radii r_1 and r_2, respectively. Gaseous species A is diffusing through the shell in the radial direction. Let $\rho_{A,1}$ be the mass concentration of species A inside the cylindrical solid at $r = r_1$ and let $\rho_{A,2}$ be the mass concentration of A inside the cylindrical solid at $r = r_2$. At steady state, the concentration distribution of A within B is given by Equation 21.64 as

$$\frac{d}{dr}\left(r\frac{d\rho_A}{dr}\right) = 0 \tag{21.79}$$

$$\rho_A = \rho_{A,1} + \frac{\rho_{A,2} - \rho_{A,1}}{\ln\left(\frac{r_2}{r_1}\right)} \ln\left(\frac{r}{r_1}\right) \tag{21.80}$$

From Equation 21.63, the mass flux of A is given as

$$j_{A,r} = -D_{AB}\frac{d\rho_A}{dr} = -\frac{D_{AB}\left(\rho_{A,2}-\rho_{A,1}\right)}{\ln\left(\frac{r_2}{r_1}\right)}\left(\frac{1}{r}\right) \tag{21.81}$$

Thus, the concentration distribution of species A is nonlinear (see Equation 21.80) and the mass flux of A decreases with the increase in r. Note that with the increase in r, the area of mass transfer increases and consequently, the mass flux decreases for the same mass transfer rate ($\dot{m}_A$ = constant, at steady state). Similar results can be obtained in terms of molar units. From Equation 21.66

$$\frac{d}{dr}\left(r\frac{dC_A}{dr}\right) = 0 \tag{21.82}$$

$$C_A = C_{A,1} + \frac{C_{A,2}-C_{A,1}}{\ln\left(\frac{r_2}{r_1}\right)}\ln\left(\frac{r}{r_1}\right) \tag{21.83}$$

where $C_{A,1}$ is the molar concentration of A within B at $r = r_1$ and $C_{A,2}$ is the molar concentration of A within B at $r = r_2$. The molar flux of species A is given as

$$J_{A,r} = -D_{AB}\frac{dC_A}{dr} = -\frac{D_{AB}\left(C_{A,2}-C_{A,1}\right)}{\ln\left(\frac{r_2}{r_1}\right)}\left(\frac{1}{r}\right) \tag{21.84}$$

The resistance to diffusional mass transfer in cylindrical geometry is

$$R_m = \frac{\Delta\rho_A}{\dot{m}_A} = \frac{\Delta C_A}{\dot{M}_A} = \frac{\ln\left(\frac{r_2}{r_1}\right)}{2\pi D_{AB}L} \tag{21.85}$$

where L is the length of the cylindrical shell. Using the equilibrium relationship Equation 21.75, the molar flux can also be expressed as

$$J_{A,r} = \frac{\left(p_{A,1}-p_{A,2}\right)}{\left[\frac{\ln(r_2/r_1)}{D_{AB}S}\right]}\left(\frac{1}{r}\right) \tag{21.86}$$

or

$$\dot{M}_A = \frac{\left(p_{A,1} - p_{A,2}\right)}{\left(\frac{\ln(r_2/r_1)}{2\pi SLD_{AB}}\right)} = \frac{\left(p_{A,1} - p_{A,2}\right)}{\left(\frac{\ln(r_2/r_1)}{2\pi PL}\right)} \tag{21.87}$$

where $p_{A,1}$ is the partial pressure of species A in the gas phase at gas/liquid interface (at $r = r_1$) and $p_{A,2}$ is the partial pressure of species A in the gas phase at gas/solid interface (at $r = r_2$).

21.6.2.3 Steady-State Diffusion in Spherical Geometry

For gaseous species A diffusing through a solid spherical shell of material B, Equation 21.64 reduces to

$$\frac{d}{dr}\left(r^2 \frac{d\rho_A}{dr}\right) = 0 \tag{21.88}$$

$$\rho_A = \rho_{A,1} + \frac{\rho_{A,2} - \rho_{A,1}}{\left(\frac{1}{r_2} - \frac{1}{r_1}\right)}\left(\frac{1}{r} - \frac{1}{r_1}\right) \tag{21.89}$$

where $\rho_{A,1}$ is mass concentration of species A within material B at gas/solid interface (at $r = r_1$) and $\rho_{A,2}$ be the mass concentration of A in B at gas/solid interface (at $r = r_2$). From Equation 21.63, the mass flux of A is

$$j_{A,r} = -D_{AB}\frac{d\rho_A}{dr} = -\frac{D_{AB}(\rho_{A,2} - \rho_{A,1})}{\left(\frac{1}{r_1} - \frac{1}{r_2}\right)}\left(\frac{1}{r^2}\right) \tag{21.90}$$

Thus, the concentration distribution of species A is nonlinear (see Equation 21.89) and the mass flux of A decreases with the increase in r due to an increase in the mass transfer area at constant mass transfer rate ($\dot{m}_A$ = constant, at steady state). In terms of molar units, Equation 21.66 gives

$$\frac{d}{dr}\left(r^2 \frac{dC_A}{dr}\right) = 0 \tag{21.91}$$

$$C_A = C_{A,1} + \frac{C_{A,2} - C_{A,1}}{\left(\frac{1}{r_2} - \frac{1}{r_1}\right)}\left(\frac{1}{r} - \frac{1}{r_1}\right) \tag{21.92}$$

where $C_{A,1}$ is the molar concentration of A within B at $r = r_1$ and $C_{A,2}$ is the molar concentration of A within B at $r = r_2$. The molar flux of species A is

$$J_{A,r} = -D_{AB}\frac{dC_A}{dr} = -\frac{D_{AB}\left(C_{A,2} - C_{A,1}\right)}{\left(\frac{1}{r_1} - \frac{1}{r_2}\right)}\left(\frac{1}{r^2}\right) \tag{21.93}$$

The resistance to diffusional mass transfer in a spherical geometry is

$$R_m = \frac{\Delta\rho_A}{\dot{m}_A} = \frac{\Delta C_A}{\dot{M}_A} = \frac{r_2 - r_1}{4\pi D_{AB} r_1 r_2} \tag{21.94}$$

The molar flux of species A in terms of partial pressures of A can be obtained using Equation 21.75. Thus,

$$J_{A,r} = \frac{(p_{A,1} - p_{A,2})}{\frac{r_2 - r_1}{SD_{AB} r_1 r_2}}\left(\frac{1}{r^2}\right) \tag{21.95}$$

or

$$\dot{M}_A = \frac{(p_{A,1} - p_{A,2})}{\frac{r_2 - r_1}{4\pi P r_1 r_2}} \tag{21.96}$$

where P is the permeability of A in B, given as SD_{AB}.

21.6.3 Diffusion of Species A through Stagnant B (Dilute Binary System with Chemical Reaction)

Many processes of practical interest involve the simultaneous diffusion of a chemical species and the consumption or generation of the same species through a chemical reaction. In such situations, the mass balance equations in terms of mass and molar units are as follows:

$$\frac{\partial \rho_A}{\partial t} + \nabla \cdot \vec{n}_A - r_A = 0 \tag{21.97}$$

$$\frac{\partial C_A}{\partial t} + \nabla \cdot \vec{N}_A - R_A = 0 \tag{21.98}$$

Since

$$\vec{n}_A = \vec{j}_A = -D_{AB}\nabla\rho_A \tag{21.99}$$

$$\vec{N}_A = \vec{J}_A = -D_{AB}\nabla C_A \tag{21.100}$$

Equations 21.97 and 21.98 can be rewritten as follows provided that D_{AB} is constant:

$$\frac{\partial\rho_A}{\partial t} = D_{AB}\nabla^2\rho_A + r_A \tag{21.101}$$

$$\frac{\partial C_A}{\partial t} = D_{AB}\nabla^2 C_A + R_A \tag{21.102}$$

As an example of the application of these equations, consider a plane layer of organic matter of thickness L. The oxygen is diffusing through the organic matter. The oxygen is also being consumed in the organic matter by biochemical reactions (say by bacteria that is uniformly distributed in the organic matter). The consumption of oxygen depends on the local concentration of oxygen and can be expressed as $R_A = -kC_A$ (mol/s.m^3). Let $C_{A,0}$ and $C_{A,L}$ be the molar concentrations of oxygen in the organic matter at x = 0 and x = L, respectively. Assuming that $C_{A,0}$ and $C_{A,L}$ are constant (independent of time), we can determine the concentration distribution of oxygen in the organic matter by solving Equation 21.102. Thus,

$$D_{AB}\frac{d^2C_A}{dx^2} - kC_A = 0 \tag{21.103}$$

Equation 21.103 needs to be solved subject to the boundary conditions: at x = 0, $C_A = C_{A,0}$ and at x = L, $C_A = C_{A,L}$. The solution is as follows:

$$C_A = \frac{C_{A,0}\left(e^{-\left(\sqrt{k/D_{AB}}\right)(L-x)} - e^{\left(\sqrt{k/D_{AB}}\right)(L-x)}\right) + C_{A,L}\left(e^{-\left(\sqrt{k/D_{AB}}\right)x} - e^{\left(\sqrt{k/D_{AB}}\right)x}\right)}{\left(e^{-\left(\sqrt{k/D_{AB}}\right)L} - e^{\left(\sqrt{k/D_{AB}}\right)L}\right)} \tag{21.104}$$

21.6.4 Diffusion of Species A through Stagnant B (Nondilute Binary System)

When the concentration of the diffusing species is not small, the bulk or advective effects cannot be neglected. In a binary system, where A is diffusing through stagnant B, the absolute mass and molar fluxes of A are given as

$$\vec{n}_A = -\rho D_{AB} \nabla \omega_A + \omega_A \vec{n}_A \tag{21.105}$$

$$\vec{N}_A = -C D_{AB} \nabla x_A + x_A \vec{N}_A \tag{21.106}$$

Considering only the molar quantities and one-dimensional diffusion, Equation 21.106 can be rewritten as

$$N_{A,y}\left(1 - x_A\right) = -C D_{AB}\left(\frac{dx_A}{dy}\right) \tag{21.107}$$

where $N_{A,y}$ is the absolute molar flux of A in the direction of mass transfer (y-direction). Assuming steady state ($N_{A,y}$ = constant), and constant C (total concentration of mixture), and constant D_{AB}, Equation 21.107 can be integrated over the diffusion zone of thickness L:

$$N_{A,y} \int_{y=0}^{L} dy = -C D_{AB} \int_{x_{A,0}}^{x_{A,L}} \frac{dx_A}{1 - x_A} \tag{21.108}$$

where $x_{A,0}$ is the mole fraction of species A at y = 0 and $x_{A,L}$ is the mole fraction of species A at y = L. Equation 21.108 gives

$$N_{A,y} = \frac{-C D_{AB}}{L} \ln\left[\frac{1 - x_{A,0}}{1 - x_{A,L}}\right] \tag{21.109}$$

Upon rearrangement, Equation 21.109 can be expressed as

$$N_{A,y} = \frac{C D_{AB}}{L}\left[\frac{x_{A,0} - x_{A,L}}{(x_B)_{lm}}\right] \tag{21.110}$$

where $(x_B)_{lm}$ is log mean mole fraction of B, defined as

$$(x_B)_{lm} = \left[\frac{x_{B,0} - x_{B,L}}{\ln\left(\frac{x_{B,0}}{x_{B,L}}\right)}\right] \tag{21.111}$$

If species A and B are ideal gases (at low pressures, gases can be treated as ideal gases), it follows that

$$C = \frac{p}{RT}, \quad C_A = \frac{p_A}{RT}, \quad C_B = \frac{p_B}{RT} \tag{21.112}$$

$$x_A = \frac{C_A}{C} = \frac{p_A}{p}, \quad x_B = \frac{p_B}{p}, \quad (x_B)_{lm} = \frac{(p_B)_{lm}}{p} \tag{21.113}$$

Thus, Equation 21.109 can be rewritten as

$$N_{A,y} = \frac{D_{AB}}{RT} \frac{p}{(p_B)_{lm}} \left(\frac{p_{A,0} - p_{A,L}}{L} \right) \tag{21.114}$$

21.6.5 Transient Diffusion

In steady-state analysis of mass diffusion considered in the preceding sections, the concentration and flux are independent of time. Now transient mass diffusion is considered where the concentration and flux vary with both location and time.

Consider a semi-infinite body of material B. This body is exposed to an environment consisting of species A. Species A diffuses into the semi-infinite body. We are interested in concentration distribution of species A in the body as a function of time, given that

$$\rho_A(x, t = 0) = \rho_{A,i} \tag{21.115}$$

$$\rho_A(x = 0, t) = \rho_{A,s} \tag{21.116}$$

$$\rho_A(x \to \infty, t) = \rho_{A,i} \tag{21.117}$$

Equation 21.115 represents the initial condition that the mass concentration of species A in the body is uniform at t = 0, Equation 21.116 is the surface boundary condition that the concentration of species A within the body at the surface is constant, and Equation 21.117 represents the second boundary condition that far away from the surface, the concentration of species A in the body is the same as initial concentration.

The equation governing the concentration distribution is Equation 21.64 provided that D_{AB} is constant and $\omega_A \ll 1$. Thus

$$\frac{\partial \rho_A}{\partial t} = D_{AB} \frac{\partial^2 \rho_A}{\partial x^2} \tag{21.118}$$

Equation 21.118 needs to be solved subject to the initial and boundary conditions specified in Equations 21.115 through 21.117. The solution is as follows:

$$\frac{\rho_A - \rho_{A,i}}{\rho_{A,s} - \rho_{A,i}} = 1 - \text{erf}\left[\frac{x}{2\sqrt{D_{AB}t}}\right] \tag{21.119}$$

where "erf" refers to error function. If $\rho_{A,i} = 0$, Equation 21.119 reduces to

$$\frac{\rho_A}{\rho_{A,s}} = 1 - \text{erf}\left[\frac{x}{2\sqrt{D_{AB}t}}\right] \tag{21.120}$$

These results can be applied to several problems of practical interest.

SUPPLEMENTAL READING

Bird, R.B., W.E. Stewart, and E.N. Lightfoot. 2007. *Transport Phenomena*, 2nd Edition, New York: John Wiley & Sons.

Geankoplis, C.J. 1993. *Transport Processes and Unit Operations*, 3rd Edition, Englewood Cliffs, NJ: Prentice-Hall.

Greenkorn, R.A. and D.P. Kessler. 1972. *Transfer Operations*, New York: McGraw-Hill.

McCabe, W.L., J.C. Smith, and P. Harriott. 2005. *Unit Operations of Chemical Engineering*, 7th Edition, New York: McGraw-Hill.

Welty, J.R., C.E. Wicks, R.E. Wilson, and G.L. Rorrer. 2008. *Fundamentals of Momentum, Heat, and Mass Transfer*, 5th Edition, New York: John Wiley & Sons.

22 Diffusion Mass Transfer in Composite Membranes

22.1 PARTICULATE-FILLED POLYMER COMPOSITE MEMBRANES

Particulate-filled polymer composite membranes are two-phase heterogeneous membranes consisting of filler particles dispersed uniformly or randomly in a polymer matrix [1]. The incorporation of filler particles to the polymer matrix can reduce or enhance the permeation of species through the membrane depending upon the permeability of the species in the filler particles. In some practical applications, it is desirable to reduce the permeability of a species through the membrane (barrier membranes) whereas in other applications, it is important to increase the permeability of a species (mixed matrix membranes). Barrier membranes with reduced permeability are widely used in the packaging industry [2,3]. They are also used as anticorrosive coatings [4–6]. Mixed matrix membranes (MMMs), on the other hand, are designed to have high permeability and high permselectivity for a species of interest. They are composed of porous "molecular sieve type" inorganic fillers and polymeric matrix and are very effective in the separation of gaseous mixtures [7–19]. Particulate-filled polymer composite membranes are finding applications in polymer electrolyte membrane (PEM) fuel cells as well [20]. In the PEM fuel cells, the proton permeability and the mechanical strength of polymer electrolyte membrane could be improved significantly by filling the polymer matrix with inorganic particles of high proton permeability.

To make efficient use of the particulate-filled polymer composite membranes, the variation of permeability of a penetrant with the kind and concentration of filler materials should be known. Knowledge of the permeabilities of different penetrants is required for the design and operation of composite membrane based separation processes.

22.1.1 Background

According to the solution–diffusion model of permeation, the mechanism of permeation of a species through the dense membrane consists of three steps: (1) adsorption of the permeating species from the feed stream onto the membrane surface, (2) diffusion of species through the membrane, and (3) desorption of the permeating species into the product stream.

The permeation of a species through a stationary medium (membrane) is governed by the following Fick's law of diffusion provided that the concentration of the diffusing species A is small:

$$\vec{N} = -P\nabla p \tag{22.1}$$

where $\vec{N}$ is the absolute molar flux of a diffusing species, P is the permeability of the membrane for the species, and ∇p is the gradient in partial pressure of the species diffusing through the membrane. The permeability of a membrane is a measure of its ability to permeate (pass or transfer) a species through it. When P = 0 for a particular molecular species, the membrane is impermeable to that species meaning the species under consideration cannot pass through the membrane. The higher the P, the faster the rate of the mass transfer of species for a given pressure gradient.

In the case of one-dimensional permeation in the x-direction, Fick's law reduces to

$$N = P\left(\frac{p_1 - p_2}{L}\right) \tag{22.2}$$

where L is the membrane thickness, p_1 is the partial pressure of permeating species on the feed side, and p_2 is the partial pressure of permeating species on the product side.

As noted in Chapter 21, the permeability of a species in the membrane is the product of its diffusion coefficient D and solubility S, that is

$$P = D \times S \tag{22.3}$$

The solubility of the species in the filled polymer membrane is given as

$$S = \phi S_d + (1 - \phi)S_m \tag{22.4}$$

where S_d and S_m are the solubilities of the species in the dispersed and matrix phases and ϕ is the filler volume fraction. From Equations 22.3, 22.4, and the relation

$$P_m = D_m \times S_m \tag{22.5}$$

it follows that

$$\frac{D}{D_m} = \frac{P/P_m}{\left[\phi\left(\frac{S_d}{S_m}\right) + (1-\phi)\right]} \tag{22.6}$$

Thus, one can estimate the diffusion coefficient of a species in the membrane from Equation 22.6, once the permeability is known.

When the solubilities of a species in the dispersed phase and matrix, S_d and S_m, are equal, Equation 22.6 gives

$$\frac{D}{D_m} = \frac{P}{P_m} \tag{22.7}$$

In the case of filler particles with negligible solubility for the species, $S_d \to 0$ and

$$\frac{D}{D_m} = \left(\frac{P}{P_m}\right)(1-\phi)^{-1} \tag{22.8}$$

The addition of filler particles to a polymer matrix alters the permeability of a species in at least two ways: (1) the addition of fillers increases the tortuosity of the diffusion path and (2) the solubility of the penetrant is altered due to replacement of polymer matrix with filler particles.

22.1.2 Permeation Models for Particulate-Filled Polymer Composite Membranes

As there exists a close analogy between electrical/thermal conduction phenomenon and permeation of species through membranes, the equations derived for the electrical/thermal conductivity of a heterogeneous system can be applied directly to the permeation of species through filled composite membranes by replacing the conductivity with the membrane permeability.

The simple rules of mixtures applicable to electrical/thermal conduction could also be applied to permeability of a species through a particulate-filled composite membrane. Thus,

$$P = \phi P_d + (1 - \phi)P_m \tag{22.9}$$

$$\frac{1}{P} = \frac{\phi}{P_d} + \frac{1-\phi}{P_m} \tag{22.10}$$

$$\log P = \phi \log P_d + (1 - \phi) \log P_m \tag{22.11}$$

Equation 22.9 is the Voigt rule of mixtures which gives the upper bound of permeability. Equation 22.10 is the Reuss rule of mixtures which gives the lower bound of permeability. Equation 22.11 is the Lichtenecker logarithmic rule of mixtures for permeability.

The Maxwell model [21], originally developed for the electrical conductivity of particulate-filled composites, can be adapted to permeability as

$$P_r = \frac{P}{P_m} = \left[\frac{2(1-\phi) + (1+2\phi)\lambda_{dm}}{(2+\phi) + (1-\phi)\lambda_{dm}}\right] \tag{22.12}$$

where P_r is the relative permeability of species, P is the effective permeability of species in membrane, P_m is the permeability of species in the matrix (continuous phase), ϕ is the volume fraction of the filler particles, and λ_{dm} is the permeability ratio P_d/P_m (P_d is the permeability of species in dispersed phase).

The Maxwell model generally describes the permeability well when ϕ is less than about 0.2. At higher values of ϕ, significant deviations are expected between the predictions of Equation 22.12 and actual values. Also, the Maxwell model fails to predict the correct behavior at $\phi \to \phi_m$, where ϕ_m is the maximum packing volume fraction of filler particles. Note that at $\phi = \phi_m$, the relative permeability P_r is expected to diverge especially for filled composite membranes with permeability ratio $\lambda_{dm} \to \infty$. Furthermore, the Maxwell model does not account for particle size distribution, particle shape, and aggregation of particles.

The Bruggeman model [22], originally developed for the dielectric constant of particulate-filled composites, can be adapted to permeability as

$$(P_r)^{1/3}\left[\frac{\lambda_{dm}-1}{\lambda_{dm}-P_r}\right] = (1-\phi)^{-1} \tag{22.13}$$

The Bruggeman model was developed using the differential effective medium approach. While the Bruggeman model is an improvement over the Maxwell model, as far as the effect of ϕ is concerned, it has limitations similar to that of the Maxwell model, that is, it does not give the correct behavior at $\phi \to \phi_m$. Also, it does not account for particle size distribution, particle shape, and aggregation of particles.

The Lewis–Nielsen model [23,24], originally proposed for the elastic modulus of particulate composites, can be adapted to permeability [19] as

$$P_r = \frac{P}{P_m} = \left[\frac{1+2\left(\frac{\lambda_{dm}-1}{\lambda_{dm}+2}\right)\phi}{1-\left(\frac{\lambda_{dm}-1}{\lambda_{dm}+2}\right)\phi\psi}\right] \tag{22.14}$$

where

$$\psi = 1+\left(\frac{1-\phi_m}{\phi_m^2}\right)\phi \tag{22.15}$$

and ϕ_m is the maximum packing volume fraction of filler particles (ϕ_m is 0.64 for random close packing of uniform spheres).

The Lewis–Nielsen model, Equation 22.14, gives the correct behavior at $\phi \to \phi_m$. As expected, the relative permeability P_r at $\phi = \phi_m$ diverges when the permeability ratio $\lambda_{dm} \to \infty$. As ϕ_m is sensitive to particle size distribution, particle shape, and aggregation of particles, the Lewis–Nielsen model does take into account the effects of morphology on permeability. Also note that when $\phi_m \to 1$, the Lewis–Nielsen model reduces to the Maxwell model (Equation 22.12).

The Pal model [25], originally developed for the thermal conductivity of particulate composites, can be adapted to permeability as

$$(P_r)^{1/3}\left[\frac{\lambda_{dm}-1}{\lambda_{dm}-P_r}\right]=\left(1-\frac{\phi}{\phi_m}\right)^{-\phi_m} \tag{22.16}$$

The Pal model was developed using the differential effective medium approach taking into consideration the packing difficulty of filler particles. Note that when $\phi_m \to 1$, the Pal model reduces to the Bruggeman model (Equation 22.13). The Pal model, like the Lewis–Nielsen model, gives the correct behavior at $\phi \to \phi_m$. It also takes into account the effects of morphology on permeability through the parameter ϕ_m (ϕ_m is known to be sensitive to morphology).

22.1.3 Effects of Interfacial Layer

The models discussed in the preceding section assume ideal contact between the filler particles and matrix. More often than not, the contact between the particles and matrix phase is defective; for example, dewetting of polymer chains from the filler surface often occurs resulting in void space between the two phases (filler and matrix). It is also possible that the polymer molecules in direct contact with the filler surface become somewhat rigidified in comparison to the bulk polymer molecules [9,11]. Thus, the permeability of a species in the interfacial region surrounding the filler particles is often significantly different from the permeability in the bulk polymer matrix.

The influence of interfacial layer on the permeability of species in composite membranes has been investigated by Mahajan and Koros [18]. The permeability of species in three-phase composite membranes (the three phases being bulk matrix, interfacial layer, and filler particles) can be modeled using a two-step approach. In the first step, the Maxwell equation (Equation 22.12) for two-phase composites is applied to determine the permeability of species in a single core-shell particle consisting of filler as core and interfacial layer as shell. The interfacial layer is treated as matrix with respect to the filler core particle. In the second step, the core-shell particles are treated as "homogeneous" particles of permeability obtained from the first step. The Maxwell model is applied once again to determine the permeability of three-phase composite membrane. Thus,

$$P_r=\frac{P}{P_m}=\left[\frac{2(1-\phi)+(1+2\phi)(P_{eff}/P_m)}{(2+\phi)+(1-\phi)(P_{eff}/P_m)}\right] \tag{22.17}$$

where ϕ is the volume fraction of total dispersed phase (filler core particles plus interfacial layers) and P_{eff} is the effective permeability of the core-shell particle (filler core particle plus interfacial layer) given as

$$P_{eff}=P_I\left[\frac{2(1-\phi_c)+(1+2\phi_c)(P_d/P_I)}{(2+\phi_c)+(1-\phi_c)(P_d/P_I)}\right] \tag{22.18}$$

where ϕ_c is the volume fraction of filler core particle in the combined volume of core and interfacial shell, P_d is the permeability of core particle and P_I is the permeability of the interfacial shell.

The modified Maxwell model, Equations 22.17 and 22.18, has the same limitations as observed in the case of the Maxwell model (Equation 22.12). It is valid for low volume fractions of core-shell particles. It is expected to exhibit significant deviation from the actual behavior at high values of ϕ, especially when $\phi \rightarrow \phi_m$, where ϕ_m is the maximum packing volume fraction of core-shell particles. Also the modified Maxwell model does not account for particle size distribution, particle shape, and aggregation of particles.

Using a self-consistent field concept, Felske [26] recently developed an expression for the thermal conductivity of composites of core-shell particles (core particle covered with interfacial layer). The Felske thermal conductivity model, when adapted to permeability [19], can be written as

$$P_r = \frac{P}{P_m} = \left[\frac{2(1-\phi) + (1+2\phi)(\beta/\gamma)}{(2+\phi) + (1-\phi)(\beta/\gamma)} \right] \tag{22.19}$$

where β and γ are given as

$$\beta = \frac{(2+\delta^3)P_d - 2(1-\delta^3)P_I}{P_m} = (2+\delta^3)\lambda_{dm} - 2(1-\delta^3)\lambda_{Im} \tag{22.20}$$

$$\gamma = 1 + 2\delta^3 - (1-\delta^3)(P_d/P_I) = 1 + 2\delta^3 - (1-\delta^3)\lambda_{dI} \tag{22.21}$$

δ is the ratio of outer radius of interfacial shell to core radius, ϕ is the volume fraction of core-shell particles (volume fraction of total dispersed phase, filler core particles plus interfacial layers), P_I is the permeability in the interfacial shell, P_d is the permeability in filler core particle, P_m is the permeability in matrix, λ_{dm} is the permeability ratio P_d/P_m, λ_{Im} is the permeability ratio P_I/P_m, and λ_{dI} is the permeability ratio P_d/P_I.

The Felske model gives almost the same predictions as the modified Maxwell model (Equations 22.17 and 22.18). Also, the Felske model reduces to the Maxwell model (Equation 22.12) when $\delta = 1$, that is, when the interfacial layer is absent.

The Felske model, although somewhat simpler than the modified Maxwell model, Equations 22.17 and 22.18, has the same limitations as that of the modified Maxwell model. It is valid only when the volume fraction of core-shell particles (ϕ) is small. Like the modified Maxwell model, it is expected to exhibit significant deviation from the actual behavior at high values of ϕ, especially when $\phi \rightarrow \phi_m$. Also the Felske model does not account for particle size distribution, particle shape, and aggregation of particles.

To account for the morphology and packing difficulty of particles, Pal [19] has recently proposed the following model:

$$P_r = \frac{P}{P_m} = \left[\frac{1 + 2\left(\frac{\beta-\gamma}{\beta+2\gamma}\right)\phi}{1 - \left(\frac{\beta-\gamma}{\beta+2\gamma}\right)\phi\psi} \right] \tag{22.22}$$

where β and γ are given by Equations 22.20 and 22.21, respectively and ψ is given by Equation 22.15 in terms of ϕ_m (maximum packing volume fraction of core–shell particles). In the limit $\phi \to \phi_m$, this Pal–Felske model, Equation 22.22, gives the correct behavior. When $\phi_m = 1$, the model reduces to the Felske model (Equation 22.19). When $\delta = 1$, the model reduces to the Lewis–Nielsen model (Equation 22.14). Also, when $\delta = 1$ and $\phi_m = 1$, the Pal–Felske model reduces to the Maxwell model (Equation 22.12).

The selectivity (also referred to as permselectivity) of a membrane, denoted as α_{AB}, is defined as the ratio of permeability of component A in the membrane (P_A) to permeability of component B in the membrane (P_B):

$$\alpha_{AB} = \frac{P_A}{P_B} \tag{22.23}$$

Using the Pal–Felske model (Equation 22.22), the relative selectivity $\alpha_{AB,r}$ can be expressed as

$$\alpha_{AB,r} = \frac{\alpha_{AB}}{\alpha_{AB,m}} = \frac{P_A/P_B}{P_{Am}/P_{Bm}} = \left\{\frac{1+2\phi\left(\dfrac{\beta_A-\gamma_A}{\beta_A+2\gamma_A}\right)}{1+2\phi\left(\dfrac{\beta_B-\gamma_B}{\beta_B+2\gamma_B}\right)}\right\}\left\{\frac{1-\psi\phi\left(\dfrac{\beta_B-\gamma_B}{\beta_B+2\gamma_B}\right)}{1-\psi\phi\left(\dfrac{\beta_A-\gamma_A}{\beta_A+2\gamma_A}\right)}\right\} \tag{22.24}$$

where $\alpha_{AB,m}$ is the selectivity of the matrix, P_{Am} and P_{Bm} are the permeabilities of species A and B in the matrix, respectively, and β_A, γ_A, β_B, γ_B are defined as

$$\beta_A = \frac{(2+\delta^3)P_{Ad} - 2(1-\delta^3)P_{AI}}{P_{Am}} = (2+\delta^3)\lambda_{A,dm} - 2(1-\delta^3)\lambda_{A,Im} \tag{22.25}$$

$$\gamma_A = 1 + 2\delta^3 - (1-\delta^3)(P_{Ad}/P_{AI}) = 1 + 2\delta^3 - (1-\delta^3)\lambda_{A,dI} \tag{22.26}$$

$$\beta_B = \frac{(2+\delta^3)P_{Bd} - 2(1-\delta^3)P_{BI}}{P_{Bm}} = (2+\delta^3)\lambda_{B,dm} - 2(1-\delta^3)\lambda_{B,Im} \tag{22.27}$$

$$\gamma_B = 1 + 2\delta^3 - (1-\delta^3)(P_{Bd}/P_{BI}) = 1 + 2\delta^3 - (1-\delta^3)\lambda_{B,dI} \tag{22.28}$$

where P_{Ad} and P_{AI} are the permeabilities of species A in dispersed phase (filler core particle) and interfacial shell, respectively; P_{Bd} and P_{BI} are the permeabilities of species B in dispersed phase (filler core particle) and interfacial shell, respectively; $\lambda_{A,dm}$, $\lambda_{A,Im}$, $\lambda_{A,dI}$, $\lambda_{B,dm}$, $\lambda_{B,Im}$, and $\lambda_{B,dI}$ are the various permeability ratios for species A and B defined as $\lambda_{A,dm} = P_{Ad}/P_{Am}$; $\lambda_{A,Im} = P_{AI}/P_{Am}$; $\lambda_{A,dI} = P_{Ad}/P_{AI}$; $\lambda_{B,dm} = P_{Bd}/P_{Bm}$; $\lambda_{B,Im} = P_{BI}/P_{Bm}$; and $\lambda_{B,dI} = P_{Bd}/P_{BI}$.

22.1.3.1 Predictions of the Pal–Felske Model

According to the Pal–Felske model (Equation 22.22), the relative permeability of a species in particulate-filled composite membranes (particles with interfacial layers) can be expressed as [19]

$$P_r = f(\delta, \lambda_{Im}, \lambda_{dI}, \phi, \phi_m) \tag{22.29}$$

Note that $\lambda_{dm} = \lambda_{Im}\,\lambda_{dI}$.

Figure 22.1 shows the relative permeability predicted from the model for different values of filler volume fraction (ϕ). Note that ϕ is the volume fraction of core plus shell particles. The plots are generated from Equation 22.22 under the conditions: $\delta = 4/3$, $\lambda_{dI} = 100$, $\phi_m = 0.64$. At a fixed value of ϕ, the relative permeability (P_r) remains constant initially with the increase in the permeability ratio λ_{Im}. In the range $10^{-2} < \lambda_{Im} < 100$, P_r increases with the increase in λ_{Im}. At higher values of λ_{Im} ($\lambda_{Im} > 100$), P_r again becomes constant (independent of λ_{Im}). Interestingly, P_r is less than unity for small values of λ_{Im} and P_r is greater than unity when λ_{Im} is large. For low values of λ_{Im}, P_r decreases with the increase in ϕ. For large values of λ_{Im}, P_r increases with the increase in ϕ.

Figure 22.2 shows the relative permeability P_r versus permeability ratio λ_{Im} plots for different values of radii ratio δ (δ is the ratio of outer radius of the shell to radius of the core). The plots are generated from the Pal–Felske model (Equation 22.22) under the conditions: $\phi = 0.55$, $\phi_m = 0.64$, and $\lambda_{dI} = 1000$. The radii ratio δ, and hence the thickness of the interfacial layer, has a strong influence on the relative permeability, especially in the intermediate range of permeability ratio λ_{Im}; at very low and very high values of λ_{Im}, P_r of the membrane is independent of the radii ratio δ. In the

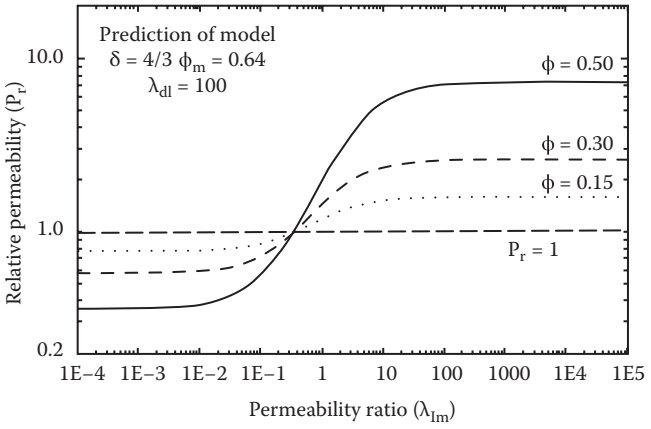

FIGURE 22.1 Relative permeability (P_r) versus permeability ratio (λ_{Im}) behavior predicted by the Pal–Felske model (Equation 22.22) under the conditions $\delta = 4/3$, $\lambda_{dI} = 100$, and $\phi_m = 0.64$. Note that λ_{Im} is the ratio of interfacial shell permeability to matrix permeability, λ_{dI} is the ratio of filler core particle permeability to interfacial shell permeability, and δ is the ratio of outer radius of interfacial shell to radius of filler core particle. (From Pal, R., *J. Colloid Interf. Sci.* 317: 191–198, 2008.)

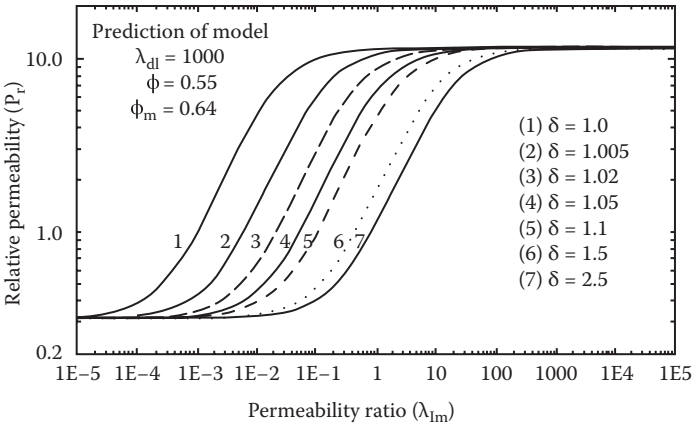

FIGURE 22.2 Relative permeability (P_r) versus permeability ratio (λ_{Im}) plots for different values of radii ratio δ under the conditions $\phi = 0.55$, $\phi_m = 0.64$, and $\lambda_{dI} = 1000$. (From Pal, R., *J. Colloid Interf. Sci.* 317: 191–198, 2008.)

intermediate range of λ_{Im}, P_r decreases with the increase in δ or the shell thickness of the core-shell particle.

The effect of permeability ratio λ_{dI} on P_r versus λ_{Im} behavior of filled composite membranes is shown in Figure 22.3, under the conditions: $\phi = 0.55$, $\phi_m = 0.64$, $\delta = 4/3$. With the increase in λ_{dI} (permeability of core material divided by permeability of shell material), the relative permeability P_r of a filled composite membrane increases for intermediate values of λ_{Im} ($10^{-2} < \lambda_{Im} < 100$).

Figure 22.4 shows the plots of selectivity α_{AB} versus permeability P_A predicted from the Pal–Felske model. The top graph of Figure 22.4 is generated under the conditions: $P_{Am} = 10$, $P_{Ad} = 45$, $P_{AI} = 4.5$, $P_{Bm} = 1$, $P_{Bd} = 1$, $P_{BI} = 0.1$, and $\phi_m = 0.64$.

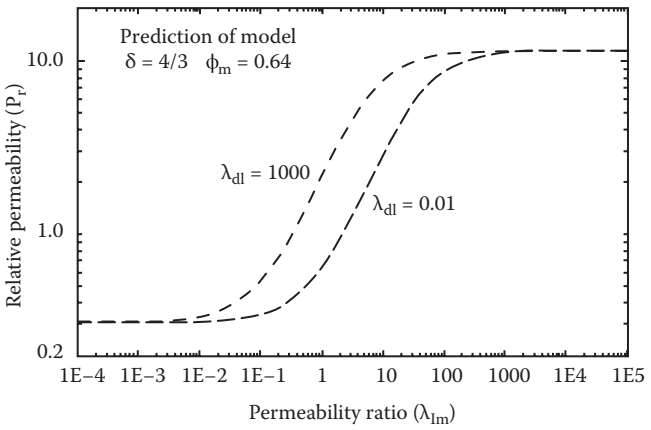

FIGURE 22.3 Effect of permeability ratio λ_{dI} (ratio of filler core particle permeability to interfacial shell permeability) on the P_r versus λ_{Im} behavior under the conditions $\phi_m = 0.64$, and $\delta = 4/3$. (From Pal, R., *J. Colloid Interf. Sci.* 317: 191–198, 2008.)

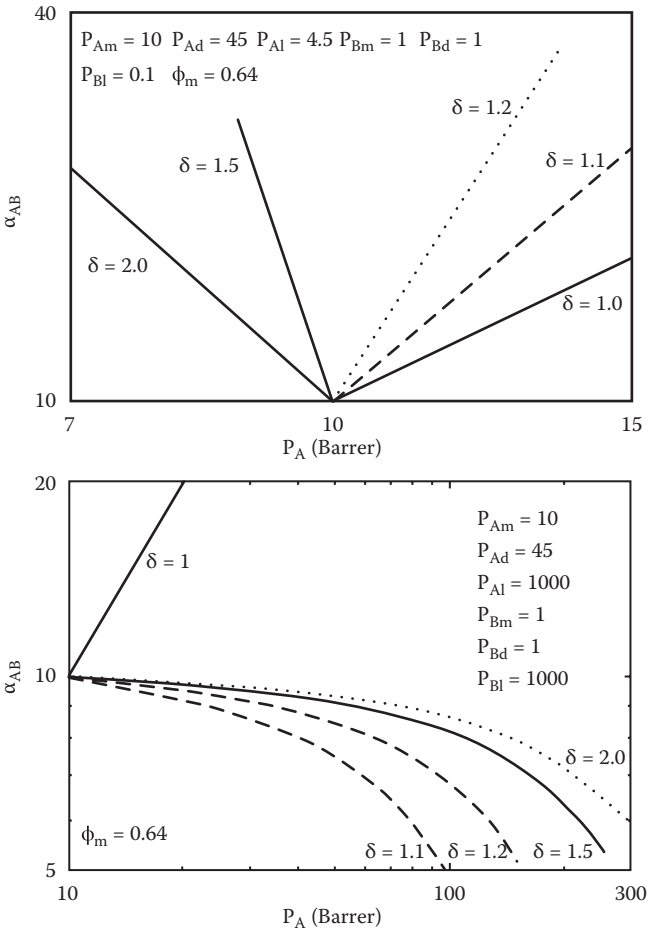

FIGURE 22.4 Plots of selectivity α_{AB} versus permeability P_A predicted by the Pal–Felske model. (From Pal, R., *J. Colloid Interf. Sci.* 317: 191–198, 2008.)

This case corresponds to *rigidified* matrix layer as the interfacial layer surrounding the particles. The bottom graph of Figure 22.4 is generated under the conditions: $P_{Am} = 10$, $P_{Ad} = 45$, $P_{AI} = 1000$, $P_{Bm} = 1$, $P_{Bd} = 1$, $P_{BI} = 1000$, and $\phi_m = 0.64$. This case corresponds to *void space* as the interfacial layer surrounding the particles. Clearly the performance of the membrane is sensitive to the thickness of the interfacial layer (radii ratio δ). For the case where the interfacial layer is rigidified (top graph of Figure 22.4) the selectivity and permeability both increase with the increase in ϕ when δ is close to unity. The performance of the filled composite membrane deteriorates with the increase in δ, that is, for the same selectivity α_{AB}, lower permeability P_A is achieved. For the case where the interfacial layer is void space (bottom graph of Figure 22.4), a dramatic change in the membrane performance occurs even when the interfacial layer is very thin (δ close to 1); when δ = 1 (ideal contact, no interfacial layer) α_{AB} and P_A both increase with the increase in the concentration of filler

particles (ϕ). For the same permeability P_A, a large decrease in selectivity α_{AB} occurs when voids are present at the interface of the filler particles.

22.1.3.2 Comparison of Model Predictions with Experimental Data

Figure 22.5 shows comparison between experimental relative permeability data (Set 1 [14]) on mixed matrix membranes and predictions of the Pal–Felske model [19]. The matrix material (6 FDA-6FpDA-DABA) is a polymer–glassy polyimide. The volume fraction of the filler core particles (ZSM-2 Zeolite) is fixed at 0.16. The permeability ratio λ_{dm} (ratio of filler core particle permeability to matrix permeability) is varied from 0.0132 to 4 by using five different gases (He, O_2, N_2, CH_4, and CO_2). The maximum packing volume fraction of particles is taken to be 0.64, corresponding to random close packing of uniform spheres. Clearly the model describes the experimental data very well. The value of δ is unity indicating that the contact between the particles and the matrix is defect free.

Figure 22.6 compares model predictions and experimental permeability data (Set 2 [15]), for Matrimid 5218/Carbon molecular sieves (CMS) system. The mixed matrix membranes consisting of carbon molecular sieves as filler particles and Matrimid 5218 (thermoplastic polyimide) as matrix were studied by Vu et al. [15] for CO_2/CH_4 separation. The experimental data are plotted as relative selectivity $\alpha_{AB,r}$ and relative permeability $P_{A,r}$ (here A refers to CO_2) versus volume fraction of filler core particles. As can be seen, the experimental data can be described reasonably well by the Pal–Felske model using the following values of the parameters: $\phi_m = 0.64$, $\delta = 1.1$, $P_{AI} = 3.333$ Barrers, and $P_{BI} = 0.035$ Barrers. As $\delta > 1.0$ and $P_{AI} < P_{Am}$ and $P_{BI} < P_{Bm}$, the filler particles are surrounded by a thin interfacial layer of rigidified matrix material.

Vu et al. [15] investigated mixed matrix membranes of Matrimid 5218/Carbon molecular sieves (CMS) type for O_2/N_2 separation. Their experimental data for relative selectivity $\alpha_{AB,r}$ and relative permeability $P_{A,r}$ (here A refers to O_2) are plotted in Figure 22.7. The model predictions are also shown. There is a good agreement

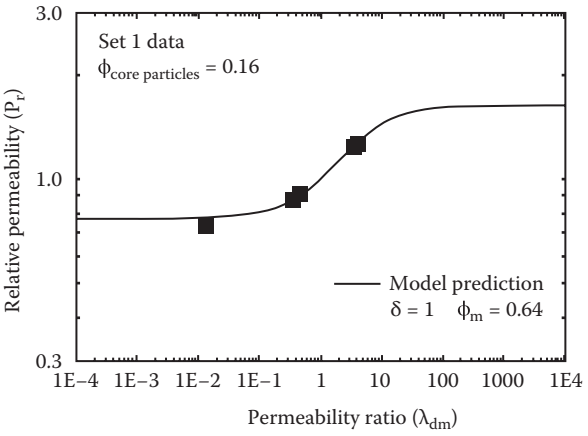

FIGURE 22.5 Comparison between experimental relative permeability data (Set 1) and prediction of the Pal–Felske model. (From Pal, R., *J. Colloid Interf. Sci.* 317: 191–198, 2008.)

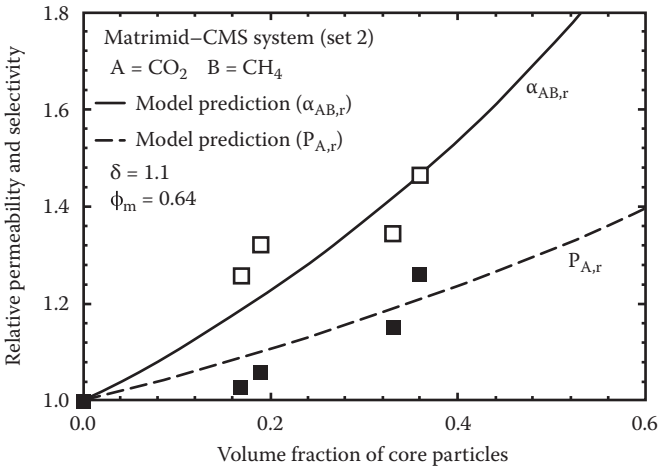

FIGURE 22.6 Comparison between model predictions and experimental data (relative permeability and relative selectivity data) of Set 2. Note that $P_{Am} = 10$, $P_{Ad} = 44$, $P_{AI} = 3.333$, $P_{Bm} = 0.28$, $P_{Bd} = 0.22$, and $P_{BI} = 0.035$. The permeabilities are in Barrers. (From Pal, R., *J. Colloid Interf. Sci.* 317: 191–198, 2008.)

between model predictions and experimental data (Set 3 [15]). The values of the relevant parameters are as follows: $\phi_m = 0.64$, $\delta = 1.1$, $P_{AI} = 0.73$ Barrers, and $P_{BI} = 0.09$ Barrers. As $\delta > 1.0$ and $P_{AI} < P_{Am}$ and $P_{BI} < P_{Bm}$, the filler CMS particles are surrounded a thin interfacial layer of rigidified matrix material.

Figure 22.8 compares model predictions and experimental permeability data (Set 4 [16]) for poly(vinyl acetate)/Zeolite 4A system. Mixed matrix membranes

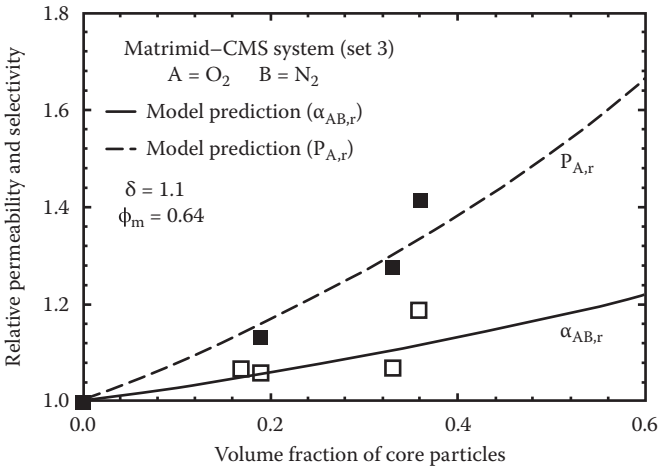

FIGURE 22.7 Comparison between model predictions and experimental data (relative permeability and relative selectivity data) of Set 3. Note that $P_{Am} = 2.12$, $P_{Ad} = 22$, $P_{AI} = 0.73$, $P_{Bm} = 0.32$, $P_{Bd} = 1.65$, and $P_{BI} = 0.09$. The permeabilities are in Barrers. (From Pal, R., *J. Colloid Interf. Sci.* 317: 191–198, 2008.)

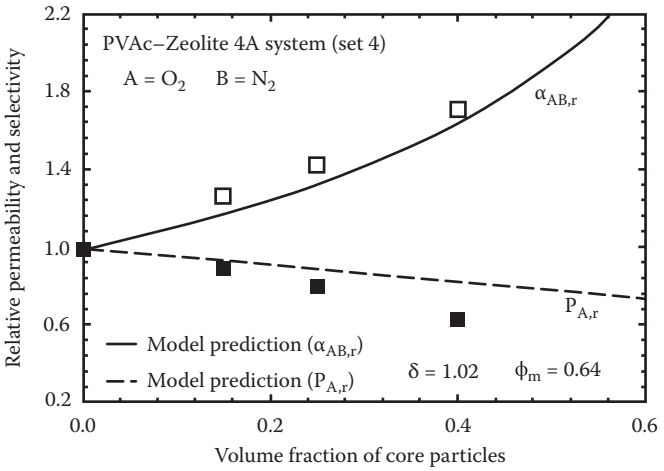

FIGURE 22.8 Comparison between model predictions and experimental data (relative permeability and relative selectivity data) of Set 4. Note that $P_{Am} = 0.5$, $P_{Ad} = 0.77$, $P_{AI} = 0.01$, $P_{Bm} = 0.085$, $P_{Bd} = 0.0208$, and $P_{BI} = 0.00001$. The permeabilities are in Barrers. (From Pal, R., *J. Colloid Interf. Sci.* 317: 191–198, 2008.)

consisting of Zeolite 4A filler particles and poly(vinyl acetate) matrix were studied by Mahajan and Koros [16] for O_2/N_2 separation. The model describes the experimental $\alpha_{AB,r}$ and $P_{A,r}$ (here A refers to O_2) data satisfactorily, with the following values of the relevant quantities: $\phi_m = 0.64$, $\delta = 1.02$, $P_{AI} = 0.01$ Barrers, and $P_{BI} = 0.00001$ Barrers. It appears that the filler particles are covered by a thin interfacial layer of rigidified matrix almost impermeable to species B.

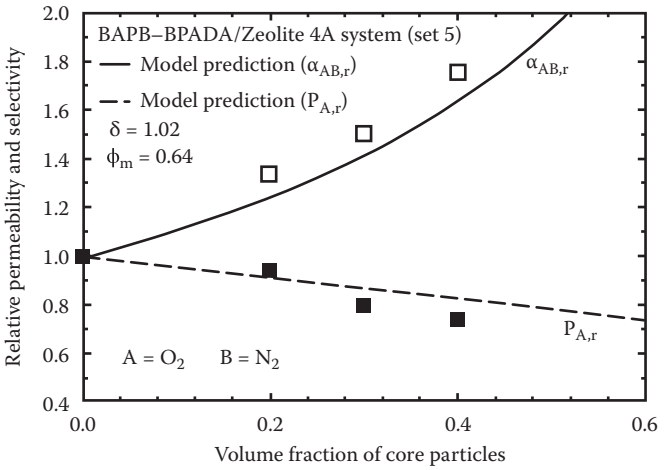

FIGURE 22.9 Comparison between model predictions and experimental data (relative permeability and relative selectivity data) of Set 5. Note that $P_{Am} = 0.5$, $P_{Ad} = 0.77$, $P_{AI} = 0.01$, $P_{Bm} = 0.0704$, $P_{Bd} = 0.0208$, and $P_{BI} = 0.00001$. The permeabilities are in Barrers. (From Pal, R., *J. Colloid Interf. Sci.* 317: 191–198, 2008.)

Mahajan and Koros [18] also investigated mixed matrix membranes of BAPB-BPADA/Zeolite 4A type for O_2/N_2 separation. The matrix material (BAPB-BPADA) was a polymer–polyimide. Figure 22.9 compares model predictions with the experimental data (Set 5 [18]). The model describes the experimental $\alpha_{AB,r}$ and $P_{A,r}$ (here A is O_2) data reasonably well, with the following values of the relevant quantities: $\phi_m = 0.64$, $\delta = 1.02$, $P_{AI} = 0.01$ Barrers, and $P_{BI} = 0.00001$ Barrers. The filler Zeolite 4A particles seem to be covered by a thin interfacial layer of rigidified matrix almost impermeable to species B.

22.2 POROUS MEMBRANES

Thus far, the discussion has focused on particulate-filled polymer composite membranes consisting of filler particles dispersed in a polymer matrix. Now diffusion through porous media and porous membranes is considered. Porous medium is a special case of composite material consisting of voids (pores) and solid phase.

Porous membranes have many interesting applications [27–29] including separation of mixture of gases. One important application of porous membranes is PEM fuel cells. Polymer electrolyte membrane (PEM) fuel cells consist of porous membranes on both sides of the dense polymer electrolyte membrane. The porous membranes are referred to as anode gas diffusion layer (GDL) and cathode GDL. Hydrogen is fed on the anode side and air/oxygen is fed on the cathode side. On the anode side, hydrogen diffuses through the GDL and reaches the anode catalyst layer where the hydrogen molecules are split into hydrogen protons and electrons. The protons then diffuse through the PEM whereas the electrons are diverted to the external circuit due to poor electrical conductivity of PEM. Meanwhile oxygen diffuses from the cathode side towards the cathode catalyst layer where the protons combine with oxygen and electrons to form water.

Both polymer and inorganic porous membranes are widely used in industrial applications. Among the polymers utilized for the preparation of porous membranes, polyvinylidene fluoride (PVDF) is popular. The inorganic porous membranes are made from metals, ceramics, or pyrolyzed carbon [28]. As the porous membranes do not have the mechanical strength to form self-supported membranes, macroporous supports made of alumina, zirconia, stainless steel, etc., are often used to provide the desired strength.

22.2.1 Diffusion in Porous Membranes and Porous Media

As compared with diffusion in free stream, diffusion in porous medium is hindered/reduced by at least two factors: (1) increase in diffusion length due to tortuous pores or tortuosity and (2) reduction in diffusion area (cross-sectional area available for diffusion) due to obstruction by solid phase.

The molar flux in porous medium is expressed by Fick's law of diffusion:

$$J_A = -D\frac{dC_A}{dx} \tag{22.30}$$

where D is the effective diffusion coefficient of species A in porous medium. The ratio of effective diffusion coefficient in porous medium to diffusion coefficient in free stream can be expressed as

$$\frac{D}{D_o} = \frac{\varepsilon}{\tau} \tag{22.31}$$

where D_o is the diffusion coefficient of the same species in the absence of solid phase (that is, free stream value), ε is the porosity and τ is the tortuosity of the porous medium.

Note that in Equation 22.31, ε is the effective porosity. The effective porosity is usually less than the actual porosity as some pores are not accessible to solute due to their small size (pore size), some are dead end pores, and some are isolated pores or blind pores. It is assumed that the diffusion is "molecular diffusion" type meaning that diffusion occurs primarily through molecule–molecule collisions. This requires the mean free path of molecules to be significantly smaller than the pore size, that is, Knudsen diffusion is negligible and the Knudsen number (defined as the ratio of mean free path to pore diameter) is less than one. In molecular diffusion, the diffusivity is independent of the pore diameter and pore size distribution. When the mean free path of the molecules is larger than the pore size, that is, the Knudsen number is greater than one, collision of the molecules with the pore wall are more important than molecule–molecule collisions. This type of diffusion is called "Knudsen diffusion." Now the diffusivity depends on the pore size and pore size distribution. It is further assumed that there occurs negligible "surface diffusion." In surface diffusion, the diffusing solute exhibits a strong affinity for the solid surface and diffuses along the pore walls.

Treating porous medium to be a dispersion of solid particles in free space, and assuming that the diffusion of mass is analogous to the conduction of electric current, the expressions derived for the electrical conductivity of composites could be adapted to the mass diffusivity. For example, the Maxwell model for mass diffusivity is as follows:

$$D_r = \frac{D}{D_o} = \left[\frac{2(1-\phi) + (1+2\phi)\lambda_{Diff}}{(2+\phi) + (1-\phi)\lambda_{Diff}} \right] \tag{22.32}$$

where D_r is the relative diffusivity of species, D is the effective diffusivity of species in membrane, D_o is the free diffusivity of species in the absence of solid phase, ϕ is the volume fraction of the filler particles, and λ_{Diff} is the diffusivity ratio D_d/D_o (D_d is the diffusivity of species in particles). Likewise, one can write the Bruggeman equivalent of mass diffusivity as

$$\frac{D_d - D}{D_d - D_o}\left(\frac{D_o}{D}\right)^{1/3} = (1-\phi) \tag{22.33}$$

Assuming solid phase to be impermeable, that is, $D_d = 0$ and substituting $\phi = 1 - \varepsilon$, one can get the following expressions:

$$D_r = \frac{D}{D_o} = \left[\frac{2\varepsilon}{(3-\varepsilon)}\right] \tag{22.34}$$

$$\frac{D}{D_o} = (\varepsilon)^{3/2} \tag{22.35}$$

where ε is the porosity. In the limit $\varepsilon \to 1$, both expressions give the same values.

REFERENCES

1. Cong, H., M. Radosz, B.F. Towler, and Y. Shen. 2007. Polymer–inorganic nanocomposite membranes for gas separation. *Sep. Purif. Technol*. 55: 281–291.
2. Chen, X. and T.D. Papathanasiou. 2007. Barrier properties of flake-filled membranes: Review and numerical evaluation. *J. Plast. Film Sheet*. 23: 319–346.
3. Sapalidis, A.A., F.K. Katsaros, G.E. Romanos, N.K. Kakizis, and N.K. Kanellopoulos. 2007. Preparation and characterization of novel poly-(vinyl alcohol)-Zostera flakes composites for packaging applications. *Compos. Part B.* 38: 398–404.
4. Yang, C., W.H. Smyrl, and E.L. Cussler. 2004. Aligning flakes in barrier coating. *J. Membrane Sci*. 231: 1–12.
5. Huang, H., T. Huang, T. Yeh, C. Tsai, C. Lai, M. Tsai, J. Yeh, and Y. Chou. 2011. Advanced anticorrosive materials prepared from amine-capped aniline trimer-based electroactive polyimide–clay nanocomposite materials with synergistic effects of redox catalytic capability and gas barrier properties. *Polymer.* 52: 2391–2400.
6. Chang, C., T. Huang, C. Peng, T. Yeh, H. Lu, W. Hung, C. Weng, T. Yang, and J. Yeh. 2012. Novel anticorrosion coatings prepared from polyaniline/graphene composites. *Carbon*. 50: 5044–5051.
7. Vinh-Thang, H. and S. Kaliaguine. 2013. Predictive models for mixed-matrix membrane performance: A review. *Chem. Rev*. 113: 4980–5028.
8. Chung,T.S., L.Y. Jiang, and S. Kulprathipanja. 2007. Mixed matrix membranes comprising organic polymers with dispersed inorganic fillers for gas separation. *Prog. Polym. Sci.* 32: 483–507.
9. Mahajan, R., W.J. Koros, and M. Thundyil. 1999. Mixed matrix membranes: Important and challenging! *Membrane Tech*. 105: 6–8.
10. Moore, T.T., R. Mahajan, D.Q. Vu, and W.J. Koros. 2004. Hybrid membrane materials comprising organic polymers with rigid dispersed phases. *Aiche J*. 50: 311–321.
11. Bouma, R.H.B., A. Checchetti, G. Chidichimo, and E. Drioli. 1997. Permeation through a heterogeneous membrane: The effect of the dispersed phase. *J. Membrane Sci*. 128: 141–149.
12. Zimmerman, C.M., A. Singh, and W.J. Koros. 1997. Tailoring mixed matrix composite membranes for gas separations. *J. Membrane Sci.* 137: 145–154.
13. Gonzo, E.E., M.L. Parentis, and J.C. Gottifredi. 2006. Estimating models for predicting effective permeability of mixed matrix membranes. *J. Membrane Sci.* 277: 46–54.
14. Pechar, T.W., M. Tsapatsis, E. Marand, and R. Davis. 2002. Preparation and characterization of a glassy fluorinated polyimide zeolite-mixed matrix membrane. *Desalination* 146: 3–9.

15. Vu, D.Q., W.J. Koros, and S.J. Miller. 2003. Mixed matrix membranes using carbon molecular sieves: II. Modeling permeation behavior. *J. Membrane Sci.* 211: 335–348.
16. Mahajan, R. and W.J. Koros. 2000. Factors controlling successful formation of mixed-matrix gas separation materials. *Ind. Eng. Chem. Res.* 39: 2692–2696.
17. Mahajan, R. and W.J. Koros. 2002. Mixed matrix membrane materials with glassy polymers. Part 1. *Polym. Eng. Sci.* 42: 1420–1431.
18. Mahajan, R. and W.J. Koros. 2002. Mixed matrix membrane materials with glassy polymers. Part 2. *Polym. Eng. Sci.* 42: 1432–1441.
19. Pal, R. 2008. Permeation models for mixed matrix membranes. *J. Colloid Interf. Sci.* 317: 191–198.
20. Alberti, G. and M. Casciola. 2003. Composite membranes for medium-temperature PEM fuel cells. *Annu. Rev. Mater. Res.* 33: 129–154.
21. Maxwell, J.C. 1954. *A treatise on electricity and magnetism*, Chapter IX, New York: Dover Publications.
22. Bruggeman, D.A.G. 1935. Berechnung verschiedener physikalischer Konstanten von heterogenen Substanzen. *Ann. Phys.-Leipzig* 24: 636–679.
23. Lewis, T. and L. Nielsen. 1970. Dynamic mechanical properties of particulate filled composites. *J. Appl. Polym. Sci.* 14: 1449–1471.
24. Nielsen, L. 1973. Thermal conductivity of particulate filled polymers. *J. Appl. Polym. Sci.* 17: 3819–3820.
25. Pal, R. 2007. New models for thermal conductivity of particulate composites. *J. Reinf. Plast. Comp.* 26: 643–651.
26. Felske, J.D. 2004. Effective thermal conductivity of composite spheres in a continuous medium with contact resistance. *Int. J. Heat Mass Tran.* 47: 3453–3461.
27. LaManna, J.M. and S.G. Kandlikar. 2011. Determination of effective water vapor diffusion coefficient in pemfc gas diffusion layers. *Int. J. Hydrogen Energ.* 36: 5021–5029.
28. Javaid, A. 2005. Membranes for solubility-based gas separation applications. *Chem. Eng. J*. 112: 219–226.
29. Bottino, A., G. Capannelli, A. Comite, and M. Oliveri. 2004. Development of novel membranes with controlled porosity from fluorinated polymer. *Filtration* 4: 130–135.

23 Fundamentals of Convective Mass Transfer

The transport of some material species (say A) from a high-concentration (C_A high) to a low-concentration (C_A low) region of a fluid in the presence of bulk/macroscopic motion of the fluid is referred to as "convective mass transfer." The transport of material species between a boundary surface (solid or liquid) and a fluid moving adjacent to the boundary surface when there exists a gradient in concentration of species between the fluid and the boundary surface is also an example of "convective mass transfer."

In a convective mass transfer process, mass of some species is transported from one region of fluid to another by two mechanisms acting simultaneously. The mechanisms are "molecular diffusion" and "advection" (advection being caused by bulk macroscopic motion of fluid).

In many industrial processes, convective mass transport takes place in or around composite materials. Therefore, a good understanding of convective mass transfer is important in these applications. In this chapter, the basics of convective mass transfer are covered. Convective mass transfer in composite materials is covered in the next chapter.

23.1 GOVERNING EQUATIONS

Consider an isothermal nonreacting binary mixture of species A and B. Let the mixture viscosity (η), mixture total mass concentration (ρ), mixture total molar concentration (C), and diffusion coefficient D_{AB} be constant. With these restrictions, the governing equations of convective mass transfer can be written as

$$\nabla \cdot \vec{V} = 0 \tag{23.1}$$

$$\frac{\partial C_A}{\partial t} + \nabla \cdot \vec{N}_A = 0 \tag{23.2}$$

with

$$\vec{N}_A = -D_{AB}\nabla C_A + C_A \vec{V}^* \tag{23.3}$$

$$\rho\left[\frac{\partial \vec{V}}{\partial t} + \vec{V} \cdot \nabla \vec{V}\right] = -\nabla p + \rho \vec{g} + \eta \nabla^2 \vec{V} \tag{23.4}$$

where $\vec{V}$ is mass average velocity of mixture, C_A is molar concentration of species A, $\vec{N}_A$ is the absolute molar flux of species A, $\vec{V}^*$ is the molar average velocity of mixture, p is pressure, and $\vec{g}$ is acceleration due to gravity. Equation 23.1 is the continuity equation for the mixture, Equation 23.2 is the continuity equation for species A, and Equation 23.4 is the equation of motion (Navier–Stokes equation) for the mixture.

Combining Equations 23.2 and 23.3 gives

$$\frac{\partial C_A}{\partial t} = D_{AB}\nabla^2 C_A - C_A(\nabla \cdot \vec{V}^*) - \vec{V}^* \cdot \nabla C_A \tag{23.5}$$

For systems dilute in A: $\eta \approx \eta_B$, $\rho \approx \rho_B$, $C \approx C_B$, $\vec{V} \approx \vec{V}_B$ and $\vec{V}^* \approx \vec{V}_B$, where fluid B is the solvent, species A is the solute present at dilute level, and η_B, ρ_B, and $\vec{V}_B$ are viscosity, density, and velocity of solvent (fluid B), respectively. Thus, the governing equations for dilute systems become

$$\nabla \cdot \vec{V}_B = 0 \tag{23.6}$$

$$\frac{\partial C_A}{\partial t} + \vec{V}_B \cdot \nabla C_A = D_{AB}\nabla^2 C_A \tag{23.7}$$

$$\rho_B\left[\frac{\partial \vec{V}_B}{\partial t} + \vec{V}_B \cdot \nabla \vec{V}_B\right] = -\nabla p + \rho_B \vec{g} + \eta_B \nabla^2 \vec{V}_B \tag{23.8}$$

These three equations need to be solved simultaneously in order to determine the velocity, pressure, and concentration distribution in the fluid.

23.2 EXTERNAL FLOWS

External flow refers to flow of unbounded fluid over a solid surface. For steady-state two-dimensional flow of a Newtonian fluid (with constant properties) over a solid surface, the boundary layer mass and momentum equations are

$$\frac{\partial V_x}{\partial x} + \frac{\partial V_y}{\partial y} = 0 \tag{23.9}$$

$$V_x \frac{\partial V_x}{\partial x} + V_y \frac{\partial V_x}{\partial y} = V_\infty \frac{dV_\infty}{dx} + \nu \frac{\partial^2 V_x}{\partial y^2} \tag{23.10}$$

where V_x and V_y are x and y components of fluid velocity, respectively, V_∞ is the free stream velocity of the fluid, and ν is the kinematic viscosity ($= \eta/\rho$). Equation 23.9 follows from Equation 23.1 and Equation 23.10 follows from Equation 23.4.

The concentration boundary layer equation is as follows:

$$V_x \frac{\partial C_A}{\partial x} + V_y \frac{\partial C_B}{\partial y} = D_{AB} \frac{\partial^2 C_A}{\partial y^2} \tag{23.11}$$

Equation 23.11 follows from the continuity equation for species A (Equation 23.5) using the boundary layer approximation that $\frac{\partial^2 C_A}{\partial y^2} \gg \frac{\partial^2 C_A}{\partial x^2}$. Equations 23.9 through 23.11 need to be solved, subject to the given boundary conditions, for the three unknowns V_x, V_y, and C_A.

23.2.1 Integral Analysis of Boundary Layer

In practical problems dealing with convective mass transfer between a solid surface and moving fluid, the quantity of most interest is the mass or molar flux at the solid/fluid interface. The following von Karman mass integral expression (given here without proof) could be used to determine the molar flux at the solid/fluid interface:

$$N_{A,w} = -D_{AB}\left(\frac{\partial C_A}{\partial y}\right)_{y=0} = \frac{d}{dx}\int_0^{\delta_c} (C_A - C_{A,\infty}) V_x \, dy \tag{23.12}$$

where $N_{A,W}$ is the absolute molar flux of species A at the solid surface, $C_{A,\infty}$ is the free-stream concentration of A, and δ_c is the thickness of the concentration boundary layer. The integral expression (Equation 23.12) is valid for dilute systems with low mass transfer rate and small concentration of diffusing species A. It can be used to determine the molar flux at the solid/fluid interface provided that both the velocity and concentration profiles are known.

23.2.2 Mass Transfer Coefficient

For external flows, the diffusional molar flux at the solid/fluid interface (normal to the interface) can be expressed in terms of the mass transfer coefficient as

$$J_{A,y}\Big|_{y=0} = k_c (C_{A,s} - C_{A,\infty}) \tag{23.13a}$$

where k_c is the mass transfer coefficient, $C_{A,s}$ is the molar concentration of species A in the fluid at the fluid/solid interface (y = 0), and $C_{A,\infty}$ is the free-stream molar concentration of species A in the fluid. Assuming low mass transfer rate and small concentration of diffusing species A, the diffusional flux J_A (flux with respect to axes moving at molar average velocity) can be equated to the absolute flux N_A (flux with respect to fixed coordinates). Therefore, one can write:

$$N_{A,y}\Big|_{y=0} = N_{A,w} = k_c (C_{A,s} - C_{A,\infty}) \tag{23.13b}$$

At the fluid/solid interface, the molar flux normal to the interface is also given by Fick's law of diffusion:

$$N_{A,y}\Big|_{y=0} = J_{A,y}\Big|_{y=0} = -D_{AB}\left(\frac{\partial C_A}{\partial y}\right)_{y=0} \tag{23.14}$$

From Equations 23.13 and 23.14, it follows that

$$k_c = \frac{-D_{AB}\left(\frac{\partial C_A}{\partial y}\right)_{y=0}}{C_{A,s} - C_{A,\infty}} \tag{23.15}$$

23.2.2.1 Laminar Flow over Flat Plate

Consider laminar flow over a solid flat plate. The concentration of species A in the fluid at the fluid/solid interface ($y = 0$) is $C_{A,s}$. The free-stream concentration of A ($y > \delta_c$) is $C_{A,\infty}$. The velocity profile for laminar flow over a flat plate is given as

$$\frac{V_x}{V_\infty} = \frac{3}{2}\left(\frac{y}{\delta}\right) - \frac{1}{2}\left(\frac{y}{\delta}\right)^3 \tag{23.16}$$

where δ is the hydrodynamic boundary layer thickness. From momentum integral analysis, it is found that

$$\frac{\delta}{x} = \frac{4.64}{Re_x^{1/2}} \tag{23.17}$$

where x is the distance from the leading edge of the plate and Re_x is the local Reynolds number defined as $\rho V_\infty x/\eta$. The concentration profile can be assumed to be a four term polynomial as

$$C_A - C_{A,s} = a + by + cy^2 + dy^3 \tag{23.18}$$

The constants in Equation 23.18 can be obtained from the boundary conditions:

$$y = 0, \quad C_A - C_{A,s} = 0 \tag{23.19}$$

$$y = \delta_c, \quad C_A - C_{A,s} = C_{A,\infty} - C_{A,s} \tag{23.20}$$

$$y = \delta_c, \quad \frac{\partial}{\partial y}(C_A - C_{A,s}) = 0 \tag{23.21}$$

$$y = 0, \quad \frac{\partial^2}{\partial y^2}(C_A - C_{A,s}) = 0 \tag{23.22}$$

The last boundary condition follows from the concentration boundary layer equation (Equation 23.11) as $V_x(\partial C_A/\partial x) = 0$ and $V_y(\partial C_A/\partial y) = 0$ at $y = 0$. Note that $C_{A,s}$ is assumed to be constant. Using the boundary conditions (Equations 23.19 through 23.22), it can be easily shown that

$$\frac{C_A - C_{A,s}}{C_{A,\infty} - C_{A,s}} = \frac{3}{2}\left(\frac{y}{\delta_c}\right) - \frac{1}{2}\left(\frac{y}{\delta_c}\right)^3 \tag{23.23}$$

To utilize the mass integral expression (Equation 23.12) knowledge of both velocity and concentration distribution is required. Assuming that $\delta_c < \delta$, the velocity distribution in concentration boundary layer is given by Equation 23.16. Substitution of concentration distribution (Equation 23.23) and velocity distribution (Equation 23.16) into the integral expression (Equation 23.12) and carrying out the integration yields the following result:

$$\frac{\delta_c}{\delta} = \frac{0.976}{Sc^{1/3}} \tag{23.24}$$

Using Equations 23.15, 23.17, 23.23, and 23.24, it can be shown that

$$Sh_x = \frac{k_c x}{D_{AB}} = 0.331(Re_x)^{1/2} Sc^{1/3} \tag{23.25}$$

where Sc is the Schmidt number, defined as ν/D_{AB}, Sh_x is the local Sherwood number, and Re_x is the local Reynolds number.

These results (Equations 23.24 and 23.25) are valid for $Sc > 0.60$ and they are very close to exact solution of the boundary layer equations (Equations 23.9 through 23.11). The exact solution gives

$$\frac{\delta_c}{\delta} = \frac{1}{Sc^{1/3}} \tag{23.26}$$

$$Sh_x = \frac{k_c x}{D_{AB}} = 0.332\, Sc^{1/3}(Re_x)^{1/2} \tag{23.27}$$

Using Equation 23.27 and the following friction factor equation for laminar flow over a flat plate

$$\frac{f}{2} = \frac{0.332}{Re_x^{1/2}} \tag{23.28}$$

it can easily be shown that

$$St_m\, Sc^{2/3} = \frac{f}{2} \tag{23.29}$$

where St_m is the mass transport Stanton number, defined as

$$St_m = \frac{Sh}{Sc\, Re} \tag{23.30}$$

Equation 23.29 is referred to as the Chilton–Colburn analogy between mass transfer and momentum transfer. It is valid for Sc > 0.6.

23.2.2.2 Turbulent Flow over Flat Plate

The local friction factor in turbulent flow over a flat plate is given by the following empirical equation:

$$f = \frac{0.0592}{Re_x^{1/5}} \tag{23.31}$$

The mass transfer coefficient in turbulent flow over a flat plate can be determined from the Chilton–Colburn analogy (Equation 23.29) using the above friction factor relation. Thus,

$$Sh_x = \frac{k_c x}{D_{AB}} = 0.0296\left(Re_x\right)^{4/5} Sc^{1/3} \tag{23.32}$$

23.2.3 Other External Flows

In the preceding section, forced convective mass transfer from a flat plate was covered. Another commonly encountered geometry in convective mass transfer applications is a solid cylinder. Consider mass transfer from a solid cylinder into fluid which is flowing normal to the axis of the cylinder. This type of mass transfer problem could be encountered in sublimation of solid into the moving fluid. Other applications may involve mass transfer of some species present at the surface of cylinder in the form of a coating.

Bedingfield and Drew [1] developed the following correlation for mass transfer from solid cylinder into gas flowing normal to the axis of the cylinder:

$$Sh = \frac{k_c D}{D_{AB}} = 0.281\left(Re_D\right)^{1/2} Sc^{0.44} \tag{23.33}$$

where D is diameter of the cylinder, and Re_D is the Reynolds number based on cylinder diameter (= $\rho DV_\infty/\eta$). This correlation is valid for $400 < Re_D < 25{,}000$ and $0.6 < Sc < 2.6$. For liquids the following correlation of Linton and Sherwood [2] could be used

$$Sh = \frac{k_c D}{D_{AB}} = 0.281\left(Re_D\right)^{0.6} Sc^{1/3} \tag{23.34}$$

This correlation is valid for $400 < Re_D < 25{,}000$ and $Sc < 3000$.

23.3 INTERNAL FLOWS

Consider a cylindrical tube (radius R) whose surface is coated with some material (species A) that can dissolve and diffuse into the fluid moving inside the tube. The molar flux of species A at the fluid/solid interface (r = R) can be expressed in terms of the mass transfer coefficient as

$$N_{A,w} = k_c(C_{A,s} - C_{A,m}) \tag{23.35}$$

where $C_{A,s}$ is the molar concentration of species A in the fluid at the fluid/wall interface (r = R), and $C_{A,m}$ is the mean concentration of species A in the fluid over a given cross section:

$$C_{A,m} = \frac{2}{\bar{V}R^2}\int_0^R rC_A V_z\, dr \tag{23.36}$$

where $\bar{V}$ is the average velocity and V_z is the local velocity. At the pipe wall, the molar flux normal to the solid surface can also be expressed as

$$N_{A,w} = J_{A,y}\Big|_{y=0} = -D_{AB}\left(\frac{\partial C_A}{\partial y}\right)_{y=0} = D_{AB}\left(\frac{\partial C_A}{\partial r}\right)_{r=R} \tag{23.37}$$

Note that we are neglecting bulk contribution to $N_{A,y}$ at the solid surface, that is, $C_A V_y^* \ll J_{A,y}$ at the interface (V_y^* is the y-component of molar average velocity). From Equations 23.35 and 23.37, it follows that

$$k_c = \frac{D_{AB}\left(\frac{\partial C_A}{\partial r}\right)_{r=R}}{C_{A,s} - C_{A,m}} \tag{23.38}$$

Thus, the mass transfer coefficient in internal flow can be obtained if both concentration and velocity distributions are known.

From material balance over a differential section of the tube, it can be readily shown that

$$\bar{N}_A = \bar{k}_c (\Delta C_A)_{lm} \tag{23.39}$$

where $\bar{N}_A$ is the average molar flux of A over the entire length of the tube, $\bar{k}_c$ is the average mass transfer coefficient, and $(\Delta C_A)_{lm}$ is the log-mean concentration difference of A defined as

$$(\Delta C_A)_{lm} = \frac{\Delta C_{A,2} - \Delta C_{A,1}}{\ln\left(\frac{\Delta C_{A,2}}{\Delta C_{A,1}}\right)} \tag{23.40}$$

In Equation 23.40, $\Delta C_{A,1} = C_{A,s} - C_{A,1}$, $\Delta C_{A,2} = C_{A,s} - C_{A,2}$, and $C_{A,1}$ and $C_{A,2}$ are average inlet and outlet concentrations of species A. The average mass transfer coefficient $\bar{k}_c$ in Equation 23.39 is given as

$$\bar{k}_c = \frac{1}{L}\int_0^L k_c \, dz \tag{23.41}$$

where k_c is the local mass transfer coefficient and L is the length of the tube.

23.3.1 Laminar Flow

For hydrodynamically fully developed laminar flow in a pipe, the velocity distribution is given as

$$\frac{V_z}{V_{max}} = 1 - \left(\frac{r}{R}\right)^2 \tag{23.42}$$

where V_z is the local velocity in axial direction, and V_{max} is the maximum velocity at the centerline (r = 0). The equation of continuity for species A under steady-state laminar flow conditions (see Equation 23.5) can be expressed as

$$V_z \frac{\partial C_A}{\partial z} = D_{AB}\left(\frac{\partial^2 C_A}{\partial r^2} + \frac{1}{r}\frac{\partial C_A}{\partial r}\right) \tag{23.43}$$

Therefore, for hydrodynamically fully developed laminar flow the concentration distribution is given by the following equation:

$$\frac{\partial C_A}{\partial z} = \frac{D_{AB}}{V_{max}\left[1-\left(\frac{r}{R}\right)^2\right]}\left(\frac{\partial^2 C_A}{\partial r^2}+\frac{1}{r}\frac{\partial C_A}{\partial r}\right) \tag{23.44}$$

This equation needs to be solved subject to the given boundary conditions.

As an example, consider the case where the wall concentration of species A is constant ($C_{A,s}$ = constant) and the flow is hydrodynamically and concentration-wise fully developed. Note that concentration-wise fully developed flow is characterized by the following condition:

$$\frac{\partial}{\partial z}\left(\frac{C_{A,s}-C_A}{C_{A,s}-C_{A,m}}\right)=0 \tag{23.45}$$

Under these restrictions, the solution to Equation 23.44 yields the following result:

$$Sh=\frac{k_c D}{D_{AB}}=3.66 \tag{23.46}$$

where D is the pipe diameter. For hydrodynamically fully developed but concentration-wise developing flows, the solution to Equation 23.44 (assuming constant wall concentration) can be expressed in the following form:

$$Sh_z=\frac{k_c D}{D_{AB}}=f(Gz_m) \tag{23.47}$$

where Gz_m is Graetz number for mass transfer, defined as

$$Gz_m=\frac{\pi}{4}\left(\frac{D}{z}\right)Re\,Sc \tag{23.48}$$

where Re is the Reynolds number for pipe flow = ($\rho\bar{V}D/\eta$). For the calculation of average mass transfer coefficient ($\bar{k}_c$) or average Sherwood number ($\bar{Sh}$), the following Hausen correlation is often used:

$$\bar{Sh}=\frac{\bar{k}_c D}{D_{AB}}=3.66+\frac{0.0668(D/L)(Re\,Sc)}{1+0.04\left[(D/L)(Re\,Sc)\right]^{2/3}} \tag{23.49}$$

The combined entry length problem where the flow is hydrodynamically and concentration-wise developing is much more difficult to solve as velocity and concentration both depend on r as well as z. For the estimation of the average Sherwood

number in the case of combined entry length problem dealing with laminar flow through a pipe (assuming constant wall concentration), the following correlation is recommended:

$$\overline{Sh} = \frac{\overline{k}_c D}{D_{AB}} = 1.86(Re\,Sc)^{1/3}\left(\frac{D}{L}\right)^{1/3} \tag{23.50}$$

23.3.2 Turbulent Flow

The mass transfer coefficient in fully developed turbulent flows can be determined from the Chilton–Colburn analogy (Equation 23.29) provided that the friction factor relationship is known. For smooth pipes, the friction factor in turbulent flow can be calculated from the following empirical relation:

$$f = \frac{0.046}{Re^{1/5}} \tag{23.51}$$

This equation can be applied over the Reynolds number range of 2×10^4 to 10^6. Substitution of Equation 23.51 into Equation 23.29 results in the following equation for Sherwood number:

$$\overline{Sh} = \frac{\overline{k}_c D}{D_{AB}} = 0.023(Re)^{4/5}(Sc)^{1/3} \tag{23.52}$$

This equation is valid for $Sc > 0.5$.

The modified versions of Equation 23.52 have been proposed in the literature. For example, Gilliland and Sherwood [3] proposed the following correlation based on experimental data on vaporization of different liquids (wetting the inner surface of the pipe) into air flowing through the tube:

$$\frac{\overline{k}_c D}{D_{AB}}\left(\frac{p_{B,lm}}{p}\right) = 0.023(Re)^{0.83}(Sc)^{0.44} \tag{23.53}$$

where p is the total pressure of the system and $p_{B,lm}$ is the log-mean partial pressure of the carrier gas, given as

$$p_{B,lm} = \frac{p_{B,2} - p_{B,1}}{\ln\left(\frac{p_{B,2}}{p_{B,1}}\right)} \tag{23.54}$$

where $p_{B,1}$ and $p_{B,2}$ are partial pressures of carrier gas at inlet and outlet, respectively.

Equation 23.53 is valid for gases under the conditions: $2000 < Re < 3.5 < 10^4$ and $0.6 < Sc < 2.5$. For dilute solutions ($y_A \ll 1.0$), $p_{B,lm}/p$ is nearly unity.

Linton and Sherwood [2] proposed another correlation based on experimental data on dissolution of solid solute (coated on the inner surface of the pipe) in liquid solvent flowing through the tube.

$$\overline{Sh} = \frac{\overline{k}_c D}{D_{AB}} = 0.023(Re)^{0.83}(Sc)^{1/3} \tag{23.55}$$

This equation is valid for liquids under the conditions: $2000 < Re < 3.5 \times 10^4$ and $1000 < Sc < 2260$.

23.4 INTERPHASE MASS TRANSFER

In the preceding sections, convective mass transfer was considered either within a single phase or between a solid surface and a fluid moving adjacent to the solid surface. For convective mass transfer between a solid surface and a moving fluid, the concept of individual mass transfer coefficient (k_c) was introduced. In many mass transfer problems of practical interest, the transfer of some material species (say A) takes place between two immiscible fluid phases (gas/liquid, liquid/liquid) in intimate contact with one another. Also the two phases are in motion and consequently, the transfer of species A from one phase to the interface and from interface to the second phase occurs by convection. Examples of interphase mass transfer processes include "absorption" and "stripping (desorption)." In the absorption process, a solute gas (for example, ammonia) is absorbed from an inert gas (for example, air) into a liquid (for example, water) in which the solute is soluble. In the desorption or stripping process, the solute is transferred from the solvent liquid phase to the gas phase. In the analysis of interphase mass transfer problems, the overall mass transfer coefficient and its relation to individual mass transfer coefficients are important concepts. Also in most situations, it is assumed that the interface itself does not offer any resistance to the transfer of the diffusing species across the interface. Thus, the rate of mass transfer between the phases is controlled by the individual mass transfer resistances in the two phases. Across the interface between the two phases, equilibrium is assumed to exist so that the adjacent concentrations of diffusing species across the interface are related by a thermodynamic equilibrium relation.

Figure 23.1 shows the concentration profile of solute A diffusing from gas phase to liquid phase. In the gas phase, the partial pressure of solute A is plotted as a concentration variable. In the liquid phase, the molar concentration of A is plotted. The bulk phase concentrations are $p_{A,G}$ (partial pressure of A in bulk gas phase) and $C_{A,L}$ (molar concentration of A in bulk liquid phase). At the interface, the partial pressure of A on the gas side is $p_{A,i}$ and the molar concentration of A on the liquid side is $C_{A,i}$. N_A is the molar flux of A from the gas phase to the liquid phase (see Figure 23.1). As equilibrium exists at the interface, the concentrations of species A across the interface are related by an equilibrium relation such as

$$p_{A,i} = f(C_{A,i}) \tag{23.56}$$

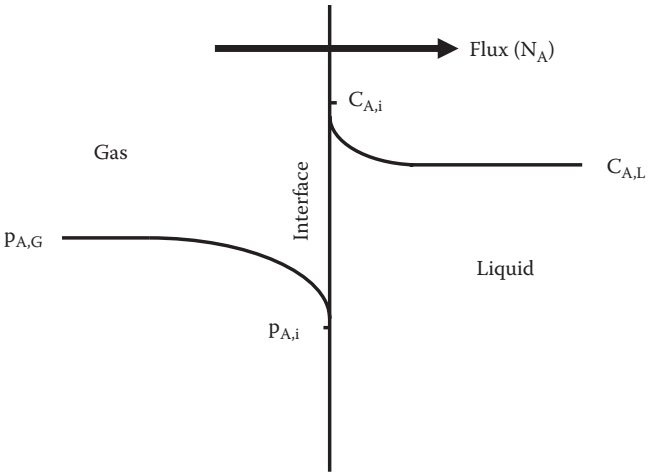

FIGURE 23.1 Concentration profile of solute A diffusing from gas phase to liquid phase.

23.4.1 Individual Mass Transfer Coefficients and Interface Concentrations

Under steady state condition, the mass flux in one phase must be equal to the mass flux in the second phase. Thus,

$$N_A = k_G(p_{A,G} - p_{A,i}) = k_L(C_{A,i} - C_{A,L}) \tag{23.57}$$

where k_G is the gas-phase mass transfer coefficient (S.I. units of k_G are moles/(m^2.s.Pa)), and k_L is the liquid-phase mass transfer coefficient (S.I. units of k_L are m/s). Note that Equation 23.57 assumes that the mass transfer rate and solute concentration are small and that the absolute and diffusional fluxes are the same.

Equation 23.57 can be rearranged as

$$-\frac{k_L}{k_G} = \frac{p_{A,G} - p_{A,i}}{C_{A,L} - C_{A,i}} \tag{23.58}$$

This expression allows the evaluation of the unknown interface concentrations ($p_{A,i}$ and $C_{A,i}$) from the knowledge of bulk concentrations ($p_{A,G}$ and $C_{A,L}$) and the individual mass transfer coefficients, provided that the equilibrium relationship (Equation 23.56) is known.

The procedure for determining $p_{A,i}$ and $C_{A,i}$ is shown graphically in Figure 23.2. From the knowledge of the bulk compositions ($p_{A,G}$ and $C_{A,L}$), point "O" is marked on the diagram. A straight line of slope $-k_G/k_L$ passing through the point "O" intersects the equilibrium curve at a point where $p_A = p_{A,i}$ and $C_A = C_{A,i}$.

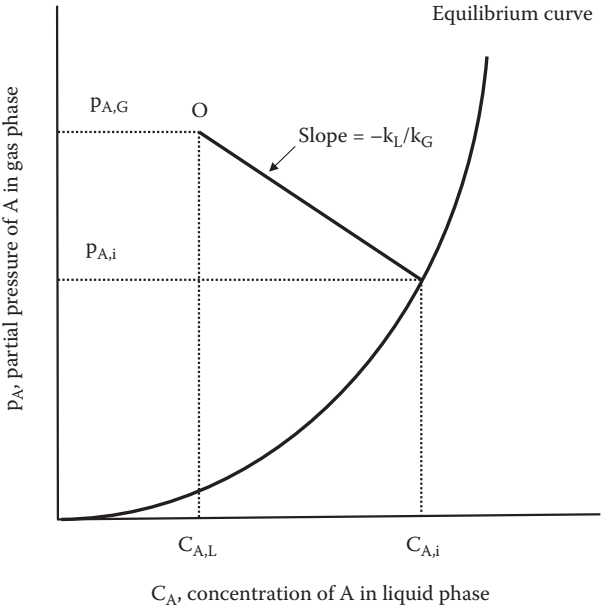

FIGURE 23.2 Graphical procedure for determining the interfacial quantities $p_{A,i}$ and $C_{A,i}$.

23.4.2 Concept of Overall Mass Transfer Coefficient

The concept of overall mass transfer coefficient is very useful in that it allows the evaluation of the mass flux without the knowledge of the interfacial concentrations ($p_{A,i}$ and $C_{A,i}$).

The overall mass transfer coefficient based on the gas phase (K_G) is defined as

$$N_A = K_G(p_{A,G} - p_A^*) \tag{23.59}$$

where p_A^* is the partial pressure of A in the gas phase if the gas phase was in equilibrium with the bulk liquid phase (having concentration of A as $C_{A,L}$). Note that p_A^* is a fictitious quantity whose value is determined from the equilibrium relation (Equation 23.56) at $C_A = C_{A,L}$. Thus, p_A^* is a measure of the bulk liquid concentration $C_{A,L}$.

Similarly, the overall mass transfer coefficient based on liquid phase (K_L) is defined as

$$N_A = K_L(C_A^* - C_{A,L}) \tag{23.60}$$

where C_A^* is the concentration of A in the liquid phase if the liquid phase was in equilibrium with the bulk gas phase (having partial pressure of A as $p_{A,G}$). Once again C_A^* (like p_A^*) is a fictitious quantity whose value is determined from the equilibrium

relation (Equation 23.56) at $p_A = p_{A,G}$. Thus, C_A^* is a measure of the partial pressure of A in the bulk gas phase. The quantities p_A^* and C_A^* are shown schematically in Figure 23.3.

The overall mass transfer coefficient can be related to individual phase coefficients if the equilibrium relationship (Equation 23.56) is known. Assuming a linear equilibrium relationship

$$p_A = mC_A \tag{23.61}$$

where "m" is the equilibrium constant. This linear equilibrium relationship is generally valid at low concentrations and is referred to as "Henry's law." As equilibrium exists at the interface, Equation 23.61 can be expressed in terms of the interface concentrations:

$$p_{A,i} = mC_{A,i} \tag{23.62}$$

From Equation 23.59, it follows that

$$\frac{1}{K_G} = \frac{p_{A,G} - p_A^*}{N_A} = \frac{p_{A,G} - p_{A,i}}{N_A} + \frac{p_{A,i} - p_A^*}{N_A} \tag{23.63}$$

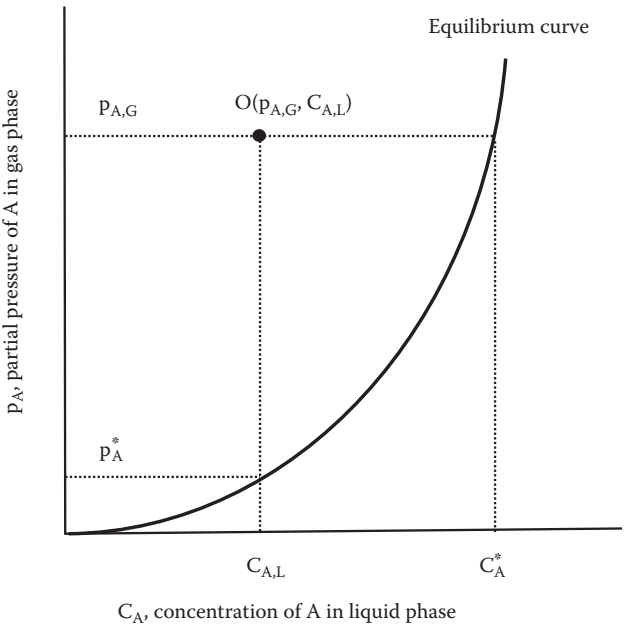

FIGURE 23.3 Graphical description of quantities p_A^* and C_A^*.

Using the relations $p_A^* = mC_{A,L}$ and $p_{A,i} = mC_{A,i}$, Equation 23.63 can be rewritten as

$$\frac{1}{K_G} = \frac{p_{A,G} - p_{A,i}}{N_A} + \frac{m(C_{A,i} - C_{A,L})}{N_A} \tag{23.64}$$

From Equations 23.57 and 23.64, it can be readily shown that

$$\frac{1}{K_G} = \frac{1}{k_G} + \frac{m}{k_L} \tag{23.65}$$

This equation expresses the relationship between overall mass transfer coefficient (K_G) and individual phase coefficients (k_G and k_L). A similar relation for K_L can be obtained as follows:

$$\frac{1}{K_L} = \frac{C_A^* - C_{A,L}}{N_A} = \frac{C_A^* - C_{A,i}}{N_A} + \frac{C_{A,i} - C_{A,L}}{N_A} \tag{23.66}$$

This equation follows from Equation 23.60. As $p_{A,G} = mC_A^*$ and $p_{A,i} = mC_{A,i}$, it follows that

$$\frac{1}{K_L} = \frac{p_{A,G} - p_{A,i}}{mN_A} + \frac{C_{A,i} - C_{A,L}}{N_A} \tag{23.67}$$

From Equations 23.57 and 23.67

$$\frac{1}{K_L} = \frac{1}{k_L} + \frac{1}{mk_G} \tag{23.68}$$

Equation 23.68 is the relationship between overall mass transfer coefficient K_L and individual mass transfer coefficients (k_G and k_L).

For systems with large values of m (solute with low solubility in liquid), Equation 23.68 gives

$$\frac{1}{K_L} \approx \frac{1}{k_L} \tag{23.69}$$

that is, the main resistance to mass transfer lies in the liquid phase. This type of system is "liquid-phase controlled" from mass transfer point of view.

For systems with small values of m (solute with high solubility in liquid), Equation 23.65 gives

$$\frac{1}{K_G} \approx \frac{1}{k_G} \tag{23.70}$$

In this case, the main resistance to mass transfer of solute lies in the gas phase. This type of system is "gas-phase controlled."

23.4.3 Mass Transfer Coefficients Using Mole Fraction Difference as the Driving Force

In the discussion so far on mass transfer coefficients, either molar concentration difference ΔC_A or partial pressure difference Δp_A was considered as the driving force for mass transfer, and the mass transfer coefficients were defined as

$$N_A = k_L(\Delta C_A) \tag{23.71}$$

$$N_A = k_G(\Delta p_A) \tag{23.72}$$

$$N_A = K_G(\Delta p_A) \tag{23.73}$$

$$N_A = K_L(\Delta C_A) \tag{23.74}$$

It is not necessary to express the driving force for mass transfer in terms of either concentration difference (ΔC_A) or partial pressure difference (Δp_A). It is equally valid to express the driving force for mass transfer in terms of mole fraction difference. Consider mass transfer of solute A from gas phase to liquid phase, as shown in Figure 23.1. For the *gas phase*, one can express the molar flux as

$$N_A = k_y(y_{A,G} - y_{A,i}) \tag{23.75}$$

where $y_{A,G}$ is the mole fraction of A in the bulk gas phase, $y_{A,i}$ is the mole fraction of A in the gas phase at the interface, and k_y is the gas-phase mass transfer coefficient with mole fraction difference as the driving force. For the *liquid phase*, the molar flux can be expressed as

$$N_A = k_x(x_{A,i} - x_{A,L}) \tag{23.76}$$

where $x_{A,i}$ is the mole fraction of A in the liquid phase at the interface, $x_{A,L}$ is the mole fraction of A in the bulk liquid phase, and k_x is the liquid-phase mass transfer coefficient with mole fraction difference as the driving force.

In a similar manner, the overall mass transfer coefficients can be expressed in terms of mole fraction difference as the driving force. Thus,

$$N_A = K_y \left(y_{A,G} - y_A^* \right) \tag{23.77}$$

$$N_A = K_x \left(x_A^* - x_{A,L} \right) \tag{23.78}$$

where K_y and K_x are overall mass transfer coefficients based on gas phase and liquid phase, respectively with mole fraction difference as the driving force. $y_{A,G}$ is the mole fraction of A in the bulk gas phase and y_A^* is the mole fraction of A in the gas phase if gas phase was in equilibrium with the bulk liquid (having mole fraction of A as $x_{A,L}$). $x_{A,L}$ is the mole fraction of A in the bulk liquid phase and x_A^* is the mole fraction of A in the liquid phase if liquid phase was in equilibrium with the bulk gas (having mole fraction of A as $y_{A,G}$). It should be noted that mole fractions y_A^* and x_A^* are fictitious quantities evaluated from the equilibrium relationship.

23.4.3.1 Liquid-Phase Mass Transfer Coefficients (k_L and k_x)

The molar flux in the liquid phase is

$$N_A = k_L (C_{A,i} - C_{A,L}) = k_x (x_{A,i} - x_{A,L}) \tag{23.79}$$

As $C_A = x_A C$, where C is the total molar concentration of the liquid mixture, Equation 23.79 gives

$$k_L C (x_{A,i} - x_{A,L}) = k_x (x_{A,i} - x_{A,L}) \tag{23.80}$$

Thus,

$$k_x = k_L C \tag{23.81}$$

23.4.3.2 Gas-Phase Mass Transfer Coefficients (k_G and k_y)

The molar flux in the gas phase is

$$N_A = k_G (p_{A,G} - p_{A,i}) = k_y (y_{A,G} - y_{A,i}) \tag{23.82}$$

As $p_A = y_A p$, where p is the total pressure of the gas mixture, it follows that

$$k_G p (y_{A,G} - y_{A,i}) = k_y (y_{A,G} - y_{A,i}) \tag{23.83}$$

Thus,

$$k_y = k_G p \tag{23.84}$$

23.4.3.3 Overall Mass Transfer Coefficients Based on Liquid Phase (K_L and K_x)

The molar flux of species A from gas phase to liquid phase is given by

$$N_A = K_L(C_A^* - C_{A,L}) = K_x(x_A^* - x_{A,L}) \tag{23.85}$$

As $C_A = x_A C$, Equation 23.85 gives

$$K_L C(x_A^* - x_{A,L}) = K_x(x_A^* - x_{A,L}) \tag{23.86}$$

Thus,

$$K_x = K_L C \tag{23.87}$$

23.4.3.4 Overall Mass Transfer Coefficients Based on Gas Phase (K_G and K_y)

The molar flux of species A from gas phase to liquid phase is

$$N_A = K_G(p_{A,G} - p_A^*) = K_y(y_{A,G} - y_A^*) \tag{23.88}$$

As $p_A = y_A p$, where p is the total pressure of the gas mixture, it follows that

$$pK_G(y_{A,G} - y_A^*) = K_y(y_{A,G} - y_A^*) \tag{23.89}$$

Thus,

$$K_y = pK_G \tag{23.90}$$

23.4.3.5 Relationship between Overall Mass Transfer Coefficient K_x and Individual Mass Transfer Coefficients k_x and k_y

From Equation 23.85, one can write:

$$\frac{1}{K_x} = \frac{x_A^* - x_{A,L}}{N_A} = \frac{x_A^* - x_{A,i}}{N_A} + \frac{x_{A,i} - x_{A,L}}{N_A} \tag{23.91}$$

Assuming that the equilibrium relationship in terms of mole fractions is linear

$$y_A = m' x_A \tag{23.92}$$

where m′ is the equilibrium constant, one can rewrite Equation 23.91 as

$$\frac{1}{K_x} = \frac{y_{A,G} - y_{A,i}}{m'N_A} + \frac{1}{k_x} \tag{23.93}$$

This implies that

$$\frac{1}{K_x} = \frac{1}{k_x} + \frac{1}{m'k_y} \tag{23.94}$$

23.4.3.6 Relationship between Overall Mass Transfer Coefficient K_y and Individual Mass Transfer Coefficients k_x and k_y

From Equation 23.88, one can write:

$$\frac{1}{K_y} = \frac{y_{A,G} - y_A^*}{N_A} = \frac{y_{A,G} - y_{A,i}}{N_A} + \frac{y_{A,i} - y_A^*}{N_A} \tag{23.95}$$

Using the equilibrium relation (Equation 23.92), Equation 23.95 can be rewritten as

$$\frac{1}{K_y} = \frac{1}{k_y} + \frac{m'(x_{A,i} - x_{A,L})}{N_A} \tag{23.96}$$

This implies that

$$\frac{1}{K_y} = \frac{1}{k_y} + \frac{m'}{k_x} \tag{23.97}$$

REFERENCES

1. Bedingfield, H. and T.B. Drew. 1950. Analogy between heat transfer and mass transfer—A psychrometric study. *Ind. Eng. Chem*. 42: 1164–1173.
2. Linton, W.H. and T.K. Sherwood. 1950. Mass transfer from solid phase to water in streamline and turbulent flow. *Chem. Eng. Progress*. 46: 258–264.
3. Gilliland, E.R. and T.K. Sherwood. 1934. Diffusion of vapors into air streams. *Ind. Eng. Chem.* 26: 516–523.

SUPPLEMENTAL READING

Bird, R.B., W.E. Stewart, and E.N. Lightfoot. 2007. *Transport Phenomena*, 2nd Edition, New York: John Wiley & Sons.

Geankoplis, C.J. 1993. *Transport Processes and Unit Operations*, 3rd Edition, Englewood Cliffs, NJ: Prentice-Hall.

Greenkorn, R.A. and D.P. Kessler. 1972. *Transfer Operations*, New York: McGraw-Hill.

McCabe, W.L., J.C. Smith, and P. Harriott. 2005. *Unit Operations of Chemical Engineering*, 7th Edition, New York: McGraw-Hill.

Welty, J.R., C.E. Wicks, R.E. Wilson, and G.L. Rorrer. 2008. *Fundamentals of Momentum, Heat, and Mass Transfer*, 5th Edition, New York: John Wiley & Sons.

24 Convective Mass Transfer in Composite Materials

Mass transport of solute across a particulate-filled composite membrane usually involves convection at the boundaries. Convective mass transport of solute within a composite system between matrix fluid and particles, in the presence of relative motion between the matrix fluid and particles, is also not uncommon in practical applications.

24.1 MASS TRANSPORT ACROSS COMPOSITE MEMBRANE WITH CONVECTION AT BOUNDARIES

In this section, mass transport across porous composite membranes and dense particulate-filled composite membranes (also called mixed matrix membranes) is considered with convection at the boundaries of the membrane. The systems are generally assumed to be dilute so that the mass transfer coefficients are the same for coordinate systems both stationary and moving at the average molar velocity. The cases considered are as follows: (1) separation of solute from one gas phase to another using porous membrane, (2) separation of solute from aqueous phase to organic phase using *hydrophobic* porous membrane, (3) separation of solute from aqueous phase to organic phase using *hydrophilic* porous membrane, (4) separation of solute from one bulk phase to another using dense mixed-matrix membrane.

24.1.1 Porous Membranes

24.1.1.1 Separation of Gas Mixtures

Consider a flat sheet porous membrane separating *two gaseous bulk phases* and controlling the transfer of solute between them, as shown in Figure 24.1. The bulk gas phases on either side of the membrane are in motion relative to the membrane. Thus, we have convection at the boundaries of the membrane.

Let the concentration of the solute A be $C_{A,F}$ in the bulk feed stream, $C_{A,1}$ at the interface between the porous membrane and feed, $C_{A,2}$ at the interface between the porous membrane and product stream, and $C_{A,P}$ in the bulk product stream. Thus, there are three resistances to mass transport, namely, convective resistance on the feed side, diffusional resistance in the membrane, and convective resistance on the product side. As the three resistances are in series, one can write:

$$R_{total} = R_{feed\text{-}side} + R_{membrane} + R_{product\text{-}side}$$

$$R_{total} = \frac{1}{k_f A} + \frac{L}{DA} + \frac{1}{k_p A} \tag{24.1}$$

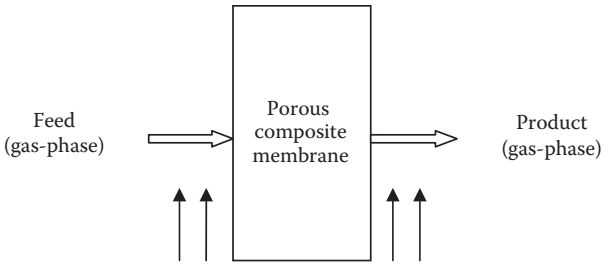

FIGURE 24.1 Separation of a gas mixture using a flat sheet porous membrane.

where k_f and k_p are the mass transfer coefficients on feed and product sides, D is effective diffusivity of solute in the porous membrane, L is the thickness of the membrane, and A is the area of mass transfer (membrane area normal to the direction of mass transport). R_{total} is related to the overall mass transfer coefficient K as follows:

$$\frac{1}{KA} = R_{total} = \frac{1}{k_f A} + \frac{L}{DA} + \frac{1}{k_p A} \tag{24.2}$$

Thus, the overall mass transfer coefficient K is as follows:

$$\frac{1}{K} = \frac{1}{k_f} + \frac{1}{D/L} + \frac{1}{k_p} \tag{24.3}$$

The individual mass transfer coefficients k_f and k_p can be estimated from the convective mass transfer correlations discussed in Chapter 23, and the effective diffusion coefficient D is given as

$$\frac{D}{D_o} = \frac{\varepsilon}{\tau} \tag{24.4}$$

where D_o is the diffusion coefficient of the same species in the absence of solid phase (that is, free-stream value), ε is the porosity, and τ is the tortuosity of porous material. Note that this expression of D assumes that the ratio of molecular size to pore size (λ) is very small. For nonzero values of λ, the diffusion is "hindered diffusion" and the expression of D modifies to [1]

$$\frac{D}{D_o} = \frac{\varepsilon}{\tau} f(\lambda) \tag{24.5}$$

where

$$f(\lambda) = (1 - \lambda)^2 (1 - 2.104\lambda + 2.09\lambda^3 - 0.95\lambda^5) \tag{24.6}$$

The flux of species A from the feed to the product side can be calculated from

$$N_A = K(C_{A,F} - C_{A,P}) \tag{24.7}$$

24.1.1.2 Separation of Liquid Mixtures

Now, consider the application of porous membranes for *liquid–liquid extraction*. The two bulk liquid phases are water and some organic liquid. The solute is present in the aqueous phase. Thus, solute needs to be transferred from the aqueous phase to the organic phase. Consider a flat sheet porous membrane of thickness L separating aqueous phase and organic liquid and controlling the transfer of solute between them. The bulk liquid phases on either side of the membrane are in motion relative to the membrane. Thus, we have convection at the boundaries of the membrane (see Figure 24.2).

The porous membrane material could be hydrophobic (such as Teflon or polypropylene) or hydrophilic (such as ceramics). Depending upon the hydrophobic–hydrophilic nature of the membrane material, the pores of the membrane could be filled with organic liquid or aqueous phase.

First, consider the membrane material to be *hydrophobic*. As the membrane is hydrophobic, the pores of the membrane would be filled with the organic liquid, and the liquid–liquid interface would exist at the pore mouths on the feed side of the membrane. Let the concentration of the solute be $C_{A,w}$ in the aqueous feed stream, $C^{i}_{A,w}$ at the interface between the porous membrane and feed on the aqueous side, $C^{m}_{A,I}$ at the interface between the porous membrane and feed on the organic phase side, $C^{m}_{A,2}$ at the interface between the porous membrane and product stream, and $C_{A,O}$ in the bulk organic phase. Note that there occurs a jump in solute concentration across the liquid–liquid interface on the feed side.

The molar flux of solute A can be expressed as

$$N_A = k_w\left(C_{A,w} - C^{i}_{A,w}\right) \tag{24.8}$$

$$N_A = \frac{D}{L}\left(C^{m}_{A,I} - C^{m}_{A,2}\right) \tag{24.9}$$

$$N_A = k_o\left(C^{m}_{A,2} - C_{A,O}\right) \tag{24.10}$$

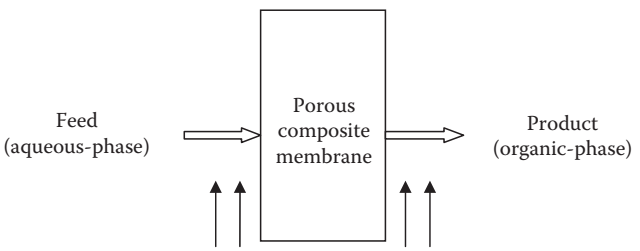

FIGURE 24.2 Separation of a liquid mixture using a flat sheet porous membrane.

where k_w and k_o are the mass transfer coefficients on the aqueous feed side and organic product side, respectively, and D is the effective diffusivity of solute in the porous membrane.

The overall mass transfer coefficient K_w based on aqueous phase could be defined as follows:

$$N_A = K_w\left(C_{A,w} - C^*_{A,w}\right) \tag{24.11}$$

where $C^*_{A,w}$ is the solute concentration in aqueous phase in equilibrium with the bulk organic phase with solute concentration of $C_{A,O}$. Note that $C^*_{A,w}$ is a fictitious quantity in that it does not exist in the system; it is determined from the following equilibrium relation:

$$C^e_{A,O} = f\left(C^e_{A,w}\right) = mC^e_{A,w} \tag{24.12}$$

where the superscript "e" refers to equilibrium condition and "m" is the distribution coefficient.

Equation 24.11 could be recast as

$$\frac{N_A}{K_w} = C_{A,w} - C^*_{A,w} = C_{A,w} - C^i_{A,w} + C^i_{A,w} - C^*_{A,w} \tag{24.13}$$

Upon substituting the following relations into Equation 24.13,

$$C^i_{A,w} = C^m_{A,l}/m \quad \text{and} \quad C^*_{A,w} = C_{A,O}/m \tag{24.14}$$

the following result is obtained:

$$\frac{N_A}{K_w} = C_{A,w} - C^*_{A,w} = C_{A,w} - C^i_{A,w} + \frac{C^m_{A,l}}{m} - \frac{C_{A,O}}{m} \tag{24.15}$$

Upon further rearrangement and using Equations 24.8 through 24.10,

$$\begin{aligned}\frac{N_A}{K_w} &= C_{A,w} - C^i_{A,w} + \frac{C^m_{A,1}}{m} - \frac{C^m_{A,2}}{m} + \frac{C^m_{A,2}}{m} - \frac{C_{A,O}}{m} \\ &= \frac{N_A}{k_w} + \frac{N_A}{m(D/L)} + \frac{N_A}{mk_o}\end{aligned} \tag{24.16}$$

Thus, the overall mass transfer coefficient K_w based on the aqueous phase is as follows:

$$\frac{1}{K_w} = \frac{1}{k_w} + \frac{1}{m}\left(\frac{1}{D/L} + \frac{1}{k_o}\right) \tag{24.17}$$

When the distribution coefficient "m" is large (low solubility of solute in aqueous phase), the system is water-controlled in that most of the resistance to mass transfer lies in the aqueous phase:

$$\frac{1}{K_w} \approx \frac{1}{k_w} \tag{24.18}$$

Now, we consider the case where the porous membrane is *hydrophilic* in nature. The pores of the hydrophilic membrane would be filled with the aqueous phase, and the liquid–liquid interface would exist at the pore mouths on the organic liquid (product) side of the membrane. Thus, there occurs a jump in solute concentration across the liquid–liquid interface on the product side.

Let the concentration of the solute (A) be $C_{A,w}$ in the aqueous feed stream, $C^m_{A,1}$ at the interface between the porous membrane and feed, $C^m_{A,2}$ at the interface between the porous membrane and product stream on the aqueous phase side, $C^i_{A,O}$ at the interface between the porous membrane and product stream on the organic phase side, and $C_{A,O}$ in the bulk organic phase.

The molar flux of solute A can be expressed as

$$N_A = k_w\left(C_{A,w} - C^m_{A,1}\right) \tag{24.19}$$

$$N_A = \frac{D}{L}\left(C^m_{A,1} - C^m_{A,2}\right) \tag{24.20}$$

$$N_A = k_o\left(C^i_{A,O} - C_{A,O}\right) \tag{24.21}$$

$$N_A = K_w\left(C_{A,w} - C^*_{A,w}\right) \tag{24.22}$$

Now, the overall mass transfer coefficient K_w based on the aqueous phase is as follows:

$$\frac{1}{K_w} = \frac{1}{k_w} + \frac{1}{mk_o} + \left(\frac{1}{D/L}\right) \tag{24.23}$$

When the distribution coefficient "m" is small ($m \ll 1$), that is, the solubility of solute in aqueous phase is large, the system is organic phase controlled in that most of the resistance to mass transfer lies in the organic phase:

$$\frac{1}{K_w} \approx \frac{1}{mk_o} \tag{24.24}$$

24.1.2 Dense Particulate Composite Membranes

Consider separation of solute from one liquid phase to another using a dense particulate composite membrane, as shown in Figure 24.3. Let the concentration of the solute A be $C_{A,F}$ in the liquid feed stream, $C^{i}_{A,F}$ at the interface between the composite membrane and feed on the feed side, $C^{m}_{A,F}$ at the interface between the membrane and feed on the membrane side, $C^{m}_{A,p}$ at the interface between the membrane and product stream on the membrane side, $C^{i}_{A,p}$ at the interface between the composite membrane and product stream on the product side, and $C_{A,p}$ in the bulk product stream. Note that there occurs a jump in solute concentration across the membrane–liquid interface on both the feed and product sides. The solute concentrations at the interface are related by the equilibrium distribution coefficient (m) as shown below:

$$m = \frac{C^{m}_{A,F}}{C^{i}_{A,F}} = \frac{C^{m}_{A,p}}{C^{i}_{A,p}} \tag{24.25}$$

Equation 24.25 assumes that the value of the distribution coefficient is the same on both sides of the membrane. The molar flux of solute A from the feed to the product stream can be expressed as

$$N_A = k_f\left(C_{A,F} - C^{i}_{A,F}\right) \tag{24.26}$$

$$N_A = \frac{D}{L}\left(C^{m}_{A,F} - C^{m}_{A,p}\right) = \frac{Dm}{L}\left(C^{i}_{A,F} - C^{i}_{A,p}\right) \tag{24.27}$$

$$N_A = k_p\left(C^{i}_{A,p} - C_{A,p}\right) \tag{24.28}$$

$$N_A = K(C_{A,F} - C_{A,p}) \tag{24.29}$$

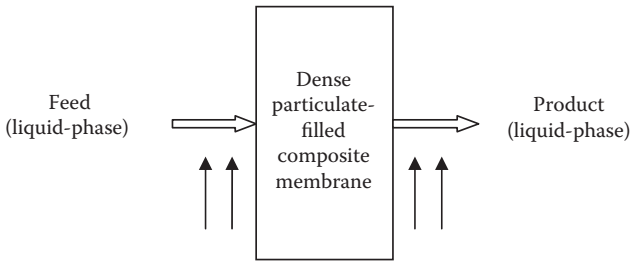

FIGURE 24.3 Separation of a liquid mixture using a dense particulate-filled composite membrane.

Using these relations, one can write

$$\frac{N_A}{K} = C_{A,F} - C_{A,p} = \left(C_{A,F} - C^i_{A,F}\right) + \left(C^i_{A,F} - C^i_{A,p}\right) + \left(C^i_{A,p} - C_{A,p}\right)$$
$$= \frac{N_A}{k_f} + \frac{N_A}{\left(\frac{mD}{L}\right)} + \frac{N_A}{k_p} \tag{24.30}$$

Thus, the overall mass transfer coefficient and molar flux can be expressed as follows:

$$\frac{1}{K} = \frac{1}{k_f} + \left(\frac{1}{mD/L}\right) + \frac{1}{k_p} \tag{24.31}$$

$$N_A = \frac{C_{A,F} - C_{A,p}}{\frac{1}{k_f} + \left(\frac{1}{mD/L}\right) + \frac{1}{k_p}} \tag{24.32}$$

where k_f and k_p are the mass transfer coefficients on the feed and product sides, D is the effective diffusivity of solute in the composite membrane, and L is the thickness of the membrane. The effective diffusivity of solute in the composite membrane can be estimated from the equations discussed in Chapter 22 (Section 22.1.1).

Dense composite membranes are also used widely for the separation of gas mixtures. Consider, for example, the separation of solute from one gas phase to another using a dense composite membrane, as shown in Figure 24.4. Let the partial pressure of the solute A be $p_{A,F}$ in the gaseous feed stream, $p^i_{A,F}$ at the interface between the composite membrane and feed on the feed side, $p^i_{A,p}$ at the interface between the composite membrane and product stream on the product side, and $p_{A,p}$ in the bulk product stream. The solute concentrations at the interface on the membrane side

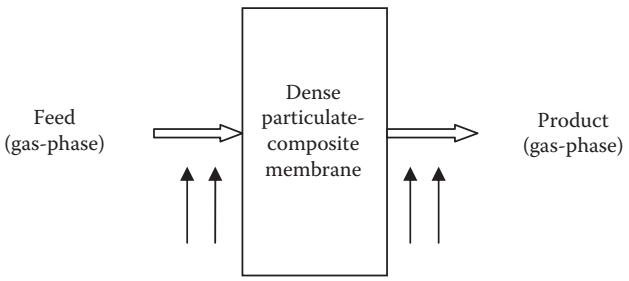

FIGURE 24.4 Separation of a gas mixture using a dense particulate-filled composite membrane.

are related to the partial pressures at the interface by the solubility of solute in the membrane (S) as

$$S = \frac{C^{m}_{A,F}}{p^{i}_{A,F}} = \frac{C^{m}_{A,p}}{p^{i}_{A,p}} \tag{24.33}$$

where $C^{m}_{A,F}$ is the solute concentration at the interface between the membrane and feed on the membrane side and $C^{m}_{A,p}$ is the solute concentration at the interface between the membrane and product stream on the membrane side.

The molar flux of solute A from the feed to the product stream can be expressed as

$$N_A = k_{G,f}\left(p_{A,F} - p^{i}_{A,F}\right) \tag{24.34}$$

$$N_A = \frac{D}{L}\left(C^{m}_{A,F} - C^{m}_{A,p}\right) = \frac{DS}{L}\left(p^{i}_{A,F} - p^{i}_{A,p}\right) \tag{24.35}$$

$$N_A = k_{G,p}\left(p^{i}_{A,p} - p_{A,p}\right) \tag{24.36}$$

$$N_A = K_G(p_{A,F} - p_{A,p}) \tag{24.37}$$

Using these relations, one can write

$$\begin{aligned}\frac{N_A}{K_G} &= p_{A,F} - p_{A,p} = \left(p_{A,F} - p^{i}_{A,F}\right) + \left(p^{i}_{A,F} - p^{i}_{A,p}\right) + \left(p^{i}_{A,p} - p_{A,p}\right) \\ &= \frac{N_A}{k_{G,f}} + \frac{N_A}{\left(\frac{DS}{L}\right)} + \frac{N_A}{k_{G,p}}\end{aligned} \tag{24.38}$$

Thus, the overall mass transfer coefficient and molar flux can be expressed as follows:

$$\frac{1}{K_G} = \frac{1}{k_{G,f}} + \left(\frac{1}{DS/L}\right) + \frac{1}{k_{G,p}} \tag{24.39}$$

$$N_A = \frac{p_{A,F} - p_{A,p}}{\frac{1}{k_{G,f}} + \left(\frac{1}{DS/L}\right) + \frac{1}{k_{G,p}}} \tag{24.40}$$

Another important membrane separation process where dense composite membranes (such as mixed matrix membranes) are utilized is *pervaporation*.

Pervaporation is a membrane separation process where one or more components of a liquid mixture diffuse through a dense membrane, vaporize due to low pressure maintained by a vacuum pump on the downstream side, and are removed by condensation. The driving force for mass transfer in the pervaporation process is the difference in partial pressures (more precisely, the difference in chemical potentials) of the permeants across the membrane. The partial pressure difference across the membrane is created by reducing the total pressure on the product side of the membrane using a vacuum pump. Pervaporation is widely used in dehydration of organic liquids, removal of organic compounds from water, and separation of organic mixtures.

Consider pervaporation separation of species A from a mixture using a dense composite membrane (polymeric membrane filled with particles). The feed is in liquid state and the product (permeate) is removed in a vapor state, as shown in Figure 24.5. Let the concentration of the solute be $C_{A,F}$ in the liquid feed stream, $C^{i}_{A,F}$ at the interface between the composite membrane and feed on the feed side, $C^{m}_{A,F}$ at the interface between the membrane and feed on the membrane side, and $C^{m}_{A,p}$ at the interface between the membrane and product stream on the membrane side. Let $p^{i}_{A,F}$ be the partial pressure of solute at the interface between the composite membrane and feed on the feed side, and $p_{A,p}$ be the partial pressure of solute on the vapor side. Let $x_{A,F}$ and $y_{A,p}$ be the mole fractions of solute in the bulk feed and permeate vapor. The resistance to mass transfer is assumed to be negligible on the vapor side.

The molar flux of solute A within the membrane can be expressed as

$$N_A = \frac{D}{L}\left(C^{m}_{A,F} - C^{m}_{A,p}\right) = \frac{DS}{L}\left(p^{i}_{A,F} - p_{A,p}\right) = \frac{P}{L}\left(p^{i}_{A,F} - p_{A,p}\right) \tag{24.41}$$

where S is the solubility of solute A in the membrane and P is the permeability of A in the membrane. The partial pressure of solute $p^{i}_{A,F}$ at the interface between the composite membrane and feed on the feed side can be expressed in terms of the activity coefficient as follows:

$$p^{i}_{A,F} = x^{i}_{A,F}\gamma_A p^{o}_{A} \tag{24.42}$$

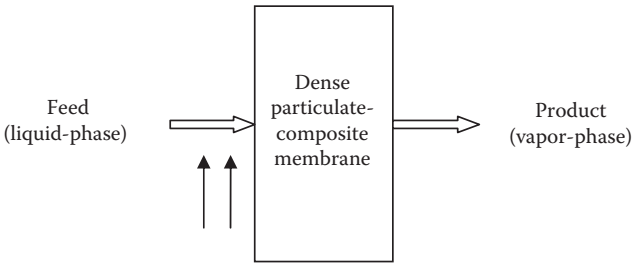

FIGURE 24.5 Pervaporation separation of a mixture using a dense polymeric membrane filled with particles.

where $x^{i}_{A,F}$ is the mole fraction of solute at the interface between the composite membrane and feed on the feed side, γ_A is the activity coefficient of A in the liquid solution, and p^{o}_{A} is the vapor pressure of pure A. Thus, the flux N_A could be written as

$$N_A = \frac{P}{L}\left(x^{i}_{A,F}\gamma_A p^{o}_{A} - p_{A,p}\right) \tag{24.43}$$

Using Henry's law,

$$p_A = x_A H_A = x_A \gamma_A p^{o}_{A} \tag{24.44}$$

one can recast the flux expression Equation 24.43 as follows:

$$N_A = \frac{P}{L}\left(x^{i}_{A,F}H_A - p_{A,p}\right) = \frac{PH_A}{L}\left(x^{i}_{A,F} - \frac{p_{A,p}}{H_A}\right) \tag{24.45}$$

If we define the mass transfer coefficient for the membrane as

$$k^{m}_{x} = \frac{PH_A}{L} \tag{24.46}$$

the flux can be expressed as

$$N_A = k^{m}_{x}\left(x^{i}_{A,F} - \frac{p_{A,p}}{H_A}\right) \tag{24.47}$$

The flux could also be expressed in terms of the overall permeability (P_o) and overall mass transfer coefficient (K_x) as follows [2]:

$$N_A = \frac{P_o}{L}\left(x_{A,F}\gamma_A p^{o}_{A} - p_{A,p}\right) = \frac{P_o H_A}{L}\left(x_{A,F} - \frac{p_{A,p}}{H_A}\right) = K_x\left(x_{A,F} - \frac{p_{A,p}}{H_A}\right) \tag{24.48}$$

Note that the overall mass transfer coefficient (K_x) and overall permeability (P_o) are related to each other as follows:

$$K_x = \frac{P_o H_A}{L} \tag{24.49}$$

The overall mass transfer coefficient can be related to the individual mass transfer coefficients by noting that

$$N_A = k^{F}_{x}\left(x_{A,F} - x^{i}_{A,F}\right) \tag{24.50}$$

and

$$\frac{N_A}{K_x} = x_{A,F} - \frac{p_{A,p}}{H_A} = x^i_{A,F} - \frac{p_{A,p}}{H_A} + x_{A,F} - x^i_{A,F} = \frac{N_A}{k^m_x} + \frac{N_A}{k^F_x} \tag{24.51}$$

Thus,

$$\frac{1}{K_x} = \frac{1}{k^m_x} + \frac{1}{k^F_x} \tag{24.52}$$

24.2 CONVECTIVE MASS TRANSFER WITHIN COMPOSITE MATERIALS

Now, consider convective mass transport of solute within a composite system, between matrix fluid and particles, in the presence of relative motion between the matrix fluid and particles. Both single-particle and multiple-particle (packed bed) systems are considered. Interphase mass transfer between two immiscible fluids moving through a packed bed of inert particles is also discussed.

24.2.1 Convective Mass Transfer from Single Particle

The Sherwood number (Sh) for forced convective mass transfer from a particle is a function of particle Reynolds number (Re) and Schmidt number (Sc). The general form of the Sherwood number relation for a single-particle system is as follows:

$$Sh = \frac{k_c D_p}{D_{AB}} = Sh_0 + C\,Re^m\,Sc^n \tag{24.53}$$

where k_c is the mass transfer coefficient, D_p is the particle diameter, D_{AB} is the diffusion coefficient, and C, m, and n are constants. Sh_0 is the Sherwood number in the limit $Re \to 0$, corresponding to diffusion from a particle in an infinite stationary fluid. For a solid spherical particle, Sh_0 is 2. Note that the particle Reynolds number is defined as $\rho D_p V_\infty/\eta$, where V_∞ is the free-stream velocity of fluid, and ρ and η are the fluid density and viscosity, respectively.

Froessling [3] proposed the following relationship for mass transfer from a solid spherical particle:

$$Sh = \frac{k_c D_p}{D_{AB}} = 2 + 0.552\,Re^{\frac{1}{2}}\,Sc^{\frac{1}{3}} \tag{24.54}$$

This equation correlates the data well for mass transfer from a spherical particle into gases with $2 < Re < 800$ and $0.6 < Sc < 2.7$.

For higher Re (1500 < Re < 12,000) and 0.6 < Sc < 1.85), Steinberger and Treybal [4] proposed the modification of the Froessling equation as

$$\mathrm{Sh} = \frac{k_c D_p}{D_{AB}} = 2 + 0.552\,\mathrm{Re}^{0.53}\,\mathrm{Sc}^{\frac{1}{3}} \tag{24.55}$$

McCabe et al. [1] recommend a slightly modified version of the Froessling equation for Re up to 1000.

$$\mathrm{Sh} = \frac{k_c D_p}{D_{AB}} = 2 + 0.6\,\mathrm{Re}^{\frac{1}{2}}\,\mathrm{Sc}^{\frac{1}{3}} \tag{24.56}$$

This equation is probably less restrictive on Sc and could be applied to liquid flow around the particle. However, for creeping flows (Re $\ll$ 1) with high Peclet number (Pe = ReSc), this equation tends to underpredict the values of the Sherwood number. In such situations, the following equation is recommended:

$$\mathrm{Sh} = \frac{k_c D_p}{D_{AB}} = \left(4.0 + 1.21\mathrm{Pe}^{\frac{2}{3}}\right)^{\frac{1}{2}} \tag{24.57}$$

This equation could be applied for Pe up to as high as 10,000. For Pe > 10,000, the following Levich equation [5] could be used:

$$\mathrm{Sh} = \frac{k_c D_p}{D_{AB}} = 1.01\left(\mathrm{Re}\,\mathrm{Sc}\right)^{\frac{1}{3}} \tag{24.58}$$

So far, mass transfer from a solid spherical particle is considered. For bubble or droplets, the mass transfer rates are somewhat higher due to internal circulation effect. Assuming that no surfactants or impurities are present at the surface of bubbles or droplets, transmission of tangential stresses occur from the external matrix fluid to internal fluid of droplets and bubbles. The transmission of stresses causes internal circulation within the droplets/bubbles. The internal circulation, in turn, enhances the mass transfer rate. McCabe et al. [1] recommend the following correlation for the estimation of mass transfer coefficient in the presence of internal circulation effect:

$$\mathrm{Sh} = \frac{k_c D_p}{D_{AB}} = 1.13\,\mathrm{Re}^{\frac{1}{2}}\,\mathrm{Sc}^{\frac{1}{2}} \tag{24.59}$$

This equation should be modified to the following form in order to take into account diffusion from a droplet/particle under no-flow condition:

$$\mathrm{Sh} = \frac{k_c D_p}{D_{AB}} = 2.0 + 1.13\,\mathrm{Re}^{\frac{1}{2}}\,\mathrm{Sc}^{\frac{1}{2}} \tag{24.60}$$

In the equations discussed thus far, *natural convection* is assumed to be absent. If natural convection is present along with forced convection, the mass transfer correlation can be expressed in the following form [4]:

$$\mathrm{Sh} = \frac{k_c D_p}{D_{AB}} = \mathrm{Sh}_{nc} + C\,\mathrm{Re}^m\,\mathrm{Sc}^n \tag{24.61}$$

where Sh_{nc} is the contribution of natural convection and the second term is the contribution from forced convection. For flow around a solid sphere, the correlation proposed by Steinberger and Treybal [4] is as follows:

$$\mathrm{Sh} = \frac{k_c D_p}{D_{AB}} = \mathrm{Sh}_{nc} + 0.347\,\mathrm{Re}^{0.62}\,\mathrm{Sc}^{\frac{1}{3}} \tag{24.62}$$

This correlation is valid over $1 < \mathrm{Re} < 30{,}000$ and $0.6 < \mathrm{Sc} < 3200$ with natural convection contribution Sh_{nc} as follows:

$$\mathrm{Sh}_{nc} = 2.0 + 0.0254\ (\mathrm{GrSc})^{\frac{1}{3}}\ \mathrm{Sc}^{0.244}\ \text{for}\ \mathrm{GrSc} > 10^8 \tag{24.63}$$

$$\mathrm{Sh}_{nc} = 2.0 + 0.569\ (\mathrm{GrSc})^{\frac{1}{4}}\ \text{for}\ \mathrm{GrSc} < 10^8 \tag{24.64}$$

where Gr is the Grashof number based on the particle diameter. The natural convection term becomes negligible at high Re.

24.2.2 Convective Mass Transfer in Packed Bed of Particles

Packed beds are widely used in industrial mass transfer operations as they provide a large mass transfer area (total surface area of particles). A number of experimental studies have been carried out to measure and correlate mass transfer coefficients in packed beds. Only a sample of the mass transfer coefficient correlations proposed in the literature is discussed here. Gupta and Thodos [6] proposed the following correlation for mass transfer between packed bed particles (spherical) and fluid (gas or liquid) moving through the bed:

$$j_M = \mathrm{StSc}^{\frac{2}{3}} = \frac{k_c}{V_s}\mathrm{Sc}^{\frac{2}{3}} = \frac{0.010}{\varepsilon} + \frac{0.863/\varepsilon}{\mathrm{Re}^{0.58} - 0.483} \tag{24.65}$$

where j_M is the Colburn factor for mass transfer, St is the Stanton number for mass transfer defined as Sh/(ReSc), V_s is the superficial velocity of fluid, ε is the bed void fraction, and Re is the particle Reynolds number defined as $\rho D_p V_s/\eta$. This correlation is valid for $1 < \mathrm{Re} < 2100$.

Sherwood et al. [7] proposed the following correlation for mass transfer between packed bed particles and gas moving through the bed under the condition $10 < \mathrm{Re} < 2500$:

$$j_M = StSc^{\frac{2}{3}} = \frac{k_c}{V_s} Sc^{\frac{2}{3}} = 1.17 Re^{0.585} Sc^{\frac{1}{3}} \tag{24.66}$$

This equation is recommended for packed beds of spherical particles with ε of about 0.40 to 0.45. It is interesting to note that the mass transfer coefficients predicted from this equation are about 2 to 3 times those for a single spherical particle when comparison is made at the same particle Reynolds number Re. One reason for this enhancement of mass transfer in comparison with a single particle is the high interstitial velocity in the bed for a given superficial velocity.

Equation 24.66 does not take into account the bed void fraction. Thus, it is applicable over a limited range of ε (about 0.40 to 0.45). Another useful empirical correlation that does take into account the bed porosity is due to Wilson and Geankoplis [8] given below:

$$j_M = StSc^{\frac{2}{3}} = \frac{k_c}{V_s} Sc^{\frac{2}{3}} = \frac{1.09}{\varepsilon} Re^{\frac{1}{3}} Sc^{\frac{1}{3}} \tag{24.67}$$

This equation is based on flow of liquids through a packed bed of spherical particles. It covers the following ranges of Re, Sc, and bed porosity ε: $0.0016 < Re < 55$, $165 < Sc < 70{,}600$, and $0.35 < \varepsilon < 0.75$.

24.2.3 Interphase Mass Transfer in Packed Bed of Inert Particles

Packed columns of inert packing material are frequently used for interphase mass transfer applications. As there are no physically distinguishable stages present in the column, the packed columns are also referred to as "continuous contacting devices." The two immiscible phases (liquid–gas and liquid–liquid) usually flow in a countercurrent manner. For example, the liquid is fed at the top of the column and gas enters the packed column at the bottom. The role of the packing material is to promote a large area of contact between the two phases with a minimum resistance to the flow of phases.

The design of the packed columns involves the specification of the column height and diameter. The height (h) of the column can be determined from the following relation:

$$h = n_{OG} H_{OG} \tag{24.68}$$

where n_{OG} is the number of overall gas transfer units and H_{OG} is the height of the overall gas transfer unit. The number of overall gas transfer units depends on the change in gas composition from one end of column to the other and the average driving force for mass transfer. The height of the overall gas transfer unit depends on the gas molar flow rate per unit area and the overall mass transfer capacity coefficient.

The diameter of the column is selected on the basis of the *flooding* characteristics of the column. The column diameter is chosen such that the mass velocity of the gas phase in the column is well below the flooding mass velocity. Typically,

$$G_{actual} = 0.5 G_{flooding} \tag{24.69}$$

where G is the mass velocity with S.I. units of $kg/s.m^2$.

As an example, consider the counter-current absorption process in a packed column where some solute A present in the gas phase is being transferred to the liquid phase. Let the molar flow rates of liquid and gas phases be L_m and V_m, respectively. Assuming low mass transfer rate with small concentration of diffusing species A, the molar flow rates of gas and liquid phases in the column can be regarded as constant. At the top of the column, let the mole fractions of solute in the liquid and gas phases be x_a and y_a, respectively. At the bottom of the column, the mole fractions of solute in the liquid and gas phases be x_b and y_b, respectively (see Figure 24.6).

The material balance for solute A on the gas phase over a section Δz of the column, under steady-state condition, gives

$$V_m y\Big|_z - V_m y\Big|_{z+\Delta z} - N_A a(S dz) = 0 \tag{24.70}$$

where N_A is the molar flux of A from gas phase to liquid phase, "a" is the interfacial area (contact area between the gas and liquid phases) per unit volume of the column, and S is the cross-sectional area of the column. Rearranging Equation 24.70 and taking the limit $\Delta z \to 0$ give

$$-\frac{d(V_m y)}{dz} = N_A aS \tag{24.71}$$

Since V_m is constant under the assumption of dilute system:

$$-\frac{dy}{dz} = \frac{N_A aS}{V_m} \tag{24.72}$$

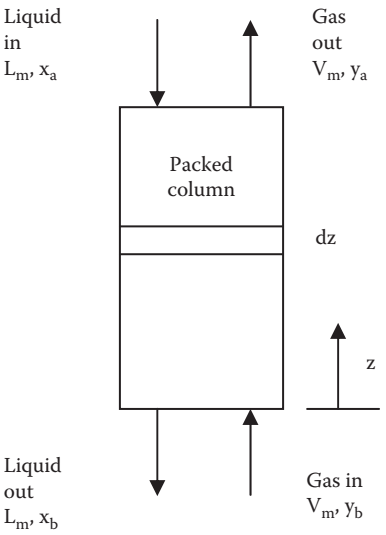

FIGURE 24.6 Counter-current absorption in a packed column.

The molar flux of A from gas phase to liquid phase at any location in the column can be expressed as

$$N_A = k_y(y - y_i) \tag{24.73}$$

where k_y is the gas phase mass transfer coefficient, y is the mole fraction of solute in the bulk gas phase at the given location in the column, and y_i is the mole fraction of solute at the interface on the gas side. From Equations 24.72 and 24.73, the height of the packed column is determined as follows:

$$h = \int_0^h dz = -\left(\frac{V_m/S}{k_y a}\right)\int_{y_b}^{y_a} \frac{dy}{y - y_i} \tag{24.74}$$

This equation could be recast as

$$h = n_G H_G \tag{24.75}$$

where n_G is the number of gas transfer units and H_G is the height of the gas transfer unit defined as

$$n_G = \int_{y_a}^{y_b} \frac{dy}{y - y_i}, \quad H_G = \frac{V_m/S}{k_y a} \tag{24.76}$$

Instead of considering material balance on the gas phase as done in the preceding analysis, it is equally appropriate to consider material balance on the liquid phase over a section Δz of the column. Thus, material balance for solute A on the liquid phase, under steady-state condition, gives

$$L_m x\Big|_{z+\Delta z} - L_m x\Big|_z + N_A a(Sdz) = 0 \tag{24.77}$$

Rearranging Equation 24.77 and taking the limit $\Delta z \to 0$,

$$-\frac{d(L_m x)}{dz} = N_A aS \tag{24.78}$$

Since L_m is constant under the assumption of dilute system,

$$-\frac{dx}{dz} = \frac{N_A aS}{L_m} \tag{24.79}$$

The molar flux of A from gas phase to liquid phase at any location in the column can be expressed as

$$N_A = k_x(x_i - x) \tag{24.80}$$

where k_x is the liquid phase mass transfer coefficient, x is the mole fraction of solute in the bulk liquid phase at the given location in the column, and x_i is the mole fraction of solute at the interface on the liquid side. From Equations 24.79 and 24.80, the height of the packed column is determined as follows:

$$h = \int_0^h dz = -\left(\frac{L_m/S}{k_x a}\right)\int_{x_b}^{x_a} \frac{dx}{x_i - x} \tag{24.81}$$

This equation could be recast as

$$h = n_L H_L \tag{24.82}$$

where n_L is the number of liquid transfer units and H_L is the height of the liquid transfer unit defined as

$$n_L = \int_{x_a}^{x_b} \frac{dx}{x_i - x}, \quad H_L = \frac{L_m/S}{k_x a} \tag{24.83}$$

In Equations 24.73 and 24.80, the molar flux of solute A was expressed in terms of the individual mass transfer coefficients. It is equally appropriate to use overall mass transfer coefficients to express N_A. When N_A is written as

$$N_A = K_y(y - y^*) \tag{24.84}$$

where K_y is the overall mass transfer coefficient based on the gas phase and y* is the mole fraction of solute in the gas phase in equilibrium with the liquid present in the column, the bed height can be expressed as

$$h = \int_0^h dz = -\left(\frac{V_m/S}{K_y a}\right)\int_{y_b}^{y_a} \frac{dy}{y - y^*} \tag{24.85}$$

From Equations 24.68 and 24.85,

$$n_{OG} = \int_{y_a}^{y_b} \frac{dy}{y - y^*}, \quad H_{OG} = \frac{V_m/S}{K_y a} \tag{24.86}$$

When N_A is written in terms of the overall mass transfer coefficient based on the liquid phase as follows:

$$N_A = K_x(x^* - x) \tag{24.87}$$

where x* is the mole fraction of solute in the liquid phase in equilibrium with the gas present in the column, the bed height can be expressed as

$$h = \int_0^h dz = -\left(\frac{L_m/S}{K_x a}\right)\int_{x_b}^{x_a} \frac{dx}{x^* - x} \tag{24.88}$$

This equation could be recast as

$$h = n_{OL}H_{OL} \tag{24.89}$$

where n_{OL} is the number of overall liquid transfer units and H_{OL} is the height of the overall liquid transfer unit defined as

$$n_{OL} = \int_{x_a}^{x_b} \frac{dx}{x^* - x}, \quad H_{OL} = \frac{L_m/S}{K_x a} \tag{24.90}$$

Table 24.1 summarizes the various expressions for the calculation of the bed height. It should be noted that various heights of the transfer units (H_G, H_L, H_{OG}, and H_{OL}) are interrelated, and their relation follows from the relationship between the

TABLE 24.1
Summary of Various Expressions for Calculation of Bed Height

Expressions for Bed Height (h)	Expressions for Number of Transfer Units (n_G, n_L, n_{OG}, and n_{OL})	Expressions for Height of Transfer Unit (H_G, H_L, H_{OG}, and H_{OL})
$h = n_G H_G$	$n_G = \int_{y_a}^{y_b} \frac{dy}{y - y_i}$	$H_G = \frac{V_m/S}{k_y a}$
$h = n_L H_L$	$n_L = \int_{x_a}^{x_b} \frac{dx}{x_i - x}$	$H_L = \frac{L_m/S}{k_x a}$
$h = n_{OG} H_{OG}$	$n_{OG} = \int_{y_a}^{y_b} \frac{dy}{y - y^*}$	$H_{OG} = \frac{V_m/S}{K_y a}$
$h = n_{OL} H_{OL}$	$n_{OL} = \int_{x_a}^{x_b} \frac{dx}{x^* - x}$	$H_{OL} = \frac{L_m/S}{K_x a}$

overall capacity coefficient $K_y a$ and individual mass transfer capacity coefficients $k_y a$ and $k_x a$:

$$\frac{1}{K_y a} = \frac{1}{k_y a} + \frac{m}{k_x a} \tag{24.91}$$

where m is the slope of the equilibrium curve. Since

$$k_y a = \frac{V_m/S}{H_G}, \quad k_x a = \frac{L_m/S}{H_L}, \quad K_y a = \frac{V_m/S}{H_{OG}} \tag{24.92}$$

it follows that

$$H_{OG} = H_G + \left(\frac{m}{L_m/V_m}\right) H_L \tag{24.93}$$

In a similar manner, one can show that

$$H_{OL} = H_L + \left(\frac{L_m/V_m}{m}\right) H_G \tag{24.94}$$

Equation 24.94 follows from the relationship between the overall capacity coefficient $K_x a$ and individual mass transfer capacity coefficients $k_y a$ and $k_x a$ given below:

$$\frac{1}{K_x a} = \frac{1}{k_x a} + \frac{1}{m k_y a} \tag{24.95}$$

Also note that

$$H_{OL} = \left(\frac{L_m/V_m}{m}\right) H_{OG} \tag{24.96}$$

This follows from Equations 24.93 and 24.94.

Although all the expressions for the calculation of bed height are equivalent, it is more convenient to use Equations 24.68 and 24.86 for the estimation of the bed height. Thus,

$$h = n_{OG} H_{OG} \tag{24.68}$$

$$n_{OG} = \int_{y_a}^{y_b} \frac{dy}{y - y^*}, \quad H_{OG} = \frac{V_m/S}{K_y a} \tag{24.86}$$

The height of the overall gas transfer unit H_{OG} can be evaluated from the knowledge of gas phase molar flow per unit area (V_m/S) and overall mass transfer capacity coefficient $K_y a$. The number of the overall gas transfer units n_{OG} requires the evaluation of the integral (see Equation 24.86). To that end, we need an equation for the operating line of the absorber. Consider the material balance for solute A over the bottom portion of the column from z = 0 to z = z:

$$y_b V_m + xL_m = yV_m + x_b L_m \tag{24.97}$$

where x and y are mole fractions of solute in the liquid and gas phases, respectively, at any location z in the column. Upon rearrangement of Equation 24.97, the following equation is obtained for the operating line:

$$y = y_b + \left(\frac{L_m}{V_m}\right)(x - x_b) \tag{24.98}$$

The operating line relates the compositions of the passing gas and liquid streams at any location z in the column.

Figure 24.7 shows the plots of operating line and equilibrium relation schematically. The driving force for mass transfer y – y* is the vertical distance between the equilibrium line and the operating line. The driving force y – y* varies with y. Thus, one can obtain graphically the values of the driving force y – y* as a function of y.

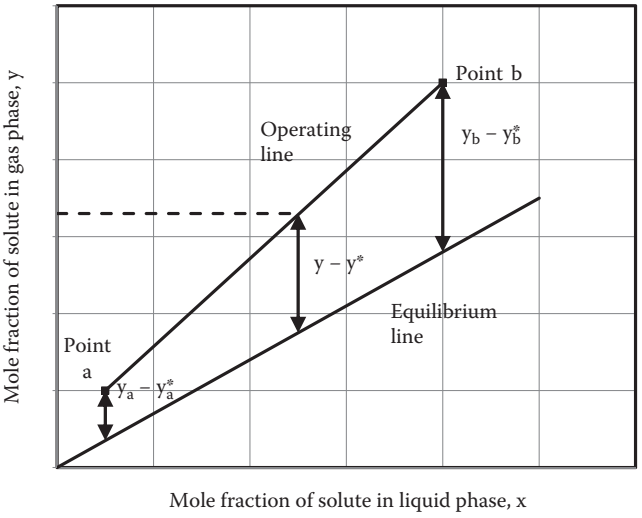

FIGURE 24.7 Schematic plots of the operating line and equilibrium relation in a counter–current absorption process.

The values are plotted as $1/(y - y^*)$ versus y and the area under the curve over the y-range of y_a to y_b gives the number of overall gas transfer units, n_{OG}. This graphical procedure for estimating n_{OG} is applicable even when the equilibrium relation is nonlinear. However, n_{OG} is given by the following expression when the operating and equilibrium lines are linear:

$$n_{OG} = \int_{y_a}^{y_b} \frac{dy}{y - y^*} = \frac{y_b - y_a}{(y - y^*)_{log-mean}} \tag{24.99}$$

where

$$(y - y^*)_{log-mean} = \frac{\left(y_b - y_b^*\right) - \left(y_a - y_a^*\right)}{\ln\left(\frac{y_b - y_b^*}{y_a - y_a^*}\right)} \tag{24.100}$$

In the special case of the operating and equilibrium lines being linear and parallel, n_{OG} is given as

$$n_{OG} = \frac{y_b - y_a}{\left(y_a - y_a^*\right)} = \frac{y_b - y_a}{\left(y_b - y_b^*\right)} \tag{24.101}$$

REFERENCES

1. McCabe, W.L., J.C. Smith, and P. Harriott. 2005. *Unit Operations of Chemical Engineering*, 7th Edition, New York: McGraw-Hill.
2. Satyanarayana, S.V., A. Sharma, and P.K. Bhattacharya. 2004. Composite membranes for hydrophobic pervaporation: Study with the toluene-water system. *Chem. Eng. J*. 102: 171–184.
3. Froessling, N. 1938. Über die Verdunstung fallender Tropfen. *Gerlands Beitr. Zur Geophyik*. 52: 170–216.
4. Steinberger, R.L. and R.E. Treybal. 1960. Mass transfer from a solid soluble sphere to a flowing liquid stream. *AIChE J.* 6: 227–232.
5. Levich, V.G. 1962. *Physicochemical Hydrodynamics*, Englewood Cliffs, NJ: Prentice-Hall.
6. Gupta, A.S. and G. Thodos. 1962. Mass and heat transfer in the flow of fluids through fixed and fluidized beds of spherical particles. *AIChE J.* 8: 608–610.
7. Sherwood, T.K., R.L. Pigford, and C.R. Wilke. 1975. *Mass Transfer*, New York: McGraw-Hill.
8. Wilson, E.J. and C.J. Geankoplis. 1966. Liquid mass transfer at very low Reynolds numbers in packed beds. *Ind. Eng. Chem. Fundamentals*. 5: 9–14.

SUPPLEMENTAL READING

Bird, R.B., W.E. Stewart, and E.N. Lightfoot. 2007. *Transport Phenomena*, 2nd Edition, New York: John Wiley & Sons.

Geankoplis, C.J. 1993. *Transport Processes and Unit Operations*, 3rd Edition, Englewood Cliffs, NJ: Prentice-Hall.

Greenkorn, R.A. and D.P. Kessler. 1972. *Transfer Operations*, New York: McGraw-Hill.

Wankat, P.C. 1988. *Equilibrium-Staged Separations*, Englewood Cliffs, NJ: Prentice-Hall.

Welty, J.R., C.E. Wicks, R.E. Wilson, and G.L. Rorrer. 2008. *Fundamentals of Momentum, Heat, and Mass Transfer*, 5th Edition, New York: John Wiley & Sons.

MATERIALS SCIENCE & ENGINEERING

In the design, processing, and applications of composite materials, a thorough understanding of the physical properties is required. It is important to be able to predict the variations of these properties with the kind, shape, and concentration of filler materials. The currently available books on composite materials often emphasize mechanical properties and focus on classification, applications, and manufacturing. This limited coverage neglects areas that are important to new and emerging applications.

For the first time in a single source, this volume provides a systematic, comprehensive, and up-to-date exploration of the electromagnetic (electrical, dielectric, and magnetic), mechanical, thermal, and mass-transport properties of composite materials. The author begins with a brief discussion of the relevance of these properties for designing new materials to meet specific practical requirements. The book is then organized into five parts examining:

- **The electromagnetic properties of composite materials subjected to time-invariant electric and magnetic fields**
- **The dynamic electromagnetic properties of composite materials subjected to time-varying electric and magnetic fields**
- **The mechanical elastic and viscoelastic properties of composites**
- **Heat transfer in composites and thermal properties (thermal conductivity, thermal diffusivity, coefficient of thermal expansion, and thermal emissivity)**
- **Mass transfer in composite membranes and composite materials**

Throughout the book, the analogy between various properties is emphasized. *Electromagnetic, Mechanical, and Transport Properties of Composite Materials* provides both an introduction to the subject for newcomers and sufficient in-depth coverage for those involved in research. Scientists, engineers, and students from a broad range of fields will find this book a comprehensive source of information.

CRC Press
Taylor & Francis Group
an **informa** business
www.crcpress.com

6000 Broken Sound Parkway, NW
Suite 300, Boca Raton, FL 33487
711 Third Avenue
New York, NY 10017
2 Park Square, Milton Park
Abingdon, Oxon OX14 4RN, UK

89218
ISBN: 978-1-4200-8921-9
90000
9 781420 089219